5-2014

Global Dynamic Characterization and Load Rating of Bridge Structures Utilizing Economical Dynamic Excitation Devices

Eric Fernstrom
University of Arkansas, Fayetteville

Global Dynamic Characterization and Load Rating of Bridge Structures Utilizing Economical Dynamic Excitation Devices

Global Dynamic Characterization and Load Rating of Bridge Structures Utilizing Economical Dynamic Excitation Devices

A dissertation submitted in partial fulfillment
of the requirements for the degree of
Doctor of Philosophy in Engineering

by

Eric Victor Fernstrom
Bucknell University
Bachelor of Science in Civil Engineering, 1997
Rutgers University
Master of Science in Civil Engineering, 2004

May 2014
University of Arkansas

This dissertation is approved for recommendation to the Graduate Council.

_____
Dr. Kirk Grimmelsman
Dissertation Director

_____
Dr. Ernest Heymsfield
Committee Member

_____
Dr. Mark Arnold
Committee Member

_____
Dr. R. Panneer Selvam
Committee Member

ABSTRACT

Experimental modal analysis (EMA) of bridges and other civil structures can be used to acquire quantitative data describing their condition, and enhance opportunities for structural health monitoring and related fields. The use of EMA on civil structures has been limited by the high cost of the excitation devices that are required for the best data quality. The objective of the research reported herein is to evaluate a low-cost excitation system for multiple-input, multiple-output (MIMO) EMA, enabling the production of accurate estimates of the global behavior of in-service bridges.

The prototype excitation system is composed of consumer entertainment devices, namely tactile transducers and subwoofer amplifiers, which are capable of providing excitation in the range of 5 Hz to 200 Hz. The use of these devices in vibration testing is unprecedented, and their low cost allows approximately 30 structural degrees-of-freedom to be excited for the price of a single purpose-built laboratory shaker device. Methods are developed to systematically characterize the operational performance of the devices. Research and testing are also performed to optimize the techniques by which the system can be used for MIMO EMA of bridges.

The excitation system is then validated for MIMO EMA by dynamically characterizing a large-scale laboratory structure and comparing the results to those from traditional excitation methods. The system is then deployed on an in-service highway bridge, representing the first time that more than two shakers have been used in MIMO EMA testing of a bridge. The identification results using MIMO EMA are shown to be superior to those found using traditional excitation methods.

Finally, the identified modal parameters of the in-service bridge are used in load rating. Direct use of the modal properties of a bridge for load rating is unprecedented, and a relatively simple method to use measured modal flexibility to help determine live load demand is developed herein. The bridge load ratings calculated from the new method are compared to traditional methods.

In summary, a low-cost excitation system is optimized and systematically evaluated for MIMO EMA testing of civil structures, and the use of the system is validated in the laboratory and in the field. A new method to improve bridge rating reliability is then developed using the high quality modal parameters found via the optimized testing process.

ACKNOWLEDGEMENTS

I thank my advisor, Dr. Kirk Grimmelsman for his interest and encouragement throughout my time at the University. I compliment his creativity in establishing the idea that tactile transducers could be used to excite civil structures, which led to the work published herein.

I also thank the dissertation committee members; Dr. Ernest Heymsfield, Dr. Panneer Selvam, and Dr. Mark Arnold for their assistance and advice.

The field testing reported herein cannot be accomplished by a single person, and I thank students Thomas Norris and James Lindsey for their help in performing this work. I also thank fellow Ph.D. students Cyrus Garner and Matt Strasser for their friendship and occasional commiseration during this long process. My thanks also go to graduate students Jeremy Rawn, Ryan Maestri, and Javier Torres for the use of data from work they performed.

Finally, I thank my wife, Thea, for supporting my decision to pursue a Ph.D. The process took longer than anticipated, and her patience with me is deeply appreciated.

TABLE OF CONTENTS

LIST OF TABLES

LIST OF FIGURES

CHAPTER ONE

INTRODUCTION

1.1 MOTIVATION AND RESEARCH CONTEXT

The work of this thesis is motivated by two complimentary goals. The first goal is to develop a new methodology to better obtain reliable modal flexibility of bridges by using experimental modal analysis. The second goal is to develop a new method by which modal flexibility can be used to enhance evaluation and management of real-world bridge structures. A brief introduction to the state-of-the-art in modal analysis and in bridge condition evaluation are provided in the following in order to frame the research presented herein.

1.1.1 Overview of Modal Analysis in Testing of Civil Structures

Experimental modal analysis (EMA) is a process in which measurable dynamic excitation is applied to a system and the response is recorded. The input-output relationship provides significant knowledge about the system. With the assumption of linear structural dynamics, the relationship between the input and the output reveals various modal parameters such as the natural frequencies, mode shapes, damping ratios, modal scaling, modal flexibility, etc. of the structure.

Modal analysis of rotating machinery, aerospace, and automotive systems has been successfully used for decades. In these industries, the work is usually performed in a controlled laboratory setting with the test subject well isolated from ambient inputs. Both the input forces applied to the structure and the outputs (velocities, accelerations, strains, etc.) of the test subject are measured and the desired modal properties are determined. The modal parameters extracted from

testing of mechanical structures are used for a variety of purposes: reduction of vibration, calibration of numerical models, damage and defect identification, etc.

Vibration testing of civil structures accelerated in the early 1980's, usually with the purpose of determining natural frequencies for the purposes of seismic and wind analyses. More recently, research into modal analysis of civil structures has been focused on structural health monitoring (SHM) and damage detection. In these subjects, the identified modal parameters of a structure are used to try to detect, localize, and quantify damage. This work coincides with the trend to continuously monitor important infrastructure systems via the application of modern technology. The availability of (relatively) inexpensive sensors, computers, and communications gear has enabled this research thrust; however, there are fundamental issues in the modal testing of civil structures that remain unresolved.

1.1.1.1 Discussion of Modal Analysis Excitation Methods

One of the most significant fundamental challenges is to adequately excite massive structures of the scale of typical civil works. Cunha and Caetano (2006) present a selection of large and very expensive excitation devices that were built to excite dams and long span bridges. Not only are these devices rare and costly, but their use typically interferes with the normal operation of the structure under test. Because of the high cost and limited availability of such devices, researchers have explored many other means of excitation. The range of excitation methods attempted is very broad – everything from shooting a structure with a bolt gun to suspending and suddenly releasing a barge from a bridge has been tried. None of these various methods have proven suitable for widespread use in research or practice.

Because of the difficulty of adequately exciting civil works with controlled inputs, vibration testing of civil structures has largely transitioned to output-only analysis methods in which the input excitation is not measured. This testing method is commonly known as operational modal analysis (OMA). With OMA, no attempt is made to purposely excite the structure. Instead, excitation is provided by naturally occurring environmental processes and only the structural outputs are recorded. With the assumption that the input is stationary, broadband, uncorrelated to prior system responses (Giraldo et al. 2009), and spatially uniformly distributed (Chauhan et al. 2008), the modal parameters can be extracted from the output measurements.

There are three main drawbacks to the use of OMA. First, although the various algorithms that have been developed have different levels of sensitivity to these underlying assumptions, significant errors can be made in the modal parameter estimation when the input is not stochastic. The nature of the environmental inputs typically makes them nearly impossible to record and analyze, and thus the stochastic assumption cannot readily be validated. The algorithms and processing methods have steadily become more elaborate to deal with this uncertainty so that the utility of the results is not reduced.

Second, without knowledge of the input forces, modal scaling cannot be directly calculated from the output measurements (Gul and Catbas 2008). Without modal scaling, modal flexibility also cannot be calculated. Some researchers have attempted to overcome this limitation by calibrating finite element models of the tested structure and using the model to provide modal scaling. Parloo et al. (2005) attempt to use a sensitivity based technique to estimate modal scaling in OMA testing by adding significant mass to the structure under test. Although the results of this technique were encouraging, the difficulty of significantly modifying the mass of civil structures seems to have discouraged its adoption.

Third, the low level of excitation provided by OMA often makes it difficult to identify higher frequency modes. The literature provides a few examples in which OMA and EMA testing are both performed on the same civil structure. Doebling et al. (1997) tested a bridge with a type of EMA known as multiple reference impact testing (MRIT) and with OMA. They found more modes of the structure and tighter confidence intervals on the modal parameters with EMA. Aktan et al. (2005) tested a large-scale laboratory bridge model with MRIT and OMA, and they identified many more modes with EMA. Deckers et al. (2008) notes that "In practice, however, it occurs that not all modes are well excited by the ambient forces and the application of an artificial excitation is necessary."

However, most researchers are willing to accept the limitations of OMA since imparting significant measurable excitation appears to be so onerous. An excerpt from Sohn (1998, 3) is indicative of the general consensus of researchers today:

> *The size of civil structures does not permit the instrumentation of a large number of sensors and actuators, and the excitation of higher modes. Furthermore, the application of forced vibration tests, which are commonly used for system identification, is difficult for civil structures in service because of the economic and social ramifications caused by service interruption due to road closure and evacuation of buildings. Ambient vibration tests are more suitable for civil structures since the tests can be conducted under normal operation of structures and can be easily repeated to collect additional modal data sets.*

Unfortunately, SHM and damage detection applications require very accurate identification of the modal parameters since localized damage only causes small changes to these that are difficult to detect. Significant effort is being expended in an effort to develop algorithms that can accurately identify such small changes in the presence of noise and environmental variations common to civil structures. The questionable quality of modal parameters determined from OMA testing makes the advancement of SHM all the more difficult. Chauhan et al. (2008)

demonstrated analytically that the bias error known as leakage is difficult to avoid with OMA, and that modal damping estimates suffer when the ambient excitations are partially correlated. Parloo et al. (2005) noted that the inability to directly identify modal scaling restricts the success of OMA for some particular damage identification techniques, dynamic structural response prediction, force identification, and vibro-acoustic applications. Aktan et al. (2005) stated, "Whether output-only modal analysis alone may serve for reliable health monitoring should be questioned."

Overall, testing of structures using EMA has been very successful in the mechanical engineering field, and is known to provide more reliable modal parameters than OMA. However, the difficulty of imparting adequate controlled excitation to civil structures has limited the use of EMA, and OMA is currently the dominant method by which vibration testing is carried out in the civil engineering field.

1.1.1.2 Discussion of Multiple Input Excitation

In the testing of structures using EMA, the input excitation is usually classified as single-input, multiple-output (SIMO) or multiple-input, multiple-output (MIMO). With SIMO, only a single point on a structure is subject to dynamic input at any given time, whereas with MIMO, excitation is *simultaneously* applied to more than one location. MIMO testing has several advantages in comparison to SIMO testing. Vold et al. (1982) developed the first algorithm that simultaneously used all of the redundant information that multiple inputs generate, which allowed the identification of closely spaced modes and repeated roots. Allemang et al. (1983) performed the first reported real-world MIMO testing of a structure by using three shakers on an aircraft. They noted that the MIMO approach gives better energy distribution, enhances data consistency, and reduces testing time. Zimmerman and Hunt (1985) also noted that MIMO

provides less distortion of measurements by noise and nonlinearities, and that increased average excitation improves signal-to-noise ratio (as compared to SIMO). Avitabile (2011a) noted that a significant advantage of MIMO testing is that an array of shakers allows a lower power input signal which diminishes excitation of nonlinearities.

The mechanical engineering industry routinely uses MIMO testing for these reasons; however, true MIMO testing of civil structures has rarely been performed. Only two examples of MIMO testing of civil structures in the field are found in the literature. First, Schwarz and Richardson (2001) analyzed data from testing of a highway bridge that was excited by two shakers. This bridge was also tested with OMA and with MRIT (which is a SIMO method), and the best modal parameters were extracted from the MIMO data. Second, Miskovic et al. (2009) used four APS shakers (expensive, laboratory grade devices) to test floor slabs in an office building. SIMO testing of civil structures with a single, large shaker or by MRIT is more prevalent than MIMO testing, but is not nearly as common as the use of OMA. Representative examples of bridge testing with single large shakers can be found in Shelley et al. (1995) and in Maas et al. (2012). A representative example of bridge testing with MRIT can be found in Catbas et al. (1998).

Overall, in the performance of EMA, MIMO testing is known to be superior to SIMO testing. However, dynamic testing of civil structures is almost never performed using MIMO EMA because of the historic difficulty and expense of obtaining, installing, or using multiple shaker devices.

1.1.2 Bridge Evaluation Overview

The aged and deteriorated condition of transportation infrastructure is a well-publicized issue facing the United States. National data on vehicular bridges are often cited to substantiate this

statement, and current reports indicate that 17,340 bridges are structurally deficient out of a total of 292,085 state and federally owned bridges (Barbaccia 2011). When bridges owned by counties and townships are included, 59,719 are structurally deficient out of a total of 602,091 bridges. The difficulty of maintaining the bridge population is compounded by limited funding for repair or replacement. The national concern regarding the budget deficit, the impasse in Congress, and the strong push in Washington to cut costs wherever possible also impacts the ability of transportation agencies to adequately care for their bridge structures. Therefore, it is of the utmost importance that the limited available funding be spent on bridges that have the greatest need for structural improvement.

It is difficult for bridge owners to determine which of their bridges are the most in need of repair or replacement because the data they have available is the result of subjective biennial inspections. The data is qualitative for a variety of reasons. The greatest limitation is that the inspection process is almost always limited to visual identification and characterization of localized defects. Additionally, bridge inspections performed for any given agency are carried out by a variety of consultants and in-house personnel, and thus the assessment is colored by the experience and background of the individual performing the inspection. The data provided by these inspections is highly useful for certain purposes. For instance, the condition of the paint system, the deck joints, and the various safety features can be established with great certainty. However, the inspection does not indicate the actual load carrying capacity of the bridge or the remaining useful life. Despite the best efforts of owners to provide guidance to inspectors, it is impossible to consistently provide a qualitative value for the condition of a single type of structural component, no less to the condition of an entire bridge.

From an operational perspective, the value of a highway bridge simply lies in its ability to carry vehicular loads. Therefore, load ratings have been calculated for every bridge by mandate, and the ratings are supposed to be reviewed during each inspection cycle so that deterioration identified in the field can be incorporated into the rating calculations. However, the rating calculations are almost always based on analytical assumptions and significant simplifications. The outcome is an indication of the load capacity that is almost always conservative, but to an unknown extent. The real carrying capacity of the structure is not known. This results in a highly qualitative system wherein the operating agency has both inspection and rating data of which neither is especially useful for prioritizing bridge work across a broad inventory of structures.

A quantitative determination of the real load carrying capacity is highly useful then, since it indicates if the subject bridge can do the job it is meant to do. Quantitative methods for establishing the load carrying capacity of bridges do exist but are seldom used in practice. These AASHTO accepted methods are load testing and dynamic testing (AASHTO 2008, Article 8.1.2). Both types of testing are typically performed in a manner that captures the global behavior of the structure. Load testing is the application of stationary or moving loads to the bridge. A proof load test can be used to show that a bridge can at least carry a load as large as the proof load. More commonly, deflections or stresses are measured for smaller loads and the results are extrapolated to indicate the bridge capacity. Load testing is uncommon due to its cost and the operational issues that it causes (e.g. bridge closure during the testing).

Dynamic testing is a quantitative, global method that can also be applied to bridges. It is the process of measuring the time-varying response of a structure relative to input dynamic excitation. Typically, the measured acceleration responses from different locations on the bridge are used to identify the modal characteristics. The identified modal characteristics usually

include the natural frequencies, mode shapes, and damping ratios. These characteristics are system properties of a structure and are a function of mass, stiffness, and damping. Changes in the structure due to damage, deterioration, and environmental effects are reflected by changes in the dynamic properties. Although not commonly used in industry, it is often easier and more economical to globally characterize a bridge with dynamic testing than it is to characterize it using load testing.

It is also recognized that load rating is an exceptionally important application of bridge management. The load capacity ratings are the single item that inform the operating agency of the ability of each structure to carry legal truck loads, and the ratings have a broad and consistent meaning to engineers. The calculation of load ratings include estimating the capacity, dead load stress, and live load stress of structural elements, and these calculations all include uncertainty that is not easily eliminated. However, the estimation of live load stress is the single most difficult part of the rating process and relies the most heavily on simplifying analytical assumptions. Therefore, reduction of the uncertainty in this portion of the bridge evaluation by use of measured physical responses is desirable.

1.2 FOCUS OF THESIS

In response to the various issues discussed, it is recognized that an inexpensive, easily deployable, spatially distributed excitation system that can provide measurable force input to civil structures is needed. Such a system could help spur advances in SHM and damage detection by providing high quality modal parameters and obviating the need for the unvalidated assumptions inherent to OMA.

Dr. Kirk Grimmelsman instigated the idea that an array of low cost linear actuators can be used to provide the measurable input that most easily enables dynamic analysis. The novel idea is to greatly reduce costs by using a consumer product that has real price competition as the dynamic excitation device. The product type that is proposed can be described as a 'bass shaker' or a 'tactile transducer', and is a device used in home theater applications to shake the floor or furniture during deep rumble noises in movies and games. The tactile feel of the shaking enhances the experience by more deeply immersing the viewer's senses in the media.

The costs of such devices generally range from $50 to $1,000. One brand of transducer that is considered in this study costs about $250 and provides an estimated 30 pounds of peak force. It is estimated that the cost per unit including a power supply, amplifier, and shaker is on the order of $1,000. A review of the literature shows that the use of such an approach for controlled dynamic testing of civil infrastructure has never been attempted. Many researchers have used purpose-built, commercial shakers as excitation devices for EMA testing of laboratory and full-scale structures. A commonly used shaker from APS Dynamics costs on the order of $13,000 for a device that can impart 30 pounds of dynamic force. A similar shaker that can provide 100 pounds of dynamic force costs about $18,000. Thus, many tactile transducers could be deployed on a structure for less than the cost of a single, purpose-built device.

The contribution of the research presented herein is summarized as:

- Develop and implement a testing protocol for evaluating shakers and amplifiers for use in EMA of civil structures.
- Develop a framework for characterizing shaker and amplifier uniformity across a population of devices.

- Determine an optimized excitation technique for MIMO EMA of civil structures.
- Validate the ability of the tactile transducer based excitation system for MIMO EMA in a laboratory environment via comparison to results from accepted means and methods.
- Perform the first real-world MIMO EMA bridge testing utilizing more than two shakers simultaneously.
- Perform the first real-world MIMO EMA bridge testing using determinate excitation signals.
- Validate the ability of the new excitation system for MIMO EMA on a real-world bridge via comparison to results from state-of-the-art methods.
- Evaluate the deterministic multisine signal for use in EMA of civil structures.
- Develop a new method to more directly use modal parameters for bridge capacity evaluation.

Characterization of the system components is necessary in order to select the most appropriate devices from which to construct the full excitation system. Also, the operational characteristics of these devices must be established so that best practices for their use can be determined. The characterization process is carried out in the laboratory via the design and implementation of a large number of tests.

After the system components are well understood, research and testing is performed to determine the optimal manner in which the system can be used for MIMO EMA. Excitation signal types, output force levels, and spatial arrangement of inputs are some issues that are considered. Data distillation and modal parameter extraction algorithms appropriate to MIMO EMA are also

evaluated for use. Particular data processing methods are selected, coded in Matlab, and tested with analytically generated data.

Laboratory testing of a large-scale model structure is then undertaken to validate that the novel excitation system does allow the capture of accurate modal parameters via MIMO EMA. Traditional dynamic testing and static testing of the model structure is also performed to provide a baseline for evaluation of the success of the new methods.

Field testing of an in-service highway bridge using MIMO EMA is also performed using a maximum of eight tactile transducers operating simultaneously. This testing is the first time that MIMO EMA using more than two shakers is ever successfully executed. Results from the new methodology are compared against results using OMA and MRIT excitation paradigms.

Finally, a simple methodology is developed by which measured modal flexibility can be used to improve the bridge load rating process. As noted, many researchers are currently working to detect damage and to continuously monitor for structural changes; however, few are attempting to provide a more straightforward and rational estimate of load capacity. Bridge owners understand and utilize ratings, and thus are more likely to adopt a testing process that provides them with load ratings.

Overall, the goal of this thesis is to evaluate the suitability of a novel excitation system for MIMO EMA dynamic characterization of bridges. Since the body of knowledge related to MIMO EMA of civil structures is very limited, this approach and the optimal design considerations for application to bridges must first be systematically evaluated and validated. An additional goal is to develop a simple method by which the identified modal parameters can be used to improve the bridge load rating process.

1.3 ORGANIZATION OF THE TEXT

The chapters of this manuscript are organized in chronological order of the system characterization and validation of the novel excitation system. This is followed by the application of the modal parameters to the calculation of bridge load ratings. A chapter-by-chapter overview of the text is provided as:

Chapter 1

Frames the subject matter of the work, highlights the original contributions, and clarifies the organization of the text.

Chapter 2

Presents a testing and evaluation program that was developed to systematically evaluate and characterize the components of the novel excitation system, including various alternate components.

Chapter 3

Presents in-depth characterization of the tactile transducer and power amplifier selected for use in the system. These characterization studies investigated the available force output across various frequencies, the ability to reproduce signals used in modal testing, the level of distortion of signals, and the level of uniformity across a population of the devices.

Chapter 4

Provides background and selection criteria for excitation techniques. Various signal types, force levels, and spatial distribution of input are discussed. Best practices to use with the array of

tactile transducers are enumerated. This provides the basis for the manner in which testing of a laboratory structure and then a real-world bridge proceeds.

Chapter 5

Discusses various data collection, reduction, and processing methods. These methods can significantly affect the quality of the modal parameters to be extracted, and justification for the processes selected are provided. Also, the detailed equations used in the selected processing algorithms are provided, and assumptions inherent to these algorithms are discussed.

Chapter 6

Laboratory testing of a model structure is undertaken and the results are presented. Several baseline tests are performed using standard methods. Results using tactile transducer excitation are presented and compared to the baseline modal parameters. Lessons learned in this testing are applied to the subsequent field testing.

Chapter 7

Field testing of an in-service highway bridge is undertaken using an array of the tactile transducer excitation devices and the results are presented. Comparison is made to results from prior testing by other University of Arkansas researchers. The results demonstrate that the tactile transducer based excitation system produces superior results to other available approaches.

Chapter 8

Bridge load rating is performed for the in-service bridge tested in the field. Baseline load ratings are developed using standard industry practice. A method by which the measured modal

flexibility matrix can be used to improve the load rating process is developed, and ratings based on this process are calculated. The load ratings from the new process are compared to those based on standard practices.

Chapter 9

Overall conclusions are presented for the entirety of the work.

CHAPTER TWO

CHARACTERIZATION AND SELECTION OF TACTILE TRANSDUCER AND POWER AMPLIFIER

2.1 INTRODUCTION

This chapter presents a laboratory testing and evaluation program that is undertaken in order to establish the operating and performance characteristics of several commercially available tactile transducer (TT) shaking devices and subwoofer amplifiers to drive the TTs. The objective of the evaluation program is to validate the selection of a transducer-amplifier pair for use in MIMO EMA testing of short to medium-span bridges. To be of use, the devices must provide acceptable excitation force amplitudes in the frequency range of interest, and reliably reproduce the deterministic and stochastic signals that are typical for modal testing of bridges. Therefore, the TTs are tested to reveal the force that they can develop over a range of frequencies, and the amplifiers are tested to determine their gain. Tests are also performed on both the amplifiers and the TTs to determine how much distortion they impart to deterministic and stochastic signal types.

Since researchers and practitioners in the field of vibration testing typically use purpose-built shaker devices, the operating parameters of the devices are either supplied by the manufacturer, or the devices are custom-built to meet the required parameters. The TTs and amplifiers evaluated herein are not designed to meet the high expectations of the vibration testing community, and their operating characteristics and responses to various excitation signals are not documented. Since shakers of this type have never before been adapted for use in vibration testing, the literature does not provide any framework for a characterization program. Therefore,

the tests devised and undertaken herein contribute to the body of knowledge by providing methods that can be used evaluate other excitation devices in the future.

2.2 SHAKER TESTING

2.2.1 Devices Evaluated

The TTs surveyed for this study are small-scale, electrodynamic shaker devices that are intended to make theater and gaming experiences more immersive. Low frequency sounds from movies or video games are sent to the TTs and they create a rumbling sensation. This is accomplished by attaching the transducers to the underside of floors or furniture so that the low frequency rumble can be felt by the audience. The devices are widely and commercially available for use in home theater applications, 4D amusement park rides, and traditional theaters. There are a number of manufacturers that market these devices, and as a result, their cost is competitive. The market includes a variety of product sizes, power ratings, packaging options, and price ranges, but a point of commonality is that practically all TTs use a voice coil as the principal motive system. In the parlance of vibration testing, these shakers are of the electrodynamic type.

Three different TTs were evaluated. Selection of the devices evaluated in this study was based on price and manufacturer specifications of power handling. The specific devices evaluated in this study are referred to as Shaker 1, 2, and 3 and they are shown in Figure 2.1 (trade names are intentionally withheld at this time). It should be noted that the largest of the devices tested measures less than 6 inches in any dimension and weighs only 10 pounds. The devices' small size would allow many of them to be easily deployed by hand on structures such as bridges and buildings.

Figure 2.1. Shakers evaluated for use in MIMO EMA. (Photo by EVF, dynamics lab, 9/14/12)

Shaker 1 and Shaker 2 are similar in style and represent the most common type of TT. They consist of a rugged metal housing with integral cooling fins and all moving parts are located within the enclosure. Unlike a traditional shaker used for laboratory modal analysis, there is no armature and no method to directly monitor the position, velocity, or acceleration of the moving mass. These two shakers are produced by different manufacturers and have significantly different specified power handling capabilities per manufacturer literature. Shaker 1 can be operated continuously at 400 Watts RMS, whereas Shaker 2 can only handle 50 Watts. As a result, Shaker 2 is about a quarter the cost of Shaker 1.

Shaker 3 is of a different style and is more similar to a typical laboratory shaker. This device does not have a moving mass contained within a rugged packaging, and instead features a load table that is intended to support the leg of a chair or couch to impart the dynamic excitation. The load table is equivalent to an armature and this enables measurement of the shaker movements.

Additionally, the load table allows the addition of mass which provides the ability to modify the force output and natural frequency of the shaker. This device can handle 30 Watts RMS.

An APS Dynamics 113-HF shaker paired with an APS 145 amplifier is also subject to the same shaker tests. This electrodynamic shaker system is representative of the types of high-quality and expensive laboratory shakers used in vibration and modal testing. Reaction masses of 20 pounds are attached to the shaker for all tests, and the APS amplifier is operated in voltage mode for all tests. The APS shaker results are presented as a point of comparison for the TTs. Table 2.1 summarizes various nominal specifications of the devices tested.

Name	Price	Rated RMS Power	Nominal Impedance	Weight
Shaker 1	$200	400 W	4 Ohm	10 lb
Shaker 2	$40	50 W	4 Ohm	3 lb
Shaker 3	$500	30 W	6 Ohm	4 lb
APS 113HF	$12,940 w/amp	600 W	2 Ohm	103 lb

Table 2.1. General information for tested shakers.

2.2.2 Testing Criteria

TTs are essentially audio components and the manufacturers provide specifications that are generally aligned with traditional subwoofer characteristics. These specifications are generally not the same as those provided by the makers of shakers for vibration and modal testing. As such, a controlled laboratory testing program must be devised and performed to establish the operational and performance characteristics of the TTs in a systematic manner. The first step in this process is to establish what characteristics will be most important for MIMO EMA testing of bridges. These important characteristics can then be used as selection criteria for choosing the best device for a MIMO testing system.

The most important characteristic of the shakers for bridge testing is the force output in the frequency range of interest. Bridges and other civil structures are massive, and a significant amount of input force is needed to adequately excite such structures beyond the ambient input level (noise floor). These large structures also typically have low frequency modes which are best excited by low frequency input. Thus, the maximum force that can be produced at various frequencies, and especially at low frequencies, is tested and evaluated.

Another important characteristic is the ability of the shaker to accurately reproduce input signals that are typical to modal testing. These signals often include swept-sine (determinate) and burst-random (stochastic). For testing the reproduction of sinusoidal signals, the periodogram is used to measure the energy content at both the input frequency and at other frequencies, and the signal to noise ratio (SNR) is calculated for the measured outputs from the devices. To evaluate the reproduction of a broadband random input signal, the energy content at all frequencies within the range of interest is compared.

2.2.3 Test Methods, Results, and Discussion

The subsections below describe the specific test methods that are employed and discuss the outcome of each test for all shakers. The results are considered in relation to the potential use of these devices in a MIMO array for dynamic testing of civil structures. The tests/criteria subsections are:

1. Shaker Force Output
2. Shaker Sinusoid Reproduction
3. Shaker Burst-Random Reproduction

For all tests, the signals are generated by an Agilent 33220A Arbitrary Waveform Generator and data is acquired by a National Instruments PXI 4472B DAQ card. All data processing is performed in MATLAB.

2.2.3.1 Shaker Force Output

As stated previously, the most important characteristic for the shakers is their ability to provide adequate excitation force over the frequency band of interest, which is taken as 0 to 100 Hz. This test is performed by attaching each shaker to an aluminum plate that is supported on three dynamic force transducers in a tripod arrangement (Figure 2.2). Sinusoidal signals are sent to Amp 1 and from there to the shaker. The power draw of the shaker is also monitored. With a sinusoidal signal input at a discrete frequency, the amplitude of the input is increased until the shaker "bottoms out" due to its stroke being exceeded or until the maximum recommended RMS power is reached, whichever comes first. The output from the three force transducers is then summed and the total force is recorded for four seconds. The mean RMS value of this measured force is taken as the maximum RMS force available at the frequency under consideration.

$$F_{RMS} = \sqrt{\frac{1}{N}\sum_{i=1}^{N}[F(t)^2]} \qquad \text{Equation 2.1.}$$

Where:

F_{RMS} = the root-mean-square force (lbf).

N = the number of discrete measurements.

$F(t)$ = the discrete measured force (lbf).

(a) (b) (c)

Figure 2.2. Force measurement apparatus. (a) - aluminum plate with tripod of force transducers. (b) – plate orientation for testing. (c) – typical testing setup. (Photo by EVF, dynamics lab, 9/14/12)

Figure 2.3 illustrates the maximum RMS force that each shaker produces over the frequency range. The APS shaker is capable of producing 50 lbf at a frequency of 4 Hz in voltage mode. The force gradually falls off to a low of about 30 lbf at 50 Hz before peaking at 100 lbf (off graph) at the natural frequency of the shaker. The shape of the APS force response demonstrates the highly nonlinear nature of force output in relation to frequency. The factors that limit the force also change depending on frequency. The force is limited by the shaker stroke length up to about 3 Hz, and this particular shaker has a long 6.25-inch stroke. Above 3 Hz the force is limited by the amplifier power. It is clear that the APS shaker can produce significantly more force than any of the TTs that were evaluated.

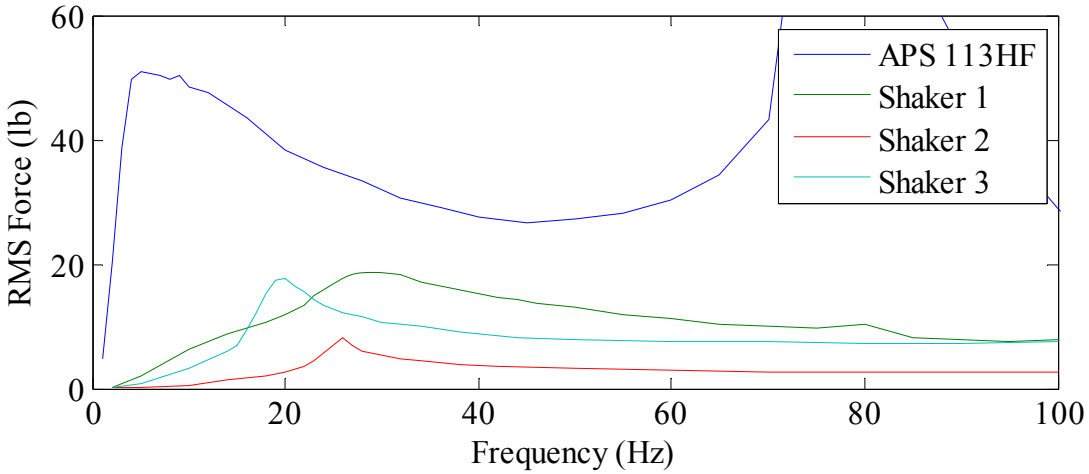

Figure 2.3. RMS force output for subject shakers in the frequency range of interest.

Of the three different TTs evaluated, Shaker 1 provides the highest level of force at low frequencies. The force rises nearly linearly from zero at 1 Hz to about 20 lbf RMS at 29 Hz and then gradually decreases with increasing frequency. The TTs all have a short stroke and this limits the low frequency force they can produce without bottoming out (Tustin 1991). Shaker 1 is limited by its stroke up to 25 Hz, and above 25 Hz the force is limited by the power of the amplifier. Compared to the other TTs, Shaker 1 has a much broader peak in the vicinity of its natural frequency and can provide much greater force across the range of 30 to 80 Hz.

Shaker 2 produces the least force of all of the shakers across the entire frequency range. The force is stroke-limited below 5 Hz and is limited by the 50 Watt shaker power capacity above this. This shaker provides very little force at low frequencies with less than 2 lbf RMS at 20 Hz. The force has a strong peak at the 27 Hz shaker natural frequency and then quickly drops down to about 3 lbf RMS at higher frequencies.

Shaker 3 differs in its construction from the other two shakers in that it has a load plate and is meant to carry additional mass. This allows a broad range of experiments to understand how the force output varies with increments of additional mass and how the reproduction quality varies simultaneously. The results shown are with an added mass of 2.26 pounds of aluminum disks (the powerful fixed magnets in the shaker preclude the use of ferrous metals for added mass). The shaker force is generally stroke limited at frequencies near and below the peak force (at 20 Hz), and is limited by the shaker power capacity at higher frequencies. The added mass allows high forces to be generated relative to power consumption, and the magnitude of the mass allows the peak to be adjusted to particular frequencies. However, the force falloff is significant away from the sharp peak at the natural frequency of the shaker/mass system.

Overall, the short stroke lengths of the TTs preclude them from producing high forces at low frequencies without bottoming out. Of the three transducers tested, Shaker 1 provides the largest force at low frequencies and provides the most consistent force response across the frequency band of interest. Shaker 3 provides the unique ability to have its peak force output tuned to a particular frequency by adding mass, and provides a high level of force given its low power input. Shaker 2 and Shaker 3 both provide a very consistent level of force at higher frequencies.

Several observations are made from these tests. First, two 'identical' shakers do not produce exactly the same force trace, and the results shown are based on testing of one individual shaker. The variance between 'identical' shakers is far less than the variance between the different shaker types, and this can be seen in the subsequent chapter in which multiple Shaker 1 samples are compared. Second, power consumption by the shakers was not measured directly. The RMS voltage across each shaker was measured and the manufacturer's stated nominal impedance was used to calculate a presumed power. This is inexact since the actual impedance across a coil varies depending on frequency, and the impedance can be significantly higher than the nominal value resulting in power consumption less than presumed and below the limit (Lang 1997). However, an actual power draw less than the manufacturer's stated limit is not considered to be a significant issue in this testing since the stated limits are fairly arbitrary and are inconsistent across the devices.

2.2.3.2 Shaker Sinusoid Reproduction

A signal to noise ratio (SNR) measurement is now used to characterize how well each shaker can convert a voltage input to a force output. A sinusoidal signal at a particular frequency is generated, amplified by Amp 1, and then sent to the subject shaker. A sinusoid at a single frequency line is generated for 6 seconds and then the next higher frequency is generated. The

signal input to the shaker and the force output are continuously recorded during this process. In data processing, the first 2 seconds of data at each frequency line are ignored so that the minor transient that occurs at frequency changes is excluded from the results, and the remaining four seconds of data are transformed to the frequency domain. The mean RMS value of the response away from the input frequency is then found and divided into the response at the input frequency to determine SNR.

$$SNR = 10 \log \left[\frac{P_{sig}}{P_{noise}} \right] \quad \text{Equation 2.2.}$$

$$P_{noise} = \frac{P_{total} - P_{sig}}{N} \quad \text{Equation 2.3.}$$

Where:

P_{sig} = the power at the discrete input frequency (lbf^2/Hz).

P_{noise} = the average power at all other frequencies (lbf^2/Hz).

P_{total} = the power at all frequencies (lbf^2/Hz).

N = the number of discrete frequency lines in the periodogram.

The power is found by taking the one-sided periodogram of the vector of force measurements. The power at the input frequency is taken as the periodogram value at that single frequency line, and the power of the noise is taken as the average value of all other frequency lines. For these experiments, the bandwidth of the periodogram was from 0 Hz to 250 Hz.

As a baseline, the APS shaker provides very good reproduction at low frequencies with an SNR of 70 dB at 3 Hz (Figure 2.4). As frequencies increase, the measured noise increases but the signal is still far more powerful than the noise. It is recognized that the degradation at higher

frequencies is partly due to a constant data acquisition rate of 1000 Hz, which causes increased aliasing in the Fourier transform as signal frequencies increase.

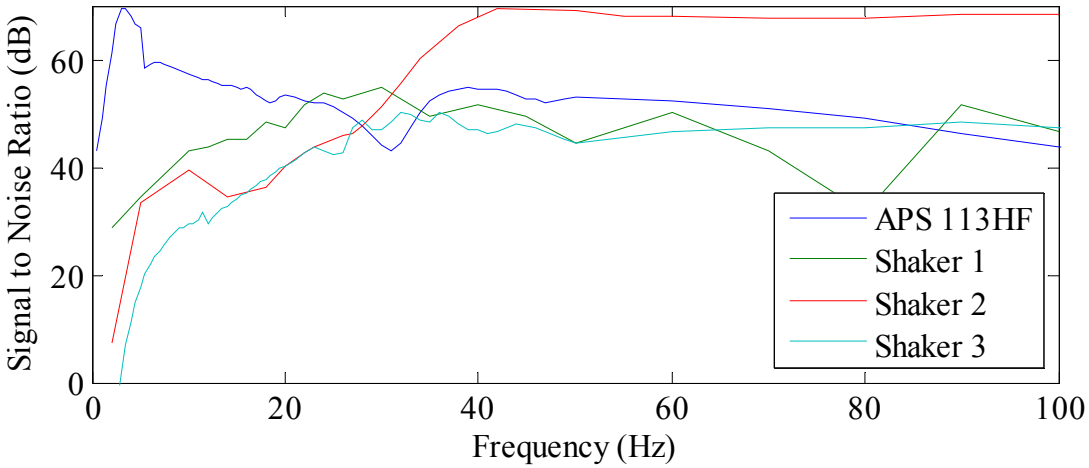

Figure 2.4. SNR for subject shakers in the frequency range of interest.

As expected, all of the TTs perform poorly at lower frequencies due to their limited strokes. To illustrate this point, Figure 2.5 shows the time data force recording for Shaker 1 operating at 5 Hz, and Figure 2.6 shows the time data for 20 Hz. It is visually obvious that low-frequency reproduction is not as good as that at higher frequencies. Of all of the TTs, Shaker 1 performs the best with a SNR of about 30 dB at 1 Hz. The signal reproduction then improves up to the natural frequency of Shaker 1 and then gradually declines in general except for a segment of poor reproduction in the vicinity of 80 Hz.

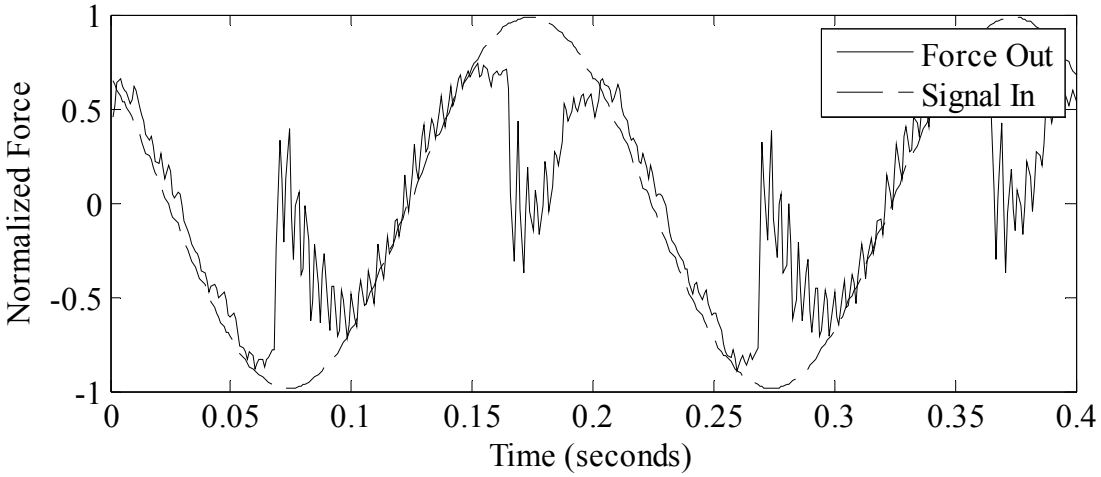

Figure 2.5. Shaker 1 force output with 5 Hz sinusoidal input. Note high noise content.

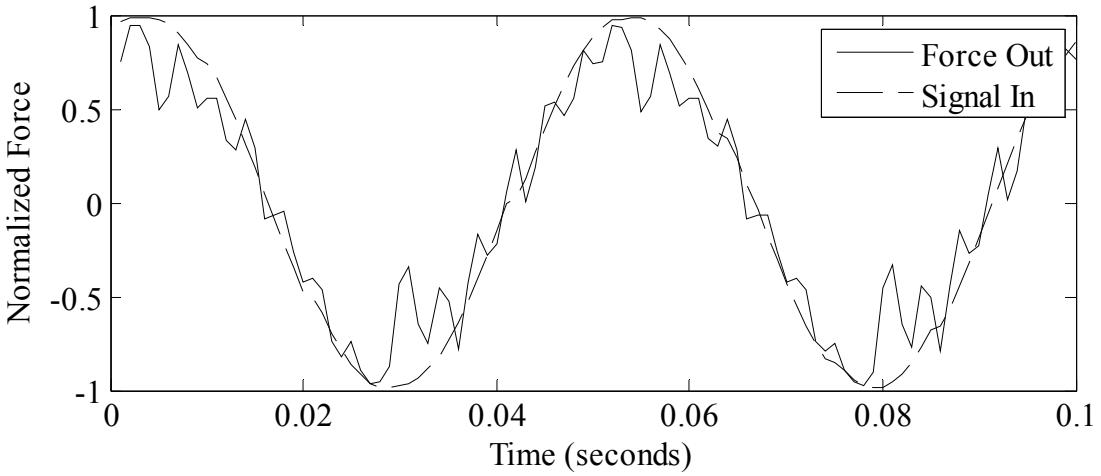

Figure 2.6. Shaker 1 force output with 20 Hz sinusoidal input. Note better performance.

Shaker 2 provides low SNR below 3 Hz but then steadily improves to the point that this shaker provides the cleanest response above about 35 Hz. Shaker 3 has very poor SNR up to about 10 Hz, and is generally the worst at reproducing lower frequency signals up through about 30 Hz. This shaker then has a fairly constant SNR which is in the same range as the APS shaker and Shaker 1. Shaker 3 has the shortest stroke of all of the devices tested, and this significantly impacts its ability to reproduce low frequencies while producing any appreciable force.

Overall, the SNR values are negatively impacted at low frequencies due to the stroke limit of the TTs. Shaker 1 has the longest stroke and is the least limited. At higher frequencies, all of the

transducers do a good job of producing a force signal that is predominantly sinusoidal with little noise. A SNR value of 40 dB corresponds to an RMS value of the signal that is 10,000 times greater than the RMS value of the noise, and all of the transducers exceed this threshold at higher frequencies except Shaker 1 at 80 Hz.

2.2.3.3 Shaker Burst-Random Reproduction

The test method for burst-random shaker testing begins by generating Gaussian white noise in MATLAB. This signal is then modified with a 5^{th} order low-pass Butterworth filter using a cutoff frequency of 100 Hz. The resulting signal is 128 seconds long with 500 points per second. This signal is amplified by Amp 2 and sent to the shaker, and the force output is recorded as before. The measured time data for the signal from the amplifier and for the force output are then transformed to the frequency domain for analysis. The high resolution (0.008 Hz) causes excessive visual noise in the graphical output, and this is diminished by reducing the resolution to 1 Hz by averaging.

The outcome of this testing is presented in Figure 2.7 with the 'Input' curve representing the power content of the signal that is output by the amplifier. The other four curves are the power content of the force signal measured from each shaker. The results generally show that the TTs reproduce random shaking to the same levels that they reproduce sinusoidal signals since the shape of the response over the frequency range is essentially the same as in Figure 2.3.

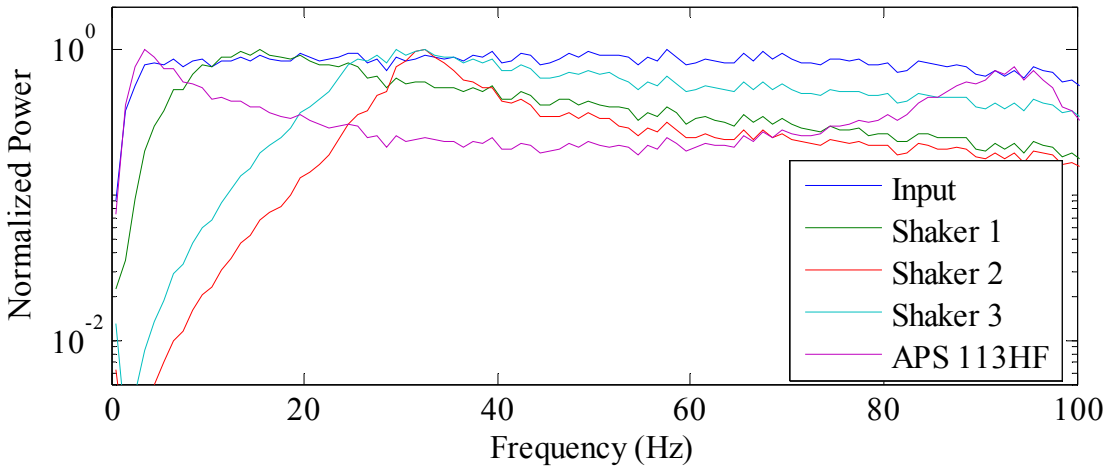

Figure 2.7. Reproduction of burst-random signal by subject shakers.

At low frequencies, stroke length is still the limiting factor. The APS shaker has very good low frequency response due to its long stroke, and all of the TTs have difficulty providing force at low frequencies due to their relatively short strokes. Shaker 1 again does the best with essentially full response available at 10 Hz. Shaker 2 performs the most poorly with a power output that is less than $1/10^{th}$ of what it should be all the way up to 20 Hz with full response not available until 30 Hz. Shaker 3 only performed marginally better than Shaker 2 but still far worse than Shaker 1.

The APS shaker and all of the TTs again produce maximum power at their own natural frequencies. As the input frequency increases above the natural frequency of the shaker, the power falls off with a shape that is consistent with the force output graphs. The conclusion can thus be drawn that these devices respond to burst-random signals in a manner that is predictable based on the response of the shaker to pure sinusoidal inputs. This is the expected outcome.

2.3 AMPLIFIER TESTING

2.3.1 Devices Evaluated

An intrinsic and cost-plus component of any shaker system is the power amplifier. Three inexpensive commercial audio amplifiers are evaluated in conjunction with the shakers for this testing program, and they are referred to as Amp 1, 2, and 3 (Figure 2.8 and Table 2.2). Amp 1 is a single channel device with an output power of 500 Watts RMS, which pairs well with Shaker 1. Amp 2 is a similarly powerful device but has two channels and a different manufacturer. Amp 3 is much less expensive and less powerful at 70 Watts and pairs with Shaker 2 or Shaker 3. Most amplifiers used for vibration testing can be set up to provide either a voltage output (voltage mode) or a current output (current mode) in proportion to the input signal. The subsequent velocity of the moving mass is proportional to voltage, and the acceleration (and force) is proportional to the current. Audio amplifiers do not have the capability to operate in current mode and thus voltage mode is used throughout this study.

Figure 2.8. Amplifiers evaluated. (Photo by EVF, dynamics lab, 9/14/12)

Name	Price	Rated RMS Power	Channels	Weight
Amp 1	$150	500 W	x 1	6.9 lb
Amp 2	$120	480 W	x 2	8.4 lb
Amp 3	$50	70 W	x 1	5.6 lb

Table 2.2. General information for tested amplifiers.

2.3.2 Testing Criteria

The performance of the amplifier impacts the shaker performance and thus amplifier testing is performed to establish the characteristics of these devices as well. These tests include gain across the frequency range of interest, reproduction of determinate signals, and reproduction of stochastic signals. These criteria essentially mirror the criteria for shaker selection.

2.3.3 Test Methods, Results, and Discussion

The subsections below describe the specific test methods that are employed and discuss the outcome of each test for all amplifiers. The tests/criteria subsections are:

- Amplifier Gain
- Amplifier Sinusoid Reproduction
- Amplifier Burst-Random Reproduction

For all tests, the signals are generated by an Agilent 33220A Arbitrary Waveform Generator and data is acquired by a National Instruments PXI 4472B DAQ card. All data processing is performed in MATLAB.

2.3.3.1 Amplifier Gain

Gain is a measure of how many times higher an output signal is than the input signal; however, gain is typically not consistent across the frequency spectrum for several reasons. First, the entire

spectrum of frequencies cannot be amplified by a single amplifier circuit, and thus the incoming signal is split into frequency windows which are separately amplified, and these signal segments are then added back together at the output. Thus the amplification within each frequency window can be different. Also, in the design of audio components, engineers often take advantage of the fact that humans typically cannot hear frequencies below about 20 Hz or above about 20 kHz. The audio amplifier may then be more economically designed to encompass the frequencies that humans hear best. For these reasons, it was important to test the gain of the various amplifiers to ensure they do not cut off low frequencies that are essential for dynamic testing of many civil structures.

Amplifier gain is tested at discrete frequencies while both the amplifier input and output voltage are monitored. All three amplifiers have a gain dial and this is set to maximum. Six seconds of data are captured at each frequency and the first two seconds are discarded as before. The RMS level of the output is then divided by the RMS level of the input to calculate gain at each tested frequency line. During all amplifier testing, a load of four shakers is powered by Amp 1 and Amp 2, and a load of a single shaker is attached to the less powerful Amp 3. For Amp 2, only a single channel is used. The results of gain testing are shown in Figure 2.9.

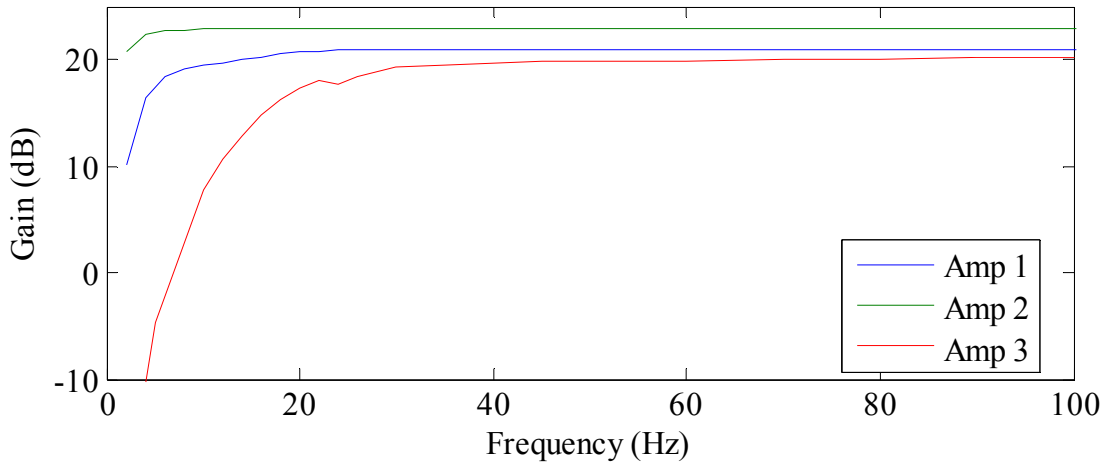

Figure 2.9. Amplifier gain.

Amp 1 does not provide much gain at low frequencies, especially below 5 Hz. The gain at 2 Hz is only about 8% of the maximum gain, and the gain at 4 Hz is about a third of the maximum. The gain rises to 71% of the maximum by 10 Hz and essentially reaches a stable plateau at 20 Hz and extending to the maximum frequency of interest. Amp 2 provides superior response at low frequencies with a gain at 2 Hz that is 61 % of the maximum and a gain at 4 Hz that is 87% of the maximum. The response is then essentially flat beyond 10 Hz. Amp 3 has very poor response at low frequencies, essentially low-pass filtering the signal below 10 Hz. At 20 Hz, the gain is still only 39% of the maximum gain and a plateau is finally reached at 30 Hz.

Both Amp1 and Amp 2 provide gain that is acceptable for use with the tested shakers. The low gain at low frequencies does not limit the force production of the shakers since they are stroke limited in this range. The flat, full response of both amps beyond 20 Hz then aligns well with the frequency range where the shakers are not stroke limited and can use their full power potential. The very poor response of Amp 3 below 10 Hz when considered in conjunction with its low maximum power output suggests that this amplifier is not well suited to bridge testing. However,

at its low cost it could still have potential use in testing lighter structures with higher fundamental natural frequencies.

2.3.3.2 Amplifier Sinusoid Reproduction

Next, an SNR measurement for the amplifiers is undertaken in exactly the same manner as that used for characterization of the shakers, except the signal input and voltage output from the amplifier are recorded and analyzed. The findings are shown in Figure 2.10 with the SNR of the input signal also shown for reference.

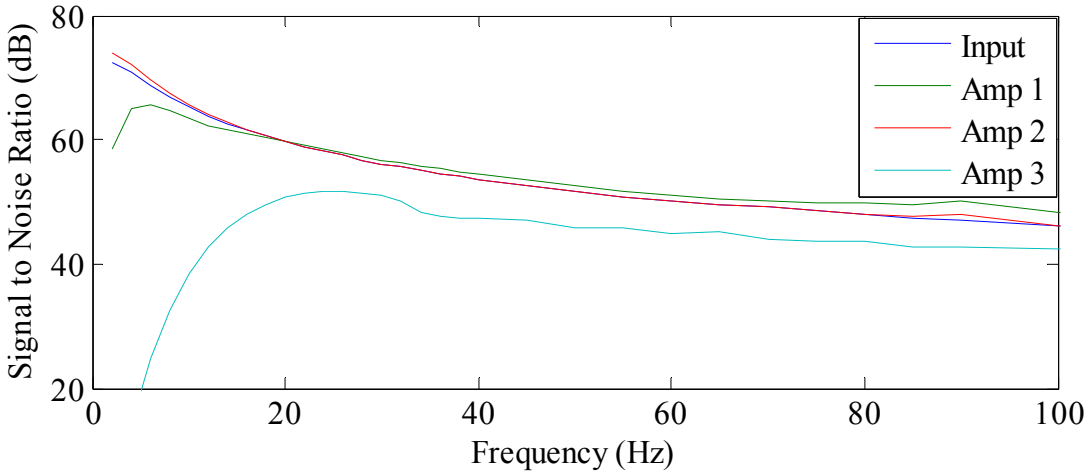

Figure 2.10. Amplifier signal to noise ratio.

Both Amp 1 and Amp 2 reproduce the input signals with high fidelity and introduce very little noise. Amp 1 is not as good at the lowest frequencies which relates to its reduced gain in this range. Amp 3 is far below the other two with significant noise introduced. It is noted that the gradual downward trend in SNR for Amps 1 and 2 is caused by a gradually decreased resolution of the input signal at higher frequencies. The SNR of the input signal is also shown on the figure to demonstrate that the decrease is caused by aliasing which is measured as noise.

2.3.3.3 Amplifier Burst-Random Reproduction

This test is also performed in exactly the same manner as the shaker testing, again with a filtered burst-random signal used as the input to the amplifiers. Both the input and output voltages are measured and the data is transformed to the frequency domain. Figure 2.11 shows how well each amplifier reproduced the frequency content of the input signal, and is normalized to a maximum value of 1.0 for each signal to generally remove the effect of gain.

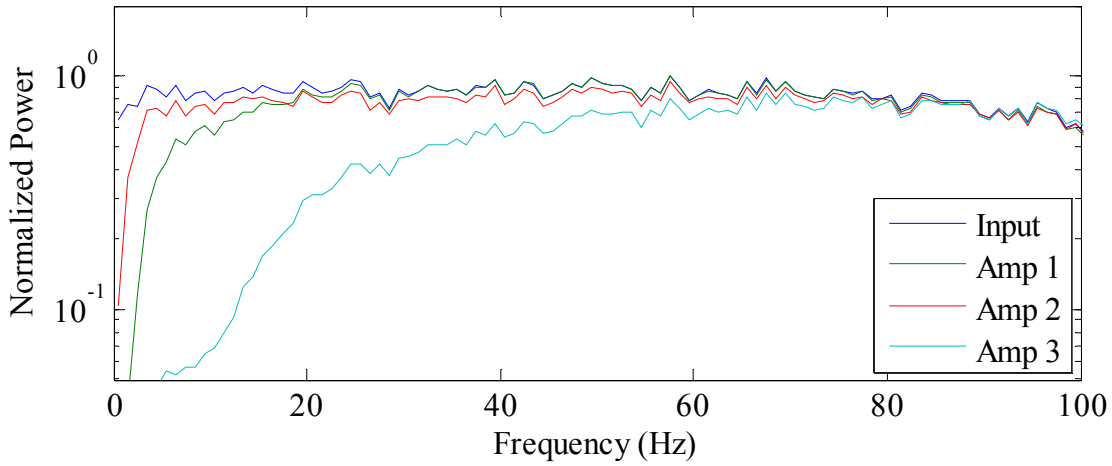

Figure 2.11. Reproduction of burst-random signal by subject amplifiers.

Amp 2 is again the best of the lot and provides output that is nearly identical to the input except below about 5 Hz. Amp 1 is as good as Amp 2 above 20 Hz, but does not reproduce the lowest frequencies as well. Amp 3 does not reproduce the random signal well, significantly reducing the power up to about 50 Hz, and essentially low-pass filtering the signal below 15 Hz.

2.4 QUALITATIVE CHARACTERISTICS OF SHAKERS AND AMPLIFIERS

In addition to the laboratory testing results, cost, perceived durability, and ease of use are also important characteristics to consider in the performance evaluation of the system components. The cost of the components is a major consideration since one of the main objectives in the development of this system is that there should be a low cost per channel, enabling the use of

many shakers in MIMO testing. Durability is also a serious consideration since the expectation is that these devices will frequently be deployed in the field where items are routinely dropped and where dirt and moisture cannot be avoided. Ease of use is important as it applies to quick and simple setup. Field deployment of the excitation system demands rapid setup and reliable connection characteristics.

The performance of Shaker 1 was the best from the laboratory studies; however, it costs nearly five times more than Shaker 2 while only providing about twice the force. Shaker 1 also requires more power input per pound of force output, necessitating a larger amp and increased power generation capacity. From a consideration of durability, Shaker 1 has a rugged housing, but air vents near the base could allow moisture and detritus to enter the unit. This shaker is very easy to connect with integral posts that accept either a bare wire or a banana plug. Overall, Shaker 1 is somewhat costly, but seems reasonably rugged and is easy to use.

Shaker 2 is significantly less expensive than any other device and can be paired with Amp 3 since this shaker has low power requirements. The cost of this combo per channel would be about $90. Additionally, Shaker 2 has a rugged housing with no air vents or other penetrations making it the most likely to have a high resistance to the rigors of repeated field use. Finally, Shaker 2 has posts that accept bare wire connections so setup is as fast as Shaker 1. Overall, Shaker 2 provides the best cost, seems the most rugged, and is easy to use.

Shaker 3 does not compare well relative to the other TTs. The cost of this shaker is more than twelve times greater than Shaker 2, it does not have a housing to protect it, and it has a delicate load plate system that can easily be damaged by the application of lateral loads (per the manufacturer). It appears as if it is intended for a laboratory environment. Also, the need to add

mass plates requires more items to be taken to the field and makes installation more complicated. This shaker also has an integral lead wire that requires addition of a connector for speedy field setup. Overall, Shaker 3 is expensive and is not a good choice for field use.

Amp 1 and Amp 2 are both very similar units in that they have a comparable size, similar controls and connections, and comparable power ratings (per channel). However, Amp 2 provides a much better cost in that a single unit can drive two shakers with separate signals whereas Amp 1 can only handle one excitation signal. This results in a cost per input location of $60 for Amp 2 compared to $150 for Amp 1. Amp 3 is of a different form than the other two and cannot compete with their power output. However, paired with Shaker 2, Amp 3 has an opportunity to provide a very low cost array of shakers for excitation of structures with fundamental frequencies greater than about 15 Hz.

2.5 CONCLUSIONS

The laboratory tests and other device attributes discussed herein were intended to characterize various alternative components for the TT-based excitation system and evaluate the suitability for field testing in a quantitative manner. In the final analysis, low frequency response is the most important segment of the spectrum for the intended bridge testing. As such, Shaker 1 and Amp 2 are the best choice since they have the best signal reproduction of the tested devices at low frequencies. Shaker 1 not only provides the highest forces at low frequencies, it also has the flattest force peak around its own natural frequency, and imparts low noise to determinate and stochastic signals. Both Amp1 and Amp 2 are powerful enough to drive the selected shaker, but Amp 2 has better gain at low frequencies, imparts less noise at low frequencies, and is far less expensive. Price, perceived durability, and ease of use are also considered and also support

selection of Shaker 1 and Amp 2. These devices are evaluated in subsequent chapters for MIMO EMA characterization of a large-scale laboratory model and a full-scale highway bridge.

CHAPTER THREE

IN-DEPTH CHARACTERIZATION OF SHAKER AND AMPLIFIER

3.1 INTRODUCTION

One major objective of this thesis is to optimize the multi-shaker excitation system for MIMO EMA of short to medium-span bridges. The previous chapter quantified the operating and performance characteristics of proposed system components. In this chapter, additional testing of the best shaker and amplifier combination is undertaken. The primary goal of the testing program presented herein is to determine if a dedicated force transducer is required at each input location for MIMO EMA. Ideally, the force output could be adequately characterized through controlled testing in the lab; however, this hypothesis must be systematically evaluated to determine if force transducers can be neglected. A secondary goal is to determine if the selected shakers and amplifiers are uniform enough across their population that they can be used interchangeably.

To maintain a low system cost, it is desirable that force transducers not be used at each shaker location. The use of force transducers not only requires the purchase of at least one transducer per shaker, but each transducer also requires a data acquisition channel. Additionally, field setup of the system is more complex if transducers are needed since an additional cable must be run for each shaker location. However, the force input at each shaker location must be known in order to calculate modal scaling and thus find modal flexibility. It is theorized that if the shakers and amplifiers operate in a highly consistent manner, then the force output for a given input signal can be measured in the laboratory and then assumed to be the same in field testing operations.

The literature on using shakers of various types in structural testing is diverse; however, the literature on testing and documenting the operation of shakers is scarce. Lang (1997) provides

significant discussion on the complexities of the interactions between the changing magnetic field and the motions of the armature in electrodynamic shakers, including equations for the change in impedance depending on frequency and load. Lang also provides test methods for determining the natural frequency, damping, and armature mass for shakers with accessible armatures. Rao (1987) builds on the efforts of several researchers in an effort to explain the phenomenon of shaker force drop off when the natural frequency of a structure is reached. He provides some recommendations on minimizing the issue during testing. Varoto and Oliveira (2002) provide further theoretical developments for the interactions that occur between a shaker and the object being excited. They note that the force drop off of the shaker is exacerbated by the use of voltage mode, which is the mode that all audio amplifiers use. Tustin (1991) discusses how shakers are limited by their available stroke and provides equations for estimating how much stroke is needed for a desired frequency. None of these authors provide guidance on whether force output can be considered to be deterministic since in practically all previous applications, the use of a force transducer was simply assumed. Therefore, a process is developed herein to establish the necessity of using force transducers with the novel MIMO EMA system.

A testing framework is developed and undertaken to establish if the force developed by a shaker can be known without recording the force during every use. The tests establish how consistently each shaker and an each amplifier reproduce a given signal, how uniform a population of 'identical' shakers and amplifiers is, and if the force output varies depending on the behavior of the structure or on the input location on the structure. A variety of tests are performed and the results are reported in subsequent subsections.

First, the selected shaker is subject to several tests to understand how uniformly a single shaker can repeatedly reproduce a signal:

- Uniformity of force output for a single shaker - 3.2.1
  - With a deterministic signal - 3.2.1.1
  - With a stochastic signal - 3.2.1.2

Second, a population of the shakers is tested to determine how uniformly these 'identical' devices operate:

- Uniformity of force output for a population of shakers - 3.2.2
  - With a deterministic signal - 3.2.2.1
  - With a stochastic signal - 3.2.2.2

Third, the effect of shaker-structure interaction on the uniformity of force output for a given input signal is evaluated:

- Uniformity of force output with the effects of shaker-structure interaction - 3.2.3

Similar testing of the selected amplifier is also carried out:

- Uniformity of signal output for a single amplifier - 3.3.1
- Uniformity of signal output for a population of amplifiers - 3.3.2
- Uniformity of signal output with the effects of both amplifier channels loaded - 3.3.3

Finally, an effort is made to model the response of the system components by use of deterministic equations:

- Use of a deterministic equation to model response of components - 3.4.1

- Equation development for amplifier - 3.4.1.2
- Equation development for shaker - 3.4.1.3

3.2 SHAKER TESTING

The following tests are undertaken to first determine how uniform the force output of a single shaker is, and how similar the output of a population of shakers is. This testing also explores if the response of a structure affects the force output measurement.

3.2.1 Shaker Force Output Uniformity

The first issue explored is whether a single shaker consistently produces the same force output for a given input signal. This is of utmost importance because if the force output has significant variation from data set to data set, then a force transducer would have to be used for every shaker during every run. The testing is performed using two types of input signals that are expected to be commonly used in bridge testing. These are swept-sine and burst-random signals, and the issue is explored separately for each of these two signal types.

3.2.1.1 Shaker Stepped-Sine Signal Reproduction Uniformity

3.2.1.1.1 Test Method

The first test consists of checking the force output given a variety of frequencies of sinusoidal input. A shaker is mounted to a test plate which is in turn mounted to the relatively massive and very stiff steel pylon (Figure 3.1). The force output is measured by three force transducers as described in the previous chapter. Both the input signal to the shaker and the force output are recorded at a 1,000 Hz sampling rate. The input signal consists of sinusoids at twenty discrete frequency lines ranging from 6 Hz to 44 Hz at 2 Hz steps. Each frequency line is individually excited for a duration of six seconds, and the signal then transitions directly to the next frequency

without any pause or delay. The amplitude of the input signal at the various frequencies is selected with the intent that the shaker operate at about 80% of its capacity. For frequencies up to 20 Hz, the amplitude is limited so that the shaker does not bottom out. For frequencies above 20 Hz, the amplifier output limit of approximately 30 volts is used. The input signal is shown in Figure 3.2 and it is referred to as the stepped-sine signal throughout this chapter. This 120-second long input signal is sent to each shaker three times, and three output data files are recorded.

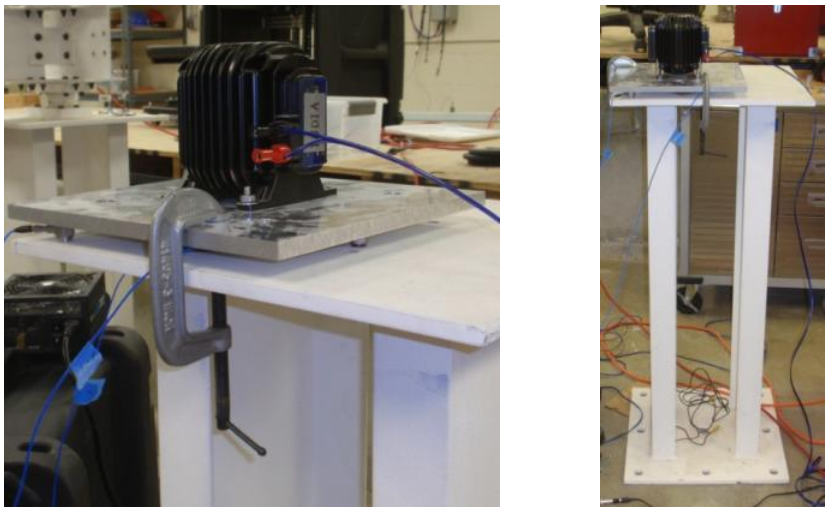

Figure 3.1. Photographs of shaker testing setup on steel pylon. (Photos by EVF, dynamics lab, 11/20/12)

This testing is undertaken in a manner such that everything is uniform from run to run so that only the differences due to the shaker response and due to random noise are expected to impact the output. The signal input file was created and loaded onto the Agilent Arbitrary Signal Generator. The signal is amplified by a single channel of an amplifier and then input into a single shaker. This testing is performed on a population of twelve shakers.

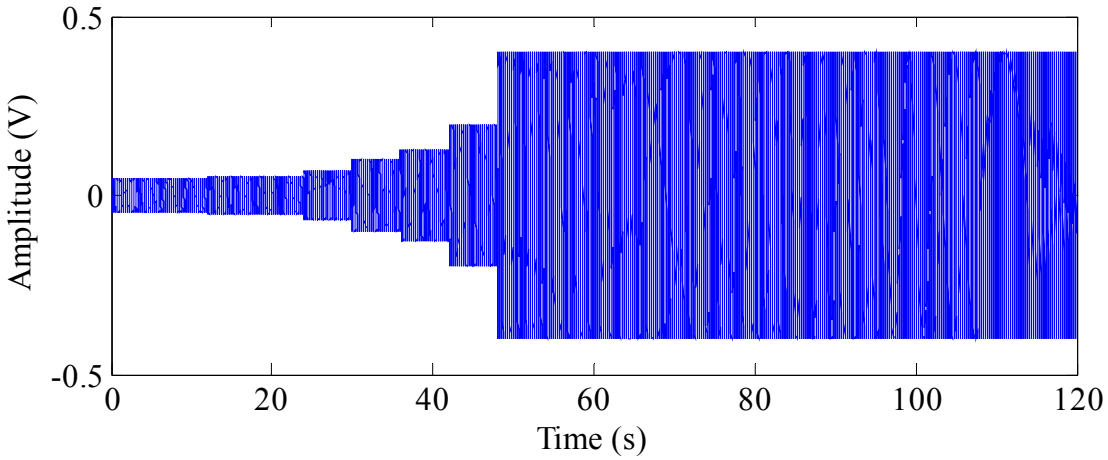

Figure 3.2. Plot of stepped-sine input signal showing lower amplitudes at lower frequencies to limit stroke.

3.2.1.1.2 Analysis and Results

The three sets of data captured for an individual shaker are scrutinized to understand how uniform the force output is with the same shaker reproducing the same signal three times in a row. First, the three sets are averaged and then the difference between each set and the average is found. Then, the RMS value of this difference is calculated for the 6,000 data points within each frequency line for each of the three sets. Finally, the resulting values are divided by the RMS value of the average force output per frequency line to normalize the result. The following equations illustrate this concept.

$$Mean = \frac{1}{n}\sum_{a=1}^{n} Sig(a) \qquad \text{Equation 3.1.}$$

$$RMS_{mean} = \frac{1}{L}\sum_{i=1}^{L} |Mean(i)| \qquad \text{Equation 3.2.}$$

$$RMS_{var}(a) = \frac{1}{L}\sum_{i=1}^{L} |Mean(i) - Sig(a)| \qquad \text{Equation 3.3.}$$

$$Normalized\ Variance(a) = \frac{RMS_{var}(a)}{RMS_{mean}}$$ Equation 3.4.

Where:

$n =$ the number of sets of data.

$Sig(a)$ = the force recording data set, set 'a'.

$L =$ the number of data points within a single excited frequency line.

The outcome is illustrated in Figure 3.3 where the results are shown for four representative shakers. The significant variance in force output represented by shakers A and B occurs in four of the twelve shakers. The more uniform results shown for shakers H and I are representative of the remainder of the 12 shaker sample. Based on these initial results, it is clear that the data must be considered in more depth to understand why the variation is so great for some of the shakers.

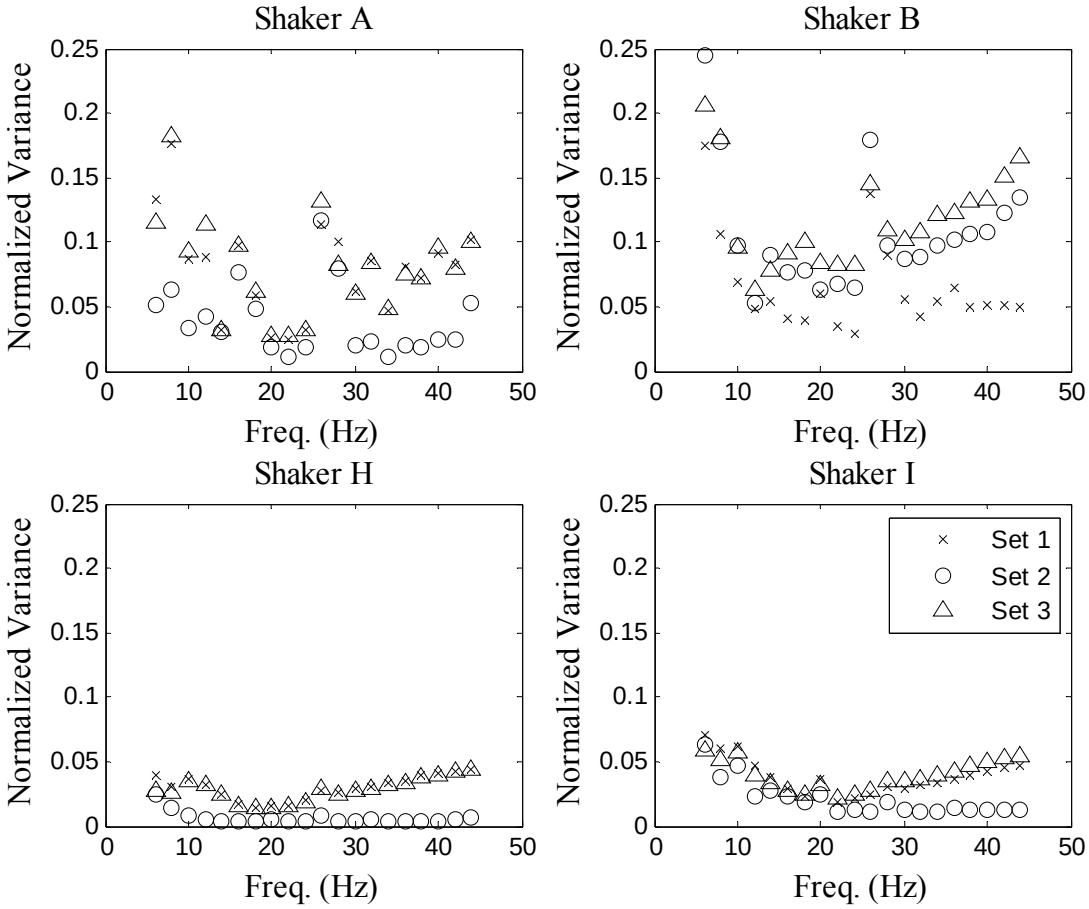

Figure 3.3. Normalized variance in RMS force output amplitude for three sets of stepped-sine input. Representative results for four shakers shown.

Next, in an effort to drill down to the cause of the large variation in force output, the force data is viewed directly. Considering the variance for Shaker A, Figure 3.3 shows good agreement between the three sets at the 20 Hz frequency line and poor agreement at the 26 Hz frequency line. To understand how this looks in the time domain force recording, representative samples of the three data sets are considered. Figure 3.4 shows two cycles of the three sets at 20 Hz and it is clear that the force is highly consistent in both phase and amplitude. Figure 3.5 shows two cycles of the three sets at 26 Hz and the difference compared to the 20 Hz data is immediately apparent. The figures demonstrate that the primary signal is both in-phase and consistent in amplitude for the case of low variance and for the case of high variance. This shows that the high variance

calculated for the time domain force signal is caused by the noise present in the sample, not by any significant difference in the force response of the shaker to the input signal. It is noted that a natural frequency of the support apparatus is excited in the vicinity of 26 Hz as is audibly apparent during testing, and thus the variance is high at this frequency for all shakers.

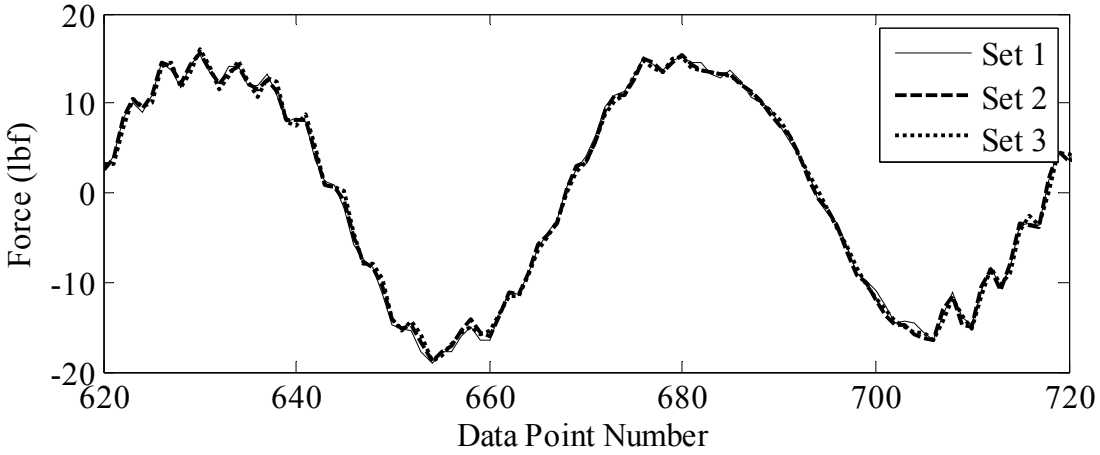

Figure 3.4. Representative segment of force output for three sets of data for Shaker A operating at 20 Hz. Note the excellent agreement.

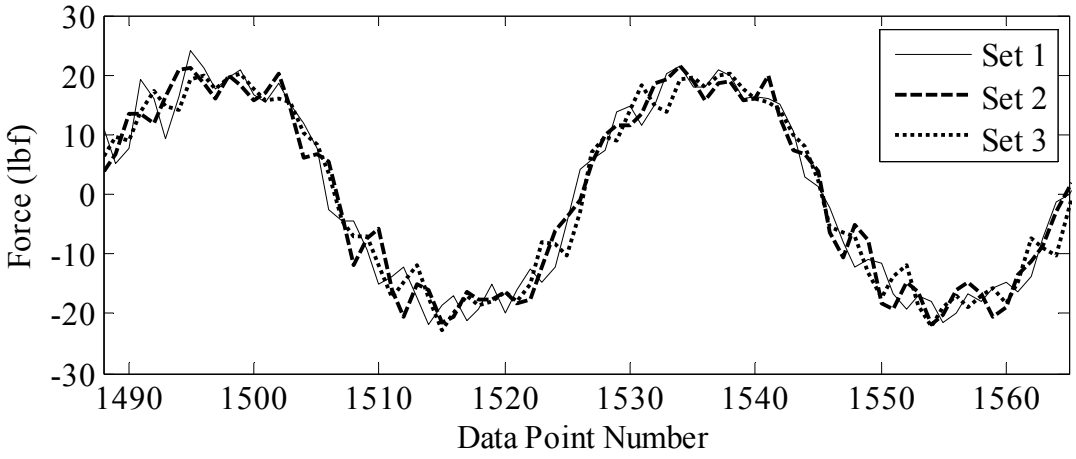

Figure 3.5. Representative segment of force output for three sets of data for Shaker A operating at 26 Hz. Note the increased noise.

The preceding demonstrates that time domain measures of variance in the force signal are not especially informative as to the homogeneity of the shaker output. Therefore, frequency domain methods will be considered. The benefit of transforming the data to the frequency domain is that

the primary signal will be separated from the noise constituents. This will enable a more direct comparison of the amplitude and phase variation of the part of the signal that is at the intended frequency.

Thus, the data is transformed to the frequency domain by performing a fast Fourier transform. Again, the three sets of force measurements for Shaker A at 20 Hz and 26 Hz are inspected to understand the general agreement between the data sets.

Figure 3.6 shows the result for the 20 Hz data, and it is clear that the power at the input frequency is far greater than at any other frequency. Harmonic distortion appears to be responsible for the predominance of the noise with power spikes visible at the next few multiples of 20 Hz; however, the power at these harmonics is less than a tenth of the power at the intended frequency. The consistency of the three data sets is such that it is difficult to distinguish any differences. Figure 3.7 shows the results for the 26 Hz data, and although the time domain analysis and plots clearly indicate more noise, the frequency domain plot provides a good indicator of how minor that noise is in relation to the power of the intended signal. Figure 3.8 shows a close-up plot of the peaks at 20 Hz and 26 Hz for the three sets with the phase angle also labeled. The scale is the same for both plots which illustrates that the variance in force is much greater at 26 Hz than at 20 Hz, just as was noted in the time domain plots.

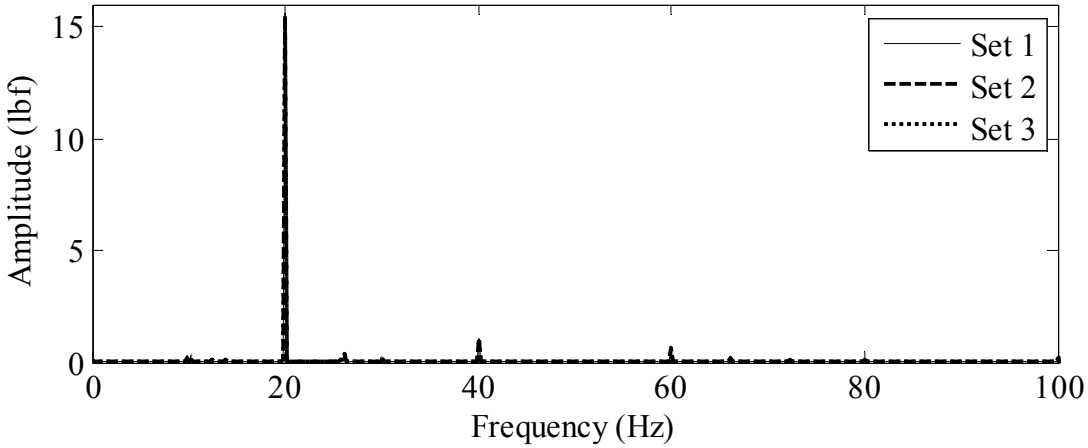

Figure 3.6. Frequency domain plot of force output for three sets of data for Shaker A operating at 20 Hz. Sets are indistinguishable.

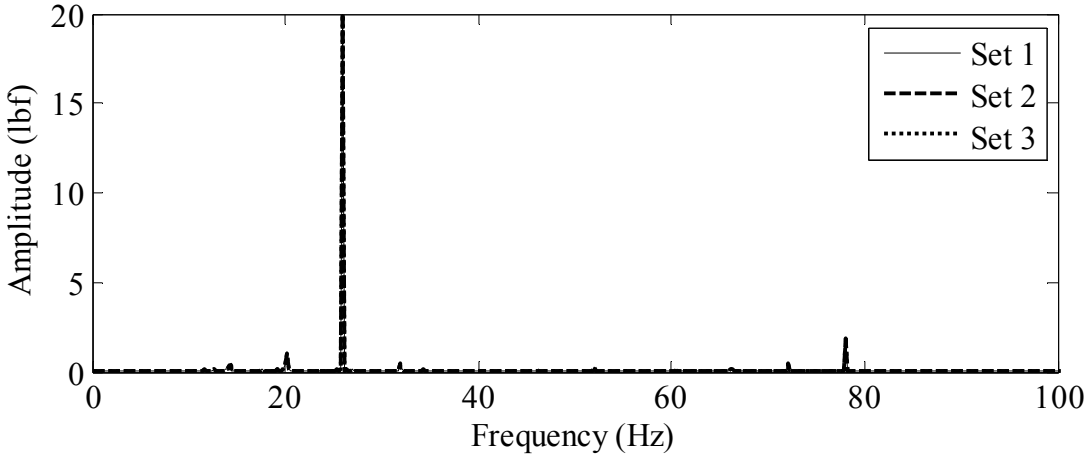

Figure 3.7. Frequency domain plot of force output for three sets of data for Shaker A operating at 26 Hz. Sets are indistinguishable.

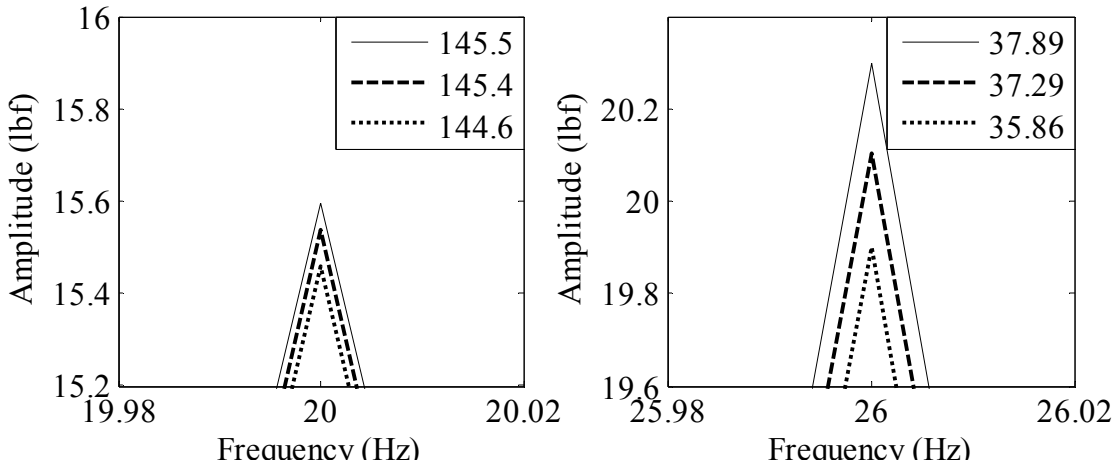

Figure 3.8. Close-up of peaks at 20 Hz (left) and 26 Hz (right). Scale of two plots is identical and illustrates the greater variance at the 26 Hz frequency line. (Phase angle shown in legend)

Finally, proceeding with frequency domain analysis of the shaker uniformity, Fourier transforms are performed for all frequency lines. At a given frequency line for a single shaker, the amplitude and phase angle for each of the three data sets is recorded. Next, the mean of these three amplitudes and phases is found, and then the average variance from the mean is found for force amplitude and for phase angle. Finally, the mean variance in force is normalized by dividing by the mean force, and the mean variance in phase angle is normalized by dividing by the 180-degree range of possible phases.

Overall, this data analysis shows that an individual shaker is not perfectly consistent in how it reacts to a sinusoidal input signal, but that the consistency is quite high. Figure 3.9 shows the average variation in magnitude and Figure 3.10 shows the variation in phase angle for each excited frequency line. This data is displayed for each of the twelve shakers with three shakers shown per plot for clarity. The variation in amplitude across the frequency range follows a very consistent shape for all twelve shakers, with more variance at low frequencies and less at higher frequencies. Below about 16 Hz, the variance reaches a maximum of about 2% of the RMS

amplitude of the force. Above 16 Hz, the variance does not exceed 1% for any of the shakers. The phase angle results indicate that the lower the frequency, the more consistent the phase. For nine of the shakers, the normalized variance in phase angle never exceeded 1% for any tested frequency line; however, three of the shakers have a variance that is about three times as great, reaching 3%.

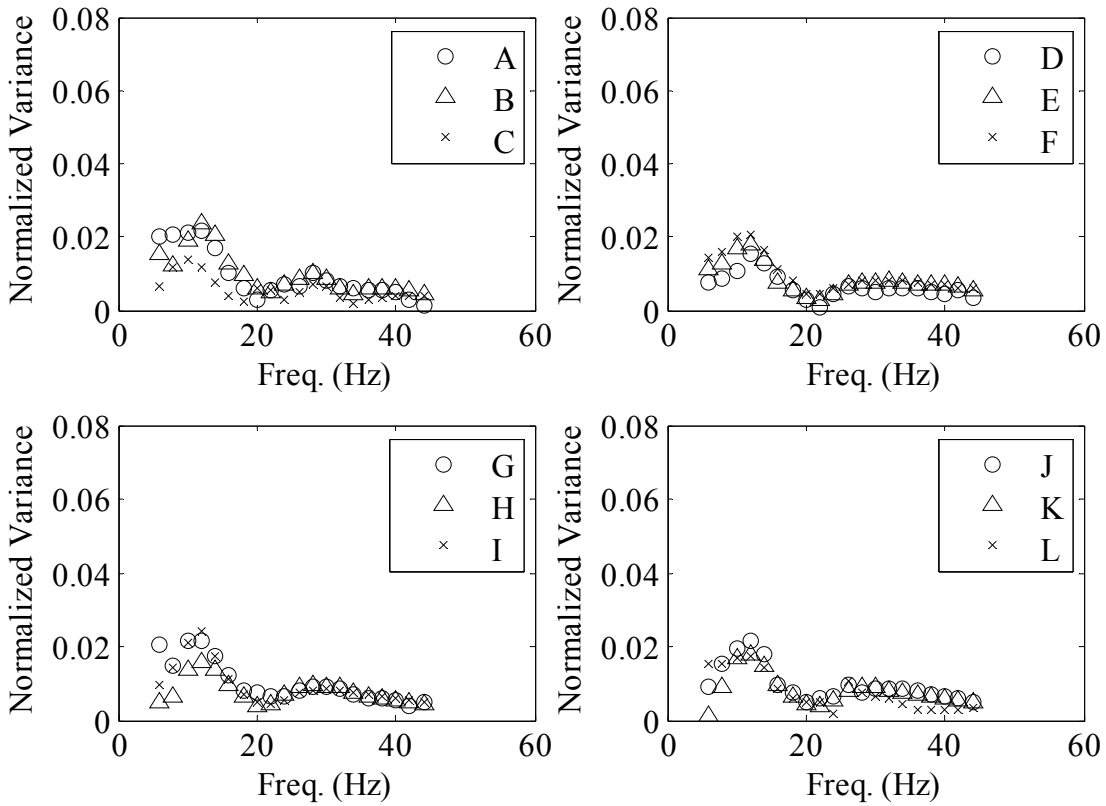

Figure 3.9. Normalized variance in force amplitude for twelve shakers.

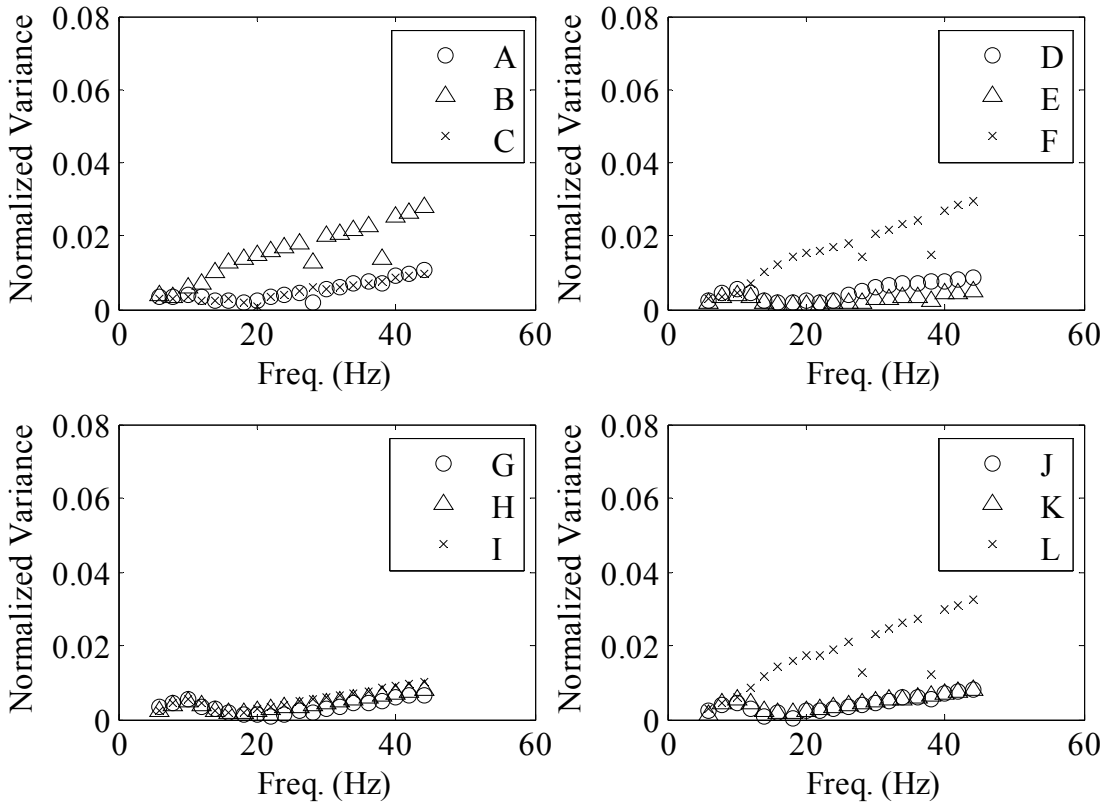

Figure 3.10. Normalized variance in phase angle for twelve shakers.

The data analysis indicates that an individual shaker can be relied upon to react to a sinusoidal input in a fairly consistent manner time after time. In general, the force amplitude does not vary by more than 2% from one run to the next, and the phase angle does not vary by more than 3%. The maximum mean normalized variance is approximately 1% for the population of 12 shakers.

3.2.1.2 Shaker Random Signal Reproduction

3.2.1.2.1 Test Method

The second test is checking the force output given a random input signal. Similar to the sinusoid testing, the signal is loaded onto the Agilent Arbitrary Signal Generator and amplified by a single channel of an amplifier. A single shaker is tested while mounted to the test apparatus described

previously. The test is repeated three times for each of the twelve shakers and the data is then processed in MATLAB.

The random input signal is generated in MATLAB starting with 60,000 random numbers selected from the normal distribution with an RMS value of unity. The intent is to convert this vector into a filtered random signal that will have a duration of 120 seconds with 500 points defining the shape of the signal per second. High frequency content is not desired and is reduced using a fifth order Butterworth filter with a cutoff frequency of 50 Hz. It is also desirable to reduce the signal amplitude at frequencies below 20 Hz where the shakers are stroke limited. This will allow the full duration of the signal to be input to the amplifier at a higher amplitude without having the shakers bottom out. Thus a second order high pass filter is applied with a cutoff frequency of 20 Hz. The unfiltered signal is shown in Figure 3.11 and the filtered signal is shown in Figure 3.12. The resulting filtered signal is used repeatedly in the testing described in this chapter and it is referred to as the random signal.

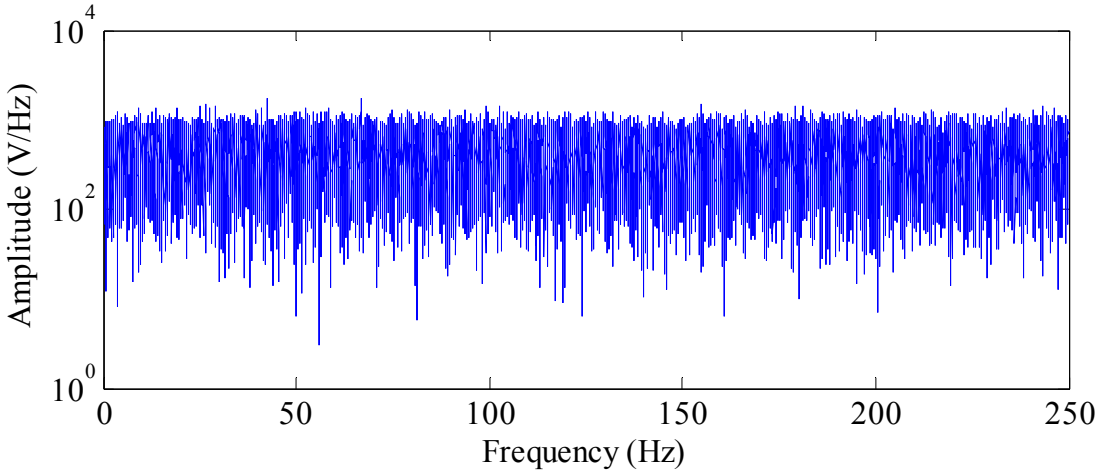

Figure 3.11. Random signal in frequency domain prior to filtering.

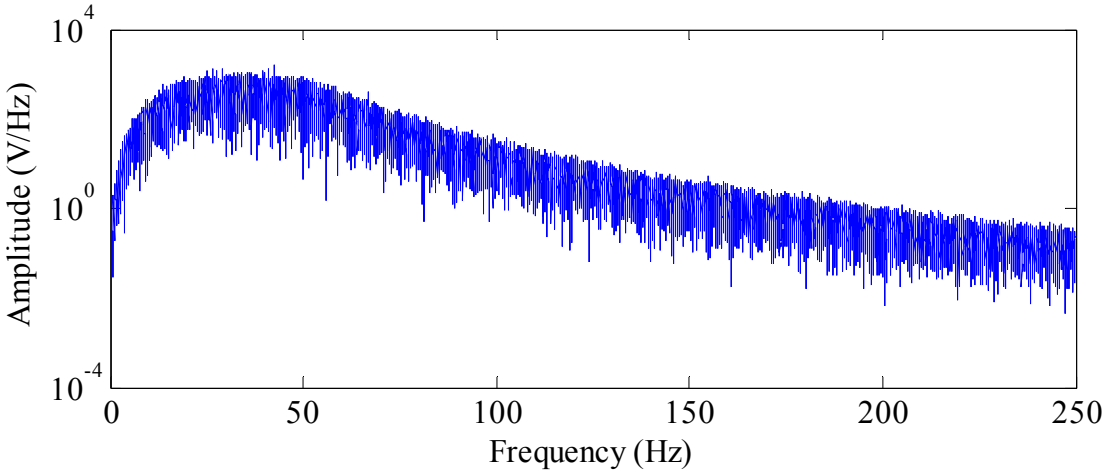

Figure 3.12. Random signal in frequency domain after filtering.

3.2.1.2.2 Analysis and Results

The three sets of data captured for an individual shaker are processed to understand how uniform the force output is with the same shaker reproducing the same signal three times in a row. Figure 3.13 shows a representative segment of the three sets of time domain data for Shaker L. The agreement between the sets appears to be excellent.

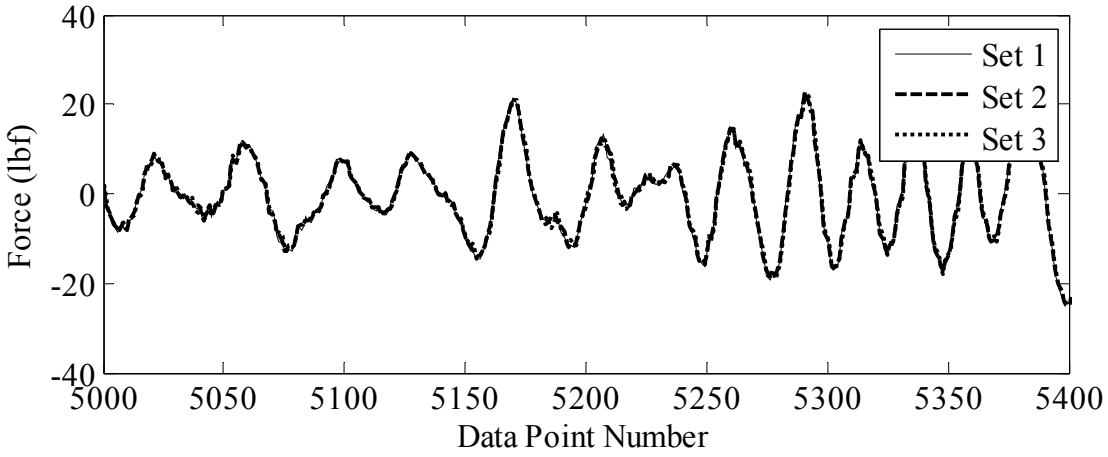

Figure 3.13. Representative segment of force output for three sets of data for Shaker L with random input.

Next, each force recording is transformed to the frequency domain to enable comparison of the sets for the full signal length. The mean of the three data sets is found, and then the variance

from the mean is found for force amplitude. Finally, the variance in force output is normalized by dividing by the mean force.

The outcome for two representative shakers is shown in Figure 3.14. The data analysis shows that an individual shaker is not perfectly consistent in how it reacts to a random input signal, but that the uniformity is quite high. The variation in amplitude across the frequency range follows a very consistent shape for all twelve shakers, with more variance at low frequencies and less at higher frequencies, similar to the outcome for the sinusoidal input testing. Below about 16 Hz, the variance reaches a maximum of about 2% of the force amplitude. Above 20 Hz, the variance typically does not exceed 1%. It is worth noting that the force decreased as each successive run occurred. The pattern shown in the figure is consistent for all twelve shakers, with the first data set providing the highest force, the second set producing a reduced force, and the third set even less force. It is theorized that the force decrease is due to the increase in temperature of the voice coil during the testing. A temperature increase would increase the resistance which would decrease the current in the coil. Electrical current in a voice coil is directly proportional to force output. A simple solution that would reduce variance is to run the shakers for several minutes to bring them up to operating temperature, and then immediately transition to testing.

An experiment is undertaken to test this theory in which Shaker J is allowed to warm up by using a 25 Hz sinusoid for three minutes prior to recording four new data sets. The results are shown in Figure 3.15, and the difference in force from set to set is reduced but is not eliminated. The force still decreases for each run performed. This indicates that a longer use is required to adequately warm the devices in preparation for testing.

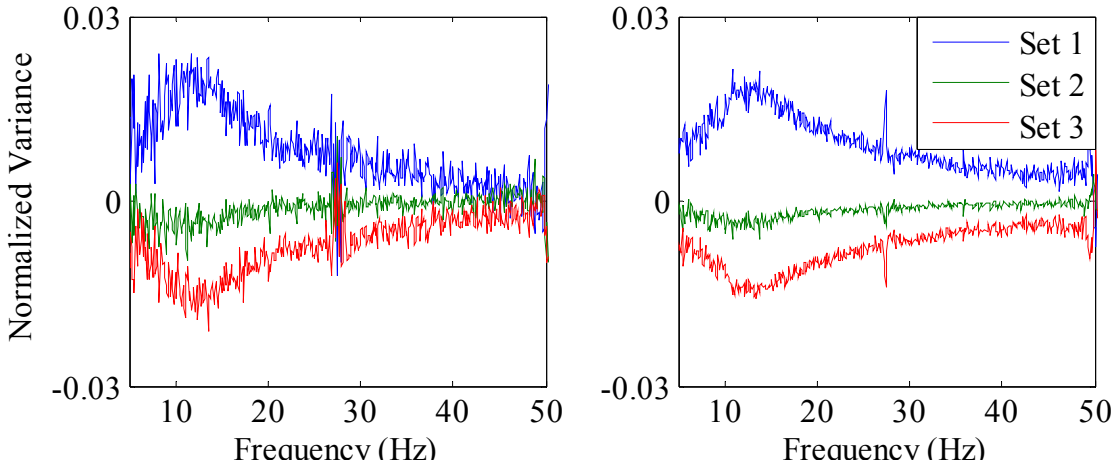

Figure 3.14. Normalized variance in force amplitude for three sets of random input. Representative Shaker B (left) and Shaker J (right) shown.

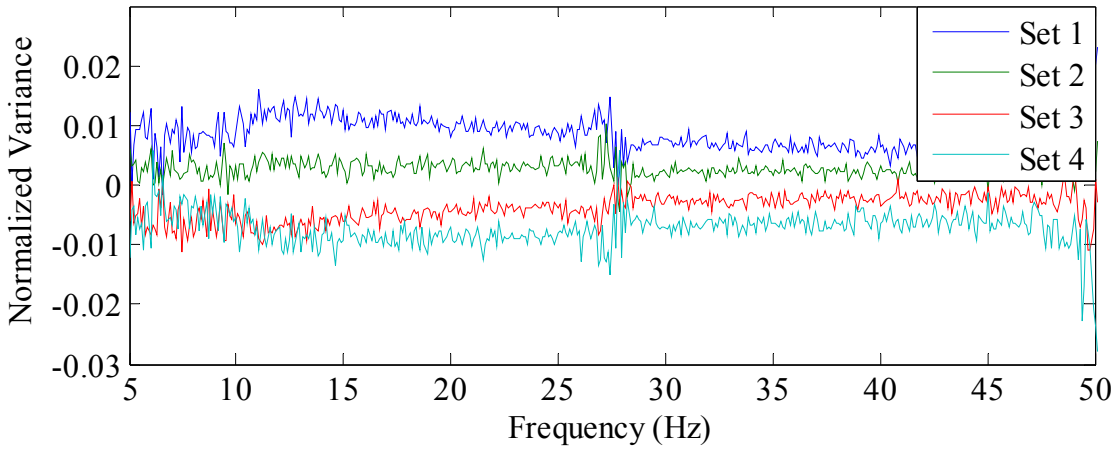

Figure 3.15. Normalized variance in force amplitude for four sets of random input, Shaker J. Shaker warmed up prior to this test.

3.2.1.3 Shaker Force Output Uniformity Conclusions

The ability of a shaker to consistently produce the same force output for a given signal input was tested. Both sinusoidal and random signals were used and the force output was recorded and analyzed. The results are that the shakers perform in a highly consistent manner. With sinusoidal input, the variance in force amplitude is typically less than 2%, and the variance in phase angle is typically less than 1%. With random input, the variance in force output is also typically less than

2%, and it is likely that a portion of the variance in all of the tests is due to the shaker coil increasing in temperature during testing.

3.2.2 Shaker Interchangeability

The second issue of concern is whether the shakers can be used interchangeably or if they must be considered as individual units. If the force output for a given input is highly consistent across a population of shakers, then the shakers can be deployed in testing without regard for which shaker is put in what location on a structure. This type of interchangeability would greatly simplify field testing since no special care would be needed for placing the shakers and documenting their individual positions. On the other hand, if the shakers are highly individual then a unique force output must be developed and stored for each shaker for each input signal used. This would add significant effort in using these devices for testing. The ability of the shakers to be interchanged is explored using both the stepped-sine and random input signals already discussed.

3.2.2.1 Shaker Interchangeability Testing with Stepped-Sine Signal

3.2.2.1.1 Test Method

This test was undertaken in order to understand how similar the force output is from twelve individual shakers for a range of sinusoidal inputs frequencies. The data used is the same as that captured for the testing performed in Section 3.2.1.1. Thus, the test method and data collection provided in that section are pertinent here. To restate the test method, a range of twenty frequencies were used consecutively with a six-second duration for each. This signal was repeated three times for each shaker and the force output was recorded by three force transducers with the shaker mounted on the steel pylon.

3.2.2.1.2 Analysis and Results

The force output recorded for all twelve shakers is first considered in the time domain. Figure 3.16 shows the force trace for four shakers at 14 Hz and Figure 3.17 shows the same but at 20 Hz. These two frequencies are selected for visualization since the previous section indicates that amplitude variance is relatively high at 14 Hz and relatively low at 20 Hz. For each shaker, the force trace shown is the mean of the three data sets.

The two force traces clearly show that there is more amplitude variation from shaker to shaker than was found between sets for a single shaker. It is also clear that phase differences are minor. It is of note that the twelve shakers were purchased in small quantities over a time range of about one year. The first four shakers purchased consistently provide less force than those acquired later, and are also 180 degrees out of phase compared to the later models (the phase flip was corrected prior to plotting). Thus, it can be inferred that the manufacturer updated the model between production runs. Since these types of changes are likely to occur in the future as well, interchangeability will be a difficult issue to resolve as new shakers are added to the testing system or old shakers are replaced.

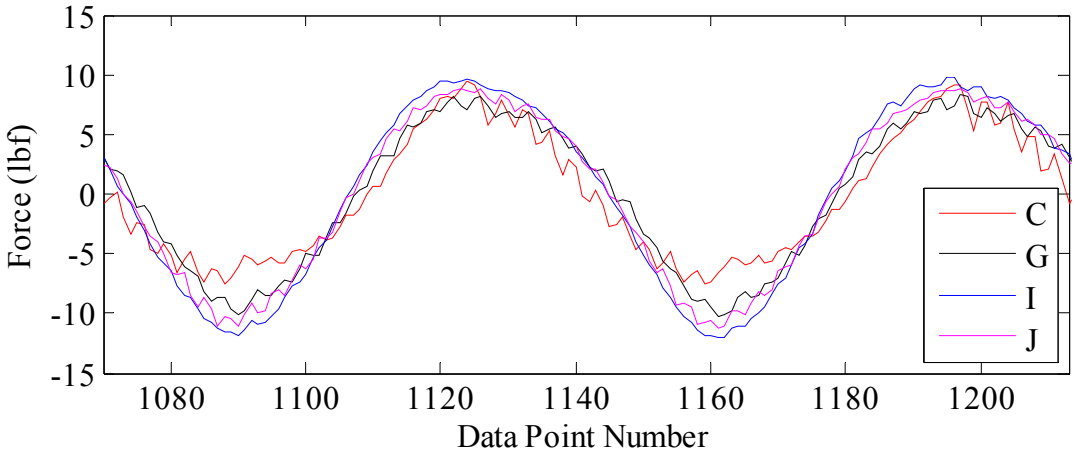

Figure 3.16. Representative segment of force output signal for four shakers operating at 14 Hz.

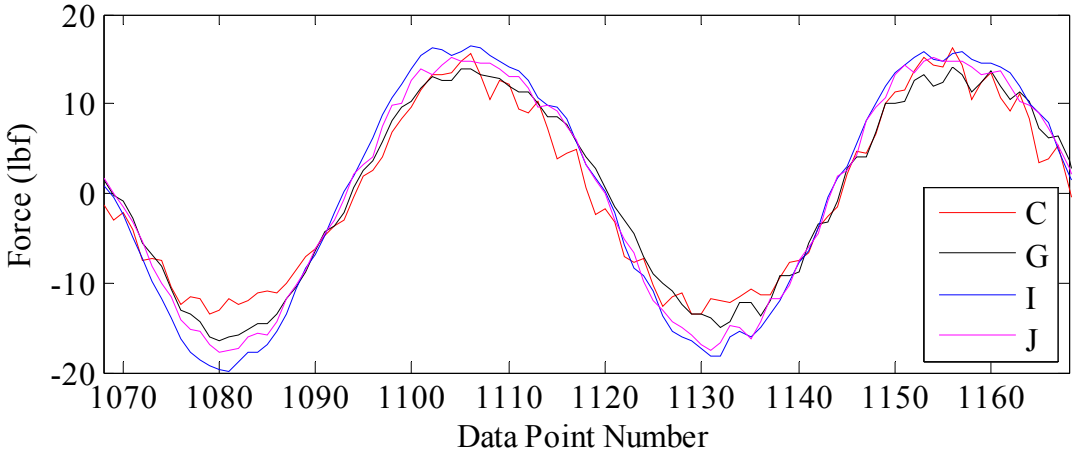

Figure 3.17. Representative segment of force output signal for four shakers operating at 20 Hz.

Next, the variation in force and phase angle between shakers is analyzed in the frequency domain as was done in the previous section. A Fourier transform is performed for each frequency line for each shaker and the amplitude and phase are recorded. Since the sample size is twelve for this analysis, the mean and variance are calculated assuming a t-distribution. The 90% confidence interval is then calculated at each frequency line as an indicator of the variability in the data. The t-distribution equations used are shown.

$$\bar{x} = \frac{x_1 + \cdots + x_n}{n} \qquad \text{Equation 3.5.}$$

$$s^2 = \frac{1}{n-1}\sum_{i=1}^{n}(x_i - \bar{x})^2 \qquad \text{Equation 3.6.}$$

$$interval = \bar{x} \pm A\frac{s}{\sqrt{n}} \qquad \text{Equation 3.7.}$$

Where:

$\bar{x}$ = the sample mean.

x_i = a sample value.

n = the number of samples.

s^2 = the sample variance.

A = 1.796 for a 90% confidence interval.

Figure 3.18 shows the values of mean force output for the twelve shakers as well as the 90% confidence interval for the mean at each tested frequency line. The results indicate that there is a fairly wide spread in the force output of the various shakers. Figure 3.19 shows the values of the mean phase angle and the 90% confidence interval. The mean variance for the amplitude is about 7% at lower frequencies and about 6% above 30 Hz. For the phase angle, the mean variance is about 1% for the full range of tested frequencies.

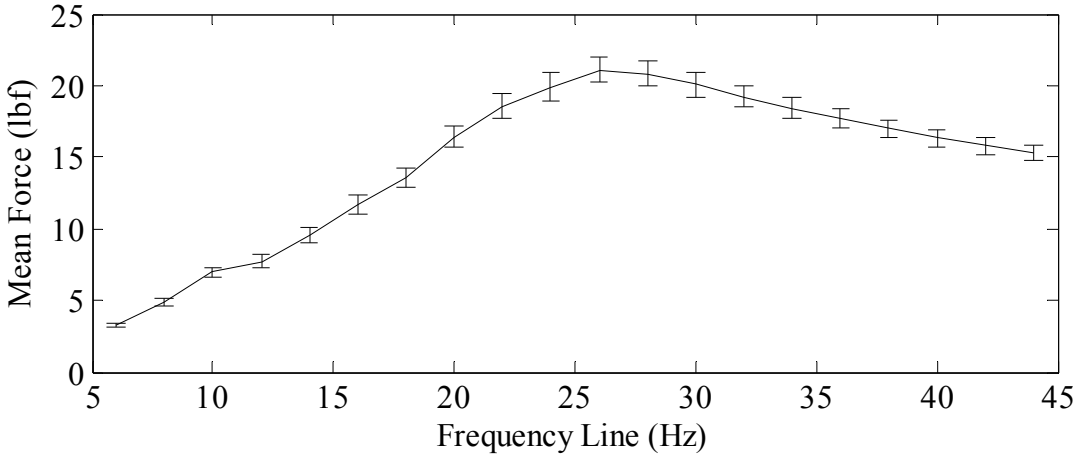

Figure 3.18. Mean force output of twelve shakers at various frequencies with 90% confidence interval shown.

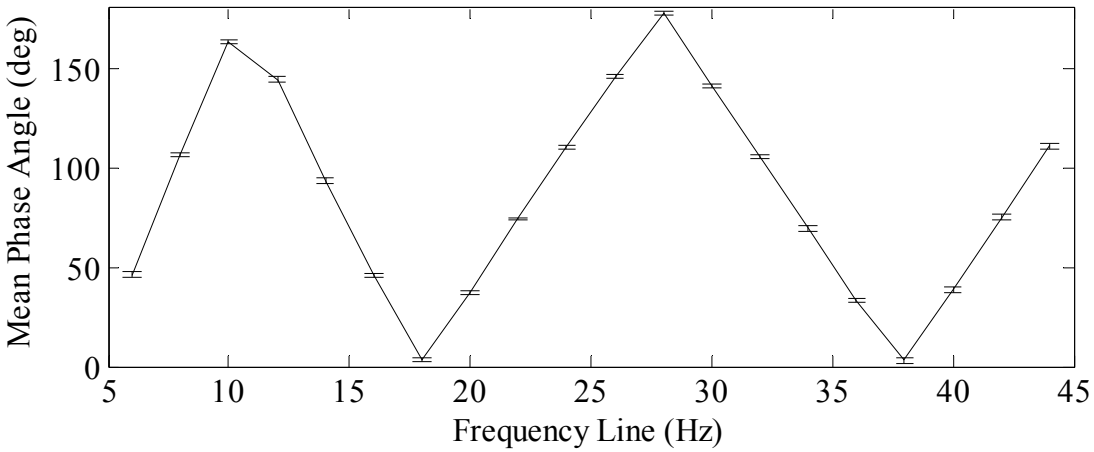

Figure 3.19. Mean phase angle of twelve shakers at various frequencies with 90% confidence interval shown.

Overall, the phase angle is highly consistent between shakers for a sinusoidal input; however, the amplitude is not as uniform.

3.2.2.2 Shaker Interchangeability Testing with Random Signal

3.2.2.2.1 Test Method

This test is undertaken in order to understand how similar the force output is from twelve individual shakers for a random input signal. The data used is the same as that captured for the testing performed in Section 3.2.1.2. Thus, the test method and data collection provided in that section are identical for this section. To briefly restate the method, a random signal from a normal distribution is generated and then band-pass filtered. The signal has a duration of 120 seconds, and is played three times through each shaker. The force output is recorded by three force transducers with the shaker mounted on the steel pylon.

3.2.2.2.2 Analysis and Results

First, the data is considered in the time domain. The three sets of data captured for an individual shaker are averaged and this resultant mean force is then processed to understand how consistent the force output is across the population of twelve shakers. Figure 3.20 shows a representative

segment of the force output for all twelve shakers. The consistency between the sets is similar to what was seen for the stepped-sine reproduction in that the phase matches quite well but the amplitude has more variation.

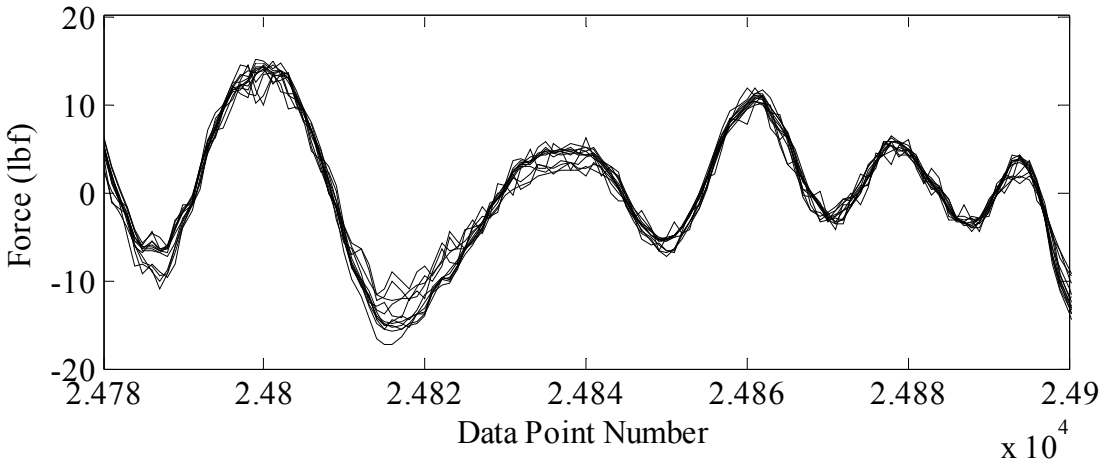

Figure 3.20. Representative segment of force output data for all twelve shakers with random input signal.

Next, the mean time domain data is transformed to the frequency domain. Averaging in the frequency domain is used to reduce the resolution to approximately 0.1 Hz. Then, the mean and variance for the twelve shakers are calculated at each frequency line, and the variance is normalized by dividing by the mean force. Figure 3.21 shows the results of the frequency domain analysis. In general, the data shows that the average shaker has a force amplitude variance that is about 7% off of the mean force across a broad range of frequencies, and this variance is in agreement with the results of the stepped-sine testing.

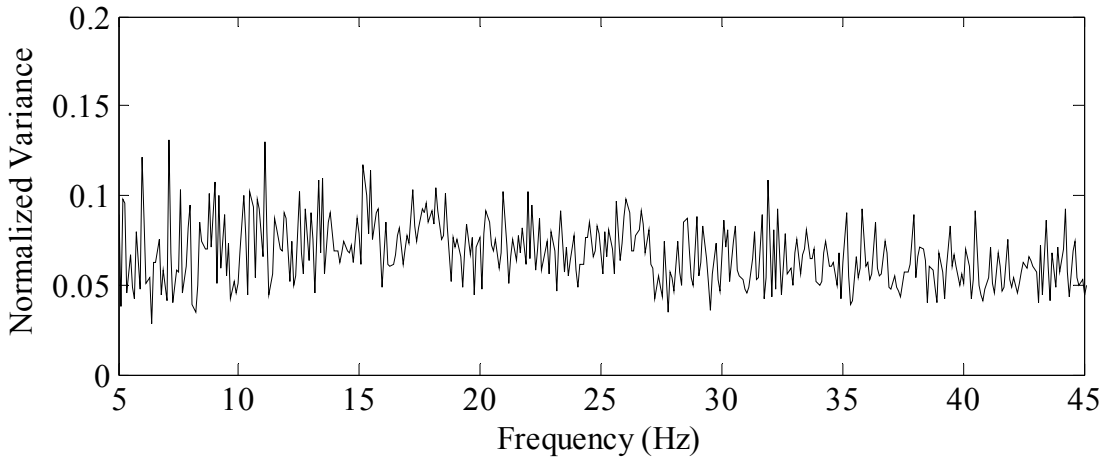

Figure 3.21. Normalized variance in force amplitude for twelve shakers with random input signal.

3.2.2.3 Shaker Interchangeability Conclusion

The ability of the population of shakers to produce a uniform force output for a given signal input was tested. Both stepped-sine and random signals were used and the force output was recorded and analyzed. The results are that the population of twelve shakers operate fairly similarly to each other, but not identically. With the stepped-sine input signal, the variance in the output force amplitude is typically about 7%. With the random input, the variance in force output is also typically about 7%. Therefore, the shakers cannot be used in an interchangeable manner in MIMO testing.

3.2.3 Shaker Force Uniformity on Laboratory Bridge Model

The next issue of concern is whether the force output varies depending on the response of the structure that the shaker is exciting (shaker-structure interaction). The testing of Section 3.2.1 suggests that the force output of a single shaker is uniform within 1% to 2% from one run to the next. In those tests, the shakers were mounted to a stiff steel pylon; however, it must be shown that the stiffness and dynamic response of the structure does not cause significant variation in the force. In this testing, the University's steel grid bridge model is used as the recipient of the

excitation force, and both the stepped-sine and random signals are again used. This testing is conducted with the shaker positioned at two different spatial locations on the model structure, namely the span third-point and the span mid-point along the north fascia girder. These points are selected since the mid-point excitation is then at a node point for the second bending and torsional modes of the model whereas the third-point excitation is not at a modal node for any mode in the frequency range tested. Again, force output needs to be uniform for the use of force transducers to be avoided.

The laboratory bridge model is a steel grid structure composed of W8 shapes. The model is supported on steel rollers and has three beams and a span length of 24'-0". The model has previously undergone modal testing by a variety of methods, and some natural frequencies that are of import to the following discussions are listed below. These are approximations of the natural frequencies reported by Herrman (2011, 144).

Mode No.	Approx. Freq.	Mode Description
1	9.6 Hz	Bending 1
2	10.9 Hz	Torsion 1
3	34.7 Hz	Bending 2
4	39.0 Hz	Torsion 2

Table 3.1. Natural frequencies of laboratory bridge model.

3.2.3.2 Test Method

This testing is performed in a very similar manner to the tests described previously. A single shaker is bolted to an aluminum plate that has three force transducers connected to it and this apparatus is clamped to the bridge model as shown in Figure 3.22. The shaker is powered by a single channel of an amplifier which has a signal input from the Agilent Arbitrary Signal Generator. The same stepped-sine signal described in Section 3.2.1.1.1 is used as is the random

signal described in Section 3.2.1.2.1. Each signal is played three times per shaker, per spatial location. A population of twelve shakers are tested.

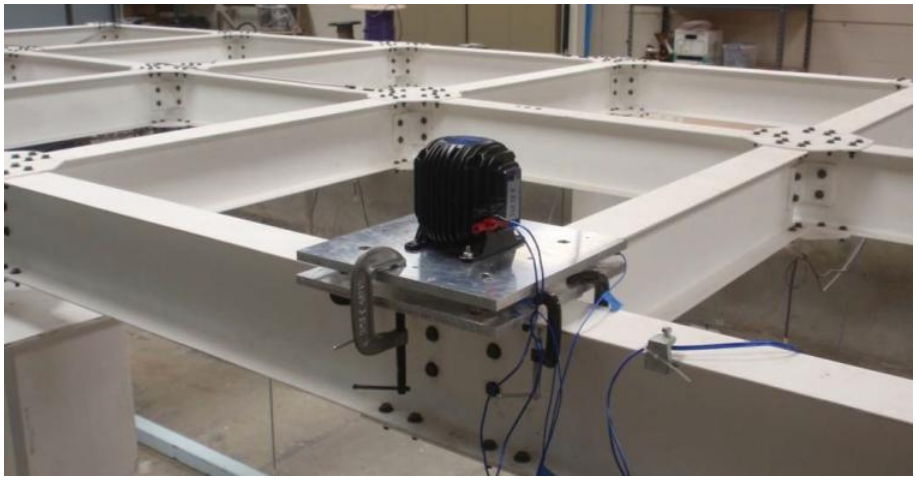

Figure 3.22. Photograph of shaker testing setup on laboratory bridge model. (Photo by EVF, dynamics lab, 11/20/12)

3.2.3.3 Analysis and Results

3.2.3.3.1 Shaker at Span Third-Point with Stepped-Sine Signal

Three sets of data are captured for each shaker with the stepped-sine input signal and the uniformity between these sets is analyzed. The time domain analysis indicates that the force output is more consistent at some frequencies than others. A representative segment of the time domain signal for Shaker B is shown at 22 Hz in Figure 3.23 and at 40 Hz in Figure 3.24. It is visually apparent that the consistency from set to set is excellent at 22 Hz but less so at 40 Hz. The bridge model has a natural frequency for its fourth mode at 39 Hz and this is partially excited by the 40 Hz signal, increasing the apparent noise in the system.

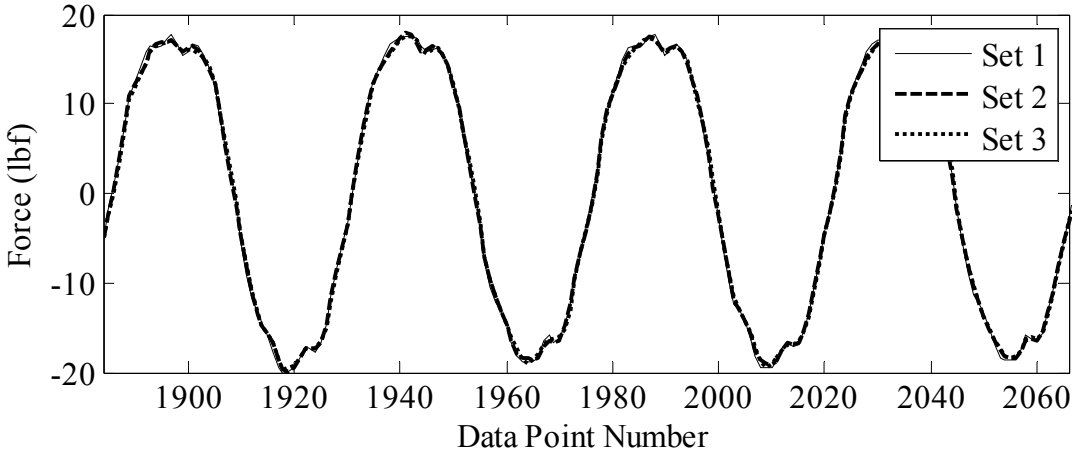

Figure 3.23. Representative segment of force output for three sets of data for Shaker B operating at 22 Hz. Note the excellent agreement.

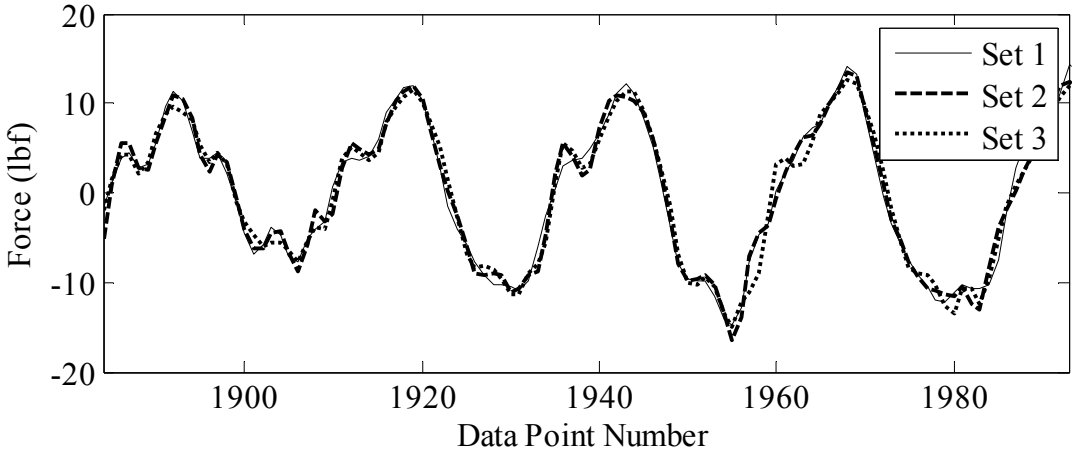

Figure 3.24. Representative segment of force output for three sets of data for Shaker B operating at 40 Hz. Note the increased noise.

Next, the data is transformed to the frequency domain. Frequency domain analysis is used to analyze the variance in force amplitude for all of the shakers. Again, the three sets of force measurements for Shaker B at 22 Hz and 40 Hz are inspected to understand the general agreement between the data sets.

Figure 3.25 shows the frequency domain result for the 22 Hz data, and it is clear that the power at the input frequency is far greater than at any other frequency. The uniformity of the three data sets is excellent. It is also noted that harmonic distortion is responsible for most of the noise with

small peaks visible at 44 Hz and 66 Hz. Figure 3.26 shows the results for the 40 Hz data sets. This plot shows that much of the noise is caused by several known modes of the bridge model being excited: mode 3 at 34 Hz, mode 4 at 39 Hz, mode 5 at 73 Hz, and mode 8 at 88 Hz. The force amplitude at 40 Hz is reduced.

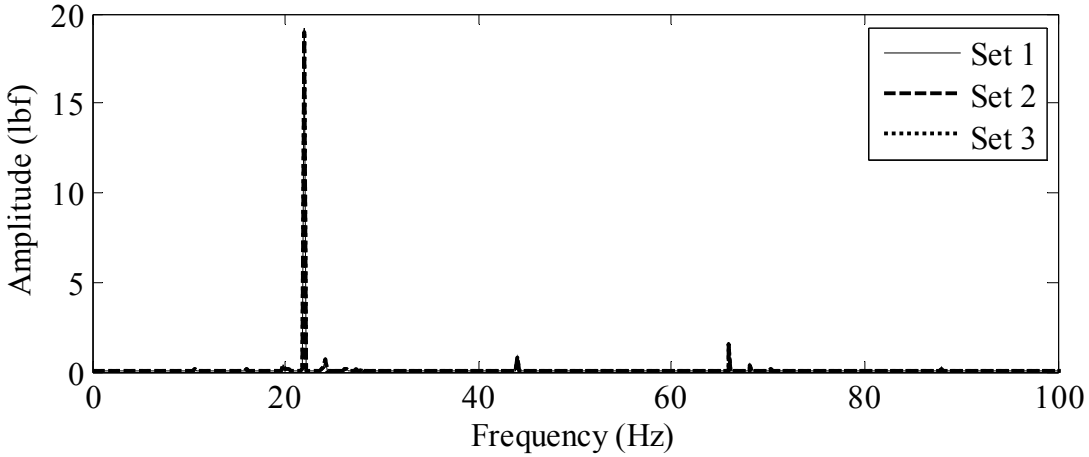

Figure 3.25. Frequency domain plot of force output for three sets of data for Shaker B operating at 22 Hz. Sets are indistinguishable.

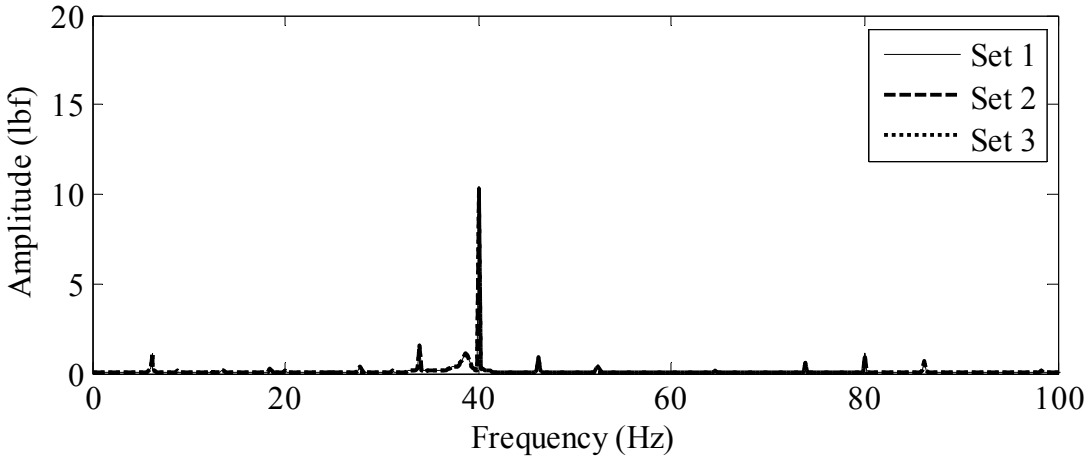

Figure 3.26. Frequency domain plot of force output for three sets of data for Shaker B operating at 40 Hz. Sets are indistinguishable but significantly more noise is present.

As before, the normalized variance in force amplitude at the intended frequency is found for each of the twenty tested frequency lines and for each of the twelve shakers. As with the stepped-sine testing of the shakers mounted to the steel pylon, the uniformity for a shaker is quite good from

one set to the next as is seen in Figure 3.27. Also, the variance is practically identical to that for the pylon testing (Figure 3.9), but with slightly more noise consistently showing up at the 38 Hz frequency line which is near a natural frequency of the structure.

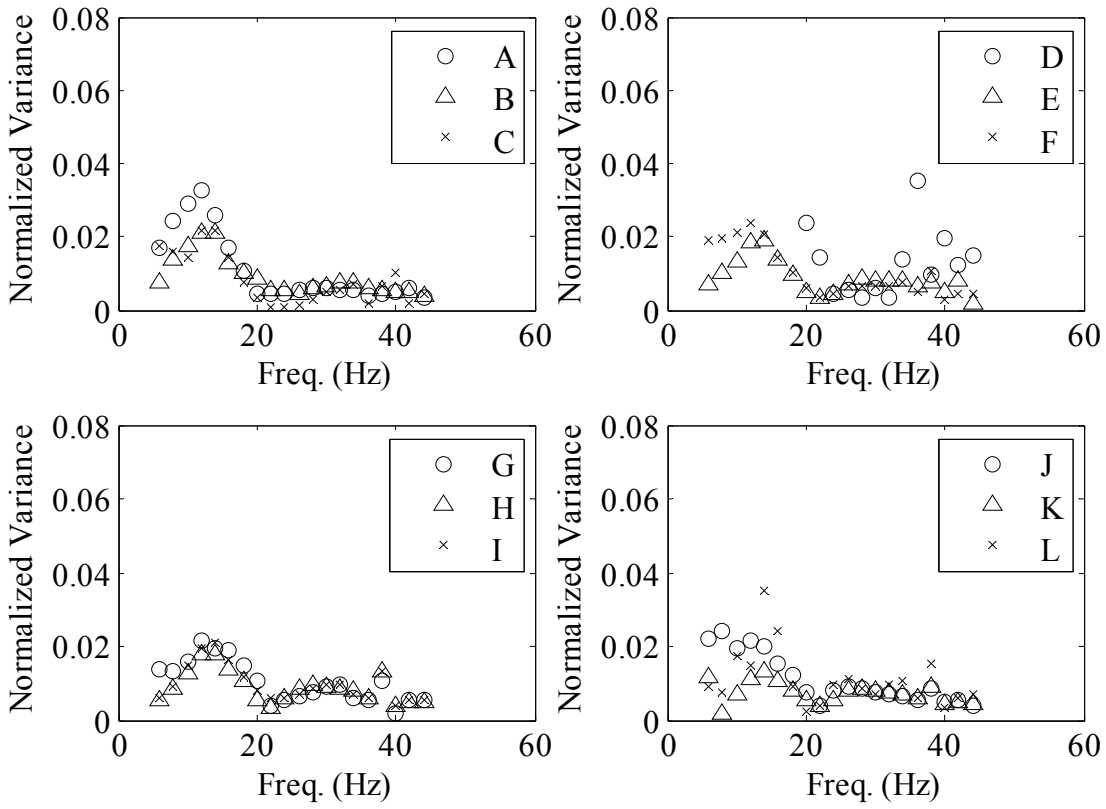

Figure 3.27. Normalized variance in force amplitude for twelve shakers with spatial position at bridge model third-point.

3.2.3.3.2 Shaker at Span Mid-Point with Stepped-Sine Signal

Three sets of data are also captured for each shaker spatially located at the mid-point of the bridge model with the stepped-sine input signal. The results are very similar to what is seen for the shaker at the third-point, and thus only the normalized variance for all twelve shakers is shown herein. Figure 3.28 shows this variance and it is seen that it is not noticeably affected by the spatial location except at 38 Hz. When the shaker was located at the third-point of the span, it excited the second torsional mode of the structure which has a natural frequency near 39 Hz.

With the shaker positioned at the mid-point, the force input occurs at a node point in the mode shape and so the amplified structural response did not occur and did not increase force variance.

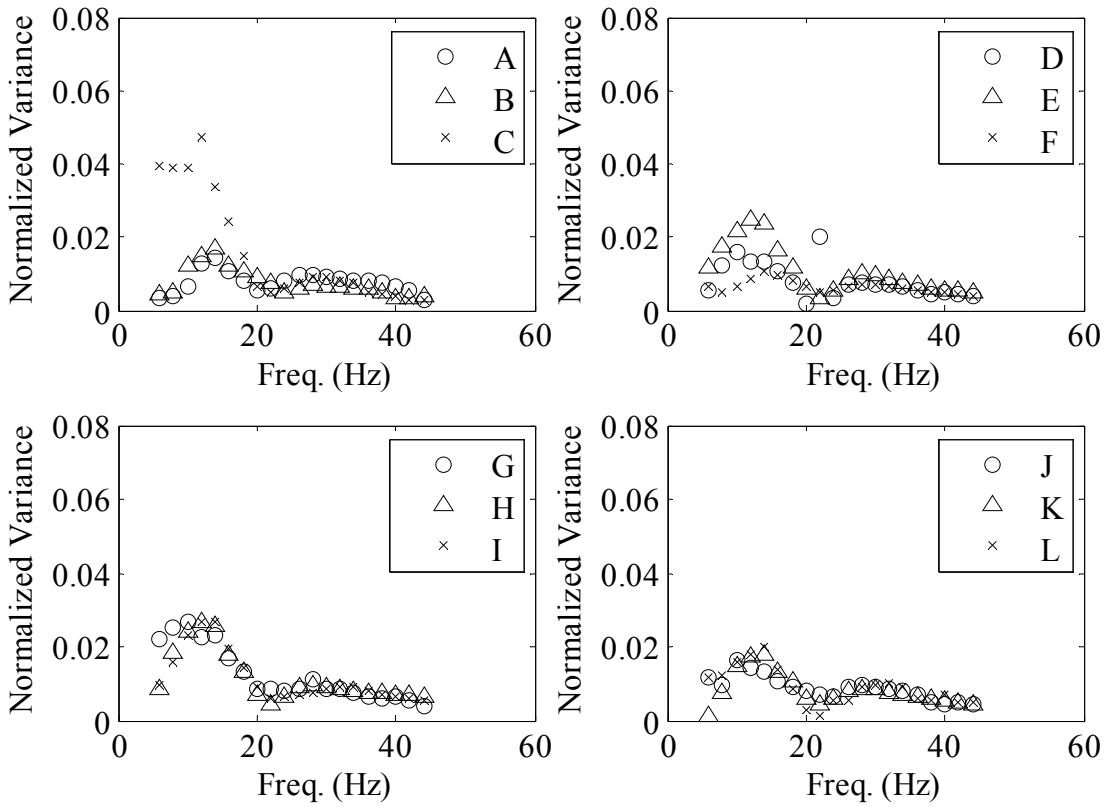

Figure 3.28. Normalized variance in force amplitude for twelve shakers with spatial position at bridge mid-point.

3.2.3.3.3 Stepped-Sine Signal Force Output Comparison

The stepped-sine testing at the bridge model third-point and mid-point locations both revealed that the variance in force output did not change appreciably due to the structural response. However, it must be determined if the force amplitude changes depending on input location. This is tested by comparing the force amplitude per frequency line for input at the bridge model third-point and at the mid-point. The mean of the force output signals is found for the three sets of data collected at a single location for a single shaker. A representative time domain comparison is shown in Figure 3.29 for Shaker I operating at 12 Hz. The force output measured during the

pylon testing is also shown as a baseline. It is visually obvious that there is very little difference in force output between the spatial locations given this input frequency. However, Figure 3.30 shows the force output at 40 Hz and the difference is significant. The phase angle is not greatly affected, but the measured force amplitude is far less at the third-point than at the span mid-point. This is due to the structure's response near this particular natural frequency.

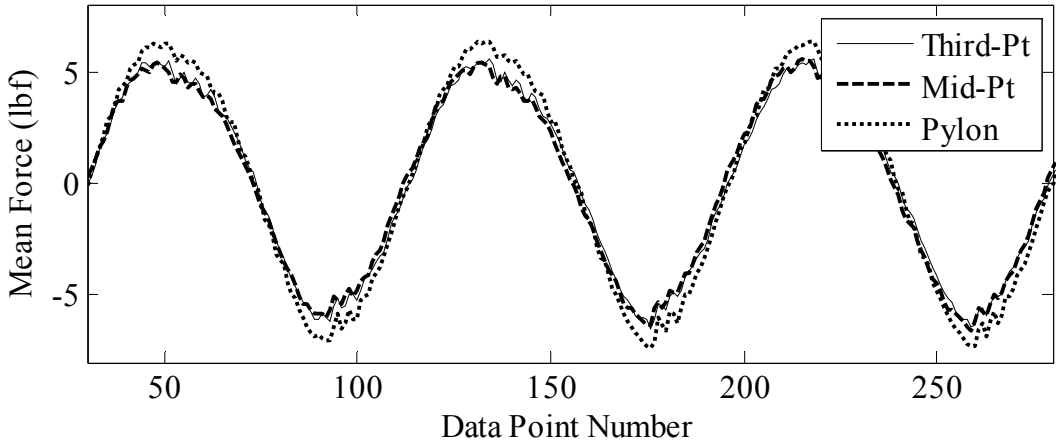

Figure 3.29. Representative segment of mean force output for Shaker I operating at 12 Hz for three different input locations.

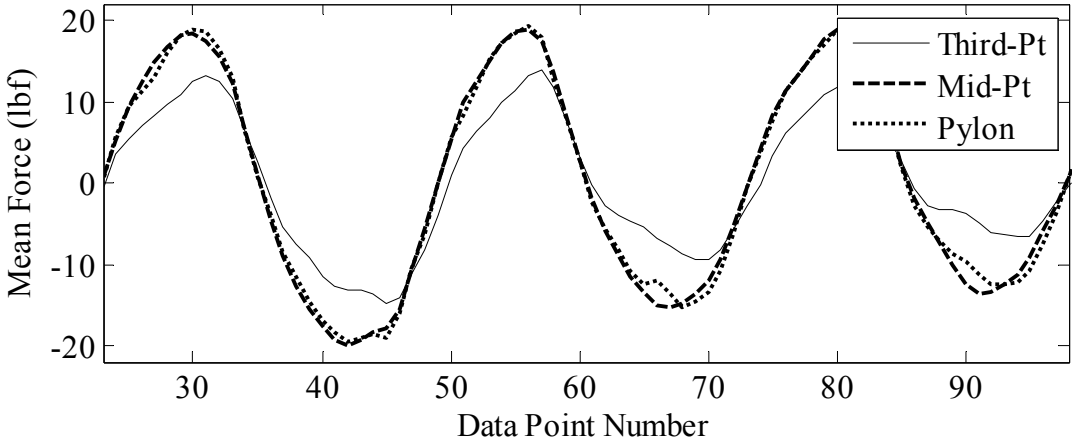

Figure 3.30. Representative segment of mean force output for Shaker I operating at 40 Hz for three different input locations.

The data is now converted to the frequency domain as in the other analyses so that all of the frequency lines can easily be considered. The outcome is shown in Figure 3.31 and it is seen that

the force output is definitely impacted by the response of the structure. The mean force amplitude for representative Shaker I is shown, with a curve for each of the various mounting positions. The first bending and first torsional modes are around 10 Hz and 11 Hz respectively, and there is no indication that these modes affect the force output since the measured force is consistent with the pylon testing. The second bending mode and second torsional mode of the bridge model are around 35 Hz and 39 Hz respectively. The mid-point shaker position is at a modal node, and thus the force output is not affected by the modal motions. However, the force output with the shaker at the model third-point is significantly affected by both of these modes and the measured force is alternately reduced or increased depending on the phase. This phenomenon is expected per the literature (Rao 1987; Varoto and Oliveira 2002).

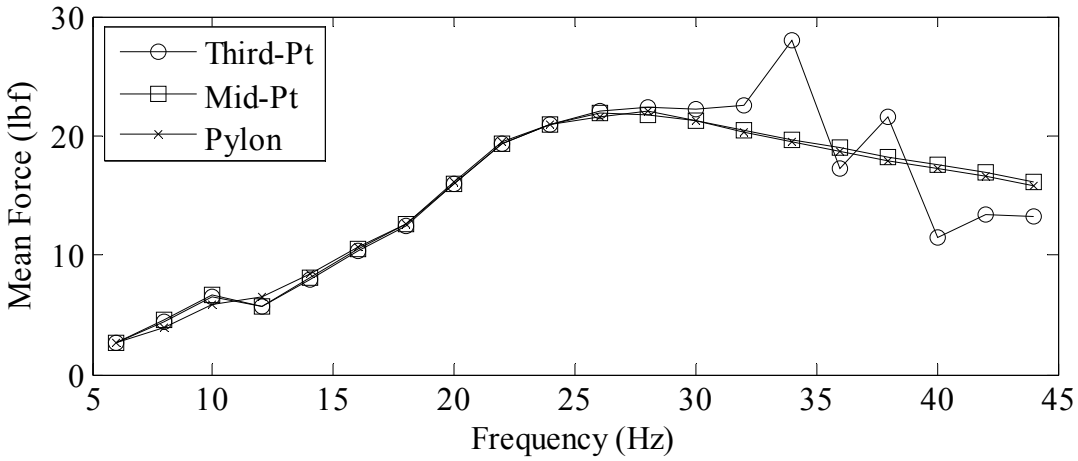

Figure 3.31. Force output of Shaker I at various frequencies for shaker mounted on model third-point, model mid-point, and on pylon.

It is shown that the amplitude of the force being introduced into the structure is sometimes affected by the modal movements of the structure. The significant change in measured force is a paramount concern in whether the force output must be measured at each shaker for all testing.

3.2.3.3.4 Shaker at Span Third-Point with Random Signal

Three sets of data are also captured for each shaker at the third-point of the bridge model with the random input signal. The data appears to have very good uniformity based on time domain review. The force measurements are also in excellent agreement with the force from the pylon testing (Figure 3.13). The data is now processed in the same manner as in Section 3.2.1.2.2. The force records are transformed to the frequency domain, averaging is used to diminish the resolution, and the normalized variance in the force amplitude at each frequency line is calculated. Representative results are shown for Shaker F and Shaker I in Figure 3.32. It is noted that the variance is essentially the same as that found for testing on the steel pylon (Figure 3.14) except for in the vicinity of the bridge model natural frequency at 39 Hz. This indicates that the structural response increases the amount of noise in the force output with random testing.

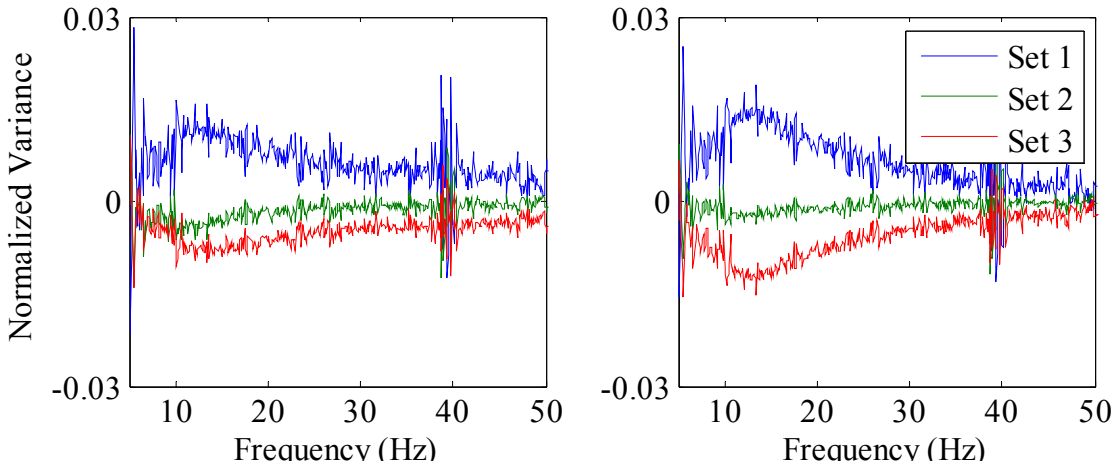

Figure 3.32. Normalized variance in force amplitude for three sets of random input at bridge model third-point. Shaker F (left) and Shaker I (right) shown.

3.2.3.3.5 Shaker at Span Mid-Point with Random Signal

Finally, three sets of data are captured for each shaker at the mid-point of the bridge model using the random input signal. The time domain data is reviewed as before and no change in consistency is noted. The normalized variance in force output is calculated using frequency

domain data and representative results are shown in Figure 3.33, again for Shaker F and Shaker I. As with the stepped-sine input analysis, the scale of the variance is essentially unchanged, but the noise in the vicinity of 39 Hz is not seen at the mid-point. Again, this can be attributed to this spatial location being a node point for the particular torsional mode that is excited at 39 Hz.

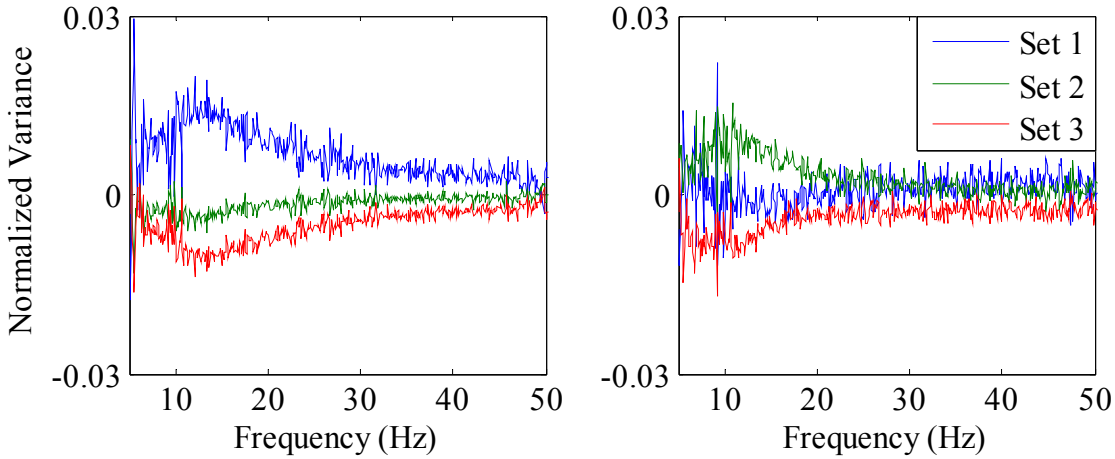

Figure 3.33. Normalized variance in force amplitude for three sets of random input at bridge model mid-point. Shaker F (left) and Shaker I (right) shown.

3.2.3.3.6 Random Signal Force Output Comparison

The amplitude of the force output is now compared for the two shaker locations on the bridge model. The pylon testing data is again used as a baseline. First, a segment of the force output recording for each spatial location is presented in Figure 3.34 for representative Shaker I. It is readily apparent that the force amplitude and phase visually present highly similar traces independent of the input location.

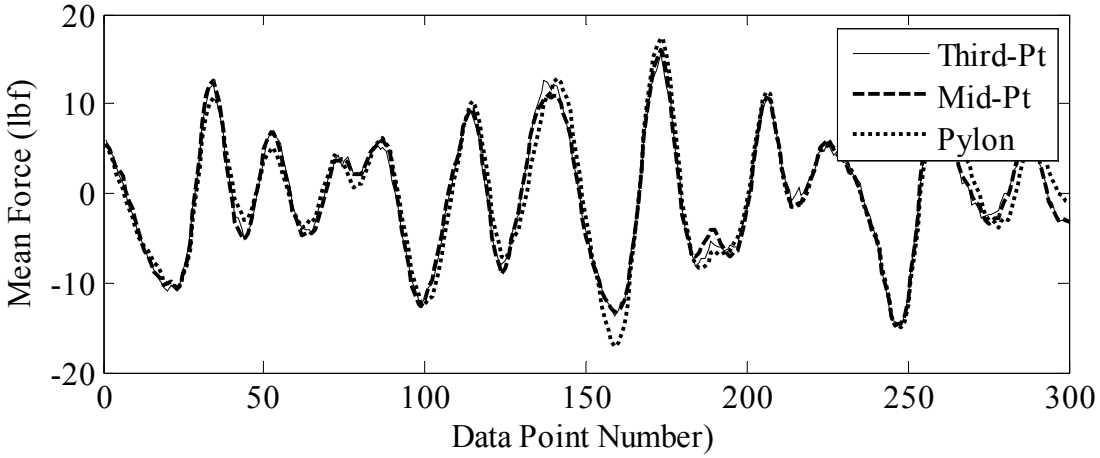

Figure 3.34. Representative segment of mean force output for Shaker I for three different input locations.

The mean force data is now transformed to the frequency domain. As in the previous sections, the resolution is decreased by averaging. The force output for the two bridge model shaker locations is normalized against the force output measured on the pylon and the result is shown in Figure 3.35. With far greater frequency resolution than the stepped-sine testing, the results clearly indicate that all of the structure's natural frequencies significantly alter the force input measurement. The first bending and first torsional modes impact both shaker locations as seen by the approximately 50% variance in force at 9 Hz and 11 Hz. The second bending mode at 35 Hz and the second torsional mode at 39 Hz both have a nodal point at the span mid-point, and thus the shaker force output is not affected by these two modes when the shaker is located at the nodal point. However, when the shaker is located at the third-point, the increase in measured force approaches 100% at the frequency of the second torsional mode. The impact of the first two modes was not seen in the stepped-sine testing since the 2 Hz steps between tested frequencies just happened to align with and thus hide the first bending mode and first torsional mode.

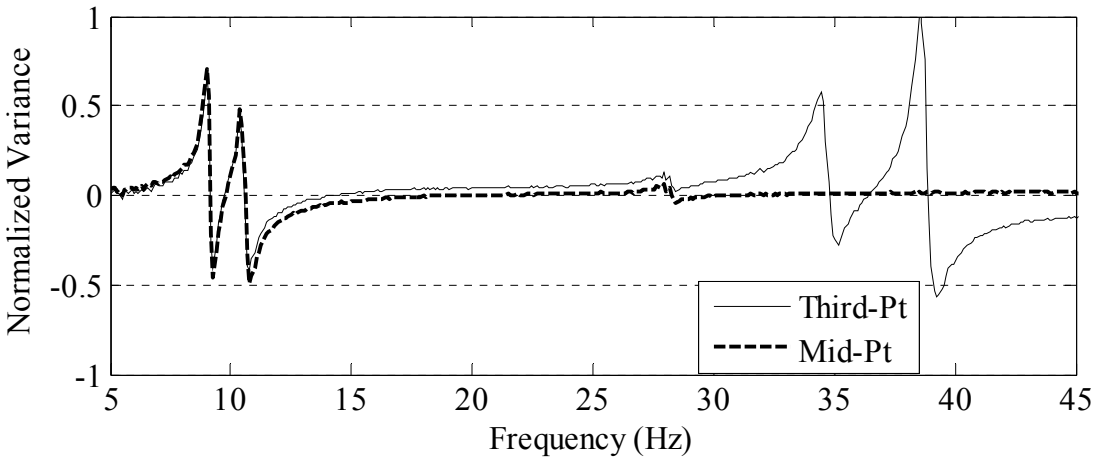

Figure 3.35. Normalized variance in force amplitude for Shaker I for two bridge model input locations normalized to pylon force amplitude.

3.2.3.4 Summary of Shaker Force Uniformity on Bridge Model

Various experiments were undertaken to understand if the force output from a shaker is uniform in various situations. The results indicate that for a given input signal, an individual shaker produces nearly identical output time after time with a variance that rarely exceeds 2%. However, the results also show that the force output can be significantly altered by the behavior of the structure to which the shaker is attached. When a shaker is operating at a frequency that is near a natural frequency of the structure being tested, the force measured between the shaker and the structure can be increased or decreased by as much as 100% compared to the force output when a mode is not excited. Rao (1987) provides some guidance to decrease the effect of this phenomenon, but it cannot be eliminated. Per the literature, this shaker-structure interaction is diminished when the modal mass of the test subject greatly exceeds the shaker mass. Therefore, this issue may be greatly reduced in real-world testing of a massive bridge.

3.3 AMPLIFIER TESTING

Each shaker requires a power amplifier to magnify the signal produced by a waveform generator. The amplifiers selected for the subject system are relatively inexpensive subwoofer amplifiers

that are intended for aftermarket use in automobiles. Similar to the purpose for the shaker testing performed in the previous sections, it must be known if the various amplifiers are uniform in gain across the range of frequencies that are anticipated for use in bridge testing. The uniformity is considered first as the ability of an individual amplifier to produce the same output signal with repeated sets of a particular input signal. This type of repeatability is important so that the force output does not have to be measured at each shaker location during bridge testing. Second, the uniformity across a group of 'identical' amplifiers must be tested. If the amplifiers are truly close to identical in output then they can be used interchangeably; however, if the gain varies significantly then each amplifier must be treated as a unique individual during bridge testing if force transducers are not used.

3.3.1 Amplifier Single Channel Uniformity

The first issue considered is whether or not an individual channel of an individual amplifier can repeatedly produce the same output signal for a given input signal.

3.3.1.1 Test Method

The test method for exploring this issue is nearly identical to the shaker testing discussed in the preceding sections. An input signal is repeatedly sent to one channel of an amplifier and the output voltage is monitored. A shaker is connected to the amplifier channel as a load and the same shaker is used throughout testing. Three sets of data are collected for each channel, and six amplifiers with two channels each are used as the population. The input signals are the stepped-sine signal shown in Figure 3.2 and the random signal shown in Figure 3.12.

3.3.1.2 Analysis and Results

The data for the stepped-sine signal appears to be quite uniform across the population of amplifiers. Figure 3.36 shows a representative segment of the three sets of voltage output for the left channel of Amp 1. The three curves are visually indistinguishable, and this level of uniformity is typical for all frequency lines and for all of the tested amplifiers.

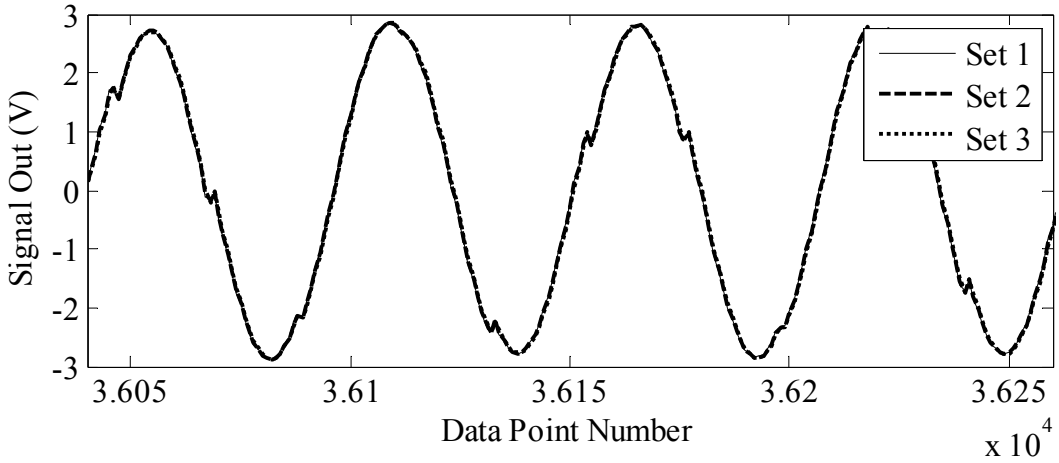

Figure 3.36. Representative segment of voltage output for three sets of data for Amp 1 operating at 18 Hz (sets are nearly indistinguishable).

The stepped-sine data is transformed to the frequency domain and the normalized variance in voltage amplitude is calculated as described in Section 3.2.1.1.2. The results for the left and right channels of three amplifiers are shown in Figure 3.37. The variance is consistently less than $1/10^{th}$ of a percent indicating that the output for an individual amplifier is extremely uniform for a given input. It is noted that significant heating of the amplifiers occurred during this testing, and it can be concluded that such heating did not affect the output.

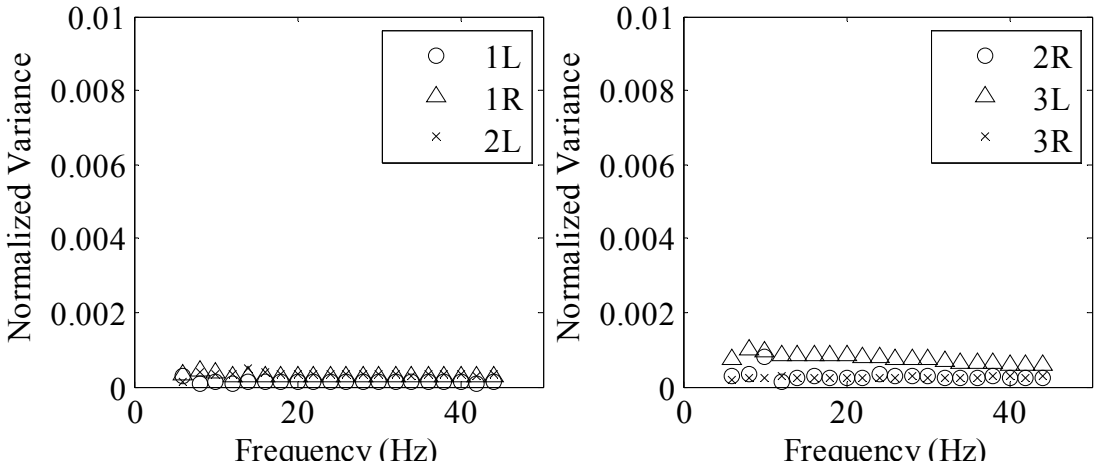

Figure 3.37. Normalized variance in voltage amplitude for left and right channels of Amps 1, 2, and 3. 'L' and 'R' indicate left and right amplifier channels.

Next, the voltage output using the random input signal is analyzed. A time domain segment for the three sets of voltage output using the left channel of Amp 1 are shown in Figure 3.38. As with the stepped-sine test, the data sets are visually indistinguishable and this is typical for all twelve tested amplifier channels.

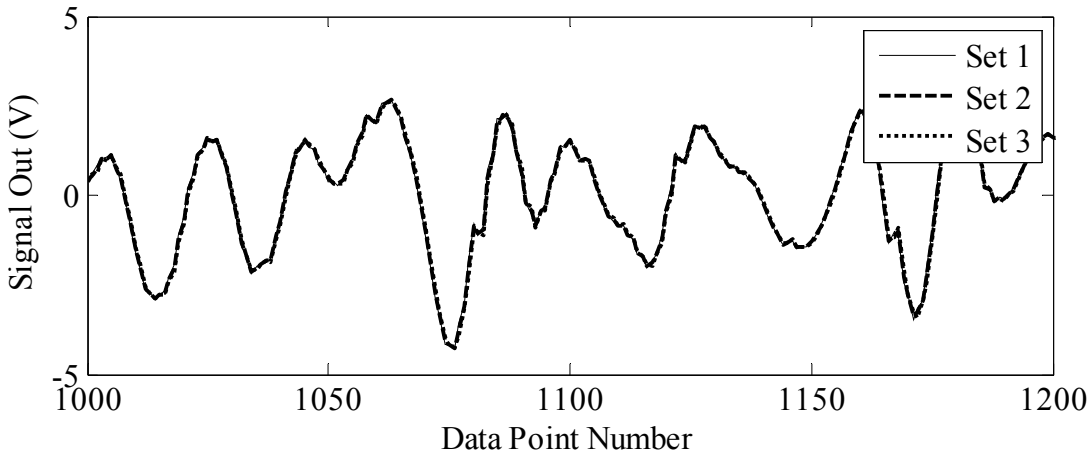

Figure 3.38. Representative segment of voltage output for three sets of data for Amp 1 (sets are nearly indistinguishable).

The data is transformed to the frequency domain and the normalized variance in voltage amplitude is calculated as before. Representative results for the left channel of Amp 1 and the left channel of Amp 5 are shown in Figure 3.39. The variance is generally close to zero with

localized higher variance of about 0.5% below 10 Hz. The higher normalized variance at low frequencies is due to a low signal amplitude.

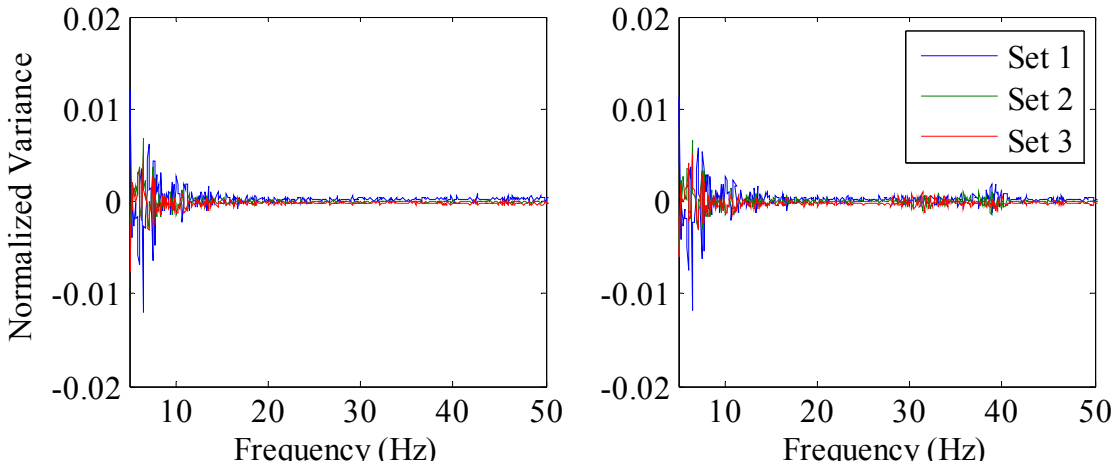

Figure 3.39. Normalized variance in voltage amplitude for three sets of random input. Representative Amp 1 (left) and Amp 5 (right) shown.

Overall, the tests demonstrate that each amplifier provides excellent uniformity in output for set after set of identical input.

3.3.2 Amplifier Interchangeability

The issue to be tested is whether the amplifiers can be used without regard for which one is used to drive a given shaker. This type of interchangeability would simplify field testing by reducing the number of items that must be arranged in a particular manner and by reducing the level of documentation (in the case that force transducers can be avoided).

3.3.2.1 Test Method

Interchangeability is explored by providing the same input signal to each channel of each amplifier and comparing the voltage output from each. Six two-channel amplifiers are tested. Both the stepped-sine and random signals are again used, and three sets of data for each signal

type are collected. The mean of the three data sets is found and then compared for the twelve tested amplifier channels.

3.3.2.2 Analysis and Results

As a first step in understanding the uniformity of the output across the population of amplifier channels, a segment of time domain data is shown in Figure 3.40. The figure illustrates the high similarity between four different amplifier channels operating at the 20 Hz frequency line of the stepped-sine signal.

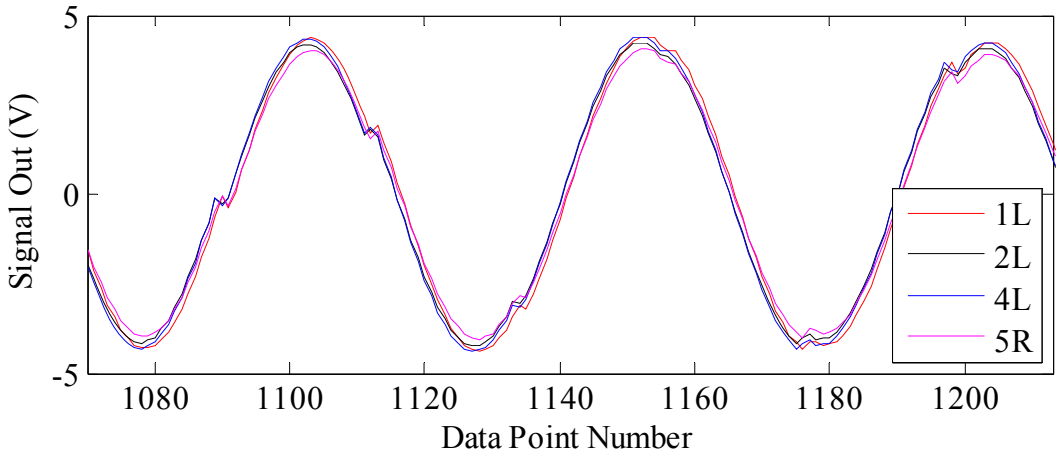

Figure 3.40. Representative segment of voltage output data for four amplifier channels operating at 20 Hz.

The output data for the stepped-sine input signal is transformed to the frequency domain and the amplitude at each frequency line is found for each of the twelve amplifier channels. A t-distribution is assumed and the mean amplitude and 90% confidence interval is found for each frequency line as in Section 3.2.2.1.2. The result is displayed in Figure 3.41 and it is clear that the amplitude variation between amplifier channels is quite small.

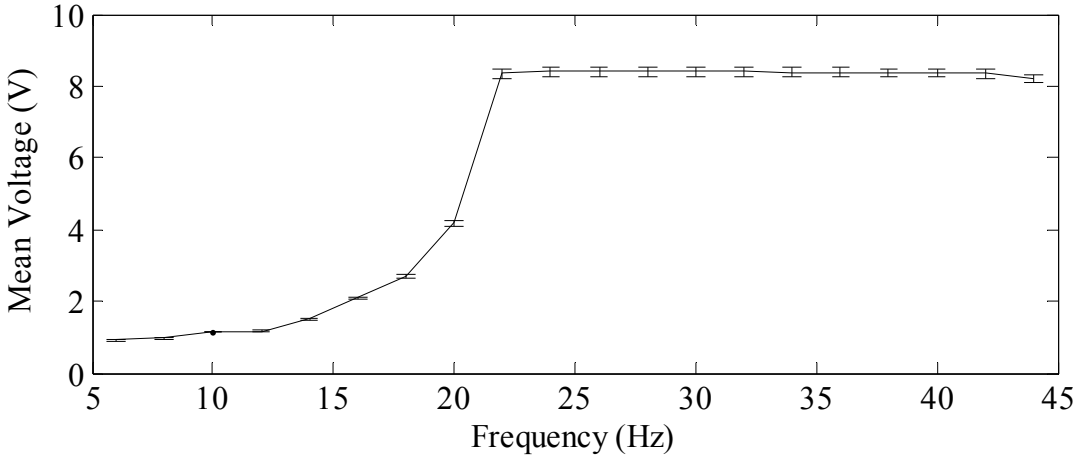

Figure 3.41. Mean voltage output of twelve amplifier channels at various frequencies with 90% confidence interval shown.

The outcome using the random signal is similar. Figure 3.42 shows a segment of time domain data for all twelve amplifier channels and the uniformity appears to be very good. The time domain data is useful for visual inspection, but frequency domain analysis is more complete.

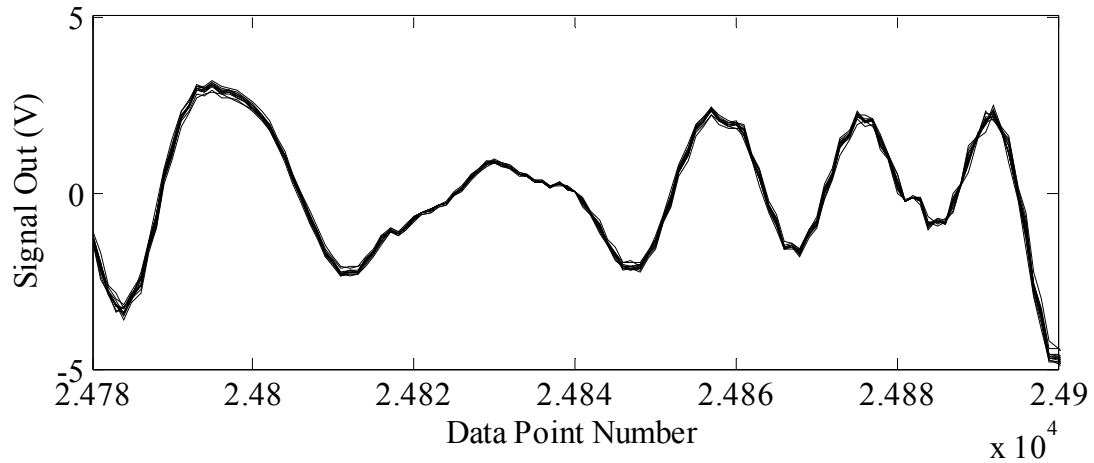

Figure 3.42. Representative segment of voltage output data for all twelve amplifier channels with random input.

The mean voltage output for each of the twelve channels is now transformed to the frequency domain. The mean and variance of the twelve channels are found and the variance is normalized via division by the mean. The result is plotted in Figure 3.43 and the normalized variance in voltage output is essentially constant at about 2%.

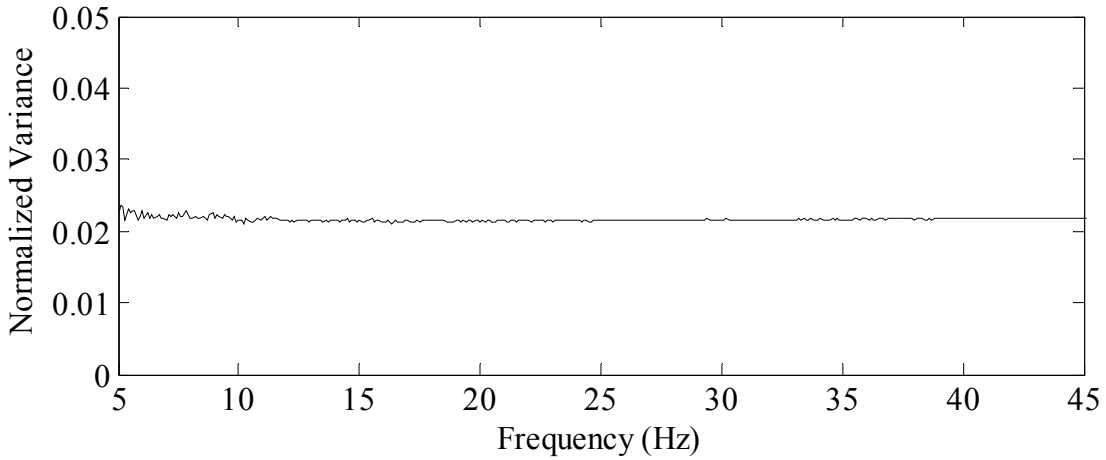

Figure 3.43. Normalized variance in voltage output amplitude for twelve amplifier channels with random input.

Overall, the uniformity between amplifiers is very good with an average variance in output voltage of about 2% for both stepped-sine and random input signals. It is likely that this will allow the amplifiers to be used interchangeably without regard to which amplifier is driving which shaker.

3.3.3 Amplifier Consistency with Simultaneous Channel Operation

Another issue of concern with the two-channel amplifiers is whether operating both channels simultaneously affects the output voltage of a single channel. The testing performed to this point was carried out using a single channel while the amplifier's other channel was not in use. It is possible that adding a load to the second channel will affect the voltage output of the first channel, and this must be evaluated.

3.3.3.1 Test Method

This test is performed on Amp 1 with each of its two channels powering a single shaker. The left channel powers Shaker I, which is attached to the force measuring apparatus mounted on the steel pylon. The right channel simultaneously powers Shaker L, and the stepped-sine signal is sent to both channels at the same amplitude as in the Section 3.2.1.1.1 testing. Thus the input

amplitude varies for frequencies below 22 Hz so that the shaker does not bottom out. For the range of frequencies from 22 Hz to 44 Hz the input amplitude is constant at 0.4 volts peak. The force output of Shaker I is recorded as before and is compared to the force output when only the left channel is in use. Three sets of data are collected for each condition.

3.3.3.2 Analysis and Results

The mean of the three data sets is calculated and then the mean is transformed to the frequency domain. The amplitude at each frequency line is shown in Figure 3.44 with and without the second channel in use. The plot clearly illustrates that when the total load is higher, the amplifier reduces the power output to a single channel. For instance, the force output is reduced by 9% at the 28 Hz frequency line. This behavior is a significant issue and thus additional testing is performed to understand if the reduction can be avoided.

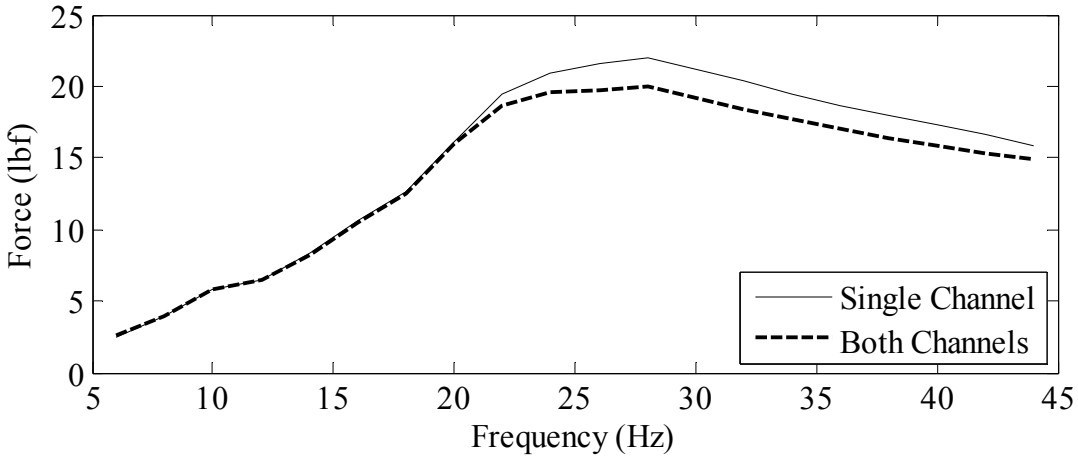

Figure 3.44. Force output of Shaker I with and without a load on the second amplifier channel. Amplifier input = 0.4 volts.

A follow-up experiment is conducted in which the amplitude of the input signal is varied. The stepped-sine signal is used and the force output of a single shaker is recorded. During one run of the signal, only a single channel is used. During a second run of the signal, the second amplifier

channel is connected to a second shaker. Eight amplitudes were tested ranging from 0.14 volts to 0.30 volts peak.

It was found that at and below 0.22 volts input amplitude, the force output is the same whether one or both channels have a load. At higher input voltages the force diverges for the two experimental conditions. This is illustrated in Figure 3.45. It is noteworthy that input amplitudes above 0.22 volts barely provide higher output voltages (and thus force) since the amplifier's limit seems to be reached. Thus, the force output from the shaker is already nearly at the maximum that the amplifier can provide. Therefore, the issue illustrated by Figure 3.44 is really not an issue at all. With careful selection of the input voltages, a high force output can be maintained that is independent of the number of channels in use.

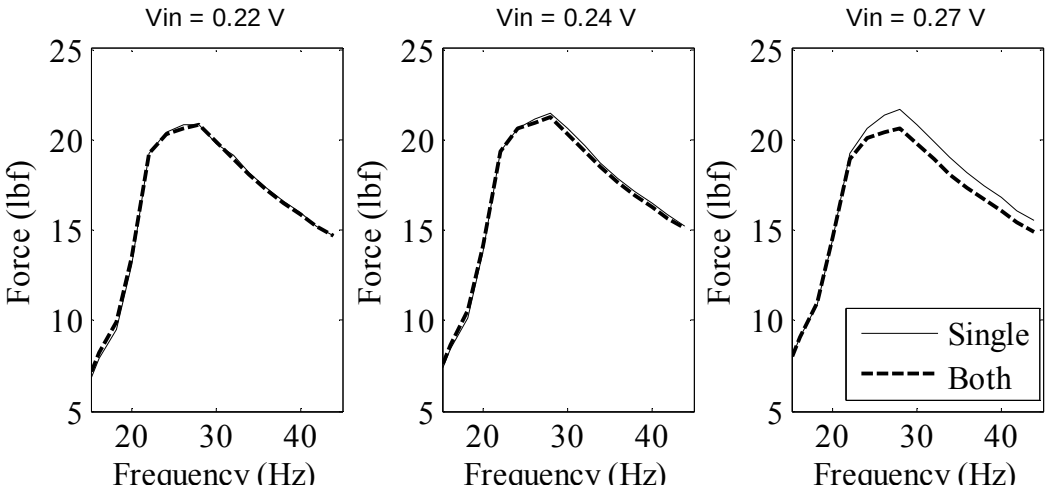

Figure 3.45. Force output of Shaker I with and without a load on the second amplifier channel and with various input voltages.

3.4 FORCE TRANSDUCER REQUIREMENT

In classical EMA of structures, FRFs are developed from measurements of both the excitation forces and structural vibrations. Measuring the excitation force at a single input location requires the use of a force transducer and a data acquisition channel. The excitation system evaluated in this research will ideally use many shakers operating simultaneously; however, it is desirable to avoid the use of force transducers (and the requisite data channels) if possible since they increase both the cost and complexity of the testing system.

One proposed method to circumvent the use of transducers is to develop deterministic equations that relate the signal input to the amplifiers to the force output from the shakers. Testing of the shakers for stepped sine and random signals earlier in this chapter demonstrated that the force output curve in the frequency domain had a uniform shape for both signal types. Thus, it is theorized that the signal gain and phase change caused by the amplifier and by the shaker may be deterministically related to the frequency. Equations of this type would be the best solution to avoiding force transducers since the output force could be predicted for any input signal type. To succeed, this approach requires that the hardware components are stable and the force output will be totally repeatable. Such equations would essentially attempt to fit the transfer function of the excitation system.

If deterministic equations fail to work, then a second method that is more cumbersome may still be effective. This method would require the force input for a given signal to be measured once for each shaker location on the structure under test. Assuming a single force transducer, this process would need to be performed separately at each input location. After the measurement of all force inputs, production testing would commence and it would be assumed that the force does

not vary during these subsequent runs of the same signal. This process would add significant effort to the testing of a structure, but would reduce equipment costs.

3.4.1 Deterministic Equation Development

In this section, an attempt is made to develop deterministic equations that relate the shaker force response to the input signal. This is done in two steps that correspond to the signal change due to the amplifier and the signal change due to the shaker. Also, the amplitude and phase change are handled separately, and a diagram of the system model is shown in Figure 3.46.

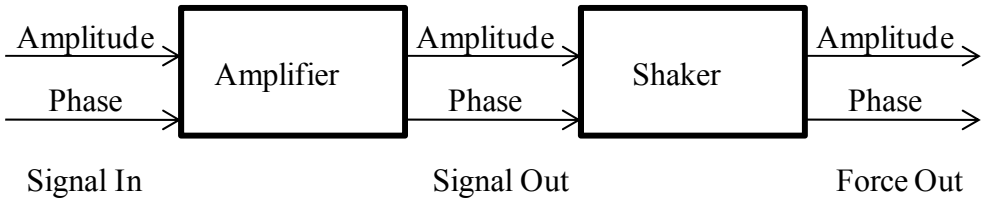

Figure 3.46. Diagram of system model.

The modeling of the system response proceeds by developing an equation for gain and phase change for each component:

- Development of amplifier model - 3.4.1.2
- Development of shaker model - 3.4.1.3

Next, the equations developed to model the response of the components are evaluated for a broad range of frequencies and input amplitudes in subsection 3.4.2.1.

Finally, the effect of shaker-structure interaction is revisited as it applies to the proposed use of a system model to predict force output in subsection 3.4.2.2.

3.4.1.2 Development of Amplifier Model

The objective of this testing is to fit a deterministic equation to the output of the amplifier for any given input signal. Based on previous testing, it is expected that the input frequency is the only independent variable.

3.4.1.2.1 Test Method

The test consists of measuring signals into and out of the amplifier so that a relation can be developed. Testing is performed using a stepped-sine input signal that consists of twenty discrete frequency lines ranging from 6 Hz to 44 Hz at 2 Hz steps. The amplitude at each frequency is limited either by the amplifier capacity or the shaker stroke. For frequency lines below 20 Hz, the amplitude is selected so that the shaker does not bottom out. For 20 Hz and above, the input is set at 0.18 volts peak to stay below the maximum amplifier threshold as established in Section 3.3.3.2. Each frequency is input for six seconds and the amplifier input and output are recorded. The left and right channels of six amplifiers are tested separately, and the stepped-sine signal is used three times per channel to enable averaging.

3.4.1.2.2 Analysis and Results

First, it is assumed that the change in amplitude and the change in phase are functions of frequency. The basic formulation is shown in the following equations and the data is analyzed to find equations for the functions of frequency.

For amplitude:

$$gain = \frac{(A_1)}{(A_o)} = f(freq.)$$ Equation 3.8.

and therefore:

$$(A_1) = (A_o) * f(freq.)$$ Equation 3.9.

For phase:

$$(\varphi_1) - (\varphi_o) = lag = g(freq.)$$ Equation 3.10.

and therefore:

$$(\varphi_1) = (\varphi_o) + g(freq.)$$ Equation 3.11.

Where:

A_o = the amplitude of the input signal.

A_1 = the amplitude of the output signal.

φ_0 = the phase of the input signal.

φ_1 = the phase of the output signal.

The amplitude is considered first. Figure 3.47 shows the gain for the twelve amplifier channels across the frequency range of interest. The shape of the curves is fairly uniform, but the level of the gain varies across the population. Thus, an equation must be developed for each amplifier.

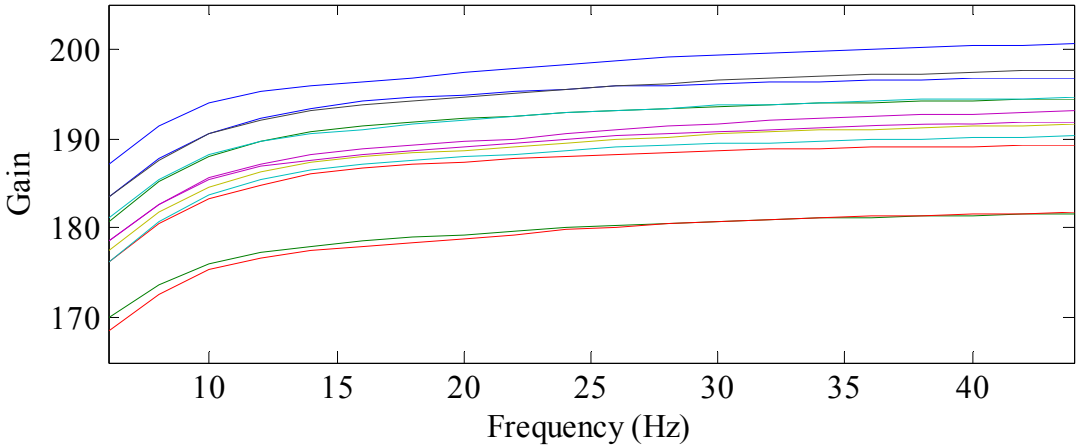

Figure 3.47. Gain for twelve amplifier channels.

The shape of the curves suggests that a 1/x function may provide a good fit. Matlab is used to perform a least squares curve fit optimization for each amplifier channel using the following basic formulation:

$$A_1 = A_o\left(C_1 + \frac{C_2}{f^{C_3}}\right) \qquad \text{Equation 3.12.}$$

Where:

f = the frequency line (Hz).

C_1, C_2, C_3 = constants that may vary for each amplifier channel.

The value of each constant was found for each amplifier channel. As an example, the value of the constants for the left channel of amplifier 1 are 197.8, -163.3, and 1.36 respectively. The fit of the equation is demonstrated in Figure 3.48, and the result is very good.

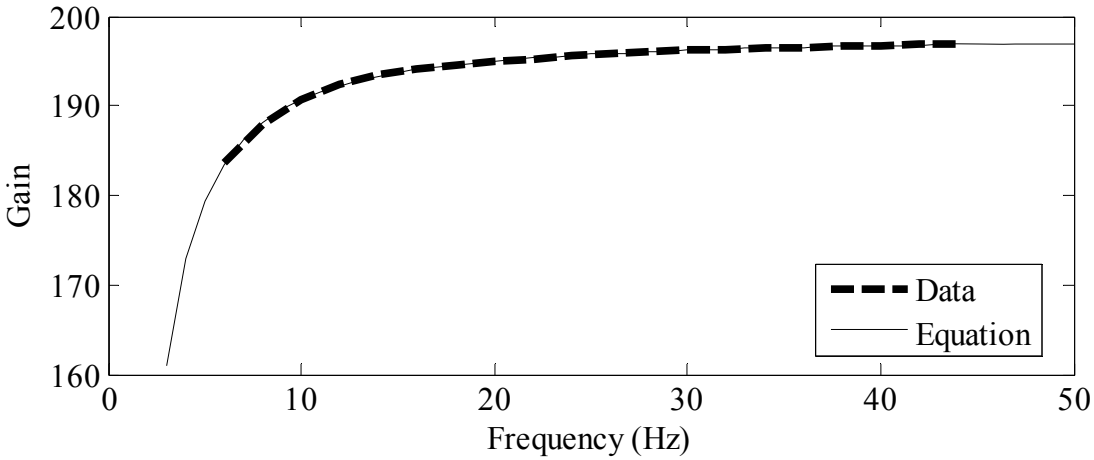

Figure 3.48. Curve fit of gain for Amplifier 1, left channel.

Next, the phase change is considered. Figure 3.49 shows the lag for the twelve amplifier channels and it is noted that the uniformity across the population is excellent. Thus, a single equation will be found and used for all of the amplifiers.

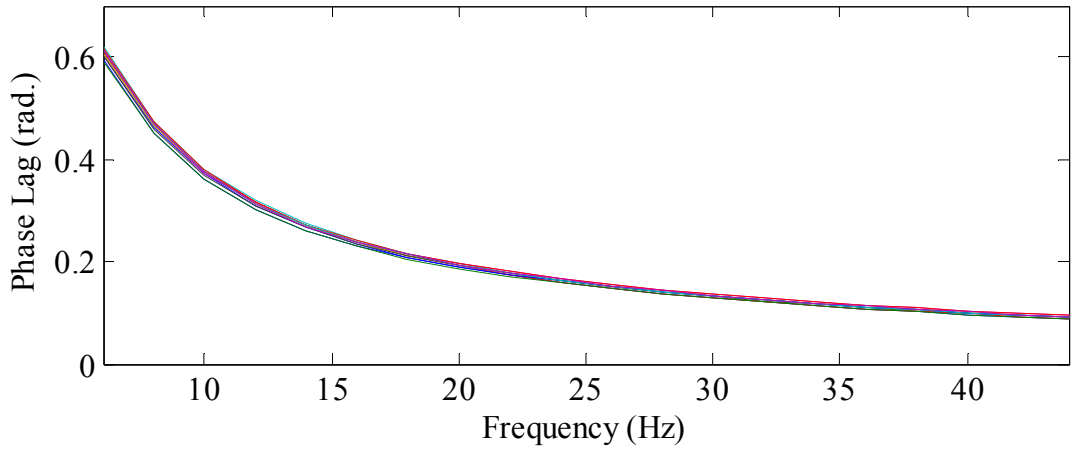

Figure 3.49. Phase lag for twelve amplifier channels.

The shape of the curves again suggests a 1/x function. Using the same formulation as for the amplifier gain, the values of the constants are found to be 0.689, 205.8, and 1.0 respectively. The excellent fit of the equation against the mean phase lag of the twelve amplifier channels is demonstrated in Figure 3.50.

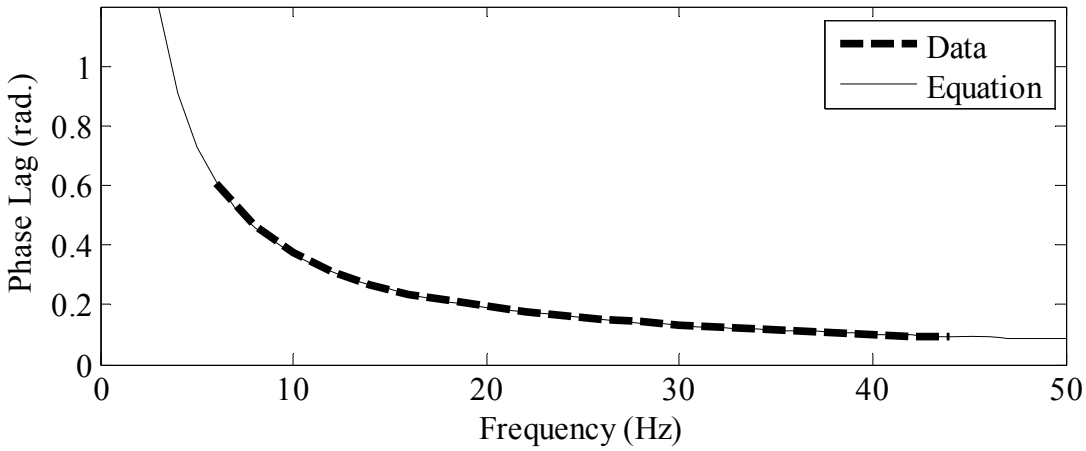

Figure 3.50. Curve fit of phase lag for twelve amplifiers.

In summary, the response of the amplifiers to an input signal appears to be well estimated by the deterministic equations given below.

For amplitude:

$$A_1 = A_o\left(C_1 + \frac{C_2}{f^{C_3}}\right) \qquad \text{Equation 3.13.}$$

For phase:

$$\varphi_1 = \varphi_o + 0.012 + \frac{3.592}{f} \qquad \text{Equation 3.14.}$$

Where:

φ = the phase (radians).

All other elements as defined previously.

3.4.1.3 Development of Shaker Model

This is carried out in the same manner as for the amplifiers. The input and output to a shaker are recorded and an attempt is made to fit a deterministic equation to the gain and phase change that occurs.

3.4.1.3.1 Test Method

The test consists of measuring signals into and out of the shaker so that a relation can be developed. Testing is performed using the stepped-sine input signal. Four shakers are tested, and each is mounted to the pylon for this experiment.

3.4.1.3.2 Analysis and Results

The same assumptions are made as in the amplifier testing. It is assumed that the gain and phase lag are only a function of frequency. The amplitude is considered first. Figure 3.51 shows the gain for the four shakers across the frequency range of interest. The shape of the curves is fairly consistent, but the level of the gain varies across the population. Thus, an equation must be developed for each shaker.

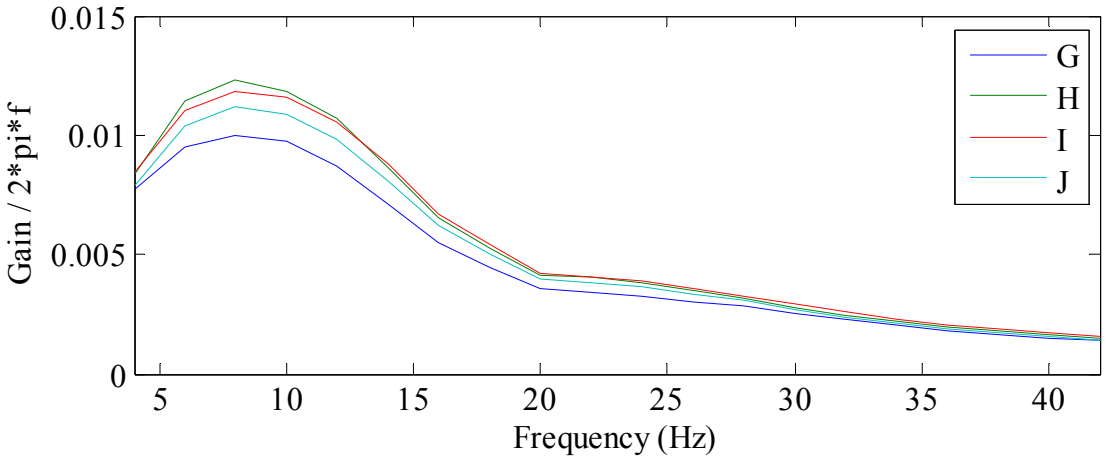

Figure 3.51. Gain characteristics of four shakers.

The shape of the curves suggests that a function as shown below may provide a good fit. Matlab is used to perform a least squares curve fit optimization for each shaker using the following basic formulation:

$$A_2 = A_1 * 2\pi f * \left(C_1 + C_2 * \sin\left(\frac{-\pi * C_3}{f^2 + C_3} + \pi + C_4\right)\right) \qquad \text{Equation 3.15.}$$

Where:

A_1 = the amplitude of the signal from the amplifier (volts).

A_2 = the amplitude of the force output from the shaker (lbf).

f = the frequency line (Hz).

C_1, C_2, C_3, C_4 = constants that may vary for each shaker.

The value of each constant was found for each of the four shakers. As an example, the value of the constants for shaker G are 0.0018, 0.0085, 67.1, and 8.82 respectively. The fit of the equation is demonstrated in Figure 3.52, and the result is fairly reasonable.

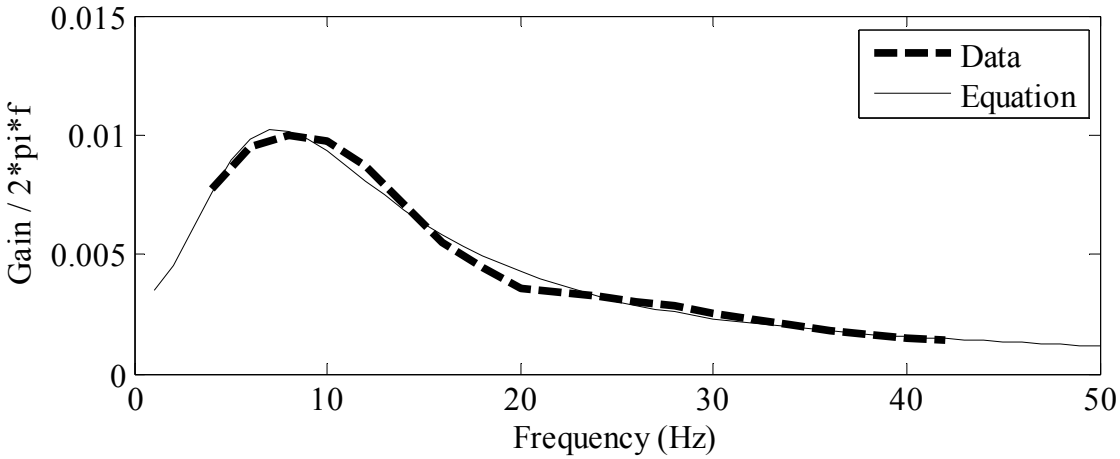

Figure 3.52. Curve fit of gain for Shaker H.

Next, the phase change caused by the shaker is considered. Figure 3.53 shows the lag for the four shakers and it is noted that the uniformity across the population is very good. Thus, a single equation will be fit to the average of the four shakers.

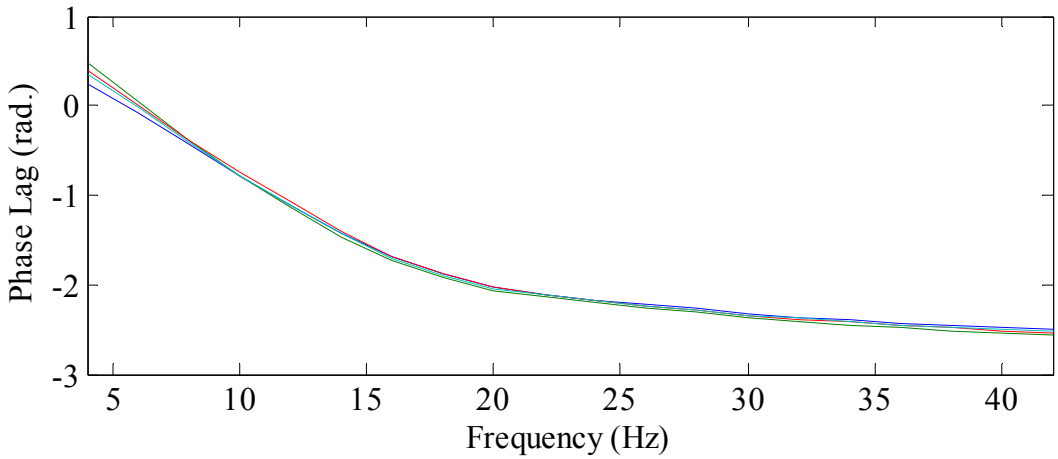

Figure 3.53. Phase lag for four shakers.

The shape of the curves again suggests a 1/x function. Using the same formulation as for the amplifier phase lag, the values of the constants are solved. The fit of the resulting equation against the mean phase lag of the four shakers is demonstrated in Figure 3.54. The curve fit is fair but not as good as for the amplifier.

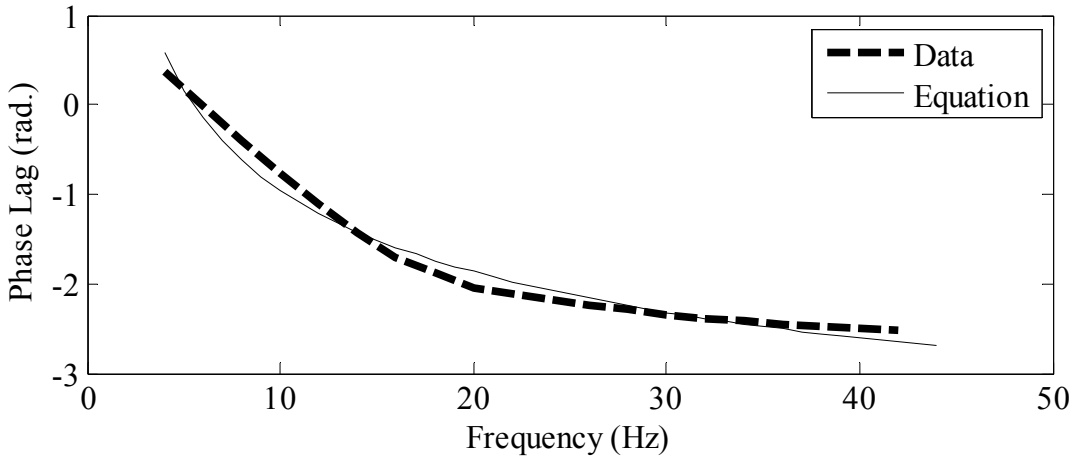

Figure 3.54. Curve fit of phase lag for four shakers.

In summary, the response of the shakers to an input signal appears to be reasonably well estimated by the deterministic equations given below.

For amplitude:

$$A_2 = A_1 * 2\pi f * \left(C_1 + C_2 * \sin\left(\frac{-\pi * C_3}{f^2 + C_3} + \pi + C_4\right)\right) \quad \text{Equation 3.16.}$$

For phase:

$$\varphi_2 = \varphi_1 + \frac{\pi}{2} - 5.89 + \frac{9.72}{f^{0.29}} \quad \text{Equation 3.17.}$$

Where:

φ_1 = the phase of the signal from the amplifier (radians).

φ_2 = the phase of the force output from the shaker.

All other elements as defined previously.

Deterministic equations have now been developed that represent each of the processes that transform an input excitation signal into a force output signal. The four equations can easily be combined for any given amplifier and shaker pairing. Thus, it is not necessary to explicitly find the intermediate phase and amplitude that occurs after the amplifier but before the shaker. Also, using complex numbers, the phase and amplitude could be operated on in a single step.

3.4.2 Deterministic Equation Applicability Check

In the previous subsection, deterministic equations were developed that transform input signals into output signals based on the behavior of the amplifiers and the shakers. The equations were developed using a stepped-sine input signal that was limited to twenty frequency lines and to a single amplitude per frequency line. Additionally, the force measurement was performed on the steel pylon. In this subsection, the validity of the developed equations will be checked with

broadband signals at various input amplitudes. Also, the force output will be measured on the steel bridge model to see if the force drop off at structure natural frequencies can be reduced.

3.4.2.1 Input Amplitude Examination

In the production of the deterministic equations, it was assumed that at any given frequency line, the output amplitude is directly proportional to the input amplitude and the output phase is a constant offset from the input phase. It is known that for both the amplifier and the shaker, this can only be true within some range of input amplitudes. For example, the amplifiers have a limited output of about 30 volts. As the input signal amplitude is increased, there is no longer a corresponding increase in the output beyond this 30 volt ceiling. Similarly, for the shaker, large amplitudes at low frequencies cause the mass to exceed the available stroke and thus the force cannot be increased beyond the limits of the stroke. Thus, the range of applicability of the assumed linear relation between input and output amplitude must be established by testing. The phase relation may also be limited and will also be studied.

3.4.2.1.1 Test Method

This testing is performed using only the left channel of Amplifier 1 and only Shaker H. A broadband signal is sent from the Agilent signal generator to the amplifier. The amplifier drives the shaker, which is mounted to the pylon via the force transducer tripod. The Agilent output, the amplifier output, and the shaker force output are all simultaneously recorded so that the amplitude and phase changes can be analyzed.

The broadband signal selected for the experiment is a multisine having energy content at 0.1 Hz steps from 6 Hz to 44 Hz. The signal is 10 seconds long and has amplitude shaping such that the shaker does not bottom out at lower frequencies. The FFT of the signal is shown in Figure 3.55.

During testing, this signal is run six times consecutively at a particular maximum input level. During processing, the first run is ignored since it contains a non-periodic transient, and the other five runs are averaged in the time domain to reduce the effects of noise. This is performed for each input amplitude test.

The Agilent signal generator output amplitude is varied over twenty voltages from 0.01 volts to 0.20 volts at 0.01 volt steps. Therefore, in the time domain, the multisine signal has a maximum amplitude of 0.01 volts in the first test and a maximum amplitude of 0.20 volts in the twentieth test. For reference, the plot of Figure 3.55 is for a time domain maximum amplitude of 1.0 volt.

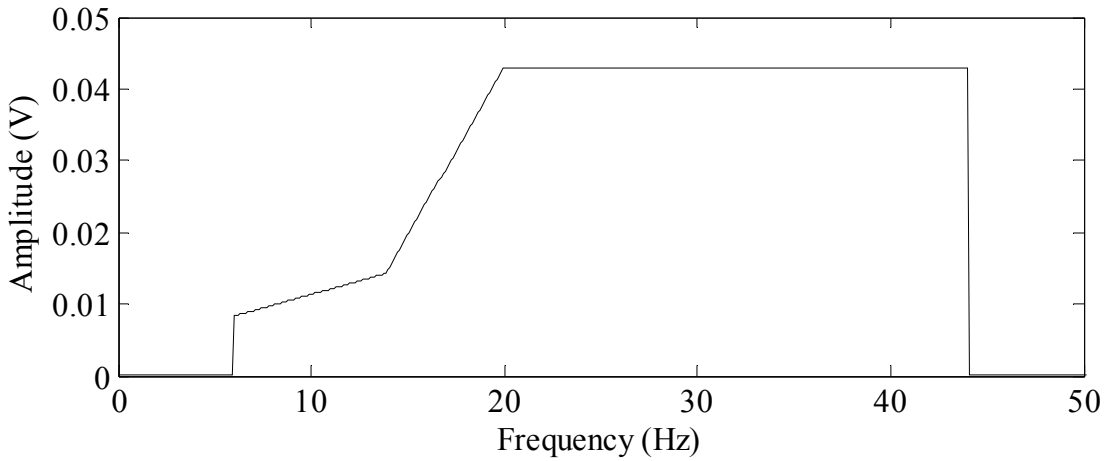

Figure 3.55. Multisine signal in frequency domain showing results of amplitude shaping at low frequencies.

3.4.2.1.2 Analysis and Results

The purpose of this testing is to establish the range of input amplitudes over which the deterministic equations developed for gain and phase lag are valid. The desirable outcome is for the shape of the response along the frequency axis to be constant over a wide swath of input voltages. This should preferably be true for both gain and phase lag.

First, the total gain is analyzed, including the amplitude change due to both the amplifier and the shaker. To enable visualization, a three dimensional plot is produced, and Figure 3.56 shows the gain relative to both input frequency and input amplitude. The input amplitudes are normalized to a minimum value of 1.0 (i.e. 0.01 volts actual input equals a normalized value of 1). The plot shows some interesting characteristics that were not noted during the stepped sine testing. First, there is significant variability in the gain of the system depending on the input amplitude, especially within the frequency range of 10 Hz to 20 Hz. Also, there is a ripple in the plot near 30 Hz and across all input amplitudes that may be a characteristic of the shaker or of the physical test setup.

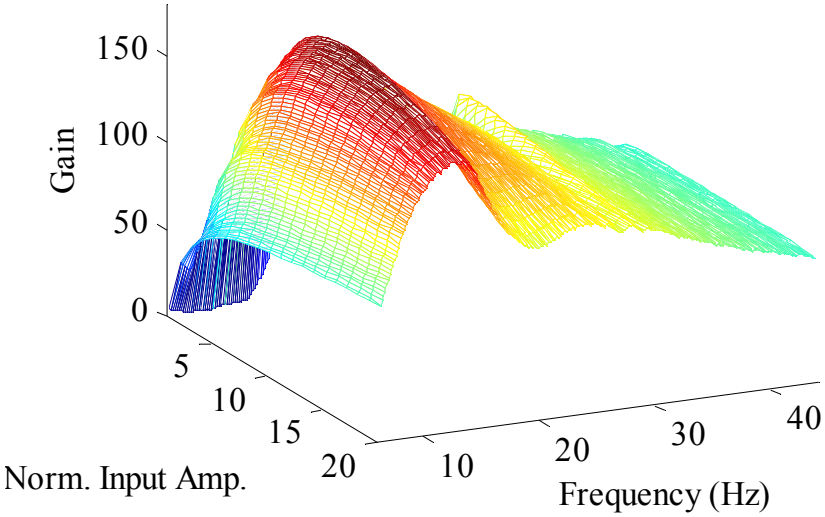

Figure 3.56. Total gain relative to input frequency and to input signal amplitude.

To further illustrate the variability across input levels, Figure 3.57 shows the same data, but on a two dimensional plot and only for four input amplitudes (4, 9, 14, and 19) along with the result of the deterministic gain equations. On this plot, it is obvious that the gain varies across the entire frequency range for any change in input amplitude. The deterministic equations were

developed based on a relative input amplitude of 18, and thus the equation best fits the displayed data for an amplitude of 19.

This high variability in gain over various input levels is not desirable. It is possible that an equation could be developed that incorporates both changes in frequency and in input amplitude, but this is not warranted based on other issues that are subsequently discussed. Overall, the complex behavior of the amplitude change through the system suggests that the use of force transducers will be required.

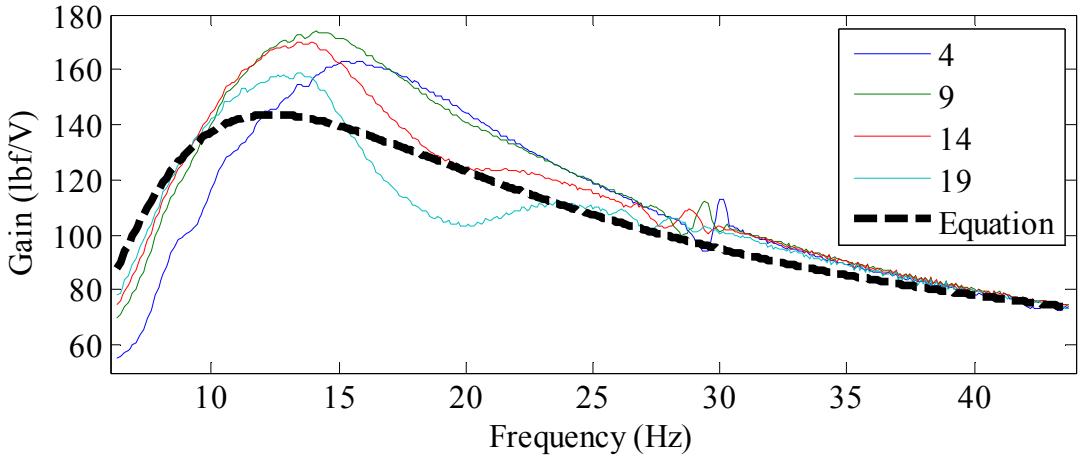

Figure 3.57. Total gain relative to input frequency for four input signal amplitudes and for deterministic equation.

Next, the total phase change is analyzed, including the change due to both the amplifier and the shaker. A three dimensional plot is produced, and Figure 3.58 shows the phase lag relative to both input frequency and input amplitude. The input amplitudes are again normalized to a minimum value of 1.0. The plot shows that the uniformity is much better than for gain.

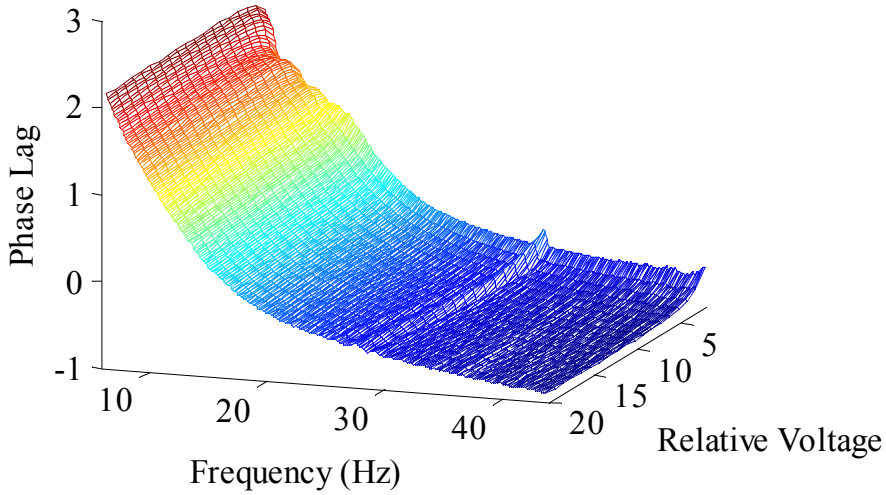

Figure 3.58. Total phase lag relative to input frequency and to input signal amplitude.

Again, to further illustrate the variability across input levels, Figure 3.59 shows the same data, but on a two dimensional plot and only for four input amplitudes (4, 9, 14, and 19) along with the result of the deterministic phase lag equations. This shows that the phase lag is quite consistent across the various input levels. Also, the deterministic equations that were developed fit the displayed data fairly well. Overall, the phase change seems to be predictable.

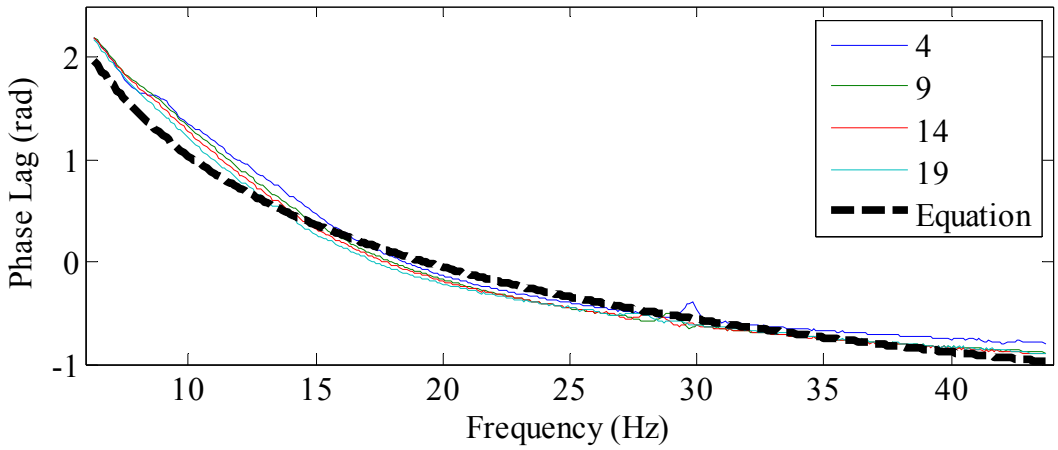

Figure 3.59. Total phase lag relative to input frequency for four input signal amplitudes and for deterministic equation.

3.4.2.2 Shaker-Structure Interaction

The next step in validating the deterministic equations is to examine whether they are valid in the presence of force drop off. The phenomenon of force drop off in shaker output has been analyzed by several authors. Rao (1987) developed equations based on the electro-mechanical construction of shakers that explain why force drop off occurs. Essentially, for lightly damped structures vibrating at a natural frequency, the velocity of the structure approaches the velocity of the moving mass and thus a reduction in the force transmitted occurs. Varoto and Oliveira (2002) revisit the issue and include effects due to the natural frequency of the shaker. They also consider the difference between an amplifier in voltage or current mode and validate that using current mode ameliorates the force drop. Davis et al. (2011) examined this issue while testing if it is better to measure input via the acceleration of the moving mass or with a force transducer. Due to force drop off, a force transducer provides the better measurement. They also found that the greater the difference between the mass of the structure and the mass of the shaker, the less the force drop. This is logical since a more massive structure will have much smaller displacements relative to the moving mass.

Overall, the literature indicates that the force drop off phenomenon is worst with lightly damped structures, amplifiers operating in voltage mode, and with less massive structures. Unfortunately, all three of these problems are unavoidable for the laboratory model structure. The inexpensive audio amplifiers only operate in voltage mode, and the steel bridge model is a light structure that is very lightly damped. However, Rao suggests that lower force input may diminish the phenomenon, and so a test is conducted on the bridge model to evaluate if the force input approaches the deterministic values at low excitation levels.

3.4.2.2.1 Test Method

This testing is essentially identical to the input amplitude testing, except that the shaker is placed on the bridge model third-point instead of on the pylon. Only the left channel of Amplifier 1 and only Shaker H are used. A multisine signal is sent from the Agilent signal generator to the amplifier. The amplifier drives the shaker, which is mounted to the bridge model via the force transducer tripod. The Agilent output, the amplifier output, and the shaker force output are all simultaneously recorded so that the amplitude and phase changes can be analyzed. The multisine signal is the same as shown in Figure 3.55 and is again run six times consecutively at each particular input level. During processing, the first run is eliminated since it contains a non-periodic transient, and the other five runs are averaged in the time domain to reduce the effects of noise. This is performed for each of twenty tested input amplitudes which again vary from 0.01 volts to 0.20 volts.

3.4.2.2.2 Analysis and Results

The results indicate that lower excitation levels have no discernible effect on the force drop off. Figure 3.60 shows the normalized output force for four levels of input amplitude. The values are normalized by dividing by the force measured on the steel pylon, which highlights the spikes in the plot at the structure natural frequencies. Note that the excitation level of 4 (0.04 volt input to amplifier) is near the lower limit of the operating capability of the shakers. Below this level, the magnetic force generated by the coil is less than the static friction of the mass, and no shaking force is produced. Thus, the curves on this plot represent nearly the full range of excitation level that the tactile transducer can provide.

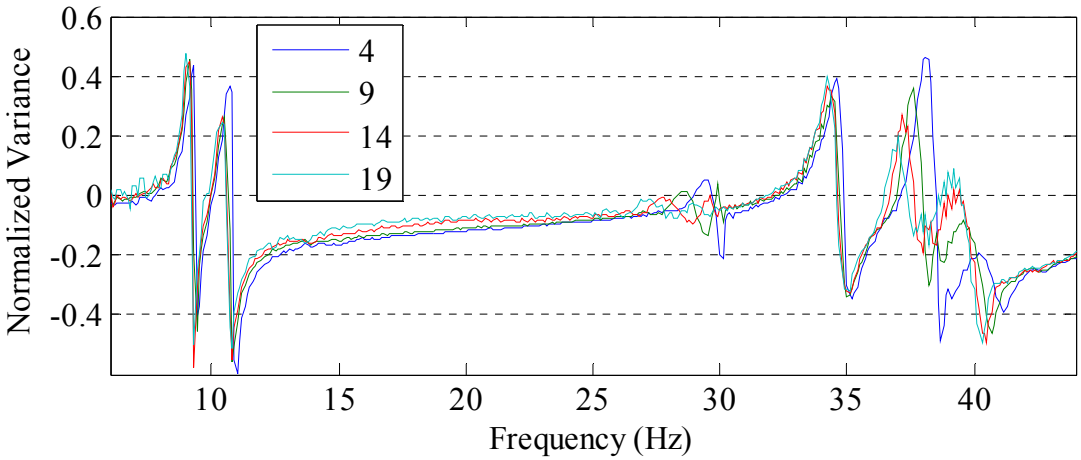

Figure 3.60. Normalized variance in force amplitude for four levels of excitation at the bridge model third-point.

3.4.3 Deterministic Equation Summary

An attempt was made to model the behavior of the amplifiers and the shakers with deterministic mathematical equations. Equations that described the amplitude and phase change of signals caused by the devices were developed, and were fit via a least squares process to experimental data. The resulting equations were then evaluated over a range of signal input frequencies and amplitudes, and on a physical structure.

The result is that the phase of the output force can be predicted; however, the amplitude of the output force is not easily predicted. Both the amplifier and the shaker have nonlinear gain responses to changes in input amplitude. The gain could potentially be fit to more variables to improve the prediction of output amplitudes, but this has little value since other issues exist. To wit, the force drop off phenomenon significantly violates the predictions of the deterministic equations, further reducing their utility. The force drop off will be different on every tested structure, and thus there is no way to incorporate this affect.

Overall, the attempt to the use deterministic equations to transfer an input signal to a force output signal failed. The output is structure specific and spatial location specific. However, it may still be possible to use pre-recorded force outputs to reduce the need for force transducers.

3.4.4 Alternative Approaches for Measuring Excitation Force

Although the use of deterministic equations failed to accurately predict the force output of the shakers, a more cumbersome method to avoid the use of a force transducer at every shaker may still be effective. This method would require the force output for a given signal to be measured once for each amplifier-shaker pair. Because of force shaker-structure interaction, the force output would have to be measured at each spatial location on the structure to be tested. After the measurement of all force inputs, production testing would commence and it would be assumed that the force does not vary during these subsequent runs of the same signal. Later, frequency response functions would be calculated using the actual output measurements and the assumed input measurements.

Although theoretically possible, this method has a number of shortcomings that make it undesirable. First, this method limits the number of unique signals that can be used. Realistically, only a small number of unique signals could be used on a given day since each signal must be recorded separately for each shaker, and this takes time. Certainly, it would be impossible to use any signals with a random component for testing since these signal types require many realizations. This includes true random, burst-random, pseudo-random, or periodic random signals. Additionally, only a few examples of a deterministic signal could be used. This limits the ability to use different amplitudes of a signal, or to perform sweeps over narrow frequency bands. However, in the context of long-term testing in which the shakers are placed on a structure for months or years, this method could be utilized.

Second, it would take significant time to measure the force input at each spatial location even with a small number of signals. The force transducer apparatus would need to be installed, several runs of each proposed input signal would occur so that averaging could be utilized, and then the apparatus would need to be removed and relocated. Not only does this elapsed time cost money, it also reduces the consistency of the data and thus reduces the accuracy of the characterization. Although it is assumed that the structures are time invariant, this is not the case and elapsed time between recording the force input and the structure output provides significant opportunities for weather or other factors to alter the structure's response.

A third issue is bookkeeping. During the recording of the various signals at the various input locations, great care would have to be taken to document these items. This is undesirable since there is always a time crunch during testing, with many people performing various activities simultaneously, and with a resultant increase in probability of mistakes. Also, if a piece of equipment such as a shaker or an amplifier malfunctions during testing and a replacement is used, the force output must be recorded again but only used for data sets subsequent to the replacement.

Finally, if the force input is not measured directly at each shaker during all testing, other errors occur. For instance, it has been noted that the force output changes by as much as 5% depending on the temperature of the shaker coil. There is also variance in the amplifier gain, and the phase output for the amplifiers and the shakers. If the force is recorded during testing, then these issues have no affect on the results of the structure characterization. However, if the force is not recorded, then the variability of these items results in errors in the characterization of the structure.

Overall, this method is attempted in subsequent testing, and is referred to as 'roving force transducers.' Despite the many potential issues, a long-term goal is to use many shakers (20+), and measuring all force input simultaneously would require a DAQ channel for each shaker. On the other hand, roving five (for example) force transducers would greatly reduce costs.

3.5 CONCLUSION

3.5.1 Shaker and Amplifier Testing Summary

This chapter focused on additional testing and characterization of the shakers and amplifiers for use in modal testing. To reduce the cost and complexity of MIMO testing using the multi-shaker excitation system, it is desirable to avoid the use of force transducers. Also, if the shakers and amplifiers operate in a uniform manner, then they can be used interchangeably. Therefore, tests were devised to validate the variability in shaker force output and amplifier gain.

- In subsection 3.2.1, the uniformity with which a shaker reproduces a force output for a repeated input was tested first. The result is that the force output is highly repeatable, with an individual shaker's output varying by only 1% to 2% for both a stepped-sine and random input signal. Also, a significant portion of the variance is caused by the increase in the temperature of the shaker voice coil during use. The affect of this can be reduced by operating the shakers for several minutes immediately prior to performing testing.
- In subsection 3.2.2, the uniformity of a population of shakers was tested. The outcome is that the shakers have an average variance in force amplitude of about 7%, but the phase angle has a lower variance of about 3%. The twelve shakers were purchased at different times and the testing results clearly show that the manufacturer changed the product since the first four shakers acquired operate differently than those acquired later.

- In subsection 3.2.3, the uniformity of shaker force output was tested on a laboratory bridge model to evaluate shaker-structure interaction. The shakers were located at two spatially distinct locations on the model and the affect of the structure response on the force measurement was analyzed. The results of this testing are that the force output is significantly affected by both the reaction of the structure and by the spatial location of the shaker on the structure. Force output varied by up to 100% for frequencies in the vicinity of a natural frequency of the bridge model; however, forces were uniform away from bridge model natural frequencies.
- In subsection 3.3.1, the uniformity of an amplifier's voltage output for a given input signal was also tested. The result is that the amplifiers produce highly repeatable output with the output voltage signal varying by less than 0.1% for both stepped-sine and random input signals.
- In subsection 3.3.2, the uniformity of a population of amplifiers was tested. The outcome of the testing shows that the amplifiers' output voltage amplitude varies by about 2% on average.
- Finally, in subsection 3.3.3, the output of a single channel of an amplifier was tested to determine whether it was affected by loading of the amplifier's other channel. The result is that for unnecessarily high input voltages, the output amplitude is reduced by as much as 10%. However, it was found that more careful selection of input voltage eliminated this issue, and that the force output was then not affected by the use of a single or both amplifier channels.

Overall, the testing showed that uniformity in force output of an individual shaker is generally within 2% of force amplitude, and that the consistency for an individual amplifier is generally

within 0.1% of voltage amplitude. The testing also indicates that the shakers must be considered as individuals since there is a large variance in force output, and since newer shakers may be added and older shakers may be replaced at any time. The amplifiers must also be considered as individuals since their gain is variable.

3.5.2 Force Transducer Requirement Summary

Ideally, money is no object and unlimited force transducers and data acquisition channels would be available. The reality for the work reported herein is that budget constraints do not permit the simultaneous measurement of force input for the number of shakers that are available. Thus, it is desirable to avoid the use of a force transducer at every input so that more DOFs can be simultaneously excited. The idea of fitting deterministic equations to the excitation system was explored, but the variability in force output due to several sources introduces excessive error.

First, every shaker operates as a unique individual and each amplifier does as well. This could possibly be overcome with careful bookkeeping, however, the use of force transducers allows the amplifiers and shakers to be used completely interchangeably with no regard for which one is used where. This greatly reduces the potential to get incorrect results due to a setup mistake. Second, force drop off near the natural frequencies of a structure under test significantly impacts the force input. Third, the excitation force can potentially change during testing due to a myriad of reasons. The shaker coil temp, the time variance of the structure, any test setup change, any accidental modification of the equipment or apparatus, etc. will all vary the force input as testing proceeds. Thus, force transducers should always be used for reliable results to be captured.

A less-desirable alternative that allows simultaneous excitation of more DOFs than the number of available force transducers is to rove the transducers. Roving incorporates the variability due

to non-uniform amplifiers and shakers, and incorporates force drop off, but does not take into account any input changes that occur during the testing time. The use of roving force transducers also increases testing time and complexity; however, due to budget limitations, using roving force transducers is tested later in this thesis.

CHAPTER FOUR

EXCITATION TECHNIQUES

4.1 INTRODUCTION

This chapter considers the important choice of excitation signal type, force level, and spatial location for the MIMO experimental modal analysis of bridge structures using multiple shakers. The quality of the measured frequency response functions (FRFs) is directly related to the parameters of the excitation. Although MIMO EMA is common in the mechanical and aerospace fields, only two examples are reported in the literature for civil structures (Schwarz and Richardson 2001 and Miskovic et al. 2009 as noted previously). Neither of these papers provide details on optimization of the input.

Thus, it is necessary to determine the best techniques for MIMO EMA excitation of short to medium-span bridges. This is performed in the following steps:

- The available literature is reviewed for context of the problem
- Issues that affect the measurements of FRFs in regards to the methods of usage of various signal types are discussed
- The variety of alternate input signal types are discussed and compared
- Methods to determine the optimal input force level are discussed
- Methods to determine the optimal spatial distribution of input are discussed
- Finally, the best signals are selected for MIMO EMA with tactile transducers, and the manner in which force level and spatial distribution will be determined for any tested structure is documented.

4.2 BACKGROUND AND CONTEXT

Because of the importance of the input signal in the accurate estimation of modal parameters, literally hundreds of papers and many books have been written on the subject by researchers and practitioners in the mechanical and aerospace fields. A brief literature review that provides a sampling of commonly cited papers is presented to provide some historic perspective on the subject and to frame the selection of excitation techniques for the research presented herein.

Prior to the availability of the digitally implemented fast Fourier transform (FFT), modal testing was performed with slowly swept sinusoidal input and a tracking filter. By the early 1970's, hardware was available that allowed the excitation of test objects with arbitrary waveforms consisting of a broadband spectrum. The switch from using a single frequency at a time to broadband input allowed a significant reduction in testing time, and this encouraged researchers to explore the use of a wide variety of signal types.

Allemang, et al. (1983) advanced the idea of multiple-input, multiple-output (MIMO) experimental modal analysis. Prior work by others had formulated the theoretical basis, but experimental work was lacking. In this paper, several experimental advantages that could be expected with the successful implementation of MIMO were mentioned, but the main advantage touted was in the great reduction of required testing time. A major concern noted was the correlation of inputs, and so only random signal types were considered. An airplane was tested with three inputs and a single output with continuous-random, periodic-random, and burst-random signals. The burst-random signal was shown to produce the best FRFs in this testing.

Zimmerman and Hunt (1985) took the idea of MIMO testing with random signals further. They tested three aircraft with burst-random and continuous-random signals and concluded that burst-

random was far superior primarily due to the reduction of leakage error. They also listed out eight reasons why MIMO testing is superior to single-input testing, although they did not validate these reasons with experimentation. They still had concerns with correlation of the signals, worrying that the forces may be correlated by the response of the structure.

Hunt (1987) was one of the first to report on using determinate excitation for MIMO testing. To avoid issues with correlation, the inputs were simply made out of phase with each other. He noted that hardware had to be developed to make this possible. Experiments were performed on rocket motor bodies, and the results indicated that the method is superior to using single-input determinate excitation. Unfortunately, this paper did not directly compare burst-random with determinate testing.

Many other researchers promoted different signal types for various testing situations, and eventually Schoukens, et al. (1988) set out to determine which signal type was best. In this paper, the writers developed a mathematical measure of the quality of a signal, which they called the time factor. This measure incorporated signal to noise ratio (SNR), peak factor, and averaging requirements. They then determined the value of the time factor for ten signal types, and summarily promoted the use of multisine signals since this excitation type had a low time factor. They also showed that the common belief that random signals average out nonlinearities is not true. However, this belief persists to this day.

Hunt and Brillhart (1991) summarized a great amount of the testing community's results of the preceeding decade using random excitation. They touted MIMO and discussed the benefits of using more exciters. They also wrote about selecting an appropriate force input level and recommended a qualitative method in which the force level that gives the smoothest FRFs is

used. Finally, they continued to recommend using burst-random excitation in testing of lightly damped structures.

In an effort to assist the testing community in selecting good locations for shakers, Imamovic and Ewins (1997) attempted to create a mathematical method that would quantitatively indicate the locations that should be excited. The method required a-priori knowledge of the mode shapes, but then did allow the calculation of a number that represents the relative value of exciting at a particular spatial location. This method does not seem to have been adopted by others.

In a further effort to evaluate the merits of random as the excitation signal of choice, Pintelon and Schoukens (1998) mathematically proved that continuous-random, burst-random, and multisines all provide the same linear approximation of nonlinearities. Despite this, other researchers do not seem to have adopted the use of multisine signals.

Guillaume, et al. (2001) also wrote about the benefits of multisines and discussed various methods for optimizing the crest factor of the signal. The authors statistically show that the FRFs are best estimated by use of a maximum likelihood estimator as opposed to the traditional H1 estimator. They also show the optimum application of multisines to MIMO testing by using a Hadamard matrix to force the testing realizations to be orthogonal. However, this requires that the number of inputs is a power of two.

Solomou and Rees (2003) presented work on developing the best linear estimate of slightly nonlinear systems using multisines. They encouraged the use of a crest factor optimization algorithm known as L_∞ which enables this best linear estimate.

Dobrowiecki, et al. (2006) set out to determine the optimum method for using multisines in MIMO testing. The authors noted several reasons why all forms of random excitation are inferior to multisines in the estimation of FRFs. They then compare three different methods of using multisines in MIMO testing with the point of not only avoiding any issues with correlation, but providing nearly orthogonal excitation realizations for any number of inputs.

Overall, a great deal has been written on selecting excitation signals for various types of modal testing of mechanical and aerospace systems. The signal types and testing procedures have changed over time as new research has been performed, and as new hardware and software have been developed. However, the literature does not demonstrate how this knowledge should be adapted to EMA of civil structures.

Therefore, for the work of this thesis, the information that exists is considered in the context of bridge testing. The optimal signal must be compatible with MIMO testing, should minimize leakage and other errors, should minimize testing time, and would preferably enable testing to proceed with the use of roving force transducers. Seven signal types are analyzed and compared herein.

4.3 DEFINITION OF TERMS AND DISCUSSION OF ISSUES IN SIGNAL SELECTION

This section introduces the issues that are important in selecting an appropriate excitation signal for the testing proposed in this thesis. It also describes and defines common procedures and terms used in testing so that the later comparison of signal types can be readily understood.

4.3.1 Overview and Issues

Excitation signals include any type of force input that is intended to produce a response in a structure under test. Four major categories of excitation exist: ambient; impact; relaxation; and

shaker. Ambient inputs are the unmeasurable excitations from the surrounding world. This ambient input can be used as the only excitation if some assumptions about the frequency content are made; however, modal flexibility cannot be calculated without a known force input, and thus ambient excitations are not adequate for the work of this thesis. Impacts are also often used to excite structures. The impact force can be applied with devices ranging from small hammers to massive drop weights. However, impact excitation has many drawbacks and is not fit for MIMO testing of bridges. Relaxation is an excitation method wherein a structure is deformed by a force which is then suddenly released. The free vibration of the structure after release is measured. This type of excitation is similar to impact in many ways, but is far more difficult to actually perform in the field.

Finally, mechanical shaking devices can be used to impart signals of any duration or character. Mechanical shakers can generally be divided into three groups. Eccentric mass shakers have a rotating mass (or masses) that is eccentric and thus generates sinusoidal signals. Reaction mass shakers position an actuation device between the structure under test and a massive object (such as the earth), and the force applied to the structure can usually be of any character. Linear mass shakers use hydraulic or electro-magnetic actuation to move a mass, resulting in an output force that can usually be of any character. The tactile transducers are linear mass shakers, and thus the signal types discussed herein are those that are commonly used with this style of shaker.

Three major issues must be considered in the selection of the best excitation signal for this research. First, the signal must minimize the bias error known as leakage. Second, the signal must be usable in a MIMO environment. Finally, to enable the use of roving force transducers, the signal should be deterministic (not a unique realization of a probability distribution). Each of these three issues is discussed in more detail below.

4.3.1.1 Leakage Error

The types of signals commonly used in testing are largely a result of the requirements of the fast Fourier transform (FFT). For the transform to give best results, the time domain input and output signals must meet one of two requirements. One requirement is that the entire time history is captured. The other requirement is that the captured signals are periodic and thus could extend in exactly the same manner infinitely into the future and past. Otherwise, a type of error known as leakage occurs.

An example of a periodic signal and its FFT are shown in Figure 4.1, and an example of a non-periodic signal and its FFT are shown in Figure 4.2. It is clear that the amplitude of the non-periodic signal gets 'smeared', or leaked, into the adjacent frequency lines. This error affects both the transform of the input signal and the output signal. For the output, peaks exist at natural frequencies, and these peaks are made shorter and wider if leakage occurs. This has a large affect on calculated damping and modal scaling values.

Leakage can be avoided by the choice of testing procedure. One procedure is to use an excitation that is periodic in the observation window, and capture a simultaneous response that is also periodic in the window. A second procedure is to use a transient excitation signal that is completely observed in the window, and capture a simultaneous response that is also completely observed.

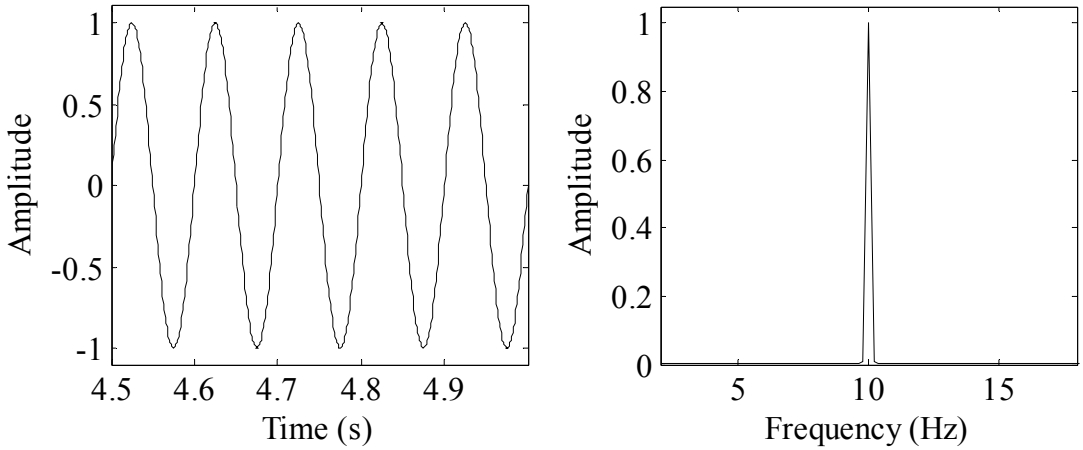

Figure 4.1. Signal that is periodic in the transform window; time and frequency domain.

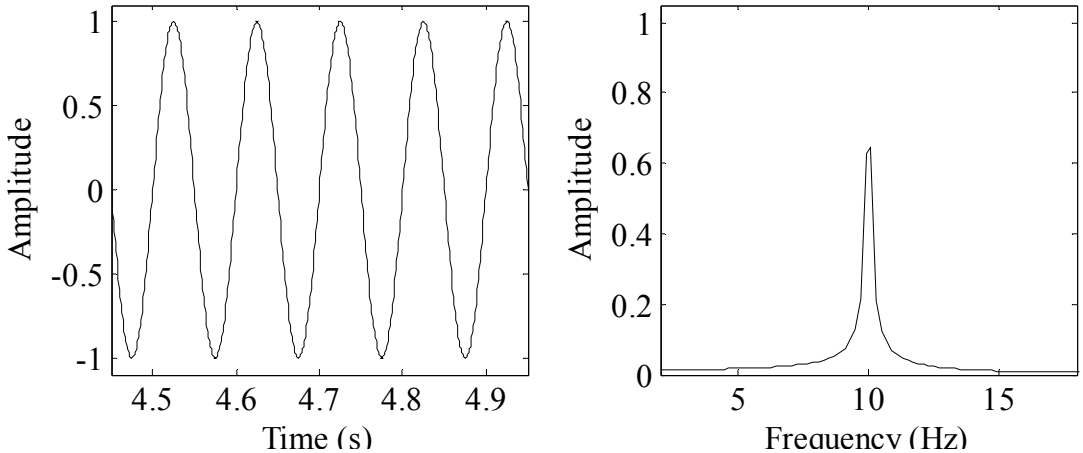

Figure 4.2. Signal that is half a period short of being periodic in the transform window; time and frequency domain.

4.3.1.2 MIMO Signal Requirements

The use of simultaneous multiple excitation creates some added requirements if frequency response functions (FRFs) are to be found. FRFs are simply a ratio of the output to the input. Several common formulations that can be used with multiple inputs exist depending on the nature of the input signal, but they all require dividing the output measurement by the measured inputs. The problem is demonstrated below at a single discrete frequency line for a system that has two inputs and two outputs. The definition of the transfer function is:

$$\begin{Bmatrix} X_1 \\ X_2 \end{Bmatrix} = \begin{bmatrix} H_{11} & H_{12} \\ H_{21} & H_{22} \end{bmatrix} \begin{Bmatrix} F_1 \\ F_2 \end{Bmatrix}$$ Equation 4.1.

Where:

X_i = the output at DOF i.

H_{ij} = the transfer function or FRF for output i due to input j.

F_j = the input at DOF j.

It is clear from the formulation that there are four unknown FRF values but only two equations. This requires that a second experiment be conducted so that additional input and output pairs can be measured. If the force inputs between the two experiments, experiments 'a' and 'b', are linearly independent, then the four unknown FRF values can be directly solved with the four independent equations:

$$\begin{Bmatrix} X_{1a} & X_{1b} \\ X_{2a} & X_{2b} \end{Bmatrix} = \begin{bmatrix} H_{11} & H_{12} \\ H_{21} & H_{22} \end{bmatrix} \begin{Bmatrix} F_{1a} & F_{1b} \\ F_{2a} & F_{2b} \end{Bmatrix}$$ Equation 4.2.

The transfer function can now easily be found by using any appropriate algorithm that solves the general linear algebra problem of $Ax = b$. However, if the two forcing functions are linearly correlated at any frequency line, then the force matrix will be singular at that frequency line, and a solution cannot be found.

Thus it is seen that for FRFs to be found in MIMO testing, two requirements must be met. First, the experiment must be realized at least N_i times, where N_i is the number of input DOFs. Second, there must be at least N_i force inputs, none of which are perfectly correlated at any frequency line. It must also be recognized that even close correlation can cause numerical issues in the solution of $Ax = b$.

4.3.1.3 Roving Force Transducer Use

As has been mentioned in earlier chapters, it is desirable to minimize the cost and the logistical complexity of the testing system. Thus, the use of roving force transducers is considered. In the best case, the force output from each shaker in a given setup, and for a given signal, can be measured once and can then be considered to be a known quantity whenever that signal is used again. In this way, force vectors would not have to be measured for every data set. The selection of an excitation signal type impacts the potential need for the transducers.

If a deterministic signal is used for each required testing realization, then the use of roving force transducers is enabled. However, if stochastic signals are used, force transducers will be difficult to avoid. The primary issue is not the number of realizations that are required for solution of $Ax = b$, the issue is that stochastic signals require many realizations to ensure that all frequency lines are adequately excited. Due to the large number of unique signals, it would take an unreasonable amount of time to record the response of each shaker, and it would also be difficult to keep track of which signal is used for which shaker in each testing realization. Thus, stochastic signals are not desirable if roving force transducers is to be attempted.

4.3.2 Averaging Methods

Averaging is the most commonly used tool for reducing stochastic errors that are present in all measurements. The two main types are cyclic averaging and power spectral averaging.

4.3.2.1 Cyclic Averaging

The cyclic averaging of data sets is a commonly used method for improving the quality of FRF measurements with periodic signals. Cyclic averaging is linear and requires that the sets to be averaged are periodic in the observation window, and that each set is due to the same input

function. As such, this averaging is most useful with deterministic signals. This type of averaging cannot be used with any true random signals since each data set would be unique. However, it is possible to use a single realization of a random signal and apply it in a periodic manner so that time domain averaging can be used to reduce the effect of noise on the output. In this way, some of the benefits of this averaging technique can be extended to random, burst-random, and periodic-random signals.

Cyclic averaging can be used in the time or frequency domain with equivalent results. However, cyclic averaging is typically performed in the time domain so that the FFT is performed on fewer data records, reducing computation time. There are two primary benefits to this type of averaging. First and foremost, the averaging reduces the random noise that is part of every real measurement. The second benefit is data reduction. If averaging is performed as each set of data is collected, then the storage requirements for the data can be greatly reduced. This was more important in the past when electronic storage was relatively expensive, whereas now experimenters are seldom limited by hard drive space. Cyclic averaging does not reduce leakage error.

The main benefit of cyclic averaging is in reduction of the random noise. Figure 4.3 shows a multisine signal that white noise has been added to. The noise has an RMS amplitude equal to 50% of the RMS amplitude of the original signal. Figure 4.4 illustrates the benefit of averaging by showing the FFT result without averaging, and with an average of five realizations of the noise. It is clear that in the presence of random noise, cyclic averaging is a good method for reduction its effects.

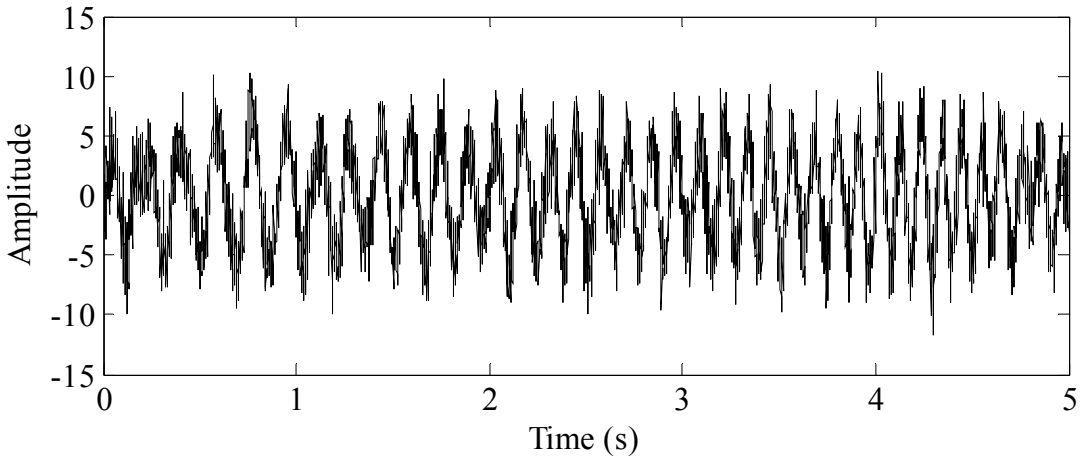

Figure 4.3. Multisine signal example in the time domain with random noise added.

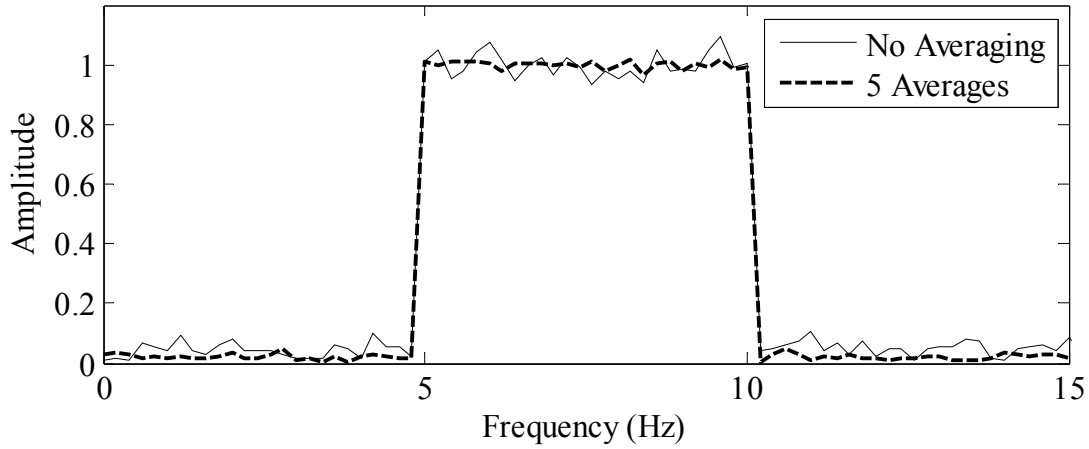

Figure 4.4. Multisine signals in the frequency domain showing the benefit of cyclic averaging in reduction of noise.

4.3.2.2 Power Spectral Averaging

Power spectral averaging is a commonly used method for improving the quality of FRF measurements with stochastic signals. The averaging is performed on the cross power and auto power spectra prior to calculation of the FRFs. Data sets are converted to the frequency domain, the auto and cross power spectra of each data set are calculated, and then linearly averaged together. After averaging, the FRFs are calculated.

This frequency domain averaging is necessary for random signals. In practical testing, relatively short periods are used for each observation window. Thus, a single realization of a random signal

is likely to have low energy at some frequencies. This is an issue in the calculation of the FRFs due to division by the force input. If the force input is very small and noise exists in the output, then the division can result in a large FRF magnitude that may be incorrectly interpreted as a system pole.

The probability that all frequencies have been adequately excited improves as more samples are collected; however, the samples cannot be averaged in the time domain since the mean value of a random signal tends to zero. Also, averaging the frequency domain signals causes the same issue. Thus, the averaging must be performed after calculation of the auto and cross power spectra. This averaging of the power spectra not only allows the combination of random signals, but also reduces the variance due to noise in the samples. Bias errors such as leakage are not reduced by use of power spectral averaging. Thus, leakage must be addressed by the choice of signal type.

An example of the benefits of power spectral averaging is illustrated. A numerical model of a cantilever beam is excited with a burst random input at a degree of freedom (DOF) that is at the tip of the beam, and the acceleration of the beam is also recorded at that DOF. White noise with an RMS amplitude of 10% of the RMS amplitude of the output signal is added to the output signal. The left half of Figure 4.5 shows the resulting FRF with the use of a single realization of the burst random signal. Spurious peaks are seen in the magnitude plot and the phase plot is very noisy. The right half of the figure shows the resulting FRF with the use of ten averages of the power spectra. The averages are the result of ten realizations of the force input signal and the noise on the output. The magnitude plot very clearly indicates the first six natural frequencies of the beam and the phase plot is also improved.

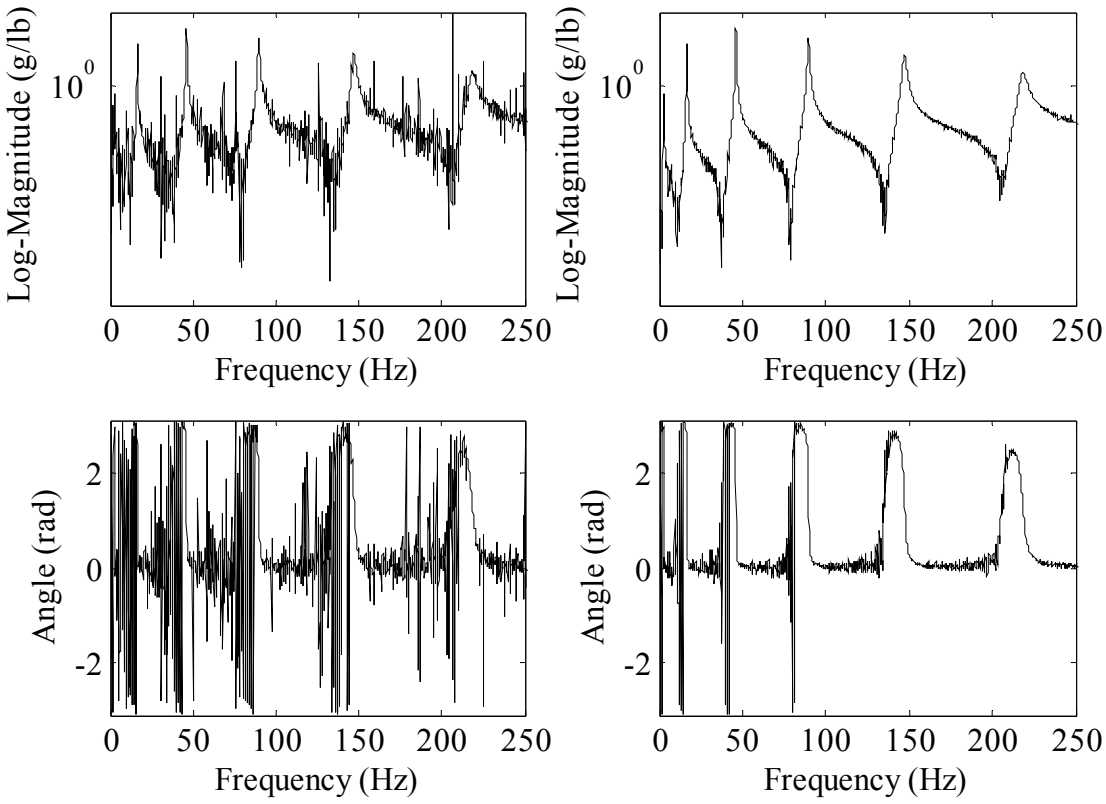

Figure 4.5. FRF magnitude and phase plots for a virtual cantilever beam. One power spectral average on left and ten averages on right.

4.3.3 Testing Time

Given any testing situation, it is beneficial to minimize the required testing time for a few reasons. First, less time spent is equivalent to less cost. Second, bridge structures are not truly stationary, and longer testing times give worse modal results due to non-stationarity decreasing the consistency of the measurements. Thus, it is desirable to select a signal that can provide equal quality of results in the least time. However, the required testing time is difficult to predict in general since it is a combination of several elements.

For periodic signals, the testing time is defined by four elements. First is the signal length. For some deterministic signals, the length is determined by the frequency content, but for others the length is selected for a desired resolution. The next element is the structure settling time. The

settling time is how long it takes for the transient response to decay so that the response is then periodic. The third element is the number of cyclic averages desired for reduction of noise. The final element of testing time is the number of multiple inputs. Each input requires a realization of the test process so that the transfer function can be determined.

For stochastic signals, the testing time is defined by only three elements. Two of the elements are the signal length and the number of inputs, the same as for deterministic signals. The final element is the number of power spectral averages required. This requirement can be controlled by either the need to reduce noise, or the need to ensure that all frequency lines have been adequately excited.

It is clear that the actual testing time for a given structure will be dependent on the level of noise, number of inputs, and frequency range of interest. However, it is possible to normalize the needed time to reach a given level of accuracy for a single frequency line. Schoukens, et al. (1988) provided a survey of excitation signals wherein they developed a measure called the time factor (TF). They defined a TF of unity as the time required to reach a selected level of FRF accuracy with a pure sine wave input. The time factor includes all of the contributing elements discussed previously except for settling time. The time factors that were found by these authors are reported within the discussion of each signal type. A lower TF is better.

4.4 SIGNAL TYPES FOR DYNAMIC TESTING

The goal of this section is to provide a description of all of the commonly used excitation signals, compare the pros and cons, and select the best signal type to use for the MIMO EMA testing of bridge structures. Seven signal types are discussed in detail, the main properties are summarized in a table, and then a signal is chosen.

4.4.1 Slow Swept Sine

The slow swept sine signal consists of sinusoidal input at discrete frequency lines over some frequency band of interest. Also referred to as stepped-sine, this signal type only has energy at a relatively small number of frequencies. In practice, a single frequency is input for a long enough time that any transient response of the structure decays prior to the start of data recording. After the desired length of data is collected, the next frequency line is tested. Sets of data for the different input frequencies are then added together in the frequency domain prior to the calculation of frequency response functions. A simple example of this type of signal is shown in Figure 4.6 after transformation to the frequency domain, and the discrete nature of the excitation is clear.

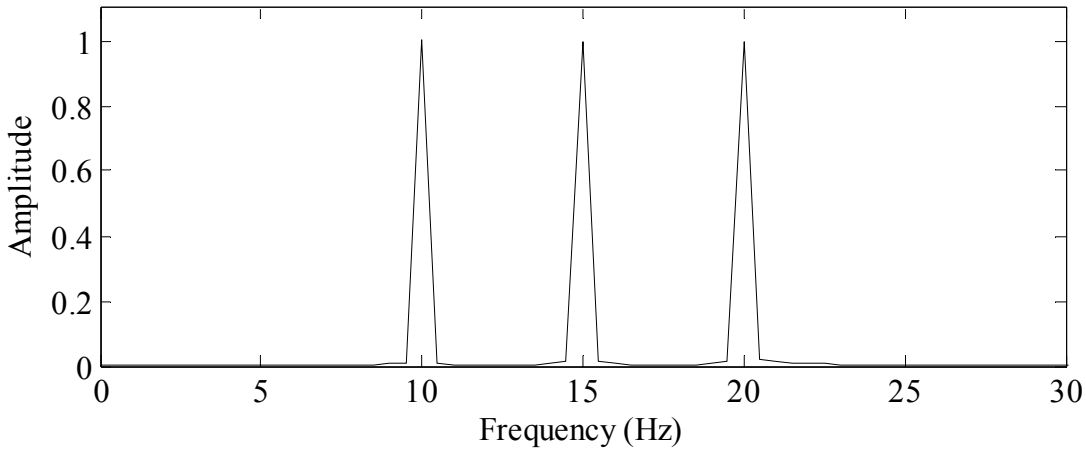

Figure 4.6. Slow swept sine example in the frequency domain.

When using the stepped-sine, leakage is controlled by the testing procedure. The recorded data blocks of both the excitation and the structural response are chosen to have a length such that they are periodic, minimizing leakage in the FFT. Also, the FFT resolution and excitation frequencies are selected so that each excitation is at one of the discrete frequencies represented in the transform.

Since the recorded data is periodic, cyclic averaging in the time domain can be used to reduce the effects of noise. Time domain averaging also reduces leakage caused by the non-periodic noise.

MIMO testing can be performed with pure sinusoidal signals. Correlation is avoided by merely altering the phase angle of inputs from one testing realization to the next. For instance, with two input locations, the first test can be performed with both input sinusoids starting each observation window at a phase of zero radians. A second test can then be performed with one of the input sinusoids starting at a phase of π radians. However, if a large number of test realizations are desired to reduce variance on the FRFs, then the phase difference between realizations will become small. This is a problem for the H1 FRF estimator, but not for other algorithms such as the maximum likelihood FRF estimator (MLE).

This type of signal has a few other advantages. First, the frequency content can be completely controlled, which allows excitation of one mode while explicitly not exciting another. Second, the TF is very good at 1.0. Finally, the use of discrete frequencies allows structural nonlinearities to be characterized.

However, the discrete frequency content causes testing using the stepped-sine to suffer from a choice of two drawbacks. One testing option is to use a large number of frequency lines so that all modes of interest are likely to be adequately excited. This option results in testing taking a very long time, potentially longer than the available time. This is because of settling time being required for each frequency change. The other testing option is to only test narrow frequency bands around the modes of interest, but this requires prior knowledge of estimated natural frequencies of the structural modes.

4.4.2 Periodic Chirp

The periodic chirp signal is composed of a sinusoid whose frequency is constantly varying from a selected minimum to a selected maximum value. This means that all frequencies in the selected band are excited to an equal amplitude. In practical testing, the chirp is typically repeated multiple times in a row and each repetition is considered as a periodic data block. This is a deterministic signal and the equation that describes a chirp signal is shown. A simple example of this signal type is shown in Figure 4.7 with the sinusoid starting at 3 Hz and finishing at a frequency of 9 Hz.

$$y(t) = A \cdot \sin\left[2\pi\left(f_{min} \cdot t + \frac{k \cdot t^2}{2} + \varphi_o\right)\right] \quad \text{Equation 4.3.}$$

$$k = \frac{f_{max} - f_{min}}{time} \quad \text{Equation 4.4.}$$

Where:

$y(t)$ = the discrete time chirp signal.

A = the signal amplitude.

f_{min} = the frequency at the start of the chirp.

f_{max} = the frequency at the end of the chirp.

k = the rate of change of the frequency.

φ_o = the phase angle at the start of the chirp.

$time$ = the total duration of the chirp.

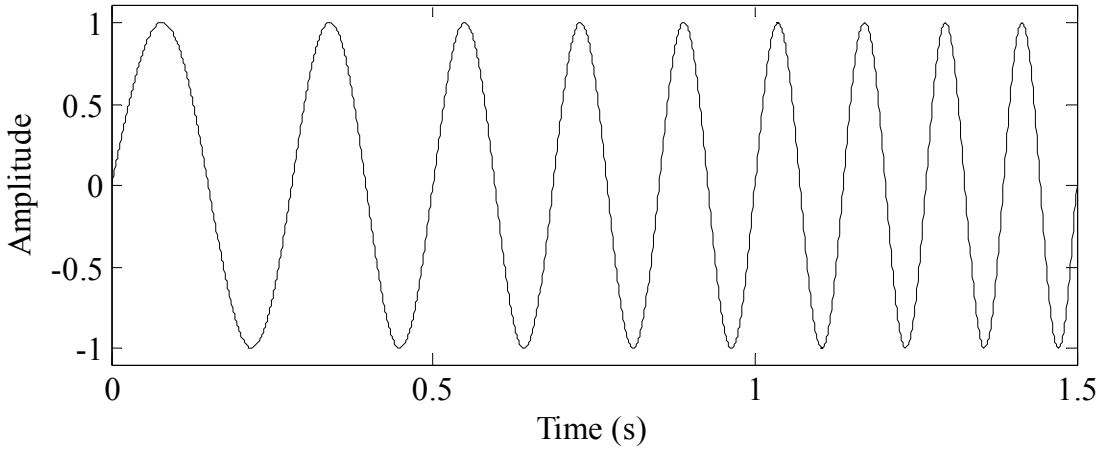

Figure 4.7. Chirp example in the time domain.

The frequency domain transform of two chirp signals are shown in Figure 4.8. This figure illustrates how the chirp provides excitation to a select range of frequencies while providing very little energy to other frequency lines. Two curves are shown to illustrate the benefits of longer chirp durations. The upper curve is for a chirp duration of 5 seconds and the lower curve is for a duration of 25 seconds. It is clear that the longer the time, the sharper the roll off at the ends of the band and the smoother the input amplitude within the band. This is largely a result of the number of oscillations within the time domain signal such that less time is needed at higher frequencies than at lower frequencies to get an equally smooth response. Since bridge testing requires generally low frequency input, chirp signals will need to be relatively long.

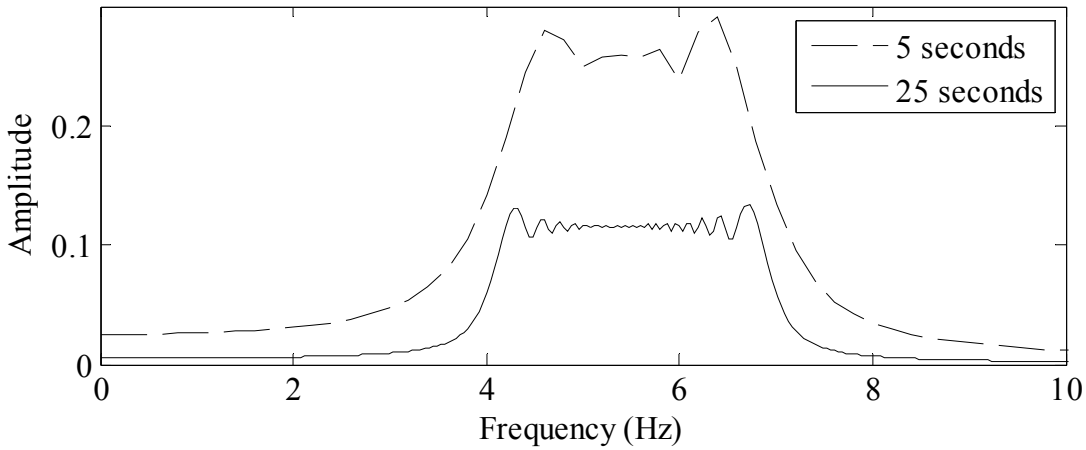

Figure 4.8. Chirp example in the frequency domain showing improvement with longer duration signal.

Leakage is reduced by the testing procedure when using a chirp. The chirp is input repeatedly and data collection begins after the transient response decays. The desired number of periodic data sets are then recorded. The periodicity of the input and output data minimizes leakage. However, since the chirp excites all frequencies, there is leakage in the FFT of the chirp that comes from between the excitation of frequencies that are between the discrete frequency lines that are represented in the FFT. Since the input amplitude is typically flat, this type of leakage is usually not an issue.

Since the chirp signal is periodic, cyclic averaging in the time domain can be used to reduce the noise and the leakage caused by the non-periodic noise.

MIMO testing with a chirp is the same as testing with a stepped-sine. The phase of the signal must be varied for each testing realization so that correlation is avoided. This can impact the choice of FRF algorithm as discussed for stepped-sine.

There are several other advantages to the chirp signal. First, the frequency content can be controlled such that desired bands can be excited while other bands are largely excluded. Second,

all frequencies within the excitation band are guaranteed to be excited for a true analog signal. For a discrete digital signal, it is necessary to select a time step in signal generation that is small enough to provide the desired resolution of excitation. Third, since the signal is deterministic, it is possible to characterize structural nonlinearities. Finally, the TF ranges between 1.5 and 4.

One disadvantage of the chirp signal is that for low frequency excitation, the signal may need to have a long duration to provide reasonably smooth frequency input amplitude (and thus the higher end of the TF is reached). Alternately, with prior estimates of the natural frequencies of the structure under test, high resolution narrow band chirps can be used.

4.4.3 Random

The pure random signal (i.e. continuous-random) is a collection of random numbers selected from a probability distribution, and the signal is described by the statistical underpinnings of the distribution. Any time domain sample generated for a given definition of a random signal would thus be theoretically unique and would have energy at all frequencies. For vibration testing, the random signals used are stationary and ergodic. Stationary mean that the probability distribution of the signal is the same at all times, and ergodic means that the statistical properties of the distribution can be deduced from any sufficiently long sample of the signal.

Figure 4.9 shows a sample of a random signal that was generated from Gaussian white noise. The definition of the signal is that it has a normal distribution, a mean of zero, and a standard deviation of one.

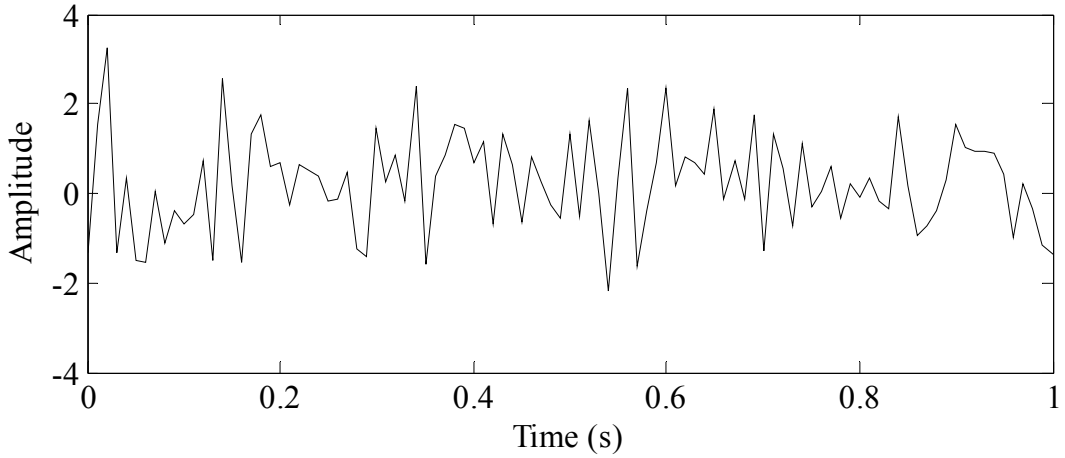

Figure 4.9. Pure random signal example in the time domain.

A random signal has several issues for use in modal testing. First, the energy content at each frequency line is highly variable and is not improved by extending the duration of the signal. Figure 4.10 shows the frequency domain results for a random signal that has a duration of 1 second and for a signal that has a duration of 5 seconds. It is seen that the resolution of the transform is increased by five times, however, the variability in the signal amplitude at discrete frequency lines is not improved. To reduce the variability, averaging must be used. This is illustrated in Figure 4.11 for 10 averages and for 100 averages. In both cases, the duration of each data set was 1 second, and it is clear that the amplitude of the frequency content is significantly improved by averaging more sets.

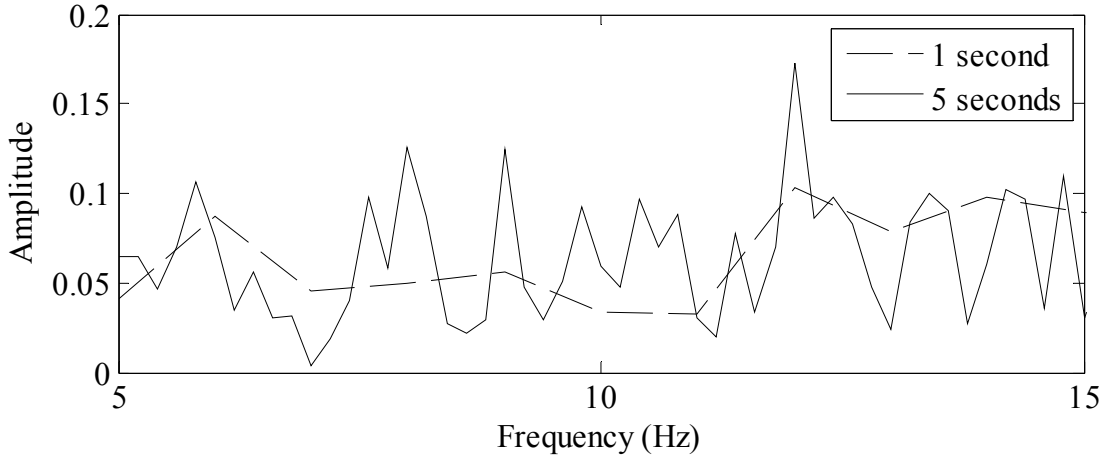

Figure 4.10. Pure random signals of different durations in the frequency domain.

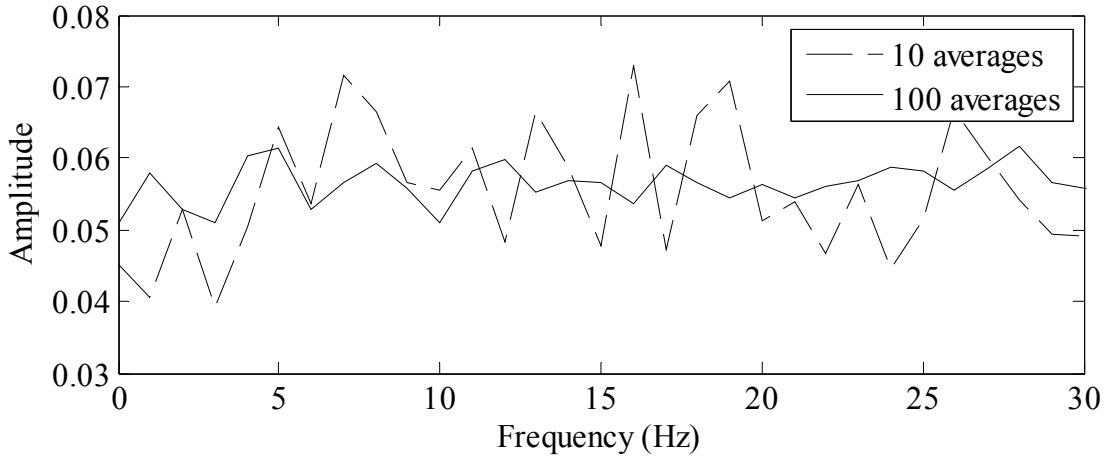

Figure 4.11. Pure random signals with different numbers of averages in the frequency domain.

Leakage is a major problem when using a pure random signal. The excitation is not periodic in the observation window, nor is it a completely observed transient. Traditionally, a Hanning window was applied to both the excitation and response time histories to reduce the leakage by forcing the data to zero at both ends of the window. Unfortunately, the Hanning window causes other bias errors. Since a random signal also excites all frequencies, leakage from between the discrete frequencies lines also occurs, and can cause issues since a single realization has significant peaks and valleys.

Averaging of the data is complicated by the continuous random signal. Time domain averaging cannot be used since the mean of a random signal is zero. Frequency domain averaging also cannot be used since the amplitude will still approach zero. Therefore, the averaging for the random signals is undertaken by averaging the auto-power and cross-power spectra of the inputs and outputs. The disadvantage of averaging in this manner is that more data storage is required and more computation time is consumed.

Random signals are desirable for MIMO testing. Since each realization of the input signal is unique, correlation of the signals if not a major concern. Typically, many realizations are performed so that all frequencies are likely to be excited, and this provides a high probability that an adequate number of uncorrelated signals exist. However, a unique realization is required at each input location, not just for each test. Also, the pure random signal has a good TF of 1.5.

4.4.4 Burst-Random

The burst-random signal is also a stationary, ergodic signal, but varies from the pure random signal in that the signal is set to a deterministic value of zero after a portion of the sampling time elapses. This is done so that the response of the structure under test has time to decay and thus both the signal and the response are almost totally captured in the observation window. An example of a burst-random signal is shown in Figure 4.12.

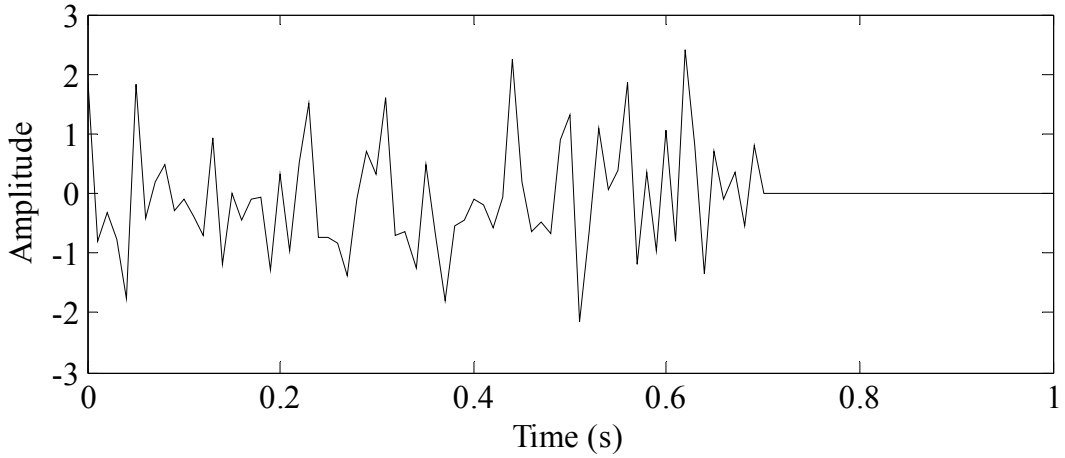

Figure 4.12. Burst-random signal example in the time domain.

The burst-random signal exists as a result of researchers attempting to reduce the leakage error while keeping the benefits of a random signal. Leakage can be nearly eliminated if the excitation ends early enough in the observation window that the structural motion has time to practically decay to zero. However, since a random signal excites all frequency lines, leakage from between the discrete frequencies represented in the FFT still occurs. As with the continuous random signal, this leakage can be significant since a single realization of the burst-random signal is likely to have peaks and valleys.

Averaging of many data sets is required to ensure that all frequency lines have been adequately excited. As with the continuous random signal, the averaging must occur after response spectra are calculated, increasing data storage and computation time.

The burst-random signal is the most commonly used excitation method for MIMO testing. Each realization is unique, so correlation is not an issue so long as many sets are collected. As with the continuous random signal, any number of test realizations can be performed, but a unique excitation realization is needed for each input location.

The TF for burst-random is dependent on the length of the signal portion that is set to zero. The longer the duration of no input, the worse the signal to noise ratio, and thus the worse the TF. For a reasonable burst that is 80% of the length of the window, the TF would be about 1.7.

4.4.5 Pseudo-Random

The pseudo-random input signal is also stationary and ergodic like the pure random signal; however, the frequency content is controlled such that there is energy input at only frequency lines that will exist in the FFT, and the amplitude is constant while the phase angle is random. An example of a pseudo-random signal is shown in Figure 4.13. The absolute value at each frequency line is shown since the random phase angle causes the amplitude to be spread between the real and imaginary parts. This signal is then transformed to the time domain using the inverse FFT and the result is shown in Figure 4.14 where it is clear that the amplitude is constant and the phase angle is random. The contributing sinusoids were separated for illustrative purposes. The actual signal is the superposition of the three sinusoids.

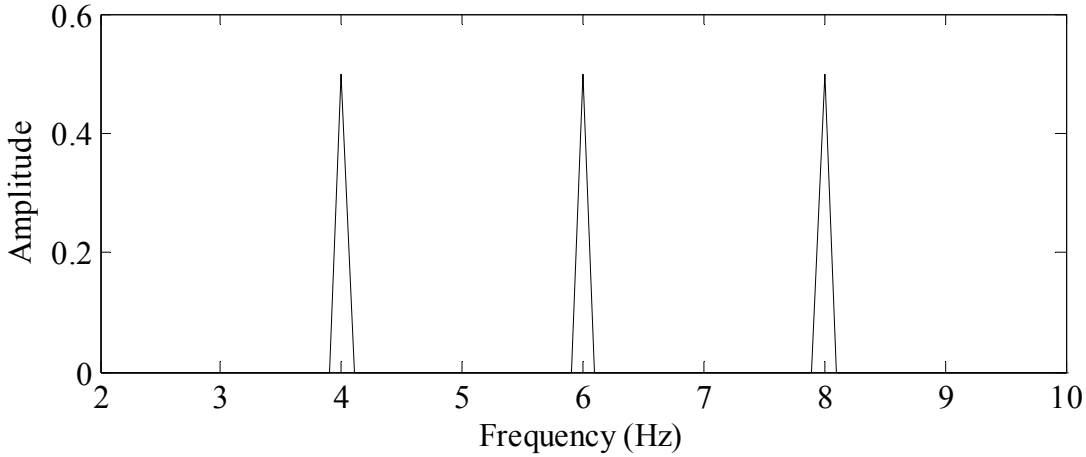

Figure 4.13. Pseudo-random signal example in the frequency domain (absolute value).

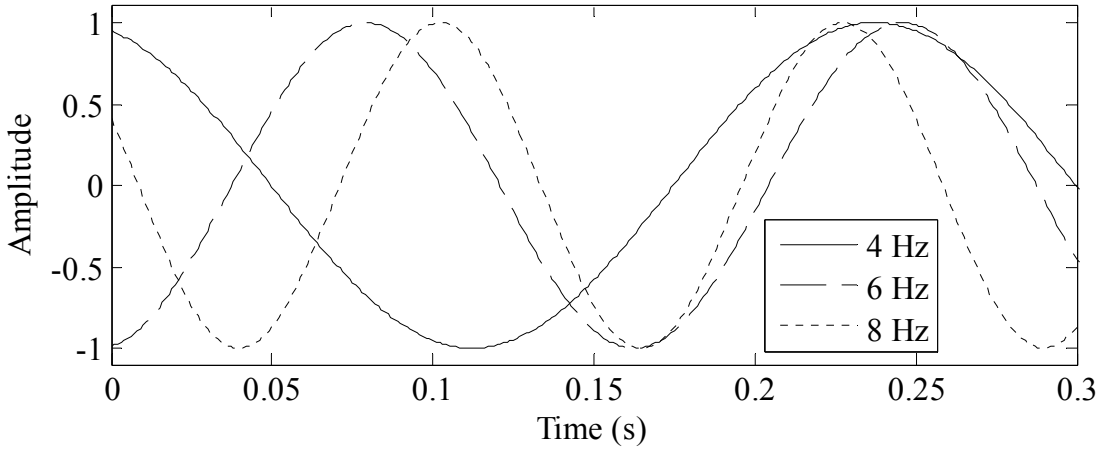

Figure 4.14. Pseudo-random signal transformed to the time domain with contributing frequencies shown separately. Note constant amplitude but random phase.

Control of the frequency content eliminates the leakage that occurs from between the discrete lines when all frequencies are excited. The test procedure is used to eliminate the leakage error that is due to nonperiodicity. In practice, the signal is input repeatedly. After the decay of the transient response, the input and output are periodic. In this way, a periodic input and response are captured in the observation window and leakage is theoretically eliminated. This testing method requires the repeated use of a single realization of the pseudo-random signal; i.e. the phase angle is not randomized on each repeated input of the signal.

Since this signal is periodic, cyclic averaging in the time domain can be used to reduce the noise and the leakage caused by the non-periodic noise. The application of deterministic amplitudes to the desired frequency lines eliminates the need for averaging of the power spectra.

This signal is a good candidate for MIMO testing. Correlation issues can be reduced by the use of random phases in many realizations. Random phases are also required for each shaker within each test.

The TF for pseudo-random signals is generally between 2 and 4.5. Since the phases are random, the superposition of the various frequency sinusoids can cause large peaks (in the time domain) in a particular realization, and this uneven input amplitude makes the TF worse.

4.4.6 Periodic-Random

A variation of the pseudo-random signal is the periodic-random signal. This is exactly the same as pseudo-random except that the amplitude at each frequency is random instead of the phase. This signal is less desirable than the pseudo-random since many averages are required so that adequate excitation can be expected at all frequencies. The TF is also worse at 4.5.

4.4.7 Multisine

The multisine signal has been the subject of much more recent research than the other signal types. Although there are several versions of multisine signals, they typically consist of a selection of sinusoids that are added together and whose phases and amplitudes are controlled in a manner that optimizes particular properties depending on the testing situation. The signal can also selectively be designed to optimize the ratio of the peak amplitude to the RMS amplitude. This significantly improves signal to noise ratio, which decreases variance on the FRF (by reducing the effect of small denominator values).

There are several methods in the literature that provide low peak to RMS ratios (Guillaume et al. 2001). A simple method for selecting the phases is known as the Schroeder multisine and is shown below. This method is used in the production of Figure 4.15 and it is apparent that the amplitude is fairly constant throughout the signal length.

$$y(t) = \sum_{k=1}^{F} A_k \cdot \cos(2\pi \cdot k \cdot f \cdot t + \varphi_k)$$ Equation 4.5.

$$\varphi_k = -\frac{\pi \cdot k(k-1)}{F}$$ Equation 4.6.

Where:

$y(t) =$ the discrete time multisine signal.

$F =$ the total number of frequency lines in the signal.

$A_k =$ the amplitude for the k-th frequency line.

$f =$ the step size between frequency lines.

$\varphi_k =$ the phase angle for the k-th frequency line.

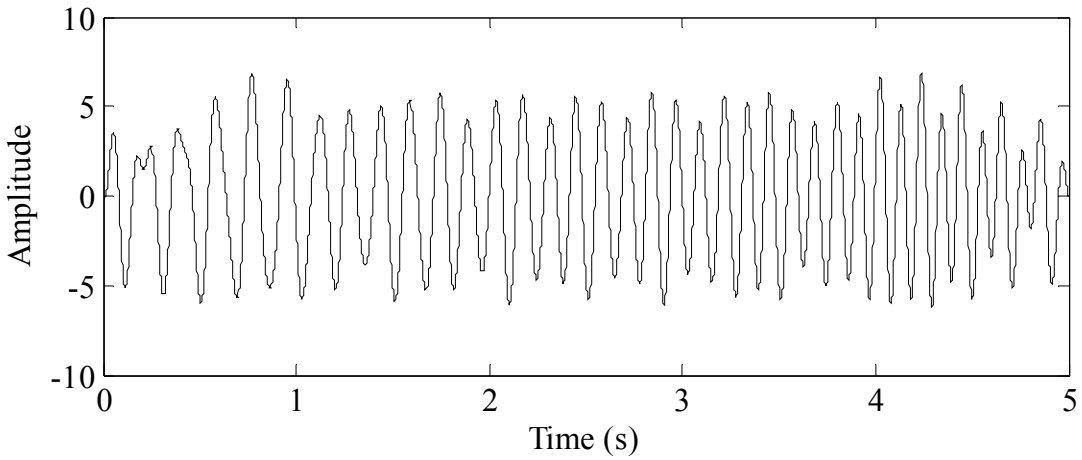

Figure 4.15. Multisine signal example in the time domain. Note consistent peak amplitudes.

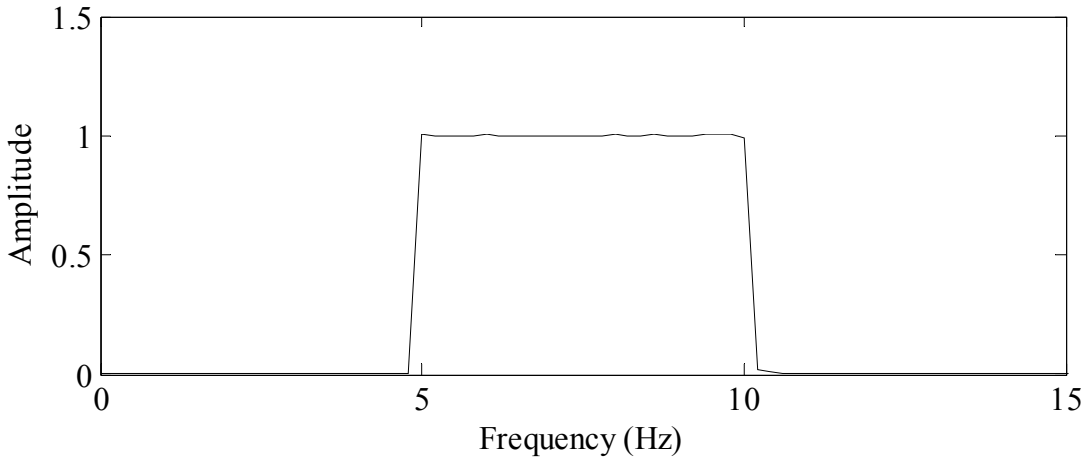

Figure 4.16. Multisine signal example in the frequency domain.

All multisines are designed to eliminate leakage on the input by using sinusoids at integer multiples of the FFT resolution. Using *f* as the step size between frequency lines, the period is chosen as $T = 1/f$. This period eliminates leakage on the input since all of the sinusoids will be periodic in the observation window and all of the frequency lines will match a frequency line of the FFT. To minimize leakage on the output, the multisine signal can be used either as a burst, or, more commonly, in a repeating fashion such that the initial transient decays out and then the response becomes periodic. An example of the multisine signal in the frequency domain is shown in Figure 4.16 and the lack of leakage and the consistent amplitude over the excitation range are clear. As with the other periodic signals, cyclic averaging can be performed in the time domain to reduce noise.

For MIMO testing, correlation of the inputs becomes a concern. Simple methods exist that will theoretically eliminate correlation, although the actual physical responses of a structure may introduce some correlation. One simple method is to choose frequency lines for the different shakers that are interleaved. For example, using the basic case of two inputs, in the first test realization one shaker excites even frequency lines and the other would excite odd frequency lines. In a second test realization, the inputs would be reversed. Other methods are available such

as using a Hadamard matrix to ensure the test realizations are orthogonal. The Hadamard matrix requires the number of inputs to be a power of two, but other methods are available so the signals can be nearly orthogonal for any number of inputs (Dobrowiecki et al. 2006).

The multisine signal has a good time factor between 1 and 1.5 depending on which method is used to select the phases. Thus, this signal provides the same level of FRF accuracy in less time than most of the other signals discussed.

4.4.8 Summary of Signal Types

The seven signals discussed are summarized in Table 4.1, and it is clear that the multisine signal should give the best results and it is selected for use in this work. However, the burst-random signal is commonly employed in the literature and has been used far more than multisine. Therefore, burst-random is also used in testing.

Signal Type	Leakage Error	MIMO Compatibility	Allows Roving Transducers	Time Factor
Slow Swept Sine	None	Fair	Yes	1.0
Periodic Chirp	Minor	Fair	Yes	1.5 - 4
Random	Significant	Best	No	1.5
Burst-Random	Minor	Good	No	1.7 - 2.5
Pseudo-Random	None	Good	No	2 – 4.5
Periodic Random	None	Good	No	4.5
Multisine	None	Good	Yes	1 – 1.5

Table 4.1. Comparison of Signal Characteristics.

4.5 SIGNAL INPUT FORCE LEVEL

The quality of the FRFs is impacted by the force level selected for the excitation input. This subject has been commented on by many authors (Allemang et al. 1983; Hunt and Brillhart 1991; Schoukens et al. 1988), and the consensus is that the force should not be too low or too high. This qualitative statement is based on the idea of balancing two conflicting issues. The first issue is that a high force level is desired so that the SNR of the measurements is maximized. The second issue is that high force levels cause noise in the structural response.

Considering a highway bridge as a test subject, noise exists in the structure due to wind, microtremors, water currents, etc. Whether these inputs are stochastic or not, the response of the structure will be magnified at natural frequencies, and thus the response due to the noise input may not be eliminated by averaging methods. If the forced excitation is not much more energetic than the ambient excitation, then the response at natural frequencies will be significantly exaggerated by the ambient inputs and the calculated modal parameters will be less accurate. As the SNR increases, the effect of the noise is reduced. Thus, increasing the force input is beneficial.

As force input to a structure increases, three problems develop that reduce the accuracy of the measurements. First, large motions of the structure cause noise to develop. This noise is due to the rattling of attachments, the opening and closing of microcracks, undesirable movement of supports, etc. Second, the response of structural nonlinearities are greatly exacerbated with larger movements. The excitation of nonlinearities and the extraneous noise both reduce the accuracy of FRFs. Finally, a phenomenon known as force drop out (Rao 1987) causes the force input to be significantly reduced at natural frequencies of the structure. With smaller input forces, the motions of the structure are small compared to the motions of the excitation mass, and force drop

out is not significant. As the magnitude of the structural response increases, the velocity of the structure can be similar to the velocity of the mass and the imparted force is greatly reduced. This phenomenon reduces the accuracy of FRFs at the natural frequencies of the structure, which are the most important parts of the FRFs.

It is obvious then that for any given structure, there is a 'sweet spot' where the force is high enough to provide good SNR, but low enough that undesirable structural responses are not created. Hunt and Brillhart (1991) have recommended that testing of a structure should start with a 'force level survey' during which a number of brief runs are conducted at increasing force levels. FRFs are calculated and their general smoothness is visually inspected. The force level that provides the smoothest FRFs is then selected for production testing. With a lack of better options reported in the literature, this method will be used for the physical structural testing of this thesis.

4.6 SPATIAL DISTRIBUTION OF INPUT

The quality of the FRFs is also impacted by the spatial location and direction of the input forces. If a force input is imparted at a location on a structure that does not excite a particular mode well, then the quality of the FRF will be poor at frequencies near that mode. Locations near a nodal point of a mode should be avoided, and imparting force in a direction that is orthogonal to a mode should also be avoided.

This issue can be quite complicated for three dimensional structures, especially those with sub-assemblies. Fortunately, in the proposed bridge testing, only vertical modes are desired since these are the modes that contribute to the vertical elements of modal flexibility. Thus, a bridge will be considered as a flat plate and all shakers can be oriented to impart force in a vertical

direction. Thus, only modal nodes need to be avoided when selecting input locations. However, FRFs will be of the highest quality when shaker locations are near the point of maximum response of a particular mode. This objective represents a challenge for even simple structures.

Considering a structure that is a one-dimensional beam. The first mode will have maximum response at midspan, as will all other odd numbered modes. However, all even numbered modes will have a modal node at midspan. Thus, midspan is the best excitation location for half of all modes and the worst excitation location for the other half of the modes. Some authors have attempted to develop functions and algorithms for the selection of the optimum excitation locations (Imamovic and Ewins 1997), but the high complexity and limited applicability of these methods makes them relatively undesirable. A simple and common method for selecting excitation locations is to sketch the locations of modal nodes and then qualitatively select locations that are away from nodes but still near points of maximum response.

For an irregularly shaped structure, it is unlikely that the mode shapes can be predicted in advance, and thus it is not possible to select good exciter locations in advance of testing. In this situation, the best results are obtained if an excitation survey is performed. The survey consists of briefly exciting the structure from a large number of input locations (one at a time), and analyzing the results. This process will provide rough estimates of the mode shapes and experimental FRFs, both of which can then be used to select good excitation locations.

It is obvious that the larger the number of excitation locations, the greater the probability that all modes will be adequately excited. Thus, the issues with selecting shaker locations are reduced by the research herein that aims to emply many shakers that are spatially well-dispersed on the structure.

For the research of this thesis, the structures to be tested are rectangular and are thus symmetric in two directions. This makes it possible to predict the more powerful lower mode shapes with confidence. The excitation locations are then qualitatively selected to be near maximum response points while avoiding many nodal locations.

4.7 CONCLUSION

This chapter focused on the importance of excitation signal type, force level, and spatial location in the performance of experimental modal analysis. The quality of the FRFs, and thus the accuracy of all calculated modal properties, are significantly impacted by these three parameters. Therefore, the many commonly used signal types were discussed and compared, and the issues that complicate the selection of force level and input location were introduced.

The choice of excitation signal type needs to balance several needs of the proposed structural testing. The signal needs to be compatible with MIMO testing, should minimize leakage and other errors, should minimize testing time, and would preferably enable testing to proceed with roving force transducers. Out of seven signal types analyzed, multisine excitation is chosen as the signal type that best satisfies these criteria. However, burst-random will also be used since it is well accepted in the field of modal testing.

The excitation force level needs to be selected as high as possible to maximize SNR, but not high enough to cause unwanted structural responses to develop. An effective way to choose the force level for any structure is to perform testing at several force levels and analyze the smoothness of the resulting FRFs.

Finally, the excitation input locations for a structure need to be chosen so that modal nodes are avoided while points of maximum response are selected. For testing that involves many exciters,

the probability that all modes will be adequately excited is high and less care is required for locating the shakers. However, for testing that uses only several shakers, the locations of modal nodes and maximum responses will be assumed if possible, and input DOFs will be selected from this mapping. Also, symmetric placement will be avoided on structures with obvious symmetry.

The exact excitation selections are unique to each unique structure. Thus, the multisine frequency range and resolution, force input level per frequency line, and input locations are noted in this thesis as part of the testing procedure for each tested structure.

CHAPTER FIVE

DATA PROCESSING AND ANALYSIS METHODS

5.1 INTRODUCTION

This chapter describes the procedures that are used to extract modal parameters of structures from the measurements of inputs and outputs. The final result of the processing is the production of a modal flexibility matrix that can be used to assist in the strength evaluation of a bridge. There are many potential pitfalls in data collection and processing, and many of these are discussed in detail, and best practices are introduced.

Common problems relating to data collection and preprocessing are discussed in detail, as are the methods by which these problems can be minimized or avoided. Serious data collection issues include quantization, inadequate frequency resolution, aliasing, and leakage. The various types of averaging that can be used to reduce variance due to noise are also discussed.

Next, the methods by which transfer functions are assembled from the data are described. Several FRF algorithms that are appropriate to different averaging methods are discussed, and the best algorithms for the work of this thesis are selected. The assembly of the transfer function is also demonstrated for systems with single force input locations (SIMO) and for systems with multiple simultaneous input locations (MIMO).

System identification procedures are also reviewed. System identification is the process of extracting the modal properties from the transfer function, and many different algorithms and commercial packages exist for this analysis step. The basis of these algorithms is shown from the

form of several mathematical models. A system identification algorithm is then selected for this work and the details of the system identification process using that algorithm are provided.

Finally, the method by which modal flexibility is synthesized from the identified modal parameters is shown. Subsequent chapters validate the entire data processing routine by comparing the outcome from physical testing to analytical results.

5.2 THEORETICAL BACKGROUND

This section introduces the theoretical development that connects the physical properties of a structure to measured dynamic force inputs and measured structure responses. First, it is assumed that the properties of the structure do not vary with time. Second, it is assumed that the structure's response is linear. Finally, it is assumed that the properties of the geometrically continuous structure can be 'lumped' into a finite number of representative degrees-of-freedom (DOFs). Based on these assumptions, the classical dynamic equation for the time domain response at any DOF to some time-varying force input(s) is given by:

$$[M]\{\ddot{x}(t)\} + [C]\{\dot{x}(t)\} + [K]\{x(t)\} = \{F(t)\} \qquad \text{Equation 5.1.}$$

Where:

$[M]$ = the mass matrix for the system.

$[C]$ = the damping matrix for the system.

$[K]$ = the stiffness matrix for the system.

$\{F(t)\}$ = the force vectors for the system.

$\{\ddot{x}(t)\}$ = the acceleration of the system DOFs.

$\{\dot{x}(t)\}$ = the velocity of the system DOFs.

$\{x(t)\}$ = the displacement of the system DOFs.

The Laplace transform can be used to solve this differential equation. The definition of the Laplace transform is:

$$\{X(s)\} = \mathcal{L}\{x(t)\} \cdot s = \int_0^\infty e^{-st} x(t) dt \qquad \text{Equation 5.2.}$$

Where:

$s = \sigma + j\omega$, a complex number.

Interpreting the transform as a conversion of steady state response from the time domain to the frequency domain, the displacement, velocity, and acceleration components are:

$$x(t) = \{X(s)\} \qquad \text{Equation 5.3.}$$

$$\dot{x}(t) = s \cdot \{X(s)\} - x(0) \qquad \text{Equation 5.4.}$$

$$\ddot{x}(t) = s^2 \cdot \{X(s)\} - s \cdot x(0) - \dot{x}(0) \qquad \text{Equation 5.5.}$$

And assuming initial conditions of zero displacement and zero velocity, the transforms reduce to:

$$\dot{x}(t) = s \cdot \{X(s)\} \qquad \text{Equation 5.6.}$$

$$\ddot{x}(t) = s^2 \cdot \{X(s)\} \qquad \text{Equation 5.7.}$$

The transform is evaluated along the frequency axis, and thus $\sigma = 0$. Therefore, substituting with $s = j\omega$ gives:

$$x(t) = \{X(j\omega)\} \qquad \text{Equation 5.8.}$$

$$\dot{x}(t) = j\omega \cdot \{X(j\omega)\}$$ Equation 5.9.

$$\ddot{x}(t) = -\omega^2 \cdot \{X(j\omega)\}$$ Equation 5.10.

Which are the expected results for converting displacement to velocity and to acceleration in the frequency domain. Substituting these results into Equation 5.1 transforms the time domain system to:

$$-\omega^2[M]\{X(j\omega)\} + j\omega[C]\{X(j\omega)\} + [K]\{X(j\omega)\} = \{F(j\omega)\}$$ Equation 5.11.

And rearranging gives the definition of the frequency response function (FRF). When multiple input or output locations are considered, this is also called the system transfer function.

$$\frac{\{X(j\omega)\}}{\{F(j\omega)\}} = \frac{1}{-\omega^2[M] + j\omega[C] + [K]} = [H(j\omega)]$$ Equation 5.12.

Where:

$\frac{\{X(j\omega)\}}{\{F(j\omega)\}} =$ the frequency response functions for the various DOFs where inputs and/or outputs were measured.

$[H(j\omega)]$ = the transfer function for the MDOF system.

If this equation is evaluated at the frequency $\omega = 0$, then the result simplifies to:

$$[H(0)] = \frac{1}{[K]} = [f]$$ Equation 5.13.

Where:

$[f] =$ the flexibility matrix for the system

This is logical since the equation of motion has reduced to the definition of flexibility of a static system. Thus, for a static load, the flexibility is the measured displacement divided by the applied load.

Unfortunately, some additional complexity is introduced when using real-world dynamic measurements. First, both the measured force input and structure response are contaminated with noise and errors. This issue is best addressed by taking multiple sets of measurements and applying an appropriate FRF algorithm that minimizes the contamination. Second, the measurements are typically made with accelerometers, and thus there is no possible measurement at $\omega = 0$. Therefore, flexibility cannot be directly found from the transfer function and other modal information will have to be manipulated to estimate flexibility. Both of these issues are discussed in detail in the following sections of this chapter.

5.3 DATA COLLECTION AND PREPROCESSING

The methods by which the applied forces and the resulting responses are measured has a large effect on the accuracy of the estimated FRFs, and thus on the accuracy of calculated modal parameters. There are many steps involved in the capture and preprocessing of the data, and many papers have been written on best practices for each step. It is not the intent of this thesis to reexamine every possible way that measurements can be compromised; however, a few issues with regards to data collection deserve special attention. These issues are quantization, frequency resolution, aliasing, averaging, and use of the FFT. Each of these subjects is discussed in detail below.

5.3.1 Quantization

Quantization is an error that affects digital electronics. In digital devices, there are a preset number of values that any element of data must conform to (i.e. quanta). The number of preset values is defined by the number of bits that are available for representation of the data. For instance, with a single bit only two values can be represented, whereas two bits allows four unique values to be represented. For 'n' bits, there are 2^n possible values, and thus it is obvious that the more bits, the more discrete values that can exist.

An example of quantization is shown in Figure 5.1. A smooth (analog) sine wave is shown as well as the signal after digitization using 21 quanta and using 9 quanta. The alteration of the data in the time domain is clear. Next, these three signals are transformed to the frequency domain and the result is shown in Figure 5.2. The error introduced is less obvious, but a closer inspection shows that the result of quantization is that there is now energy at many higher frequency lines. Also, the amplitude at the dominant frequency is reduced.

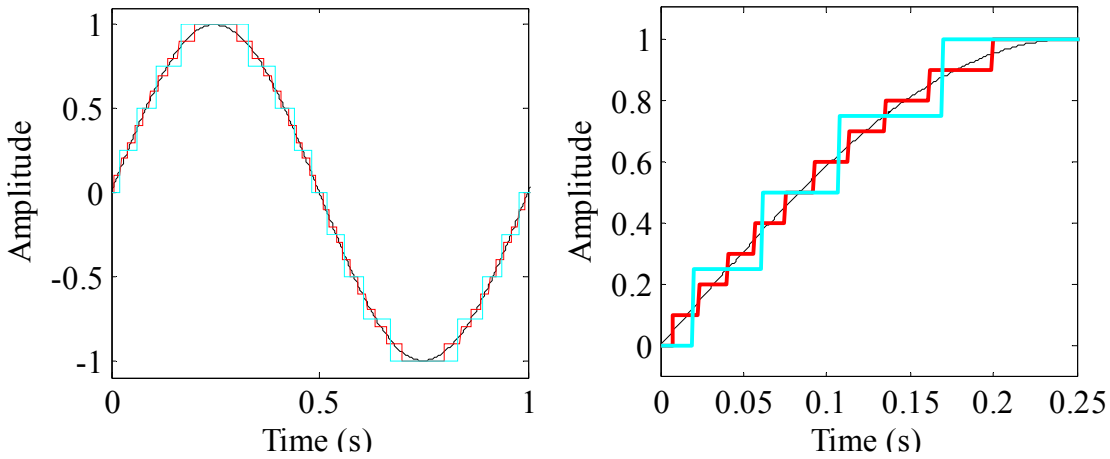

Figure 5.1. Example of quantization error in the time domain.

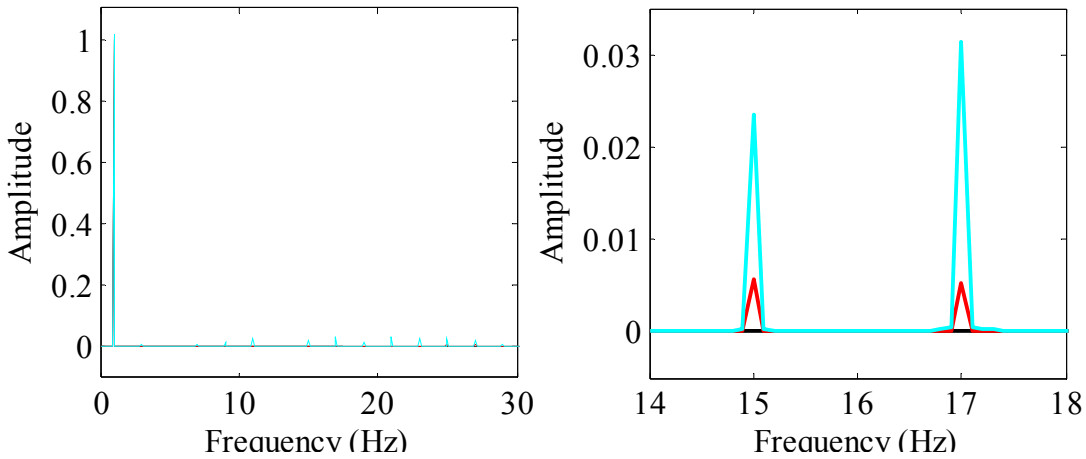

Figure 5.2. Example of quantization error in the frequency domain.

Quantization is an issue of importance with both digital sensors and analog-to-digital converters (ADCs), and the topic of dynamic range is closely related. Dynamic range is the ability of a device to reallocate the finite number of possible response levels to fit between an arbitrarily selected lower and upper bound. This allows the relatively limited number of response levels to be scaled for larger or smaller values, or to be shifted. Dynamic range is only available on some devices, has a cost associated with it, and is limited in its ability to scale or shift to a desired input range.

Many sensors are analog, and thus theoretically, have an infinite number of possible responses between their minimum and maximum values. Other sensors are digital and may have quantization issues. Digital sensors are unlikely to have any dynamic range, and thus the possible output levels are permanently fixed. The issue occurs when accelerometers are selected that have a high enough range to measure hammer impacts (for example) but low level vibrations must also be detected with good resolution. If the sensor has 16 bits (~65,000 quanta), it may be able to measure both strong and weak vibrations with adequate accuracy; however, a 12 bit sensor

(~4000 quanta) cannot. Thus it is important to know the limitations of any digital sensors and plan the testing with respect to these limitations.

Quantization is a potential issue with all ADCs. Older ADCs may have 8 or 12 bits, whereas newer versions generally have 16 or 24 bits. Most ADCs have dynamic range and this can be set prior to an experiment to maximize the number of possible levels that are actually in the range of the input. Setting the dynamic range is very important with older systems but less so with newer systems.

Consider a 24 bit ADC which has about 17,000,000 available quanta that is being used to measure a voltage that only ranges from 0 to 0.1 volts. If the ADC is set to a range of 0 to 10 volts, only about 1% of the available quanta will actually be used to measure the input. However, even if the noise in the system being measured is at the very low level of 1% of the signal amplitude, the ADC still provides about 1,700 quanta just for the noise amplitude. Another way to consider this example is to say that system noise dominates the measurement at input levels that are three orders of magnitude higher than quantization errors. If dynamic range had been used to set the ADC to read from 0 to 1 volt, then the noise would be four orders of magnitude larger than any potential quantization errors, and thus the change in range would not have improved the measurement in any way. If this same example were considered for a 16 bit system then the noise would be at the same order of magnitude as the quantization and thus the use of dynamic range might improve the measurement.

In summary, for any ADC with less than 16 bits, quantization must be carefully considered as part of the experiment planning process. Also, any digital sensor must be used with caution and the range and accuracy of the output must be evaluated.

5.3.2 Frequency Resolution

The frequency resolution of a measurement is the size of the gap between frequency lines that are represented in the FFT. For any recorded signal, the resolution in the frequency domain is just the inverse of the length of the signal in the time domain. Therefore, the signal length must be selected to provide the desired frequency resolution, but there are several issues to consider when making this choice. The benefits of greater resolution are that the probability of finding all natural frequencies increases, the accuracy of the curve fit for modal parameters is improved, and closely spaced modes can be differentiated. The drawback of higher frequency resolution is that the testing takes longer, with an order of magnitude greater resolution taking an order of magnitude longer. Thus the benefits must be balanced against the required testing time.

Consider a signal that consists only of energy at 2 Hz and at 3 Hz. If the signal is sampled for 0.5 seconds, then the resolution in the frequency domain will be 2 Hz, and the energy at 3 Hz will not be properly represented. This is illustrated in Figure 5.3 and it is shown that the energy from the 3 Hz frequency line has leaked to the nearby frequency lines that are represented. If the sampling period is increased to 5 seconds then the resolution is more than adequate to accurately identify the energy at 3 Hz as shown in Figure 5.4. This simple example demonstrates that inadequate frequency resolution not only worsens leakage, but can also make it more difficult to identify natural frequencies by suppressing the corresponding peaks.

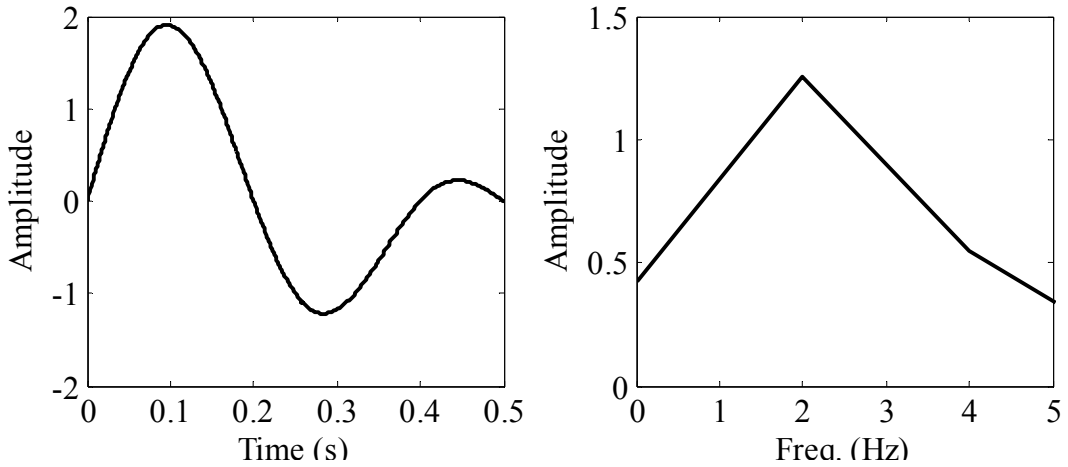

Figure 5.3. Example of the effect of inadequate frequency resolution for a signal with energy at only 2 Hz and 3 Hz.

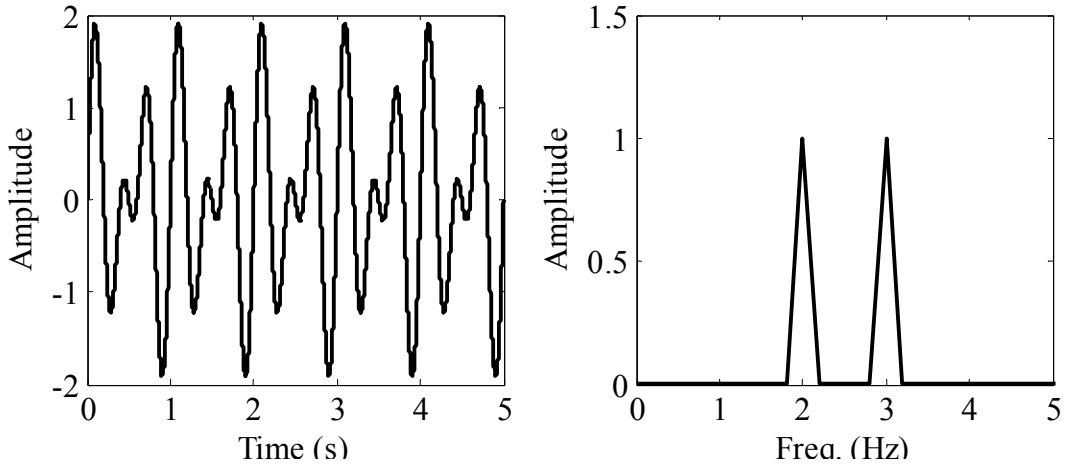

Figure 5.4. Example of adequate frequency resolution for a signal with energy at only 2 Hz and 3 Hz.

To select an appropriate frequency resolution, an estimate of the order of magnitude of the desired natural frequencies is needed as a first step. For short to medium span bridges, the first ten global modes are typically between 1 and 100 Hz. For long-span bridges, many natural frequencies will exist below 1 Hz. With this knowledge, it is easy to set a lower bound on the resolution, but it is not as obvious what a good upper bound would be. The lower bound would be perhaps $1/50^{th}$ of the lowest expected natural frequency. However, without prior knowledge or

good estimates of the natural frequencies and damping of the structure, it will be unknown if there are closely spaced modes.

In the absence of specific knowledge, initial testing must be conducted to select an appropriate frequency resolution for any structure. The initial testing should be set up with a few signals of significantly differing lengths, perhaps resulting in frequency resolutions of $1/50^{th}$, $1/100^{th}$, and $1/500^{th}$ of the base natural frequency. Only a small number of averages would be used such that the initial testing time is limited. The natural frequencies and mode shapes should then be compared and the usefulness of the extra resolution can be evaluated. A resolution to use for the production testing can then be selected. This process is used in the testing reported in this thesis.

5.3.3 Aliasing

Aliasing is an issue that is caused by discretizing a continuous signal, and it decreases the accuracy of modal testing. If too few points in time are chosen when discretizing, then the shape of the resulting digital signal will not closely match the original signal and the frequency content found by the FFT will be altered. The recording frequency (sampling rate) of the data acquisition system (DAQ) is the variable that determines the amount of aliasing. Theoretically, any component of the signal that has a frequency less than the Nyquist frequency will be free of aliasing in the FFT (Stiltz 1961, 89). The Nyquist frequency is simply half of the data collection frequency, implying that a sinusoid represented by greater than 2.0 samples per period will have no aliasing. However, in the presence of noise, the identification of signal components is more accurate when the data collection frequency is higher, and thus more digitized points per period represent the particular signal component.

Aliasing can be practically eliminated by sampling at a high rate; however, this has costs associated with it. The primary cost is that the recording equipment must be able to handle the data rate. The DAQ, the busses or network, and the computer hardware and software must all have adequate bit rates, memory buffers, data write speeds, etc. The second issue is data file size as it relates to hard disk usage and to data processing time.

Consider a test setup with 15 channels of force input and 30 channels of acceleration output. For a resolution of 0.02 Hz, a 50-second signal is needed. Assume 10 averages in the time domain, 15 unique runs of the inputs for MIMO processing (discussed later in this chapter), and 5 experiments for reducing variance on the transfer function. At a data collection rate of 200 Hz and double precision, the data will occupy 2.7 GB. If 1000 Hz is used to reduce aliasing, then 13.5 GB of hard disk space are required to store the data. While these values are not especially daunting given the proliferation of terabyte hard drives, it is apparent that collecting data at an unnecessarily high rate can easily result in a volume of data that is unwieldy. Computation time and RAM space can also become an issue due to high data rates.

In summary, the data collection rate must be chosen for each structure to be tested. The rate must be more than two times greater than the highest natural frequency of interest, but results are more reliable with rates significantly in excess of this minimum. However, to reduce issues that can be caused by storing excess data, the collection rate should not be excessively high. Similar to the selection of resolution, the selection of an appropriate data rate must be based on some initial testing of the structure that indicates what the highest frequency of interest is.

5.3.4 Averaging

In modal testing, many types of averaging are used to improve measurements in various situations. Three types of averaging are applicable to the type of testing proposed herein. Namely, these are asynchronous averaging, synchronous averaging, and cyclic averaging (Allemang 1999, 4_46-48). Each of these methods relies on the idea that redundant data is collected during testing. The redundant data is produced by conducting an experiment several times over, and then the best estimate of the results is found by averaging information from each separate experiment. How the experiments relate to each other generally defines which averaging method can be used. Each of the averaging methods is discussed in detail below.

Asynchronous averaging is used to reduce the variance on the measurement of FRFs when the data sets from the separate experiments are expected to be unrelated. This is the case when a new realization of a random input is used for each experiment, when the duration of the input is varied for each experiment, or when different signal types are used for each experiment. In any of these situations, neither the time domain nor frequency domain signals can be averaged since the phase will vary between experiments. However, power spectra can be averaged since the unique phase information is canceled out by the calculation of the spectra. Consider an input signal for an experiment that has an amplitude of one and a phase of zero degrees at the 10 Hz frequency line. If the subsequent experiment has an input signal with an amplitude of 1 but a phase of 180 degrees at 10 Hz, then the average of the inputs for the two experiments will indicate that there was no energy at 10 Hz in either experiment. Asynchronous averaging is most applicable to stochastic signals, but can also be used for deterministic signals of any type.

If the same input signals are used in each experiment, then synchronous averaging can be used to reduce the variance on the measurement of FRFs. Synchronous averaging not only requires that

the inputs be consistent from experiment to experiment, but that the recorded data sets be synchronized. The data sets from different experiments can either be synchronized by use of an electronic trigger that starts the input signal and the data logging simultaneously, or the sets can be aligned during processing. With synchronous data, the phase information will be consistent between experiments and the averaging can thus be carried out in the time domain or the frequency domain without the calculation of power spectra. Synchronous averaging is most appropriate with deterministic signals.

Cyclic averaging is a special form of averaging that specifically helps eliminate leakage error. For cyclic averaging to be used, the same input signal must be used successively without any elapsed time between recurrences. The transient response of the structure that occurs due to the initiation of the input will decay during the first few runs of the input signal. These runs are called 'delay blocks' and will be discarded. After the transient decays, the response of the structure is completely periodic in relation to the duration of the input signal and several repetitions will be recorded. The recorded runs are called 'capture blocks'. Since the response of the structure is periodic in the capture block, each frequency that is contributing to the total response is also periodic in the capture block. Since each frequency is periodic and the capture block has a set duration, then the response of the structure has been filtered such that only frequencies that will be represented in the FFT are active, and leakage has thus been eliminated.

The capture blocks from an experiment that utilizes cyclic averaging will still be contaminated by noise. The variance due to the noise can be reduced by using synchronous or asynchronous averaging on the collection of capture blocks from one or many experiments. Cyclic averaging is most commonly used with deterministic signals, but can be used with stochastic signals as well. For use with any type of stochastic signal, the same realization of the signal is repeated until the

structure response is periodic and then capture blocks are recorded. This process is then repeated with additional realizations until all frequency lines have been adequately excited. Asynchronous averaging is then used to combine capture blocks resulting from different input realizations.

Figure 5.5 illustrates the benefits of asynchronous averaging. Ten unique realizations of burst-random input were used to excite a numerical model of a cantilevered beam, and random noise was added to the input and response signals. An FRF was then found for a single experiment and is compared to an FRF found using asynchronous averaging of all ten experiments. The averaging benefits the FRF by reducing the variance caused by the added noise, and by improving the excitation of all frequency lines.

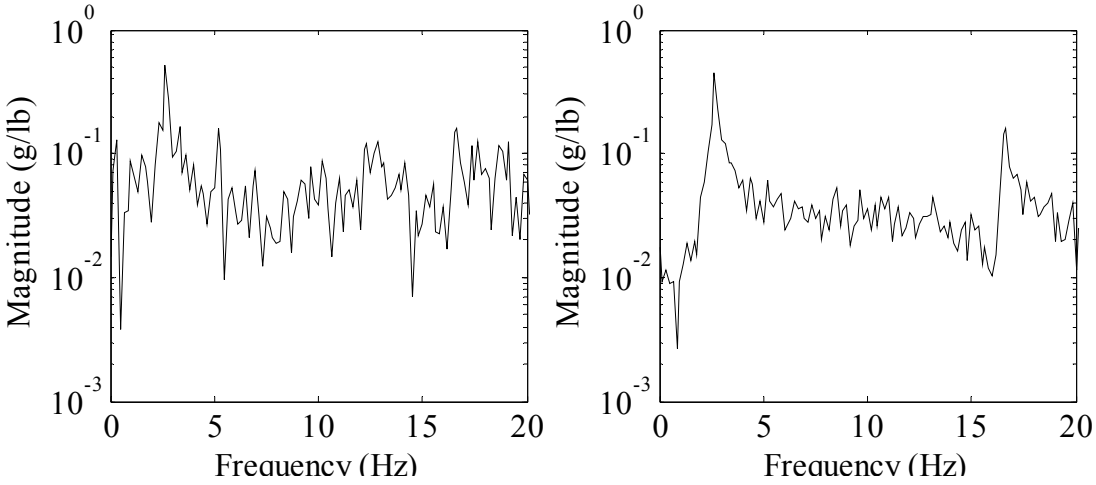

Figure 5.5. FRF for a cantilever beam with burst-random excitation illustrating asynchronous averaging. One average at left and ten averages at right.

Figure 5.6 illustrates the benefits of synchronous averaging. A multisine signal was used to excite a numerical model of a cantilevered beam, and random noise was again added to the data. An FRF was found for a single experiment and is compared to an FRF found using synchronous averaging of ten experiments. The noise is clearly reduced by the averaging. It is also noteworthy that a single average with the multisine signal provides a much better FRF than ten averages with

the burst random signal. The reason for this is that by design, the multisine signal evenly excites every frequency line in the FFT, whereas the burst random signal requires many realizations to do this.

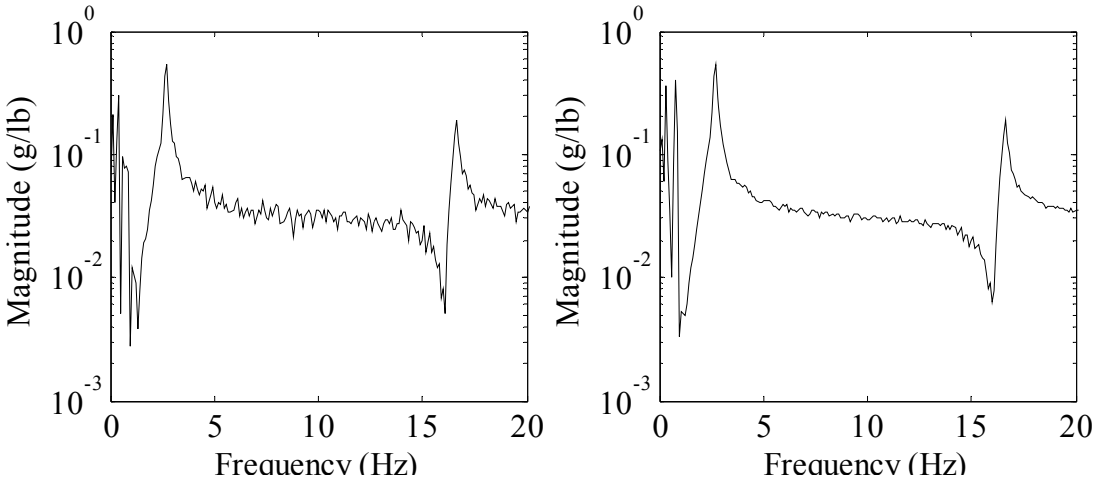

Figure 5.6. FRF for a cantilever beam with multisine excitation illustrating synchronous averaging. One average at left and ten averages at right.

Finally, Figure 5.7 illustrates the use of cyclic averaging on the cantilevered beam. A multisine signal is used five times successively and an FRF is found by using the first and fifth recurrences. The transient structural response causes the FRF from the first recurrence to suffer from leakage, as is evident by the wider, flatter peak near 17 Hz in the left plot. The right plot shows the FRF from only the fifth recurrence and the improvement is significant.

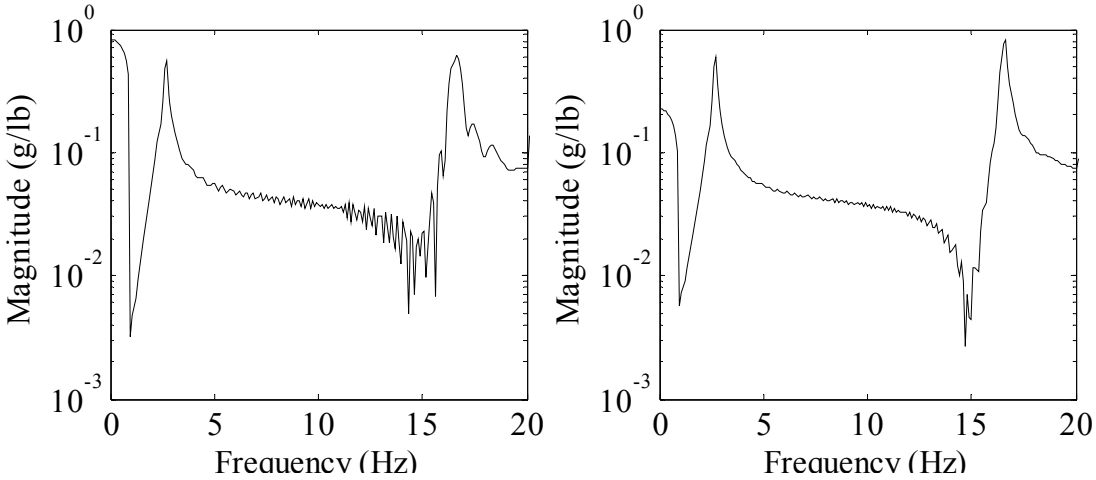

Figure 5.7. FRF for a cantilever beam with multisine excitation illustrating cyclic averaging at right compared to measurement without cyclic averaging at left.

Overall, averaging is the method by which variance is reduced in the measurement of FRFs. The method of averaging that can be utilized is limited by the types of excitation signals used during testing, and by the experimental process. Asynchronous and synchronous averaging are two methods for using the results of multiple experiments to reduce the measurement variance due to noise. Cyclic averaging is a related experimental method that practically eliminates leakage errors.

5.3.5 Fast Fourier Transform

The Laplace transform was used to simplify the equation of motion from a differential equation in the time domain to an algebraic equation in the frequency domain. Because of this, time domain data that is collected during testing must be transformed to the frequency domain. Various methods exist for performing this transformation, but the fast Fourier transform (FFT) is the most commonly used. The definition of the transform can be found in any text and is shown, but the algorithms that are actually used in commercial software use a variety of different solution procedures to enable a very fast computation.

$$F(\omega) = \int_{-\infty}^{\infty} f(x) \cdot e^{-j\omega \cdot x}\, dx$$ Equation 5.14.

Use of the FFT can result in a poor frequency domain representation of the data, especially in consideration of leakage errors, aliasing, and inadequate frequency resolution as discussed previously. Assuming that each of these items has been appropriately handled by the testing procedure, then the transformed data can be used further. However, the result of the transform may be presented in different forms depending on the software being used. The details of using the data after a transformation in MATLAB are discussed.

In MATLAB, the command for performing the FFT on time domain data is $fft(data)$ where $data$ is a vector of N measurements taken at discrete, but consistent, time intervals. The result of this command is a vector of complex numbers that is the same length as the input vector. The complex numbers provide phase and amplitude information for each of the discrete frequency lines that are represented. The number of frequency lines represented is equal to $1 + N/2$ when N is even, and $1.5 + N/2$ when N is odd. Although not precisely true, the vector will be considered as two halfs: the first element in the vector is the frequency content at 0 Hz, and each successive element is the content at uniformly increasing frequency lines at consistent intervals up to the middle of the vector. The second half of the vector is just a mirror image of the first half with each element being the complex conjugate of the corresponding element in the first half. As such, the amplitude information at a frequency line is divided evenly between the first half and second half of the vector.

During the calculation of the FFT by Matlab, the amplitude is scaled by the length of the vector (N) and this needs to be divided back out of the data to preserve the correct amplitude.

Considering an element from the first half of the vector that is of the form $a + bi$, the total amplitude at that frequency line is $2/N \cdot \sqrt{a^2 + b^2}$ and the phase is $\tan^{-1}(b/a)$.

5.4 TRANSFER FUNCTION ESTIMATION

The transfer function is the collection of FRFs that describe the input-output behavior of a structure. The estimation of an accurate transfer function is critical to the estimation of modal parameters. Since the transfer function is composed of FRFs, the consistent and accurate estimation of FRFs is needed. As discussed previously, the methods of data collection and processing have a significant effect on the FRFs, and proper selection of several key criteria will lead to the highest quality data within the constraints of the testing equipment. The proper assembly of the FRFs into the transfer function is the next step in the data processing procedure.

At its most basic, the transfer function at some discrete frequency ω is calculated as $H(\omega) = X(\omega)/F(\omega)$. This is identical to the formulation of the FRF when there is a single input location, a single output location, and a single realization of the experiment. However, the assembly of the transfer function becomes more complicated when multiple inputs, multiple outputs, and multiple experiments are used. Thus, the manner in which the transfer function is found will be explained in detail for three increasing levels of complexity. First, the formulation will be described for one realization of an experiment using a single input but multiple outputs (commonly referred to as 'SIMO'). Second, the required experimental process and transfer formulation will be described for a single realization of an experiment using multiple inputs and multiple outputs (commonly referred to as 'MIMO'). Finally, the added complexity of using multiple realizations of the experiment will be discussed.

5.4.1 Transfer Function Calculation With SIMO Testing

A SIMO experiment consists of providing an exciting force at a single location on a structure while recording the response at multiple locations. An FRF will exist for each output location, and these are collected together to form the transfer function. At a discrete frequency line, the transfer function is defined as (and dropping the (ω) notation):

$$[H] = [X][F]^{-1} \qquad \text{Equation 5.15.}$$

Given a test setup with a single input and three outputs, the full equation for solution of the transfer function at a discrete frequency line becomes:

$$\begin{bmatrix} H_{11} \\ H_{21} \\ H_{31} \end{bmatrix} = \begin{bmatrix} X_1 \\ X_2 \\ X_3 \end{bmatrix} [F_1]^{-1} \qquad \text{Equation 5.16.}$$

Thus, the transfer function consists of a column of three FRFs that are calculated by dividing the response at each location by a scalar. There is no matrix inversion in this case. However, computational issues can still occur if the force is nearly zero at any frequency line. This is a common issue with random and burst-random input signals and is the reason why averaging of many realizations is required to get smooth FRFs.

In structural testing, it is often desirable to have the input occur at multiple locations, but commonly only one excitation device is available. The typical solution is to perform a SIMO test for each desired input location and then to assemble a larger transfer function. The transfer function gets augmented by one new column of FRFs for each input location. This type of testing is sometimes referred to as MRIT (multiple reference impact testing) when the input is caused by

an impact, and is often erroneously called MIMO when other input excitation signals are used. In any case, the new column of the transfer function is found as shown below:

$$\begin{bmatrix} H_{12} \\ H_{22} \\ H_{32} \end{bmatrix} = \begin{bmatrix} X_1 \\ X_2 \\ X_3 \end{bmatrix} [F_2]^{-1} \qquad \text{Equation 5.17.}$$

This type of testing has a significant issue in that the columns of data are often inconsistent. This inconsistency can be caused by several problems. First, positioning the force input device in various places on the structure, or attaching it to different locations alters the response of the structure. Second, time elapses during the testing, and it is often several hours from the time the first location is excited until the final location is excited. Ideally, the structure under test is time-invariant; however, in practical testing, environmental factors typically cause bridge structures to vary over time. Thus, the data is inconsistent because of changes that occur during testing. The consistency of the data can be improved by exciting many inputs at once, and thus collecting the data for multiple columns of the transfer function simultaneously.

5.4.2 Transfer Function Calculation With MIMO Testing

A MIMO experiment consists of providing simultaneous exciting forces at multiple locations on a structure while recording the response at multiple locations. An FRF will exist for each input-output pair, and these are collected together to form the transfer function. Given a test setup with two inputs and three outputs, the equation for calculation of the transfer function at a discrete frequency line is shown. The force input is moved to the left side of the equation to make some issues with calculation that are discussed subsequently more obvious:

$$\begin{bmatrix} H_{11} & H_{12} \\ H_{21} & H_{22} \\ H_{31} & H_{32} \end{bmatrix} \begin{bmatrix} F_1 \\ F_2 \end{bmatrix} = \begin{bmatrix} X_1 \\ X_2 \\ X_3 \end{bmatrix} \qquad \text{Equation 5.18.}$$

This formula has six unknown FRF values but only three independent equations, and thus cannot be solved. Physically, this indicates that for a measured structural response, there is no way to distinguish what portion of the response was caused by either input force. In order to solve, a second experiment must be run. The subscripts 'a' and 'b' are now introduced to indicate the measurements from the first experiment and from the second experiment respectively.

$$\begin{bmatrix} H_{11} & H_{12} \\ H_{21} & H_{22} \\ H_{31} & H_{32} \end{bmatrix} \begin{bmatrix} F_{1a} & F_{1b} \\ F_{2a} & F_{2b} \end{bmatrix} = \begin{bmatrix} X_{1a} & X_{1b} \\ X_{2a} & X_{2b} \\ X_{3a} & X_{3b} \end{bmatrix} \quad \text{Equation 5.19.}$$

By running a second experiment, there are now six equations and six unknowns. So long as all six equations are linearly independent, the six FRF values can be solved for. To ensure that this stipulation is satisfied, the force inputs must not be completely correlated between the two experiments. If they are, then the determinant of the force matrix will be zero and an inverse will not exist.

As more input locations are included, more experiments are required. In general, MIMO testing requires that for N_i input locations, N_i experiments must be run so that the transfer function can be solved. It should be noted that various FRF algorithms use different methods to combine the data from additional experiments, however, the basic principle remains. Guillaume, et al. (2001) show that the optimal experimentation scheme is the one in which the force vectors are all mutually orthogonal. In practical experiments, this can be accomplished by using a single deterministic excitation signal and applying a gain of 1 or -1. For instance, if the number of inputs is a power of two, then a Hadamard matrix provides values of 1 or -1 to apply to the input signals so that the columns of the force matrix are orthogonal. For the example of two inputs and three outputs, the transfer function would thus be found from:

$$\begin{bmatrix} H_{11} & H_{12} \\ H_{21} & H_{22} \\ H_{31} & H_{32} \end{bmatrix} \begin{bmatrix} 1 \cdot F & 1 \cdot F \\ 1 \cdot F & -1 \cdot F \end{bmatrix} = \begin{bmatrix} X_{1a} & X_{1b} \\ X_{2a} & X_{2b} \\ X_{3a} & X_{3b} \end{bmatrix} \quad \text{Equation 5.20.}$$

In practice, MIMO testing is often performed in a manner similar to SIMO testing. Consider a test that requires eight input locations but with only two shakers available for excitation. In this situation, two columns of the transfer function are found simultaneously, but four total testing setups are still required to find all eight columns of the transfer function. This again introduces issues with data consistency. If many shakers are available, then the testing setup does not need to be varied to find the entire transfer function. The benefit of this is that inconsistency is greatly reduced and more accurate modal properties can be determined. Another benefit is a reduction of testing time.

5.4.3 Transfer Function Calculation With Redundant Information

Measurements are inherently affected by noise. If there is reason to believe that the noise is random in nature, then averaging of multiple measurements will result in the noise approaching zero as the number of measurements approaches infinity. Actual testing will result in a number of data sets that is not nearly infinity, but increasing the number of averages still decreases the variance that is caused by random noise. Therefore, whether SIMO or MIMO is used, multiple measurements are typically made so that the variance can be reduced. These multiple measurements cause redundant information to be available during data analysis, and one of several different methods can be selected for best utilizing this redundant information. Six methods will be described below and the formulation and implementation of each will be shown.

5.4.3.1 H_1 Algorithm

The H_1 algorithm was the first method for utilizing the data from redundant experiments and still remains popular. In the formulation of this algorithm, it is assumed that noise exists on the measurements of system response, but that no noise exists on the measurement of force inputs. A least-squares approach is then used to minimize the effect of the noise on the responses (Leuridan and Vanderauweraer 1986). The equation is shown below.

$$[H_1] = \frac{\frac{1}{M}\sum_{m=1}^{M}\left([X^{(m)}][F^{(m)}]^*\right)}{\frac{1}{M}\sum_{m=1}^{M}([F^{(m)}][F^{(m)}]^*)} \qquad \text{Equation 5.21.}$$

Where:

M = the number of redundant experiments.

$X^{(m)}$ = the measured response for the mth experiment.

$F^{(m)}$ = the measured input for the mth experiment.

$[-]^*$ = the complex conjugate transpose.

From the formulation, it is clear that the H_1 algorithm cancels out the phase information during the calculation of the cross-power spectra, $X * F^*$, and the auto-power spectra, $F * F^*$. This allows the algorithm to be used for unrelated realizations of experiments, which is very useful for random signal inputs. The drawback of the H_1 algorithm is that it does not account for noise (or leakage error) on the input measurements. Thus, the transfer function will suffer from bias error in the presence of input noise.

For SIMO testing, the implementation of the H_1algorithm is demonstrated below. In this example, it is assumed that there are three outputs and that two experiments are run. Again using

'a' and 'b' to denote the two experiments, the transfer function for a discrete frequency line is found as:

$$\begin{bmatrix} H_1 \\ H_2 \\ H_3 \end{bmatrix} = \left(\begin{bmatrix} X_{1a} \\ X_{2a} \\ X_{3a} \end{bmatrix} F_{1a}^* + \begin{bmatrix} X_{1b} \\ X_{2b} \\ X_{3b} \end{bmatrix} F_{1b}^* \right) (F_{1a} \cdot F_{1a}^* + F_{1b} \cdot F_{1b}^*)^{-1} \quad \text{Equation 5.22.}$$

As described previously for MIMO testing, a number of experiments with uncorrelated inputs equal to the number of input locations is required. With the H_1 algorithm, the information from the additional experiment(s) is incorporated just by averaging the power spectra. Since many more than the minimum number of experiments may be desired to reduce variance, random excitations are most commonly used with H_1. In this way, it can reasonably be expected that there will be no difficulty with inverting the force auto-power spectra due to a lack of unique force inputs.

Since the spectra are averaged, the calculation of H_1 for MIMO testing is practically identical to SIMO. Keeping all else the same but using two force inputs, the implementation of H_1 is shown below:

$$\begin{bmatrix} H_{11} & H_{12} \\ H_{21} & H_{22} \\ H_{31} & H_{32} \end{bmatrix} = \left(\begin{bmatrix} X_{1a} \\ X_{2a} \\ X_{3a} \end{bmatrix} \begin{bmatrix} F_{1a} \\ F_{2a} \end{bmatrix}^* + \begin{bmatrix} X_{1b} \\ X_{2b} \\ X_{3b} \end{bmatrix} \begin{bmatrix} F_{1b} \\ F_{2b} \end{bmatrix}^* \right) \left(\begin{bmatrix} F_{1a} \\ F_{2a} \end{bmatrix} \begin{bmatrix} F_{1a} \\ F_{2a} \end{bmatrix}^* + \begin{bmatrix} F_{1b} \\ F_{2b} \end{bmatrix} \begin{bmatrix} F_{1b} \\ F_{2b} \end{bmatrix}^* \right)^{-1}$$

Equation 5.23.

5.4.3.2 H_2 Algorithm

The H_2 algorithm is similar to H_1, except that noise is assumed to exist on the input measurements but not on the response measurements. A least-squares approach is again used to minimize the effect of the noise on the inputs (Allemang 1999). The formulation is shown below.

$$[H_2] = \frac{\frac{1}{M}\sum_{m=1}^{M}\left([X^{(m)}][X^{(m)}]^*\right)}{\frac{1}{M}\sum_{m=1}^{M}([F^{(m)}][X^{(m)}]^*)} \qquad \text{Equation 5.24.}$$

The formulation again shows that phase information is canceled out, allowing this algorithm to be used with unique experiments. The denominator also indicates that a square matrix will only exist if the number of inputs is equal to the number of outputs. Thus, for the usual situation in which the number of inputs does not equal the number of outputs, the transfer function cannot be directly found. It may be possible to use the Moore-Penrose pseudoinverse to solve for the transfer function; however, it is likely that the problem will be ill-conditioned at some frequency lines. This is especially true for random inputs in which some frequency lines may not have been well excited. Additionally, it is uncommon to assume that the output noise is zero but that the input noise is significant. As such, the H_2 algorithm is not commonly used.

5.4.3.3 H_v Algorithm

The H_v algorithm uses a total least squares approach to minimize the effect of noise on the inputs and the outputs. It has been shown that the transfer function determined from H_v is always bracketed by the results of H_1 and H_2, and the result is thus more accurate in the presence of noise on the inputs and the outputs (which is always the case) (Vold et al. 1984, 38). However, the H_v algorithm performs best when the input and output noise are similar in magnitude and are uncorrelated. Also, the H_v algorithm is more computationally intensive than the others in that it requires an eigenvalue decomposition to be performed at every frequency line.

The process for using the H_v algorithm begins by calculating a matrix of power spectra. For the SIMO case, at each frequency line the following is assembled for each output location (output location '1' shown):

$$[GFFX_1] = \begin{bmatrix} F_1F_1^* & F_1X_1^* \\ X_1F_1^* & X_1X_1^* \end{bmatrix}$$ Equation 5.25.

This 2x2 matrix is then subject to eigenvalue decomposition, and the eigenvector associated with the minimum eigenvalue is selected. The eigenvector must then be normalized to conform to the following:

$$[V_1]_{\lambda_{min}} = \begin{bmatrix} H_1 \\ -1 \end{bmatrix}$$ Equation 5.26.

Again, the subscript of '1' indicates that this calculation is being performed for output location '1'. This process must then be repeated for each output location in order to assemble a column of the transfer function. The process is nearly identical for the MIMO case, except that the power spectra matrix, $GFFX_1$, will include all of the inputs but still just a single output. Thus, the normalized eigenvector will provide an entire row of the transfer function.

The H_v algorithm is also not commonly used for a few reasons. First, the extra computational effort can be a significant factor for large data sets. Second, in the common case where the output noise has a significantly larger magnitude than the input noise, the H_v algorithm will not noticeably outperform the simpler H_1 algorithm. Finally, if the input and output noise are partially correlated, then other algorithms discussed below will outperform H_v by providing more consistent results.

5.4.3.4 EIV Algorithm

The EIV algorithm uses an errors-in-variables formulation to minimize the effect of noise on the inputs and on the outputs (Pintelon and Schoukens 2001).

$$[H_{EIV}] = \frac{\frac{1}{M}\sum_{m=1}^{M}([X^{(m)}])}{\frac{1}{M}\sum_{m=1}^{M}([F^{(m)}])} \qquad \text{Equation 5.27.}$$

It is clear from the formulation that the frequency domain data from each experiment is being linearly averaged and thus phase information is preserved. Because of this, only synchronized deterministic signals can be used as the inputs since any phase differences would cause the averages to tend to zero.

For SIMO testing, the implementation of the EIV algorithm is demonstrated below. It is assumed that there are three outputs and that two experiments are run. Again using 'a' and 'b' to denote the two experiments, the transfer function for a discrete frequency line is found as:

$$\begin{bmatrix} H_1 \\ H_2 \\ H_3 \end{bmatrix} = \left(\begin{bmatrix} X_{1a} \\ X_{2a} \\ X_{3a} \end{bmatrix} + \begin{bmatrix} X_{1b} \\ X_{2b} \\ X_{3b} \end{bmatrix} \right) (F_{1a} + F_{1b})^{-1} \qquad \text{Equation 5.28.}$$

For MIMO testing, this algorithm functions differently than those that use power spectra. A number of experiments, M, equal to the number of inputs, N_i, must be undertaken for each average of the EIV algorithm. This is demonstrated for the case of two inputs with lower case letters again used to denote the experiment:

$$\begin{bmatrix} H_{11} & H_{12} \\ H_{21} & H_{22} \\ H_{31} & H_{32} \end{bmatrix} = \left(\begin{bmatrix} X_{1a} & X_{1b} \\ X_{2a} & X_{2b} \\ X_{3a} & X_{3b} \end{bmatrix} + \begin{bmatrix} X_{1c} & X_{1d} \\ X_{2c} & X_{2d} \\ X_{3c} & X_{3d} \end{bmatrix} \right) \left(\begin{bmatrix} F_{1a} & F_{1b} \\ F_{2a} & F_{2b} \end{bmatrix} + \begin{bmatrix} F_{1c} & F_{1d} \\ F_{2c} & F_{2d} \end{bmatrix} \right)^{-1}$$

Equation 5.29.

It is seen that the experiments must be arranged into groups so that a square matrix results for the inversion. Within each group, the input vectors must not be completely correlated; however, since the measurements are synchronous, each group of measurements should use the exact same

inputs as every other group. This property enables averaging of many experiments while still using deterministic inputs.

An additional benefit of the EIV algorithm is that it provides more consistent estimates of the FRFs than the power spectra algorithms if there is correlation between the input and output errors, and also in cases where there is a difference in the magnitude of the input and output errors (Pintelon and Schoukens 2001; Guillaume et al. 2001). The drawback of using EIV is that testing equipment must be available that enables accurate synchronization of experiments.

5.4.3.5 ARI Algorithm

The ARI algorithm uses an arithmetic mean formulation to minimize variance on the estimate of the transfer function:

$$[H_{ARI}] = \frac{1}{M}\sum_{m=1}^{M}\frac{[X]^{(m)}}{[F]^{(m)}} \qquad \text{Equation 5.30.}$$

With the ARI algorithm, the phase is canceled by the division prior to the summation, which again allows the combination of unique experiments. However, with MIMO testing, care must be taken such that each experiment within a group is linearly independent. This can be noted by inspection of the example implementation given below for the case of two inputs and four total experiments:

$$\begin{bmatrix} H_{11} & H_{12} \\ H_{21} & H_{22} \\ H_{31} & H_{32} \end{bmatrix} = \left(\begin{bmatrix} X_{1a} & X_{1b} \\ X_{2a} & X_{2b} \\ X_{3a} & X_{3b} \end{bmatrix} \begin{bmatrix} F_{1a} & F_{1b} \\ F_{2a} & F_{2b} \end{bmatrix}^{-1} + \begin{bmatrix} X_{1c} & X_{1d} \\ X_{2c} & X_{2d} \\ X_{3c} & X_{3d} \end{bmatrix} \begin{bmatrix} F_{1c} & F_{1d} \\ F_{2c} & F_{2d} \end{bmatrix}^{-1} \right)$$

Equation 5.31.

The ARI estimator is similar to the popular H_1 algorithm in that the phase information is canceled out and thus stochastic excitation can be used. ARI has the benefit that it is more

accurate in the presence of input errors than H_1. However, H_1 can be expected to be more stable during the inversion of the force matrix since, for H_1, there are typically many unique realizations averaged prior to the inversion. ARI requires an inversion for each group of N_i measurements with a correspondingly greater probability that the stochastic inputs are correlated at some frequency line. Thus, for ARI, the calculation process should be monitored to ensure that force matrices that are nearly singular are not included in the transfer function calculation.

5.4.3.6 GEO Algorithm

The GEO algorithm uses a geometric mean formulation to minimize variance on the estimate of the transfer function (Pintelon and Schoukens 2001):

$$[H_{GEO}] = \left(\prod_{m=1}^{M} \frac{[X]^{(m)}}{[F]^{(m)}} \right)^{1/M} \qquad \text{Equation 5.32.}$$

This algorithm is essentially the same as the arithmetic mean algorithm since no matter the magnitude of the inputs, the FRF will always be of the same magnitude. Since a geometric mean is typically used in the case of combining values of different magnitude, it is no more attractive than the ARI algorithm for the work of this thesis. In fact, since the root of a matrix must be found, use of the geometric mean can be considered to be less attractive than the arithmetic mean due to computational difficulty.

5.4.3.7 Coherence Functions

Coherence is an indication of how much of the measured output power of the system is caused by the measured input power, per frequency line. A coherence value of unity indicates that all of the output is coherent with the input, whereas a value less than unity generally indicates that unmeasured sources also contributed input to the system. However, low coherence can also be

caused by measurement errors, such as quantization, and by data processing errors, such as leakage.

For the case of SIMO, the ordinary coherence function between the single input location, q, and a particular output location, p, is calculated as:

$$COH_{pq} = \frac{\sum_{m=1}^{M}\left(X^{(m)}F^{(m)*}\right)\sum_{m=1}^{M}\left(F^{(m)}X^{(m)*}\right)}{\sum_{m=1}^{M}(F^{(m)}F^{(m)*})\sum_{m=1}^{M}(X^{(m)}X^{(m)*})} \qquad \text{Equation 5.33.}$$

Where:

M = the number of redundant experiments.

$X^{(m)}$ = the measured response at location p for the mth experiment.

$F^{(m)}$ = the measured input at location q for the mth experiment.

$[-]^*$ = the complex conjugate.

For the case of MIMO, ordinary coherence functions can be calculated between any input and output, but the multiple coherence function is deemed to be the most useful. Multiple coherence indicates how much of a measured output is caused by the summation of all of the measured inputs. Again, a value of unity indicates that all of the output is coherent with the inputs. The equation for calculating multiple coherence for a particular output location, p, due to all measured inputs is taken from Allemang (1999), and is shown below:

$$MCOH_p = \sum_{q=1}^{N}\sum_{t=1}^{N}\frac{H_{pq}GFF_{qt}H_{pt}^*}{GXX_{pp}} \qquad \text{Equation 5.34.}$$

Where:

N = the number of measured inputs.

H_{pq} = the FRF for output p and input q.

H_{pt} = the FRF for output p and input t.

GFF_{qt} = the cross-power spectrum between output q and input t.

GXX_{pp} = the auto-power spectrum for output p.

$[-]^*$ = the complex conjugate transpose.

5.4.3.8 Summary

Six algorithms for utilizing the data from multiple experiments to reduce variance on FRFs have been discussed. If many realizations of random input are to be used, then the H_v algorithm provides the best results. However, the H_1 algorithm is often preferred since it is much easier to implement and is only marginally inferior to H_v when errors on the input measurements are much smaller than errors on the output measurements (a common assumption). If testing equipment is available that enables synchronization of the measurements over multiple experiments, then the EIV algorithm should be used. The EIV algorithm allows the use of deterministic signals so that leakage can be practically eliminated, and provides consistent FRF estimates even when the input and output errors are somewhat correlated. For these reasons, the H_1 algorithm is used when random excitations are selected for testing performed in the work of this thesis, and the EIV algorithm is used when deterministic excitation signals are selected. The calculation of coherence in this thesis always uses the ordinary coherence function for SIMO testing and the multiple coherence function for MIMO testing, independent of the input signal types.

5.5 SYSTEM IDENTIFICATION BACKGROUND AND ALGORITHM SELECTION

System identification is the process of extracting the modal properties of the tested structure from the measured FRFs. These modal properties are the natural frequencies, modal damping, mode shapes, and modal scaling. Over the last thirty years, many algorithms have been developed for this purpose, with many commercial software packages now available. Along with this multitude of algorithms, there have been many attempts to compare and contrast them with the point of determining which is best. Unfortunately, most of the work in this realm is not especially useful since the comparisons were made in respect to a single specific situation. Also, it is possible that the authors of some of these comparisons may be biased by their relative amount of experience with particular algorithms. In any case, the algorithms are all equally valid from a theoretical standpoint. However, a system identification algorithm that is robust in the case of MIMO bridge testing must be selected.

The selection process begins by discussing the formulation of the mathematical models that are used in system identification. The models relate the measured data to the identifiable modal properties, and the three most common formulations are known as partial fraction, matrix fraction, and state space. The partial fraction model is used in the work of this thesis, and is thus developed in detail. The other two models are also described.

After these formulations are presented, some of the historically most popular algorithms are briefly discussed, including the CMIF algorithm which is then selected. The details of how this selected algorithm determines the modal properties are then provided.

5.5.1 Partial Fraction Model

One mathematical model that relates the physical properties of the structure to the measured data is the partial fraction model (Richardson 1977). This formulation begins with Equation 5.12, but remaining in the Laplace domain provides:

$$\frac{X(s)}{F(s)} = H(s) = \frac{1}{s^2M + sC + K} \qquad \text{Equation 5.35.}$$

Where:

$X(s)$ = the response of the DOF.

$F(s)$ = the force input to the DOF.

$H(s)$ = the transfer function.

M = the mass that is assumed lumped at the DOF.

C = the damping that is associated with the DOF.

K = the stiffness that is associated with the DOF.

$s = \sigma + j\omega$, a complex number.

The goal is to use this equation to derive an expression that relates the transfer function to modal properties. The derivation of the partial fraction model is illustrated below, assuming a single degree of freedom (SDOF) system. First, dividing through by the mass gives:

$$H(s) = \frac{1/M}{s^2 + s(C/M) + (K/M)} \qquad \text{Equation 5.36.}$$

Next, the roots of the denominator are found. This is done by setting the denominator equal to zero and using the quadratic equation to solve. The roots are thus:

$$s = \frac{-C}{2M} \pm \sqrt{\left(\frac{C}{2M}\right)^2 - \left(\frac{K}{M}\right)} \qquad \text{Equation 5.37.}$$

Now define critical damping, C_c, as the damping that makes the radical equal to zero. By setting the radical equal to zero and solving for the critical damping, and by noting that $\sqrt{K/M}$ is the definition of the undamped natural frequency:

$$C_c = 2M\sqrt{K/M} = 2M\Omega \qquad \text{Equation 5.38.}$$

Where:

Ω = the undamped natural frequency.

And defining the damping ratio as:

$$\zeta = C/C_c \qquad \text{Equation 5.39.}$$

This allows the variables in Equation 5.37 to be replaced as follows:

$$\frac{C}{2M} = \zeta\Omega \qquad \frac{\mathrm{K}}{\mathrm{M}} = \Omega^2 \qquad \text{Equation 5.40.}$$

And now substituting gives:

$$s = -\zeta\Omega \pm \sqrt{(\zeta\Omega)^2 - \Omega^2} \qquad \text{Equation 5.41.}$$

The damped natural frequency and damping can be combined on the complex plane, and the undamped natural frequency and the damping ratio can be found as:

$$\Omega = \sqrt{\omega_n^2 - \sigma^2} \qquad \text{Equation 5.42.}$$

$$\zeta = -\sigma / \sqrt{\omega_n^2 + \sigma^2} \qquad \text{Equation 5.43.}$$

Where:

ω_n = the damped natural frequency.

σ = the damping factor.

Substituting these expressions into Equation 5.41 results in a final expression for the roots, which are also the poles of the SDOF system:

$$s = \sigma \pm j\omega_n \qquad \text{Equation 5.44.}$$

$$\lambda = \sigma + j\omega_n \qquad \text{Equation 5.45.}$$

$$\lambda^* = \sigma - j\omega_n \qquad \text{Equation 5.46.}$$

Therefore, Equation 5.36 can now be rewritten as:

$$H(s) = \frac{1/M}{(s-\lambda)(s-\lambda^*)} \qquad \text{Equation 5.47.}$$

This expression can be modified by writing it in terms of partial fractions as:

$$H(s) = \frac{c_1}{(s-\lambda)} + \frac{c_2}{(s-\lambda^*)} \qquad \text{Equation 5.48.}$$

Setting Equation 5.48 equal to Equation 5.47 and solving for the new variables results in:

$$c_1 = \frac{1/M}{(\lambda-\lambda^*)} = \frac{1/M}{(\sigma+j\omega_n)-(\sigma-j\omega_n)} = \frac{1/M}{2j\omega_n} \qquad \text{Equation 5.49.}$$

$$c_2 = \frac{1/M}{-2j\omega_n} = c_1^* \qquad \text{Equation 5.50.}$$

These expressions for c_1 and c_2 are commonly referred to as the residue and are typically denoted by the variable A. Evaluating the expression along the $j\omega$ axis since this is where the FRFs are measured results in the final partial fraction equation below:

$$H(\omega) = \frac{A}{(j\omega - \lambda)} + \frac{A^*}{(j\omega - \lambda^*)} \qquad \text{Equation 5.51.}$$

For systems that have multiple DOFs, the development of the partial fraction equation is identical, except that the transfer function is a summation of the contribution from each mode, and there is one mode for each DOF. Also, for an SDOF system, each variable in Equation 5.51 is a scalar, whereas for an MDOF system with N DOFs, H and A will be matrices of size NxN. Thus, for an MDOF system, the partial fraction expression becomes:

$$[H(\omega)] = \sum_{r=1}^{N} \frac{[A]_r}{(j\omega - \lambda_r)} + \frac{[\mathrm{A}^*]_\mathrm{r}}{(j\omega - \lambda_r^*)} \qquad \text{Equation 5.52.}$$

Where:

r = the mode number

N = the total number of DOFs

$\lambda_r = \sigma_r + j\omega_{n_r}$ = pole of mode r

For Equation 5.52, the values within each residue matrix, $[A]_r$, become far more complicated to derive than those shown for an SDOF system in Equations 5.49 and 5.50. However, this is not an issue since the residue matrix is directly related to the mode shapes (also referred to as modal vectors). The relationship between the residues and the modal vectors is developed below.

First, starting with Equation 5.12, but in the Laplace domain:

$$[B(s)] = 1/[H(s)] = s^2[M] + s[C] + [K] \quad \text{Equation 5.53.}$$

Where:

$[B(s)]$ = the system impedance matrix.

And it is known that:

$$[B(s)][B(s)]^{-1} = [I] = [B(s)][H(s)] \quad \text{Equation 5.54.}$$

Where:

$[I]$ = the identity matrix.

Substituting Equation 5.50 into Equation 5.52 for $[H(s)]$ gives:

$$[I] = \sum_{r=1}^{N} \frac{[B(s)][A]_r}{(s-\lambda_r)} + \frac{[B(s)][\mathrm{A}^*]_\mathrm{r}}{(s-\lambda_r^*)} \quad \text{Equation 5.55.}$$

Now pre-multiplying both sides of the equation by $(s-\lambda_r)$ gives:

$$(s-\lambda_r)[I] = \sum_{r=1}^{N} [B(s)][A]_r + \frac{(s-\lambda_r)[B(s)][\mathrm{A}^*]_\mathrm{r}}{(s-\lambda_r^*)} \quad \text{Equation 5.56.}$$

And evaluating at $s = \lambda_r$ results in the following expression for each mode:

$$0 = [B(\lambda_r)][A]_r \quad \text{Equation 5.57.}$$

The columns of $[B(\lambda_r)]$ are all proportional to modal vector r (denoted by ψ_r). Thus, each column of the residue matrix for mode r must be proportional to ψ_r. It can also be shown that the residue matrix must have the same structure as $[B(\lambda_r)]$. Thus, the following equation can be written:

$$[A]_r = Q_r\{\psi\}_r\{\psi\}_r^T$$ Equation 5.58.

Where:

Q_r = the modal scaling factor for mode r.

$\{\psi\}_r$ = the scaled modal vector (mode shape) for mode r.

This allows Equation 5.50 to be rewritten as:

$$[H(\omega)] = \sum_{r=1}^{N} \frac{Q_r\{\psi\}_r\{\psi\}_r^T}{(j\omega - \lambda_r)} + \frac{Q_r{}^*\{\psi\}_r\{\psi\}_r^T}{(j\omega - \lambda_r^*)}$$ Equation 5.59.

This equation demonstrates that the measured FRFs can be modeled as a superposition of the system properties at each mode. These system properties are the modal scaling, modal vector, damping ratio, and damped natural frequency. A number of algorithms solve for the system properties from this formulation.

5.5.2 Matrix Fraction Model

The matrix fraction model is another common formulation that is used to extract modal properties from measured data. This derivation starts with Equation 5.35 which is repeated here:

$$\frac{X(s)}{F(s)} = H(s) = \frac{1}{s^2M + sC + K}$$ Equation 5.60.

The transfer function can also be expressed as:

$$H(s) = \frac{1}{s^2M + sC + K} = (G(s))^{-1} = \frac{G_{adj}(s)}{|G(s)|}$$ Equation 5.61.

Where:

$G(s)$ = the dynamic stiffness.

$G_{adj}(s)$ = the adjoint matrix.

$|G(s)|$ = the determinant.

For an MDOF system, this can be rewritten as:

$$H(s) = \frac{B(s)}{A(s)} = \frac{\begin{bmatrix} B_{1,1}(s) & \cdots & B_{1,N}(s) \\ \vdots & \ddots & \vdots \\ B_{N,1}(s) & \cdots & B_{N,N}(s) \end{bmatrix}}{A(s)} \quad \text{Equation 5.62.}$$

Where:

N = the total number of DOFs.

The numerator is composed of a matrix of polynomials in s of order $2(N-1)$, and the denominator is a single polynomial in s of order $2N$. From this point, various algorithms solve for the system poles in $A(s)$ in different ways.

5.5.3 State Space Model

The third model for extracting modal parameters uses a state space relationship. The formulation begins with Equation 5.1 which is shown again:

$$[M]\{\ddot{x}(t)\} + [C]\{\dot{x}(t)\} + [K]\{x(t)\} = \{F(t)\} \quad \text{Equation 5.63.}$$

This can be reformulated as:

$$\begin{bmatrix} \dot{x}(t) \\ \ddot{x}(t) \end{bmatrix} = \begin{bmatrix} 0 & I \\ -M^{-1}K & -M^{-1}C \end{bmatrix} \begin{bmatrix} x(t) \\ \dot{x}(t) \end{bmatrix} + \begin{bmatrix} 0 \\ M^{-1} \end{bmatrix} F(t) \quad \text{Equation 5.64.}$$

The state vector is defined as:

$$y(t) = \begin{bmatrix} x(t) \\ \dot{x}(t) \end{bmatrix} \quad \text{Equation 5.65.}$$

The output and the direct input-output transmission matrices (C and D respectively) are defined as:

$$C = [I \quad 0] \qquad D = [0]$$ Equation 5.66.

From this, a state space description of the system is given:

$$\dot{y}(t) = A \cdot y(t) + B \cdot F(t) + w(t)$$ Equation 5.67.

$$x(t) = C \cdot y(t) + D \cdot F(t) + v(t)$$ Equation 5.68.

Where:

A = the dynamic system matrix, size 2N x 2N.

B = the input matrix.

$w(t)$ = a model for noise on the input.

$v(t)$ = a model for noise on the output.

The state space description represents the response of the structure at any time to a known input signal. The poles are found from the eigensolution of the dynamic system matrix. The mode shapes are then found from the C matrix, and the modal participation factors are found from the D matrix.

The state space formulation can also be developed in the frequency domain. With the noise terms set to zero, the formulation becomes:

$$H(s) = C[s \cdot I - A]^{-1}B + D$$ Equation 5.69.

5.5.4 Overview of System Identification Algorithms

Some historically important and popular algorithms that solve for the modal properties based on the mathematical models are discussed below. In general, each of the algorithms described has several variants and the naming is not always consistent from different references. Also, over time, more general models have been developed that have been shown to incorporate several of the listed algorithms in a consistent mathematical format. References for this overview include Maia and Silva (2001), Zhang (2004), and Avitabile et al (2005).

The Peak Picking (PP) algorithm was one of the earliest frequency domain approaches. Peaks in the plots of the FRFs are assumed to be natural frequencies. Curve fitting is then applied to each peak to estimate the damping, and mode shapes are estimated directly from a column of FRFs at the assumed natural frequencies. This method will provide incorrect estimates of damping when closely spaced or repeated modes exist. Also, this method is difficult to use in the presence of noise since the peaks will be more difficult to identify.

The Ibrahim Time Domain (ITD) method is a low order time domain algorithm that uses the state space model formulation. For FRF data, the inverse FFT is used to produce free response (decay) functions. These functions are then reformulated into an eigenvalue problem and solved to find the natural frequencies, damping, and mode shapes. Modal scaling cannot be found since free response functions are used.

The Eigensystem Realization Algorithm (ERA) is a first order time domain algorithm that uses the state space formulation. The noise vectors are assumed to equal zero, and the minimum realizations of the system matrices are found. For FRF data, the inverse FFT is used to produce impulse response functions which are assembled into a block Hankel matrix. This matrix is then

decomposed using singular value decomposition (SVD) to find the system poles, damping, and modal vectors. ERA-FD is an equivalent algorithm formulated in the frequency domain. The FRFs are formed into a block matrix and SVD is again used to solve. Both methods produce a large number of computational poles, requiring that various strategies be used to determine which are real system poles and which are not.

The Autoregressive Moving Average (ARMA) is another popular time domain method. This algorithm has a large number of variants including frequency domain incarnations. This method uses a low polynomial order of the matrix fraction model, which results in large matrix coefficients. A drawback of this method is that it also produces many computational poles.

The Least Squares Complex Exponential (LSCE) algorithm is a high order time domain method that uses impulse response functions (IRFs) and the matrix fraction model. The coefficients of the denominator characteristic equation are computed and then the roots are found, which are the system poles. The mode shapes are found in a second step. This method also generates many computational poles and determination of the real modes is required. In the presence of noise, determining the real modes can be difficult. The Polyreference Time Domain (PTD) algorithm is a MIMO version of LSCE.

The Frequency Domain Direct Parameter Identification (FDPI) method uses the state space model to solve for the modal properties. This method can only locate a number of modes equal to or less than the number of output measurements within any frequency band. Also, this method is computationally and memory intensive.

The Rational Fraction Polynomial (RFP) is a frequency domain algorithm that also has many variations, including the Matrix Fraction Description (MFD). These algorithms attempt to minimize the error between the measured and the modeled transfer function.

The Complex Mode Indicator Function (CMIF) is a frequency domain algorithm that uses SVD of the transfer function to indicate the location of modes and to provide estimates of the mode shapes (Shih et al 1989). In a second step, the partial fraction model is used to estimate the modal parameters. A significant benefit of CMIF is that computational poles are not needed in order to enable a good fit to the data.

5.5.5 Complex Mode Indicator Function

CMIF is selected for the work of this thesis for two main reasons. First, CMIF does not require the inclusion of computational poles. This is important in bridge testing since bridges are time-variant structures. In laboratory testing of mechanical systems, the ambient conditions (such as temperature and humidity) and the support conditions can be carefully maintained. This provides excellent data consistency and allows stabilization diagrams to accurately sort the computational modes from the actual modes. For time variant structures, it is far more difficult to sort out computational modes since the actual modes will drift in the stabilization diagram due to data inconsistency (Lembregts et al 1987). The second reason CMIF is selected is purely pragmatic. CMIF is a relatively simple algorithm to code and implement. Thus, CMIF is used and the process of extracting modal parameters with this algorithm is described in detail below.

Like many system identification algorithms, CMIF uses a two stage process. In the first stage, modal vectors are estimated and are then used to filter the transfer function into what are essentially a collection of SDOF systems. These filtered FRFs are referred to as enhanced

frequency response functions (eFRFs). In the second stage, the pole and modal scaling are found from each SDOF system. Of course, the actual implementation of these two stages is somewhat more complicated and thus the entire process is described in detail below.

5.5.5.1 Step 1 – Perform Singular Value Decomposition

Singular value decomposition (SVD) is a common matrix factorization that is useful in many applications. In the CMIF algorithm, SVD is used to provide estimates of the modal vectors (mode shapes) of the system. To use SVD, it is first necessary to rewrite the mathematical model in a form that more closely relates to the form of the decomposition. From before, the partial fraction model of the transfer function can be derived as:

$$[H(\omega)] = \sum_{r=1}^{N} \frac{Q_r\{\psi\}_r\{\psi\}_r^T}{(j\omega - \lambda_r)} + \frac{Q_r{}^*\{\psi\}_r\{\psi\}_r^T}{(j\omega - \lambda_r^*)} \qquad \text{Equation 5.70.}$$

If the complex conjugate terms are now included in the first term of the summation, and the limit of the sum is thus increased to $2N$, then the equation may be rewritten as:

$$[H(\omega)] = \sum_{r=1}^{2N} \frac{Q_r\{\psi\}_r\{\psi\}_r^T}{(j\omega - \lambda_r)} \qquad \text{Equation 5.71.}$$

Now defining the modal participation factor as the transpose of the modal vector multiplied by the modal scaling, per mode:

$$\{L\}_r = Q_r\{\psi\}_r^T \qquad \text{Equation 5.72.}$$

Substituting Equation 5.72 into Equation 5.71 gives:

$$[H(\omega)] = \sum_{r=1}^{2N} \frac{\{\psi\}_r \{L\}_r}{(j\omega - \lambda_r)}$$ Equation 5.73.

It is now possible to reorganize this equation into the completely equivalent form shown below which eliminates the summation (with the assumption of normal modes):

$$[H(\omega)] = \sum_{r=1}^{2N} \frac{\{\psi\}_r \{L\}_r}{(j\omega - \lambda_r)} = [\Psi][\Lambda][L]$$ Equation 5.74.

Where each column of the matrix $[\Psi]$ contains a modal vector as shown below (up to $2N$ modes):

$$[\Psi] = [\{\psi_1\}\ \{\psi_2\}\ \cdots\ \{\psi_{2N}\}]$$ Equation 5.75.

And the matrix $[\Lambda]$ is a diagonal matrix containing the poles (with a size of $2Nx2N$):

$$[\Lambda] = \begin{bmatrix} \frac{1}{j\omega - \lambda_1} & 0 & 0 & 0 \\ 0 & \frac{1}{j\omega - \lambda_2} & 0 & 0 \\ 0 & 0 & \ddots & 0 \\ 0 & 0 & 0 & \frac{1}{j\omega - \lambda_{2N}} \end{bmatrix}$$ Equation 5.76.

And where each row of the matrix $[L]$ contains a modal participation factor vector:

$$[\mathrm{L}] = \begin{bmatrix} \{L\}_1 \\ \{L\}_2 \\ \vdots \\ \{L\}_{2N} \end{bmatrix}$$ Equation 5.77.

Singular value decomposition (SVD) of the transfer function at each frequency line provides a very similar structure as the mathematical model of Equation 5.74:

$$[H(\omega)] = [\mathrm{U}(\omega)][\Sigma(\omega)][V(\omega)] \quad \text{Equation 5.78.}$$

Where:

$[U(\omega)]$ = the left singular vectors, a unitary matrix.

$[\Lambda(\omega)]$ = a diagonal matrix of singular values that are real and non-negative.

$[V(\omega)]$ = the right singular vectors, a unitary matrix.

From basic dynamics, it is known that the mode shapes are eigenvectors of the system equation. As such, finding the eigenvectors of a transfer function at some discrete frequency will provide the mode shapes that are most dominant at that frequency (up to the size of the system matrix). The SVD is closely related to the eigenvalue decomposition, and can be used in place of it. The eigenvalue decomposition of the transfer function is given as:

$$[H(\omega)][H(\omega)]^* = [\Psi(\omega)][\Lambda(\omega)][\Psi(\omega)]^* \quad \text{Equation 5.79.}$$

Where:

$[\Psi(\omega)]$ = the eigenvectors.

$[\Lambda(\omega)]$ = the eigenvalues.

The eigenvalue decomposition can also be written in terms of the SVD terms as (and dropping the omegas):

$$[H][H]^* = [\mathrm{U}][\Sigma][V]^*[V][\Sigma]^*[\mathrm{U}]^* = [\mathrm{U}]([\Sigma][\Sigma]^*)[\mathrm{U}]^* \quad \text{Equation 5.80.}$$

From inspection of Equations 5.79 and 5.80, it is obvious that the left singular vectors are the eigenvectors, and that each singular value is the square root of each eigenvalue. The right singular vectors can also be shown to be eigenvectors by reformulated Equation 5.80 as $[H]^*[H]$. Thus, the SVD provides the same basic information as an eigenvalue decomposition would.

The SVD is used in place of eigenvalue decomposition for computational purposes. First, the matrix product of the transfer function is not required when using SVD. Also, the SVD algorithm is computationally more efficient than eigenvalue decomposition.

Some important properties of the SVD are noted. First, the singular values are unique, but the singular vectors are not. If the transfer function is generally complex, than the singular vectors may also be generally complex (Fladung et al 1997). It is also important to understand the shape of the various matrices and how many elements each will contain. The equation below indicates the dimensions of the various matrices, and these dimensions are correct regardless of the number of input locations or output locations.

$$[H(\omega)]_{N_o x N_i} = [\mathrm{U}(\omega)]_{N_o x N_o}[\Sigma(\omega)]_{N_o x N_i}[V(\omega)]_{N_i x N_i} \qquad \text{Equation 5.81.}$$

Where:

N_o = the number of output measurement locations.

N_i = the number of input measurement locations.

5.5.5.2 Step 2 – Select CMIF Peaks and Extract Modal Vectors

The purpose of the SVD was to capture estimates of the mode shapes. However, the singular vectors provide the best estimate of a mode shape at frequency lines that are near the natural frequency corresponding to the mode shape of interest. Thus, it is necessary to select approximate natural frequencies of the system so that good estimates of the mode shapes can be selected.

To enable selection of natural frequencies, the singular values are plotted against frequency, and this is referred to as a CMIF plot. Peaks in the CMIF plot are selected as potential natural

frequencies. Considering Equation 5.73, it is noted that the numerator is a constant for each mode, but the denominator varies with ω. The denominator is a minimum when $j\omega = \lambda_r$, and thus a local maxima will occur in the CMIF plot. Given perfect data, each peak would be at a frequency line that is nearest to a damped natural frequency.

Selection of peaks near natural frequencies is trivial in the case of clean data, and this is illustrated in Figure 5.8. This figure shows a CMIF plot for a numerical model of a cantilevered beam with three natural frequencies in the frequency band. The asterisks on the plot indicate the peaks that were automatically selected. The frequency resolution of the CMIF is 0.1 Hz for this example, and all three selected peaks are at a frequency line that is immediately adjacent to the theoretical natural frequency.

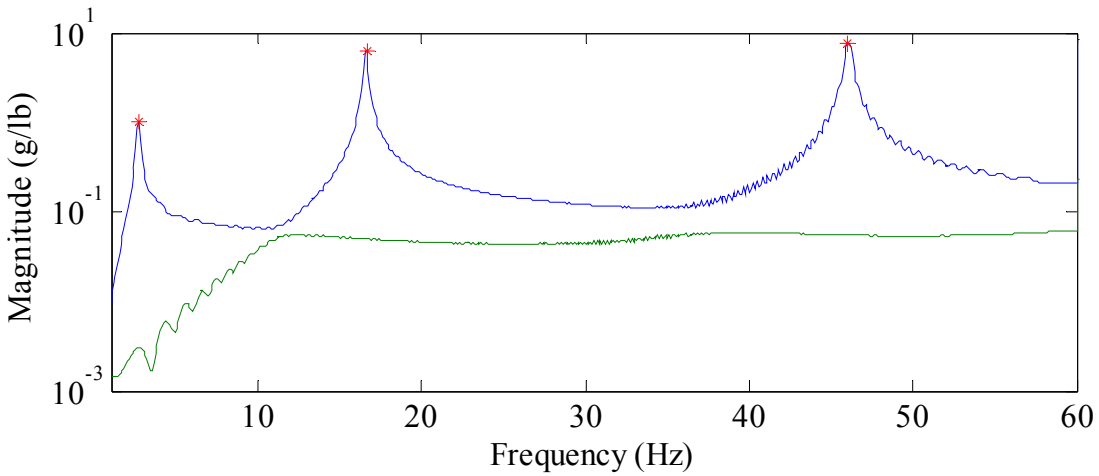

Figure 5.8. CMIF plot showing peak selection near natural frequencies with very low noise.

In the presence of noise, the peaks may be jagged and the highest point may not be at the frequency line closest to the damped natural frequency. This is not typically an issue since the mode of interest will be dominant anywhere in the vicinity of the peak. However, the variance in the mode shape can be reduced by averaging the modal vectors from several adjacent lines of the CMIF (Leurs et al 1993). In the case where there are closely spaced modes, the mode shapes to

be averaged must be inspected to ensure they are consistent. Also, using only the imaginary portion of the transfer function in the calculation of the SVD provides better discrimination between closely spaced modes (Allemang and Brown 2006). The SVD of purely imaginary values returns purely real valued modal vectors.

A more serious issue in the presence of noise is that false peaks may be selected. This is especially an issue with the use of random inputs if there are an inadequate number of averages. Peaks are then likely to exist at any frequency that was not well excited. To avoid selection of these peaks, the modal vectors near the peak are inspected to ensure they are consistent with the mode shape at the peak.

Figure 5.9 illustrates a CMIF plot in the presence of noise. This plot was prepared using the same numerical cantilevered beam model as before, but adding 5% noise to the inputs and 20% noise to the outputs. Also, the SVD was performed only on the imaginary part of the transfer function. It is noteworthy that the magnitude of the peak singular values are not affected by operating on only the imaginary part, but the singular values away from the peaks are affected. This figure also shows that although the noise is significant, it does not have a large effect in the vicinity of the peaks, validating that CMIF is a robust algorithm.

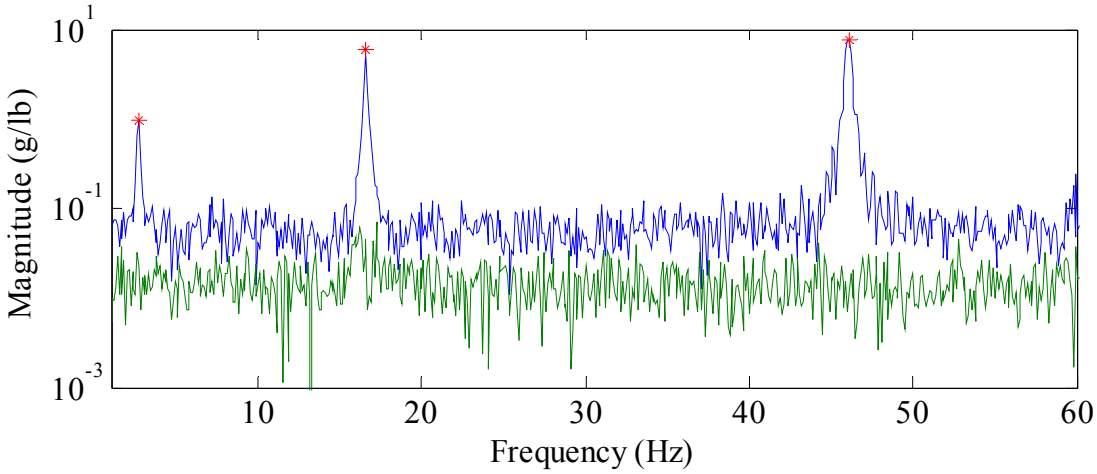

Figure 5.9. CMIF plot showing peak selection in the presence of noise.

The mode shapes are also affected by the noise. Figure 5.10 shows the mode shape for the first bending mode of the cantilever beam. The mode shape from the left singular vector at the frequency line of the peak singular value is shown in the central plot. The two plots on the left side are from the two frequency lines prior to the peak, and the two plots on the right side are from the two frequency lines after the peak. The mode shapes are practically identical for any frequency line near the peak since the modes are widely spaced and since there is very low noise. Figure 5.11 shows the same mode shape plots, but for the noisy data. The mode shape is noticeably affected by the noise.

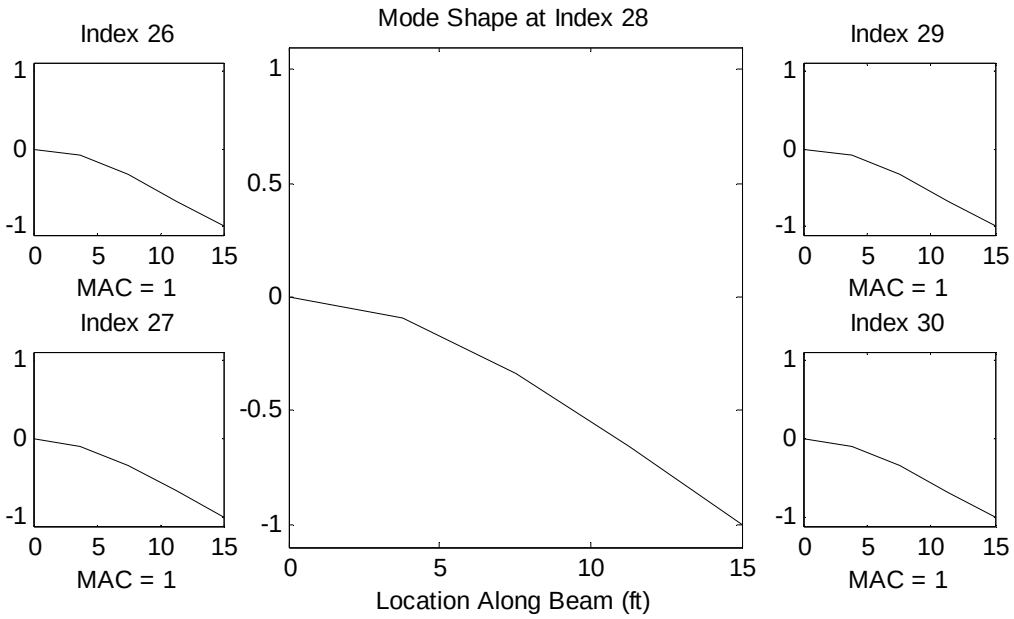

Figure 5.10. Plot of mode shapes in the vicinity of the first CMIF peak with very low noise.

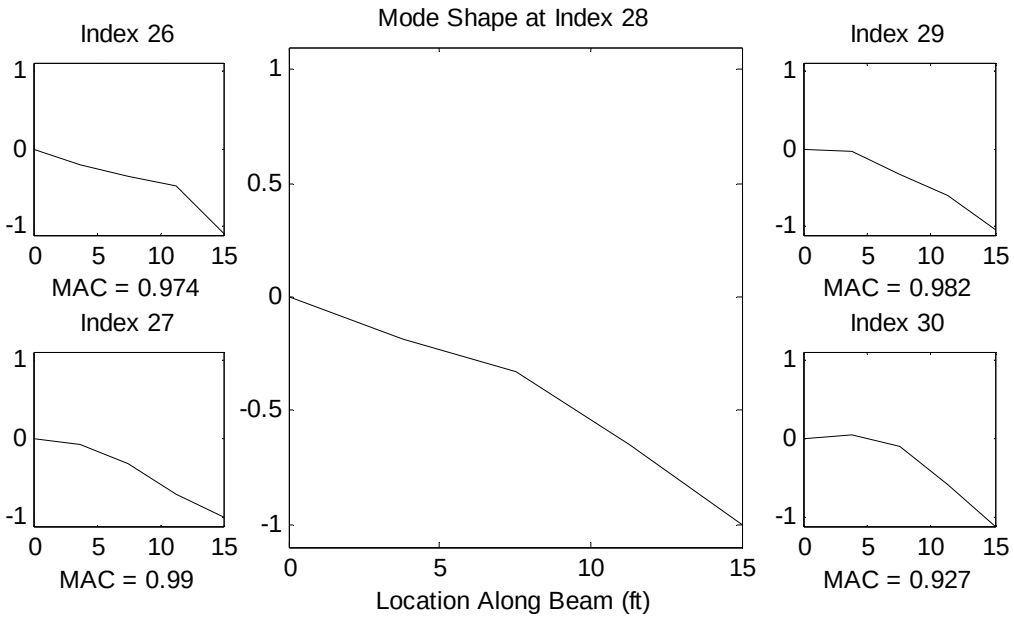

Figure 5.11. Plot of mode shapes in the vicinity of the first CMIF peak in the presence of noise.

Figure 5.12 illustrates how mode shapes in the vicinity of a peak can be used to help evaluate if the peak is due to a natural frequency or not. This figure again illustrates the mode shapes for two frequency lines before and after a selected peak. The mode shapes are not consistent, and this indicates that the peak is not due to a mode.

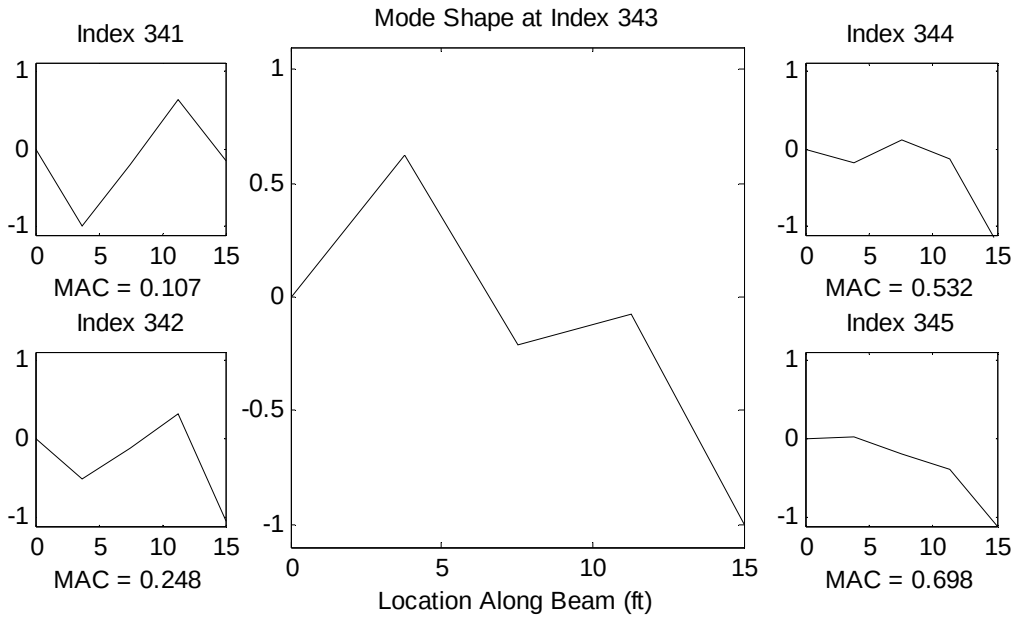

Figure 5.12. Plot of mode shapes in the vicinity of a false peak. Note inconsistent mode shapes.

If the testing was well planned and the data was properly collected, then the FRFs should be fairly smooth. Given good FRFs, the CMIF plot will also be reasonably smooth, and the selection of peaks and modal vectors can be confidently carried out.

5.5.5.3 Step 3 – Generate Enhanced Frequency Response Functions

With good estimates of the mode shapes, the FRFs can be transformed from physical coordinates to modal coordinates. This transformation is done by using the modal vectors as a basis. If the modes are orthogonal, then a transformed FRF will only be due to a single mode, and will be referred to as an enhanced FRF (eFRF). The eFRF is essentially the FRF for an SDOF system, and the purpose of this transformation is to enable the poles and modal scaling to be easily extracted. The eFRF is defined as shown below:

$$EFRF_r(\omega) = \frac{Q_r}{(j\omega - \lambda_r)}$$ Equation 5.82.

Where:

Q_r = the modal scaling factor for mode r.

$\lambda_r = \sigma_r + j\omega_{n_r}$ = pole of mode r.

To get the transfer function into this form requires a few steps. First, starting with Equation 5.71 and pre and post-multiplying both sides by a basis for the transformation (e.g. a modal vector) gives:

$$\{\varphi_r\}^T[H(\omega)]\{\varphi_r\} = \{\varphi_r\}^T \sum_{k=1}^{2N} \frac{Q_k\{\psi_k\}\{\psi_k\}^T}{(j\omega - \lambda_k)}\{\varphi_r\}$$ Equation 5.83.

Where:

φ_r = a column vector that is representative of mode r.

Assuming orthogonal modes, the contribution from any mode k that is not mode r will equal zero because of the vector product:

$$\{\varphi_r\}^T\{\psi_k\} = 0 \;\; if \;\; k \neq r$$ Equation 5.84.

In actual testing, the modes may not be completely orthogonal since only a small number of spatial locations are sampled. This is usually not important since only the eFRF information near a peak is used in estimating the modal properties, and the contribution from other modes will thus be orders of magnitude less than the contribution of the mode of interest in this vicinity. Assuming the contribution from other modes is nearly zero, Equation 5.83 reduces to:

$$\{\varphi_r\}^T[H(\omega)]\{\varphi_r\} \approx \{\varphi_r\}^T \frac{Q_r\{\psi_r\}\{\psi_r\}^T}{(j\omega - \lambda_r)}\{\varphi_r\}$$ Equation 5.85.

The contribution due to the conjugate pole, λ^*, is neglected. This contribution is equal to 50% of the eFRF magnitude at $\omega = 0$, and reduces at a rate proportional to $1/\lambda$. Thus, at very low frequencies, neglecting this term leads to large errors. However, the error in the magnitude of the eFRF at ω = 1 Hz is 0.8% (assuming 1% damping). At ω = 5 Hz the error is 0.16%, and the error is 0.08% at 10 Hz. Thus, for structures with fundamental frequencies in the range that can be excited by the TTs, neglecting the conjugate pole is satisfactory.

Moving terms from Equation 5.85 to the left side results in:

$$\frac{\{\varphi_r\}^T[H(\omega)]\{\varphi_r\}}{\{\varphi_r\}^T\{\psi_r\}\{\psi_r\}^T\{\varphi_r\}} = \frac{Q_r}{(j\omega - \lambda_r)} = EFRF_r(\omega) \qquad \text{Equation 5.86.}$$

Thus the eFRFs can be found from the transfer function so long as good estimates of the mode shapes exist and so long as the mode shape estimates are essentially orthogonal.

Equation 5.86 is general, and needs to be slightly adapted for the CMIF algorithm. Using CMIF, the modal vectors are estimated as the left singular vectors taken at a frequency that is near a natural frequency of the system. In general, the left singular vectors, like eigenvectors, are not unique and may be scaled by some complex number. As a first step, all of the singular vectors that have been selected as modes of the system must be commonly scaled. After a modal scaling method is selected and applied to each modal vector, then the modal scaling factor that relates the residues to the scaled mode shapes can be calculated. Three common methods of scaling the modal vectors are described below.

A simple and common scaling method is to set the largest absolute value in the modal vector equal to one and to scale the other values proportionally. This is known as ‘unity modal

coefficient' scaling. A second method is to set the vector length equal to one. This is known as 'unity modal vector length' and consists of dividing each element in the modal vector by the 2-norm. Finally, if the modal scaling factor is set equal to the inverse of $2j\omega$, then the modal mass will be calculated equal to one. This is 'unity modal mass' scaling, and is only applicable when the modal masses are extracted prior to the modal vectors. Unity modal coefficient scaling is used in this thesis since it is easily implemented. The scaling can be represented as:

$$\{\psi\}_r = \frac{\{u\}_r}{u_i} \qquad \text{Equation 5.87.}$$

Where:

$\{\psi\}_r$ = the scaled modal vector for mode r, which is real and has maximum value of 1.0.

$\{u\}_r$ = the left singular vector selected as the estimate of the mode shape.

u_i = the scalar from $\{u\}_r$ that has the largest absolute value.

It must also be recognized that $[H(\omega)]$ has a size of $N_o x N_i$ and thus the mode shape vector on the left side must have length N_o and the mode shape vector on the right side must have length N_i. The left singular vector has length N_o and so the scaled modal vector does as well, and can be used on the left side. However, the vector on the right side must be a subset of the modal vector that only represents the spatial locations of the inputs. While it is possible to simply use the appropriate coefficients from the modal vector, in CMIF it is preferred to use the right singular vectors instead, which already have a length of N_i.

To use the right singular vectors, they must be scaled in a consistent manner with the modal vector (Catbas et al 2004). For perfect data, there is merely a linear relation between the elements of the left singular vector and the right singular vector. In the presence of noise, this is not true

and a linear least-squares estimate is used to find a scale factor for the right singular vector. Assuming the following relation for the vectors selected at a single mode:

$$\overline{\psi_i} = C \cdot v_i + \varepsilon_i \qquad \text{Equation 5.88.}$$

Where:

C = a constant.

$\overline{\psi_i}$ = the element of the scaled mode shape that corresponds to the spatial location of v_i.

v_i = the ith element of the right singular vector.

ε_i = the error on the ith element.

And the least-squares solution for the constant is then:

$$C = \frac{\sum_{i=1}^{n}(v_i \overline{\psi_i})}{\sum_{i=1}^{n}(v_i^2)} \qquad \text{Equation 5.89.}$$

In practical coding, the pseudo inverse is often used to find the solution to linear least-squares problems. Thus, for any mode, the calculation of the constant can be equivalently represented as:

$$C_r = \{v\}_r^+ \{\bar{\psi}\}_r \qquad \text{Equation 5.90.}$$

Where:

$\{v\}_r^+$ = the pseudo inverse of the left singular vector for mode r.

$\{\bar{\psi}\}_r$ = the elements of the scaled mode shape that correspond to the input locations.

The right singular vectors can now be properly scaled in relation to the scaled modal vectors:

$$\{v_{sc}\}_r = C_r \cdot \{v\}_r \qquad \text{Equation 5.91.}$$

Substituting the modified left and right singular vector data into Equation 5.86 provides the final equation that is used to calculate the eFRFs:

$$EFRF_r(\omega) = \frac{\{\psi\}_r^T [H(\omega)] \{v_{sc}\}_r}{\{\psi\}_r^T \{\psi\}_r \{v_{sc}\}_r^T \{v_{sc}\}_r} \qquad \text{Equation 5.92.}$$

Equation 5.92 is effective at filtering the transfer function such that an eFRF will primarily be composed of the contribution from a single mode. However, with modal vectors that have low spatial resolution, and in the presence of noise, the filtering will be imperfect and more than one mode may noticeably contribute to a single eFRF. This is not usually an issue since only a few points near the peak of the eFRF are used to estimate the poles and modal scaling.

5.5.5.4 Step 4 – Extract Poles and Modal Scaling

5.5.5.4.1 Least-Squares Local DOF Method

The eFRFs are essentially the transfer functions for SDOF systems, and thus SDOF methods can be used to extract the poles and modal scaling from the eFRFs (Allemang 1999). Since the poles and modal scaling are constants, the eFRF provides a highly overdetermined set of equations from which to solve for these paramaters. Starting with the SDOF Equation 5.82:

$$EFRF_r(\omega) = \frac{Q_r}{(j\omega - \lambda_r)} \qquad \text{Equation 5.93.}$$

Using a least-squares formulation, a number of points along the eFRF are selected. The points are selected in the vicinity of the peak since this is where the eFRF should be least affected by other modes. The exact number of points to use depends on balancing two criteria: using more points reduces the variance due to noise; selecting points away from the peak reduces accuracy due to the contribution of other modes. A method is developed for use in this work to select a

'good' number of points, and is discussed later. To solve for the modal scaling and the pole for a single mode, Equation 5.93 is rearranged (and dropping the r notation):

$$j\omega_i \cdot EFRF_i - \lambda \cdot EFRF_i = Q \qquad \text{Equation 5.94.}$$

And further rearranging to:

$$j\omega_i \cdot EFRF_i = [EFRF_i \quad 1]\begin{bmatrix}\lambda \\ Q\end{bmatrix} \qquad \text{Equation 5.95.}$$

Which can finally be expressed as:

$$\begin{bmatrix}\lambda \\ Q\end{bmatrix} = \frac{1}{[EFRF_i \quad 1]} \cdot j\omega_i \cdot EFRF_i \qquad \text{Equation 5.96.}$$

And using the pseudo inverse to find the least-squares solution:

$$\begin{bmatrix}\lambda \\ Q\end{bmatrix} = \begin{bmatrix}EFRF_1 & 1 \\ EFRF_2 & 1 \\ \vdots & \vdots \\ EFRF_n & 1\end{bmatrix}^{+} \begin{bmatrix}j\omega_1 \cdot EFRF_1 \\ j\omega_2 \cdot EFRF_2 \\ \vdots \\ j\omega_n \cdot EFRF_n\end{bmatrix} \qquad \text{Equation 5.97.}$$

Where:

n = the number of points along the eFRF selected for the solution.

$[\cdot]^+$ = the pseudo inverse.

It must be noted that the least-squares formulation does not return the complex conjugate poles, although an eigenvalue formulation would. However, the conjugate poles are assumed to exist and are applied when the modal properties are used to synthesize FRFs and when modal flexibility is calculated.

Figure 5.13 shows the result of using least squares to fit a solution for the pole to the noisy numerical cantilevered beam model data. The thick black line shows the SDOF FRF synthesis over the range of points that were used to solve for the pole. The thin line is the eFRF, and it is clear that the extracted natural frequency and damping ratio match the data.

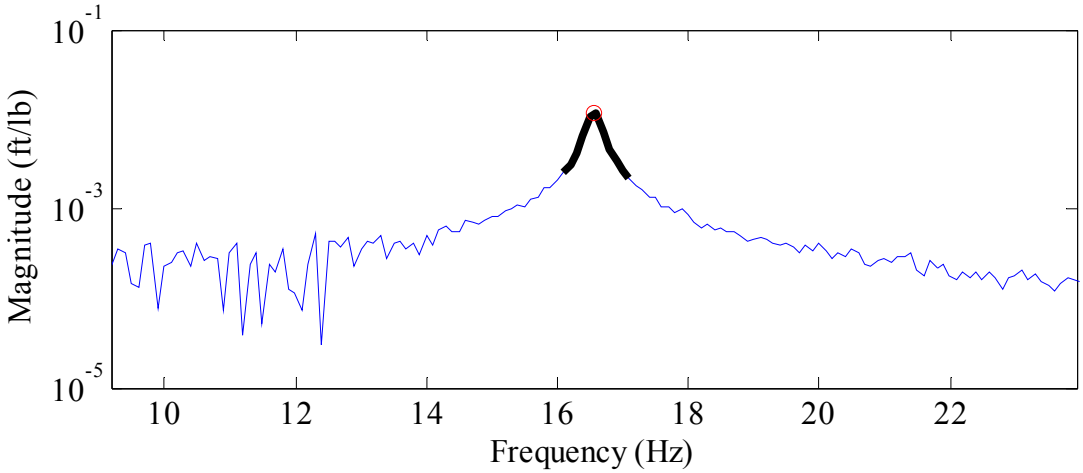

Figure 5.13. eFRF plot showing curve fit of modal parameters.

The undamped natural frequencies and damping ratios can be calculated directly from the poles by using Equation 5.42 and Equation 5.43 respectively. At this point, the mode shapes, damping ratios, natural frequencies, and modal scaling are all known and the CMIF algorithm is complete.

5.5.5.4.2 Selection of Portion of eFRF for Least-Squares

The selection of the number of points from the eFRF to use in the least-squares solution to Equation 5.97 is not often discussed in the literature, and anecdotal evidence suggests that a constant number of points is often selected *a-priori* and used for all parameter extraction. Experimentation within this work demonstrated that the number of points used can significantly affect the solution for damping and modal mass if the subject eFRF peak is affected by noise. Therefore, an algorithmic method by which a 'good' number of points is automatically selected is developed.

First, it is recognized that in the absence of noise, the few points closest to the eFRF peak are the least affected by the contribution of other modes. Second, it is recognized that if the peak is affected by noise, then additional points should be used to increase the probability that the noise will be 'averaged' out. Therefore, the algorithm works as follows:

- The peak eFRF point and the closest points to either side (3 points total) are selected and λ and Q are calculated.
- This is repeated with 5 total points and 7 total points so that three values of λ and Q exist.
- If the value of Q varies by less than 5% amongst these three samples, then the λ and Q values using five points are selected.
- If the value of Q varies by more than 5%, then the algorithm proceeds by adding two additional points in each iteration.
- If the value of Q varies by less than 5% amongst the three most recent samples, then the λ and Q values of the second most recent iteration are selected.
- If a local minima in Q is found, and the last three values vary by less than 10%, then the λ and Q values at the minima are selected.
- If a local maxima in Q is found, and the last three values vary by less than 10%, then the λ and Q values at the maxima are selected.
- If the value of Q does not adequately stabilize by the 10th iteration (21 total points in least-squares calculation), then the algorithm stops and the λ and Q values of the 10th iteration are selected.

Using this method provided much more consistent values of modal mass across various experiments, and it is used for all laboratory bridge model and field bridge testing data processing.

5.5.5.5 Step 5 – Evaluate Results

The final step of the system identification process is to verify that the extracted modal parameters accurately represent the system. The most common method to check the validity of the parameters is to synthesize FRFs from the parameters. The synthesized FRFs can then be plotted on the measured FRFs and the fit can be evaluated. A second method for checking for errors is to use reciprocity. Per Maxwell's reciprocity theorem, the response at DOF 'B' to a force at DOF 'A' is equal to the response at DOF 'A' for the same force at DOF 'B'. This implies that the FRF for input location 'A' and output location 'B' should be identical to the FRF for input location 'B' and output location 'A'.

FRFs are synthesized using the partial fraction model as shown below. Because the transfer function is usually not square due to a different number of inputs and outputs, a subset of the full modal vector must be used as before. The transfer function is synthesized as:

$$[A]_r = Q_r\{\psi_r\}\{\overline{\psi_r}\}^T \qquad \text{Equation 5.98.}$$

Where:

$[A]_r$ = the residue matrix for mode r.

$\{\overline{\psi_r}\}$ = the subset of modal vector r for the DOFs at driving point locations.

$$\left[H_{syn}(\omega)\right] = \sum_{r=1}^{N} \frac{[A]_r}{(j\omega - \lambda_r)} + \frac{[A^*]_r}{(j\omega - \lambda_r^*)} \qquad \text{Equation 5.99.}$$

Where:

N = the number of modes captured.

$[A^*]_r$ = the complex conjugate of each term of the residue matrix.

For the common situation in which a single FRF is synthesized at a time, the equation is simplified as:

$$FRF_{pq}(\omega) = \sum_{r=1}^{N} \frac{Q_r \cdot \psi_{p_r} \cdot \psi_{q_r}^*}{(j\omega - \lambda_r)} + \frac{\left(Q_r \cdot \psi_{p_r} \cdot \psi_{q_r}^*\right)^*}{(j\omega - \lambda_r^*)} \qquad \text{Equation 5.100.}$$

Where:

p = the output DOF number.

q = the input DOF number.

ψ_{p_r} = the scalar value of modal vector r at DOF location p.

$\psi_{q_r}^*$ = the complex conjugate of the scalar value of modal vector r at DOF location q.

Figure 5.14 and Figure 5.15 illustrate the use of synthesized FRFs for solution validation. These figures use the noisy data from the numerical cantilevered beam model, and the black line is the FRF that has been synthesized from the extracted modal properties. The first plot illustrates the magnitude of the FRF, and the fit is reasonable, especially at the peaks. The second plot illustrates the phase angle of the FRF, and the fit is reasonable. The significant apparent noise in the measured FRF below 15 Hz is due to the selected limits of the 'y' axis. Since the FRF should have a value near -180 degrees, values that are slightly less than -180 are plotted as positive values, causing the plot to appear noisier than it actually is in this region. This can be greatly improved by choosing different limits for the axis as is shown in Figure 5.16. This is a common problem with phase plots.

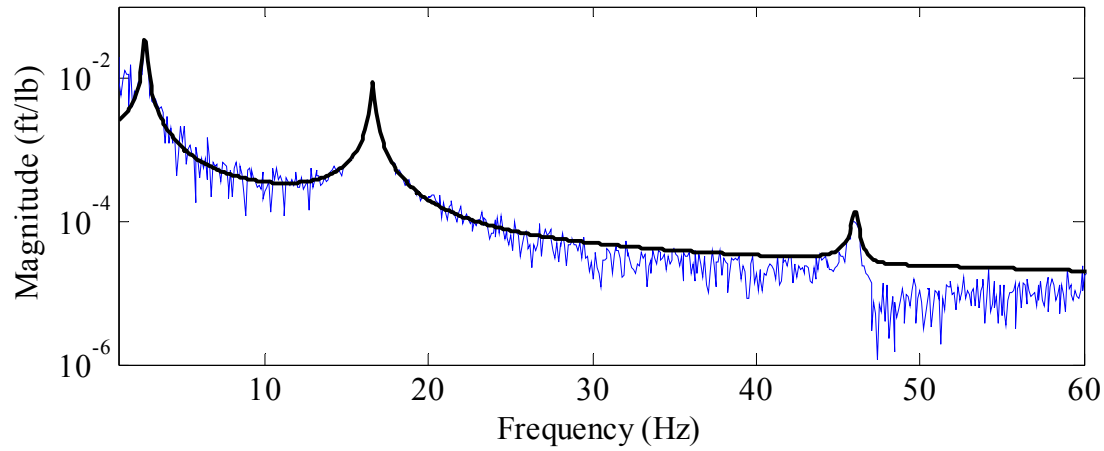

Figure 5.14. Magnitude plot - synthesized FRF overlay on measured FRF in the presence of noise.

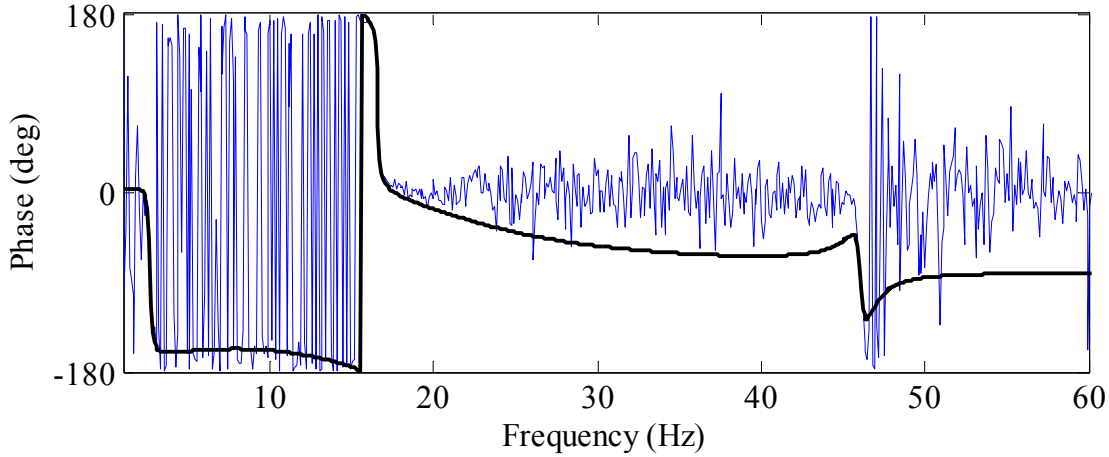

Figure 5.15. Phase angle plot – synthesized FRF overlay on measured FRF in the presence of noise.

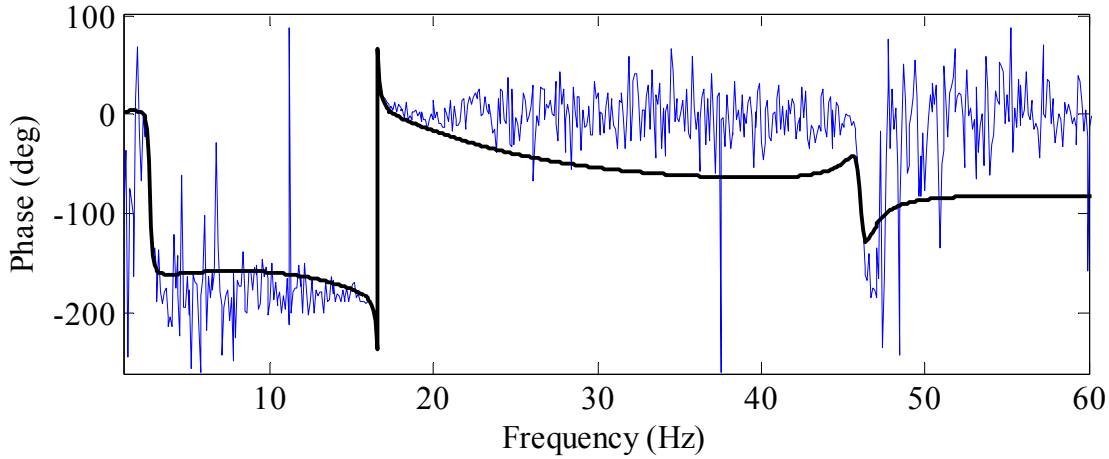

Figure 5.16. Phase angle plot – revised y-axis reduces apparent noise below 15 Hz.

Reciprocity is also checked by overlaying the FRFs synthesized for any pair of DOFs. However, the overlays will be perfectly aligned so long as an error was not made in the calculation of the synthesized FRFs. This is apparent by inspection of Equation 5.100, in which it is clear that the exact same modal properties are used to calculate the pair of FRFs that can exist between two points. It is noted that reciprocity is more commonly used to check for nonlinearities during the testing stage by comparing the measured FRFs between a pair of DOFs.

5.6 MODAL FLEXIBILITY ESTIMATION

After the modal properties have been estimated from experimental data for some number of identifiable modes, it is possible to calculate an estimate of modal flexibility. From before, if the transfer function is evaluated at $\omega = 0$ then the Newtonian equation of motion in the Laplace domain reduces to:

$$[H(0)] = \frac{1}{[K]} = [f] \qquad \text{Equation 5.101.}$$

Since the transfer function can be synthesized from the estimated modal properties, modal flexibility can also be synthesized. Using the partial fraction model of the transfer function from before:

$$[H(\omega)] = \sum_{r=1}^{N} \frac{Q_r\{\psi\}_r\{\psi\}_r^T}{(j\omega - \lambda_r)} + \frac{(Q_r\{\psi\}_r\{\psi\}_r^T)^*}{(j\omega - \lambda_r^*)} \qquad \text{Equation 5.102.}$$

Evaluating the partial fraction model at a frequency of $\omega = 0$ gives:

$$[H(0)] = \sum_{r=1}^{N} \frac{Q_r\{\psi\}_r\{\psi\}_r^T}{(-\lambda_r)} + \frac{(Q_r\{\psi\}_r\{\psi\}_r^T)^*}{(-\lambda_r^*)} = [f] \qquad \text{Equation 5.103.}$$

All of the modal parameters needed for the solution of Equation 5.103 have now been estimated by the system identification process. It is noteworthy that in the synthesis of the transfer function, the size is not limited to the $N_o x N_i$ size of the measured transfer function. Using the full length of the modal vectors results in a flexibility matrix of size $N_o x N_o$.

From a theoretical standpoint, the modal flexibility is exactly equal to the static flexibility. However, in actual testing, only some modes will be found and thus the calculated flexibility will be less than the real value. This issue is known as modal truncation, and it is important to evaluate its effect. The method used to determine if enough modes have been included is to check if the flexibility is converging as more modes are included in the summation. Typically, a unit load vector is applied to the flexibility matrix and deflections are used as a proxy for the convergence of flexibility.

This is illustrated for the case of a numerical model of a two-span continuous beam. Figure 5.17 shows the convergence by using the mean of the deflected shape. A deflection profile is found using a unit load vector applied to the modal flexibility matrix found with the inclusion of all identified modes. Then, deflection profiles are found starting with only the first mode included, and repeatedly as the contribution of each mode is added to the modal flexibility matrix. The mean of the absolute value of the deflected shapes is found. Then, the mean with all modes included is used to normalize the mean from the cases with less modes. These normalized values are plotted as shown, and it is clear for the two-span beam that the second mode is responsible for nearly 100% of the modal flexibility. Not surprisingly, the shape of the second mode is closely matched to the deflected shape.

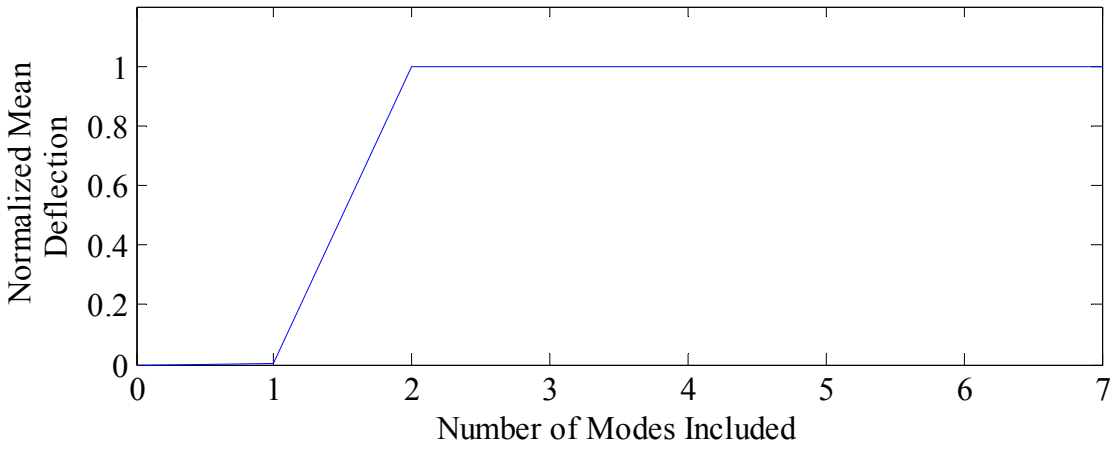

Figure 5.17. Convergence of modal flexibility for a 2-span continuous beam.

Convergence can also be assessed by the direct use of the measured deflections. Figure 5.18 shows the deflected shape as modes are added. The curves for two modes, three modes, and four modes are almost right on top of each other since the second mode has such a dominant contribution. It is noted that the second mode alone is responsible for 99% of the analytical maximum deflection. For real world structures, the major contributions to flexibility are usually shared amongst several modes, and thus the evaluation of modal truncation is more critical.

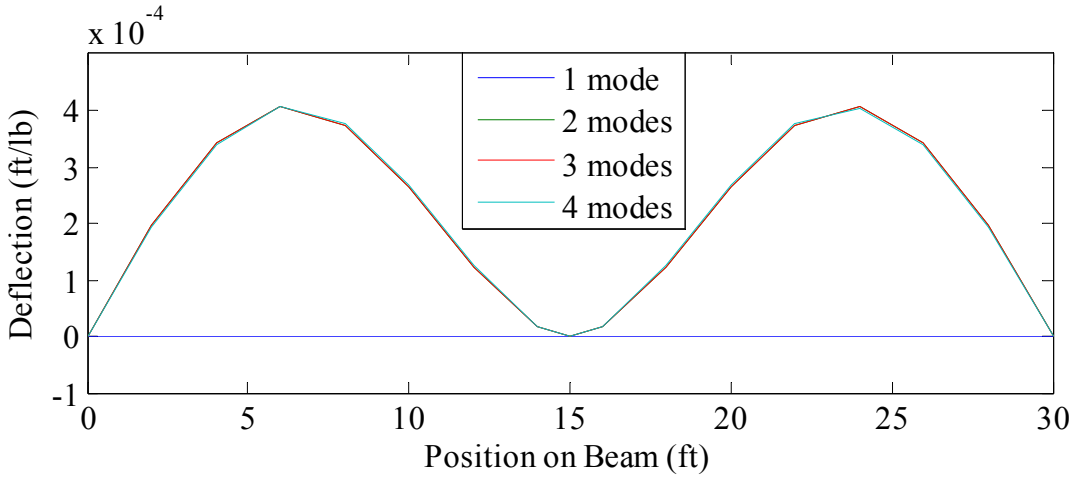

Figure 5.18. Deflection profile illustrating convergence of modal flexibility for a 2-span continuous beam.

Another issue that must be discussed in regards to modal flexibility is the topic of units. Modal flexibility has a real physical meaning and is measured in absolute units of distance per force.

However, data is usually collected in units of acceleration and force. Also, there are many opportunities during data processing to inadvertently scale the data improperly. Thus, care must be taken to convert units properly and to carry them through calculations. The following illustrates appropriate units for the various steps during data processing, and the proper conversions.

Assuming the typical situation of a force input measurement in pound-force units, and an output measurement of acceleration in units of the constant g, then the correct units and conversions are as follows:

Initial Units:

lbf = units of input measurement.

g = units of output measurement.

Perform FFT:

lbf/Hz = units of input measurement.

g/Hz = units of output measurement.

Calculate FRFs (acceleration / force):

g/lbf = outputs divided by inputs for any FRF algorithm.

Convert FRFs from g/lbf to $ft/lbf \cdot s^2$:

$FRF * 32.2\ ft/s^2$ = converted FRF in units of $ft/lbf \cdot s^2$.

Convert FRFs from receptance to dynamic compliance:

$FRF/j^2\omega^2$ = FRF in terms of ft/lbf.

The SVD portion of the CMIF algorithm may be performed on the FRFs in any units since only unitless mode shapes result from this calculation. The eFRFs must be found from the FRFs that are in terms of distance per force so that modal scaling is correct. The eFRFs will then have the same units as the FRFs, and then the units of the poles and of modal scaling will be:

rad/s = units of λ_r when found from eFRF that is in terms of ft/lbf.

$ft/lbf \cdot s$ = units of Q_r when found from eFRF that is in terms of ft/lbf.

Finally, modal flexibility is calculated:

ft/lbf = units of modal flexibility.

The modal mass can also be found from modal scaling as is shown below.

$$M_r = \frac{1}{2j\Omega_r \cdot Q_r} \qquad \text{Equation 5.104.}$$

Where:

M_r = the modal mass in units of lbm (equally represented by lbf/g).

Ω_r = the undamped natural frequency in units of rad/s.

Q_r = the modal scaling in units of $ft/lbf \cdot s$.

5.7 CONCLUSION

This chapter provided the methods by which measurements of force signal inputs and structure vibration outputs can be used to determine the modal parameters of a structure. From the context of bridge testing, it was shown how modal flexibility can be calculated, which can then be used for evaluating the structure.

Common problems relating to data collection and preprocessing were discussed in detail, as were the methods by which these problems can be minimized or avoided. The issue of quantization can be minimized by the proper selection of sensors, and by the use of dynamic range on analog to digital converters. Errors due to inadequate frequency resolution can be avoided by performing initial testing on a structure, and evaluating the necessary resolution based on the frequency and spacing of the modes of interest. The different methods by which data can be averaged to reduce variance due to noise were discussed. For deterministic signals, the best averaging method is synchronous averaging, whereas stochastic signals require the use of asynchronous averaging methods. Finally, the bias errors that can be introduced by using the FFT to transform the data to the frequency domain were discussed. Leakage is a significant issue that can be greatly reduced by the choice of excitation signal and by using cyclic averaging.

The methods by which transfer functions are assembled from FRF data were described. In modal testing, it is standard to collect many repeated sets of data. The sets of data from the repeated experiments can be combined together in a variety of ways to reduce the variance on the measurements. It was shown that the H_1 algorithm is a good choice when stochastic input signals are used, and that the EIV algorithm is a good choice when deterministic signals are used. The methods by which the transfer function is assembled were also illustrated for the cases of SIMO and MIMO testing.

System identification was also reviewed. This is the process of extracting the modal properties from the transfer function, and many competing algorithms and commercial packages exist. The broad categories of algorithm formulation were described, and some of the most popular algorithms were briefly mentioned. The CMIF algorithm was selected for the system identification needs of this thesis due to its robust identification of modes even in the presence of inconsistent data, and since the algorithm can be implemented in-house. The explicit details of how the system identification is performed using CMIF were then illustrated.

Finally, the method by which modal flexibility is synthesized from the identified modal parameters was shown. The issue of modal truncation was also discussed, and methods to assess the convergence of modal flexibility were given. It is noted that although deflections converge with the inclusion of several modes (typically), the modal flexibility matrix will still be statically incomplete (Doebling 1997), and the effects of this issue are addressed in Chapter 8. Subsequent chapters also validate the entire data processing routine by comparing the outcome to analytical results.

CHAPTER SIX

LABORATORY BRIDGE MODEL TESTING

6.1 INTRODUCTION

The overarching goal of this research is to evaluate the use of an array of tactile transducers for experimental modal analysis (EMA) of bridges and to determine the optimal experimental procedures for such testing. This chapter discusses various experiments that are undertaken to determine if the TTs will provide an EMA characterization of a large-scale bridge model that is comparable to using a more conventional excitation device. This testing is important since EMA is a totally different use for the shakers than the manufacturer intended. Thus, these shakers have never been validated for this use by the maker or by any other researcher. The various tests reported herein are designed to use the TTs in the same manner that purpose-built shakers are typically used, enabling the functionality of the TTs to be evaluated in realistic situations. The laboratory setting is used for this work so that experiments are more repeatable, variability and uncertainty from environmental factors are reduced, test setup changes can be quickly executed, and required manpower is minimized.

All experiments are performed on a steel bridge model. The TTs are used in single input, multiple output (SIMO) and multiple input, multiple output (MIMO) test setups with burst-random and multisine excitation signals. The use of roving force transducers is also tested. Baseline system identification is performed with conventional APS SIMO testing to provide a point of comparison for the tactile transducer results. Additionally, static load testing of the bridge model is performed to provide an accurate static flexibility matrix against which all modal results can be compared. The organization of the chapter is summarized in Figure 6.1:

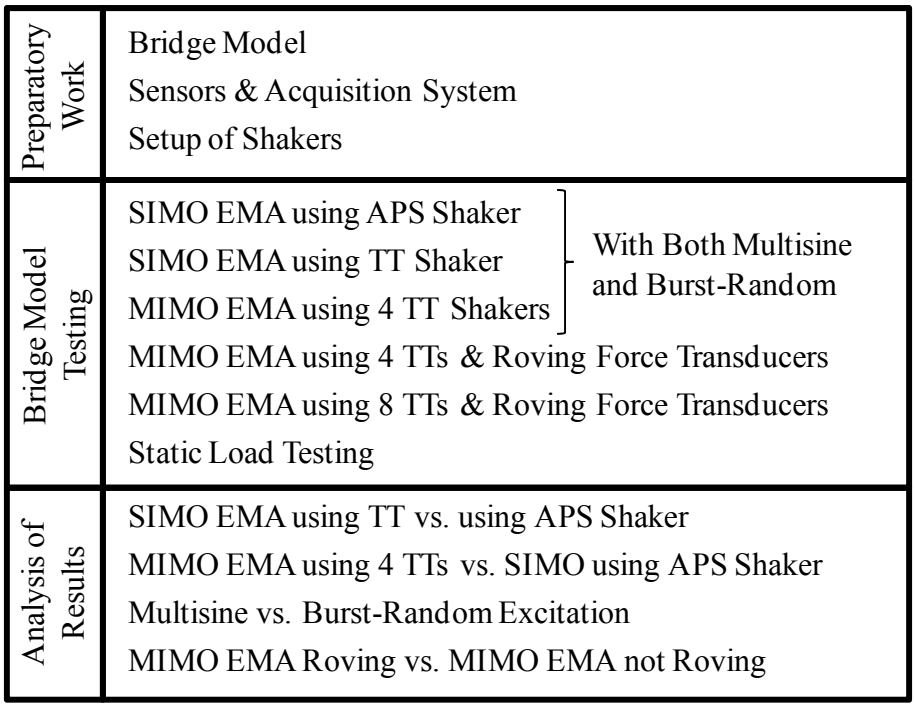

Figure 6.1. Organization of bridge model testing chapter.

6.2 PREPARATIONS FOR TESTING

This section describes the physical preparation of the laboratory bridge model, sensors, shakers, and data collection system. Each of these elements impacts the quality of the results, and thus careful attention is paid so that the best possible data is obtained.

6.2.1 Bridge Model Preparation

The bridge model is intended to represent a relatively simple structure so that correct results are easily identified. The model is nominally doubly symmetric and is a single span, simply supported on rollers. The model was previously used for a variety of tests by other students and was in a particular configuration (Figure 6.2). The previous results indicated that the model essentially acted as a plate structure due to the significant stiffness provided in the lateral direction by the seven lines of diaphragms. Consideration was given to decreasing the lateral stiffness so that the three beam lines act more independently, and thus three lines of diaphragms

were removed to decrease the ability of the structure to distribute loads laterally (Figure 6.2). Many tests with the APS shaker and with the TTs were carried out, and the results were generally poor. Local modes of the individual beams dominated the response of the model, and consistent values for modal mass and modal flexibility could not be attained due to the local modes interacting with the more important global modes. Thus, the model was reconstructed to its original arrangement with seven diaphragm lines, and the testing reported herein was undertaken. The structure dimensions and member sizes are provided in Figure 6.3.

The bridge model has bolted joints at all diaphragm lines. Noise and nonlinearities can occur in the model due to loose connections, and thus all 712 bolts are tightened. Also, many cables are attached to the structure for strain gauges and accelerometers, and all cables are checked to ensure they are tight to the structure and cannot cause much noise due to swinging and bumping. The structure is supported on steel rollers at both ends, and the east end also has bolts near the rollers to provide lateral restraint (Figure 6.4). All six rollers are reset into their proper alignment by jacking up the ends of the bridge. Overall, all obvious potential causes of noise in the structure are minimized.

Figure 6.2. Photographs of bridge model. Original and final arrangement at left and failed trial arrangement at right. (Photos by EVF, dynamics lab, 7/9/13)

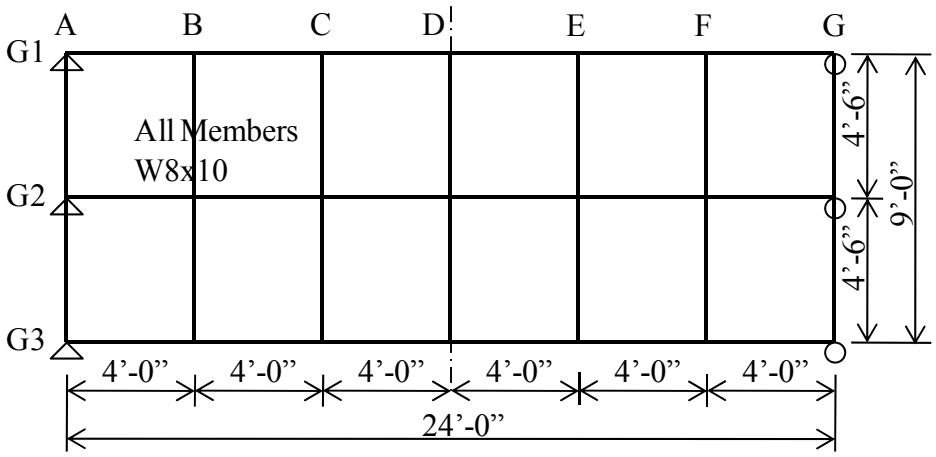

Figure 6.3. Bridge model plan view sketch.

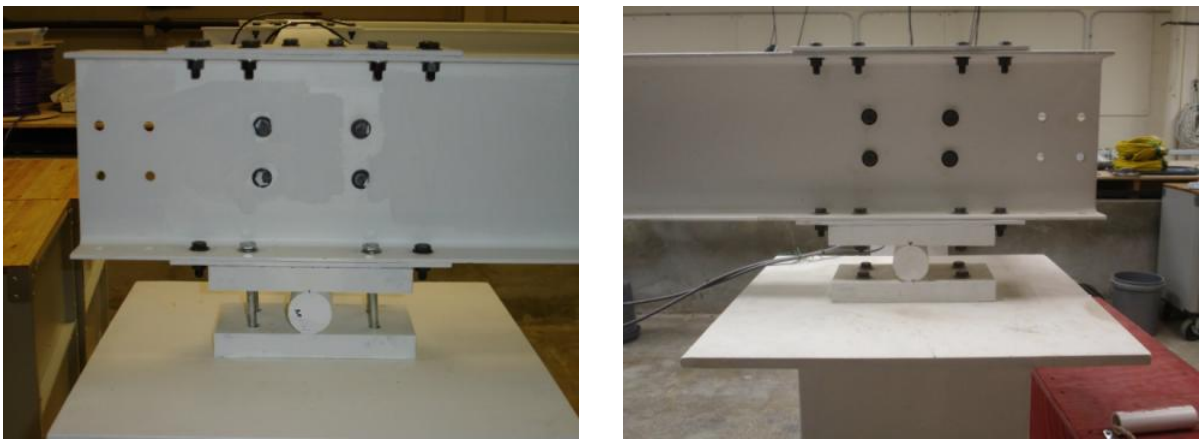

Figure 6.4. Photographs of bridge model bearings. 'Pinned' at left and 'roller' at right. (Photos by EVF, dynamics lab, 7/9/13)

6.2.2 Sensor Preparation and Data Acquisition Setup

Similar to the preparation of the bridge model, the sensors, wiring, and data acquisition are setup to provide the best possible testing results.

6.2.2.1 Accelerometers

For all dynamic testing, the structure output is captured by accelerometers. Each accelerometer is factory calibrated by back-to-back testing with a high-quality accelerometer of known response. However, the available accelerometers have all been used for a variety of tests over several years, and thus the calibration of each must be rechecked. The factory calibration process is repeated in the lab by back-to-back method as shown in Figure 6.5. A special calibration

accelerometer (the reference sensor or REF) is attached to the APS shaker, and the sensor under test (SUT) is attached directly to the calibration accelerometer. A 100 Hz sine wave is input to the APS shaker, and the output of both accelerometers is recorded. After 20 seconds of settling time elapses, 10 seconds of data are collected, and the RMS acceleration of both the REF sensor and SUT are recorded.

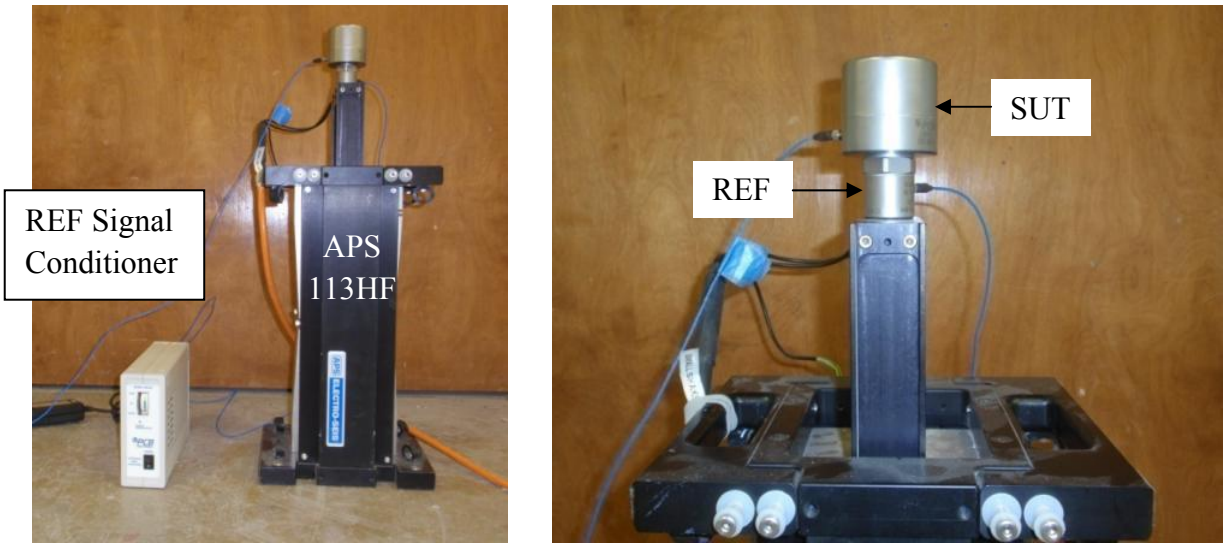

Figure 6.5. Photographs of accelerometer calibration setup. (Photos by EVF, dynamics lab, 7/9/13)

The sensors return a voltage that is proportional to the acceleration they undergo. The sensitivity is reported in units of mV/g, and thus the sensitivity of the SUT is simply found as the sensitivity of the REF multiplied by the ratio of the SUT RMS voltage to the REF RMS voltage. The calibration process discovered three accelerometers that were no longer functional and several others that were several percent off of the factory value. For the bridge model testing, the factory sensitivity value is used if the lab calibration result is within 1.5%, and the lab calibration result is used otherwise. Fifteen accelerometers, all supplied by PCB Piezotronics, are used in the lab testing, and the sensitivity and other information for each is reported in Table 6.1.

Grid Loc.	Type	Serial No.	Sensitivity (mV/g)	Range (g)	Range (Hz)
1B	393B05	24706	10269	±0.5	450
1C	393C	23502	1081	±2.5	800
1D	393C	23606	1057	±2.5	800
1E	393C	23526	1070	±2.5	800
1F	393B05	28707	9654	±0.5	450
2B	393C	23752	1073	±2.5	800
2C	393C	23525	1081	±2.5	800
2D	393C	23443	1096	±2.5	800
2E	393C	23499	1092	±2.5	800
2F	393B05	25409	9951	±0.5	450
3B	T393B05	22839	9862	±0.5	450
3C	393C	23522	1070	±2.5	800
3D	393C	23523	1089	±2.5	800
3E	393C	23500	1097	±2.5	800
3F	393B05	28696	9928	±0.5	450

Table 6.1. Accelerometer information for devices used in laboratory testing.

6.2.2.2 Force Transducers

Also for the dynamic testing, the force input to the structure by a shaker is measured with a dynamic force transducer. These devices return a voltage that is proportional to the average tensile or compressive force that they are subjected to. All force transducers are also supplied by PCB, and the relevant data for the four available transducers is provided in Table 6.2.

Type	Serial No.	Sensitivity (mV/lbf)	Range (lbf)	Range (Hz)
208C02	LW36746	47.87	±100	36,000
208C02	LW36262	49.94	±100	36,000
208C02	LW36271	51.29	±100	36,000
208C02	LW36231	49.13	±100	36,000

Table 6.2. Force transducer information for devices used in laboratory testing.

6.2.2.3 Displacement Transducers

Static load testing is also performed on the bridge model to capture its static flexibility. Displacement transducers are used to measure the vertical deflection of the structure under static loads. The inner workings of these devices are based on the use of strain gauges, and thus the sensitivity is measured in units of mV/cm per applied excitation voltage. The twelve available devices are all model number CDP-25 manufactured by Tokyo Sokki Kenkyujo Company and all have identical properties. The available stroke is 25 mm and the sensitivity is 0.25 mV/V/mm. A 0.5 V excitation was provided in all testing with these devices, and thus the sensitivity becomes 0.125 mV/mm. A photograph of all the sensor types used is provided in Figure 6.6.

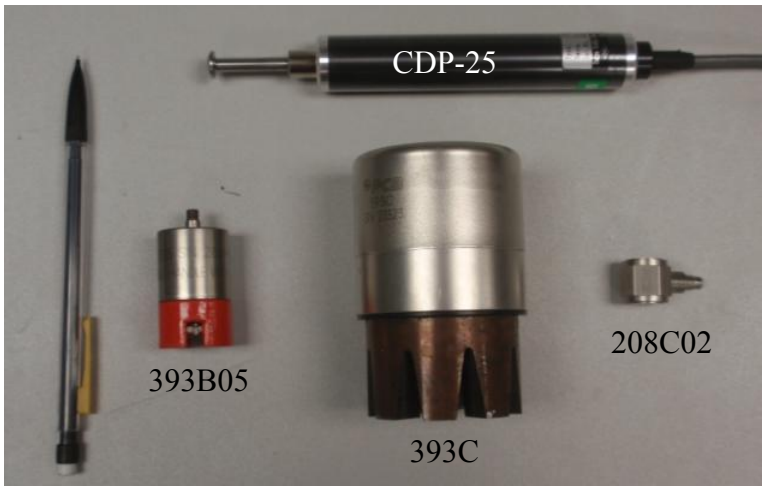

Figure 6.6. Photograph of sensors used in laboratory testing. (Photo by EVF, dynamics lab, 7/9/13)

6.2.2.4 Wiring and Data Acquisition

For dynamic testing, a National Instruments (NI) PXI-1042Q controller with four NI PXI-4472B data acquisition (DAQ) cards is used to simultaneously capture all force transducer and accelerometer readings. Each PXI-4472B card provides eight dynamic input channels with 24-bit resolution. A laptop computer running NI Labview Signal Express software is used to control the DAQ system.

Signals are generated for dynamic excitation by a NI 9264 card with 16 output channels, each with 16-bits. This is a USB device that is also controlled by the Signal Express software running on the laptop. These excitation signals are input to a power amplifier to drive the shakers. An APS-145 amp is used when driving the APS shaker, and the two-channel subwoofer amps are used when driving the TTs. A schematic wiring diagram is provided in Figure 6.7 illustrating the interconnectivity of the various devices for dynamic testing.

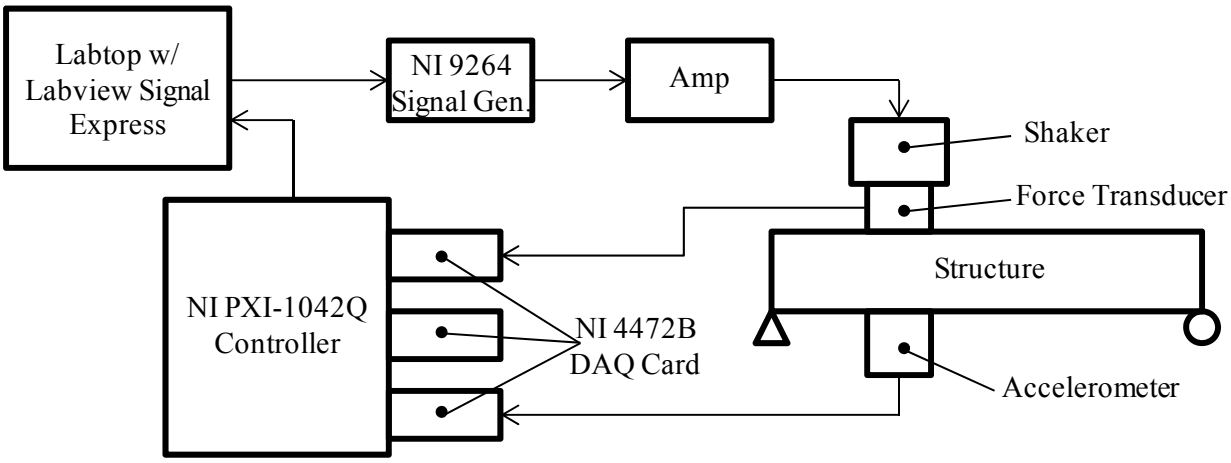

Figure 6.7. Schematic of devices used for dynamic testing.

For static load testing, a NI SCXI-1001 controller with three NI SCXI-1314 terminal blocks attached to NI SCXI-1520 DAQ cards are used to capture all displacement transducer inputs. Each SCXI-1520 card provides eight dynamic input channels. Labview Signal Express software running on a laptop is again used to control the DAQ system. A schematic wiring diagram is provided in Figure 6.8 illustrating the static testing setup.

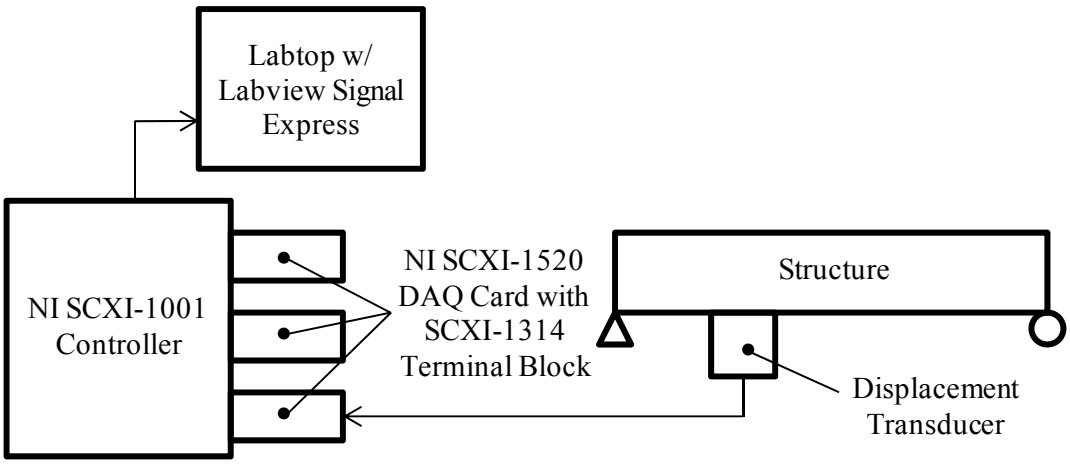

Figure 6.8. Schematic of devices used for static testing.

6.2.3 Shaker Setup

The method of connection from the shakers to the force transducers and from the force transducers to the structure impacts the accuracy of the force measurement and can cause improper excitation of the structure. Over time, numerous papers have been written on best practices for dynamic excitation of structures when using shakers (Mitchell and Elliot 1984; Cloutier et al. 2009 for example). Most such publications are focused on excitation of mechanical devices such as airframes and automobiles wherein the structure can be well isolated and the shakers can be mounted separate from the item being tested. The first recurring theme of such writings is to only apply excitation axial to the force transducer so that all of the input is accurately measured. The method most commonly used is to apply the force through a long, thin rod that has a low ability to transfer moments or shears along its length. This rod is referred to as a 'stinger'. The second recurring theme is to mount the force transducer on the structure end of the stinger so the force that actually enters the structure is measured, without being affected by losses in the stinger. For testing of the bridge model with the APS shaker, these methods are applied as is shown in Figure 6.9.

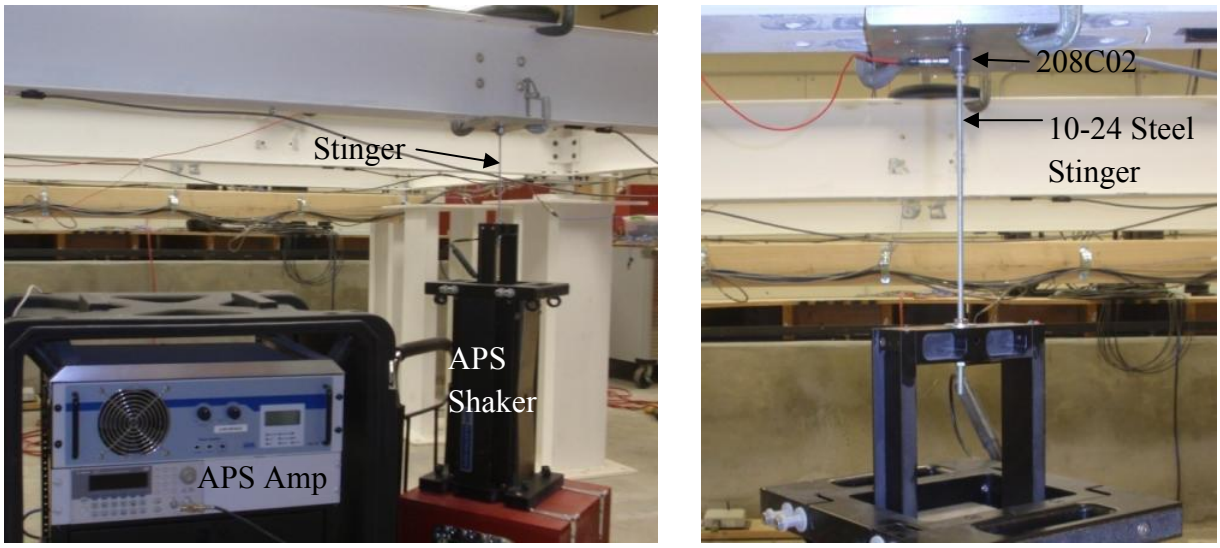

Figure 6.9. Photographs of APS shaker setup and stinger arrangement. (Photos by EVF, dynamics lab, 7/9/13)

Using the TTs for dynamic excitation is more complicated than using the APS shaker for several reasons. First, the TTs do not have an armature for connection of a stinger and the resulting isolation of the mass of the shaker body from the structure. The moving mass of the TTs is housed within the closed body and the body itself is used to transmit the shaking force. Thus, the entire TT must be connected to the structure and supported by it. This increases the mass of the structure, nominally for a real-world bridge but perhaps significantly for the light laboratory model. The effect of the shaker mass is offset in the lab testing by preloading the model with steel plates. When a TT is attached to the structure, an equivalent amount of mass is removed from that location so that the total structure mass remains the same. The mean weight of twelve TTs was found to be 10.007 pounds, and thus 10-pound steel plates are used as offset masses (Figure 6.10).

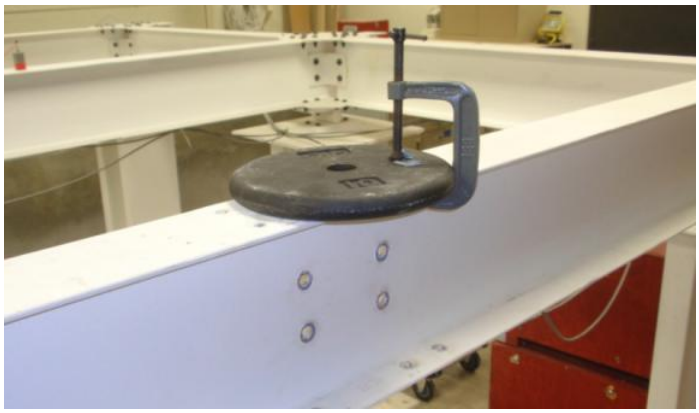

Figure 6.10. Photograph showing added masses to offset TT shaker weight. (Photo by EVF, dynamics lab, 7/9/13)

The second issue with use of the TTs is to accurately measure the force input to the structure. Each force transducer costs about twice as much as a shaker, and each requires an input DAQ channel, which is even more expensive. Thus, the goal is to only use one force transducer per shaker. It was initially theorized that a tripod arrangement could be used for the purpose of transferring force to the structure while accurately measuring it. Figure 6.11 shows a tripod setup with each leg of the tripod consisting of a force transducer. The tripod was aligned with the center of the shaker and the expectation was that each leg would carry an equal third of the total force. If this was proven true, then the intent was to only use a transducer at one leg of the tripod (Figure 6.11).

Figure 6.11. Photograph showing three-transducer tripod (left) and one-transducer tripod (right). (Photo by EVF, dynamics lab, 7/9/13)

Testing of the tripod demonstrated that the force carried by the legs varied significantly. Figure 6.12 shows a portion of the results of a swept-sine test. This plot shows the force recorded by each transducer over a small frequency band, and it is noted that the transducers carry significantly different forces and that the portion of the force carried by each also varies with frequency. It was deduced that this was partially due to moment transfer through the transducer body. A simple change was made in which one end of the transducers was not attached to the load plate and only a round screw head could transfer force, eliminating moment transfer. Testing showed that this system was an improvement, but that the force was still not equal in the three transducers. Rocking of the shaker was determined to be the cause, and no obvious way to eliminate this effect while using a tripod was identified.

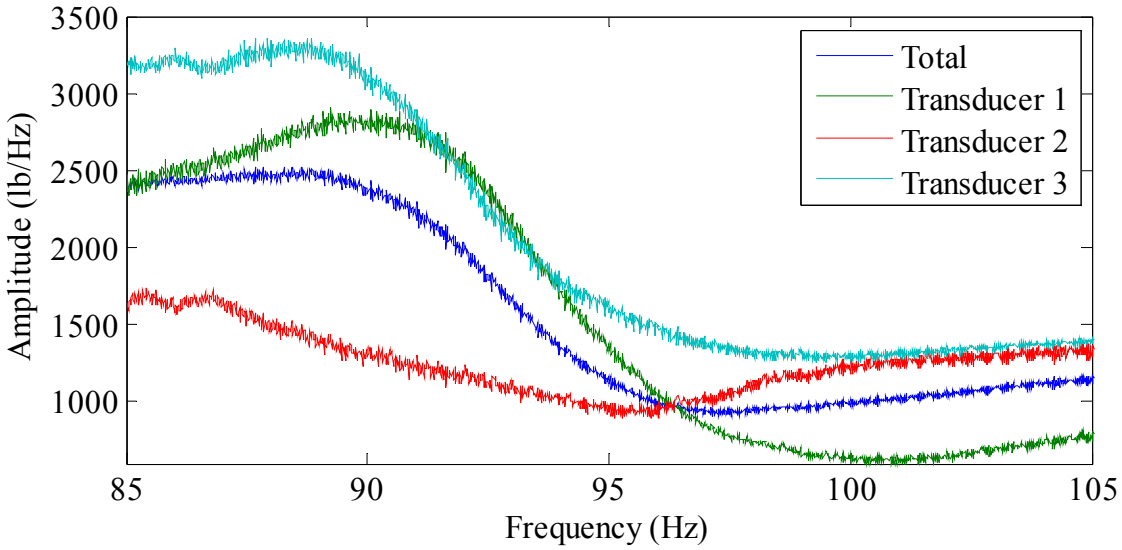

Figure 6.12. Force measurements for three transducers in a tripod arrangement under a single TT. Note poor agreement in force carried by each leg.

Finally, a new setup was proposed that emulates the use of a stinger (Figure 6.13). The TT is suspended by a single thin rod, and a single force transducer is mounted along the rod. The single support eliminates the issues due to rocking, and the thin rod reduces the ability of the system to transfer non-axial forces into the structure. The limitation with this arrangement is that the shakers must be attached to the underside of the structure. This attachment method is used for all testing reported herein.

For test cases that do not use a transducer, a setup as shown in Figure 6.13 is used so that the force input from the shaker can be assumed to be nearly identical to that measured when a transducer is present. The transducer is simply replaced by a sleeve nut.

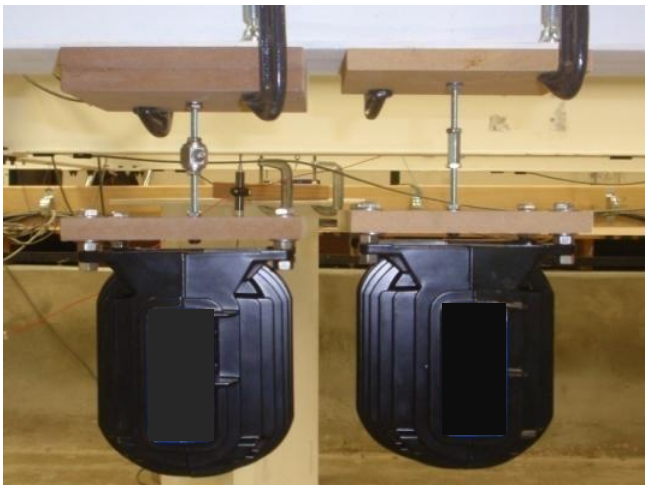

Figure 6.13. Suspended force transducer and TT with stinger type setup (left) and arrangement without force transducer (right). (Photo by EVF, dynamics lab, 7/9/13)

6.2.4 Tactile Transducer Beating Phenomenon

An unusual phenomenon was observed with use of the TTs. When using deterministic signals that gradually vary in frequency, the force output would quickly oscillate (Figure 6.14). This phenomenon had been observed by Napolitano and Linehan (2009), and those researchers called the phenomenon 'beating'. Unfortunately, they mistakenly identified the cause as interference between several shakers operating in a MIMO environment, and diminished the apparent affect by decreasing frequency resolution until the beating could no longer be detected in the frequency domain. The phenomenon actually occurs even when using a single shaker, and the variation in force is detected by the accelerometers in the structure output. Variations of the input force level and the signal length were explored, but the 'beating' was not reduced. Further testing revealed that the APS shaker also demonstrates the issue, although the 'beating' has about $1/10^{th}$ the amplitude compared to the TT. It is theorized that the 'beating' is caused by feedback between the shaker and the amplifier as the frequency is gradually varied, since the phenomenon is not detected when using stochastic signals.

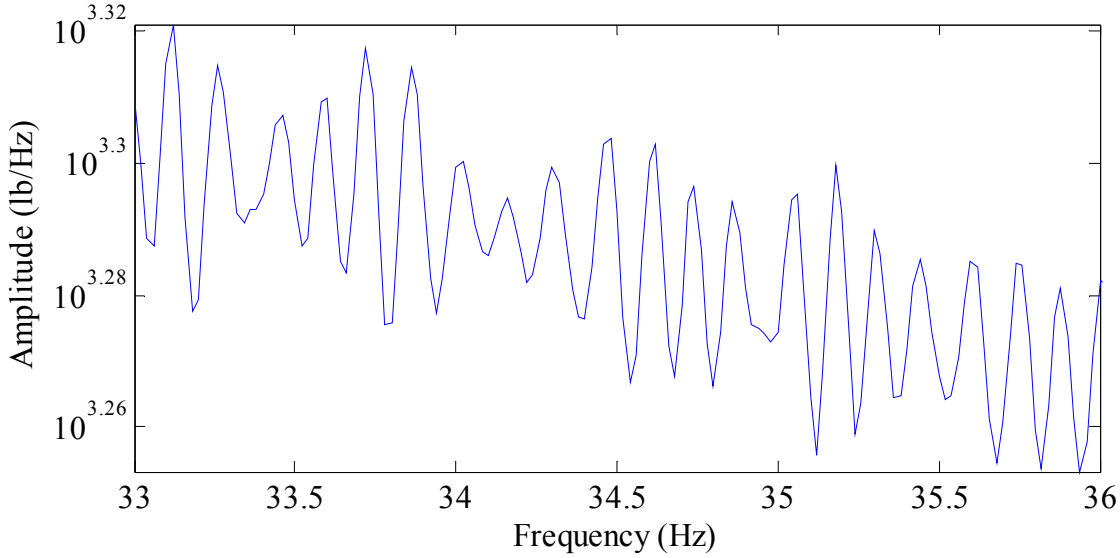

Figure 6.14. Sample of 'beating' phenomenon on force measurement in frequency domain.

Since the 'beating' is detected by both the force transducers and the accelerometers, the effect is properly canceled out in the calculation of FRFs in frequency ranges where the data is not very noisy. Unfortunately, the 'beating' has a relatively small amplitude and is significantly affected by noisy measurements. In frequency ranges with more noise, the FRFs are significantly worsened by the phenomenon and subsequent identification of modal properties fails.

To alleviate this issue, the FRFs were subject to a low-pass filter which effectively removes the 'beating' while maintaining resolution and essentially preserving the true FRF shape. An example of an FRF with and without filtering applied is shown in Figure 6.15. For testing of the bridge model, the FRFs calculated from deterministic signals are all filtered. It is noted that 'beating' was detected in the subsequent field testing, but to a lesser degree, and filtering was not necessary.

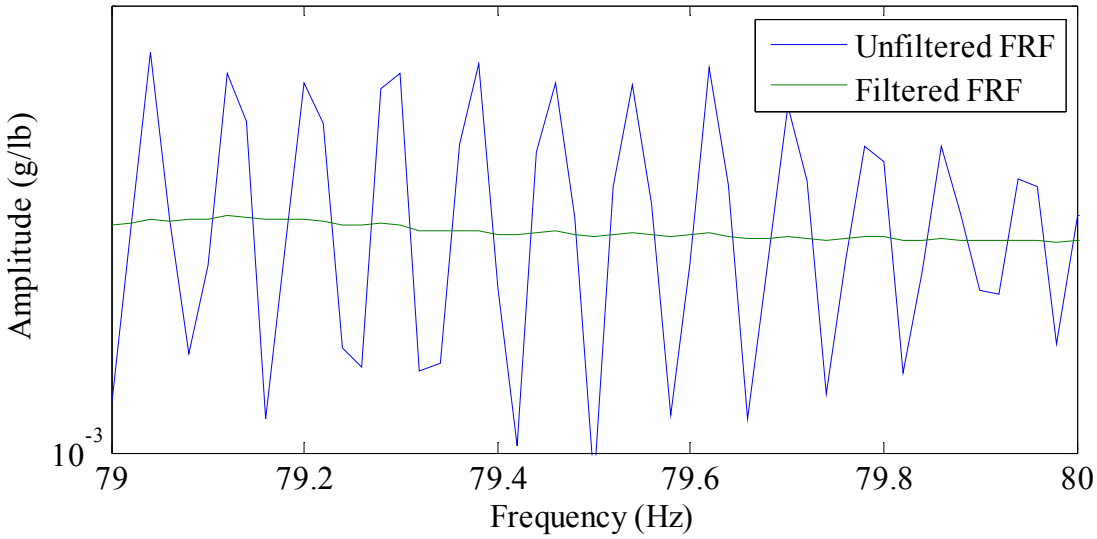

Figure 6.15. Sample of FRF with 'beating' phenomenon and the same FRF with 'beating' filtered out.

6.3 TESTING PROCEDURES

Many different tests are performed while changing system variables such as number of shakers, excitation signal type, shaker spatial locations, input force amplitude, and shaker type. The specifics of each test setup are reported in this section. Several other parameters should be kept constant throughout all testing and the selection of these values is discussed as well.

6.3.1 Determine Consistent Testing Parameters

Several parameters that will be used during production testing must initially be selected by experimentation. These parameters are input force amplitude, data acquisition frequency, and frequency resolution. The methods by which these parameters are selected are described below.

6.3.1.1 Force Amplitude Selection

The best input force amplitude is a balance between providing high signal to noise ratio while not exciting nonlinearities, rattles, etc. Selection of the amplitude is performed by trying various levels and then subjectively choosing the one that gives the smoothest FRFs (Hunt and Brillhart

1991). A multisine signal is used for this purpose since it has a fairly uniform amplitude and causes essentially no leakage (and thus cleaner FRFs). The APS shaker and amplifier are also used since they provide the cleanest input force.

The gain of the APS amp is set to its approximate midpoint and the input amplitude from the signal generator is varied. Peak force values of approximately 1, 5, 10, 15, and 20 lbf are dialed in with the APS shaker providing input at DOF 3E. The data is recorded with one delay block and three capture blocks per force level, the FRFs are calculated, and the smoothness compared. The FRF between input DOF 3E and output DOF 3E is shown in Figure 6.16 for the five input levels.

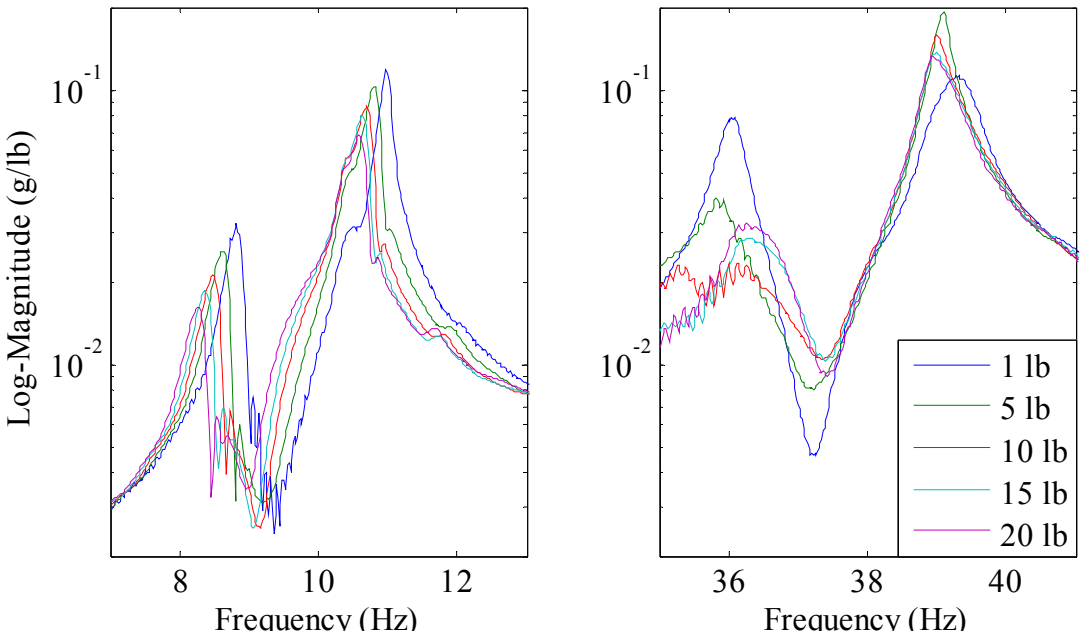

Figure 6.16. FRFs for input DOF 3E and output DOF 3E for five different force levels.

Figure 6.16 shows three interesting features. First, the apparent stiffness of the structure decreases with increasing force level and the damping increases with increasing force level for the first bending mode (between 8 and 9 Hz) and the first torsion mode (between 10 and 11 Hz).

Second, the 'beating' phenomenon is worse with increasing force. Finally, the lowest force produces the smoothest and sharpest peaks except at the second torsion mode at 39 Hz.

Overall, the 1-pound force level produces the best FRFs; however, the TTs have difficulty overcoming their own internal friction at this low of an output. Thus, the 5-pound force level is selected and is used for multisine excitation. For burst-random, the standard deviation of the normal distribution from which the signal is generated is set to 50% of the multisine force level. This input level provides an RMS force that is generally similar to that of the multisine signal.

6.3.1.2 Data Acquisition Frequency

The DAQ recording frequency is a balance between providing enough data points to prevent aliasing while not wasting electronic storage with unnecessary information. In the absence of noise, the discrete Fourier transform to the frequency domain is essentially perfect for all frequencies below the Nyquist frequency, which is half of the acquisition frequency. In the presence of noise, higher acquisition frequencies are beneficial. The bridge model has modes of interest up to about 170 Hz, and thus the minimum acceptable data collection rate is 340 Hz. However, a rate of 1000 Hz is selected for use since this is the minimum data rate of the data acquisition cards used. During data post-processing, the frequency is reduced to 500 Hz using Matlab's 'decimate' function to reduce data storage and to expedite later processing steps.

6.3.1.3 Frequency Resolution (Signal Length)

The selection of frequency resolution is also a balance of two opposing criteria. First, the excitation signal length is inversely proportion to the resolution, and thus greater resolution comes at the cost of longer testing times. Second, higher resolution allows better identification of closely spaced modes. Adequate resolution is a function of the density of modes. For this

structure, it is known that some modes are closely spaced, and thus a relatively high resolution may be needed, although the testing time will be increased.

The necessary resolution is evaluated by initial experimentation using a multisine signal. Three lengths of signal are tested: 20, 50, and 100 seconds (0.05, 0.02, 0.01 Hz resolution respectively). The first two modes of the structure are the most closely spaced and they are used to analyze the effect of resolution. The lowest resolution that provides good results is selected. The testing is again performed using one delay block and three capture blocks. A 5-pound input force level is used with the APS shaker and amplifier.

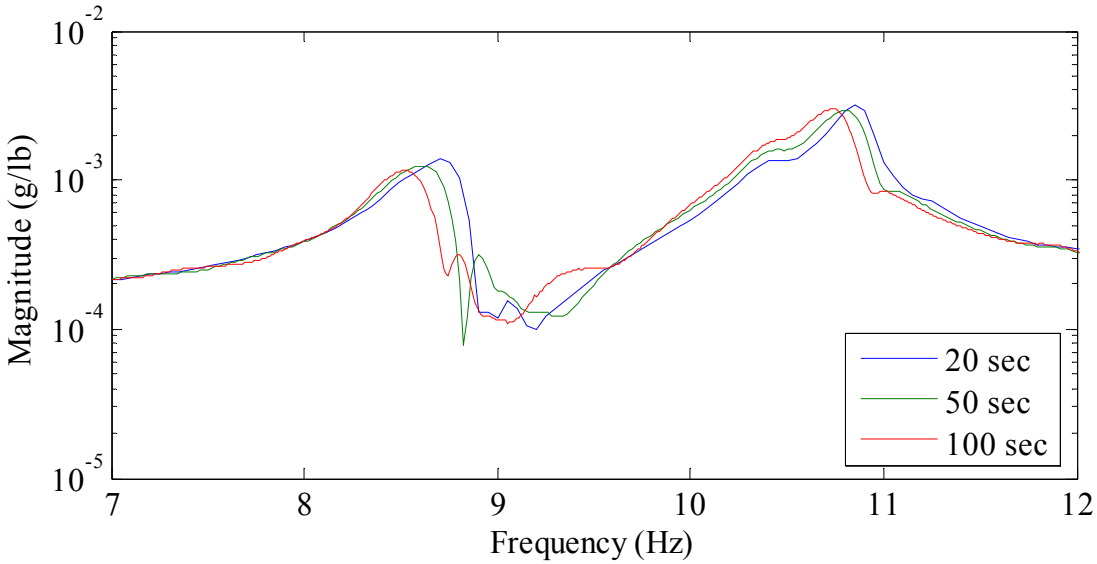

Figure 6.17. Enhanced FRFs for Mode 1 using three different signal lengths.

Figure 6.17 shows the enhanced FRFs (eFRFs) for the first bending mode of the bridge model using the various frequency resolutions. Again, there is a frequency shift due to more force being applied with higher resolutions. Although all three signals are input at the same force level, the extra frequency lines excited by a longer signal effectively provides more total force within a frequency window of equal width. Visually, the eFRF plot does not indicate a best resolution. However, the modal identification based on fitting the eFRFs does change due to the resolution.

The identified damping of the second mode decreases by 10% for the 20-second signal as compared to the other two signals (which are nearly equal). This change in damping is a result of using points farther from the modal peak in the least-squares solution for the pole. These farther points are more affected by other modes and thus the solution accuracy is diminished. The higher resolution of the 50-second and 100-second signals reduces the effect of other modes. Overall, the 50-second signal is selected as the shortest signal that allows a good identification of these two closely spaced modes. This signal length is used for both multisine and burst-random production testing.

6.3.2 Single Input, Multiple Output Testing

Single Input, Multiple Output (SIMO) testing is undertaken using both the APS and the TT shakers. SIMO is a relatively simple testing procedure that is commonly used on civil structures when only one input device is available. The process consists of applying input force at a single DOF, recording outputs at all DOFs, and then moving the shaker to another DOF and repeating until input has been applied to all DOFs (or some desired subset). In post-processing, the FRFs developed for a single input location provide a single column of the transfer function. The details of the SIMO testing procedure for the laboratory bridge model are provided below.

6.3.2.1 SIMO Testing Using APS Shaker

The APS shaker is known to provide very clean input over the frequency range of interest. Thus, the results from APS testing can be used as a baseline for evaluating the TT results. The APS shaker is connected to the first DOF using the stinger as illustrated in Figure 6.9. Both burst-random and multisine signals are used with equal testing time allotted to each. The shaker is then moved to the next DOF and the testing is repeated. This process was undertaken for 15 DOFs of the structure. The six support DOFs were not excited.

For multisine testing, a 50-second signal with a Schroeder crest factor was used that excited frequencies from 4 Hz to 170 Hz. The APS amplifier gain was adjusted to provide approximately a 5-pound peak excitation force. To eliminate leakage, the same signal was input seven times without pause between sets (cyclic averaging), and the first and last set were discarded resulting in five capture blocks. The exact same multisine signal is used for all input locations.

For burst-random testing, relatively equal excitation of all frequency lines requires the averaging of multiple realizations of random signals. Thus, five unique realizations are used at each input location. This allows five asynchronous power spectra averages to be used in post-processing. The realizations are generated by Signal Express for each run, and thus they are also unique for each input location.

For burst-random, it is also of great importance that the structure's response is almost totally damped out by the end of the data set. For the lightly damped bridge model, the burst-random signal is set to zero for the final ten seconds of the capture window. Several seconds of additional settling time is allowed before the next set is started.

6.3.2.2 SIMO Testing Using a Tactile Transducer Shaker

SIMO testing with a TT was intended to proceed exactly the same as the APS SIMO testing. However, multiple issues were discovered including the tripod / stinger issue and the 'beating' phenomenon issue discussed previously. Other problems included inconsistent force production over some frequency ranges, high noise levels at higher frequencies, and poor performance by older versions of the TT. These issues caused more noticeable effects on multisine testing than on burst-random testing, and significant effort was expended to understand and troubleshoot

these problems. The analysis section of this chapter provides details, but the various experimental procedures are reported here.

For multisine testing, a 50-second signal with a Schroeder crest factor is prepared, and then the amplitude is modified over several frequency ranges as shown in Figure 6.18. This signal is input seven times without pause and the first and last sets are discarded resulting in five capture blocks.

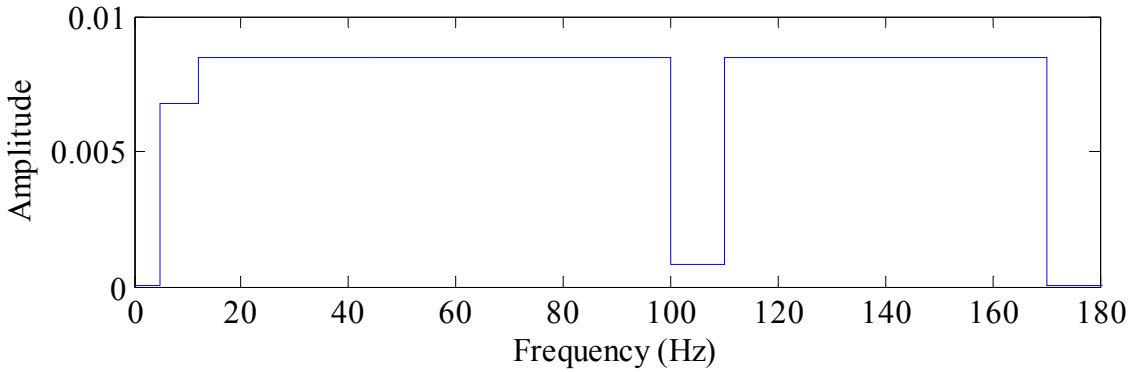

Figure 6.18. Multisine signal used for TT SIMO testing, frequency domain.

For burst-random testing, the procedure is identical to that described for the APS MIMO testing. TT shaker 'Oscar' is used throughout the SIMO testing, and is supported by the stinger apparatus shown in Figure 6.13.

6.3.3 Multiple Input, Multiple Output Testing

Multipe Input, Multiple Output (MIMO) testing is undertaken using TTs. The MIMO testing process consists of applying input force at several DOFs simultaneously while recording outputs at all DOFs. The input locations are selected in a manner that is expected to enable excitation of all modes of interest without a need for moving the shakers to any additional input locations. For this testing, a variety of MIMO tests are conducted. First, four shakers are used in two different spatial arrangements. These arrangements are illustrated in Figure 6.19 and Figure 6.20 and show

Spatial Setup A and Spatial Setup B respectively. Second, the possibility of using roving transducers is explored with four shakers arranged in Spatial Setup A. Finally, testing is conducted using eight shakers and roving transducers in Spatial Setup C (Figure 6.21).

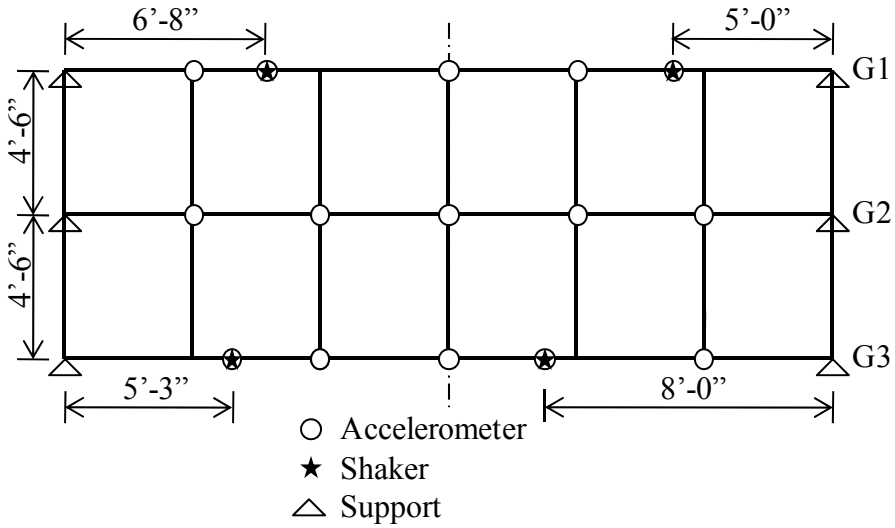

Figure 6.19. Spatial Setup A for MIMO testing with four TTs.

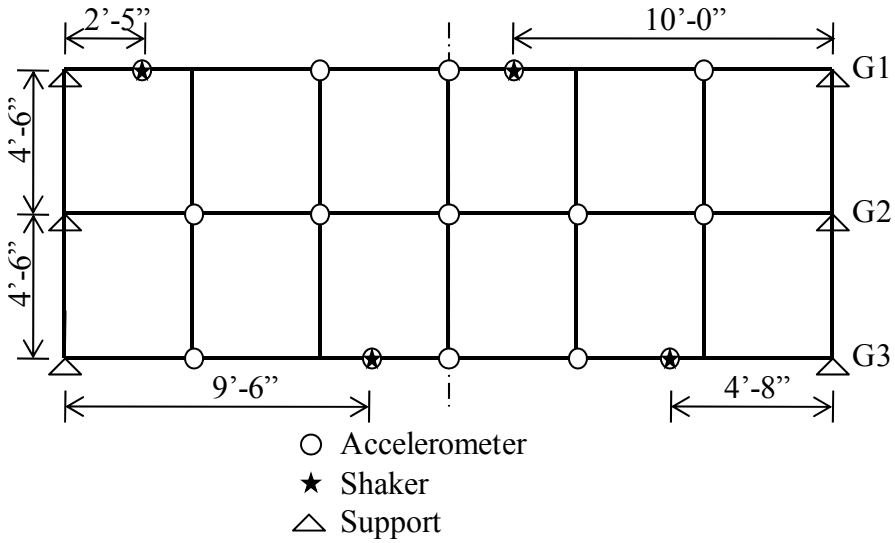

Figure 6.20. Spatial Setup B for MIMO testing with four TTs.

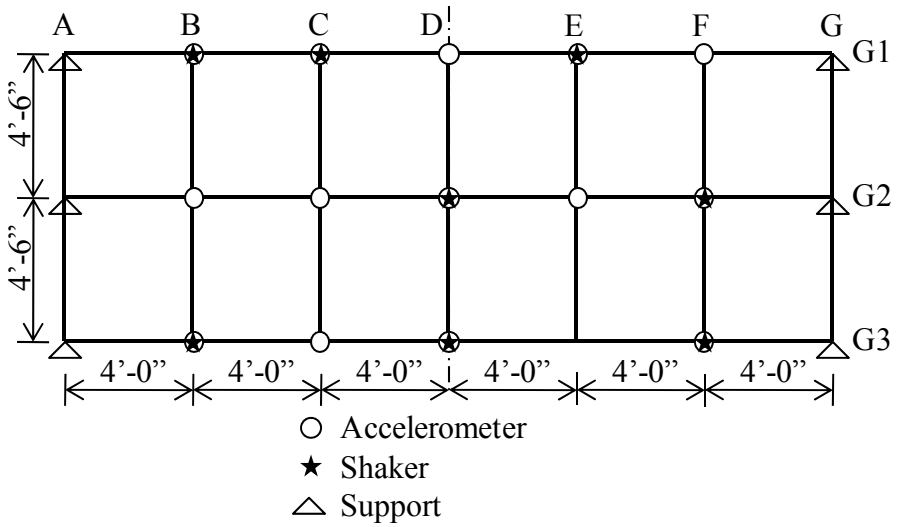

Figure 6.21. Spatial Setup C for MIMO testing with eight TTs.

An added level of complexity exists with MIMO testing in that a number of unique input sets equal to or greater than the number of inputs must be collected to enable calculation of FRFs. This requirement is handled differently for multisine and burst-random testing as described in the following subsections.

6.3.3.2 MIMO Testing With All Inputs Recorded

6.3.3.2.1 Burst-Random

Burst-random testing requires that all inputs be recorded since each realization generates a unique excitation signal. With the four input locations of Setup A and Setup B, a minimum of four sets of data with unique signals must be collected so that the matrix of force values at any frequency line is not singular. In practice, far more than the minimum number of sets are collected, which allows asynchronous averaging and greatly reduces the chance of attempting to divide by an ill-conditioned matrix. For this testing, 20 burst-random sets are collected. Each set is 50 seconds long and leakage is reduced by setting the first 0.5 seconds and the last 10 seconds of each random signal equal to zero. Several additional seconds of settling time are allowed between each set.

6.3.3.2.2 Multisine

For multisine testing, the exact same signal is used at all input locations. In order to ensure that the force matrix is invertible, the polarity of select signals is reversed so that the force matrix consists of orthogonal columns. Since the number of inputs is a power of two, a Hadamard matrix is used to determine which signals to reverse in each set. A Hadamard matrix of size eight is shown in Figure 6.22, and the top left quarter is used for four input locations.

Cyclic averaging with the multisine signal is also used. As in the MIMO testing, the signals are input seven times without pause and five capture blocks are recorded to minimize leakage and to reduce noise. Next, the polarity of the inputs is altered per the Hadamard matrix, and then seven more sets are input with five captured. The process proceeds until a number of columns of the Hadamard matrix equal to the number of inputs have been used.

$$\begin{bmatrix} +1 & +1 & +1 & +1 & +1 & +1 & +1 & +1 \\ +1 & -1 & +1 & -1 & +1 & -1 & +1 & -1 \\ +1 & +1 & -1 & -1 & +1 & +1 & -1 & -1 \\ +1 & -1 & -1 & +1 & +1 & -1 & -1 & +1 \\ +1 & +1 & +1 & +1 & -1 & -1 & -1 & -1 \\ +1 & -1 & +1 & -1 & -1 & +1 & -1 & +1 \\ +1 & +1 & -1 & -1 & -1 & -1 & +1 & +1 \\ +1 & -1 & -1 & +1 & -1 & +1 & +1 & -1 \end{bmatrix}$$

Figure 6.22. Hadamard matrix of size eight.

6.3.3.3 MIMO Testing Using Roving Force Transducers

Due to the expense of force transducers and a lack of funding, only four are available for this work. However, it is desirable to use more than four shakers in the testing of a real-world bridge. As such, it is explored whether good system identification can occur if the force transducers are used in a roving manner. This testing consists of two parts as described in the following paragraphs.

In the first part, four shakers are used in a MIMO setup, and all inputs are recorded. Then, the force transducers at input locations 1 and 2 are replaced with sleeve nuts as shown in Figure 6.13, and the experiment is performed again. Next, the transducers are reinstalled at inputs 1 and 2, and the transducers at input points 3 and 4 are removed before performing the experiment again. Finally, all transducers are reinstalled and the experiment is run a last time. This process allows all input locations to be disturbed, which may affect the force input. Since all four input locations are recorded before and after the disturbance, the input data can be compared to evaluate what effect the disturbance has. It is noted that two channels of force data are missing from the second and third experiments. Thus, these two experiments must be combined to allow FRF calculation. This combination requires an implicit assumption that the force input is the same whether a force transducer or a sleeve nut was used. The accuracy of this assumption is the most important part of this testing.

In the second part, eight shakers are used in a MIMO setup. An experimental run is performed with the first four input locations outfitted with force transducers. Next, the transducers are moved to the last four input locations and the experiment is run again. Each experiment uses a 50-second long multisine signal, repeated seven times as described previously. Also, eight variations of polarity using the Hadamard matrix of Figure 6.22 must be used for each of the two experiments. Therefore, this testing produces 80 capture blocks of data (5 capture blocks per polarity setting x 8 polarity settings x 2 experiments). It is obvious that this type of testing using roving force transducers can only be performed with deterministic signals since stochastic signals would produce a different force for every realization.

An issue with data file alignment was found during this testing. It was initially assumed that the Labview software begins the data recording process at the same elapsed time after the software

begins the excitation for any experiment. The data was processed using this assumption, and the FRFs appeared to be nothing but noise. Investigation of the issue showed that a variable and unpredictable amount of time passes after the software begins the excitation step but before it starts recording the force and acceleration data. This means that data sets from separate experiments are not aligned. An algorithm was written that finds the best alignment of separate experiments by shifting the data of the second experiment until the total difference between all data points is minimized. The acceleration outputs that are common to all experiments are used by the algorithm to find the proper alignment. Figure 6.23 shows unaligned force data for input DOF 1B from the MIMO shaker testing using eight inputs, and Figure 6.24 shows the same data after being aligned by the algorithm.

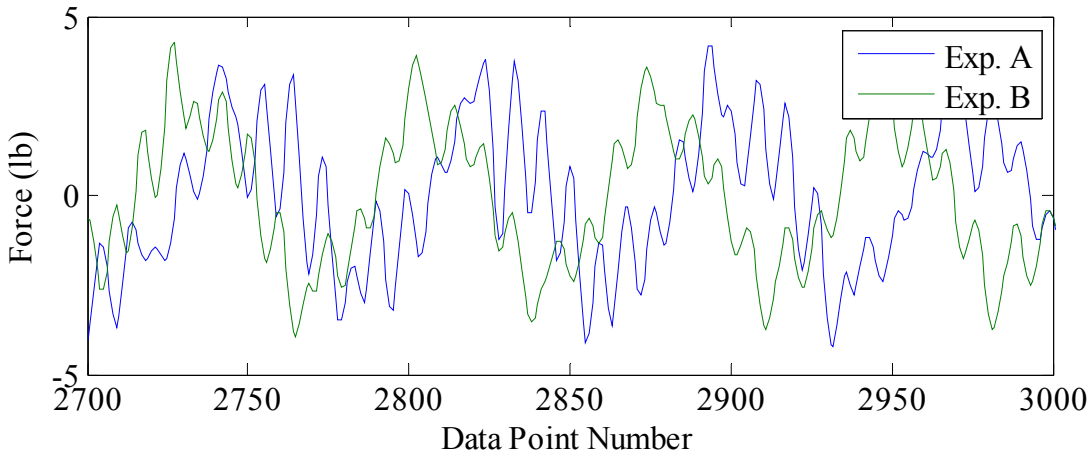

Figure 6.23. Force input data for DOF 1B that is not aligned.

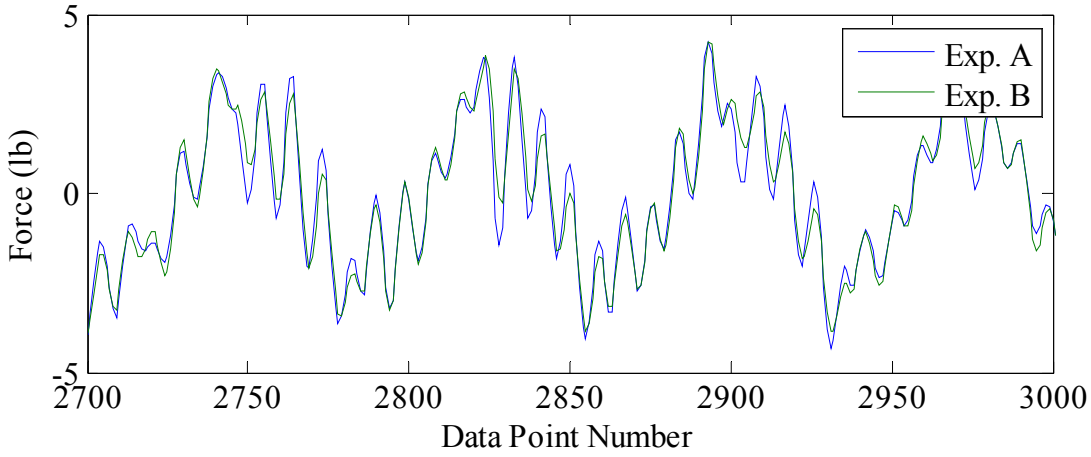

Figure 6.24. Force input data for DOF 1B after alignment.

6.3.4 Static Load Testing

The bridge model is also subject to static load testing so that an accurate flexibility matrix can be acquired. This testing is performed by suspending 410 pounds from a single DOF and measuring the displacement at all DOFs (Figure 6.25). This provides a single column of the flexibility matrix. The load is moved to each DOF in turn, and the displacements are measured with the load suspended, and then again immediately after release of the load. Loading each DOF creates a full flexibility matrix that corresponds to the same DOFs that were used in the dynamic testing.

The testing uses the 12 available CDP-25 displacement transducers, arranged as is shown in Figure 6.26. Since there are not enough of these devices for all 15 unsupported DOFs, the flexibility coefficients for DOF columns E and F are found by interpolation using a cubic spline.

Figure 6.25. Photographs of suspended load and displacement transducers used for static load testing. (Photos by EVF, dynamics lab, 7/9/13)

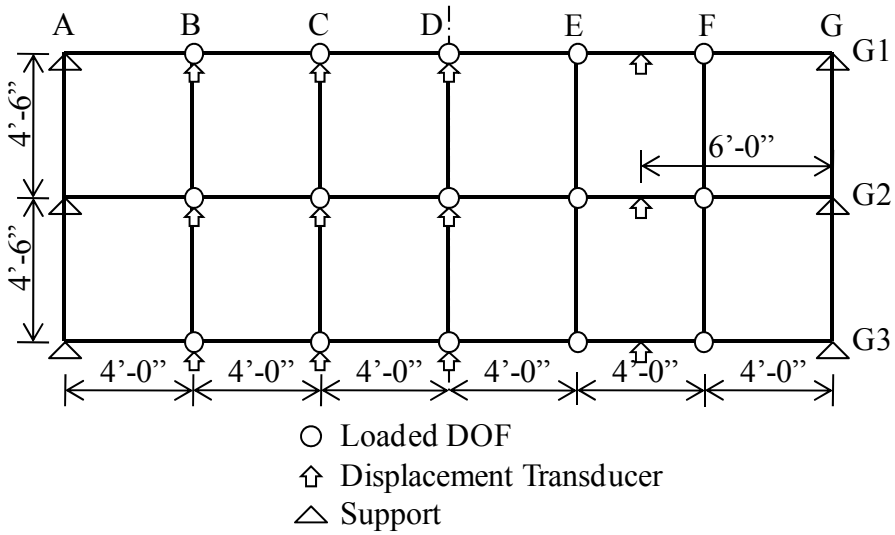

Figure 6.26. Setup of displacement transducers for static load testing.

6.4 ANALYSIS AND RESULTS

6.4.1 Introduction

The analysis and results are presented in several subsections with a different experimental technique validated in each. These subsections relate to the following:

- Ability of a TT to produce accurate modal parameters when used in SIMO testing.
- Ability of the TT shaker system to produce accurate modal parameters when used in MIMO testing.
- Validation of the use of multisine excitation signals by comparison to results acquired with burst-random excitation.
- Evaluation of the use of roving force transducers in MIMO testing.

A variety of mode shapes were frequently captured by the various testing methods, and are presented in this single location for reference (Figure 6.27). The description of each mode shape is provided as well as an abbreviated description that is used in various tables to conserve space.

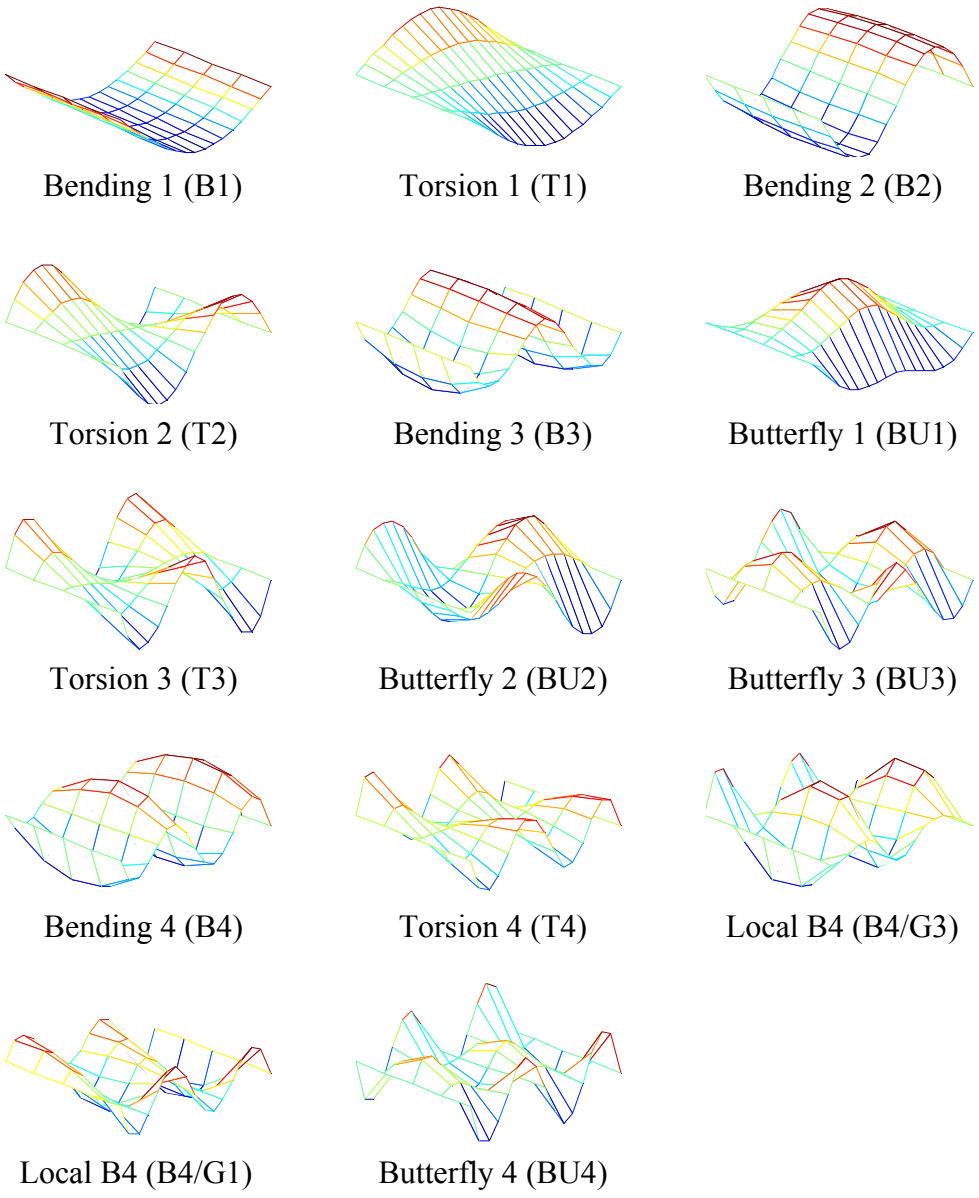

Figure 6.27. Bridge model mode shapes captured by various testing methods.

6.4.2 Validation of Tactile Transducer for Experimental Modal Analysis

The primary goal of the laboratory bridge model testing is to demonstrate that the TTs and subwoofer amps can be used to enable system identification via experimental modal analysis

(EMA). If there is good agreement between the results found using the new testing approach and those from accepted approaches, then the feasibility of the new approach will be considered to be supported by the laboratory testing. A common and accepted testing method is to use an APS shaker and amplifier, a burst-random excitation signal, and a SIMO procedure. As such, the TT SIMO results are compared to the baseline APS SIMO results for validation of the new excitation device.

For a proper comparison, it is important that as many variables as possible are held constant between the baseline APS testing and the experimental TT testing. A list of commonalities between the two tests are: the bridge model is unchanged between tests; the same sensors are used in the same locations; the same wiring, DAQ, and software are used; the same signal types are used; and the data processing methods are identical. Some minor variations are unavoidable: the temperature in the laboratory varies by a few degrees from day to day; each realization of burst-random signals is unique; the multisine signal amplitude over some frequencies is altered to enable better TT performance; and the input force level between the two shaker types cannot be made exactly equal.

The performance of the TT system is evaluated by comparison of the modal properties identified to those found with the APS testing. The modal properties to be evaluated are:

- Natural Frequencies
- Modal Damping
- Modal Mass
- Modal Vectors (mode shapes)
- Modal Flexibility

Modal mass is typically found as a complex number with an angle of nearly zero degrees. As such, the real part is only slightly different than the magnitude. The magnitude of modal mass is thus reported herein as a more easily understood and compared value than a complex number is.

6.4.2.1 Natural Frequencies, Modal Damping, and Modal Mass

The CMIF algorithm is used to identify the existence of modes, and then SDOF methods are used to estimate values for the natural frequencies, damping, and modal mass of each mode. The comparison of these parameters from the APS and the TT experiments is made in Table 6.3 for burst-random excitation and in Table 6.4 for multisine excitation.

Mode	Undamped Nat. Freq. (Hz)			Damping Ratio (%)			Modal Mass (lbf/g)		
Desc.	APS	TT	Diff.	APS	TT	Diff.	APS	TT	Diff.
B1	8.9	9.0	1%	0.86	0.58	47%	21.4	23.4	9%
T1	10.2	10.3	1%	0.57	0.58	2%	13.0	11.6	11%
B2	32.6	32.7	0%	0.62	0.67	6%	27.3	27.2	1%
T2	36.8	37.1	1%	0.40	0.42	4%	16.3	15.5	5%
B3	67.9	68.2	0%	1.09	1.08	1%	16.5	18.6	11%
BU1	73.9	74.3	1%	0.47	0.61	23%	14.1	15.1	7%
T3	76.3	79.0	3%	0.75	0.70	7%	19.0	16.8	13%
BU2	82.3	82.5	0%	0.66	0.80	17%	18.9	17.4	8%
BU3	105.7	107.8	2%	1.64	0.72	128%	14.7	21.6	32%
B4	110.7	112.5	2%	1.00	1.46	31%	18.5	27.5	33%
T4	131.5	131.8	0%	1.76	1.43	24%	18.7	21.9	14%
B4/G3	139.4	139.3	0%	1.24	1.08	14%	115.6	117.2	1%
B4/G1	141.2	148.4	5%	0.74	0.78	6%	81.1	60.1	35%
BU4	156.3	156.1	0%	0.74	0.62	20%	22.9	26.5	14%

Table 6.3. Comparison of natural frequencies, damping, and modal mass found from APS SIMO and TT SIMO testing using burst-random excitation.

Mode Desc.	Undamped Nat. Freq. (Hz)			Damping Ratio (%)			Modal Mass (lbf/g)		
	APS	TT	Diff.	APS	TT	Diff.	APS	TT	Diff.
B1	8.8	8.9	1%	1.05	0.77	36%	21.7	22.9	5%
T1	10.1	10.2	1%	0.92	0.67	38%	14.2	11.7	22%
B2	32.6	32.7	0%	0.61	0.72	14%	28.3	26.0	9%
T2	36.8	37.1	1%	0.35	0.42	17%	18.2	15.1	21%
B3	67.8	68.0	0%	1.07	1.12	5%	17.6	19.2	8%
BU1	73.8	74.4	1%	0.62	0.56	11%	13.5	16.5	18%
T3	76.1	79.0	4%	1.73	0.86	103%	11.8	14.3	18%
BU2	82.2	82.5	0%	0.75	0.80	6%	21.5	17.0	26%
BU3	105.9	107.5	2%	1.43	0.85	69%	16.7	18.5	10%
B4	110.7	110.7	0%	0.98	1.35	27%	19.3	19.1	1%
T4	131.5	131.8	0%	1.58	0.92	72%	20.9	35.3	41%
B4/G3	*	*	--	*	*	--	*	*	--
B4/G1	140.9	*	--	0.71	*	--	84.2	*	--
BU4	156.3	156.1	0%	0.73	0.57	28%	22.8	29.9	24%

* Mode not found.

Table 6.4. Comparison of natural frequencies, damping, and modal mass found from APS SIMO and TT SIMO testing using multisine excitation.

The tables show that the natural frequencies found using the TT shaker are always within a few percent of those found using the APS shaker. For the multisine testing, the B4/G3 and B4/G1 local modes are more difficult to identify than with burst-random. These two modes are closely spaced, and the B4/G1 mode still dominates at the frequency where the B4/G3 mode is expected to exist for the APS testing. For the TT multisine testing, neither local mode can be identified and the T4 mode is dominant throughout this frequency range. The burst-random signal may allow easier identification of these local modes since 'beating' does not occur for the stochastic input.

The damping ratio is far more sensitive than the natural frequency, and the variability is high between the values found with the TT and with the APS shaker. The damping is found as the real part of the pole divided by the magnitude of the pole. Since the damping is very low for this structure, the angle (or phase) of the pole is very close to 90 degrees. Thus, a small inaccuracy in

the phase angle results in a large change in the damping ratio. For example, if the true damping ratio is 1% but the phase is off by 1% (0.9 degrees), then the damping will be found as 2.6%. However, if the true damping is 10% but the phase is off by 1%, then the damping will be found as 11.6%. Thus, the magnitude of the change is consistent, but the percent error is greatly increased for low damping values. Because of this, the damping ratio is not considered to be very important in comparisons of modal data for lightly damped structures.

The modal mass values are in relatively good agreement for many modes. In a number of cases, three of the four values found are in good agreement and only a single value differs from the others. For mode T2, the APS multisine value is 16% higher than the mean of the other three values of modal mass. For mode B4, the TT burst-random value is 45% higher than the mean of the other three. For mode T4 and mode BU4, the TT multisine values are 72% and 24% higher respectively than the mean of the other three values. Since these variations are not consistent to one signal type or to one shaker type, there is little evidence that modal mass is estimated worse due to any single testing parameter. However, the poor values of modal mass found with TT multisine testing for modes T4 and BU4 are due to incomplete removal of the 'beating' phenomenon.

Considering the consistency of modal mass values found from APS testing (burst-random versus multisine) and TT testing, the TT values have less spread for seven of the first eight modes. For the four higher modes that were captured by both shakers, the APS shaker outperforms the TT shaker. The better APS performance at higher frequencies is expected since the force output is quite consistent whereas the TTs produce significantly less force as frequency increases.

Some error in modal mass value is always expected with EMA since the modal mass is inversely proportion to the value of the eFRF at the modal frequency. Thus, if a mode other than the mode of interest is contributing height to the modal peak due to imperfect modal filtering, then the modal mass will be directly affected. Modal filtering is always imperfect due to limited spatial resolution of the mode shapes. If there is a powerful mode or a closely spaced mode that is not adequately removed from the eFRF by filtering, then inaccuracies in the calculation of modal mass will result. This is a difficult problem to solve for any system with closely spaced and similarly shaped modes, and the bridge model is no exception. In the discussion of modal vectors below, it is noted that the local modes have some similarity to global shapes, resulting in the greater variation in modal mass for the higher modes.

Overall, the natural frequencies and modal masses found demonstrate that the TT shaker is capable of adequately exciting the modes and producing results similar to those found by use of the APS shaker.

6.4.2.2 Modal Vectors

The modal vectors are taken as the columns of [U] from the singular value decomposition of the transfer function. In the vicinity of a peak in the CMIF, the corresponding column of [U] is dominated by the mode shape that has a natural frequency nearly equal to the frequency at the CMIF peak. General examples of the mode shapes for the bridge model found from the testing are shown in Figure 6.27, however, the exact shapes found for each testing method are not identical. The level of similarity between mode shapes found from different experiments can be compared by calculating a value known as the modal assurance criteria (MAC) (Allemang 2003). The MAC value is found using the following equation, and a value of unity represents an exact

match, whereas a value of zero indicates that the modes are orthogonal. The agreement between mode shapes found using the TT shaker and the APS shaker are compared using MAC values.

$$MAC = \frac{(A^T * B)(B^T * A)}{(A^T * A)(B^T * B)} \qquad \text{Equation 6.1.}$$

Where:

$A =$ a vector representing a mode shape

$B =$ a vector representing a different mode shape

For comparison of the mode shapes found by the two different test methods, all modes found by both methods are compared to each other and a bar graph is used to display the results in Figure 6.28 for burst-random and Figure 6.29 for multisine excitation.

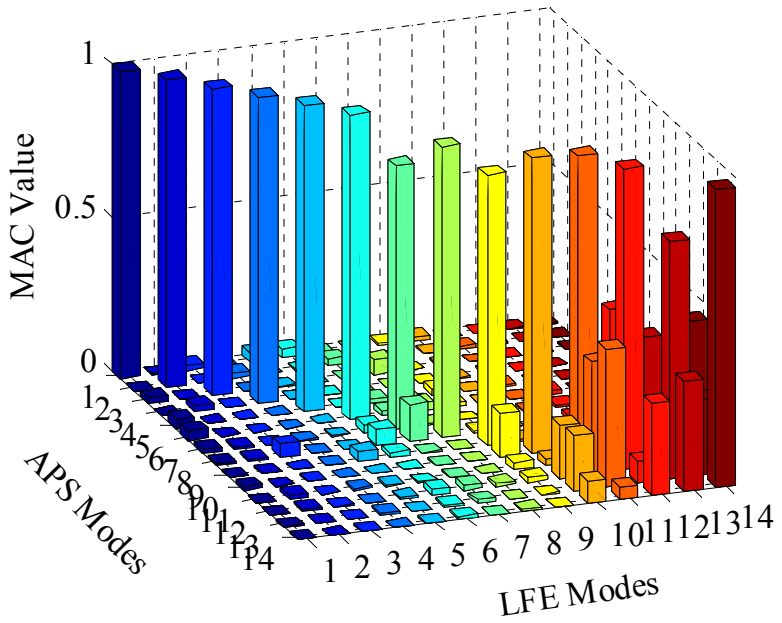

Figure 6.28. MAC values for comparison of mode shapes found from APS SIMO and TT SIMO testing using burst-random excitation.

When analyzing Figure 6.28, it is noted that the best result is for all values on the diagonal to be unity and all off-diagonal terms to be zero. The values of unity would indicate perfect agreement between the APS and TT modal vectors, and the values of zero would indicate that all other modes are orthogonal. Considering the diagonal terms first, the figure shows that for the burst-random excitation, the modal vectors found using the TT are in excellent agreement with the APS modal vectors. Most of the modes have MAC values that are nearly unity. The sixth mode (BU1) and the eighth mode (BU2) have MAC values of approximately 0.8, indicating that the TT results vary somewhat from that of the APS. The thirteenth mode (B4/G1 local) also has a low MAC value between the two shaker types.

Considering the off-diagonal terms, the first six modes are essentially orthogonal to all other modes. The seventh TT mode (T3) has about 10% correlation with the eighth APS mode (BU2), indicating that the modal vector from [U] was somewhat contaminated by the BU2 mode. For the highest five modes, there is significant correlation between the vectors. For the local modes (12 – B4/G3 and 13 – B4/G1) there is significant similarity to modes 10, 11 and 14 (B4, T4, and BU4 respectively). The existence of actual local modes is supported by the fact that these two modes are identified from many different experiments, and the inclusion of these modes improves the accuracy of synthesized FRFs. The correlation between the two local modes and the nearby global modes is largely due to the arrangement of the sensors and the resulting lack of adequate spatial resolution to fully discern the mode shapes. The high correlation is also somewhat due to these modes both being strongly excited at similar frequencies, causing the identified shapes to be a combination of two modes that are actually orthogonal.

Other non-zero terms in the figure are probably due to a lack of spatial resolution and noise. These terms are generally between modes that are spaced farther apart in frequency and are thus unlikely to be related in any real way.

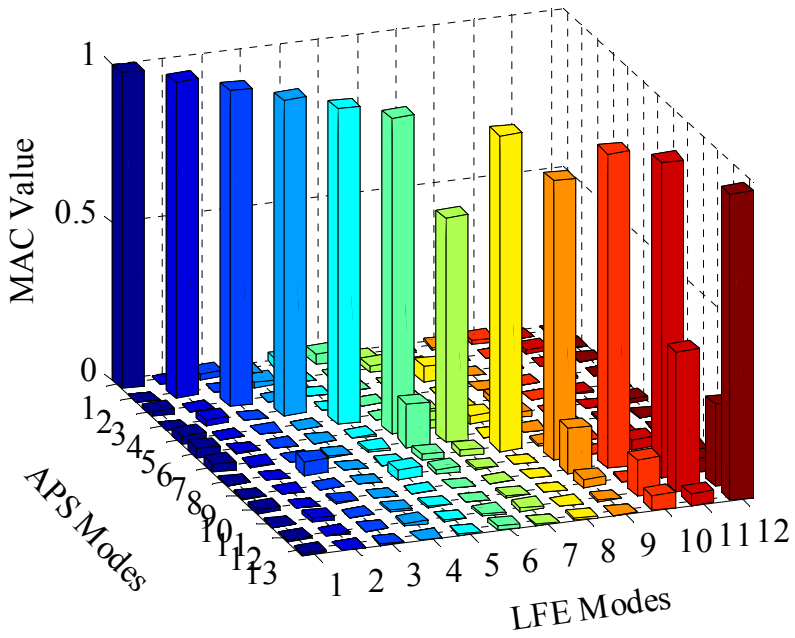

Figure 6.29. MAC values for comparison of mode shapes found from APS SIMO and TT SIMO testing using multisine excitation.

Figure 6.29 shows the MAC values using multisine excitation with the APS and TT shakers. The terms on the diagonal are generally nearly unity, indicating excellent agreement between the modal vectors captured by use of the two excitation devices. The seventh mode (T3) has a MAC value of about 0.7 indicating some difference between the vectors. Considering Table 6.4, mode T3 is found at frequencies that differ by about 3 Hz between the two shaker types. The twelfth mode captured using the APS shaker (B4/G1) is not captured with the TT, and thus there should be no agreement. However, as noted before, the local mode is correlated with the nearby global modes.

The off-diagonal terms of Figure 6.29 are generally nearly zero. However, the seventh APS mode (T3) is correlated to both the sixth and seventh TT modes (BU1 and T3). Also, as noted before, the local mode (twelfth APS mode) is correlated with the nearby global modes.

Overall, the modal vectors captured for the global modes of the bridge model using a single TT shaker are in excellent agreement with the baseline vectors from the APS testing. The MAC analysis also indicates that the selected modes are essentially orthogonal, except for the B4/G1 and B4/G3 local modes.

6.4.2.3 Modal Flexibility

6.4.2.3.1 Overview

Modal flexibility is found by extrapolating the results of dynamic testing to a forcing frequency of 0 Hz. The resulting modal flexibility matrix is square with a length equal to the number of DOFs. For the bridge model, the number of DOFs is equal to the number of accelerometers used, which is 15. A common method used to enable visualization of a flexibility matrix is to plot a deflected structural shape that is found by applying a load vector to the flexibility matrix. Most commonly, a unit load is applied to every DOF, and the global deflected shape that is roughly equivalent to applying a uniform load to the entire structure is thus produced. For civil structures, this deflected shape is useful since most engineers can immediately identify if it 'looks wrong'.

The shortcoming of using the global deflected shape as a proxy for validating the accuracy of the modal flexibility matrix is that the lowest few modes dominate the result. For the subject bridge model with a unit load at all DOFs, the maximum deflection is altered by less than 1% if none of the modes except B1 are included. However, even the inclusion of the highest captured mode (BU4 at ~156 Hz) changes some elements of the modal flexibility matrix by 5%. The inclusion

of the second butterfly mode (BU2 at ~82 Hz) alters some elements of the matrix by more than 20%. Thus, the commonly used comparison of deflected shapes with unit loading is not the best method to assess the agreement between a pair of flexibility matrices.

A better way to compare two matrices is to consider the difference between each element, and then to report a single number that represents the difference of all elements. With a flexibility matrix, some elements differ in scale by orders of magnitude and so it is also important to scale the gross difference by the magnitude of the element. The Frobenius norm is then used to collect the difference of all of the elements into a single number. The equation below illustrates the method by which two flexibility matrices are compared in this thesis. In this formulation, $f1$ is considered to be the more accurate flexibility matrix. For the data reported in this chapter, the static flexibility matrix is considered to be the most accurate result and is always used as $f1$ unless otherwise specified.

$$D = \sqrt{\sum_{i=1}^{n}\sum_{j=1}^{n}\left(\frac{f1_{i,j} - f2_{i,j}}{f1_{i,j}}\right)^2} \qquad \text{Equation 6.2.}$$

Where:

$D =$ the value representing the overall difference between two matrices.

$n =$ the size of the square matrix.

$f1 =$ the flexibility matrix considered to be more accurate.

$f2 =$ the flexibility matrix being compared.

A final consideration for comparing flexibility matrices is that the accuracy is expected to be best for DOFs spatially close to each other, and worse for DOFs that are farther apart. Thus, the most accurate elements in the matrix should be those on the diagonal, and the least accurate should be

those the farthest from the diagonal. For the DOF numbering system and the method of assembly of the matrix for the bridge model, the first element in the flexibility matrix represents the vertical deflection at DOF 1B for a unit load at DOF 1B. This element should be less affected by noise and measurement inaccuracies than off-diagonal elements. The element in the first column, fifteenth row represents the deflection at DOF 3F for a unit load at DOF 1B, and since these DOFs are far apart, it is expected that noise and other errors would have a greater impact on the accuracy of this value.

Large differences between two flexibility matrices are likely to occur at some off-diagonal terms, and this can significantly affect the value of D. Thus, a second measure of the agreement between two flexibility matrices is also proposed that only considers the elements on the main diagonal (equation shown below). Both the value of D and the value of D_d are reported herein so that a more complete comparison is presented.

$$D_d = \sqrt{\sum_{i=1}^{n} \left(\frac{f1_{i,i} - f2_{i,i}}{f1_{i,i}} \right)^2} \qquad \text{Equation 6.3.}$$

Where:

D_d = the value representing the difference between two matrix main diagonals.

An example that illustrates the preceding discussion is shown in Figure 6.30. This figure graphically depicts the deflected shape of the structure due to unit loading at each DOF using the static flexibility matrix and using the modal flexibility matrix found from the TT SIMO testing with burst-random excitation. The graph depicts that the deformed shapes appear similar, but that in general, the static result is more flexible than the modal result. The D and D_d values provide a

numerical representation of the size of the difference, which is more easily compared over a broad variety of testing methods.

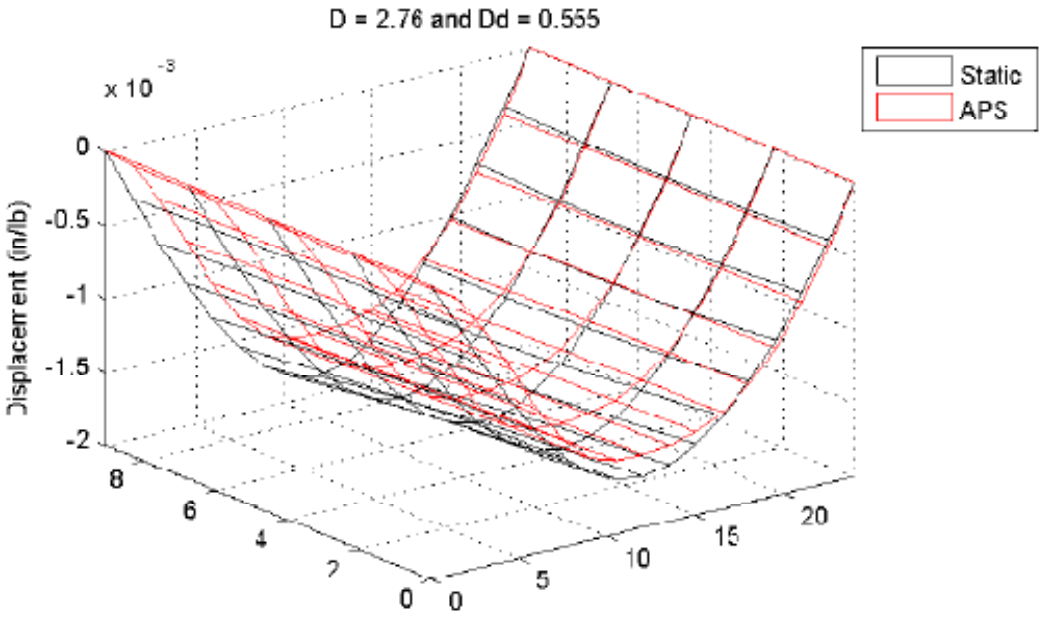

Figure 6.30. Illustration of the use of deflected shapes for comparison of flexibility matrices.

6.4.2.3.2 Analysis

The modal flexibility matrices derived from the APS SIMO testing and from the TT SIMO testing are compared as discussed above, and the results are shown in Table 6.5. In all cases, D and D_d are calculated using the static flexibility matrix as a baseline.

Desc.	Static Load	Burst-Random		Multisine	
		APS	TT	APS	TT
D		3.032	2.757	6.328	2.280
Dd		0.501	0.555	0.550	0.492
DOF 1D*	1.65	1.72	1.54	1.80	1.58
DOF 3D*	1.89	1.74	1.63	1.84	1.71

* Displacement at DOF due to 1 kip load at all DOFs (inches)

Table 6.5. Comparison of modal flexibility found from APS SIMO and TT SIMO testing.

The modal flexibility results show that in most cases the structure appears stiffer in modal testing than in static testing (bottom two rows of table). Recalling Figure 6.16, the stiffness appears to decrease as the shaking force is increased. For this testing, a low input force level was selected to minimize noise in the FRFs, and a higher apparent stiffness is one outcome of this choice.

Considering the agreement of all modal flexibility matrix elements to the static flexibility matrix, the TT shaker has lower (and thus better) D values than the APS shaker for both signal types. However, D_d values are similar in all cases. This indicates that the TT provides better excitation than the APS shaker to DOFs that are farther from the driving point. A possible explanation for this is that the TT provides more force than the APS shaker at low frequencies, and many of the matrix elements are predominantly controlled by the first two modes.

The poor value of D for the APS multisine testing is surprising. A closer analysis shows that the modal flexibility elements that relate girder 1 to girder 3 are significantly worse for the APS multisine testing than for any other case, and this drives the high value of D. No single mode is responsible for the poor results, instead, slight inaccuracies in modes B1 and T1 cause the problem. Since the matrix elements of concern are always small values compared to those closer to the diagonal, slight changes to the powerful modes have a large impact. In this case, the elements of interest nearly cancel out when modes B1 and T1 are added together. This result helps justify comparing values of both D and D_d to get a full understanding of the overall accuracy of the flexibility matrix.

The purpose of analyzing flexibility is to validate that the TT results are similar to the APS results, and they are. For both input signal types, the TT shaker provides lower D values than the APS shaker. For the elements on the diagonal, the APS shaker provides better results than the TT

shaker for burst-random, but worse results for multisine. The displacement values show that the APS shaker is slightly better than the TT for both signal types. Overall, the TT provided modal flexibility accuracy that is similar to that provided using the APS shaker.

6.4.2.4 Summary of Tactile Transducer Shaker Validation

The preceding subsections considered the results of experimental modal analysis using a single TT to excite the laboratory bridge model. The purpose of the testing was to assess whether the TT can provide system identification results similar to those found with a purpose-built shaker. Thus, the system identification results were compared to those acquired using an APS shaker, which is a device commonly used by many researchers for EMA. The comparisons demonstrate that accurate modal properties can be identified using the TT shaker as the system excitation device.

All of the global modes of the bridge model found with the APS shaker were also found with the TT shaker, and the natural frequencies and mode shapes are in close agreement. The damping and modal mass values did not agree well for all modes, but these parameters are quite sensitive to noise and to imperfect filtering caused by poor discrimination for some local modes. Modal flexibility found using the TT was as good as that found with the APS shaker.

However, the TT is inferior to the APS shaker in some regards. First, a phenomenon known as 'beating' can cause identification to fail in some frequency ranges, requiring the FRFs to be filtered. Second, the TTs have a short stroke and thus the amplitude of the input signal at low frequencies must be adjusted to prevent bottoming out. Third, the TTs provide excessive force in the vicinity of 100 Hz when they reach their own natural frequency, and care must be taken to

avoid over-ranging the sensors. Thus, the TTs require the user to exercise more care for accurate system identification to occur.

6.4.3 Validation of Tactile Transducer Shakers in MIMO Array for EMA

The SIMO testing discussed above was undertaken to demonstrate that a single TT can provide input similar to the industry-standard APS shaker. However, there is no intent to use single TTs for any real-world testing. The goal of this work is to demonstrate that a large array of TTs can be used with MIMO testing. MIMO testing is superior to SIMO testing for many reasons, but the high cost of shakers like the APS is prohibitive for most researchers. The low-cost TTs enable many spatially distributed inputs to be used simultaneously, and this application is tested herein.

An array of four TTs is used for MIMO testing of the laboratory bridge model, and modal parameters are captured as before. The APS SIMO testing results are again used as a baseline, and the various modal properties are compared. The use of an array of TTs is considered to be validated if the results are comparable to the APS results.

6.4.3.1 Natural Frequencies, Modal Damping, and Modal Mass

As before, peaks in the CMIF plot indicate potential modes of the structure, and mode shapes are taken as the left and right singular vectors of the SVD. The mode shapes are used to filter the FRFs, resulting in eFRFs. SDOF methods are then used to estimate values for the natural frequencies, damping, and modal mass of each mode. The parameters found using TT MIMO excitation are compared to the baseline APS SIMO values in the following tables: burst-random in Table 6.6; multisine in Table 6.7.

Mode Desc.	Undamped Nat. Freq. (Hz)			Damping Ratio (%)			Modal Mass (lbf/g)		
	APS	TT	Diff.	APS	TT	Diff.	APS	TT	Diff.
B1	8.9	9.0	1%	0.86	0.65	25%	21.2	29.3	38%
T1	10.2	10.4	2%	0.57	0.65	13%	13.1	13.8	6%
B2	32.6	33.0	1%	0.62	0.64	2%	27.2	27.4	0%
T2	36.8	37.8	3%	0.40	0.42	5%	16.3	17.4	7%
B3	67.9	68.3	1%	1.09	1.03	5%	16.5	13.1	21%
BU1	73.9	75.2	2%	0.47	0.50	6%	14.1	16.2	14%
T3	76.3	79.5	4%	0.75	0.79	5%	19.0	9.2	51%
BU2	82.3	83.7	2%	0.66	0.57	14%	18.9	15.2	19%
BU3	105.7	106.9	1%	1.64	1.05	36%	14.7	7.0	53%
B4	110.7	110.6	0%	1.00	0.89	11%	18.5	9.3	50%
T4	131.5	144.8	10%	1.76	0.57	68%	18.7	89.3	377%
B4/G3	139.2	137.7	1%	1.15	0.82	29%	124.5	8.7	93%
B4/G1	141.2	*	--	0.74	*	--	81.1	*	--
BU4	156.3	162.1	4%	0.74	0.64	14%	22.9	21.9	4%

* Mode not found.

Table 6.6. Comparison of natural frequencies, damping, and modal mass found from APS SIMO and TT MIMO testing using burst-random excitation.

Mode Desc.	Undamped Nat. Freq. (Hz)			Damping Ratio (%)			Modal Mass (lbf/g)		
	APS	TT	Diff.	APS	TT	Diff.	APS	TT	Diff.
B1	8.8	8.8	1%	1.05	0.61	42%	21.7	27.2	25%
T1	10.1	10.2	1%	0.92	0.76	18%	14.2	20.6	45%
B2	32.6	32.9	1%	0.61	0.60	3%	28.3	29.4	4%
T2	36.8	37.6	2%	0.35	0.83	139%	18.2	14.4	21%
B3	67.8	68.4	1%	1.07	0.92	13%	17.6	14.4	18%
BU1	73.8	75.1	2%	0.62	0.73	18%	13.5	13.9	3%
T3	76.1	79.5	4%	1.73	0.61	65%	11.8	10.2	13%
BU2	82.2	83.7	2%	0.75	0.55	26%	21.5	14.8	31%
BU3	105.9	107.4	1%	1.43	0.23	84%	16.7	18.1	9%
B4	110.7	110.4	0%	0.98	0.53	46%	19.3	13.3	31%
T4	131.5	144.9	10%	1.58	0.48	70%	20.9	103.7	395%
B4/G3	*	137.7	--	*	1.04	--	*	6.0	--
B4/G1	140.9	*	--	0.71	*	--	84.2	*	--
BU4	156.3	162.2	4%	0.73	0.36	50%	22.8	33.6	48%

* Mode not found.

Table 6.7. Comparison of natural frequencies, damping, and modal mass found from APS SIMO and TT MIMO testing using multisine excitation.

The tables show that for almost all modes, the frequencies found with TT MIMO testing are slightly higher than with APS SIMO testing. Since the bridge model's mass was constant for all testing, the frequency increase suggests that the model appears to be stiffer for MIMO testing. A possible explanation for this is that the shakers are operating out of phase with each other 75% of the time in the case of multisine, and 50% of the time with burst-random, producing added resistance to the model moving in any particular natural mode shape.

For the burst-random signal, the damping found with the TT MIMO testing is in good agreement with the APS SIMO testing. For the multisine signal, the damping from TT MIMO testing varies more widely than for burst-random. However, as discussed, the damping estimates are very sensitive and are not relied upon.

For both burst-random and multisine, the modal mass is in good agreement for many of the modes. For mode B1, the TT modal mass is high for both signal types, indicating that the eFRF magnitude is lower than it should be. This is probably due to the mode not being excited as well when the shakers operate out of phase with each other.

For mode T4, the modal mass found from the TT MIMO testing with either signal type is far too high. The frequency at the peak is also significantly different than what was found with APS SIMO testing. All MIMO testing finds the T4 mode at approximately 145 Hz, and all SIMO testing finds the T4 mode at approximately 132 Hz. Also, the MAC value between the SIMO and MIMO mode shape is low, indicating that these are not actually the same mode. It is theorized that the spatial arrangement used for the MIMO testing is poor for exciting the T4 mode, and the actual mode is not found. The peak selected at 145 Hz is not near the natural frequency, but the

T4 mode is still more dominant at this frequency than any other mode. The eFRF magnitude is low since the true peak is not found and the modal mass is therefore far too high.

Overall, the natural frequencies and modal masses found demonstrate that the TT MIMO testing produces results similar to those found using baseline APS SIMO testing. However, the high frequency modes are not identified as well as the low frequency modes.

6.4.3.2 Modal Vectors

The modal vectors found with TT MIMO testing are again compared to the vectors from APS SIMO testing using MAC values.

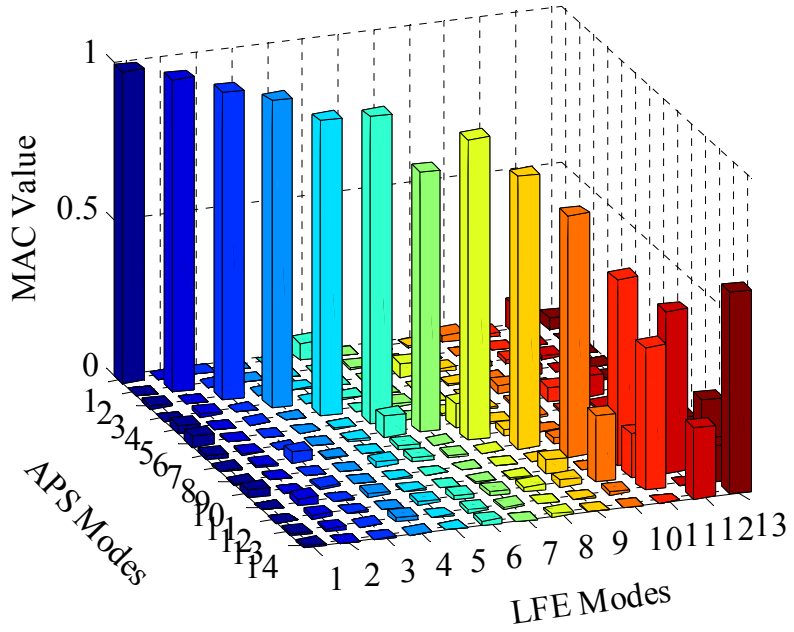

Figure 6.31. MAC values for comparison of mode shapes found from APS SIMO and TT MIMO testing using burst-random excitation.

The MAC values for the first nine modes are generally nearly unity on the diagonal of Figure 6.31, indicating very good agreement between the mode shapes identified by the two testing

methods. Mode 7 (T3), mode 9 (BU3), and mode 10 (B4) have MAC values of about 0.8, indicating some difference between the shapes. Mode 11 (T4) has poor agreement with a MAC value of about 0.6. Inspection of the mode shapes reveals that the T4 shape from the TT MIMO burst-random testing is inferior to the APS shape, with girder 2 somewhat in phase with girder 3. Mode 12 (B4/G3) also has a low MAC value, and this is because in the TT MIMO mode, girder 3 has a smaller amplitude than the mode from APS testing. For mode 13 (BU4), inspection of the mode shapes again shows that the APS testing produced a better estimate.

For values off of the diagonal of Figure 6.31, the correlation between mode shapes is generally nearly zero as expected. However, there is correlation between the local modes (APS modes 11 and 12, TT mode 12) and the nearby global modes. This was noted and discussed for the TT SIMO testing in subsection 6.4.2.2.

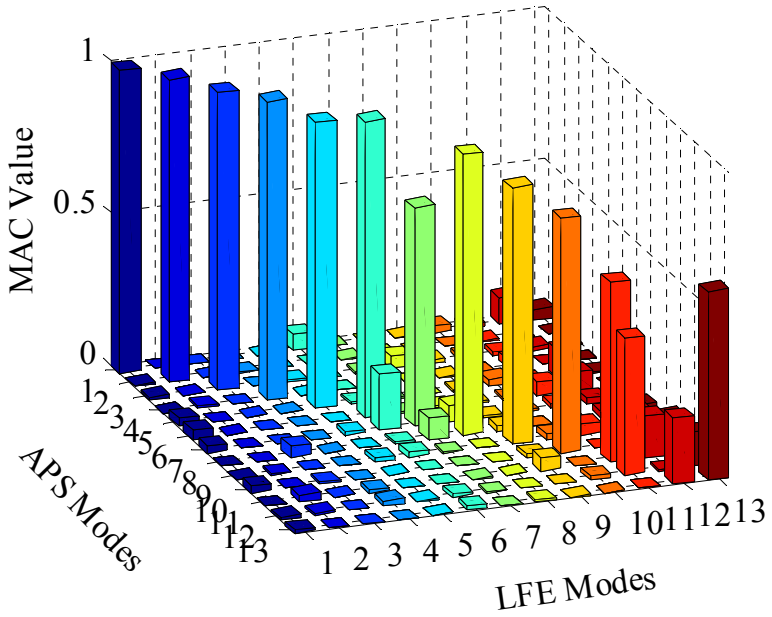

Figure 6.32. MAC values for comparison of mode shapes found from APS SIMO and TT MIMO testing using multisine excitation.

Considering Figure 6.32, the diagonal terms are nearly unity in most cases. The diagonal elements with lower MAC values are the same as in Figure 6.31 and the same explanations apply. Again, the shapes found from the APS testing are superior to those found with the TT MIMO excitation for modes 11 and 13.

Most terms off of the diagonal of Figure 6.32 are nearly zero. However, the local modes are again correlated with the global T4 and BU4 modes. Other modes with some correlation off of the diagonal are most likely due to spatial aliasing and noise.

Overall, the modal vectors captured via TT MIMO testing are generally in good agreement with those from the baseline APS SIMO testing. The analysis also shows that the modes are nearly orthogonal, except for the high frequency local modes. In a few cases at higher frequencies, the TT MIMO testing provided mode shapes that are inferior to the APS shapes.

6.4.3.3 Modal Flexibility

The modal flexibility matrices derived from the TT MIMO testing and from the APS SIMO testing are compared in Table 6.8.

Desc.	Static Load	Burst-Random		Multisine	
		APS	TT	APS	TT
D		3.032	3.760	6.328	8.722
Dd		0.501	0.829	0.550	0.981
DOF 1D*	1.65	1.72	1.23	1.80	1.43
DOF 3D*	1.89	1.74	1.37	1.84	1.56

* Displacement at DOF due to 1 kip load at all DOFs (inches)

Table 6.8. Comparison of modal flexibility found from APS SIMO and TT MIMO testing.

For the burst random testing, the maximum values of deflection at DOFs 1D and 3D are an average of 25% less for TT MIMO than the values for APS SIMO. Also, both the D and D_d

values are worse than the APS values. The high value of 0.829 for D_d indicates that some diagonal terms of the TT MIMO flexibility matrix are especially poor. These results are not surprising since the modal mass found for mode B1 is poor.

For the multisine testing, the TT MIMO results are also poor. The maximum deflection values are an average of 13% less than the deflections from the APS testing, and the D and D_d values are also significantly worse than the APS values. A check of the modal flexibility matrix shows that the terms relating the DOFs of the first girder to those of the third girder are especially poor, resulting in the high value of D. The high modal mass of mode B1 is driving much of the trouble with D, whereas the high modal mass of mode T1 is causing the high value of D_d.

6.4.3.4 Summary of MIMO Validation

Overall, the MIMO testing with four TTs identified all global modes that the SIMO testing with the APS shaker identified. Natural frequencies and mode shapes were generally in very good agreement between the two excitation methods. However, modal mass and modal flexibility were not as good with the MIMO testing as with the SIMO testing.

The less accurate modal mass and modal flexibility results are due to only exciting four DOFs with MIMO testing as opposed to exciting fifteen DOFs with SIMO testing. The SIMO testing thus provided fifteen columns in the transfer function and a better average estimate of the eFRF for each mode. With only four columns in the transfer function from MIMO testing, less redundant information is available and the eFRF quality suffers. This can be improved by using more shakers simultaneously or by relocating the shakers and performing a second experiment.

However, exciting the additional DOFs with SIMO testing required far more testing time. Considering the multisine experiments, the SIMO testing required 82 minutes of excitation plus

about two hours for moving the shaker from DOF to DOF. The MIMO testing required about 30 minutes of setup and then 23 minutes of excitation for a total testing time that is only 25% of the SIMO testing time. This time savings is one of the significant benefits of MIMO testing on a real-world structure, especially in the presence of non-stationarity due to environmental changes over the course of a test. Also, more shakers are intended for use on real-world structures, and thus more redundant information will be available for system identification. Therefore, even though the MIMO results were not as good as the SIMO results on the laboratory structure, the opposite is expected on real-world structures.

6.4.4 Validation of Multisine Excitation

Another goal of the laboratory bridge model testing is to validate that the somewhat novel multisine signal gives system identification results that are as good as the very popular burst-random signal. This is important for use of the TTs since fewer force transducers are available than shakers. To use more than four shakers (given the current funding constraints), roving transducers must be used and thus deterministic signals must be used.

As previously discussed, the multisine signal has several theoretical advantages over burst-random signals. The multisine signal is defined to excite each selected frequency evenly, there is no leakage when an experimentation process that incorporates cyclic averaging is used, and orthogonal signals can be used for MIMO testing, greatly reducing the number of averages required. Also, deterministic signals possibly allow some shakers to be operated without a force transducer, whereas force transducers are absolutely required if burst-random signals are used.

In practice, it was found that the TTs provide a good reproduction of the multisine signal, but that the excitation to each frequency line is not equal due to the characteristics of the amplifiers

and the shakers. For example, the TTs display a large increase in force between about 100 Hz and 110 Hz as their own natural frequency is excited. This frequency band is much more strongly excited than other frequencies.

Also, the Signal Express software used to control the experiments creates a slight pause between cyclic averages, offsetting the data sets by about $1/4000^{th}$ of a second, which, for example, changes the phase of a 100 Hz signal by nine degrees. Leakage is still almost totally eliminated since the complete system response is captured in the same data window as the complete excitation force; however, the apparent phase shift requires the use of the H1 FRF algorithm as opposed to the superior EIV FRF algorithm.

Finally, the 'beating' phenomenon discussed previously does not occur with stochastic signals, but does occur with any slowly varying deterministic signal such as multisine or chirp. Although filtering of the FRFs was found to effectively reduce the effect of 'beating', the true FRF shape is necessarily somewhat altered by the filtering. Experimental results indicate that the effect of filtering is small enough that it cannot be distinguished from the typical variability that is due to normal changes in the experimental setup, however, some increase in damping values should be expected as well as a decrease in modal mass.

Validation of the multisine signal is performed by comparison of system identification results from multisine excitation to the results from baseline burst-random excitation. The results of both SIMO and MIMO test setups are considered. As before, natural frequencies, damping, modal mass, modal vectors, and modal flexibility are compared.

6.4.4.1 Natural Frequencies, Modal Damping, and Modal Mass

SDOF methods are again used to estimate natural frequencies, damping, and modal mass for both SIMO and MIMO experiments using multisine (MS) and burst-random (BR) excitation. The results are compared in Table 6.9 for TT SIMO testing and in Table 6.10 for TT MIMO testing.

Mode Desc.	Undamped Nat. Freq. (Hz)			Damping Ratio (%)			Modal Mass (lbf/g)		
	BR	MS	Diff.	BR	MS	Diff.	BR	MS	Diff.
B1	9.0	8.9	1%	0.58	0.77	25%	23.4	22.9	2%
T1	10.3	10.2	1%	0.58	0.67	13%	11.6	11.7	1%
B2	32.7	32.7	0%	0.67	0.72	7%	27.2	26.0	5%
T2	37.1	37.1	0%	0.42	0.42	1%	15.5	15.1	3%
B3	68.2	68.0	0%	1.08	1.12	3%	18.6	19.2	3%
BU1	74.3	74.4	0%	0.61	0.56	9%	15.1	16.5	8%
T3	79.0	79.0	0%	0.70	0.86	18%	16.8	14.3	18%
BU2	82.5	82.5	0%	0.80	0.80	0%	17.4	17.0	3%
BU3	107.8	107.5	0%	0.72	0.85	15%	21.6	18.5	17%
B4	112.5	110.7	2%	1.46	1.35	9%	27.5	19.1	44%
T4	131.8	131.8	0%	1.43	0.92	55%	21.9	35.3	38%
B4/G3	139.3	*	--	1.08	*	--	117.2	*	--
B4/G1	148.4	*	--	0.78	*	--	60.1	*	--
BU4	156.1	156.1	0%	0.62	0.57	9%	26.5	29.9	12%

* Mode not found.

Table 6.9. Comparison of natural frequencies, damping, and modal mass found from burst-random and from multisine TT SIMO testing.

Mode Desc.	Undamped Nat. Freq. (Hz)			Damping Ratio (%)			Modal Mass (lbf/g)		
	BR	MS	Diff.	BR	MS	Diff.	BR	MS	Diff.
B1	9.0	8.8	2%	0.65	0.61	7%	29.3	27.2	8%
T1	10.4	10.2	2%	0.65	0.76	15%	13.8	20.6	33%
B2	33.0	32.9	0%	0.64	0.60	6%	27.4	29.4	7%
T2	37.8	37.6	1%	0.42	0.83	49%	17.4	14.4	21%
B3	68.3	68.4	0%	1.03	0.92	12%	13.1	14.4	9%
BU1	75.2	75.1	0%	0.50	0.73	32%	16.2	13.9	17%
T3	79.5	79.5	0%	0.79	0.61	29%	9.2	10.2	10%
BU2	83.7	83.7	0%	0.57	0.55	3%	15.2	14.8	3%
BU3	106.9	107.4	0%	1.05	0.23	360%	7.0	18.1	62%
B4	110.6	110.4	0%	0.89	0.53	70%	9.3	13.3	30%
T4	144.8	144.9	0%	0.57	0.48	19%	89.3	103.7	14%
B4/G3	137.7	137.7	0%	0.82	1.04	21%	8.7	6.0	45%
BU4	162.1	162.2	0%	0.64	0.36	78%	21.9	33.6	35%

Table 6.10. Comparison of natural frequencies, damping, and modal mass found from burst-random and from multisine TT MIMO testing.

The tables show that the natural frequencies are in excellent agreement for burst-random and multisine excitation. For SIMO testing, the two local modes were not found with multisine but were found with burst-random. For MIMO testing, the B4/G1 mode was not found with either excitation signal.

The damping ratios found from the SIMO testing agree well between the two signal types, and the multisine signal returns a higher ratio for most modes. This is partially due to the filtering. For the eleven modes higher than T1 that were identified by the SIMO multisine testing, six cannot be identified without filtering. For the remaining five, the damping is always lower without filtering, and the average reduction in the damping ratio is 0.16%. The damping ratios found from the MIMO testing do not agree as well as those found with SIMO, and this again stems from the smaller amount of redundant data available in the transfer function.

The modal mass is in excellent agreement between the two excitation signals for SIMO testing, but the variability is greater for MIMO testing. For the B4 mode from SIMO testing, the multisine modal mass is more accurate based on comparison to the APS results. For the T4 mode, the burst-random result is in better agreement with the APS results. For the MIMO testing, the multisine signal provided better results for the B1, BU1, BU3, and B4 modes, and burst-random provided better results for the T1, T2, and BU4 modes. Thus, although the modal masses with the two signal types for MIMO testing are not in good agreement, it is not clear that one signal is outperforming the other.

6.4.4.2 Modal Vectors

The modal vectors found with multisine excitation are compared to those found with burst-random excitation in Figure 6.33 for TT SIMO testing and in Figure 6.34 for TT MIMO testing.

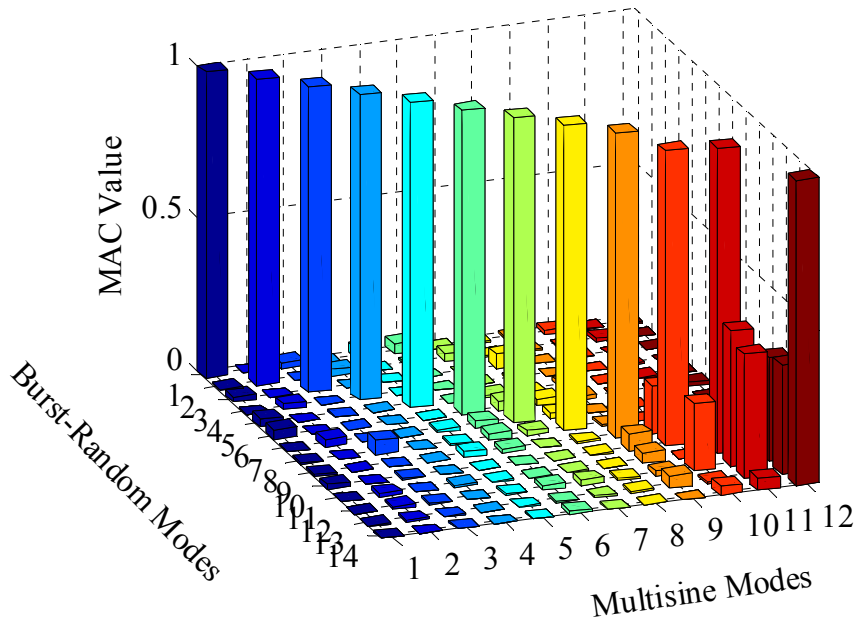

Figure 6.33. MAC values for comparison of mode shapes found from burst-random and from multisine TT SIMO testing.

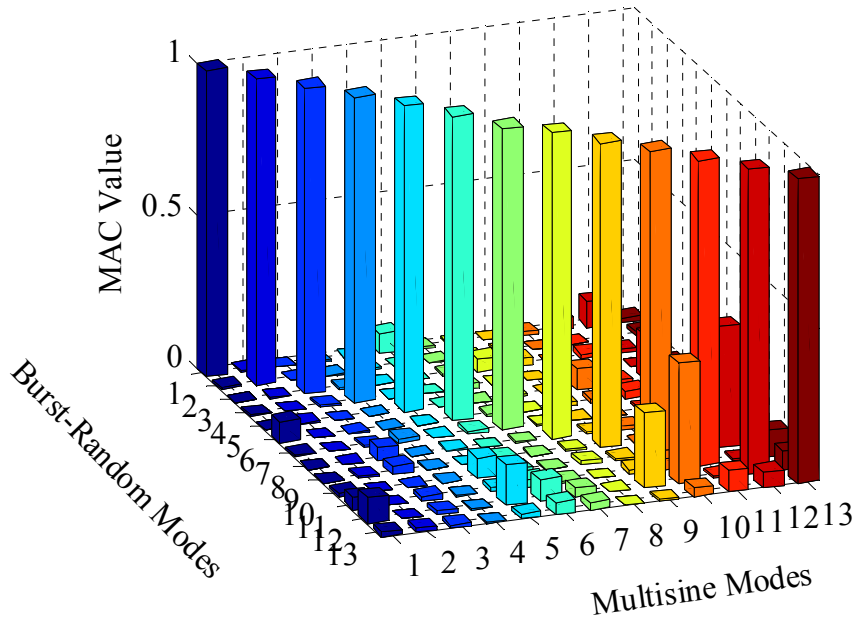

Figure 6.34. MAC values for comparison of mode shapes found from burst-random and from multisine TT MIMO testing.

The comparison of MAC values is very similar to what has been discussed previously. The elements on the diagonal are nearly unity for modes that are common to both excitation signals, and the off diagonal terms are generally nearly zero. For the MIMO testing, the two local modes found with burst-random excitation (modes 12 and 13 in Figure 6.33) are correlated with the T4 and BU4 modes. For the MIMO testing, only the B4/G3 mode was found, and it is correlated with the B4 and BU3 modes.

6.4.4.3 Modal Flexibility

Modal flexibility matrices found from the multisine testing and from the burst-random testing are compared to static load results in Table 6.11.

Desc.	Static Load	SIMO		MIMO	
		BR	MS	BR	MS
D		2.757	2.280	3.760	8.722
Dd		0.555	0.492	0.829	0.981
DOF 1D*	1.65	1.54	1.58	1.23	1.43
DOF 3D*	1.89	1.63	1.71	1.37	1.56

* Displacement at DOF due to 1 kip load at all DOFs (inches)

Table 6.11. Comparison of modal flexibility found from burst-random and from multisine TT testing.

Table 6.11 shows that use of the multisine signal gives better flexibility results for SIMO testing, but generally worse results for MIMO testing. For both SIMO and MIMO, the multisine testing gives better results for total maximum deflection, indicating that the identification of the controlling first mode is better with multisine. The high value of D for MIMO multisine testing is again largely driven by the high value of modal mass found for mode T1.

6.4.4.4 Summary of Multisine Validation

The testing shows that the multisine signal performs as well as the burst-random signal. The natural frequencies are essentially identical for both signal types, as are the mode shapes. The modal mass differs somewhat with a MIMO setup, but the multisine signal provides better accuracy as often as the burst-random signal does. The modal flexibility results are also better in some cases with burst-random, and better in other cases with multisine. Overall, use of the multisine signal is supported by the testing.

6.4.5 Validation of Using Roving Force Transducers

Only four force transducers are available at the University, however, it is desirable to use more than four shakers in the testing of a real-world bridge. As such, it is explored whether good system identification can occur if the force transducers are used in a roving manner so that more than four shakers can be used simultaneously. The FRFs can only be calculated if there is force

data for all inputs. It is hypothesized that for a given set of input signals to an array of shakers on a particular structure, the output of any shaker is consistent enough that it does not need to be measured more than once. If this is true, then the four transducers can be 'roved' and more than four shakers can be used. An initial test is performed using four shakers, and a subsequent test is performed using eight shakers.

6.4.5.1 Roving Force Transducer Testing With Four Shakers

Previous testing has shown that the TTs produce force output that is quite uniform from set to set with deterministic input signals. The purpose of the current testing is to evaluate if structural identification can succeed using force inputs and acceleration outputs that are recorded during disparate experiments. This testing is performed in four parts as described below.

In the first part, four shakers are used in a MIMO setup and all inputs are recorded. Multisine excitation is provided seven times in a row and five capture blocks are retained. As always, four experiments with orthogonal inputs must be undertaken to allow FRF calculation. The purpose of this part is to provide a baseline against which roving results can be compared.

In the second part, the force transducers at input locations 1 and 2 are replaced with sleeve nuts, and the four experiments with five capture blocks each are performed again. Removing the force transducers requires the entire shaker and stinger apparatus to be removed from the structure, causing some level of disturbance to the installation, which could potentially affect the force input. If budget permitted, a quick-connect system could be developed for swapping out force transducers with less disturbance to the installation.

In the third part, the transducers are reinstalled at inputs 1 and 2, and the transducers at input points 3 and 4 are removed. Another four experiments with five capture blocks each are

undertaken. At this point, neither the data from the second part nor the third part can independently be used to calculate FRFs since half of the force input information is missing in each. The force inputs recorded from the two different parts must be combined to enable FRF calculation, which is tantamount to assuming that the unrecorded input forces from one part are equal to the recorded input forces from the other part. This is accomplished as follows:

- Align the data from the two parts as described in subsection 6.3.3.3.
- Insert the recorded forces from the third part as the inputs at locations 1 and 2 for the second part.
- Insert the recorded forces from the second part as the inputs at locations 3 and 4 for the second part.
- This results in 40 total sets of data (5 capture blocks x 4 experiments x 2 parts).

Finally, in the fourth part, all transducers are reinstalled and the four experiments are run a last time. This process allows all input locations to be disturbed, which may affect the force input. Since all four input locations are recorded before and after the disturbances, the input data from the first and last parts can be compared to evaluate what effect the disturbance has.

The modal parameters captured from the various tests are compared in the following subsections. As before, frequencies, damping, modal mass, modal vectors, and modal flexibility are analyzed.

6.4.5.1.1 Natural Frequencies, Modal Damping, and Modal Mass

The parameters captured from the testing of part one are used as a baseline, and the parameters from the combined data of part two and part three are evaluated against this baseline. Parameter calculation was performed in the same manner as described previously. The results are presented in Table 6.12 for all inputs measured simultaneously (All) and for the combined data (Roving).

Mode Desc.	Undamped Nat. Freq. (Hz)			Damping Ratio (%)			Modal Mass (lbf/g)		
	All	Roving	Diff.	All	Roving	Diff.	All	Roving	Diff.
B1	8.8	8.8	0%	0.62	0.55	13%	25.1	24.4	3%
T1	10.2	10.2	0%	0.82	0.76	7%	21.7	20.6	5%
B2	32.8	32.8	0%	0.49	0.47	3%	32.8	33.0	1%
T2	37.6	37.6	0%	0.71	0.73	3%	15.6	14.9	5%
B3	68.2	68.0	0%	1.31	1.29	1%	16.5	17.3	5%
BU1	75.5	74.7	1%	0.66	0.68	3%	17.2	25.1	32%
T3	77.2	78.7	2%	1.92	2.09	8%	13.8	11.6	19%
BU2	83.5	83.1	0%	0.79	1.03	23%	12.7	9.3	36%
B4	111.1	111.3	0%	1.03	1.46	29%	11.7	10.9	7%
T4	134.8	*	--	0.70	*	--	44.9	*	--
B5	140.6	141.0	0%	0.61	0.66	7%	4.5	4.0	10%
BU4	161.7	162.0	0%	0.21	**	--	63.4	**	--

* Mode not found. ** Poor identification.

Table 6.12. Comparison of natural frequencies, damping, and modal mass found from baseline and roving transducer testing.

Table 6.12 shows that the agreement for all parameters is generally better than for any previously discussed testing. The natural frequencies are nearly identical, the damping ratios are in very good agreement, and the modal mass is in very good agreement for modes below about 70 Hz. However, with roving force transducers, the T4 and BU4 modes could not be identified due to high noise in the FRFs. The noise is due to poor response of some of the TTs at higher frequencies, resulting in low and inconsistent force input. This is illustrated in Figure 6.35 which shows the typical force output from two of the TTs used in this testing.

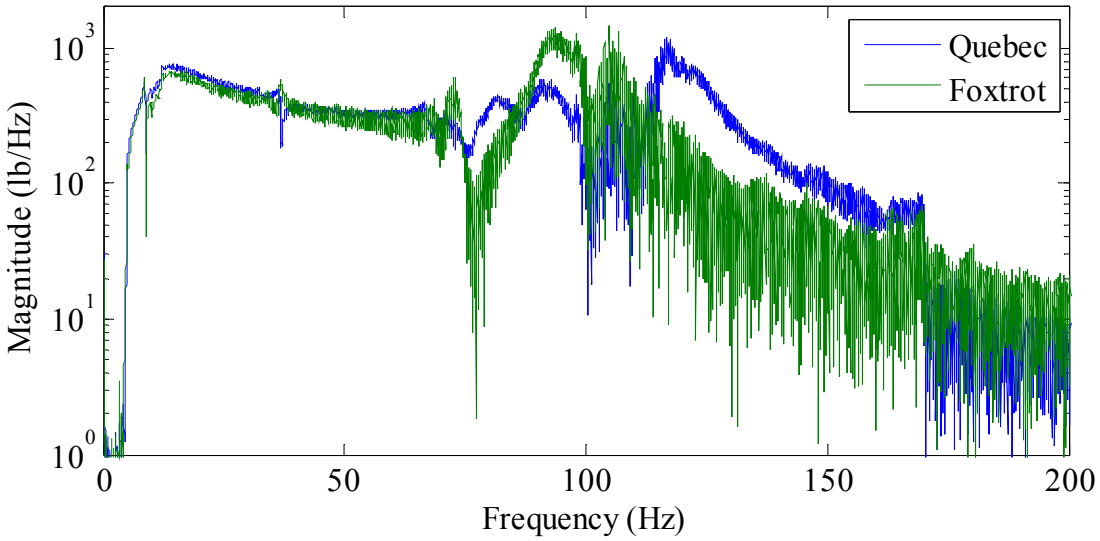

Figure 6.35. Frequency domain data showing relatively poor response of shaker 'Foxtrot' compared to shaker 'Quebec'.

Figure 6.35 demonstrates that shaker 'Quebec' maintains good force output up to the 170 Hz cutoff frequency of the multisine signal, but shaker 'Foxtrot' has a force output that decreases towards the noise floor. Because the force input from 'Foxtrot' is noisy, it varies from set to set and thus a recorded force input from one experiment is a poor match for the accelerations from a different experiment. This is very clear in Figure 6.36 which shows the multiple coherence for output DOF 3D. The multiple coherence represents how much of the measured output is due to the measured inputs. A value of unity indicates that the output is completely due to the measured inputs, and a value of zero indicates that none of the output is due to the inputs. The coherence is very good up to about 70 Hz, and then it is poor. Thus, the output is not highly correlated with the assumed inputs.

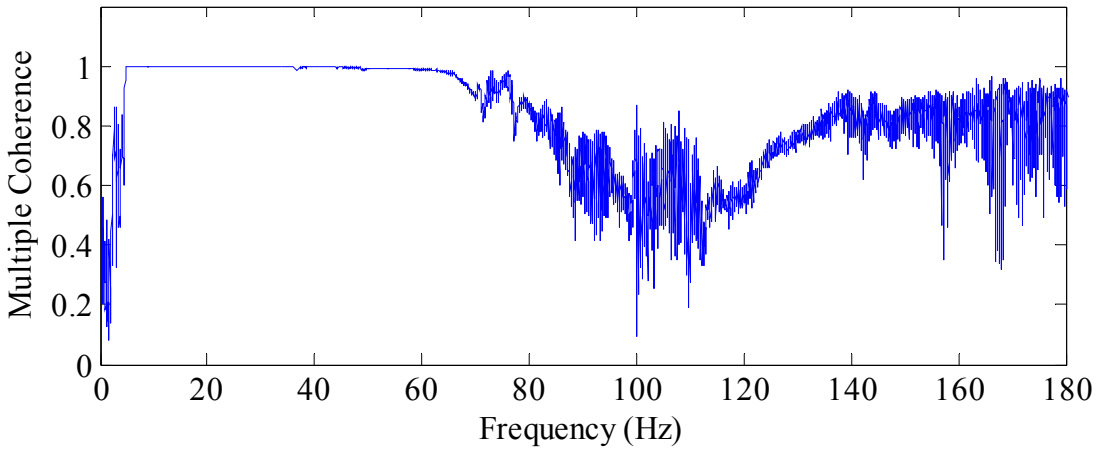

Figure 6.36. Multiple coherence for output at DOF 3D showing poor results above 70 Hz.

6.4.5.1.2 Modal Vectors

Comparison of the modal vectors uses MAC values (Figure 6.37). The figure shows values of nearly unity for all of the elements on the diagonal except for mode T3. Review of the mode shapes reveals that neither test method captured this mode well, but the shape from the roving transducer testing is superior. The cause of the poor capture is a combination of two factors. First, the four shakers used in this testing are all located relatively close to the nodes of this mode shape, and thus it is not well excited. Second, the output of two of the shakers ('Foxtrot' and 'Mike') is generally poor in this frequency range, decreasing the excitation of this mode even more.

The off-diagonal terms are generally close to zero as they should be. None of the modes from the roving testing are highly correlated with baseline modes 10 and 12 (T4 and BU4 respectively), which is appropriate.

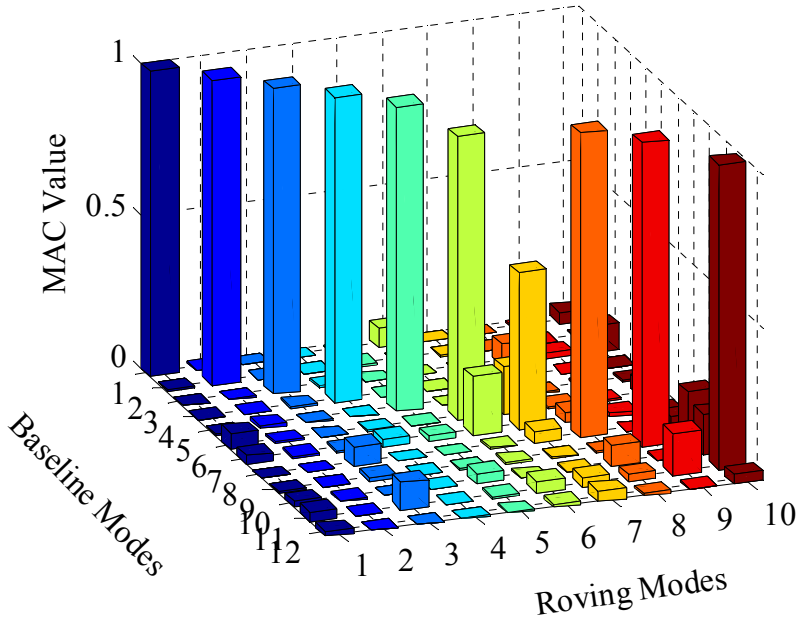

Figure 6.37. MAC values for comparison of mode shapes found from baseline testing and from roving transducer testing.

6.4.5.1.3 Modal Flexibility

The modal flexibility results are again compared to the static flexibility matrix. For this testing, the values of D and D_d are poor whether the force transducers are used in a roving manner or not. The displacement values are better than those from some of the previously reported tests, indicating that the B1 mode is identified well; however, the contribution of other modes to elements away from the diagonal are clearly inaccurate. This is largely due to the values of modal mass found for modes T1, B2, and T2, which are all significantly higher than those found from other tests. High modal mass is most directly related to a low eFRF peak, indicating that the measured FRFs are too low. In any case, the values captured using roving transducers are approximately the same as those captured with all inputs measured.

Desc.	Static Load	All	Roving
D		10.098	9.928
Dd		1.059	0.949
DOF 1D*	1.65	1.53	1.59
DOF 3D*	1.89	1.55	1.61

* Displacement at DOF due to 1 kip load at all DOFs (inches)

Table 6.13. Comparison of modal flexibility found from baseline and roving transducer testing.

6.4.5.1.4 Effect of Disturbance

The effect of disturbing the input apparatus is also investigated. As noted, in the first step of this testing, all force inputs were recorded. The successive steps required the removal and reinstallation of the input apparatus, and in the final step all force inputs were again recorded. The sensitivity of the apparatus to this disturbance is investigated by comparing the force inputs from before and after the disturbance.

This comparison is accomplished by finding the average difference in the frequency domain between the mean force output of each shaker for the before and after cases. The values are reported in the following tables. Table 6.14 shows the results for the entire range of excited frequencies, which is from 4 Hz to 170 Hz. Table 6.15 shows the results for the frequency range from 4 Hz to 60 Hz since it is clear from Figure 6.36 that the response is less consistent at higher frequencies.

Shaker	Mike	Papa	Quebec	Foxtrot
Mean Diff.	49%	16%	11%	12%

Table 6.14. Mean difference in force output between initial shaker installation and final shaker installation, 4 Hz to 170 Hz.

Shaker	Mike	Papa	Quebec	Foxtrot
Mean Diff.	15.6%	2.5%	2.4%	3.6%

Table 6.15. Mean difference in force output between initial shaker installation and final shaker installation, 4 Hz to 60 Hz.

The results reported in the tables show that the uniformity in force input is not significantly affected by the removal and reinstallation of the shakers for frequencies below 60 Hz. Above 60 Hz, the force output is much more sensitive to any setup changes. The tables also show that shaker 'Mike' is far more sensitive than the others. Separate analysis also indicates that 'Mike' has far higher variance from set to set than the other three shakers used in this testing.

Overall, this testing indicates that shakers with low variability in force output from set to set can be removed and reinstalled without a large effect on force output below 60 Hz. For higher frequencies, and for shakers with higher variability, the force output is less reliable.

6.4.5.2 Roving Force Transducer Testing With Eight Shakers

In this test, eight shakers are used in a MIMO setup. Since only four force transducers are available, this testing requires that half of the input forces must be assumed. The testing proceeds as follows: an experimental run is performed with the first four input locations outfitted with force transducers. Next, the transducers are moved to the last four input locations and the experiment is run again. This testing produces 80 capture blocks of data (5 capture blocks per polarity setting x 8 polarity settings x 2 experiments), with the last four input forces assumed for the first 40 blocks and the first four input forces assumed for the second 40 blocks. As before, the data is aligned in time by comparing output accelerations.

The benefit of using more shakers is that better spatial distribution of input, greater total excitation force, and increased volume of redundant information will produce more reliable

results for a real-world structure. However, the light bridge model does not require this much input and better system identification results are not expected. The goal of this testing is merely to demonstrate that using assumed inputs for four of eight shakers can produce reliable results. All system identification parameters are again compared. The APS SIMO burst-random results are used as a baseline against which to compare the outcome of this testing.

6.4.5.2.1 Natural Frequencies, Modal Damping, and Modal Mass

These parameters are compared in Table 6.16. The natural frequencies are in good agreement for many of the modes, but are consistently high for modes above 70 Hz. The damping values show unusually poor agreement with the damping consistently low above 70 Hz. The modal mass values are in reasonable agreement below 70 Hz, except for mode B1. The modal mass is too high for mode B1 and modal flexibility will be significantly affected by this. The peak at this mode appears to be affected by leakage, decreasing the magnitude of the peak and thus increasing modal mass. Leakage is not apparent on any of the peaks of the other modes.

For the roving transducer testing, modes BU3, T4, and BU4 were found by CMIF, but SDOF identification results were significantly in error and are not reported. As with the four input roving transducer testing, the variability in force input at higher frequencies causes the FRFs to be poor. Also as before, the multiple coherence plots indicate that the outputs are not well correlated with the inputs above 60 Hz, which informs the user that modal parameters will not be reliable in this range.

Mode Desc.	Undamped Nat. Freq. (Hz)			Damping Ratio (%)			Modal Mass (lbf/g)		
	APS	TT	Diff.	APS	TT	Diff.	APS	TT	Diff.
B1	8.9	8.8	1%	0.86	0.42	52%	21.4	30.8	44%
T1	10.2	10.4	2%	0.57	1.37	138%	13.0	14.7	14%
B2	32.6	33.3	2%	0.62	0.63	2%	27.3	27.6	1%
T2	36.8	38.4	4%	0.40	0.71	78%	16.3	14.6	10%
B3	67.9	67.9	0%	1.09	1.57	44%	16.5	21.0	27%
BU1	73.9	77.3	5%	0.47	0.12	74%	14.1	65.1	360%
T3	76.3	80.9	6%	0.75	0.17	78%	19.0	29.1	54%
BU2	82.3	84.0	2%	0.66	0.55	16%	18.9	31.1	65%
BU3	105.7	112.0	6%	1.64	**	--	14.7	**	--
B4	110.7	112.7	2%	1.00	0.16	84%	18.5	17.7	4%
T4	131.5	145.0	10%	1.76	**	--	18.7	**	--
BU4	156.3	164.0	5%	0.74	**	--	22.9	**	--

* Mode not found. ** Poor identification.

Table 6.16. Comparison of natural frequencies, damping, and modal mass found from baseline APS SIMO testing and from roving transducer testing.

6.4.5.2.2 Modal Vectors

The MAC values for the roving transducer testing versus the APS SIMO burst-random testing are shown if Figure 6.38. The elements on the diagonal are nearly unity for most of the modes, except for roving transducer modes seven and nine (T3 and B4 respectively). Visual inspection indicates that the T3 mode from the roving transducer testing is superior to that found with the APS SIMO testing. The B4 mode from the APS testing is superior. The off-diagonal terms are generally near zero, except some small amount of correlation between roving transducer mode nine (B4) and APS modes nine and twelve (BU3 and BU4). Overall, the modal vectors found with the roving transducer testing are in good agreement with the baseline modal vectors.

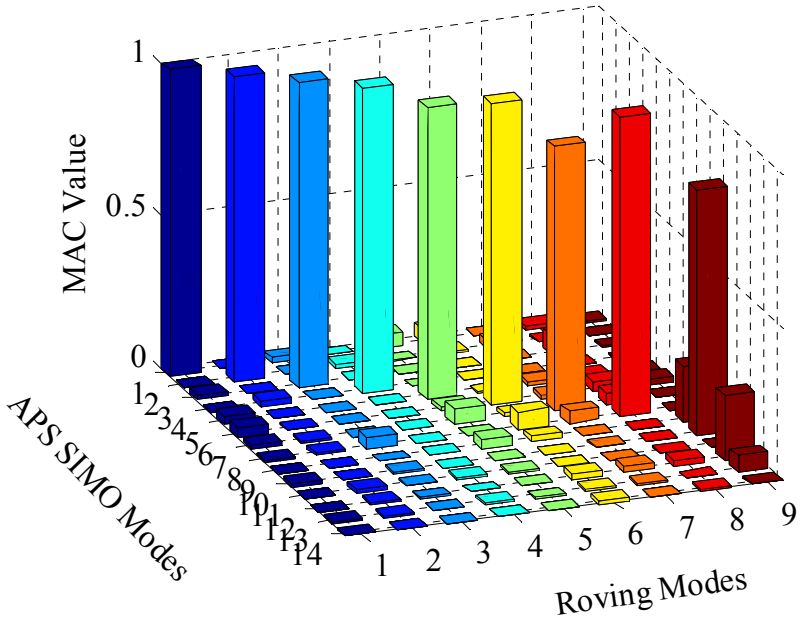

Figure 6.38. MAC values for comparison of modes shapes found from baseline APS SIMO testing and from roving transducer testing.

6.4.5.2.3 Modal Flexibility

The modal flexibility results are compared to the static flexibility matrix. For this testing, the value of D is much better than for the testing using only four shakers. This improvement is primarily due to the much more accurate value of modal mass found for the T1 mode, which strongly affects many off-diagonal terms. The value of D_d is poor and the displacements are poor due to the high value of modal mass found for mode B1.

Desc.	Static Load	Roving
D		4.392
Dd		1.223
DOF 1D*	1.65	1.16
DOF 3D*	1.89	1.28

* Displacement at DOF due to 1 kip load at all DOFs (inches)

Table 6.17. Comparison of modal flexibility found from roving transducer testing.

6.4.5.3 Summary of Roving Force Transducer Validation

The results generally show that the use of roving force transducers results in less accurate system identification than if all inputs are simultaneously measured. However, with only four transducers available, using roving transducers may still be desirable on a real-world bridge. Closer inspection of the results reveals that using roving transducers gives good identification of modes below about 60 Hz. All modes are found, and reasonably accurate values of damping and modal mass are calculated. Since all important modes of real-world bridges are usually below 60 Hz, reliable results may be captured.

It was also found during this testing that some of the TTs have poor uniformity of force output compared to others. For subsequent testing using roving transducers, it is important to select the best shakers of the 16 available. Also, disturbing the input apparatus does affect the force input, and subsequent testing must be planned in such a way that disturbance is minimized. Finally, the available testing software begins recording data at an unpredictable delay time after excitation begins. This requires that the assumed inputs be aligned as best as possible with the actual output measurements during data post-processing. Automated alignment worked well for laboratory data, but the higher noise levels of real-world data may make alignment more difficult.

Overall, the use of roving force transducers should be avoided if possible. When roving is required, results for modes with frequencies above 70 Hz should be considered to be unreliable. Care must also be taken to select the most consistent transducers, and disturbance of the input apparatus must be avoided to the greatest extent possible. If these guidelines are followed, then accurate results can be acquired with roving force transducers.

6.5 CONCLUSION

This chapter discussed various experiments intended to confirm that the TTs can be successfully used for EMA. All experiments were carried out in a controlled laboratory setting on a steel bridge model. TTs were used in SIMO and MIMO test setups with burst-random and multisine excitation signals. The use of roving force transducers was also tested. Baseline system identification was performed with conventional APS SIMO testing to provide a point of comparison for the TT results, and static load testing was performed to provide a baseline flexibility matrix.

SIMO testing with a TT shaker was undertaken to determine how well these devices can excite a structure in comparison to a purpose-built shaker. The result was that all modes were found at nearly identical frequencies to the baseline. Some variation in damping and modal mass was found, but modal flexibility was as good as with the APS shaker. This testing demonstrated that a single TT can successfully excite a laboratory-scale structure.

MIMO testing with four TTs was undertaken to validate that these shakers can successfully function in an array to allow excitation of larger structures. The APS SIMO results were again used as a baseline. The system identification provided accurate natural frequencies and modal vectors, but less accurate modal mass and modal flexibility. The decrease in accuracy was attributed to having only four columns in the transfer function as opposed to fifteen for the SIMO testing. Fewer columns provide less redundant data and the quality of the eFRFs was reduced. Nonetheless, the MIMO testing did demonstrate that an array of TTs can be used to successfully excite a structure from a variety of spatial locations.

The use of the multisine signal for SIMO and MIMO excitation was also tested. This signal has multiple theoretical advantages over the standard burst-random signal, but very little literature exists demonstrating its use in EMA. System identification results were compared from excitation with burst-random signals and with multisine signals. Overall, the multisine signal provided identification results that were just as good as the burst-random results. One issue is that a phenomenon referred to as 'beating' affects the FRFs, and they must be filtered to enable identification of all modes. This phenomenon is not limited to multisine signals, and occurs with other deterministic signals as well. However, filtering is not required for the real-world testing discussed in the next chapter.

Finally, the idea of using roving force transducers was tested. The use of roving transducers allows MIMO testing to occur with fewer transducers than shakers. Testing showed that the TTs have less uniform output and are more sensitive to setup disturbances above about 70 Hz, but that modal identification below this frequency is adequate. Thus, roving force transducers is expected to be a viable test method on real-world structures.

Overall, the testing reported in this chapter indicates that the TTs can be used as excitation devices for experimental modal analysis of structures. These shakers operate well in SIMO and MIMO tests and with stochastic burst-random and deterministic multisine input signals. Validating that similar results can be achieved on a real-world structure must still be explored.

CHAPTER SEVEN

TESTING OF AN IN-SERVICE HIGHWAY BRIDGE

7.1 INTRODUCTION

The tactile transducer excitation system was evaluated on a laboratory bridge model and the results were promising. The capabilities of this system for MIMO EMA are now evaluated on a full-scale, in-service highway bridge. The objective of this test is to evaluate the effectiveness of MIMO EMA, and to determine optimal experimental design parameters for this approach. In the course of this experimentation, other items of interest to be analyzed are:

- Evaluation of the pros and cons of combining data from disparate experiments.
- Evaluation of the effects of traffic disturbances on modal identification.
- Comparison of burst-random and multisine excitation techniques.
- Evaluation of employing roving force transducers in structure excitation.

Combining data from separate experiments is a commonly employed experimental method that aims to improve modal identification by increasing the amount of redundant data in a system transfer function. The danger with this technique is that the data from disparate experiments may be inconsistent due to the time-variant nature of real structures, and the modal identification may thus be inferior. Whether combining data improves modal identification or impairs it is evaluated.

The presence of vehicular traffic adds unmeasured excitation to a structure, while potentially altering the mass and damping. It is not desirable to close bridges to traffic to enable testing, and thus the importance of collecting data without disturbance by traffic is evaluated in this work.

Multisine signals have many theoretical advantages over commonly used excitation signals, but have scarcely been used in testing of civil structures. This work evaluates how the use of multisine excitation compares to the popular burst-random excitation technique. Superior results with multisine would suggest that this signal type should be adopted for MIMO EMA testing of bridges.

Finally, the cost of the dynamic excitation system can be reduced by employing a number of force transducers that is less than the number of operating shakers. A single force transducer has a cost that is similar to the combined cost of a TT shaker and a subwoofer amplifier. There must also be a data acquisition channel available for each force transducer. However, there are attendant technical challenges and data consistency risks if not all force inputs are recorded. Thus, an experiment using eight shakers with only four force transducers is conducted to evaluate the feasibility of roving force transducers on the real-world bridge.

7.2 TEST SUBJECT

The test subject for the experiments described in this chapter is an in-service highway bridge located in Fayetteville, Arkansas. This bridge is selected for testing for several reasons. First, the structural arrangement is highly representative of a large proportion of the national bridge population, thus successful results would indicate that this testing method will be applicable to many other bridges. Second, the close proximity to the University decreases travel time and costs. Third, the underside of the tested span is only about eleven feet above grade and water is not usually present, simplifying installation of testing equipment. Fourth, this bridge has already been evaluated by other dynamic testing approaches, which provides previous results against which the current results can be compared. For all of these reasons, this bridge is attractive as a test specimen.

The bridge was constructed in 1987 and has ten simply-supported spans (Figure 7.1). Each span has a length of 50'-0", a total width of 27'–0", and a roadway width of 24'-0" curb-to-curb. The substructures consist of concrete abutments at the ends and concrete pier bents for all intermediate supports (Figure 7.2). Each bent consists of a pair of square concrete columns spanned by a concrete cap. Bearings composed of sliding steel plates are used to support all beams. At the fixed end of each span, anchor bolts project up from the cap through round holes in steel bearing plates, sole plates, and beam bottom flanges to prevent transverse and longitudinal movement of the beams. The expansion end of each span utilizes a similar arrangement, except slotted holes in the sole plates allow longitudinal translation while still preventing transverse movement (Figure 7.3).

The superstructure of each span consists of four rolled W27x94 girders spaced at 7'-6". These girders support a composite concrete deck of nominal 8-inch thickness. The deck was cast by placing forms tight to the underside of the top flange, and thus the top and sides of each top flange are enveloped by concrete. Each edge of the bare concrete deck has a cast-in-place concrete barrier curb that is 3'-9" tall with expansion joints spaced at 10'-0". These open joints extend 1'-7" down into the barrier.


Figure 7.1. Photographs showing overall view of bridge deck (left) and underside of a typical span (right). (Photos by EVF, Fayetteville, 10/18/13)


Figure 7.2. Photographs showing typical pier (left) and typical abutment (right). (Photos by EVF, Fayetteville, 10/18/13)


Figure 7.3. Photographs showing typical fixed bearing (left) and expansion bearing (right). (Photos by EVF, Fayetteville, 10/18/13)

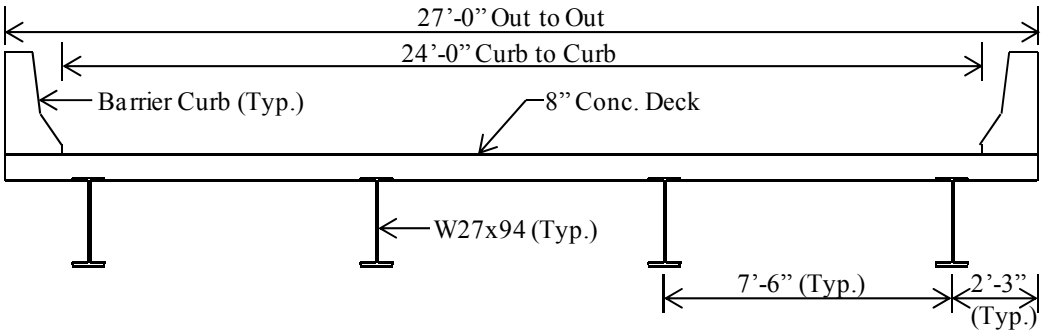

Figure 7.4. Schematic drawing of bridge superstructure section.

7.3 TEST PREPARATIONS

This section describes the work performed in preparation for the field testing. The various sensors are described, the data acquisition setup and equipment are detailed, and the best TT shakers to use are selected. The excitation signal types, amplitudes, and durations are also determined.

7.3.1 Accelerometers

The response of the structure to dynamic input is captured with accelerometers. Twenty accelerometers are used in the bridge testing, and all are type 393C as supplied by PCB Piezotronics, Inc.

As noted for the laboratory testing, the calibration of all accelerometers is checked prior to field testing. The calibration process is the same as described previously, and all sensors used except one are within 1.5% of the factory calibration. Sensor 23499 was found to be 2% off of the factory data, and so the measured sensitivity is used instead of the factory value. The various important characteristics of the accelerometers used are provided in Table 7.1.

Bridge Loc.	Type	Serial No.	Sensitivity (mV/g)	Range (g)	Range (Hz)
1	U393C	8204	1066	±2.5	800
2	393C	23444	997	±2.5	800
3	393C	23500	1097	±2.5	800
4	393C	23525	1081	±2.5	800
5	393C	23608	1061	±2.5	800
6	U393C	8957	1050	±2.5	800
7	393C	23499	1092	±2.5	800
8	393C	23502	1081	±2.5	800
9	393C	23526	1070	±2.5	800
10	393C	23721	1044	±2.5	800
11	393C	23271	1054	±2.5	800
12	393C	23501	1110	±2.5	800
13	393C	23522	1070	±2.5	800
14	393C	23606	1057	±2.5	800
15	393C	23752	1073	±2.5	800
16	393C	23443	1096	±2.5	800
17	393C	23717	1031	±2.5	800
18	393C	23523	1089	±2.5	800
19	393C	23607	1042	±2.5	800
20	393C	23753	1067	±2.5	800

Table 7.1. Accelerometer information for devices used in bridge testing.

7.3.2 Force Transducers

The force input to the structure by a shaker is measured with a dynamic force transducer. These devices return a voltage that is proportional to the average tensile or compressive force that they are subject to. All force transducers are also supplied by PCB, and the relevant data for the four available transducers is provided in Table 6.2.

Type	Serial No.	Sensitivity (mV/lbf)	Range (lbf)	Range (Hz)
208C02	LW36746	47.87	±100	36,000
208C02	LW36262	49.94	±100	36,000
208C02	LW36271	51.29	±100	36,000
208C02	LW36231	49.13	±100	36,000

Table 7.2. Force transducer information for devices used in laboratory testing.

7.3.3 Data Acquisition and Equipment Connectivity

The electronic devices used for the bridge testing are the same as those used for the laboratory testing. The various characteristics of each device, such as number of channels and resolution, are reported in the previous chapter. A schematic connectivity diagram for all of the devices used is shown in **Figure 6.7**. Up to eight shakers and twenty accelerometers are used in the testing.

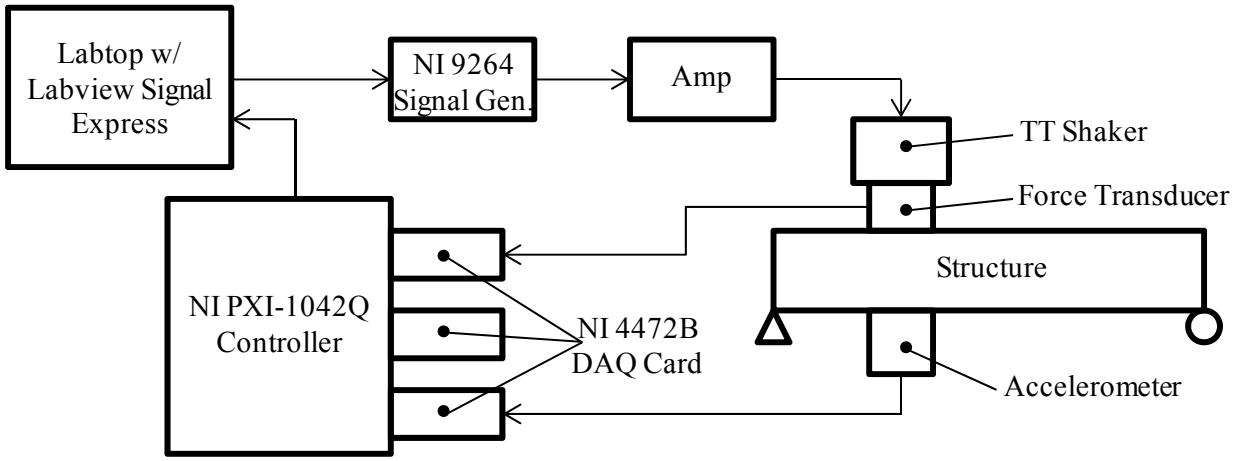

Figure 7.5. Schematic of devices used for bridge testing.

7.3.4 Shakers and Mounting Apparatus

7.3.4.1 Ranking of Shakers by Quality

Sixteen of the TTs have been acquired, but only a maximum of eight are used in the bridge testing. As such, it is necessary to select which shakers to use. It has become apparent during various prior evaluations of these shakers that they do not all have equal quality. The shakers were purchased at various times and from various suppliers, and it is clear that the manufacturer produced the shakers in different production runs. Additionally, during the many uses of these shakers in different testing, certain levels of damage may have accrued. Therefore, it is determined that each shaker should be ranked by output quality and the best performers should be used in the bridge testing.

A testing process is set up that repeatedly sends the same multisine signal to a shaker while the shaker output is measured by a force transducer. The level of uniformity of the output is then used to rank the shakers from best to worst. The details of the testing and the data analysis are provided in the following paragraphs.

A shaker is mounted to the support apparatus used for the laboratory bridge model testing. The apparatus is then connected to a very stiff steel pylon that is not expected to have any natural frequencies in the range of the input signal. A multisine signal with excitation from 4 Hz to 70 Hz and a length of 25 seconds is produced and is input to the shaker seven times in a row without pause. The force output of the shaker is recorded, saved, and processed.

The processing begins by eliminating the first and last data blocks, resulting in five capture blocks. If the shaker operates perfectly (and if there was no noise in the system) then the five capture blocks will be identical. Of course the devices are not perfect, and the amount of imperfection is quantified by comparing the five capture blocks to each other. A single number that indicates the relative quality of signal reproduction is desired so that the shakers can simply be ranked from best to worst.

The first step in condensing the data to a single number is to transform the capture blocks from the time domain to the frequency domain. The data capture rate was 1000 Hz and so the transformed data spans the frequency range of 0 Hz to 500 Hz. The transformed data is truncated so that only the excited range of 4 Hz to 70 Hz is maintained, and the absolute value of the data is taken so that only the magnitude at each frequency line is preserved.

For each frequency line, the mean magnitude is now found, and the absolute value of the difference of each capture block from the mean is calculated at each frequency line. The

differences are summed for the five capture blocks and the total magnitude of the difference is normalized by the mean magnitude of the force at each frequency line. The normalization is performed so that each frequency line has equal importance. This calculation is illustrated by the equation below, and is applied at each frequency line.

$$F_{mean} = \sum_{n=1}^{5} \frac{F_n}{5} \qquad \text{Equation 7.1.}$$

$$Total\ Difference = \sum_{n=1}^{5} \frac{|F_{mean} - F_n|}{F_{mean}} \qquad \text{Equation 7.2.}$$

Where:

F_n = absolute value of the force output at a frequency line for the nth capture block (lbf/Hz).

This value of total difference is a positive real number at each frequency line. The mean of the total difference is now found for all frequency lines, which results in a single number per shaker. This number is the mean normalized variance of the shaker force output, and essentially represents how uniform the force output of the shaker is over the range of 4 Hz to 70 Hz. The results for the sixteen shakers are provided in Table 7.3.

Shaker Name	Rank	Mean Norm. Var.	Shaker Name	Rank	Mean Norm. Var.
O	1	0.99%	A	9	2.25%
E	2	1.00%	B	10	2.43%
P	3	1.01%	D	11	2.44%
K	4	1.14%	C	12	2.47%
H	5	1.41%	N	13	2.49%
F	6	1.46%	M	14	3.37%
I	7	1.65%	J	15	3.54%
G	8	1.84%	L	16	3.88%

Table 7.3. Ranking of shakers by mean normalized variance of force output.

These rankings indicate that the worst shaker has about four times more variability in force output than the best shaker. To demonstrate how significant this is, representative figures are prepared. The figures show the magnitude of the force output in the frequency domain for the five capture blocks of data. Figure 7.6 is focused on a small but representative frequency band in the vicinity of 11 Hz, and Figure 7.7 is focused in the vicinity of 50 Hz. Both figures clearly demonstrate that the best shaker has very clean and uniform force output, while the worst shaker adds significant noise to the force output. The plots for the best shaker also show that there is a steady decrease in force output as the device warms up over the duration of the testing.

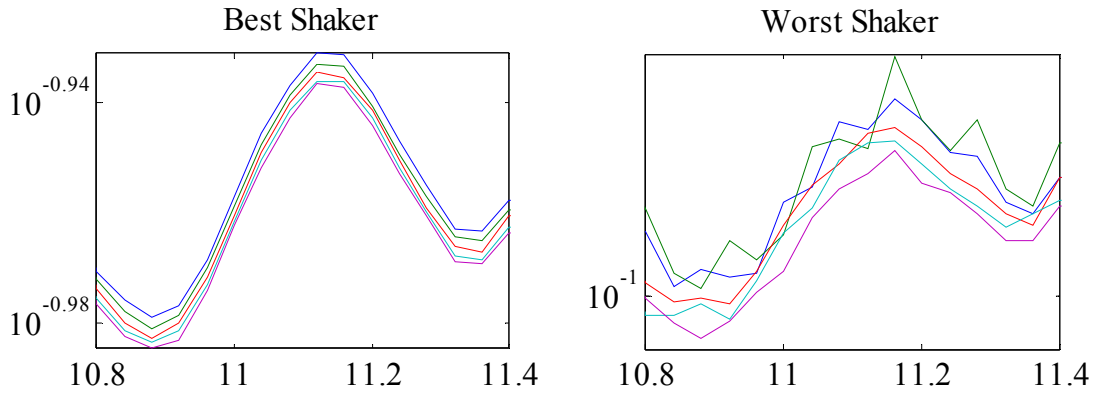

Figure 7.6. Best and worst shaker performance near 11 Hz.

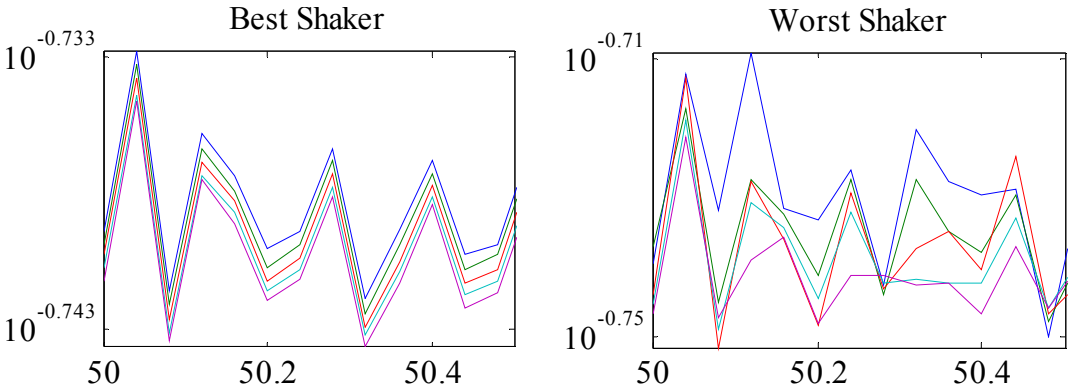

Figure 7.7. Best and worst shaker performance near 50 Hz.

The four top-ranked shakers are used for the bridge testing when only four shakers are used, and the eight top-ranked shakers are used for the roving force transducer testing.

7.3.5 Preparation of Excitation System for Field Use

Field ruggedized boxes were constructed for transport of the TT shakers, and for housing the amplifiers. These boxes are necessary for protecting the system components during the rigors of field use. A photograph of an amplifier box is shown in Figure 7.8. Each box is capable of driving four of the TTs.

Figure 7.8. Photograph of field ruggedized amplifier enclosure. (Photo by EVF, dynamics lab, 10/18/13)

7.3.6 Excitation Signals

Multisine and burst-random excitation signals are used for the bridge testing for the same reasons as described for the laboratory testing. Multisine signals have a number of theoretical advantages that should provide superior results, while burst-random signals are a popular and traditional choice for structure identification. However, several characteristics of the signals need to be selected specifically for the bridge. These characteristics are signal length, frequency range of excitation, and signal amplitude.

7.3.6.1 Length

The signal length is inversely proportional to the frequency resolution. Longer signals provide higher resolution while shorter signals provide lower resolution. Higher resolution is generally

desirable so that closely spaced modes can be better identified, but higher resolution requires increased testing time.

There are two main reasons why shorter signals are desirable for the bridge testing. First, traffic control is not used during testing and vehicles cross the bridge at frequent intervals. Data sets that include vehicle crossings provide far less accurate results than sets without crossings, and thus multiple sets without crossings must be captured. Shorter signal durations provide a benefit by increasing the probability of an individual set being captured without disturbance by traffic.

The second reason why shorter signals are desirable is because the structure is not time-invariant. As time passes, the temperature and other environmental factors change, and the bridge properties are affected by this. Thus, the more time that the testing requires, the more inconsistent the data may be. The testing is planned to be completed within one day, and the signal length to use is impacted by this decision.

Overall, signal lengths for both multisine and burst-random testing are set at 25 seconds. This signal length provides a frequency resolution of 0.04 Hz, and is expected to allow all testing to be completed in a 7-hour window. It is recognized that if the resolution seems to be too low during data processing, two sets can be appended to each other increasing the resolution to 0.02 Hz. Of course, this improvement in resolution would come at the cost of less noise reduction due to fewer averages.

7.3.6.2 Frequency Range

The range of frequencies to excite with each signal type must also be selected. For the multisine signal, an integer number of discrete frequency lines are selected in order to create the signal. Thus there is both a frequency resolution and a frequency band of excitation to select.

For the frequency band, the minimum is set to satisfy two considerations. First, it is known that the shakers do not operate well at frequencies below about 5 Hz. Second, previous testing indicated that the lowest mode of the bridge exists at about 7 Hz. Thus, 4 Hz is selected as the low end of the excitation band. This frequency should allow the TTs to operate reasonably well, and should provide enough bandwidth below the lowest mode for determination of the damping and modal mass associated with that mode.

The upper limit of the frequency band is selected such that all modes of interest are within the excited band. Based on previous results, 70 Hz is selected as the upper limit. The resolution is determined by the signal and is defined to match the resolution of the FFT of the output data. Thus, excitation lines are spaced at 0.04 Hz from 4 Hz to 70 Hz.

For the burst-random signal, it is possible to control the band of excitation by applying filters to each unique realization. However, designing and applying a filter adds complexity to the testing. Also, the TTs essentially filter the output automatically by the way they respond to various frequencies. This greatly reduces force output below about 5 Hz, and gradually reduces the force output at frequencies above about 110 Hz. Thus, the realizations of random signals are not altered, and excitation of all frequencies is theoretically permitted.

7.3.6.3 Amplitude

The amplitude of the input to the shakers determines the force output, up to the maximum capacity of the shakers. In the laboratory testing, the force output was limited to prevent excess excitation of the light model structure. For the bridge testing, the mass of the structure precludes the issue of excess input. It is assumed that the maximum force that the shakers can produce will generate the best results by maximizing SNR. The force output is limited by the stroke of the

shakers at frequencies below about 20 Hz, and is limited by the power capacity of the amplifiers and shakers above this frequency.

For the multisine signal, the amplitude can be selected individually for each frequency line. This is highly beneficial since the stroke can be controlled at low frequencies while the full potential of the shakers can be utilized at higher frequencies. To set the amplitudes for lower frequencies, experiments are conducted to identify the maximum signal amplitude that does not cause the stroke to be exceeded. To set the amplitudes for higher frequencies, experiments are conducted to identify the maximum signal amplitude that results in high force but does not cause noticeable distortion in the force output.

For the burst-random signal, the amplitude over various frequency ranges can be controlled by using filters. The application of a high pass filter would potentially allow larger forces at higher frequencies while helping to prevent stroke exceedance at lower frequencies. Testing revealed that high total force output could be achieved without using filters, and thus filtering of each realization is not performed. The amplitude to use for all realizations is instead selected as the largest gain possible that results in only infrequent stroke exceedance (on average, stroke is exceeded less than once per three realizations).

7.3.6.4 Signal Summary

The multisine signal that is generated for use in bridge testing is illustrated. Figure 7.9 shows the relative magnitude of the signal over the excited frequency band. The time-domain version of the multisine signal is generated by the NI 9264 with a maximum amplitude of 200 mV. This signal is then increased by approximately 22 dB by the amplifiers which drive the TTs. Thus, the TTs receive a peak signal amplitude of approximately 30 V. Actual peak forces are approximately 25

pounds throughout the bridge testing. Figure 7.10 shows a typical example of the force output produced by a TT shaker during the actual bridge testing. The actual force output matches the input signal well.

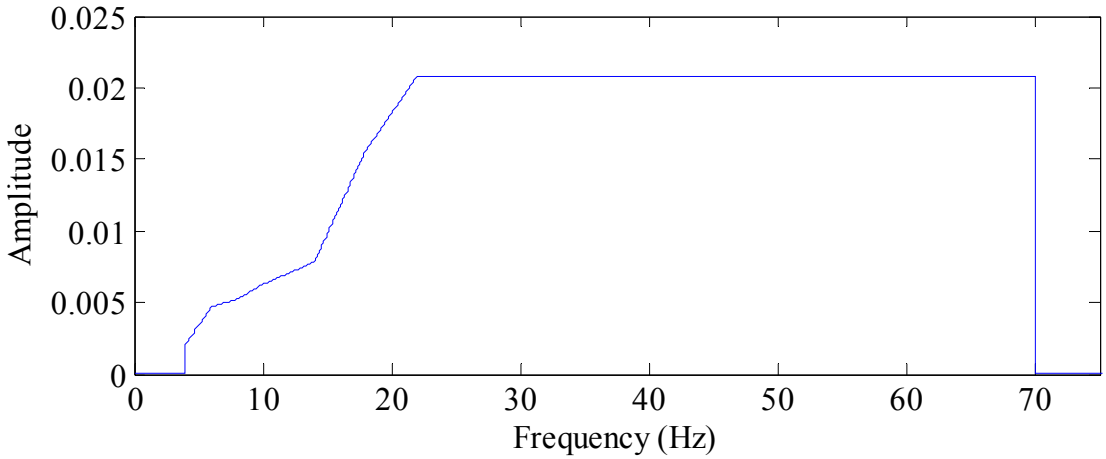

Figure 7.9. Magnitude of multisine signal used for bridge testing in frequency domain.

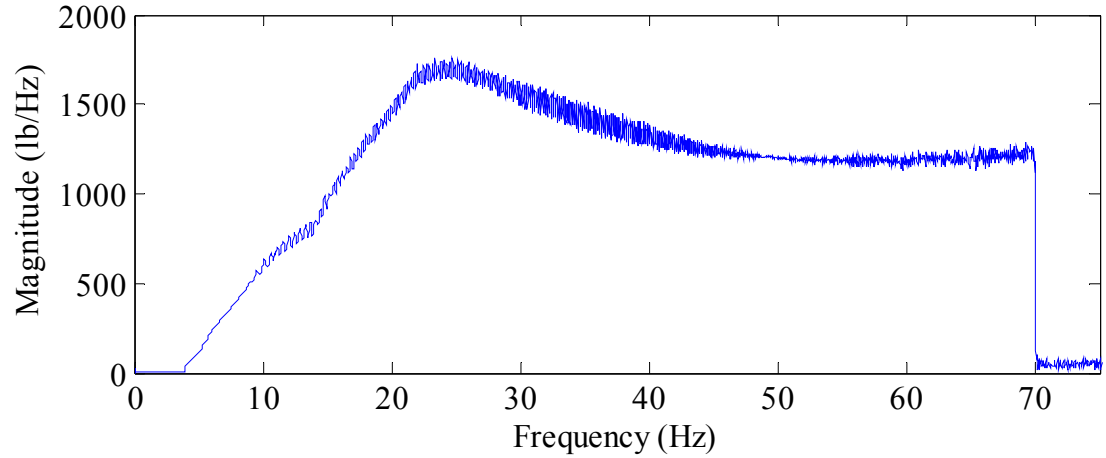

Figure 7.10. Typical recorded force output of a shaker in the frequency domain due to the multisine signal input.

Figure 7.11 shows how the phase of the multisine signal varies over a representative segment of the excited band. Figure 7.12 shows a typical example of the phase of the recorded force output from the bridge testing. As was identified during laboratory testing of the amplifiers and shakers, there is a phase shift caused by the devices. However, the phase reproduction is excellent.

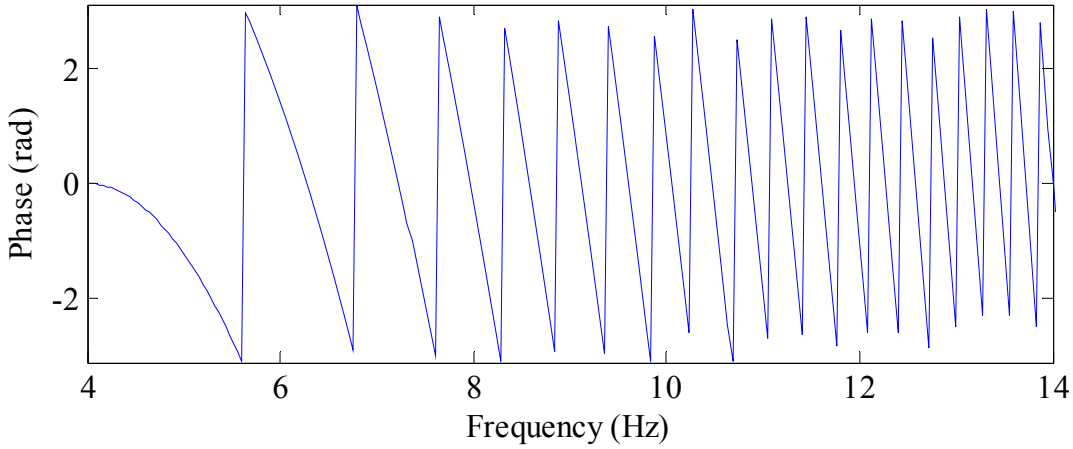

Figure 7.11. Sample of phases for multisine signal used for bridge testing.

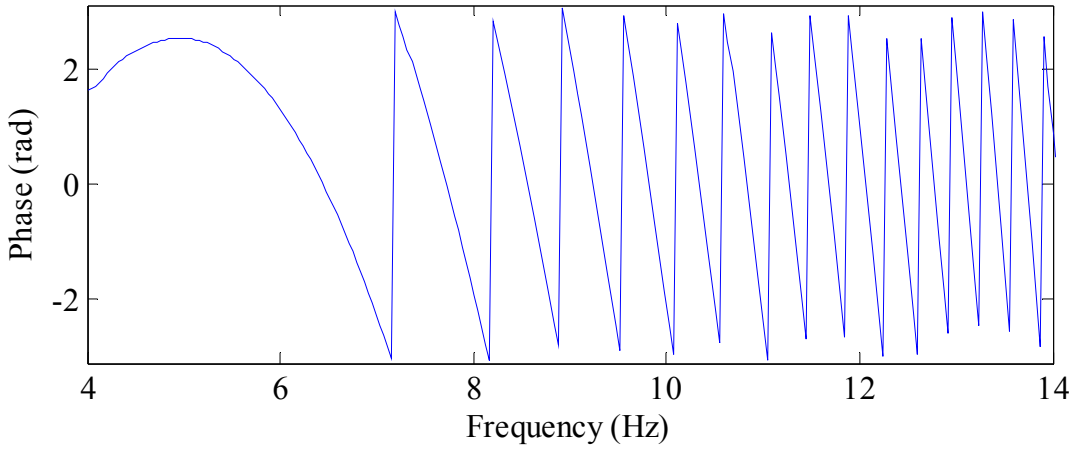

Figure 7.12. Sample of phases for typical recorded force output due to the multisine signal input.

The burst-random signals used in testing are obviously unique for every realization. Samples are shown for illustrative purposes. The beginning 0.5 seconds and the final 5 seconds of the signal are set to zero to reduce leakage. This leaves 19.5 seconds of excitation per 25-second data set (Figure 7.13). A single realization of a random signal is well known to result in unequal excitation to various frequency lines, as demonstrated in Figure 7.14. Many data sets are captured and averaged to result in more equal excitation. Figure 7.15 shows an example of the recorded force output of a shaker from the actual bridge testing. The shape of the plot demonstrates again that the TTs cannot provide significant force below about 5 Hz, that the force

output peaks between 10 Hz and 20 Hz, and that the force decreases at higher frequencies similar to what is seen for the multisine signal in Figure 7.10.

Generation of the burst-random realizations is performed using the Signal Express software from National Instruments, and an RMS level of 80 mV is selected as a maximum value that seldom causes stroke exceedance. The actual peak voltage varies for every realization. As with the multisine signals, the amplifiers provide a gain of about 22 dB. Actual peak forces produced by the TT shakers are approximately 35 pounds throughout the bridge testing.

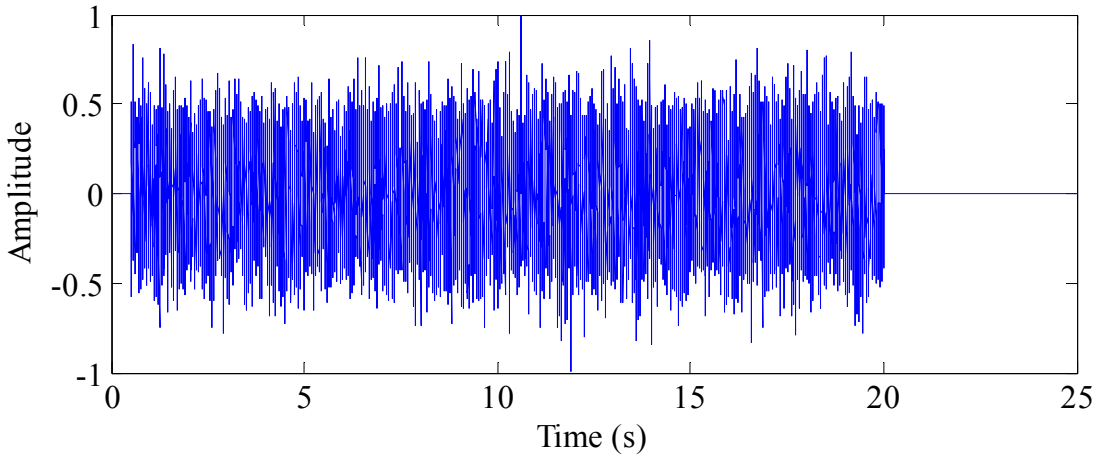

Figure 7.13. Sample of a burst-random signal in the time domain.

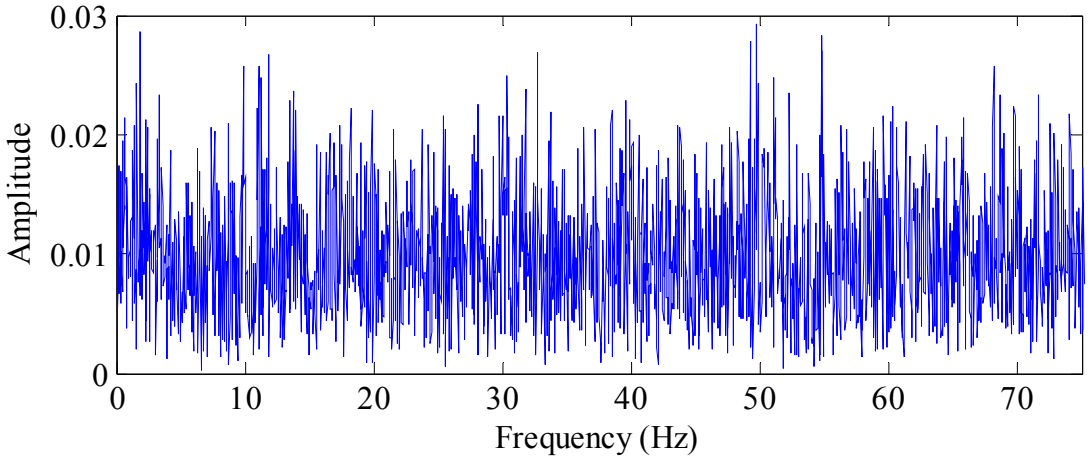

Figure 7.14. Sample of a burst-random signal in the frequency domain.

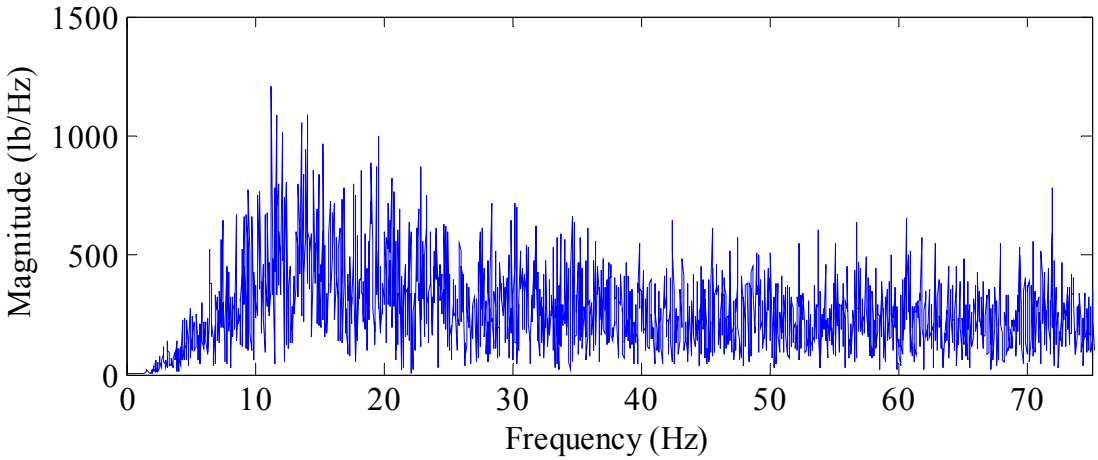

Figure 7.15. Typical recorded force output of a shaker in the frequency domain due to a burst-random signal input.

7.4 TESTING PROCEDURE

The best possible outcome of the testing is to capture modal properties of the structure that are accurate and complete. The testing procedure is established by choosing test parameters that have the highest probability of leading to accurate and complete modal data, while constrained by the available time and equipment. Unlike with the laboratory testing, the in-service bridge has no attributes that can be modified to get better results. Only the setup and arrangement of the testing equipment is variable. The procedure described in this section outlines the choices made in regards to the controllable variables of the bridge testing.

7.4.1 Sensor Locations

The available data acquisition system provides 24 input channels, of which 4 will be used for the available force transducers. This leaves 20 channels available for accelerometers. The placement of the accelerometers affects the quality of the modal data that can be captured. Since we are only interested in global vertical modes of the structure, all sensors will be oriented vertically. The selected accelerometers have strong magnetic bases, and thus they will be placed on steel

elements, i.e. the girders. Also, as has been discussed previously, a few guidelines apply to selecting sensor locations:

- Avoid symmetric placement
- Avoid placement at obvious nodal locations
- Place in a spatially well-distributed arrangement

This bridge is essentially symmetric about midspan, and thus obvious nodal locations for the second, third, and fourth order bending modes will be avoided. Also, the sensor placement will not be symmetric about midspan. Finally, the sensors will be relatively evenly distributed across the structure. Figure 7.16 schematically shows the sensor locations selected in consideration of the criteria discussed. Note that the sensors are organized into lines transverse to the bridge, labeled 'B' through 'F'. Figure 7.17 presents a photograph of the typical method of accelerometer installation for the testing.

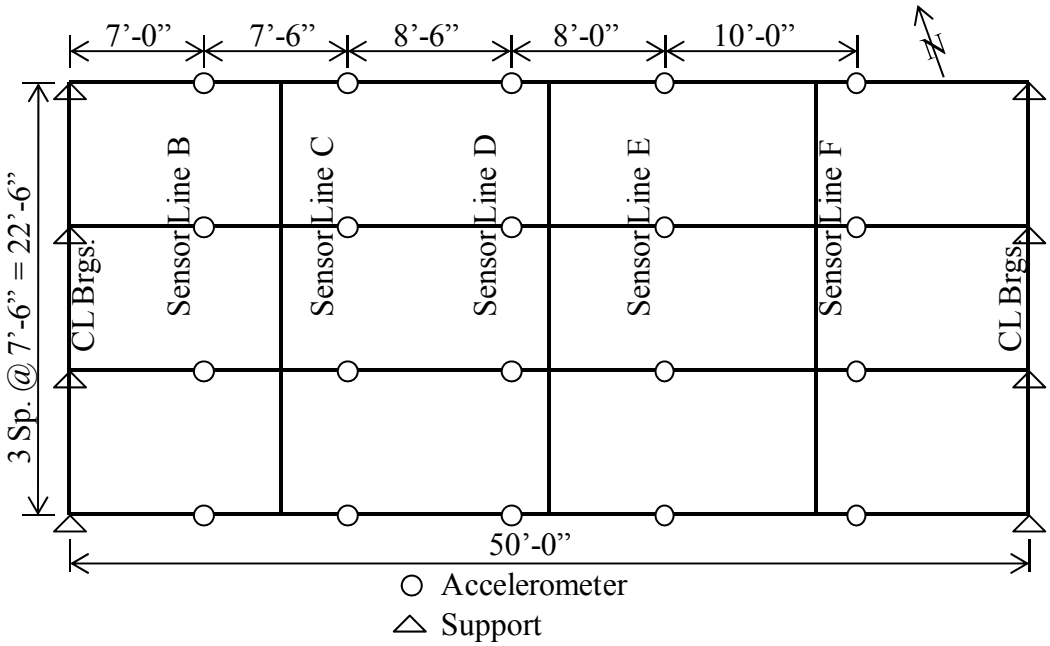

Figure 7.16. Spatial arrangement of accelerometers shown on bridge framing plan.

Figure 7.17. Photograph of typical accelerometer installation. (Photo by EVF, Fayetteville, 10/18/13)

7.4.2 Shaker Locations

The locations at which to impart excitation are largely driven by the sensor locations. It is best to excite the structure at the same DOFs where the outputs are being measured. This allows the right singular vectors to be used in the generation of eFRFs. However, with only four force transducers available, the spatial distribution of excitation is limited. Two different methods will be used considering this limitation; a method that only uses four shakers, and a method that uses eight shakers.

7.4.2.1 Four-Shaker Testing with Roving Force Transducers

This testing consists of using only the best four shakers, and all input forces are recorded during every experiment. It is known that excitation at different DOFs excites various modes to different levels. For this reason, various experiments are performed with the shakes in different locations so that all output DOFs are eventually excited. The shakers are organized into a transverse line corresponding to the transverse lines of sensors, ‘B’ through ‘F’. The first experiment has four shakers along sensor line ‘B’, the second experiment has the shakers along line ‘C’, etc. While the shakers are installed along a line, data sets are collected for multisine excitation and then for burst-random excitation.

In data processing, it is possible to create a larger transfer function by simply assembling additional columns from the separate four-shaker experiments. This approach is commonly used in MRIT testing. The success of this method can be evaluated by comparison to results from transfer functions from a single experiment.

7.4.2.2 Eight-Shaker Testing

This testing consists of using eight shakers in a spatially well-distributed arrangement. The force output from four of the shakers is recorded in one experiment, then the force transducers are moved and the force output from the other four shakers is recorded in a second experiment. This results in a transfer function with eight columns. Only multisine excitation is used in this testing. The spatial arrangement of the shakers is shown in Figure 7.18.

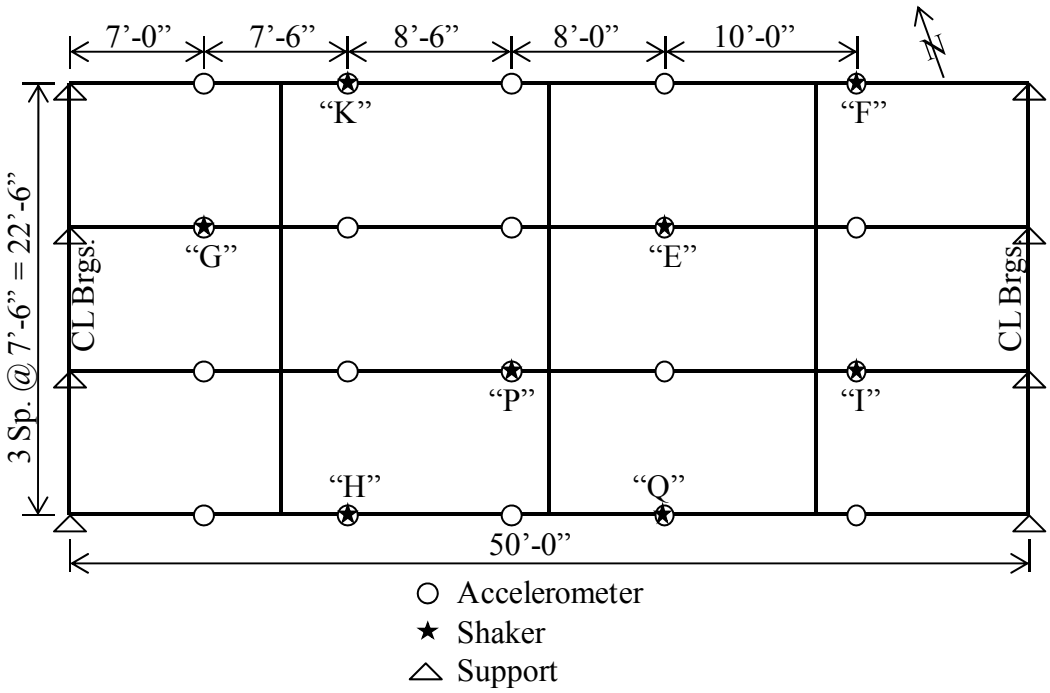

Figure 7.18. Spatial arrangement of shakers shown on bridge framing plan for testing using eight shakers.

7.5 DATA CAPTURE AND PROCESSING METHODS

This section discusses various issues that impact the methods used to capture and process the data from the bridge testing. These issues generally consist of vehicle crossings during data collection, the methods by which data from disparate experiments can be combined, the technical issues with using roving force transducers, and the explicit manner in which data from this testing is processed.

7.5.1 Traffic Issues

Traffic was anticipated during testing since the bridge would not be closed. The test plan was created with this in mind. The Signal Express software was set up to continuously record data sets for both multisine and burst-random testing. For multisine, ten clean data sets per polarity setting per experiment are desired, and the software was configured to collect fifteen sets per polarity setting. Thus, one car crossing every 75 seconds was expected. Twenty clean data sets per experiment are desired for burst-random testing, and the software was configured to collect 25 sets automatically.

While the software was running and collecting measurements, each vehicle crossing was recorded by hand and the data sets affected by the crossing were noted. This enabled additional sets to be collected to meet the minimum number of clean sets desired. Actual traffic was far in excess of expectations, and 30 multisine sets were collected per polarity setting for most experiments. Many extra burst-random sets were also recorded due to the heavy traffic volumes. In retrospect, the testing should have been planned to occur at night when traffic is greatly reduced. Future testing using this method should be performed at night to be able to capture the most data in the shortest time.

In post-processing, it was necessary to determine which data sets are best and should thus be used for system identification. The field notes were helpful, but it was found that the free vibrations caused by vehicle crossings took longer to damp out than expected. Thus, some sets thought to be clean are actually affected by traffic. It is determined that the data sets should be sorted from best to worst, and the best can then be used for further processing. The multisine data and the burst-random data must be sorted differently because of the difference in the signal types. An algorithm was developed to perform the sorting work for each signal type.

7.5.1.1 Multisine Data Sort

The multisine data is the result of imparting the same excitation 15 times in a row without pause. Because of this, the output accelerations for all 15 sets should be identical except for the effects of the transient at the start of excitation, noise in the system (including environmental excitation), and traffic excitation. The transient error is taken care of by eliminating the first set. The noise and environmental errors are small compared to the level of excitation. The traffic, however, causes large disturbances to the affected data sets. These observations lead to a method for sorting the sets.

The first step is to identify the best set (of 30 sets for most polarity settings). This is accomplished by using the field notes of vehicle crossings. The set that had the greatest amount of settling time after the most recent crossing is selected for use as a baseline against which to compare all other sets. The output measurements at DOFs 2, 8, and 14 are selected as representative of all 20 DOFs.

Next, all data sets are transformed to the frequency domain and only the magnitude at each frequency line within the range of excitation is kept. The percent difference between the baseline

set and all sets is found at each frequency line. The mean percent difference for all frequency lines is then found. Finally, to make the numbers more meaningful, they are normalized. A second-best set is selected by analysis of the field notes, and the mean percent difference for all sets is normalized by the mean percent difference for this set.

At this point, each data set is represented by a single number that expresses the level of agreement of that set to the baseline set. The lowest numbers indicate the sets the most similar to the baseline set, and high numbers indicate poor agreement with the baseline set. The method makes it easy to sort the sets into three groups:

- Unaffected by traffic
- At least one vehicle crossed
- No vehicle crossed, but set is affected by a recent crossing

Sample results are shown in Table 7.4 for polarity setting four with excitation at sensor line 'B'. The set ranked first is of course the set used as a baseline. The set ranked 8th was thought to be the second-best set, and it has a difference of 1% from the baseline set due to normalizing. The best ten sets all have very little difference from the baseline set, and are not affected by traffic. Sets ranked 11th through 17th are significantly different from the baseline set, and have been affected by traffic. Comparison with the field notes shows that these sets did not include a vehicle crossing, but did begin shortly after a crossing. Sets ranked 18th and worse all include at least one vehicle crossing per the field notes, and this is clearly indicated in their normalized percent difference from the baseline set.

Polarity 4 Data Set Analysis								
			Baseline Set:		23			
			Comp Set:		28			
Rank	Diff. (%)	Set No.	Rank	Diff. (%)	Set No.	Rank	Diff. (%)	Set No.
1	0.0	23	11	4.0	11	21	243	30
2	0.3	21	12	5.2	16	22	245	7
3	0.4	19	13	7.7	3	23	311	6
4	0.5	20	14	8.1	27	24	346	25
5	0.5	18	15	26	10	25	436	29
6	0.6	22	16	34	5	26	440	14
7	0.9	12	17	35	2	27	451	8
8	1.0	28	18	111	26	28	458	15
9	1.4	17	19	174	9	29	647	1
10	1.6	4	20	210	24	30	785	13

Table 7.4. Sample results for ranking data sets to identify traffic disturbance.

The magnitude of the difference is further illustrated in Figure 7.19. These three plots are focused in on a single peak in the output FFT that is due to a mode. The baseline set is shown in all three plots as a comparison point for the other sets. The left plot also shows the 10th ranked set, and the difference between it and the baseline set is nearly invisible. The middle plot shows the 17th ranked set, and although the peak is little affected, the effects of traffic are noticeable in the lower segments. The right plot shows the 30th ranked set, which is significantly different than the baseline set. This data is from DOF 2, polarity setting 4 of the experiment with input at sensor line ‘B’.

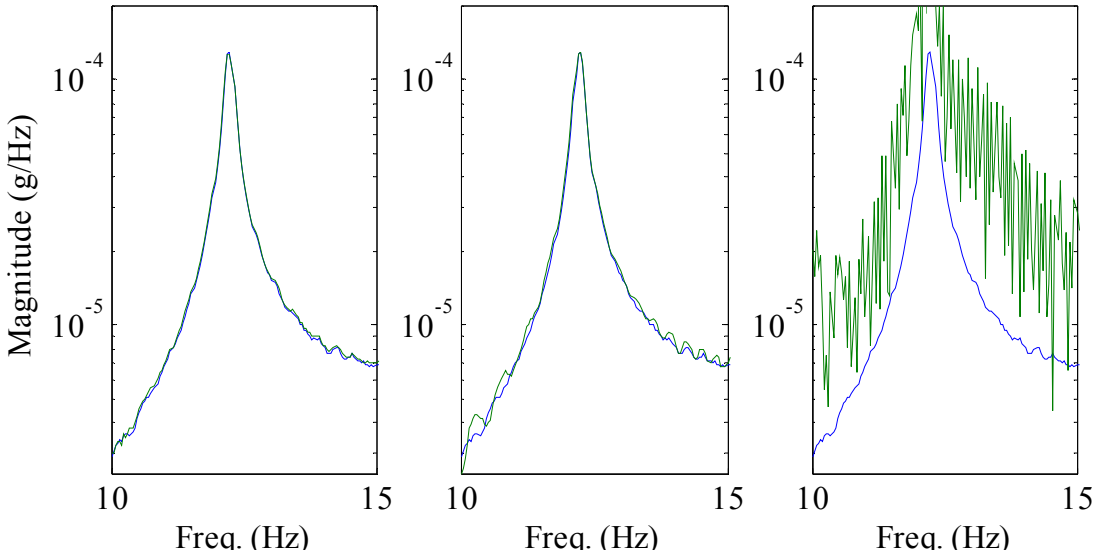

Figure 7.19. Plots showing difference in magnitude of FFT with baseline data set 23 shown in all. Left plot shows set ranked 10th, middle plot shows set ranked 17th, and right plot shows set ranked 30th.

Overall, the method developed for ranking the multisine data sets is simple and successful. This ranking process is performed for each polarity setting and for input at each line of sensors. The ten data sets least affected by traffic are selected and used in further processing.

7.5.1.2 Burst-Random Data Sort

For the bridge testing with burst-random signals, traffic is an equally significant issue. However, since every realization is unique, a different method for selecting the cleanest sets must be developed. It is recognized that the total energy input into the bridge is about the same for all sets without traffic, but is higher when traffic also excites the structure. Thus, the RMS level of the output accelerations is used for ranking the data sets.

An algorithm is written that calculates the RMS level of each data set by using the 2-norm. The data sets are then ranked from lowest RMS level to highest RMS level. The 20 data sets with the lowest RMS level are then used in further processing. This method is far less sensitive than the

one used for multisine excitation, but does prevent data sets that include traffic crossings from being included. Typical ranking results are shown in Table 7.5. The RMS level is normalized by the lowest value found, and the 20th ranked set has total output accelerations that are 6% higher than the lowest set. The sets ranked 27th and worse have RMS values that are far higher and did include a vehicle crossing per the field notes.

Excitation Line B Data Set Analysis								
Rank	Norm. RMS Level	Set No.	Rank	Norm. RMS Level	Set No.	Rank	Norm. RMS Level	Set No.
1	1.00	6	12	1.05	22	23	1.09	29
2	1.03	24	13	1.05	26	24	1.14	21
3	1.03	4	14	1.05	7	25	1.15	3
4	1.03	18	15	1.05	13	26	1.18	16
5	1.04	31	16	1.05	5	27	1.75	15
6	1.04	23	17	1.05	33	28	1.99	27
7	1.04	1	18	1.06	10	29	2.01	28
8	1.04	25	19	1.06	30	30	2.11	20
9	1.04	11	20	1.06	17	31	2.76	8
10	1.04	19	21	1.07	12	32	2.90	14
11	1.04	32	22	1.09	9	33	3.40	2

Table 7.5. Sample results for ranking burst-random data sets to exclude traffic disturbance.

7.5.1.3 Summary of Traffic Issues

The actual traffic volumes during bridge testing exceeded expectations. Also, the excitations caused by vehicle crossings did not damp out as quickly as expected. Because of this, many extra data sets had to be collected so that the minimum desired number of clean sets could be captured. For multisine excitation, the 10 cleanest sets were found by comparing each data set to a known clean data set. For burst-random excitation, the 20 least affected sets were found by calculating the RMS level of each set and ranking the sets from lowest RMS level to highest RMS level.

Both methods clearly differentiate sets with traffic crossings from sets without traffic crossings. System identification proceeds using only the cleanest data sets.

7.5.2 Analysis Groups

Only four force transducers are available for the bridge testing. This generally constrains the testing such that only four shakers can be used in any single experiment since all input forces must be known. A test method is developed that uses four shakers spatially arranged along a single transverse line of accelerometers per experiment. There are five transverse lines of accelerometers, and five experiments are performed with the shakers at a different transverse line per experiment. The testing proceeds with the shakers first positioned along line 'B', then line 'C', line 'D', line 'E', and finally line 'F' (Figure 7.16).

The testing method generates FRFs for all 400 combinations of input DOFs and output DOFs (20 inputs x 20 outputs). With these 400 FRFs, there are many possible ways to construct a transfer function that consists of some subset of the FRFs. There are two considerations that affect the choice:

- More columns in the transfer function increases the amount of redundant information and thus improves the accuracy of modal parameters.
- The time elapsed between experiments makes the data inconsistent and thus the combination of columns from different experiments may decrease the accuracy of modal parameters.

Since these two considerations provide conflicting guidance on whether more columns are better, several combinations of columns are used and system identification is undertaken on each. The resulting modal parameters are then compared.

Table 7.6 lists the nine combinations of excitation lines that are used to construct transfer functions. These same combinations are used for both multisine and burst-random excitation. The rationale for these combinations is as follows:

- Single line of inputs – the data is consistent since all input and output data is captured simultaneously. However, excitation along a single line may not adequately excite some modes, and there is less redundant data in the transfer function.
- Three lines of inputs – the elapsed time between the first and last line excited is not great, and the risk of data inconsistency is thus not very high. It is also more likely that all modes of interest will be excited, and there is more redundant data in the transfer function.
- All input lines – the elapsed time between the first and last line excited is the greatest, and thus the risk of data inconsistency is the greatest. However, the maximum amount of redundant data is available, and the greatest probability of exciting all modes is realized.

Analysis Group	Included Inputs	Included Outputs
1	Line 'B'	All
2	Line 'C'	All
3	Line 'D'	All
4	Line 'E'	All
5	Line 'F'	All
6	‘B' + 'C' + 'D'	All
7	‘C' + 'D' + 'E'	All
8	‘D' + 'E' + 'F'	All
9	All Lines	All

Table 7.6. Combinations of excitation locations used to form transfer functions for system identification.

The method by which the transfer function is constructed with data from different experiments is simple. A transfer function with 20 rows for the 20 output DOFs and 4 columns for the 4 input

DOFs is constructed from the FRFs for each of the five experiments. The arrangement of the transfer function from a single experiment is demonstrated in Figure 7.20. The data within each of these transfer functions is consistent. Larger transfer functions are constructed by including the columns of FRFs from the desired input lines. The numbering system of the DOFs used for the bridge testing requires the columns from separate experiments to be interleaved as shown in Figure 7.21. The FRFs from separate experiments may be inconsistent due to the environmental changes that occur during the elapsed time between the execution of the experiments.

$$\begin{bmatrix} FRF_{1,1} & FRF_{1,6} & FRF_{1,11} & FRF_{1,16} \\ FRF_{2,1} & FRF_{2,6} & FRF_{2,11} & FRF_{2,16} \\ \vdots & \vdots & \vdots & \vdots \\ FRF_{20,1} & FRF_{20,6} & FRF_{20,11} & FRF_{20,16} \end{bmatrix}$$

Figure 7.20. Transfer function for data from a single experiment (line 'B' excited).

$$\begin{bmatrix} FRF_{1,1} & FRF_{1,2} & FRF_{1,6} & FRF_{1,7} & FRF_{1,11} & FRF_{1,12} & FRF_{1,16} & FRF_{1,17} \\ FRF_{2,1} & FRF_{2,2} & FRF_{2,6} & FRF_{2,7} & FRF_{2,11} & FRF_{2,12} & FRF_{2,16} & FRF_{2,17} \\ \vdots & \vdots & \vdots & \vdots & \vdots & \vdots & \vdots & \vdots \\ FRF_{20,1} & FRF_{20,2} & FRF_{20,6} & FRF_{20,7} & FRF_{20,11} & FRF_{20,12} & FRF_{20,16} & FRF_{20,17} \end{bmatrix}$$

Figure 7.21. Transfer function with interleaved data from two experiments (line 'B' combined with line 'C').

7.5.3 Bridge Testing with Eight Shakers and Roving Force Transducers

An experiment is also performed using eight shakers although only four force transducers are available. The methodology for such an experiment was described for the laboratory model and the laboratory results were promising. For the bridge testing, the eight shakers are arranged in a spatially well-distributed manner and multisine excitation is applied to all shakers. Four of the shakers are outfitted with force transducers. Eight different polarity settings of input signal are used to enable calculation of the FRFs. The force transducers are then moved to the other four

shakers and the exact same experiment is undertaken a second time. These two individual parts of the experiment are referred to as 'part 1' and 'part 2' in the following discussion.

Assuming that the force input from each shaker is not affected by the relocation of the force transducers, then the force input would be the same whether the transducers are present or not. Thus, the force recordings from part 2 of the experiment would be applicable to the unmeasured shakers from part 1 of the experiment and visa-versa. This experimental method allows for more simultaneous force inputs than the available number of force transducers.

A complication arises in this method due to the behavior of the Signal Express software. A separate run of the software is used for each polarity setting, and a small but random amount of time passes after the software starts to generate the excitation signals but before it starts to record the force and acceleration data. Thus, the force data from part 1 is not aligned with the acceleration data from part 2. As discussed previously for the similar laboratory testing, an algorithm is developed that finds the best alignment of the acceleration data for part 2 compared to part 1 for each polarity setting.

7.5.4 Identification of Modal Parameters

A complicated structure like a bridge presents many challenges in system identification. Noise, local modes, and transverse modes all affect the data and make it more difficult to isolate the desired global vertical modes of the structure. These spurious modes must be eliminated through the identification process, and various methods are used to determine which modes to discard.

7.5.4.1 Step 1 – Selection of CMIF Peaks

The CMIF method is used for the bridge data, and begins by performing singular value decomposition on the transfer function. This first step provides mode shape estimates as the left singular vectors and singular values that indicate the relative strength of a mode at each frequency line. The CMIF plot for multisine excitation with combined excitation lines 'C', 'D', and 'E' is shown in Figure 7.22. Only the three largest singular values are plotted for presentation quality. It is notable that there are many peaks in the plot, all of which may indicate a mode of the structure. Since it is unknown which peaks indicate desired modes, all peaks must initially be selected (red asterisks indicate selected peaks).

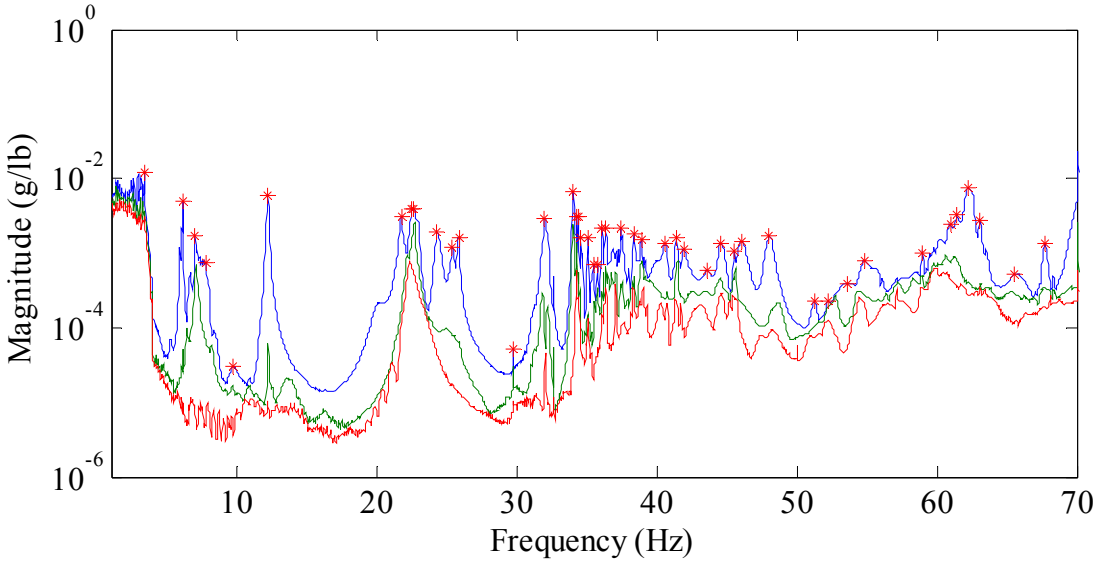

Figure 7.22. Typical CMIF plot from bridge testing data.

7.5.4.2 Step 2 – Review of Mode Shapes

The initial activity in evaluating the validity of a peak is to use the estimated mode shapes from the left singular vectors. In the vicinity of a peak, the mode shape should be a reasonably obvious global vertical mode, and the mode shape should be consistent for several frequency lines on

each side of the peak. Plots are generated for every selected CMIF peak that enable an evaluation of these criteria.

As an example, Figure 7.23 shows the mode shape corresponding to a peak in the CMIF curve, as well as the mode shape for two frequency lines before and after the peak. It is first noted that the mode shape does not appear to be an expected shape for a relatively symmetric structure. It is also noted that the stability of the shape is poor. The MAC values are very low for the frequency lines on either side of the peak. Thus, this mode is discarded.

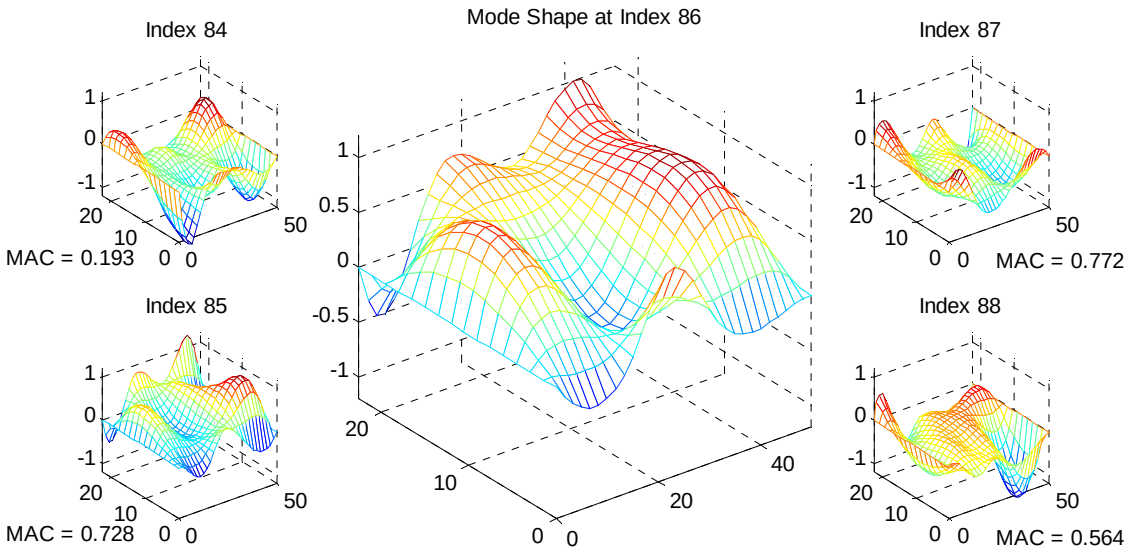

Figure 7.23. Typical plot of mode shapes in the vicinity of a CMIF peak. Lack of stability indicates a spurious mode.

As a second example, Figure 7.24 shows the mode shape corresponding to a different peak in the CMIF curve. This mode shape has a clear and symmetric appearance that is easily imagined as a true mode of vibration of the structure. Also, the mode shapes of nearby frequency lines are highly consistent as demonstrated by the MAC values that are near unity. Thus, this mode shape is selected for further processing.

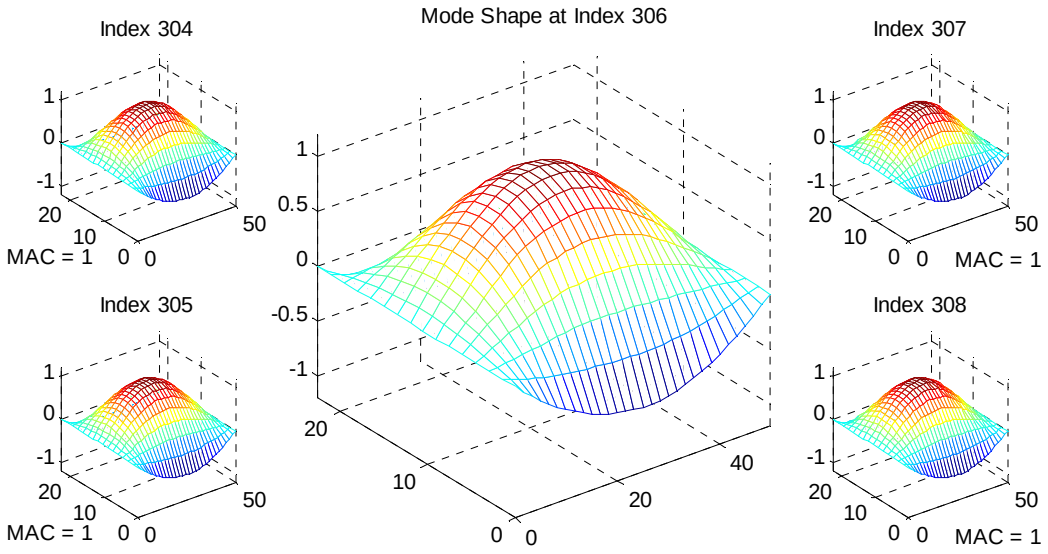

Figure 7.24. Typical plot of mode shapes in the vicinity of a CMIF peak. Clear shape and good stability indicate a real mode.

7.5.4.3 Step 3 – Calculation of Natural Frequencies, Damping, and Modal Mass

After mode shapes are selected, the estimated modal vectors are used to filter the transfer function. As discussed in previous chapters, with orthogonal modes and adequate spatial resolution, the filtering would eliminate the contribution of all modes except the mode of interest from the transfer function. The filtering process results in a single vector that is referred to as an eFRF, which is the FRF of an SDOF system. Several points in the vicinity of the peak are selected to solve for the system pole and Modal A (λ and M_a). The natural frequency and damping ratio can be found from λ and the modal mass can be found from λ and M_a.

The values of these modal properties can be reviewed to help eliminate additional spurious modes as well as real modes that are poorly identified by the experiment. Damping ratios should be in the range of 1%. Very low damping or negative damping values indicate a spurious mode. Modal mass values are calculated as a complex number, but should be predominantly real. If the imaginary part is similar in magnitude to the real part, then the mode is either spurious or real but poorly identified. Also, as additional experiments are processed, the variation in modal mass can

be used to help identify spurious modes. Real modes will have modal mass that tends to a mean, while spurious modes will have much more widely scattered values of modal mass.

Finally, the extracted modal parameters can be used to synthesize an eFRF. The overlay of the actual eFRF and the synthesized eFRF visually indicates if poor identification occurred. A poor fit of the synthesized eFRF is cause for eliminating the subject mode from further processing. Again, poor synthesis can be caused by either a spurious mode or by a real mode that is poorly identified. Poor identification can occur due to excessive noise, poor excitation of the mode, or inadequate modal filtering.

Figure 7.25 shows the synthesis of an eFRF in the vicinity of a peak. This is an example of a good fit on both the phase plot and the magnitude plot. Also, the modal mass value is predominantly real. Figure 7.26 shows an example of a poor eFRF fit. Neither the synthesized phase nor the amplitude closely matches the actual data. The modal mass is also generally complex. The mode corresponding to Figure 7.25 would be maintained and the mode corresponding to Figure 7.26 would be discarded.

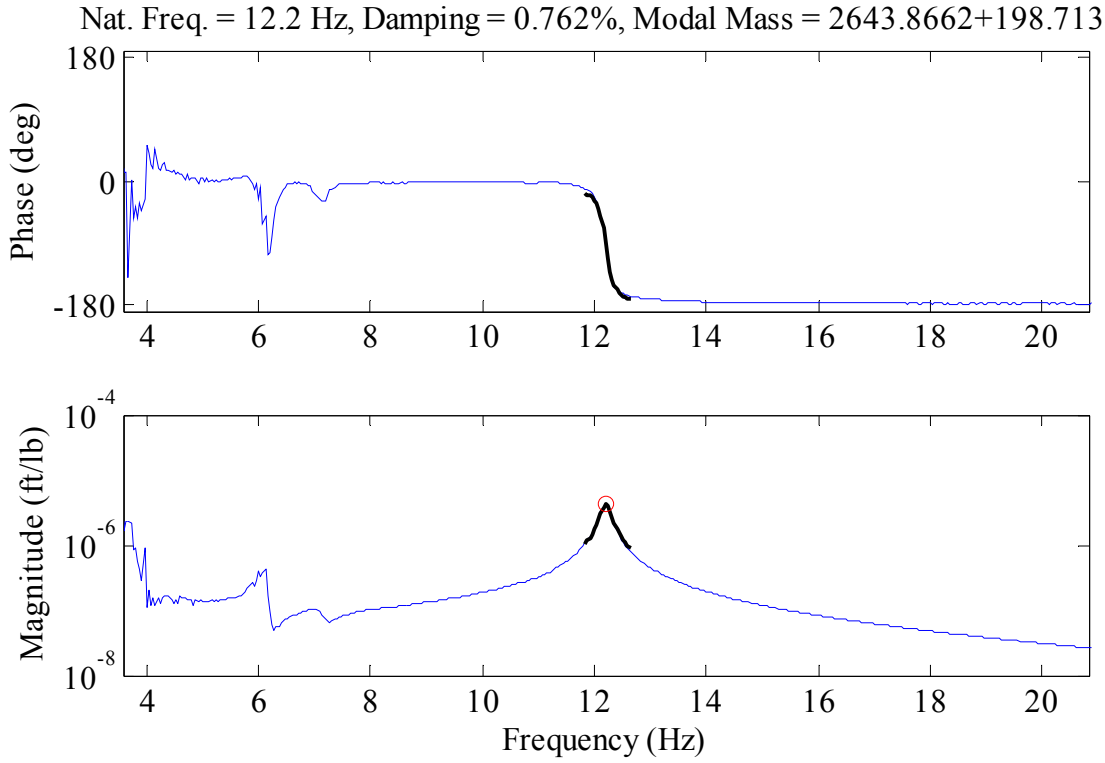

Figure 7.25. Overlay of eFRF synthesis and eFRF. Example shows good fit.

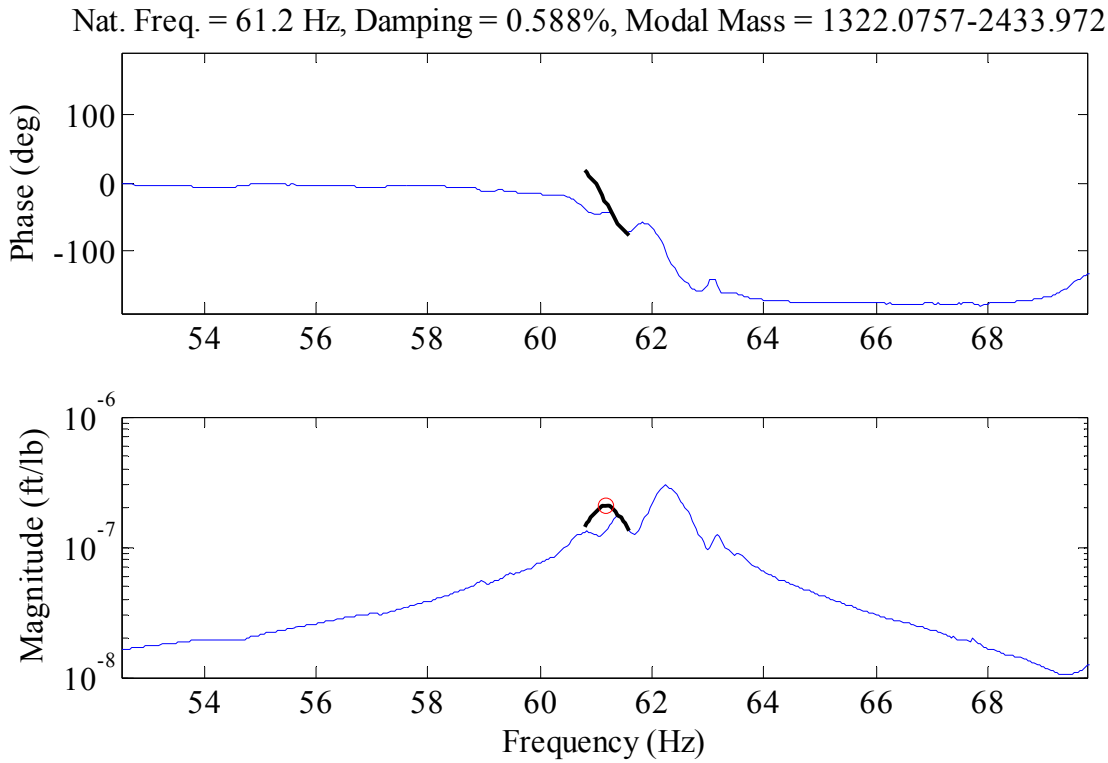

Figure 7.26. Overlay of eFRF synthesis and eFRF. Example shows poor fit.

7.6 ANALYTICAL MODEL PREPARATION FOR RESULTS VALIDATION

It is important to have other results with which to compare the system identification from the new experimental process. Finite element models are commonly used for this purpose since natural frequencies, mode shapes, and static flexibility matrices can all be found. However, real-world structures are difficult to accurately model for a number of reasons.

First, actual material properties are unknown and may vary between different structural elements. For example, the modulus of elasticity of the steel beams and diaphragms will be in the vicinity of 29,000 ksi, however, the exact value is unknown. Also, the diaphragms may have a different modulus of elasticity than the girders. The modulus of elasticity of the concrete deck must be assumed, and it is likely that the multiple batches of concrete that make up the deck have slightly varying elasticity. The parapets were cast separately and may have used a different mix design than the deck.

Second, the connectivity of various elements can be difficult to model. For example, the bolted connections from the diaphragms to the girder connection plates are composed of six bolts through the web of the diaphragms. This connection is quite stiff, but less so than the full fixity that is assumed in a typical framed connection in a finite element program. The connection from the beams to the deck is made with shear studs and the top flanges are partially encased in concrete. The composite section of steel and concrete also causes modeling challenges.

Third, the boundary conditions at the supports are difficult to model. This bridge uses bearings composed of sliding steel plates that allow the bridge to expand and contract without developing large forces, but, due to corrosion, the bearings do develop some longitudinal forces. Additionally, rotations at the bearings are resisted by the anchor bolts to some extent. Also, this

span is connected to the adjacent spans with neoprene strip seal deck joints. These joints are quite flexible, but do provide some resistance to motion. Finally, the piers have some level of flexibility that also contributes to a reduction of fixity at the bearings.

Fourth, modal parameters are very sensitive to the distribution of mass and stiffness of the structure. The bridge must be highly discretized so that the various elements are able to behave in a manner that closely matches the real structure. The parapets provide significant added mass overhanging the fascia girders, and also provide some amount of added stiffness. The expansion joints in the parapets reduce their bending stiffness at 10-foot intervals. This level of detail is difficult to model.

These various items that cause unknowns to exist in the creation of a finite element model require calibration. Calibration of a nominal model is performed by varying the parameters that cannot be explicitly known in such a way that the modal properties of the model more closely match the most accurately known modal properties of the real structure.

7.6.1 Nominal Finite Element Model Generation and Details

The nominal FE model is created to closely match the known geometry of the bridge. The horizontal location of all elements is known from field measurements, and the model is assembled to closely match the measurements. The deck is modeled using rectangular plate elements. The elements generally have a size of 1’-0” in the longitudinal direction and 1’-6” in the transverse direction. These dimensions vary along the overhangs, and along the 5” deck extension beyond the centerline of bearings. The 969 deck plates all have a uniform thickness of 8”, a density of 150 pcf, and a modulus of elasticity of 3150 ksi (based on 3000 psi concrete). In the nominal model, the parapets are not included as physical elements, but the mass of the

parapets is included as an evenly distributed load on the portion of the deck overhangs where the parapets exist.

It is considered to be important that the steel girders are in the proper vertical position from the deck so that the composite section stiffness is accurate. Additionally, local modes of the bottom flanges and the diaphragms can only be found from the finite element model if those elements are discretely modeled. To accomplish this goal, the girders and diaphragms are also modeled using plates (as opposed to simply using beam elements). Figure 7.27 illustrates the arrangement of the physical section and the method by which it is modeled. The flanges are modeled as plate elements with each plate 5" wide and 12" long. The girder web is modeled as plate elements with each plate 13.08" high and 12" long. The girder is connected to the deck with the equivalent of shear studs. A single stud is used every 12" along the girder, and each stud is 4" long and 2"x2" in section. The diaphragms and connection plates are also modeled with plate elements. A segment of the STAAD model is shown in Figure 7.28 and illustrates how the girder, connection plates, and diaphragms are framed into each other. The shear studs, girder elements, and diaphragm elements are steel with a density of 490 pcf and a modulus of elasticity of 29,000 ksi.

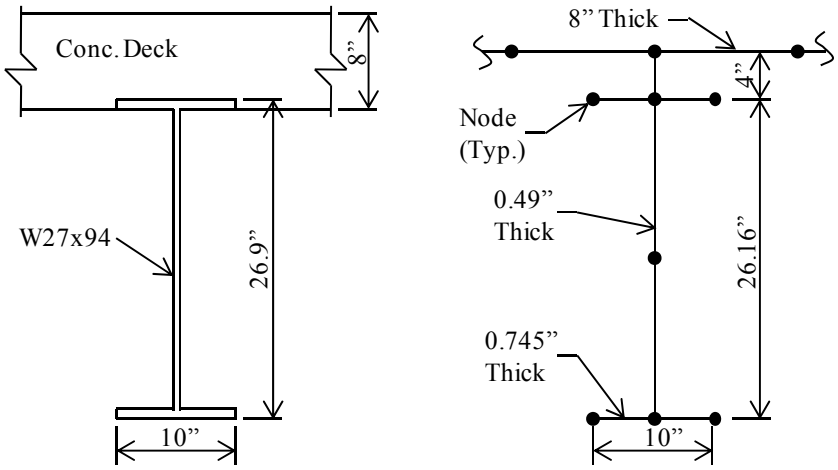

Figure 7.27. Physical composite section (left) and method of modeling section (right).

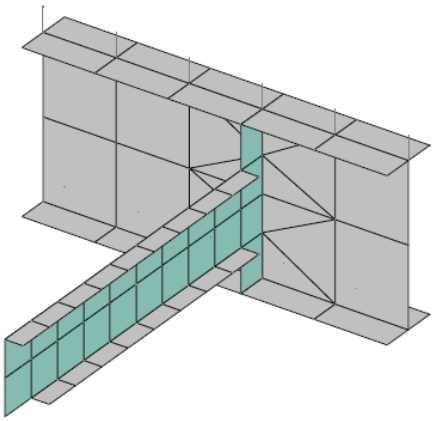

Figure 7.28. Illustration of diaphragm and girder modeling in STAAD.

The boundary conditions for the nominal model consist of pinned supports at the bearing locations along the bottom flange at one end of the span and as rollers at the other end of the span. Figure 7.29 shows the spatial location of the supports in the STAAD model.

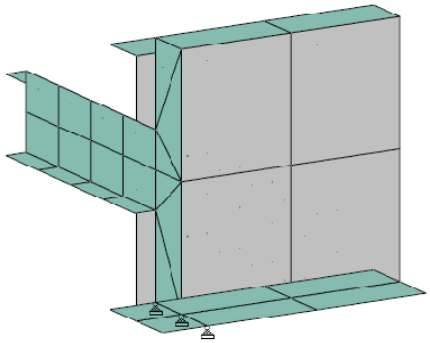

Figure 7.29. Illustration of girder end and location of supports in STAAD model.

STAAD uses a hybrid finite element formulation for plate (a.k.a. shell) elements. A complete quadratic stress distribution is assumed, and there are six degrees of freedom per node. This allows the various segments of the girder to translate and carry stress in a physically accurate manner. This enables the many powerful local modes of the girders to be solved for in the model, and helps explain some of the actual modal testing results. The natural frequencies and mode shapes are found in STAAD using eigenvalue analysis.

7.6.2 Calibration of Model

The nominal model is calibrated in an iterative manner to more closely match the field testing results. The field results that are used as a baseline are the natural frequencies of the global modes. These natural frequencies are highly consistent independent of the excitation method, and are a direct result of the actual distribution of mass, stiffness, and boundary conditions of the bridge. The calibrated finite element model should have global natural frequencies in close agreement with the test results.

The first step in calibration is to perform a sensitivity analysis. The uncertain parameters are increased and decreased, and the sensitivity of the natural frequencies of the model to these changes is noted. In the case of this bridge, the following parameters are experimented with:

- Deck stiffness – the modulus of elasticity of the concrete is varied from 3,152 ksi to 4,070 ksi (assumed concrete strength ranging from 3 ksi to 5 ksi).
- Deck thickness – the deck thickness of 8” is based on measurements at the edge of the overhang. Deck thickness in the model is varied from 7.5” to 9”.
- Steel stiffness – the modulus of elasticity of the steel is assumed to be within 5% of 29,000 ksi, so it is varied from 27,550 ksi to 30,450 ksi.
- Boundary conditions – the longitudinal stiffness of the bearings is varied from zero to 100 kip/in per bearing.
- Shear studs – the stiffness of the shear studs affects the relative amount of deformation between the top flange and the deck. The 2”x2” section in the nominal model is based on probable actual shear stud areas. However, the 4” clear height of the studs allows more relative movement than is realistic. Thus, the area is varied up to a 4”x4” section.

- Parapet stiffness – the parapet adds stiffness to the bridge at the deck overhangs, but the open joints in the parapets reduces the effectiveness of this stiffness. The nominal model has no added stiffness for the parapets. The stiffness will be varied up to a level that includes the full concrete section of the parapets with no joints.

The results of the sensitivity analysis are presented in Table 7.7. The natural frequencies of the first five global modes are shown. For each model, only the noted change was made from the nominal model. The table also provides the field results in the second column.

Mode Name	Field	Modal Frequencies for Various Models (Hz)						
		1	2	3	4	5	6	7
B1	6.1	4.8	2.7	4.7	4.9	5.0	4.9	6.2
T1	7.0	5.9	4.9	6.0	6.0	5.1	6.1	8.3
BU1	12.2	12.2	13.5	12.9	12.4	11.3	12.5	12.7
B2	21.7	16.2	9.1	16.0	16.5	16.9	16.8	19.4
T2	22.8	16.7	14.0	16.7	17.0	16.4	17.6	20.0

Model Descriptions:
1 - Nominal model.
2 - Concrete stiffness increased to 4070 ksi.
3 - Deck thickness increased to 9".
4 - Steel stiffness increased to 30,450 ksi.
5 - Bearing restraint increased to 100 k/in per bearing.
6 - Stud cross section increased to 4"x4".
7 - Parapet added - 9" wide by 32" tall each overhang.

Table 7.7. Select results for sensitivity analysis.

The sensitivity analysis provides a framework for calibrating the model to the field results by indicating how the variation of each parameter affects the various modes. It is noteworthy that the addition of the parapet is the single most important parameter for moving the natural frequencies closer to the field values. Using the results of the sensitivity analysis for guidance, parameters are varied in a trial and error method to calibrate the model.

7.6.3 Final Model Parameters

Several iterations are performed in an effort to calibrate the model. It is noted that there is no unique correct solution. The parameters could be varied in many different ways to achieve similar results, and thus the close match between the modal frequencies does not guarantee that the model is a good representation of the real structure. Nonetheless, the results for the modal frequencies are presented in Table 7.8, and the final properties of the calibrated model are listed.

- Modulus of elasticity of concrete: 3,640 ksi (4 ksi concrete strength)
- Modulus of elasticity of steel: 29,500 ksi
- Deck thickness: 8.5 inches
- Parapet dimensions: 8” wide by 32” high. Partial depth open joints (16” deep) added at 10-foot spacing along parapets.
- Bearing longitudinal stiffness: 90 kip/inch each bearing
- Shear stud section dimensions: 3” x 3”
- Model statistics: 200 beams, 3623 plates, 3994 nodes

Mode Name	Modal Frequencies		Error (%)
	Field (Hz)	Model (Hz)	
B1	6.1	6.1	0%
T1	7.0	6.9	1%
BU1	12.2	12.2	0%
B2	21.7	21.2	2%
T2	22.8	23.2	2%
BU2	25.9	24.7	5%
B3	40.6	41.3	2%
BU3	54.8	53.6	2%
B4	65.6	61.7	6%

Table 7.8. Comparison of natural frequencies from bridge testing and from calibrated finite element model.

The calibrated model is also used to generate a static flexibility matrix for comparison to the modal flexibility matrices found from the testing of the real bridge. The static flexibility matrix is developed by applying a unit load in the calibrated model to a single node at the position of an accelerometer used in the field. The vertical displacements at all other DOFs are recorded, and these values are a row or a column of the static flexibility matrix.

7.6.4 Comments Regarding Local Modes

The finite element model revealed many strong local modes that involve the lower portions of the girders and the diaphragms. The diaphragm modes are of little concern since no accelerometers were mounted to diaphragms. The girder modes are of concern since all accelerometers were mounted to the bottom flanges of the girders. The flanges vibrate in a number of different lateral modes, and the frequencies of these modes are generally within the band of 26 Hz to 40 Hz.

The manufacturer reports that the lateral sensitivity of the 393C accelerometers is less than or equal to 5%. This means that a 1g lateral acceleration of the bottom flange would be seen in the data as a vertical acceleration with a magnitude of up to 0.05g. Many peaks in the CMIF curves correlate to mode shapes that are suspected to be a result of these lateral flange modes. In retrospect, the accelerometers should have been attached to the underside of the top flanges to eliminate detection of these bottom flange lateral, local modes.

7.7 RESULTS OF PREVIOUS TESTING OF BRIDGE BY OTHERS

Dynamic testing of this bridge was carried out over several years by other students in the research group at the University of Arkansas. The testing that conformed to the generally accepted methods that are frequently used in the literature are used in this thesis as a point of

comparison for the current work. These accepted methods are MRIT (impact testing) and ambient testing. The details of the tests and the modal parameters captured are provided below.

7.7.1 Ambient Testing 1

Ambient testing was performed by Ryan Maestri, a graduate student at the University. A brief list of the details of his testing are provided below, and further details are available in Maestri et al. (2012). This was pure ambient testing with only environmental inputs; there were no traffic crossings or other intentional force inputs to the structure.

- Date: 12/10/2010
- Weather: ~45˚F, sunny, calm winds, low humidity
- Data processing method: Cross-power spectral density at each frequency line, then singular value decomposition to identify mode shapes and damped natural frequencies.
- Frequency resolution: 0.024 Hz.
- Number of output DOFs: 24

7.7.2 Ambient Testing 2

Ambient testing was also performed by Javier Torres, a graduate student at the University. Results of this testing have not been published as of the date of this writing, and thus pertinent details are provided herein, and a summary of the testing details are provided below.

This ambient testing used seven accelerometers along each girder for a total of 28 output DOFs. The bridge outputs were recorded continuously for four hours, with ambient inputs consisting of environmental disturbances and occasional traffic crossings. The raw data was processed using the 'NeXT' algorithm (James et al. 1993). This algorithm calculates auto-correlation and cross-correlation functions from the data for a pair of DOFs. Impulse response functions (IRFs) are

estimated from the correlation functions, and each IRF is a time-domain estimate of the natural decay of a mode. Pseudo FRFs are calculated from the IRFs based on the assumption of white noise input with a magnitude of unity. The CMIF algorithm is then applied to the pseudo FRFs to find modal vectors and poles.

- Date: 11/14/2011
- Weather: ~40˚F, clouds, calm winds, low humidity
- Data processing method: NeXT algorithm to produce pseudo FRFs and then the CMIF algorithm operating on the pseudo FRFs
- Frequency resolution: 0.0305 Hz
- Number of output DOFs: 28

7.7.3 Impact Testing 1

Impact testing was performed by Jeremy Rawn, a graduate student at the University. Results of this testing have not been published as of the date of this writing. The testing consisted of impacting the top surface of the bridge deck with an instrumented sledge hammer to impart excitation. Averaging was based on three hits per DOF, and the testing took about 1.5 hours. Due to the short total testing time, no significant effects due to time-variance are expected. Twenty-four accelerometers were used to measure outputs, with eight of the accelerometers at the support locations.

The data from this testing was reprocessed as part of the work of this thesis, but the output data for the eight accelerometers at the supports was neglected due to very low signal-to-noise ratio. Data was recorded for 16 seconds for each impact at a sampling rate of 512 Hz. For the current processing, the input force data is windowed to remove noise that results from vibration of the

hammer after force is no longer being imparted to the structure. This is a common practice in impact testing, and typical results of windowing are shown in Figure 7.30 for the first hit at DOF 1.

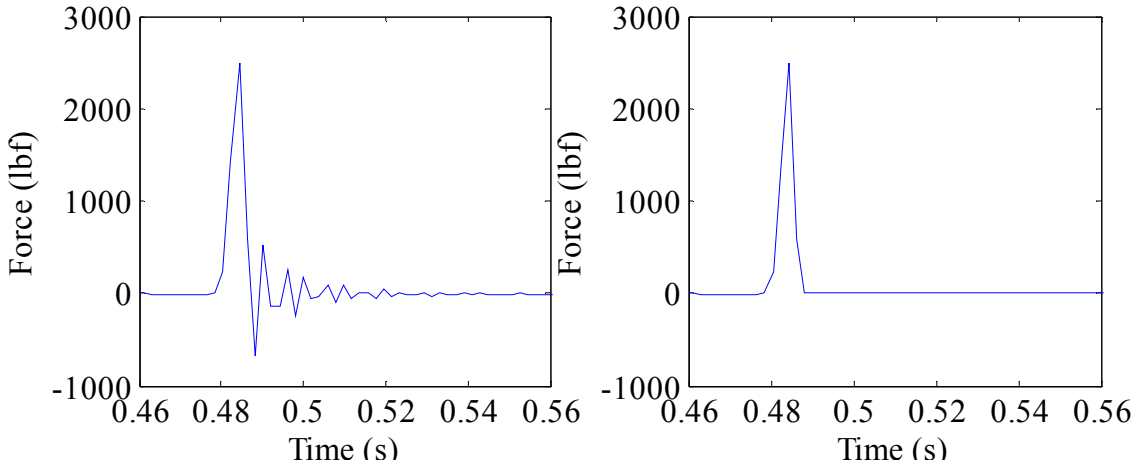

Figure 7.30. Force input data for a typical impact before windowing (left) and after windowing (right).

The input and output data are then transformed to the frequency domain, the H1 FRF algorithm is applied, and a single transfer function is assembled by using each experiment as a column of the transfer function. Thus, a transfer function with 16 rows and 16 columns of FRFs is formed. The CMIF algorithm is then carried out as described elsewhere, modal vectors and damped natural frequencies are estimated from SVD of the transfer function, and then SDOF methods are used to estimate the poles and modal mass for each mode.

- Date: 11/15/2010
- Weather: ~60˚F, sunny, calm winds, low humidity
- Data processing method: FRFs from the 16 individual SIMO tests are combined into a single transfer function, and then modal properties are extracted using the CMIF algorithm.

- Frequency resolution: 0.0625 Hz
- Number of output DOFs: 16

7.7.4 Impact Testing 2

Impact testing was also performed by Javier Torres. Again, results have not been published as of the date of this writing. The testing was nearly identical to that performed by Mr. Rawn, except that five impacts were imparted at each DOF, and 28 output DOFs were used. Data was recorded for 16 seconds for each impact at a sampling rate of 1024 Hz. The input force data was windowed to remove noise from the measurment that occurs after the impact. The data had not been properly analyzed, and thus further processing is performed as part of the work of this thesis.

The input and output data are transformed to the frequency domain using the FFT. The H1 FRF algorithm is applied for each input location, resulting in a transfer function with a single column. The columns for all 28 experiments are organized into a single transfer function, and then the CMIF algorithm is applied to estimate modal parameters.

- Date: 11/14/2011
- Weather: ~40˚F, clouds, calm winds, low humidity
- Data processing method: FRFs from the 28 individual SIMO tests are combined into a single transfer function, and then modal properties are extracted using the CMIF algorithm.
- Frequency resolution: 0.00098 Hz
- Number of output DOFs: 28

7.7.5 Modal Parameters Captured

The previous testing of the bridge provided various modal parameters. The natural frequencies for the modes captured are provided in Table 7.9, and the modal damping and modal mass values are provided in Table 7.10. Mode shapes corresponding to each of the mode numbers are provided in Figure 7.31 and Figure 7.32. Finally, parameters relating to modal flexibility are provided in Table 7.11, and the meaning of each parameter is discussed in detail in subsequent sections.

Mode No.	Natural Frequencies (Hz)			
	Ambient 1	Ambient 2	Impact 1	Impact 2
1	6.03	6.04	6.10	6.02
2	7.03	7.02	7.04	6.94
3	12.38	12.39	12.50	12.46
4	22.09	*	21.67	21.60
5	*	*	23.35	23.45
6	*	22.71	22.81	22.61
7	24.59	25.57	24.57	24.37
8	32.25	32.50	32.46	32.48
9	*	34.21	*	34.19
10	*	36.50	36.34	*
11	40.55	41.50	*	40.34
12	*	45.53	46.47	*
13	*	*	*	48.47
14	*	*	51.72	51.30
15	*	*	*	*
16	*	56.15	55.88	56.86
17	*	63.69	63.74	64.25
18	*	*	*	*
19	*	*	*	67.82
20	*	*	71.68	71.66
21	*	*	73.87	73.53

* Mode not found.

Table 7.9. Natural frequencies found from various previous dynamic tests.

Mode No.	Modal Damping (%)			Modal Mass (lbf/g)	
	Ambient 2	Impact 1	Impact 2	Impact 1	Impact 2
1	0.75	0.80	0.44	3117	3409
2	1.02	0.91	0.98	3302	2311
3	1.06	0.76	0.70	3551	2374
4	*	2.29	1.80	3058	2409
5	*	0.64	0.52	3289	2349
6	1.76	1.20	0.89	2346	1863
7	0.75	0.97	1.16	4323	3248
8	0.37	0.36	0.38	4082	3986
9	0.19	*	0.11	*	2902
10	0.17	0.24	*	2781	*
11	0.37	*	0.73	*	5638
12	0.51	1.23	*	3809	*
13	*	*	0.67	*	2100
14	*	0.91	0.98	4839	3432
15	*	*	*	*	*
16	1.24	1.25	0.88	5534	5872
17	0.32	0.58	0.48	2875	1950
18	*	*	*	*	*
19	*	*	0.30	*	1303
20	*	0.73	0.70	1959	1719
21	*	0.71	0.51	5239	946

* Mode not found.

Table 7.10. Modal damping and modal mass found from various previous dynamic tests.

Desc.	Impact 1	Impact 2
D	48.7	23.8
Dd	1.01	0.94
Disp.	99%	89%

Table 7.11. Parameters relating to modal flexibility found from various previous dynamic tests.

The data presented from previous testing was collected over a time span of several years, and in varying weather conditions. Also, test methods varied, data processing methods varied, and the skill of the researchers performing the testing varied. For all of these reasons, variation in the

estimated modal parameters is expected. The following general observations about the data are made:

- Ambient techniques failed to capture many of the modes that were found with measured input.
- Damping ratios were not calculated for the 'Ambient 1' testing.
- Modal mass and thus modal flexibility cannot be estimated from output-only ambient testing.
- 'Ambient 2' testing used more data and a more advanced processing algorithm than 'Ambient 1', and thus far more modes were identified.
- Natural frequencies were highly consistent for almost all modes.
- Damping ratios were consistent for some modes (e.g. 2 and 8), but were inconsistent for others (e.g. 1 and 6).
- Modal mass found from 'Impact 2' was consistently lower than from 'Impact 1', except for Mode 1.
- The displacement parameter found using 'Impact 1' is in excellent agreement with the finite element model results, indicating that the modal mass for Mode 1 is accurate.
- The 'D' parameter found using 'Impact 1' is large, indicating that the modal mass or modal vectors of some modes are significantly in error.

7.8 ANALYSIS AND RESULTS OF CURRENT TESTING

The primary goal of the bridge testing is to validate that the tactile transducer excitation system can provide meaningful MIMO EMA characterization of real-world structures. However, the test plan also allows the evaluation of several other issues that are important considerations in the

design of such testing. The success of combining the transfer functions from different experiments is analyzed since this allows the testing to be performed with fewer force transducers. The system identification from traditional burst-random excitation is compared to that from multisine excitation since the use of multisine signals is unproven on civil structures. Also, the results of system identification in the presence of traffic are evaluated to help determine if testing can succeed without regard to vehicle crossings. Finally, the success of only measuring some inputs to allow simultaneous excitation of more DOFs than the available number of force transducers is evaluated.

7.8.1 Methods for Comparisons

Comparisons of mode shapes utilize MAC values (Allemang 2003) as described in the previous chapter. These values are again calculated using the following equation:

$$MAC = \frac{(A^T * B)(B^T * A)}{(A^T * A)(B^T * B)} \qquad \text{Equation 7.3.}$$

Where:

$A =$ a vector representing a mode shape.

$B =$ a vector representing a different mode shape .

Flexibility matrices are also compared as in the previous chapter. Again, two values are calculated: D is a measure of the agreement between two matrices, and D_d is a measure of the agreement between the main diagonal of two matrices. The equations used to calculate these quantities are:

$$D = \sqrt{\sum_{i=1}^{n}\sum_{j=1}^{n}\left(\frac{f1_{i,j} - f2_{i,j}}{f1_{i,j}}\right)^2} \qquad \text{Equation 7.4.}$$

$$D_d = \sqrt{\sum_{i=1}^{n} \left(\frac{f1_{i,i} - f2_{i,i}}{f1_{i,i}} \right)^2} \qquad \text{Equation 7.5.}$$

Where:

$D =$ the value representing the overall difference between two matrices.

$D_d =$ the value representing the difference between two matrix's main diagonals.

$n =$ the size of the square matrix.

$f1 =$ the flexibility matrix considered to be the more accurate of the two.

$f2 =$ the flexibility matrix being compared.

A displacement due to uniform load applied to the flexibility matrices is also used in comparisons. The average displacement of the four DOFs along sensor Line D (near midspan) was found from the finite element model. The average displacement along this line is also found from an experimental result by multiplying the modal flexibility matrix by a vector of ones. The experimental average displacement is divided by the analytical average displacement and the result is displayed as a percentage. Thus, a value of 90% indicates that the displacement of the structure under uniform load based on an experimental result is 90% of the finite element model displacement. These displacements are primarily controlled by the accuracy of modal mass for Mode 1.

Finally, throughout the discussions, reference is made to various modes by mode number. The shapes of those modes are provided in Figure 7.31 and in Figure 7.32 for reference.

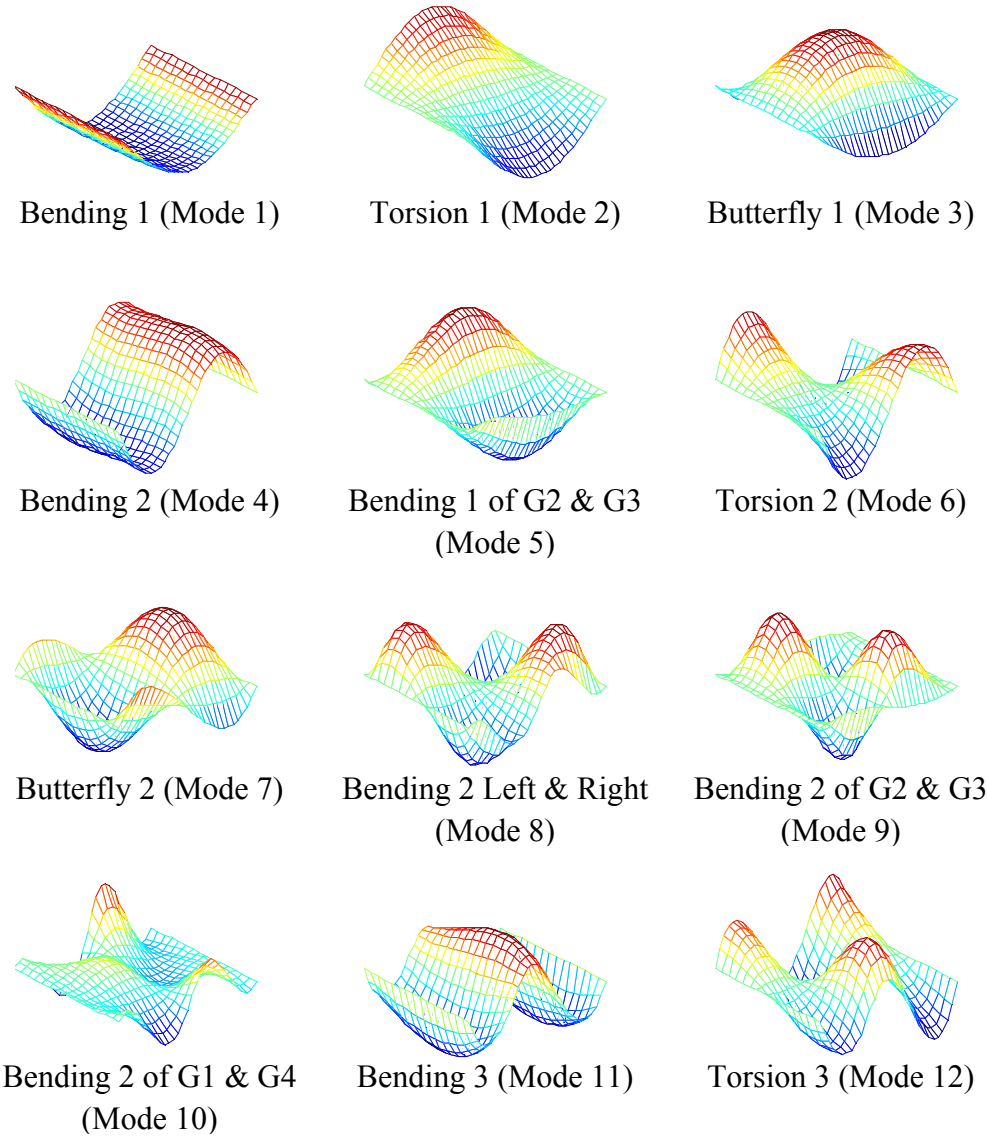

Figure 7.31. Most commonly identified modes of vibration of the Hartbarger Bridge (modes 1 through 12).

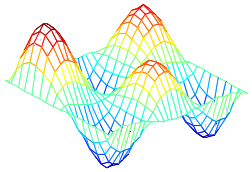

Bending 3 of G2 & G3 (Mode 13)

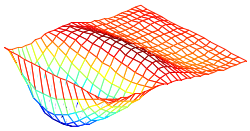

Bending 2 Near of G2 & G3 (Mode 14)

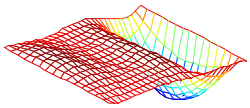

Bending 2 Far of G2 & G3 (Mode 15)

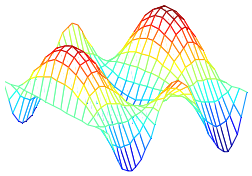

Butterfly 3 (Mode 16)

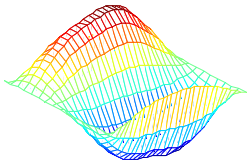

Bending 1 of G1, G2, G3, & G4 (Mode 17)

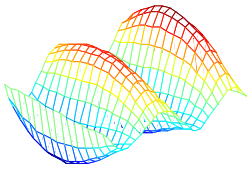

Bending 4 (Mode 18)

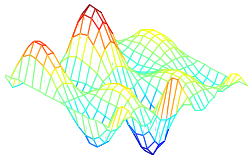

Bending 5 of G1, G2, G3, & G4 (Mode 19)

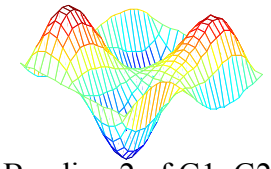

Bending 2 of G1, G2, G3, & G4 (Mode 20)

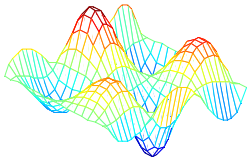

Bending 3 of G1, G2, G3, & G4 (Mode 21)

Figure 7.32. Most commonly identified modes of vibration of the Hartbarger Bridge (modes 13 through 21)

7.8.2 Validation of Excitation System on a Full-Scale Bridge

One goal of the bridge testing is to validate that the excitation system consisting of low-cost TTs can adequately excite a large structure. Adequate excitation means that the magnitude of the measured force input is sufficiently large that it greatly exceeds the ambient excitation of the structure. Adequate excitation also means that all modes of interest are excited to a level that allows accurate modal properties to be extracted.

Whether or not the bridge was adequately excited is determined by comparing the outcome of the testing using the novel approach to the outcome using traditional and accepted methods. All of the modal parameters are compared including natural frequencies, modal damping, modal mass, modal vectors, and modal flexibility. The results from the new approach are compared to the results from prior testing and to the predictions of the finite element model.

Only a portion of the total data captured during bridge testing is used in this part of the analysis. The experiments using four shakers and multisine excitation with all excitation lines combined into a single transfer function are used here. The data from the other experiments is considered in other analyses later in this chapter. The reason for this is that having a force transducer at each shaker and using multisine excitation is the preferred approach for the multi-shaker system. Additionally, only using a single experimental result makes the discussion and presentation of tables and figures more clear.

7.8.2.1 Natural Frequencies

The number of natural frequencies found and the agreement of those frequencies to previous results from accepted techniques is analyzed. The finite element results are not considered since the natural frequencies of the model were calibrated to match the current data. The natural frequencies of the modes found from the current testing and from the four previous tests are presented in Table 7.12.

Mode	MS MIMO	Ambient 1	Ambient 2	Impact 1	Impact 2
1	6.12	6.03	6.04	6.10	6.02
2	6.98	7.03	7.02	7.04	6.94
3	12.21	12.38	12.39	12.50	12.46
4	21.69	22.09	*	21.67	21.60
5	22.48	*	*	23.35	23.45
6	22.71	*	22.71	22.81	22.61
7	24.32	24.59	25.57	24.57	24.37
8	32.18	32.25	32.50	32.46	32.48
9	34.04	*	34.21	*	34.19
10	36.07	*	36.50	36.34	*
11	40.54	40.55	41.50	*	40.34
12	46.02	*	45.53	46.47	*
13	48.00	*	*	*	48.47
14	50.56	*	*	51.72	51.30
15	52.12	*	*	*	*
16	54.77	*	56.15	55.88	56.86
17	62.26	*	63.69	63.74	64.25
18	65.47	*	*	*	*
19	67.74	*	*	*	67.82

* Mode not found.

Table 7.12. Comparison of natural frequencies (Hz) found from MIMO multisine testing and from various previous tests.

Two observations are made based on Table 7.12. First, the MIMO EMA testing captured many more modes of vibration than any of the previous test methods. This is the expected outcome due to the many benefits of MIMO testing and multisine signals that have been discussed at length. The low level of excitation from ambient testing and the likelihood of unequal excitation at various frequency lines makes it more difficult to identify the many closely spaced modes of this bridge. For the impact testing, the low signal to noise ratios of the force and response data makes it more difficult to identify less powerful modes and closely spaced modes.

Second, in almost all cases, the frequencies found from the previous testing are higher than those found from the MIMO EMA multisine testing. Excluding Mode 1, all of the previous results

combined are an average of 1.3% higher than the current results. This outcome is attributed to the effects of temperature. The ambient temperature was approximately 90˚F during the current testing, but was much cooler for all of the previous tests. Higher temperatures reduce the stiffness of materials, resulting in lower natural frequencies, however, the effect of temperature is not related to any particular testing method.

7.8.2.2 Modal Damping

The estimated damping ratios from the current testing and from the previous tests are compared in Table 7.13. As discussed, damping ratios tend to be highly variable for lightly damped structures since small errors in the calculation of the poles results in large errors in the damping ratios. For most of the modes, the damping found from the MIMO multisine testing lies within the range of the values found from previous tests. For Modes 2 and 6, the previous results are consistently higher than the current results, and for Mode 8, the previous results are consistently lower than the current results. Overall, no specific conclusions can be drawn from the comparison of damping ratios.

Mode	MS MIMO	Ambient 2	Impact 1	Impact 2
1	0.59	0.75	0.80	0.44
2	0.89	1.02	0.91	0.98
3	0.78	1.06	0.76	0.70
4	0.76	*	2.29	1.80
5	0.98	*	0.64	0.52
6	0.80	1.76	1.20	0.89
7	0.90	0.75	0.97	1.16
8	0.42	0.37	0.36	0.38
9	0.21	0.19	*	0.11
10	0.17	0.17	0.24	*
11	0.70	0.37	*	0.73
12	1.06	0.51	1.23	*
13	0.74	*	*	0.67
14	0.77	*	0.91	0.98
15	0.57	*	*	*
16	1.03	1.24	1.25	0.88
17	0.54	0.32	0.58	0.48
18	1.60	*	*	*
19	0.34	*	*	0.30

* Mode not found.

Table 7.13. Comparison of damping ratios (%) found from MIMO multisine testing and from various previous tests.

7.8.2.3 Modal Mass

The estimated values of modal mass found from the MIMO multisine testing and from the previous tests are compared in Table 7.14. The calculated value of modal mass is primarily controlled by the magnitude of the eFRF at the natural frequency of the mode. This magnitude can be significantly affected by processing issues such as imperfect modal filtering, and by testing issues such as leakage, measurement noise, and system noise due to ambient excitation. Thus, variability in calculated values of modal mass is not surprising.

Comparing the impact testing results to the MIMO results for the 17 modes that were found by the impact tests, the modal mass values from impact are consistently higher than the MIMO

results for five modes and are consistently lower for nine modes. For four modes, the MIMO results are within the range of the impact results. Considering all modes, the average modal mass for 'Impact 1' is 5.2% higher than MIMO, and the average modal mass for 'Impact 2' is 20.6% lower than MIMO. Thus, there is no obvious relation for the modal mass results between any of the tests. Also, based strictly on this comparison, there is no indication that one testing method provides more accurate results than another testing method. However, since the modal mass is extremely important to the calculation of accurate modal flexibility, further discussion ensues in subsection 7.8.2.5.

Mode	MS MIMO	Impact 1	Impact 2
1	2831	3117	3409
2	2214	3302	2311
3	2615	3551	2374
4	3992	3058	2409
5	2083	3289	2349
6	4393	2346	1863
7	5158	4323	3248
8	5007	4082	3986
9	3945	*	2902
10	2642	2781	*
11	6563	*	5638
12	3168	3809	*
13	2370	*	2100
14	4770	4839	3432
15	801	*	*
16	7755	5534	5872
17	2365	2875	1950
18	6845	*	*
19	3360	*	1303

* Mode not found.

Table 7.14. Comparison of modal mass (lbf/g) found from MIMO multisine testing and from various previous tests.

7.8.2.4 Modal Vectors

The modal vectors found from the MIMO multisine testing and from the previous tests are compared to the vectors from the finite element model using MAC values. To enable MAC calculations, the DOFs must all be at the same spatial locations. The sensor locations for the previous tests were at a variety of locations that are not the same as the DOF locations for the current testing. Since the mode shapes must be smooth curves, interpolation using a cubic spline is performed along the length of each girder to estimate the modal vector amplitudes at consistent DOF locations.

The MAC values as compared to the finite element modal vectors are given in Table 7.15. The 'Ambient 1' testing provides relatively poor estimates of the modal vectors. This can be attributed to the low signal to noise ratio that results from very low excitation. The impact testing gives good modal vectors for the first five modes listed, but at higher frequencies the agreement is generally not as good. The MIMO testing is not as good for Mode 6 as the impact, but is better for Modes 12, 16, and 18 than the impact testing. Overall, the MIMO testing outperforms the impact and ambient testing methods in regards to capturing accurate modal vectors.

Mode	MS MIMO	Ambient 2	Impact 1	Impact 2
1	0.99	1.00	0.99	1.00
2	1.00	0.86	0.98	0.98
3	1.00	0.99	0.99	1.00
4	0.94	*	0.95	0.95
6	0.88	0.45	0.94	0.96
7	0.77	0.56	0.70	0.70
11	0.85	0.81	*	0.94
12	0.81	0.63	0.79	*
16	0.95	0.45	0.71	0.92
18	0.95	*	*	*

* Mode not found.

Table 7.15. Comparison of MAC values for MIMO multisine testing and for various previous tests.

7.8.2.5 Modal Flexibility

Modal flexibility matrices found from the various tests are compared to the static flexibility matrix from the finite element model. As described previously, D is used to compare all matrix elements, D_d is used to compare just the matrix main diagonals, and $Disp.$ is used to compare the average midspan displacement due to a unit load vector. The results for the MIMO multisine testing and for the two impact tests are shown in Table 7.16. Modal flexibility cannot be calculated for the ambient testing since modal mass cannot be calculated without measured inputs.

The MIMO testing significantly outperforms the impact tests based on the D and D_d values. The better results with MIMO testing are due to the identification and inclusion of more modes in calculating modal flexibility. The results are also improved by better estimates of modal mass due to better SNR. The $Disp.$ result is best from the 'Impact 1' testing, with average midspan deflections that are nearly identical to those predicted by the finite element model. This outcome suggests that the modal mass for Mode 1 is best estimated by the 'Impact 1' testing. This is not

surprising since the TTs do not generate much force at the frequency of Mode 1, and thus signal to noise ratio is diminished at this frequency.

Desc.	MS MIMO	Impact 1	Impact 2
D	12.2	48.7	23.8
Dd	0.77	1.01	0.94
Disp.	94%	99%	89%

Table 7.16. Comparison of modal flexibility from MIMO multisine testing and from various previous tests.

7.8.2.6 Summary Evaluation of Excitation System

The goal of this analysis is to evaluate whether the MIMO excitation system provides results on par with commonly used and accepted ambient and impact excitation methods. Overall, the MIMO system outperforms both ambient and impact methods. Many more modes are identified and generally more accurate modal vectors are found using the novel system. Also, the modal flexibility matrix is a better match to the static flexibility matrix, indicating that the MIMO system also provides more accurate estimates of modal mass. Thus, using the TTs in a MIMO array to excite bridges similar to the tested bridge can be expected to provide superior modal parameters so long as fundamental natural frequencies are not too low.

7.8.3 Evaluation of Combining Data from Disparate Experiments

Combining data from several different experiments is a common technique used in modal testing of civil structures, and is commonly referred to as MIMO testing even though it is more accurately described as multiple-SIMO testing (it is also sometimes referred to as multiple reference impact testing (MRIT)). A common application of this technique is to use an instrumented hammer to apply impacts to a structure. An individual hit generates a single set of data, and multiple hits are performed at a single input location to allow averaging of sets. The

process is repeated at as many DOFs as desired. A single column of the transfer function is assembled from the FRFs due to the hits at a single input location. Columns are then added for each input location. Because time elapses between the inputs, the FRFs from different columns of the transfer function cannot be completely consistent with each other. During the elapsed time, equipment may be moved, environmental conditions may change, etc., causing inconsistencies in the data.

The benefit of this technique is that the additional columns of FRFs in the transfer function provide more redundant data, and the system identification becomes more accurate. The drawback of this technique is that the data from separate experiments are inconsistent, potentially making the system identification less accurate.

For the bridge testing, four inputs in a transverse line were excited simultaneously, allowing the formation of a transfer function with four columns of completely consistent FRFs. Five experiments were performed with the inputs at different line of DOFs in each experiment. This allows the formation of a larger transfer function by augmenting with columns of FRFs fro additional experiments. A transfer function with up to twenty columns can be formed for the current testing. However, the data from the different experiments will be inconsistent due to the elapsed time between the experiments. The goal of the following analyses is to determine if the system identification improves with the inclusion of more redundant data, or if the identification gets worse due to inconsistent data.

As discussed in subsection 7.5.2, system identification was performed for each experiment separately; for each group of three experiments that were performed successively; and for all five

experiments combined together. The results from these combinations of experiments are compared in the following subsections.

7.8.3.1 Natural Frequencies

The first item to be analyzed is the number of modes captured and identified accurately. It is noted that almost all modes are found in every experiment, but if the damping and modal mass estimates are poor for a mode then that mode is considered to not have been identified by the experiment. The results are presented in Table 7.17 for multisine excitation and in Table 7.18 for burst-random excitation.

Mode	Excitation Lines Used in Transfer Function								
No.	B	C	D	E	F	B+C+D	C+D+E	D+E+F	All
1	6.10	6.11	6.12	6.12	6.09	6.12	6.12	6.12	6.12
2	6.99	7.00	6.98	6.99	7.00	6.98	6.98	6.98	6.98
3	12.23	12.19	12.18	12.24	12.26	12.19	12.21	12.23	12.21
4	21.62	21.67	21.67	21.69	21.69	21.66	21.68	21.69	21.69
5	*	22.51	22.49	22.66	*	22.48	22.48	22.49	22.48
6	22.76	22.83	22.87	*	22.76	22.71	22.70	22.86	22.71
7	24.36	24.29	24.29	24.35	24.34	24.31	24.30	24.35	24.32
8	32.17	32.01	32.04	*	32.18	32.02	32.01	32.19	32.18
9	34.11	34.04	34.13	*	34.18	34.04	34.04	34.18	34.04
10	36.27	36.08	36.15	36.05	36.20	36.08	36.08	36.05	36.07
11	40.58	*	40.50	40.56	40.56	40.50	40.52	40.55	40.54
12	46.12	46.13	45.97	46.12	45.99	46.01	46.00	45.99	46.02
13	47.98	48.11	47.98	48.14	47.98	47.99	48.04	48.00	48.00
14	50.56	51.31	51.33	*	*	50.56	51.31	*	50.56
15	52.09	52.23	52.27	*	52.12	52.20	52.27	52.12	52.12
16	54.83	54.72	54.65	54.75	*	54.78	54.68	54.70	54.77
17	62.31	62.22	62.30	62.53	*	62.27	62.25	62.56	62.26
18	65.36	65.38	65.91	65.81	*	65.43	65.66	65.80	65.47
19	67.72	67.75	67.78	*	*	67.75	67.74	67.77	67.74

* Mode not found.

Table 7.17. Natural frequencies (Hz) identified from the various single experiments and combinations of experiments using multisine excitation.

Mode No.	Excitation Lines Used in Transfer Function								
	B	C	D	E	F	B+C+D	C+D+E	D+E+F	All
1	6.11	6.09	6.13	6.11	*	6.12	6.12	6.12	6.12
2	6.99	7.01	7.00	7.02	6.99	6.98	7.00	6.98	6.99
3	12.26	12.24	12.18	12.26	12.27	12.20	12.24	12.25	12.25
4	21.64	21.66	21.68	21.70	21.72	21.65	21.69	21.72	21.71
5	*	22.84	22.62	22.73	22.77	22.61	22.72	22.74	22.74
6	*	*	*	*	*	*	22.94	22.92	22.95
7	24.39	24.37	24.30	24.36	24.38	24.36	24.37	24.37	24.36
8	32.24	32.18	32.11	32.19	32.24	32.20	32.18	32.23	32.21
9	34.13	34.09	34.14	34.00	34.21	34.10	34.09	34.00	34.09
10	*	36.09	36.12	36.04	36.19	36.07	36.06	36.04	36.07
11	40.47	40.71	40.51	40.58	40.57	40.51	40.53	40.56	40.54
12	46.12	46.29	46.12	46.15	46.07	46.12	46.13	46.10	46.12
13	47.98	48.29	48.13	48.14	48.02	48.09	48.13	48.08	48.07
14	50.68	51.39	*	*	*	50.68	*	*	50.68
15	52.24	52.15	*	52.48	52.10	52.24	*	52.10	52.11
16	54.88	54.96	54.73	*	*	54.81	54.76	54.77	54.79
17	62.59	62.61	62.50	62.74	62.72	62.55	62.61	62.73	62.62
18	65.41	65.47	65.82	65.97	65.73	65.42	65.74	65.86	65.61
19	67.81	67.82	67.78	67.55	67.74	67.80	67.79	67.77	67.80
20	70.60	70.66	70.23	70.57	70.57	70.64	70.63	70.57	70.58
21	73.28	73.38	73.42	73.67	73.70	73.37	73.41	73.44	73.37

* Mode not found.

Table 7.18. Natural frequencies (Hz) identified from the various single experiments and combinations of experiments using burst-random excitation.

The tables indicate that modes are more consistently found when more columns are included in the transfer function. For the multisine data, excitation at only line B, C, or D enables almost all modes to be identified, but six modes are missed if only line E or F is used. For burst-random, three modes are typically missed when using only a single line. Including three excitation lines improves the capture of modes, and all modes of interest are found when all five experiments are included in the formation of the transfer function.

The natural frequencies vary by small amounts for all modes depending on the location of excitation. However, there is no indication that the accuracy suffers by combining data from

separate experiments. This is not surprising since an accuracy decrease is more likely to occur in damping and modal mass.

7.8.3.2 Modal Damping

Modal damping is also compared for each experiment and for the various combinations of experiments. When experiments are combined, the expectation is that a modal peak becomes 'smeared' due to the slight changes in frequency that result from the time-varying nature of the structure. Smearing of the peak often results in an increase in calculated damping since the damping is related to the sharpness of the peak. Thus, an increase in damping for the combined experiments would indicate that more error is introduced by data inconsistency. This phenomenon is checked for in the results from the multisine testing presented in Table 7.19, and the burst-random results presented in Table 7.20.

Mode	Excitation Lines Used in Transfer Function								
No.	B	C	D	E	F	B+C+D	C+D+E	D+E+F	All
1	0.52	0.57	0.50	0.64	0.46	0.55	0.53	0.56	0.59
2	0.43	1.26	1.53	0.98	0.88	0.81	1.48	1.48	0.89
3	0.70	0.67	0.68	0.57	0.64	0.71	0.76	0.69	0.78
4	1.34	1.07	0.90	0.70	0.70	1.11	0.79	0.70	0.76
5	*	1.42	0.57	0.51	*	0.62	0.80	0.98	0.98
6	1.13	1.46	1.30	*	0.64	1.34	1.15	1.21	0.80
7	0.81	0.76	0.78	0.92	0.87	0.83	0.86	1.03	0.90
8	0.38	0.41	0.43	*	0.33	0.55	0.45	0.35	0.42
9	0.15	0.16	0.18	*	0.17	0.20	0.17	0.18	0.21
10	0.20	0.12	0.13	0.14	0.12	0.14	0.15	0.16	0.17
11	0.79	*	0.72	0.67	0.59	0.76	0.74	0.64	0.70
12	0.90	0.87	0.91	0.96	1.11	0.99	0.96	1.00	1.06
13	0.84	0.64	0.70	0.63	0.63	0.79	0.75	0.68	0.74
14	0.76	0.86	1.08	*	*	0.76	0.96	*	0.77
15	0.63	0.69	0.70	*	0.57	0.63	0.70	0.57	0.57
16	0.85	1.29	1.12	1.17	*	0.95	1.14	1.14	1.03
17	0.41	0.40	0.42	0.34	*	0.45	0.54	0.37	0.54
18	1.33	1.33	1.97	1.67	*	1.42	1.69	1.70	1.60
19	0.35	0.33	0.32	*	*	0.34	0.33	0.33	0.34

* Mode not found.

Table 7.19. Damping ratio (%) identified from the various single experiments and combinations of experiments using multisine excitation.

Mode No.	Excitation Lines Used in Transfer Function								
	B	C	D	E	F	B+C+D	C+D+E	D+E+F	All
1	0.13	0.03	0.46	0.13	*	0.10	0.18	0.21	0.18
2	0.49	1.02	1.49	1.22	0.75	0.70	1.33	0.83	0.72
3	0.73	0.71	0.67	0.60	0.59	0.79	0.75	0.76	0.75
4	1.37	1.12	0.97	0.73	0.72	1.19	0.83	0.73	0.78
5	*	0.50	0.45	0.43	0.59	0.50	0.58	0.55	0.60
6	*	*	*	*	*	*	1.43	0.82	1.32
7	0.85	0.81	0.74	0.79	1.00	0.79	0.79	0.94	0.83
8	0.35	0.35	0.38	0.34	0.31	0.39	0.35	0.35	0.39
9	0.16	0.16	0.17	0.19	0.19	0.18	0.18	0.19	0.20
10	*	0.15	0.10	0.12	0.12	0.12	0.12	0.15	0.15
11	0.77	0.19	0.72	0.63	0.64	0.78	0.74	0.67	0.71
12	0.89	0.82	0.85	0.94	0.95	0.90	0.90	0.92	0.97
13	0.87	0.67	0.66	0.65	0.63	0.77	0.69	0.66	0.73
14	0.78	0.83	*	*	*	0.79	*	*	0.80
15	0.62	0.76	*	0.50	0.53	0.65	*	0.53	0.54
16	0.85	1.27	1.01	*	*	0.97	1.09	1.04	1.07
17	0.36	0.32	0.33	0.27	0.26	0.37	0.44	0.29	0.44
18	1.33	1.38	1.92	1.65	1.55	1.01	1.61	1.70	1.59
19	0.34	0.34	0.34	0.66	0.30	0.34	0.33	0.33	0.34
20	0.59	0.57	0.49	0.59	0.46	0.58	0.60	0.62	0.49
21	0.61	0.47	0.58	0.72	0.58	0.57	0.60	0.75	0.70

* Mode not found.

Table 7.20. Damping ratio (%) identified from the various single experiments and combinations of experiments using burst-random excitation.

For both excitation signals, the damping ratios vary widely as expected since a small error in the angle of the pole results in a large error in the damping ratio when damping is low. Additionally, different input locations have varying capability to excite each mode causing further variability. However, an attempt is still made to analyze if combining inconsistent experiments diminishes accuracy by only considering the modes that have relatively consistent results.

For the multisine data, Mode 3 is considered first. This mode is well separated from other modes and always has a strong and well-shaped peak. The damping ratio varies between 0.57% and 0.70% when only a single experiment is considered. When three experiments are combined, the

damping ratio is always higher than any individual value from the lines included. When all five experiments are combined, the damping ratio is 0.78%. This is more than 10% higher than the ratio found from any individual experiment. Thus, it appears as if the combination of experiments does cause smearing of the peak and an increase in calculated damping. Modes 7, 9, 10, 12, and 17 show similar results.

For the burst-random data, the results are the same. Modes 3, 8, 9, 12, and 17 have relatively consistent damping ratios when single experiments are used, and the calculated damping increases when experiments are combined. For these five modes, the damping found using all experiments is an average of 19% higher than the average damping found from the individual experiments. However, modes 7 and 20 have a lower damping ratio from all experiments than the average of the individual experiments. This result is attributed to an increase in accuracy due to the extra redundant data.

For modes that have less consistent estimates of damping, the results using combined experiments are as likely to be lower as they are to be higher than those from single experiments. Also, the combination of experiments enables calculation of reasonable damping values for almost all modes, whereas an acceptable damping value could not be found with data from only a single experiment in some cases.

Overall, the results indicate that calculated damping values are increased and made less accurate by combining experiments. However, damping is not well-estimated by individual experiments in many cases. In these instances, accuracy of damping seems to be improved by combining several experiments. Therefore, the logical course of action is to use the average damping from

several individual experiments when the results are consistent. When the individual results are not consistent, then combinations of experiments should be used to estimate damping.

7.8.3.3 Modal Mass

Modal mass is also compared in the same manner as frequencies and damping. The magnitude of modal mass is most directly related to the magnitude of the eFRF peak, and thus smearing of the peak due to inconsistent data is not expected to have a significant effect on modal mass. The values calculated are presented in Table 7.21 for multisine excitation and in Table 7.22 for burst-random excitation.

Mode No.	Excitation Lines Used in Transfer Function								
	B	C	D	E	F	B+C+D	C+D+E	D+E+F	All
1	2673	2584	2940	2374	3209	2949	2983	2784	2831
2	1517	1674	1579	3229	3315	2050	2021	2288	2214
3	2697	2790	2849	2925	2742	2764	2646	2835	2615
4	3559	4355	3686	3544	3623	4213	4068	3597	3992
5	*	1970	2699	2992	*	2770	2363	2091	2083
6	3244	2574	5369	*	4435	2861	2551	2650	4393
7	5630	5645	5333	4827	5450	5405	5098	4660	5158
8	5213	3918	3294	*	6071	3606	3971	5467	5007
9	2117	3733	5914	*	3233	3276	4544	4623	3945
10	708	5702	11101	10417	4849	5453	2740	7531	2642
11	6962	*	6336	5506	7254	6399	5927	6775	6563
12	4385	5818	3167	2851	2786	3431	3156	2968	3168
13	2161	3503	2490	1562	3118	2290	2311	2602	2370
14	4731	11999	4183	*	*	4791	7806	*	4770
15	5585	9578	3964	*	777	2831	3028	772	801
16	9857	6867	7105	9523	*	8763	6816	6030	7755
17	2036	2852	2684	2771	*	2479	2392	2842	2365
18	8229	12465	9006	5887	*	7841	6614	5918	6845
19	3543	1708	13995	*	*	3755	6935	10764	3360

* Mode not found.

Table 7.21. Modal mass (lbf/g) identified from the various single experiments and combinations of experiments using multisine excitation.

Mode No.	Excitation Lines Used in Transfer Function								
	B	C	D	E	F	B+C+D	C+D+E	D+E+F	All
1	1438	687	2977	1216	*	4681	3417	1790	3382
2	1307	1499	2022	2365	4437	2113	1806	3379	2390
3	2762	2575	2583	2648	2639	2417	2537	2526	2538
4	3682	4212	3981	3352	3376	4015	3935	3435	3862
5	*	2919	2401	2817	3212	2504	2583	2629	2620
6	*	*	*	*	*	*	3013	3795	3214
7	5473	5214	5438	5114	4740	5395	5213	4815	5205
8	5350	4003	3460	3551	6908	4313	3894	5833	4586
9	1974	2804	5710	2379	2606	2626	3097	2572	2841
10	*	4125	12610	8211	5524	5624	3813	5676	3666
11	6638	31400	6461	5839	6800	6403	6020	6578	6555
12	4429	6199	3326	2807	2888	3760	3236	3020	3242
13	2051	3440	2575	1609	3105	2309	2398	2641	2364
14	5107	12398	*	*	*	5155	*	*	5093
15	6472	10286	*	7819	1317	3203	*	1302	1309
16	8918	6856	7436	*	*	7883	6267	6690	7162
17	1558	2552	2453	2811	2654	2257	2150	2890	2102
18	7665	14273	8833	6132	6190	10442	7265	5938	6768
19	3018	1586	14047	16823	13867	3403	7025	10932	3161
20	2076	2134	1501	1943	2354	2113	1975	1822	2343
21	1796	2371	2178	1751	1471	2098	2104	1521	1623

* Mode not found.

Table 7.22. Modal mass (lbf/g) identified from the various single experiments and combinations of experiments using burst-random excitation.

There is significant variation in the calculated values of modal mass with either excitation signal. With multisine excitation, modes 3, 4, 7, and 17 have the most consistent results. The average values of modal mass for the individual experiments are 2801, 3753, 5377, and 2586 lbf/g respectively. The modal masses for these four modes found with all five experiments combined vary from the averages noted by -7%, 6%, -4%, and -9% respectively. The modal mass from all experiments combined is also within the range of values of the individual experiments for 17 of the 19 modes.

For the burst-random data, modes 3, 4, 7, 17, 20, and 21 have the most consistent results. The modal masses for these six modes calculated with all five experiments combined vary from the averages of the individual experiments by -4%, 4%, 0%, -13%, 16%, and -15% respectively. The modal mass from all experiments combined is within the range of values of the individual experiments for 17 of the 21 modes.

Overall, there is no evidence of a consistent bias error in the magnitude of modal mass caused by combining experiments. Also, the modal mass found from combined experiments usually lies within the range of the values found from the included individual experiments. The modal mass found from individual experiments is sometimes highly variable (see burst-random mode 19), and thus including more data in the transfer function helps reduce the impact of poor results from single experiments.

7.8.3.4 Modal Flexibility

The modal flexibility matrix calculated for any experiment is assembled by superposition of the contributions of each mode. The contribution of a mode is driven by a few factors. The modal vector determines the distribution to the various input/output DOFs as $U * U^T$, where U is a modal vector. The magnitude of the contribution is inversely proportional to modal mass (M_r) and is approximately inversely proportional to the square of the undamped natural frequency (Ω) when damping is low. For modes at higher frequencies, the magnitude of the contribution to modal flexibility is greatly reduced due to the Ω^2 term, and those higher frequency modes are thus less important.

The accuracy of modal flexibility is primarily driven by the accuracy of M_r. The natural frequencies are highly accurate, and the modal vectors are usually accurate as well, and can be

visually verified for many structures. However, the modal mass is largely controlled by the magnitude of the eFRF. This magnitude can be significantly affected by processing issues such as imperfect modal filtering, and by testing issues such as leakage and noise. As is quite noticeable in Table 7.21 and Table 7.22, the modal mass calculated varies significantly and will thus have a significant impact on the accuracy of modal flexibility.

The accuracy of modal flexibility is determined by calculating D and D_d with respect to the static flexibility matrix from the finite element model. The various comparisons of experimental modal flexibility to the baseline static flexibility are made in Table 7.23 for multisine excitation and in Table 7.24 for burst-random excitation.

Desc.	Excitation Lines Used in Transfer Function								
	B	C	D	E	F	B+C+D	C+D+E	D+E+F	All
D	19.3	22.5	11.3	50.2	32.2	7.7	11.3	20.5	12.2
Dd	0.48	0.71	0.85	1.07	1.40	0.73	0.87	0.82	0.77
Disp.	109%	108%	93%	108%	84%	92%	89%	94%	94%

Table 7.23. Comparison of modal flexibility from the various single experiments and combinations of experiments using multisine excitation.

Desc.	Excitation Lines Used in Transfer Function								
	B	C	D	E	F	B+C+D	C+D+E	D+E+F	All
D	108.1	85.3	10.4	38.7	32.1	27.8	14.2	51.5	12.0
Dd	1.81	2.43	0.95	1.75	3.02	1.57	0.98	1.10	1.01
Disp.	23%	4%	88%	42%	1%	52%	76%	96%	79%

Table 7.24. Comparison of modal flexibility from the various single experiments and combinations of experiments using burst-random excitation.

Considering the analysis groups from multisine excitation, modal flexibility generally improves when multiple experiments are combined. The best value of D (7.7) is found when excitation lines B, C, and D are combined. The value of D is worst when only the Line E data is used. The

average value of D is 27.1 for the five single lines, and is 13.2 for the three groups of three lines. For the elements on the main diagonal of the flexibility matrix, the best result is found using only Line B, and the worst result is found using only Line E. The results using combinations of lines are much more consistent than the results using single lines. The average of D_d is 0.90 for the five individual experiments, and is 0.81 for the three groups of three experiments. Finally, the calculated displacements using modal flexibility range from 84% to 109% of the static displacements when only a single experiment is considered. The range of values is much tighter with multiple lines, only varying from 89% to 94%.

The results using burst-random excitation are similar. The values have far less variability when multiple lines are used as compared to single lines. Overall, the data presented suggests that providing more columns in the transfer function improves the accuracy of modal flexibility.

7.8.3.5 Summary of Results for Combining Data

Combining data from inconsistent experiments made no noticeable difference in the highly stable natural frequencies of the various modes. The calculated modal damping noticeably increases and presumably becomes less accurate due to combining data. However, in cases when damping significantly varies between experiments, combining data improves the result. The calculated value of modal mass is not obviously better or worse when data is combined, but the stability of the result seems to improve when data is combined. Finally, the accuracy of modal flexibility is improved by combining columns, and the variability is also significantly decreased. Overall, combining multiple experiments improves the calculated modal properties of the subject bridge in more cases than it diminishes them.

Despite the apparent improvement in modal parameter accuracy that results from having additional columns in the transfer function, it is recognized that larger magnitude changes to the structure over time will diminish accuracy. It is always better to excite as many DOFs as possible in a single experiment to circumvent any issues with inconsistent data. However, if this is not feasible, then combining several experiments to produce a larger transfer function is shown herein to be acceptable.

7.8.4 Comparison of Multisine and Burst-Random Excitation Techniques

Exciting a structure with burst-random input is one of the common techniques used in modal testing. The benefits of this signal type have been discussed elsewhere in this thesis, and burst-random inputs are used as a baseline for comparison. Multisine excitation signals are not commonly used, and very little literature exists describing its use for testing of civil structures. However, the signal has many benefits and may have been overlooked by many researchers. The use of deterministic signals is preferred with the tactile transducers because of the ease with which the amplitude can be controlled at any frequency. Amplitude control is desirable to prevent stroke exceedance at lower frequencies while still generating high force at other frequencies. Since the selected type of multisine signal has not been validated in testing of civil structures, the results using this signal are compared to the results using burst-random excitation herein.

For this analysis, only the results based on combining all lines of shakers into a single large transfer function are presented. This is done to simplify and clarify figures, tables, and discussions. Also, the previous section demonstrated that using a transfer function that includes all excitation DOFs results in generally more stable modal parameters. Also, Modes 20 and 21 are not considered since they were not identified in the multisine testing. The multisine signal

was constructed to only excite frequencies up to 70 Hz, and thus these two modes were not excited.

7.8.4.1 General Remarks Regarding Burst-Random and Multisine

Although the results of modal parameter identification are compared in detail for the two excitation techniques, there are other indications about the success of each signal that are considered first. A major issue with burst-random excitation is that a choice between leakage and low SNR must be made. If the excitation is stopped early enough in the capture window, then the structure response will be almost completely damped out by the end of the window and leakage will be small, but SNR will also be lower. If excitation is stopped later in the capture window, then SNR improves, but leakage gets worse.

For the current testing, a relatively long capture window was used so that SNR could be reasonably high while still having low leakage. Excitation occurs during 19.5 seconds of the 25-second capture window, and 5 seconds are provided for the response to damp out. The combined effects of leakage and SNR can be evaluated by reviewing coherence. Coherence is a measure of how much of the structure output can be attributed to the known input. This is a frequency domain measurement, and thus leakage and noise effects are automatically incorporated. A coherence value of unity indicates that the output is purely due to the input, and a coherence of zero indicates that there is no relation between the input and output.

Figure 7.33 shows an example of the difference between coherence using multisine excitation and using burst-random excitation. The data shown is for excitation with four shakers at Line D, and the coherence is for the output measurement at DOF 3. The multisine coherence is low outside of the 4 Hz to 70 Hz excitation band as expected, since only ambient inputs should have

excited those frequencies. Coherence is generally nearly unity for the band that was excited. By contrast, the coherence is not nearly as good for burst-random excitation. This indicates that the output does not agree well with the input forces at numerous frequency lines. The cause is some combination of leakage and low SNR. If the output accelerations and input forces have low coherence at a frequency line that is nearby a natural frequency of the structure, then it can be expected that modal mass will be estimated poorly.

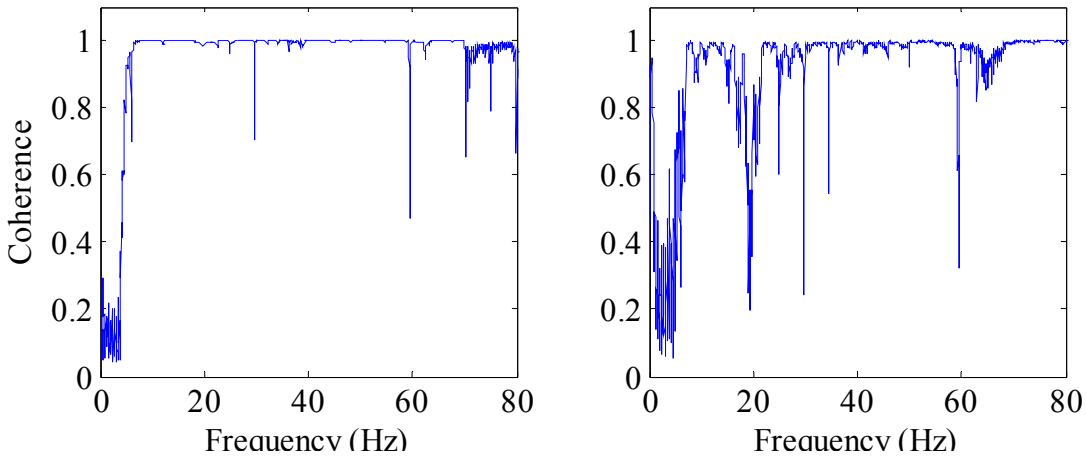

Figure 7.33. Typical example of coherence using multisine excitation (left) and burst-random excitation (right).

7.8.4.2 Natural Frequencies, Modal Damping, and Modal Mass

The undamped natural frequencies, damping ratios, and modal mass found for each mode using multisine excitation and using burst-random excitation are compared in Table 7.25. The published percent difference values are calculated as the difference between the two excitation methods divided by the mean of the two methods.

Mode	Natural Frequency (Hz)			Damping Ratio (%)			Modal Mass (lbf/g)		
No.	MS	BR	Diff.	MS	BR	Diff.	MS	BR	Diff.
1	6.12	6.12	0.1%	0.59	0.18	109%	2831	3382	18%
2	6.98	6.99	0.1%	0.89	0.72	22%	2214	2390	8%
3	12.21	12.25	0.3%	0.78	0.75	4%	2615	2538	3%
4	21.69	21.71	0.1%	0.76	0.78	3%	3992	3862	3%
5	22.48	22.74	1.1%	0.98	0.60	48%	2083	2620	23%
6	22.71	22.95	1.0%	0.80	1.32	49%	4393	3214	31%
7	24.32	24.36	0.2%	0.90	0.83	8%	5158	5205	1%
8	32.18	32.21	0.1%	0.42	0.39	9%	5007	4586	9%
9	34.04	34.09	0.2%	0.21	0.20	5%	3945	2841	33%
10	36.07	36.07	0.0%	0.17	0.15	12%	2642	3666	32%
11	40.54	40.54	0.0%	0.70	0.71	2%	6563	6555	0%
12	46.02	46.12	0.2%	1.06	0.97	9%	3168	3242	2%
13	48.00	48.07	0.1%	0.74	0.73	1%	2370	2364	0%
14	50.56	50.68	0.2%	0.77	0.80	5%	4770	5093	7%
15	52.12	52.11	0.0%	0.57	0.54	6%	801	1309	48%
16	54.77	54.79	0.0%	1.03	1.07	4%	7755	7162	8%
17	62.26	62.62	0.6%	0.54	0.44	21%	2365	2102	12%
18	65.47	65.61	0.2%	1.60	1.59	1%	6845	6768	1%
19	67.74	67.80	0.1%	0.34	0.34	1%	3360	3161	6%

Table 7.25. Comparison of various modal parameters found from multisine excitation (MS) and burst-random excitation (BR).

The undamped natural frequencies found are essentially identical for both excitation techniques. The largest differences are 1.1% for Mode 5 and 1.0% for Mode 6. The average difference for all other modes is less than 0.2%. Also, both methods identified all modes of interest.

The damping ratios and modal masses are in very good agreement between the two methods for most modes. The burst-random signals did not excite Mode 1 well, and thus the eFRF was significantly more noisy than with multisine input. This is demonstrated in Figure 7.34 which shows the eFRF peak at Mode 1 for both excitation techniques, and the difference in noise is apparent. This diminishes the accuracy of the estimated damping and modal mass.

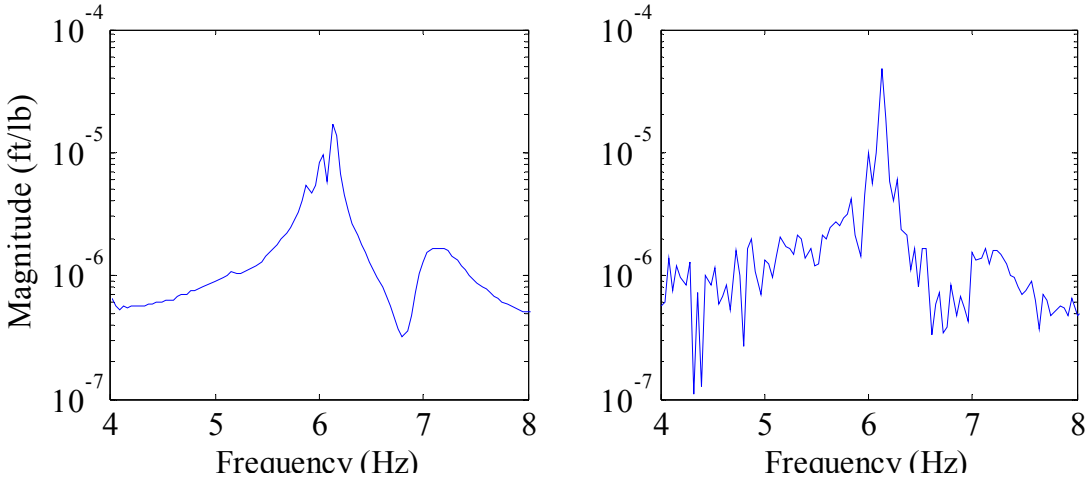

Figure 7.34. eFRF for Mode 1 from multisine excitation (left) and from burst-random excitation (right).

Modes 5 and 6 are also not in good agreement. A review of the mode shapes shows that for burst-random, Mode 5 was more affected by the nearby Mode 6 than with multisine. However, the modal vector for Mode 6 was more accurate with burst-random excitation. The mode shape accuracy impacts modal filtering and the resulting damping ratios and modal masses found from the eFRFs. Thus, the Mode 5 results are more accurate from the multisine testing and the Mode 6 results are more accurate from the burst-random testing.

Modes 9 and 10 have good agreement for damping but not for modal mass. The mode shapes are nearly identical, and the eFRFs are very similar in appearance between multisine and burst-random. However, the eFRF peaks are different in magnitude. Using the impact testing performed previously as a guide, burst-random is more accurate for Mode 9 and multisine is more accurate for Mode 10.

The modal mass for Mode 15 also has poor agreement between the two excitation methods. A review of the modal mass estimated from various combinations of excitation lines shows that this mode is generally poorly identified in many experiments.

Excluding Modes 1, 5, 6, 9, 10, and 15, the average percent difference in damping ratio for 13 modes is 7%, and for modal mass is 5%. Overall, the agreement between the two methods is very good.

7.8.4.3 Comparison of Modal Vectors

Modal vectors found using the two excitation signals are compared to each other using MAC values. Table 7.26 shows the results and the MAC values are essentially unity for all modes except Modes 5 and 6. For Mode 5, the vector using burst-random excitation is affected by the Mode 6 vector. For Mode 6 (torsion 2 shape), both excitation techniques result in suboptimal mode shape plots, neither of which is a good approximation of the expected second torsion mode. It is noted that this mode was difficult to find with burst-random excitation (Table 7.18), largely because of the very closely spaced and dominant Mode 5. A higher frequency resolution may have improved this issue, but in any case, a low MAC value is the result.

Mode	MAC	Mode	MAC	Mode	MAC	Mode	MAC
1	1.00	6	0.23	11	1.00	16	1.00
2	1.00	7	1.00	12	1.00	17	1.00
3	1.00	8	0.99	13	1.00	18	1.00
4	1.00	9	0.98	14	1.00	19	1.00
5	0.87	10	1.00	15	1.00		

Table 7.26. Comparison of modal vectors using MAC values for multisine and burst-random excitation.

7.8.4.4 Comparison of Modal Flexibility

Modal flexibility matrices are again compared using the criteria discussed previously, and which are presented in Table 7.27. The value of D is essentially identical for both excitation signals. However, the value of D_d and the average midspan deflection are much better with multisine

excitation than with burst-random excitation. This can largely be attributed to the better identification of Mode 1 with multisine testing.

Desc.	MS	BR
D	12.2	12.0
Dd	0.77	1.01
Disp.	94%	79%

Table 7.27. Comparison of modal flexibility for multisine and burst-random excitation.

7.8.4.5 Summary of Results for Comparison of Excitation Signals

Both burst-random and multisine excitation identify all modes of interest and the natural frequencies are essentially identical. Values of modal damping and modal mass are in good agreement between the two methods with one notable exception: damping and modal mass for Mode 1 are estimated poorly using the burst-random signal. The modal vectors are also practically identical between the two excitation techniques, except for two modes that are very closely spaced and which interfere with each other. The resulting modal flexibility matrix is more accurate using the multisine signal, largely because of the better identification of Mode 1. Overall, the estimated modal parameters are slightly more accurate with multisine excitation than with burst-random excitation.

7.8.5 Effects of Traffic Disturbances on Modal Parameter Identification

The modal results presented above were found from data sets that were minimally affected by vehicular use of the subject bridge. However, for structures on roads with higher ADT, it will be more difficult to capture such clean data. Additionally, it is not desirable to interrupt the normal operation of a bridge to perform testing. Thus, the level to which the results are affected by including data that is compromised by vehicular crossings is studied. If the results are little affected, then testing can be performed without regard to traffic. If the results are significantly

worse with traffic, then testing must be performed either during low traffic periods (e.g. at night) or during temporary bridge closings.

This analysis is performed using the Line D multisine data. This single excitation line is selected since all modes were found with the clean data and because there were many vehicle crossings during the period during which this experiment was undertaken. For the results presented, ten clean data sets for each of the four polarity settings are used, and ten data sets with traffic for each polarity setting are used. Thus, both methods use the exact same amount of data for modal identification.

7.8.5.1 General Comparisons of Clean Data and Data With Traffic

Before discussing the modal parameters, it is useful to investigate the differences between the clean data and the data that includes traffic crossings. First, the measured force input (in the frequency domain) at DOF 8 is shown in Figure 7.35 for a typical clean data set and for a typical data set during which a vehicle crossed the bridge. It is noted that the force input was essentially unchanged, and the two curves are indistinguishable in the plot. Next, the measured acceleration at DOF 8 is shown in Figure 7.36 for a clean data set and for a set with a vehicle crossing (also in the frequency domain). This demonstrates that the output measurements are significantly affected by vehicles. The curve with traffic is far more noisy, and the magnitude is far greater below about 30 Hz.

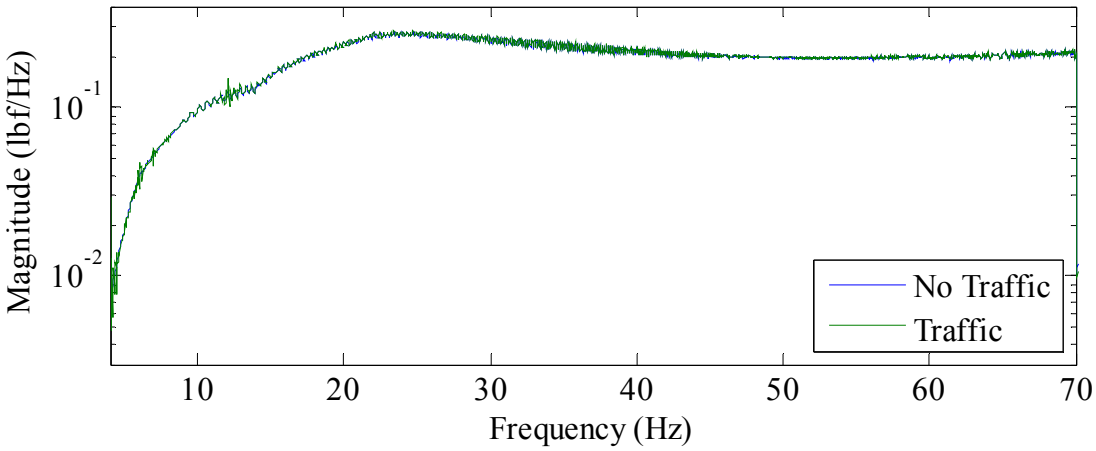

Figure 7.35. Typical measured force input without traffic and with traffic.

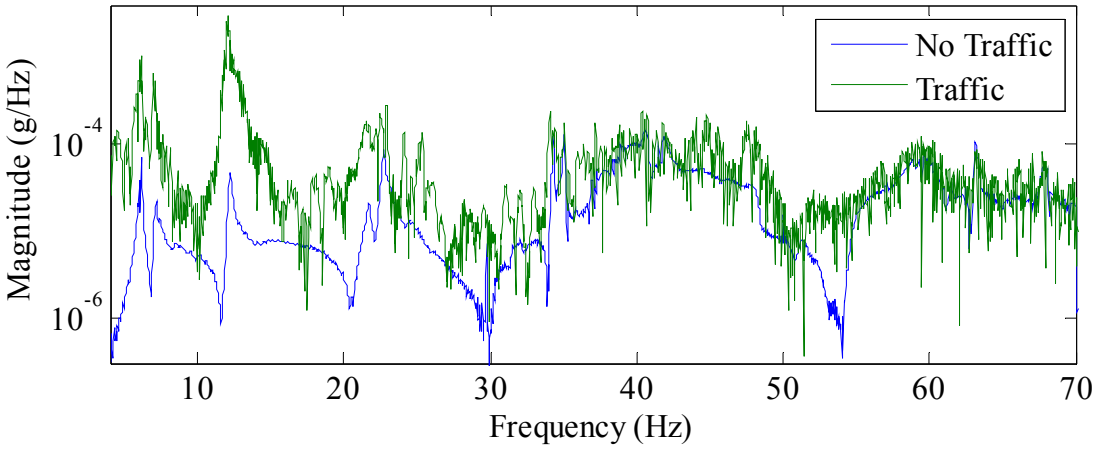

Figure 7.36. Typical measured acceleration output without traffic and with traffic.

Naturally, the FRFs are impacted by traffic as well. The FRF for DOF 8 is shown in Figure 7.37 from data with traffic and without traffic. The added noise on the outputs is reflected throughout the length of the FRF, but the magnitude is only significantly affected below about 20 Hz. It is obvious that the modal properties for Mode 1 (6 Hz) and for Mode 2 (7 Hz) will be inaccurate. Interestingly, though, the peak at about 22 Hz for Mode 4 is not very noisy and the magnitude is nearly unaffected by the traffic. Many of the peaks at frequencies higher than 30 Hz have accurate magnitudes, although most are more noisy than the peak at 22 Hz.

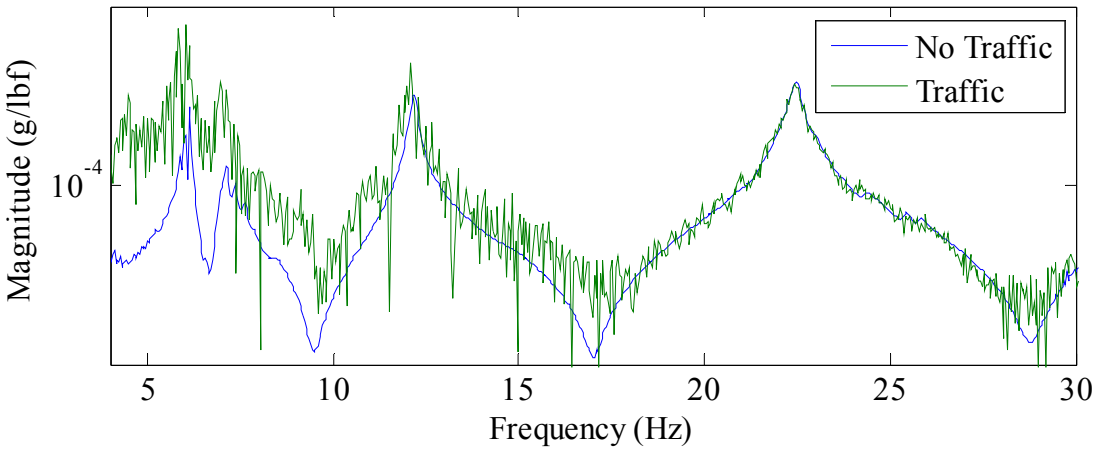

Figure 7.37. Typical measured FRF without traffic and with traffic.

Coherence is a measure of how much of an output measurement can be attributed to the input measurements. A value of unity indicates that the output is entirely due to the inputs, and a value of zero indicates that the output is completely unrelated to the inputs. Again, DOF 8 is used as an illustrative example and coherence with clean data and with traffic is plotted in Figure 7.38. Not surprisingly, the coherence is poor when data with traffic is used. It is also noted that traffic has the greatest effect at lower frequencies.

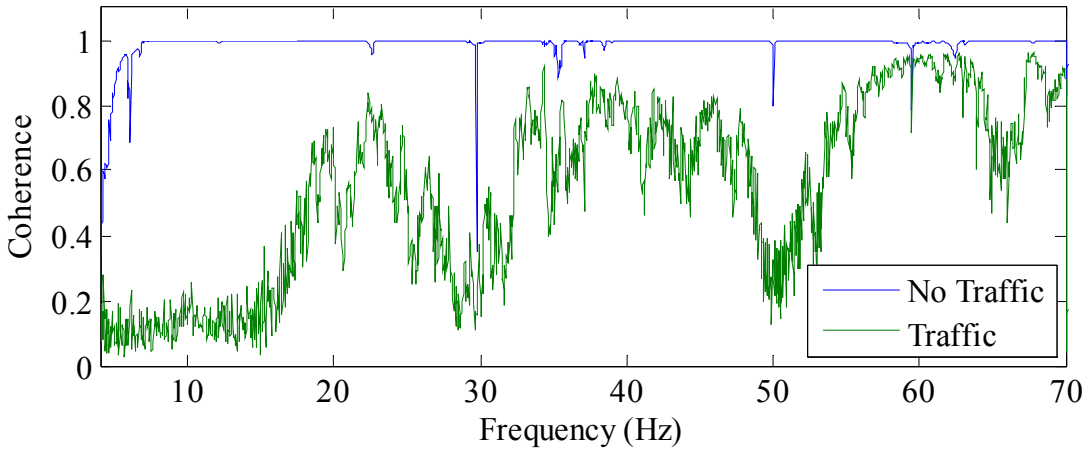

Figure 7.38. Typical plot of multiple coherence without traffic and with traffic.

Based on the general comparisons of data with and without traffic provided, it can be expected that the presence of traffic will decrease the accuracy of modal parameters, especially at lower frequencies.

7.8.5.2 Natural Frequencies, Modal Damping, and Modal Mass

The undamped natural frequencies, damping ratios, and modal mass found for each mode using clean data and using data with traffic crossings are compared in Table 7.28. The published percent difference is calculated as the difference between the two values divided by the value found with clean data.

Mode	Natural Frequency (Hz)			Damping Ratio (%)			Modal Mass (lbf/g)		
No.	Clean	Traffic	Diff.	Clean	Traffic	Diff.	Clean	Traffic	Diff.
1	6.12	6.02	1.6%	0.50	0.04	92%	2940	12	100%
2	6.98	*	*	1.53	*	*	1579	*	*
3	12.18	12.12	0.5%	0.68	0.34	50%	2849	2166	24%
4	21.67	*	*	0.90	*	*	3686	*	*
5	22.49	22.46	0.2%	0.57	0.63	10%	2699	2635	2%
6	22.87	*	*	1.30	*	*	5369	*	*
7	24.29	24.08	0.9%	0.78	0.33	58%	5333	6911	30%
8	32.04	31.98	0.2%	0.43	0.31	27%	3294	3246	1%
9	34.13	34.12	0.0%	0.18	0.23	26%	5914	5516	7%
10	36.15	36.14	0.0%	0.13	0.13	3%	11101	15055	36%
11	40.50	40.50	0.0%	0.72	0.68	5%	6336	6777	7%
12	45.97	45.88	0.2%	0.91	0.77	16%	3167	3750	18%
13	47.98	47.94	0.1%	0.70	0.68	4%	2490	2800	12%
14	51.33	*	*	1.08	*	*	4183	*	*
15	52.27	52.26	0.0%	0.70	0.76	9%	3964	3428	14%
16	54.65	54.61	0.1%	1.12	1.39	24%	7105	6168	13%
17	62.30	62.27	0.1%	0.42	0.49	18%	2684	2481	8%
18	65.91	*	*	1.97	*	*	9006	*	*
19	67.78	67.76	0.0%	0.32	0.33	3%	13995	13903	1%

* Mode not found.

Table 7.28. Comparison of various modal parameters found from data without traffic (clean) and from data with traffic.

The undamped natural frequencies are barely affected by the presence of traffic; however, 5 of the 19 modes could not be identified due to the high noise. The damping ratios and modal masses are significantly affected by the presence of traffic for many modes. The worst result is for Mode 1, where both the damping and modal mass are nearly zero. The low modal mass indicates that the mode appears to be significantly excited by small force inputs, which is a direct result of the high output accelerations caused by the unmeasured traffic input. The damping is similarly affected. At higher frequencies vehicular crossings provided little excitation, and thus the damping and modal mass are not nearly as affected.

Figure 7.39 shows the synthesized eFRF (thick black curve) and the actual eFRF (thin curve) for Mode 1 with and without traffic, and the difference is significant. Noise is very high, especially in the phase plot, and the peak magnitude with traffic is nearly three orders of magnitude higher. Figure 7.40 shows the same information but for Mode 13. Within the frequency band shown, the added noise is visible, but of low amplitude. The magnitude of the eFRF is nearly unaffected by traffic excitation.

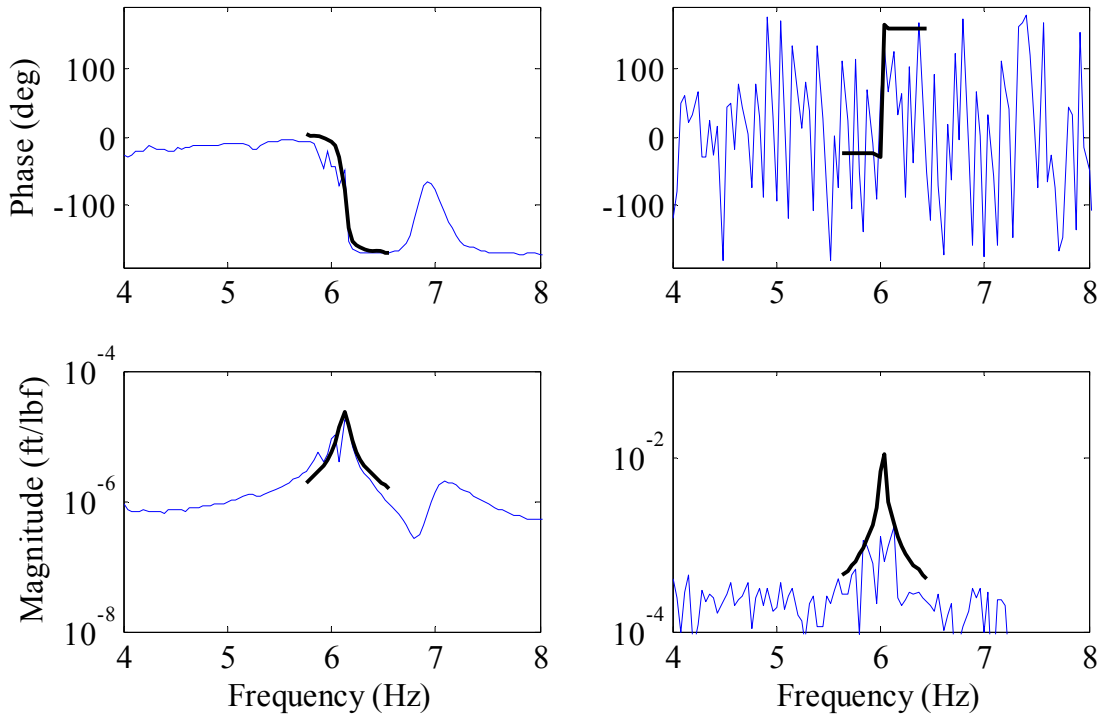

Figure 7.39. Results of SDOF identification of Mode 1 without traffic (left) and with traffic (right).

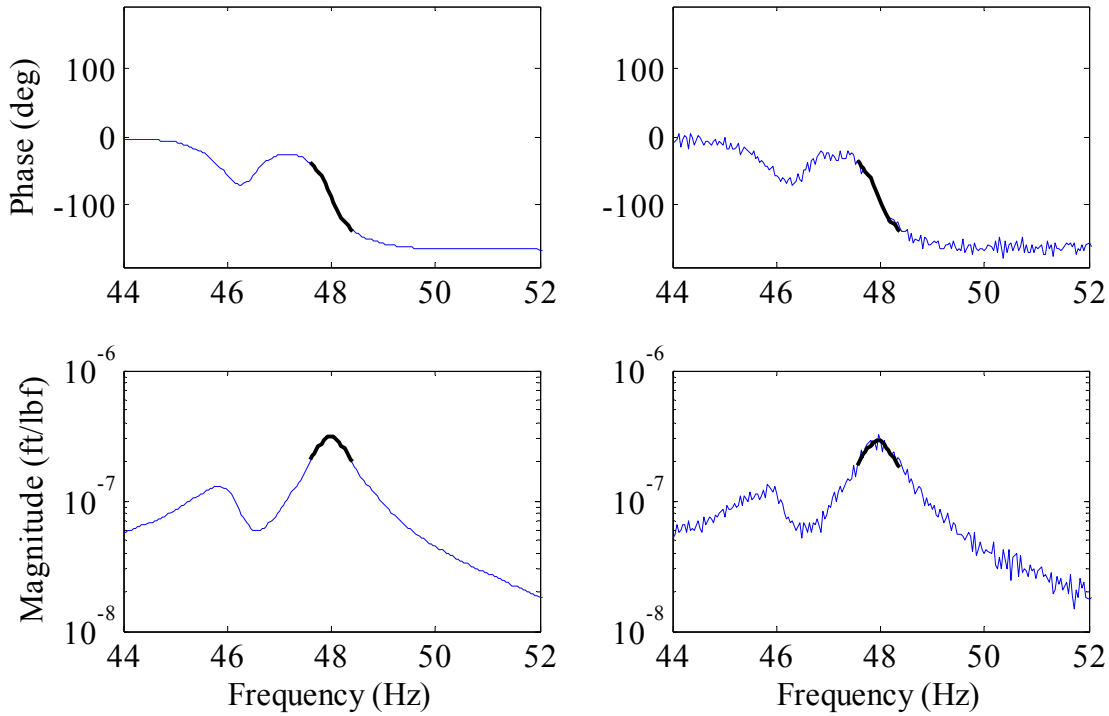

Figure 7.40. Results of SDOF identification for Mode 13 without traffic (left) and with traffic (right).

It is also noted that the traffic excitation causes a serious leakage error. The multisine signal is designed to be free of leakage, exciting only frequency lines that are present in the FFT, and being completely periodic in the observation window. The traffic excitation meets neither requirement, and leakage must occur. The effects of leakage are not easily identified in the frequency domain data because noise is so prevalent; however, leakage is diminishing the accuracy of the modal parameters by some unknown amount.

Many researchers use traffic excitation as an ambient input in output-only analysis, and assume that the traffic input can be approximated as white noise. The results of this testing indicate that traffic does not remotely excite all frequencies evenly, and that the assumption of white noise would give highly erroneous results. For this bridge, the damping and modal mass of modes below 20 Hz are inaccurate due to the magnitude error on the FRFs. The damping and modal mass values above 20 Hz are inaccurate due to more noise in the FRFs.

7.8.5.3 Comparison of Modal Vectors

Modal vectors found from data with traffic present are compared to modal vectors found from the clean data. MAC values are used to compare how similar the vectors are to each other. The outcome for each mode is shown in Table 7.29. The MAC values are all nearly unity, and thus the captured mode shapes are essentially identical with or without traffic present.

Mode	MAC	Mode	MAC	Mode	MAC
1	1.00	9	0.98	15	0.99
3	1.00	10	0.99	16	1.00
5	1.00	11	1.00	17	1.00
7	1.00	12	1.00	19	1.00
8	1.00	13	1.00		

Table 7.29. Comparison of modal vectors using MAC values for clean data and for data with traffic present.

7.8.5.4 Comparison of Modal Flexibility

Modal flexibility found using data with traffic crossings can be expected to be highly inaccurate since the modal mass for powerful Mode 1 is highly inaccurate. Additionally, five modes were not captured, including the important Mode 2. The results are presented in Table 7.30, and it is clear that the modal flexibility matrix found is in no way similar to the static flexibility matrix. This can largely be attributed to the very low modal mass of Mode 1, and the missing Mode 2.

Desc.	Clean	Traffic
D	11.3	18,180
Dd	0.85	358
Disp.	93%	18,700%

Table 7.30. Comparison of modal flexibility for data without traffic (clean) and for data with traffic.

7.8.5.5 Summary of Results for Traffic Crossings

The results of this analysis show that in general, data must be collected without traffic on the bridge in order to capture accurate modal parameters. Natural frequencies and modal vectors are not significantly affected by the presence of traffic, but modal damping and modal mass are affected. For this bridge, traffic causes a large increase in output accelerations for frequencies below about 20 Hz, and all frequency bands are affected by added noise. Both of these phenomena decrease the accuracy of modal damping and modal mass. The scale of the error at low frequencies is great enough that the modal masses are orders-of-magnitude different than the correct values.

7.8.6 Evaluation of Employing Roving Force Transducers

The final item to be analyzed for the bridge testing is the level of success that is achieved by simultaneously exciting more DOFs than the number of available force transducers. It is believed

that a greater spatial distribution of inputs will result in better results for the reasons discussed previously. As such, and similar to the laboratory testing, an experiment was performed with eight TTs operating simultaneously, but with only four of them outfitted with force transducers. Two nearly identical experiments were performed, with the force transducers measuring the output of four shakers in the first experiment, and measuring the output of the other four shakers in the second experiment.

If this technique is successful, then the modal parameters found should be as good as or better than those found using only four shakers. However, any unintended differences between the two parts of the roving experiments will result in inconsistent data, and the modal parameters found may be less accurate. For this analysis, the multisine results with all lines of shakers combined into a single transfer function are used as a baseline against which to compare the results of using roving force transducers (referred to as 'Baseline' in various tables and figures).

7.8.6.1 Natural Frequencies, Modal Damping, and Modal Mass

The estimated undamped natural frequencies, damping ratios, and modal mass for each mode are compared in Table 7.31. The natural frequencies with roving are nearly identical to the baseline, and all modes of interest are identified. The damping ratios are generally in good agreement, with the damping for ten of the modes within 10% of the baseline values. The modal mass shows more variability: excluding Mode 15, the modal masses using eight shakers are an average of 25% off of the baseline values. Ten of the values are lower than the baseline and nine are higher than the baseline. Overall, there is no obvious bias in the generally poor agreement between the roving modal masses and the baseline.

Mode	Natural Frequency (Hz)			Damping Ratio (%)			Modal Mass (lbf/g)		
No.	Baseline	Roving	Diff.	Baseline	Roving	Diff.	Baseline	Roving	Diff.
1	6.12	6.11	0.2%	0.59	0.59	0%	2831	2600	8%
2	6.98	7.00	0.2%	0.89	1.10	24%	2214	1870	16%
3	12.21	12.25	0.3%	0.78	0.84	8%	2615	2559	2%
4	21.69	21.67	0.1%	0.76	1.06	40%	3992	4974	25%
5	22.48	22.75	1.2%	0.98	0.56	43%	2083	3116	50%
6	22.71	22.99	1.2%	0.80	1.06	32%	4393	4252	3%
7	24.32	24.28	0.2%	0.90	0.94	4%	5158	5573	8%
8	32.18	32.13	0.2%	0.42	0.39	9%	5007	4868	3%
9	34.04	34.00	0.1%	0.21	0.21	2%	3945	1936	51%
10	36.07	36.02	0.1%	0.17	0.13	19%	2642	3436	30%
11	40.54	40.54	0.0%	0.70	0.65	7%	6563	4238	35%
12	46.02	46.01	0.0%	1.06	0.88	17%	3168	2054	35%
13	48.00	47.88	0.2%	0.74	0.79	8%	2370	1381	42%
14	50.56	50.57	0.0%	0.77	0.64	17%	4770	6015	26%
15	52.12	51.89	0.4%	0.57	0.72	25%	801	3128	290%
16	54.77	54.90	0.2%	1.03	0.95	8%	7755	6622	15%
17	62.26	62.46	0.3%	0.54	0.37	31%	2365	3711	57%
18	65.47	65.44	0.0%	1.60	1.65	3%	6845	5881	14%
19	67.74	67.68	0.1%	0.34	0.34	1%	3360	4564	36%

Table 7.31. Various modal parameters found from roving force transducer testing compared to baseline parameters.

7.8.6.2 Comparison of Modal Vectors

The modal vectors for the roving testing are compared to the baseline testing using MAC values. The results are shown in Table 7.32 and the mode shapes are nearly identical for most modes. For Modes 5, 6, and 9, the mode shapes from the roving testing are not as symmetric about midspan as they should be. For Mode 18, symmetry of the mode shape about the bridge centerline is poor. However, fifteen of the mode shapes are accurate.

Mode	MAC	Mode	MAC	Mode	MAC	Mode	MAC
1	1.00	6	0.64	11	1.00	16	0.96
2	0.97	7	1.00	12	0.98	17	0.99
3	1.00	8	1.00	13	0.98	18	0.89
4	1.00	9	0.60	14	0.98	19	0.91
5	0.73	10	0.93	15	0.99		

Table 7.32. Comparison of modal vectors using MAC values for roving force transducer testing and baseline testing.

7.8.6.3 Comparison of Modal Flexibility

Modal flexibility matrices are compared to static flexibility from the finite element model, and the results are presented in Table 7.33. The baseline results are included as a point of reference. The value of D for the roving testing is much higher than the baseline, indicating that the elements of the full matrix are less accurate. Similar results are found for the elements on the main diagonal as represented by the D_d value. However, the average midspan deflection found from the roving testing is closer to the finite element result than the baseline deflection is. This indicates that the modal mass for Mode 1 is more accurate with the roving force transducer testing.

Desc.	Baseline	8 TTs
D	12.2	33.1
Dd	0.77	0.92
Disp.	94%	104%

Table 7.33. Comparison of modal flexibility for testing with roving force transducers and for the baseline testing.

7.8.6.4 Summary of Results for Roving Force Transducers

Overall, the modal parameters found from the roving testing are not as accurate as those found using the traditional method of combining experiments where all inputs are measured. A few mode shapes are less accurate with roving and the estimated modal masses show significant

variation for many modes. The modal mass issues suggest that the measured force input from a shaker does not agree well with the input when a force transducer is not present. This conclusion is supported by the results of the laboratory testing, wherein it was noted that the disturbances caused by moving the force transducers results in changes to the force input. In summary, the use of roving force transducers should be avoided. The benefits of better spatial distribution of excitation are overwhelmed by the harmful effects of inconsistent data.

7.9 CONCLUSION

The tactile transducer excitation system was evaluated for MIMO EMA testing of an in-service highway bridge. The data from the testing program was used to evaluate the following experimental design characteristics:

- Evaluation of the pros and cons of combining data from disparate experiments.
- Comparison of burst-random and multisine excitation techniques.
- Evaluation of the effects of traffic disturbances on modal identification.
- Evaluation of employing roving force transducers.

The excitation system using TTs and subwoofer amplifiers successfully excited the real-world bridge. The system outperforms the accepted and more widely used ambient and impact excitation methods. More modes are identified and generally more accurate modal vectors are found using the tactile transducer MIMO EMA approach. Also, the modal flexibility matrix is a better match to the static flexibility matrix, indicating that the system also provides more accurate estimates of modal mass. Thus, the identification of more accurate modal parameters can be expected by utilizing the newly developed excitation system for bridges similar to the tested bridge.

For this testing, combining data from disparate experiments improved the accuracy of most modal parameters by increasing the amount of redundant information in the system transfer function. However, damping ratios noticeably increased and became less accurate due to inconsistencies between the various experiments. Thus, it is best to excite as many DOFs simultaneously as possible to get the most consistent data since all structures are time-variant. A major benefit of the novel excitation system is that a large number of exciters can be used at a reasonable cost.

Multisine signals have many theoretical advantages over commonly used excitation signals, but have scarcely been used in testing of civil structures. The testing reported herein demonstrates that multisine excitation results in modal parameters that are nearly identical to those found using the more conventional burst-random technique, except for a few important modes that were better identified with multisine excitation. Based on testing of this bridge, the use of multisine excitation provides results that are superior to results using burst-random excitation.

Vehicular traffic crossing the bridge during experimental modal testing causes significant amplitude change and noise in the output accelerations. While natural frequencies and modal vectors are barely affected by this, the noise diminishes the accuracy of damping and modal mass. For modes in frequency bands that are significantly excited by the traffic, the modal mass can be incorrect by orders-of-magnitude. Thus, MIMO EMA testing using the TT system should be conducted such that an adequate amount of data with no traffic disturbances can be collected.

Finally, an experiment was conducted to evaluate if the excitation system could be used by employing roving force transducers. The result is that the modal parameters found with this method are less accurate than when all inputs are measured. The disturbance to the test system

caused by relocating the force transducers causes data inconsistencies that may be significant. Overall, the benefits of better spatial distribution of excitation are overwhelmed by the negative impacts of processing inconsistent data.

7.10 FUTURE WORK

Some of the results presented in this chapter may be specific to the individual bridge that was tested, and thus future work should be conducted on other bridges, especially with different structural arrangements. It was also recognized that traffic did not evenly excite all frequencies, although this is a common assumption made by other researchers. Testing should be conducted to determine to what level various frequencies are excited by traffic, and how this is affected by various bridge types.

CHAPTER EIGHT

BRIDGE LOAD RATING USING MEASURED MODAL FLEXIBILITY

8.1 INTRODUCTION

A goal of this work is to use the high quality modal parameters to provide a bridge load rating. Load ratings indicate the capacity of a bridge to carry specific truck loads, and are thus valued by transportation agencies. These agencies use ratings to make operational decisions and to help decide where limited maintenance dollars should be invested. Although many researchers are attempting to develop methods by which damage to civil structures can be isolated by modal testing, few are working to provide bridge owners with actual load capacity.

In this chapter, the current standard process for the development of load ratings is discussed, and some of the shortcomings of the current methods are called out. Second, the ways in which modal parameters can be used to improve the process are analyzed, and a specific use for this work is developed. In essence, it is proposed that the measured modal flexibility can be used to determine live load demand more accurately than standard industry practice. Third, the challenge of using modal flexibility to calculate internal structural forces is discussed. A two-step process is developed based on work published by others in which the rank of the measured flexibility matrix is increased, and then this global flexibility matrix is disassembled to determine local stiffness parameters. Finally, a full-scale multi-girder bridge (Hartbarger Bridge) is rated by various competing methods, and the results of the ratings are compared and discussed.

8.2 BRIDGE CONDITION EVALUATION BACKGROUND

8.2.1 Bridge Inspection

Routine bridge inspection began with the inception of U.S. Code Title 23, Section 151 in 1968, requiring inspection of all federal-aid highway bridges in the United States. This law was a reaction to the collapse of the Silver Bridge over the Ohio River on December 15, 1967 that resulted in 46 deaths (Coleman 1996). In 1978 the law was extended to include all publicly owned bridges greater than 20 feet long (White et al. 1992). It was recognized that experienced engineers should visually verify the condition of each and every bridge at regular temporal intervals to ensure that loss of life due to bridge collapse would be avoided.

Since the passage of this landmark law, the means of bridge inspection have only been updated whenever bridge failures have occurred despite regular inspection. For instance, the Mianus River Bridge in Connecticut collapsed in 1983 due to a fracture in a pin-and-hanger connection. Now pins of this type are inspected for visually undetectable cracks using ultrasound techniques. The Schoharie Creek Bridge in New York collapsed in 1987 due to foundation scour. As a result, bridges are now given a baseline description as scour-critical or not scour-critical. Bridges classified as scour-critical are routinely inspected for scour by divers. More recently, the I-35 West Bridge over the Mississippi River in Minnesota collapsed in 2007 due to fracture of a gusset plate. As a result, all gusset plates are now load rated. It can be recognized that these failures have merely added tasks for the inspection team to perform; neither fundamental nor revolutionary changes in the process of bridge inspection or evaluation has occurred. Additionally, inspection is mandated for safety, not for maintenance management.

Four categories of bridge inspections exist; routine, fracture-critical, underwater, and damage (23 U.S.C. § 650 (2004)). Routine inspections occur at regular intervals not to exceed 24 months and

document any changes in the bridge condition that have occurred subsequent to the previous inspection. Fracture-critical inspections are typically performed during a routine inspection, but include a more careful examination of the fracture-critical elements. Underwater inspections are also typically performed during a routine inspection and are meant to check for scour at foundations. Damage inspections are non-routine and occur after a hazard event may have harmed a bridge. Examples include events such as a girder being impacted by a vehicle or a foundation potentially being scoured during a flood. Damage inspections are reactive, whereas many researchers are attempting to develop proactive evaluation systems. No matter the inspection type, the key similarity between all four is that visual evaluation processes are the cornerstone of the effort.

Visual inspection (VI) has many limitations. The foremost limitation is that VI is a subjective process with individual inspectors assigning widely varying condition ratings to the same deteriorated element. The FHWA performed a study on this subject and found that 56% of the average condition ratings are incorrect (Phares et al. 2004). Another limitation of VI is that although degradation of elements may be easily recognized, a change in strength is not. For instance, chlorides cause corrosion of reinforcing and the resulting spalling of bridge decks is documented by inspectors. However, the loss of reinforcing steel area and the loss of strength in the deck due to cracking are not easily determined. Furthermore, visual inspection is not an exhaustive survey and defects are often undetected as only surface defects can be seen. Finally, VI is an element by element procedure and the global interaction of various deteriorated segments is seldom considered.

In summary, bridge owners invest significant time and money into mandated inspections. The inspections are largely successful at ensuring bridges are safe, but the overall work product of inspections is qualitative.

8.2.2 Bridge Load Rating

Bridge load rating is a process of calculating the capacity of a bridge to carry various types of trucks. Load rating is required for all bridges by U.S. Code Title 23 Section 650; however, each state may have different laws that govern what axle arrangements and axle weights comprise the legal maximum load permitted on state roads. In addition to any truck configurations for a particular state, AASHTO provides several legal load configurations for national use as well as notional live loads that do not represent any particular highway vehicle. The notional loads have been developed to cause stresses in bridges that mimic the measured stresses in real bridges under a variety of load types. Load ratings are typically calculated for both the design loads and for the legal loads. The design loads and legal loads are illustrated in Figure 8.1 through Figure 8.4. The diagrams are adapted from AASHTO (2008, App. D6A).

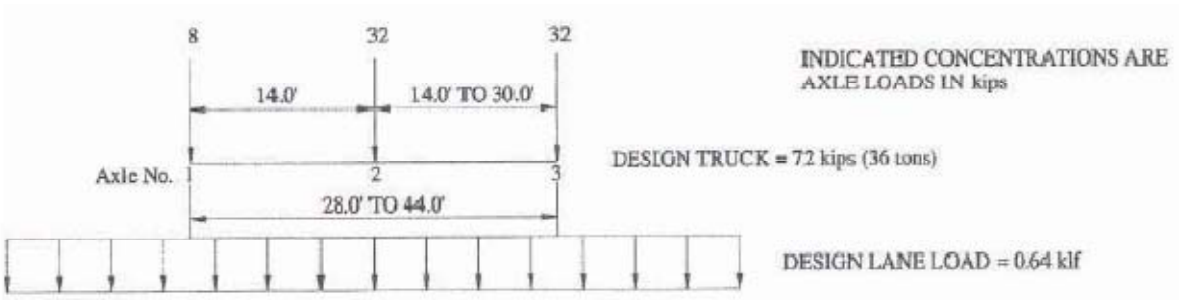

Figure 8.1. Diagram of AASHTO HL-93 notional design load. HS-20 truck is similar but excludes the lane load.

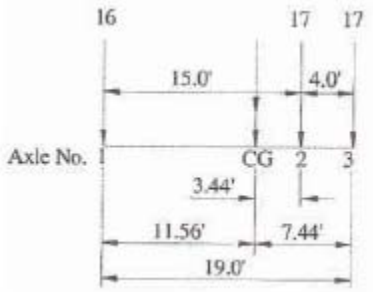

Figure 8.2. Diagram of AASHTO Type 3 legal truck load. Axle weights in kips.

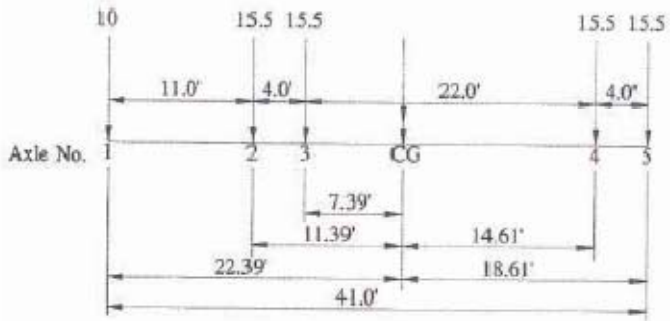

Figure 8.3. Diagram of AASHTO Type 3S2 legal truck load. Axle weights in kips.

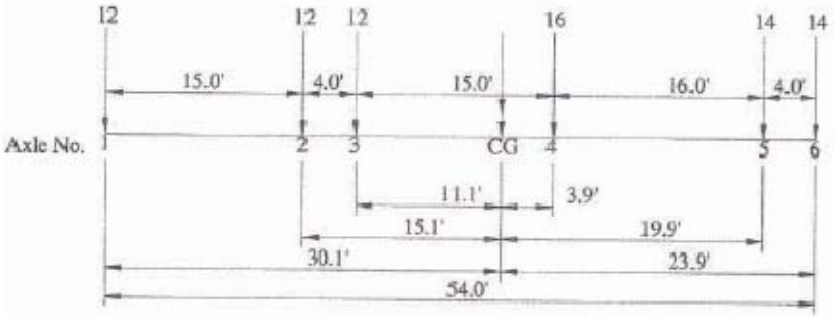

Figure 8.4. Diagram of AASHTO Type 3-3 legal truck load. Axle weights in kips.

The calculated load ratings provide a numeric value that indicates the carrying capacity of the bridge for each given truck type. A rating greater than unity is taken to mean that the element under consideration can safely carry the particular truck, whereas a rating less than unity indicates that only the calculated fraction of the particular truck can be supported. Ratings less than unity suggest that the operating agency must either strengthen the bridge or post the bridge for reduced truck weights.

Per U.S. Code, load ratings must be performed in accordance with AASHTO. The basic format of the load rating equation for any structural element is:

$$RF = \frac{C - D}{L} \qquad \text{Equation 8.1.}$$

Where:

$RF =$ the rating factor for the element under consideration.

$C =$ the structural capacity of the element.

$D =$ the dead load demand on the element.

$L =$ the live load demand on the element due to the selected truck load (plus impact).

A rating factor exists for any location along any component of the bridge superstructure. It is usually not difficult to select a small subset of locations at which critical ratings will exist, and ratings are typically only calculated for these critical locations. The single final rating for the bridge as a whole is then taken as the minimum rating factor found for any part of the structure. The units of the variables on the right hand side of the rating equation must be consistent, but may be in terms of stress, force, or bending moment for any given structural element.

Load ratings are supposed to be updated in cases where a bridge inspection reveals conditions that might impact the ratings (AASHTO 2008 Article 6A.1.1); however, this can be difficult to implement for two primary reasons First, field determination of the damage or deterioration must be quite precise in order to be accurately incorporated into an analytical capacity calculation. Second, incorporation of the damage often requires a higher level of analytical analysis than the existing ratings are based on. This results in a rating for the subject component that is inconsistent with the rating of all other components, or the entire structure must be re-rated at the higher analysis level.

8.2.2.2 Calculation of Section Capacity

For the purposes of rating, capacity values must be found in accordance with AASHTO. The capacity of any bridge element is based on a combination of the physical section properties and the material strengths. AASHTO provides equations by which these physical properties are converted into a capacity. Although the AASHTO equations must be used in the determination of capacity, it is permissible for some physical properties to be modified based on field inspection or testing. It is common for both steel and concrete to have higher strengths than the minimums specified in the contract documents. It is also common for elemental section properties to degrade over time due to use and corrosion. AASHTO permits the use of increased material strengths in the calculation of ratings if laboratory testing supports such use (e.g. coupon testing of steel, compression testing of concrete cores), and AASHTO encourages the use of reduced section properties for apparent corrosion and damage.

8.2.2.3 Calculation of Dead Load Demand

The dead load force or stress is calculated in consideration of the construction sequence. Dead load stresses are nearly deterministic in many bridge types such as simple span, multigirder bridges. However, dead load stresses on bridges continuous over at least one support can be significantly altered due to small support settlements or locked in erection stresses. This and other sources of uncertainty are incorporated into the AASHTO specifications.

8.2.2.4 Calculation of Live Load Demand

The most onerous task in bridge design and bridge rating is the application of the live load for maximum effect at the detail under consideration. First, the spatial positioning of the load vehicles can be complicated and the use of influence surfaces may be required. Second, the flow of forces through the structure to the various supporting elements is usually highly complex. For

expediency and cost control, most designs and ratings are performed using AASHTO live load distribution factors (AASHTO 2010). These factors are easily calculated by inserting a few geometric bridge properties into an equation, and then the distribution factor reduces the loading problem from two-dimensional to one-dimensional.

The current AASHTO distribution factors presented in the LRFD specifications (AASHTO 2010) were developed through a study commissioned by the NCHRP in 1985. The results were published in NCHRP Report 12-2611 (Zokaie et al. 1991) and were incorporated into the AASHTO LRFD Bridge Design Specifications in 1992. Plans of several hundred bridges randomly selected from the national bridge inventory file were collected, and finite element and grillage models were prepared (Zokaie 2000). Various bridge geometric properties were correlated with the analytical results of distribution of live load to the girders for moment and shear. From the correlations, equations were developed extending the results to a wide range of bridge types.

AASHTO does not require the use of the distribution factors that they provide (AASHTO 2008, Article 6A.3.2). Designers are permitted to use any rational analysis that satisfies equilibrium, compatibility, and material constitutive relationships (AASHTO 2010, Article 4.4). AASHTO lists some commonly acceptable examples such as finite element and grillage analogy analysis. However, industry is cost competitive and the easiest permissible analysis method is used so that expenses are controlled. Thus, the simple AASHTO distribution factors are used for design and rating in almost all cases when they are applicable.

8.2.3 Load Rating Using Physical Testing

AASHTO also allows load ratings to be performed by physical load test (AASHTO 2008, Article 6A.3.4). Physical load tests can consist of diagnostic or proof loading. Diagnostic testing uses loads of various intensities to verify the behavior of the structure in response to the loading. The results are used to validate analytical models and enable load rating. Proof loading simply ascertains that the subject bridge can carry the proof load. This provides a lower bound on the true capacity of the structure.

The benefit of any type of physical bridge testing is that the true global behavior of the structure, including its present actual condition, drives the results. In the case that an adequate array of strain gauges is installed prior to load tests, the actual flow of forces through the structure is documented. This eliminates the need to use any type of analytical load distribution approaches. Load rating still relies on estimates of section capacity and dead load stress, but the uncertainty of live load distribution is greatly reduced by the physical testing.

Lenett et al. (1999) tested a bridge in Ohio using various NDT techniques including load testing and vibration testing. The capacity based on the physical testing was far in excess of the existing load rating based on standard analytical procedures and subjective inspection data. The paper concludes that subjective methods of condition assessment are inconsistent and unreliable. Similar conclusions are readily available in the literature, and it is widely recognized that physical testing is superior to analytical modeling.

Nonetheless, this type of rating based on physical testing is uncommon due to the high costs of performing the testing and the operational issues involved. The costs include engineering and testing personnel, loaded trucks and drivers, and testing equipment such as deflection and strain

gauges. Load testing also typically requires temporary closure of the bridge, causing operational issues. Thus, it is not commonly used on important structures with high ADT.

Overall, mandated load rating is intended to provide owners with the current live load capacity of a bridge. However, simplifying assumptions reduce accuracy by an unknown amount, and the difficulty of including deterioration identified by VI generally results in ratings that do not incorporate current structural condition. Physical testing results via modal analysis can automatically incorporate the current, as-built condition of a bridge and reduce the reliance on analytical assumptions.

8.3 PRIOR RESEARCH IN MODAL ANALYSIS AND BRIDGE LOAD RATING

It has been recognized by many researchers that the current bridge inspection and rating process can be improved by the application of modern technology. Although there are competing methods being considered, modal analysis has received a significant amount of attention. Hartle et al. (2007) provides a detailed review of published research on 'early bridge testing' that used vibration data. The chronicle lists 154 papers from 1937 to 1998 and makes it clear that modal analysis of bridges has a long history. However, only a small number of bridges were tested until the 1970's when greater access to computing resources enabled modal analysis to expand, and modal analysis significantly increased in the 1980's. Although testing of structures using vibrations was increasing, the purpose of the testing was typically for one of the following reasons: behavior under wind load; behavior under seismic load; accuracy of impact factors for design; and calibration of analytical models. Vibration or modal testing with a purpose of directly estimating the load capacity of a bridge was limited.

A literature review focusing on using modal analysis results to help determine vertical load capacity of bridges has been performed. Select publications from the review are mentioned below and provide an in-depth representation of the type of work that has been performed by researchers in this field.

Ward (1984) recorded ambient vibrations of 18 bridges in Hong Kong and natural frequencies and damping ratios were found. In the paper, Ward suggested that bridge condition for carrying capacity could be diagnosed from monitoring of modal properties. One idea was to occasionally measure the fundamental frequency with the assumption that a frequency drop would be due to a stiffness drop. A second idea was to compare the fundamental frequencies of geometrically similar bridges with the assumption that a below average frequency would correspond to a weaker bridge.

Brownjohn et al. (1987) measured ambient vibrations of the Humber Bridge in England and determined natural frequencies and damping ratios. These values were used to verify analytical modeling assumptions made during the bridge design.

Agardh (1991) used drop-weight impact testing to measure the vibrations of a bridge before and after strengthening. Other bridges were also tested after several types of intentional beam damage occurred. Agardh concluded that the modal properties can be used to calibrate analytical models and to assess bridge condition.

Aktan et al. (1992) tested a concrete bridge in an effort to determine if vibration tests can be used to assess bridge condition. Impact testing was performed and modal flexibility was found and compared to static flexibility. The static and modal flexibility did not agree well and excitation of

nonlinearities by impact testing was pointed to as a cause. The authors came to a similar conclusion as Agardh in that modal properties can be used to determine bridge condition.

Miller et al. (1992) tested a concrete bridge using hammer impacts to try to determine the bridge capacity. Natural frequencies, damping ratios, and mode shapes were found. The bridge had known deterioration and the author discussed the issues with the industry and AASHTO process for subjectively calculating the remaining load-carrying capacity.

Wood et al. (1992) attempted to use a novel excitation device for excitation of bridges. A nail gun was fired into a plate to produce a sharp impact. This work indicates the difficulty in finding cost-effective methods for adequately exciting bridge structures.

Aktan et al. (1993) tested a three-span steel bridge using forced input (impact and actuator). They found the natural frequencies, damping ratios, mode shapes, and modal flexibility. These modal properties were used to calibrate a finite element model and the finite element model was then used to determine live load demand for bridge rating. The bridge was also rated using standard AASHTO distribution factors and the two results were compared. The calibrated finite element model produced much higher load ratings than the AASHTO analysis.

Rotter et al. (1994) tested an old steel railroad bridge in an attempt to determine the remaining load capacity. An impact hammer was used to excite the bridge and the modal properties were compared to a finite element model. The measured natural frequencies were lower than the analytical model and the authors attributed this to section loss of the girders.

Aktan et al. (1995) discussed the results of testing seven bridges with the purpose of damage detection via modal analysis. Impact excitation was used and natural frequencies, damping

ratios, mode shapes, and modal flexibility were found in all cases. The authors indicated that the modal flexibility agreed well with static flexibility and that modal flexibility could be used to help indicate damage.

Deger et al. (1995) tested a prestressed concrete bridge in Germany. Data was collected before and after repairs and finite element models were calibrated to the measured modal properties.

Haritos et al. (1995) tested four concrete bridges in Australia in an attempt to assess their condition. The modal data was used to calibrate finite element models.

Zhang and Aktan (1996) performed impact vibration tests on a bridge in Ohio and found natural frequencies, damping ratios, mode shapes, and modal flexibility. These properties were used to calibrate a finite element model which was then used to determine live load demand.

Wang et al. (2005) discuss a process that has been used to rate nearly 40 Ohio bridges. Modal analysis is used to calibrate finite element models of the bridges and then rating is based on the analytical model output. Excitation for the modal analysis is provided by instrumented hammer and natural frequencies, modal mass, and modal flexibility are found. The authors found that ratings based on the physical testing significantly exceed conventional ratings.

Catbas et al. (2006) provided a good synopsis of issues with and the state of the art of damage detection and condition assessment using modal analysis. In this paper, the authors describe a process of using modal flexibility to detect bridge damage and describe some of the challenges that go along with detection. They also compare deflection results based on measured modal properties to deflection results from a physical load test. They show that even significant damage

is hard to detect in structures that are redundant. However, the authors do not mention or attempt to determine the load carrying capacity of the bridges discussed.

Siswobusono et al. (2006) performed load testing and vibration testing of a bridge in Alabama with a purpose of providing a load rating. The tested bridge had a span length of 20 feet and consisted of steel beams with the upper half encapsulated in the concrete deck. The authors rated the bridge by determining the midspan deflection for a given load and then extrapolating the load that would cause a deflection equal to the AASHTO comfort limit for pedestrian use. It was assumed that the bridge load capacity equaled the load that would cause a deflection equal to the comfort limit deflection (L/800 for bridges without sidewalks and L/1000 for bridges with sidewalks). A major flaw in this paper is the assumption that structural failure would not occur for any reason prior to the selected deflection threshold.

Gangone et al. (2009) reports on vibration testing performed for bridge condition assessment and health monitoring; however, this paper is highly representative of the predominance of publications in that the authors were only trying to identify local damage. An assessment of the global load capacity of the bridge was not performed.

Catbas (2010) developed revised equations for distribution of truck loads for moment and shear using modal parameters. In this work, 40 concrete T-beam bridges were modeled using finite element software. Regression analysis was then used to correlate the modal properties found by the FE software with the maximum moment and shear found by the FE software. The purpose was to demonstrate that alternate distribution factor equations that incorporate measurable modal properties can be developed for common bridge types. The paper then compares the developed

distribution factor equations against a finite element model that had been calibrated to measured modal data and also against the AASHTO distribution factors.

Gangone et al. (2011) outfitted a bridge with more than 100 sensors for diagnostic monitoring. Strain gauge data was used to produce load ratings for the bridge. Accelerometers were used for modal characterization and natural frequencies and mode shapes were found; however, this data was not used for vertical load capacity analysis.

Gokce et al. (2011) reported on load rating and system reliability of a bascule bridge in Florida. The authors performed vibration analysis, load testing, and finite element modeling of the subject bridge. The finite element model was calibrated using strains measured during load testing. The model was then used for live load stress determination. This finite element output was used for the load rating. Reliability analysis was significantly discussed and was performed for the bridge system; however, the authors did not express how an operating agency should use output of the reliability analysis to inform decision making.

Yi et al. (2011) performed vibration testing of a bridge in Korea. They used modal analysis to update a finite element model and then verified the accuracy of the model by comparing deflections predicted by the calibrated model to deflection measurements of the physical bridge.

Analysis:

The literature review shows that physical vibration testing is seldom used to help estimate load carrying capacity of bridges. When researchers have used modal data to enhance load capacity estimates, they have in nearly all cases taken the intermediate step of calibrating a highly detailed finite element model. They then use the model to determine live load stresses. Many researchers

are also attempting to isolate the location and severity of structural damage using vibration testing and modal analysis. This is an open research topic and the literature does not demonstrate a method by which any damage should be incorporated into bridge load ratings. Also, no method has been developed for directly incorporating the results of vibration testing in the production of bridge load ratings.

8.4 METHOD OF ADVANCE

Bridge owners use bridge ratings to make operational and maintenance decisions, and more accurate ratings enable better decisions. However, if a potential improvement in accuracy comes at a high cost, owners are unlikely to utilize the method. As has been discussed at length, the novel excitation system greatly reduces the cost of performing experimental modal analysis, but the method by which rating calculation is undertaken must also be achievable at a low cost. This requirement eliminates the common method of generating and calibrating a complicated finite element model since such a process requires many man-hours by skilled engineers. It is desirable to use the modal results in a much more direct manner. Additionally, FE models are colored by the experiences of the person creating the nominal model, and calibrated models are neither unique nor guaranteed to correctly represent force flow through the physical structure.

Considering the three parts of the rating equation that can be manipulated, the biggest 'bang for the buck' can be achieved by selecting the live load demand. This can be recognized in the literature since most researchers only use their results to determine live load forces. Using modal results, structural capacity can be slightly modified by altering section properties, although an increase in section properties would be difficult to justify versus those resulting from the as-built dimensions. AASHTO does encourage the use of reduced section properties for apparent corrosion and damage, however, damage is usually localized and the characterization of the local

damage is an open research topic, may not alter the controlling ratings in any case, and is outside the scope of this thesis.

The dead load demand typically cannot be modified based on the results of modal testing. Although it is possible to estimate a mass matrix based on the modal testing, the original construction sequence largely determines the dead load forces that must exist within each structural element. If a higher mass (and higher dead load forces) than expected based on as-builts is suspected based on modal results, then direct measurements of the structural components would be a far more accurate way to determine the correct mass. Dead load stress is also dependent on section properties, and could thus be affected slightly by revised section properties. However, this is again dependant on localizing and characterizing any suspected damage that may reduce the section.

The live load demand is the most appropriate variable to manipulate since it includes the most uncertainty. As discussed, most bridges are designed and rated using approximate distribution factors that are calculated from a single equation for a broad range of bridge geometries. There is a significant volume of literature that challenges the accuracy of both the older ASD/LFD and the newer LRFD load distribution factors (for example Cai (2005) and Suksawang and Nassif (2007). AASHTO even provided a guide specification to enhance the older distribution factors since for some bridge geometries, the resulting live load shear or moment in a girder could be up to 50% off of accurate values (AASHTO 1994). If the actual flow of forces through the structure is known, then the use of distribution factors can be discarded, generally resulting in more accurate and less conservative bridge ratings. Therefore, this work will advance the state of the art by using measured modal parameters to determine more accurate live load demand.

8.5 USE OF MODAL FLEXIBILITY FOR BRIDGE RATING

It is desirable to use the results of the modal analysis to accurately determine the live load demand at all critical sections within the bridge. The live load demand can then be used in the rating equation to find the capacity of the bridge for the specified legal or design load. To proceed with this method, it is necessary to develop influence surfaces for each local element force or stress that may be critical. These influence surfaces can then be used to position truck loads to cause maximum response.

8.5.1 Problem Definition

The measured modal flexibility cannot be directly used for determining the local distribution of force through a structure. The problem is that the measured flexibility matrix does not usually contain the necessary information from which local stiffness could be determined. The flexibility matrix relates global responses to global applied loads as:

$$[f]\{P\} = \{u\} \qquad \text{Equation 8.2.}$$

Where:

$[f]$ = the measured modal flexibility matrix.

$\{P\}$ = a vector of externally applied global loads.

$\{u\}$ = a vector of global displacements.

This equation demonstrates that for any applied external loads, the flexibility matrix can be used to calculate the displacements. In order to determine the local element forces, a different equation must be solved:

$$[F_{ele}] = [k_{ele}][\beta_{ele}]\{u\}$$ Equation 8.3.

Where:

$[F_{ele}]$ = the internal element forces in local coordinates.

$[k_{ele}]$ = the stiffness parameters of the element in local coordinates.

$[\beta_{ele}]$ = a matrix that relates the local and global coordinate systems.

$\{u\}$ = a subset of the global displacements for the element under consideration.

In this equation, the local forces are desired but only $\{u\}$ is known. Local stiffness must be estimated in order for local forces to be found and used in the rating process. On the surface, it would seem quite possible to estimate local stiffness values based on the known flexibility matrix, since flexibility can be assembled directly from known local stiffnesses. However, modal flexibility is typically rank deficient and thus a unique solution does not exist.

Consider the simple propped cantilever shown in Figure 8.5, which is indeterminate to the first degree. Assuming that modal flexibility was determined for a single DOF in the vertical direction at midspan, it is obvious that a unique solution for the stiffness of the two elements, I_1 and I_2, does not exist. An infinite number of combinations of the two stiffness parameters would provide the same measured deflection for an applied load. A unique solution does not exist because the flexibility matrix (a scalar value in this case) is rank deficient. However, if the rotational DOF at midspan had also been measured, then the measured flexibility matrix (of size 2x2) would be adequate to uniquely determine the local stiffness parameters, I_1 and I_2.

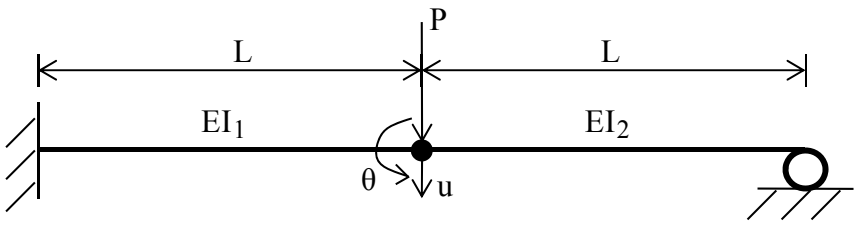

Figure 8.5. Propped cantilever beam with variable stiffness.

Additionally, in order to determine local stiffness parameters from which internal forces can be found, a model must be assumed that creates connectivity between the measured DOFs. The assumption of a model determines the range of solutions that can exist, and since any number and complexity of models could be assumed and justified, the final results will not be unique and will be dependent on the model assumptions.

8.5.2 Assumption of a Model

The first step in estimating the internal structural forces from the measured flexibility matrix is the assumption of a model. The need to develop a model leads many researchers to turn to complex finite element programs and calibration methods. As stated before, it is desirable to avoid this level of complexity, and thus the simplest model that can adequately represent the structure should be selected. The tested bridge is essentially planar, and deformations due to vertical loads primarily consist of vertical displacements and rotations about axes that lie in the plane of the structure. This suggests that Bernoulli-Euler beam elements are adequate. The most simple connectivity is also desired. Since the measured DOFs were arranged in a grid along the parallel beams of the bridge, one possible model is as shown in Figure 8.6. Each element in the model is assumed to be capable of carrying vertical shear, vertical bending, and torsion as shown in Figure 8.7.

This model has a few benefits. First, the simplicity allows quick and easy calculation without undue complexity that may not improve the estimate of forces. Second, since the beams are the critical rating elements in bridges of this type, it is essential that model elements exist that will provide the internal forces along the beam lines. Finally, a grid or grillage analysis is consistent with past practice in the design of bridges, and is thus more easily accepted by industry.

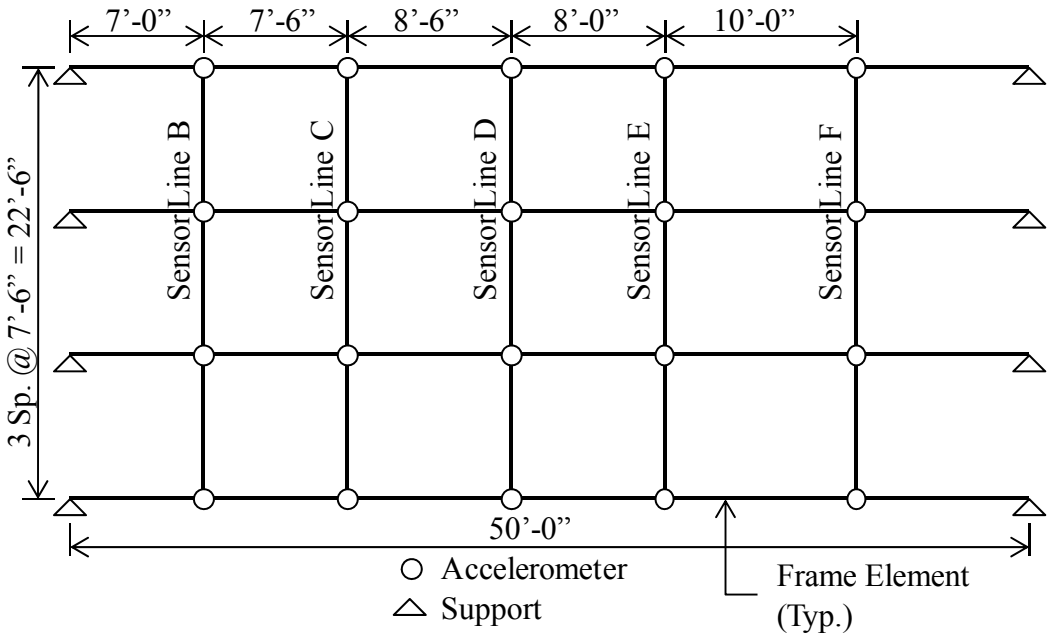

Figure 8.6. Proposed model for estimating internal forces.

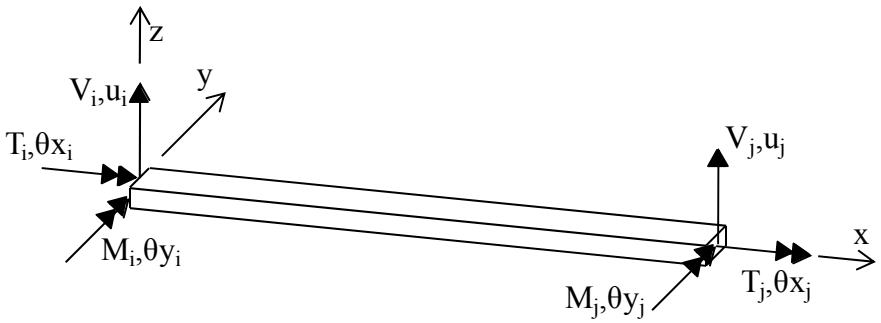

Figure 8.7. Detail of local frame element DOFs.

8.5.3 Estimation of a Full-Rank Flexibility Matrix

In order to estimate the local stiffness parameters from the flexibility matrix, the rank must be sufficient for the proposed model. The measured matrix only includes vertical displacement at

the DOFs, but the assumed elements for the model require rotations as well. Since the rotations were not measured, values must be estimated that are consistent with the measured displacements.

A method is used that was proposed by Doebling and Peterson (1997). In this method, a full rank flexibility matrix is assembled based on assumed values of local stiffness for the proposed model. Scaling values are then determined that modify the full rank matrix so that the elements in common with the measured flexibility match as closely as possible (in a least-squares sense). The final fullirank matrix is then composed of the measured flexibility values augmented by the values from the scaled model. The steps in the method given by Doebling and Peterson are shown below.

The first step is to generate a full rank flexibility matrix based on an assumed model. The assumed model is the same as given above with all stiffness parameters set to a value of unity. A global stiffness matrix is assembled from the local stiffness of each beam, its connectivity, and its orientation. The local stiffness matrix and the beta matrix used are as shown in Figure 8.8 and Figure 8.9 respectively, and are taken from Sennett (1994, 89-90). The global flexibility matrix is the inverse of the global stiffness matrix.

$$\begin{Bmatrix} T_i \\ M_i \\ V_i \\ T_j \\ M_j \\ V_j \end{Bmatrix} = \begin{bmatrix} GJ/L & 0 & 0 & -GJ/L & 0 & 0 \\ 0 & 4EI/L & -6EI/L^2 & 0 & 2EI/L & 6EI/L^2 \\ 0 & -6EI/L^2 & 12EI/L^3 & 0 & -6EI/L^2 & -12EI/L^3 \\ -GJ/L & 0 & 0 & GJ/L & 0 & 0 \\ 0 & 2EI/L & -6EI/L^2 & 0 & 4EI/L & 6EI/L^2 \\ 0 & 6EI/L^2 & -12EI/L^3 & 0 & 6EI/L^2 & 12EI/L^3 \end{bmatrix} \begin{Bmatrix} \theta x_i \\ \theta y_i \\ u_i \\ \theta x_j \\ \theta y_j \\ u_j \end{Bmatrix}$$

Figure 8.8. Definition of local stiffness matrix for assumed elements.

$$[\beta] = \begin{bmatrix} \cos\theta & \sin\theta & 0 & & & \\ -\sin\theta & \cos\theta & 0 & & 0 & \\ 0 & 0 & 1 & & & \\ & & & \cos\theta & \sin\theta & 0 \\ & 0 & & -\sin\theta & \cos\theta & 0 \\ & & & 0 & 0 & 1 \end{bmatrix}$$

Figure 8.9. Definition of transformation matrix for assumed elements.

The second step is the parameterization of the flexibility matrix by using the singular value decomposition:

$$[G] = [V][\Sigma][V]^T \qquad \text{Equation 8.4.}$$

Where:

$[G]$ = the assumed full rank flexibility matrix.

$[V]$ = the singular vectors of $[G]$.

$[\Sigma]$ = the singular values of $[G]$ (on the main diagonal).

The third step is the selection of a correlation set. The correlation set is selected as the values in the measured flexibility matrix that are considered to be the most accurate. The scaling of the assumed matrix will be such that the assumed matrix matches the correlation set as closely as possible. The correlation set is given as:

$$[h] = \begin{bmatrix} i_1 & j_1 \\ i_2 & j_2 \\ \vdots & \vdots \\ i_n & j_n \end{bmatrix} \qquad \text{Equation 8.5.}$$

Where:

i = the row co-ordinate of the correlation element within the measured flexibility matrix.

j = the column co-ordinate.

The fourth step is to construct a problem such that the $[h]$ entries in $[V][\Sigma][V]^T$ are a least-squares fit to the correlation set from the measured flexibility matrix. Doebling and Peterson formulate the problem in this way:

$$\{\hat{\Sigma}\} = [C]^{-1}\{B\} \qquad \text{Equation 8.6.}$$

$$[C_r] = [V(i_r, 1) * V(j_r, 1) \quad \cdots \quad V(i_r, n_s) * V(j_r, n_s)] \qquad \text{Equation 8.7.}$$

Where:

$[C_r]$ = the r[th] row of $[C]$.

$\{B\}$ = the vector of the correlation elements from measured flexibility.

n_s = the number of non-zero singular values in $\{\hat{\Sigma}\}$.

From this, a scalar value is found that will scale the assumed flexibility as:

$$\alpha = \{\Sigma\}_{n_s}^{+}\{\hat{\Sigma}\} \qquad \text{Equation 8.8.}$$

Where:

$\{\Sigma\}_{n_s}^{+}$ = the pseudo inverse of the n_s largest singular values.

The fifth step is to scale the assumed flexibility matrix as:

$$[\tilde{G}] = [V]\alpha\{\Sigma\}[V]^T \qquad \text{Equation 8.9.}$$

Where:

$[\tilde{G}]$ = the scaled assumed flexibility matrix.

The sixth step is to assemble a flexibility matrix that is composed of the measured values augmented by the scaled assumed values:

$$[G^c] = [G^o(h) \quad \tilde{G}(\bar{h})] \qquad \text{Equation 8.10.}$$

Where:

$G^o(h)$ = the measured flexibility matrix entries.

$\tilde{G}(\bar{h})$ = the scaled values from the assumed flexibility matrix that complement h.

The final step is to iterate using $[G^c]$ as the starting assumed flexibility matrix until a desired level of convergance is achieved.

Using this method, a full-rank flexibility matrix can be estimated that preserves the values for the measured DOFs, while augmenting with nearly consistent rotations for the unmeasured DOFs.

8.5.4 Solution for Local Element Stiffness

Now that a full rank global flexibility matrix has been attained, estimates for the local stiffness values (I and J) are needed so that local forces can be calculated. The local stiffness can be found by disassembly of global flexibility. The process is thoroughly documented in Doebling et al. (1998), but only highlights of the process are restated herein.

The disassembly is performed by formulating a problem:

$$[C]\{P\} = [B] \qquad \text{Equation 8.11.}$$

Where:

$\{P\}$ = a vector of the unknown stiffness parameters.

The $[C]$ and $[B]$ matrices are formed from the flexibility matrix and from the assumed connectivity and support conditions of the assumed structural model. In particular:

$$C_{\alpha,\beta} = \{A_\alpha\}^T[G]\{A_\beta\}\{A_\beta\}^T[G]\{A_\alpha\} \quad \text{Equation 8.12.}$$

$$B_\alpha = \{A_\alpha\}^T[G]\{A_\alpha\} \quad \text{Equation 8.13.}$$

Where:

$[G]$ = the known flexibility matrix.

$[A]$ = the stiffness connectivity matrix.

$\{B\}$ = a vector of the complementary strain energy (per row) associated with the applied 'load vector' $\{A_\alpha\}$.

The formulation of $[A]$ is based on combining the static eigenvectors of the local stiffness of the various elements in the model via a transformation to the global DOF. This stiffness connectivity matrix is assembled as:

$$[A] = [[T]_1^T[\kappa]_1 \quad [T]_2^T[\kappa]_2 \quad \cdots \quad [T]_n^T[\kappa]_n] \quad \text{Equation 8.14.}$$

Where:

$[T]$ = an elemental to global DOF transformation matrix.

$[\kappa]$ = a matrix of static eigenvectors for an element of the structural model.

n = the number of elements in the structural model.

The vector $\{P\}$ is assembled in the same organization as the global DOF such that:

$$\{P\} = \begin{bmatrix} \{p\}_1 \\ \{p\}_2 \\ \vdots \\ \{p\}_n \end{bmatrix}$$ Equation 8.15.

Where:

$\{p\}$ = a vector of static eigenvalues for an element of the structural model.

For the beam elements used in this writing, the static eigenvalues and eigenvectors for an individual element are calculated as shown below:

$$\{p\} = \begin{bmatrix} \frac{2GJ}{L} & 0 & 0 \\ 0 & \frac{2EI}{L} & 0 \\ 0 & 0 & \frac{6EI(L^2+4)}{L^3} \end{bmatrix}$$ Equation 8.16.

$$[\kappa] = \begin{bmatrix} 0 & 0 & \frac{\sqrt{2}}{\sqrt{L^2+4}} \\ 1/\sqrt{2} & 0 & 0 \\ 0 & -1/\sqrt{2} & \frac{L}{\sqrt{2}\sqrt{L^2+4}} \\ 0 & 0 & \frac{-\sqrt{2}}{\sqrt{L^2+4}} \\ -1/\sqrt{2} & 0 & 0 \\ 0 & 1/\sqrt{2} & \frac{L}{\sqrt{2}\sqrt{L^2+4}} \end{bmatrix}$$ Equation 8.17.

$$[k_{ele}] = [\kappa][p][\kappa]^T$$ Equation 8.18.

Where:

G = the shear modulus of an element.

J = the torsional stiffness of an element.

L = the length of an element.

E = the modulus of elasticity of an element.

I = the moment of inertia of an element.

With this disassembly process, the unknown stiffness parameters can be solved for. With the local stiffness now known for each element of the structural model, elemental stiffness matrices can be generated and then a global stiffness matrix can easily be assembled. Thus, at this point a simple model exists that was developed directly from the measured modal flexibility matrix.

8.5.5 Local Stiffness Results

The two-step process described above is used on a measured modal flexibility matrix from the Hartbarger Bridge. Since the best modal results were found using the multisine signal with all excitation lines combined, only this modal flexibility matrix is used herein. The matrix is of size 20 x 20 with only vertical DOFs included. In the first step, the matrix is augmented with compatible rotations, and in the second step, the augmented matrix is disassembled to find local stiffness values.

It is desirable to ensure that the calculated local stiffness is reasonable, and thus hand calculations are performed to determine I and J values as well. The hand calculations assume composite action and follow AASHTO guidelines for the width of deck that contributes to each girder. Table 8.1 and Table 8.2 summarize and compare the results from the disassembly of modal flexibility and the results calculated using the as-built section dimensions. In these tables, the segment numbers refer to the portions of each main girder that comprise one element of the assumed model.

Segment	Girder 1	Girder 2	Girder 3	Girder 4
1	11,548	12,077	12,195	11,481
2	11,760	13,514	11,433	10,949
3	11,597	11,929	14,016	12,519
4	9,473	10,380	10,846	12,772
5	8,213	10,998	10,498	9,678
6	8,363	12,857	10,592	10,762
7	16,920	11,021	12,109	11,148
8	11,844	12,683	11,989	11,195
As-Built	9,498	9,967	9,967	9,498

Table 8.1. Moment of inertia values found by disassembly of flexibility and by hand calculations using as-built dimensions (in^4).

The moment of inertia values shown in Table 8.1 demonstrate the success of using disassembly to find local stiffness. The average bending stiffness found via disassembly is 19% higher than the as-built stiffness for the fascia girders, and is also an average of 19% higher for the interior girders. The stiffness values calculated from the as-builts do not include any stiffness benefit due to the barriers per industry standard. In general, the bridge also seems stiffer near the ends of the span than toward the middle. Some significant variation in local stiffness values is the result of assumed rotations that are not completely consistent with the measured deflections. Although a case could be made for smoothing the values, these local stiffness values are used without modification in the generation of a global stiffness matrix for application of live load.

Segment	Girder 1	Girder 2	Girder 3	Girder 4
1	26,448	50,394	52,501	27,286
2	9,895	14,522	14,748	10,212
3	10,346	15,406	15,946	10,531
4	10,229	15,829	16,464	10,565
5	10,586	16,719	17,133	10,847
6	10,612	16,802	17,129	10,811
7	10,124	15,166	15,721	10,198
8	21,758	48,756	50,292	22,977
As-Built	12,288	15,360	15,360	12,288

Table 8.2. Torsional stiffness values found by disassembly of flexibility and by hand calculations using as-built dimensions (in^4).

Table 8.2 displays the torsional stiffness of each girder segment as found from disassembly of the flexibility matrix and found by calculation using the as-built dimensions of the bridge. The torsional stiffnesses of the girders from disassembly are highly consistent for the fascia girders and for the interior girders, except at the girder ends. The high stiffness at the ends is attributed to the wrap-around deck detail which largely prevents rotation in the vicinity of the supports. Not including the girder end segments, the fascia girders are an average of 15% less stiff than the as-built value, and the interior girders are an average of 4% stiffer than the as-built value. Again, the local stiffness values found from disassembly of the augmented flexibility matrix are used without modification in the generation of global stiffness for live load effect.

8.6 GENERATION AND USE OF INFLUENCE SURFACES

The maximum live load effects for the selected critical structural elements of the bridge must be found. For the various types of truck loads, which have deterministic wheel locations, but which may exist in nearly any location on the bridge, influence surfaces are commonly used to position the trucks for maximum effect. Thus, influence surfaces are generated for each critical rating element. The potential critical ratings for this bridge are:

- maximum moment at midspan of fascia girder
- maximum moment at midspan of interior girder
- maximum shear near support of fascia girder
- maximum shear near support of interior girder

An influence diagram is generated for each of these four force effects by applying a unit load to the structural model developed from the modal flexibility matrix. The internal force effect of interest is found with the following process. First, the global stiffness matrix is partitioned (Sennett 1994, 42):

$$\begin{Bmatrix}\{F_p\}\\ \{F_s\}\end{Bmatrix} = \begin{bmatrix}[K_{pp}] & [K_{ps}]\\ [K_{sp}] & [K_{ss}]\end{bmatrix}\begin{Bmatrix}\{u_p\}\\ \{u_s\}\end{Bmatrix} \quad \text{Equation 8.19.}$$

Where the subscript 'p' denotes the forces and displacements at free DOF, and the subscript 's' denotes the forces and displacements at supported DOF. The global displacements at the free DOF are solved for as (assuming zero support displacements):

$$\{u_p\} = [K_{pp}]^{-1}\{F_p\} \quad \text{Equation 8.20.}$$

And then the unknown reactions are found as:

$$\{F_s\} = [K_{sp}]\{u_p\} \quad \text{Equation 8.21.}$$

Finally, the local element forces are found using the known displacements and local element stiffnesses as:

$$[F_{ele}] = [k_{ele}][\beta_{ele}]\{u\} \quad \text{Equation 8.22.}$$

A unit load is applied across a grid of locations and the solution process is repeated until a surface of response amplitudes is known. For the work reported herein, only the free vertical DOF of the simple frame model are used as load points in the development of the surfaces.

The influence surfaces are now used to find the maximum responses due to the various truck and lane loads. First, a given truck is selected as the current load. The truck is applied in many locations within the deck limits per AASHTO requirements, and the maximum response is saved. For this project, truck positions follow a 1-foot grid in the longitudinal and transverse directions. In most cases, wheel loads do not align with influence surface ordinates. Linear interpolation of the influence ordinates is then used to estimate the response amplitude at the wheel location.

8.7 RESULTS AND ANALYSIS

Results of the rating of the Hartbarger Bridge are presented and discussed in this section. For all critical sections, ratings are developed using three different methods to estimate the live load effect:

- AASHTO live load distribution factors
- Calibrated finite element model
- Measured modal flexibility

The calibrated finite element model used for this work is the same one used in the previous chapter, and which was calibrated to closely match the measured natural frequencies. Influence surfaces are also developed for this model and loaded with the various rating trucks to find maximum response. For ratings based on bending moment, the average stresses in the plate

elements at the locations of maximum response are used. For shear ratings, the support reactions from the model are used.

8.7.1 Overview of Rating Philosophies

Over time, AASHTO has promulgated different design and rating philosophies. These philosophies are Allowable Stress Design (ASD), Load Factor Design (LFD), and Load and Resistance Factor Design (LRFD). AASHTO only currently supports the LRFD method, but various state and local transportation agencies still use ASD and LFD due to their lengthy experience with those design methods. Also, AASHTO still permits bridges to be rated using any of these three methods. In the interest of completeness, each of these philosophies is used to rate the bridge, and the ways in which the philosophies differ are discussed below.

The ASD philosophy is largely based on empirical data and historic successes and failures. All loads are applied at their nominal (or service) levels, but a factor of safety is applied to structural capacity. For example, a steel section in tension is limited to a design allowable stress of $0.55F_y$. Thus, a factor of safety of approximately 1.82 has been applied for tensile stress in steel (with the implicit assumption that first yield is the failure criteria). Therefore, in the rating equation, capacity is based on allowable stresses. Dead load and live load demand are calculated based on their expected actual load levels. The rating equation is:

$$RF = \frac{C - D}{L}$$ Equation 8.23.

The LFD design philosophy attempted to institute a more rational approach by applying load factors based on the level of uncertainty (i.e. the statistical spread) of the loads. For example, dead loads are factored by 130% whereas the more highly variable live loads are factored by

167%. However, the capacity is not modified by a safety factor. A steel section in tension is limited to a design stress equal to the yield stress, F_y (although plastification is permitted for some sections in bending). The rating equation is:

$$RF = \frac{C - A_1 D}{A_2 L}$$ Equation 8.24.

Where:

A_1 = the dead load factor of 1.3.

A_2 = the live load factor of 2.17 for inventory and 1.3 for operating level.

The LRFD design philosophy attempts to provide the same statistical probability of failure for all elements of a structure. With ASD and LFD, at the completion of design, an engineer has no idea what the overall factor of safety is for the structure in its entirety. With LRFD, theoretically, the probability of failure is known and all elements have the same probability of failing first. This is accomplished by providing both load factors that account for the variability inherent in the various types of loads, and resistance factors that account for the variability in the strength of materials. Thus, the rating equation is:

$$RF = \frac{\phi C - \gamma_D D}{\gamma_L L}$$ Equation 8.25.

Where:

ϕ = a resistance factor for the material and type of stress applied.

γ_D = a load factor applicable to the type of dead load.

γ_L = a load factor applicable to the type of truck load.

Traditionally, there are also two rating levels. The inventory rating determines a live load level that the bridge can carry daily without restriction of any kind. The operating rating determines a live load level that can be considered as a maximum load that the bridge may experience occasionally and that the bridge can carry safely. For all three design philosophies, inventory ratings essentially align with the normal design strength of the structure. However, operating ratings are handled somewhat differently for the three philosophies.

In ASD, a higher allowable stress is permitted in the calculation of operating ratings. For example, allowable tensile stress in steel is increased from $0.55F_y$ for inventory to $0.75F_y$ for the operating level (an increase of 36%). The amount of increase in capacity is not consistent across all material stresses in ASD.

For LFD, a smaller load factor of 1.3 is applied to the live load for operating ratings, whereas the load factor is 2.17 for inventory ratings. Thus, in LFD, the operating rating for any element is always 167% of the inventory rating.

LRFD is similar to LFD, in that the only modification is to the load factor for live load. For LRFD, when using the HL-93 design load, a load factor of 1.35 is used at the operating level, whereas the factor is 1.75 at the inventory level. Thus, the operating rating is always 130% of the inventory rating. For legal loads, a single load factor of 1.40 is used (based on the low ADTT at this bridge), and there is no separate rating for the inventory and operating levels. Instead, the rating is interpreted as a safe load carrying capacity for the type of legal truck.

The results using the three different methods for determining live load stress are separated based on the rating philosophy. The following subsections present the rating results for the Hartbarger

Bridge using ASD, LFD, and LRFD respectively. Rating calculations are voluminous and are included in the appendices.

8.7.2 ASD Rating Results

The ASD inventory ratings are presented in Table 8.3 and Table 8.4 for the three live load stress calculation methods. The ratings headed 'DF' are due to the use of AASHTO distribution factors, those headed 'FE' are due to the use of the calibrated finite element model, and those headed 'MF' are due to the use of the disassembled, augmented modal flexibility matrix. For the ASD and LFD philosophies, interior girder forces are based on distributing S/5.5 lanes of trucks to the girder (where 'S' is the girder spacing). For the fascia girder, the lever rule is used as illustrated in Figure 8.10.

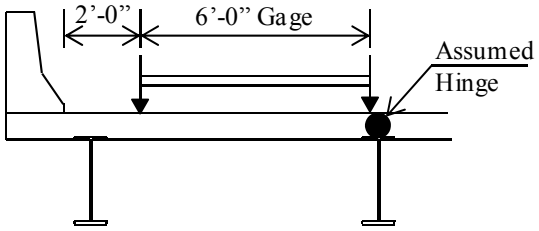

Figure 8.10. Location of wheel loads when using the lever rule per AASHTO.

The ratings are divided into rows for the critical sections. The 'Deck' row contains ratings based on maximum bending stress at the extreme fiber (top) of the deck. The 'Flange' row contains ratings based on bending in the extreme fiber (bottom) of the bottom flange. The 'Shear' row contains ratings based on average shear stress in the web at the end of the girder.

Critical Section		HS-20 Design Load			Type 3 Legal Truck		
		DF	FE	MF	DF	FE	MF
Interior	Deck	1.80	0.96	1.93	2.48	1.30	2.53
	Flange	0.67	1.04	0.72	0.89	1.35	0.95
	Shear	3.49	3.42	3.24	4.80	4.58	4.38
Fascia	Deck	1.66	1.65	2.05	2.21	2.23	2.70
	Flange	0.85	1.49	1.04	1.13	1.97	1.38
	Shear	3.81	4.56	5.11	5.07	6.49	7.13

Table 8.3. ASD inventory ratings for HS-20 and Type 3 truck loads.

Critical Section		Type 3S2 Legal Truck			Type 3-3 Legal Truck		
		DF	FE	MF	DF	FE	MF
Interior	Deck	2.33	1.41	2.77	2.47	1.56	2.77
	Flange	0.98	1.48	1.04	1.07	1.58	1.04
	Shear	4.52	4.72	4.34	4.78	5.00	4.60
Fascia	Deck	2.43	2.44	2.96	2.65	2.59	3.04
	Flange	1.24	2.16	1.51	1.35	2.21	1.55
	Shear	5.56	5.64	6.48	6.05	6.00	6.84

Table 8.4. ASD inventory ratings for Type 3S2 and Type 3-3 truck loads.

The results are consistent for all four load types, so only the HS-20 results are discussed in detail for brevity. First, it is noted that the deck ratings are much lower using the FE model, but the flange ratings are much higher. For maximum bending, a wheel load is applied in the immediate area from which the deck stress is extracted. The stress concentrations due to the wheel load have not yet spread out through the deck width and steel section, resulting in higher stresses in the deck and lower stresses in the bottom flange. The other two methods proceed by calculating a moment due to the loads and finding the stress assuming linear elastic behavior and full participation by the steel and concrete. Thus, this result is not surprising, but does help indicate some of the types of unexpected issues that can occur even when using detailed FE models for design or rating.

Second, the modal flexibility flange ratings are 7% higher than the distribution factor ratings for the interior girder but are 22% higher for the fascia girder. Also, the finite element flange ratings are 55% higher than the distribution factor ratings for the interior girder but are 75% higher for the fascia girder. This indicates that the distribution factor ratings are more conservative for the interior girders than for the fascia girders for bending. For shear, the interior girder distribution factor rating is the least conservative of all methods, but the fascia girder distribution factor rating is the most conservative.

Third, the ratings for bending stress from modal flexibility are always higher and less conservative than the distribution factor ratings, but the rating increase is not large for the interior girders. This suggests that the distribution factor for interior girders is fairly accurate for bridges with no skew (which has been documented historically).

Overall, both the FE model and the flexibility model indicate that bending stresses spread across the full structure to a greater extent than is estimated by the distribution factors. Also, both models agree that interior girders take slightly more shear and that fascia girders take significantly less than predicted by distribution factors.

The operating ratings using the ASD method are shown in Table 8.5 and Table 8.6, and show the same relationships as the inventory ratings do.

Critical Section		HS-20 Design Load			Type 3 Legal Truck		
		DF	FE	MF	DF	FE	MF
Interior	Deck	2.89	1.54	3.10	3.97	2.09	4.06
	Flange	1.23	1.89	1.32	1.64	2.47	1.73
	Shear	4.95	4.84	4.59	6.80	6.49	6.20
Fascia	Deck	2.68	2.66	3.30	3.57	3.59	4.36
	Flange	1.43	2.52	1.77	1.91	3.33	2.34
	Shear	5.37	6.43	7.19	7.17	9.15	10.03

Table 8.5. ASD operating ratings for HS-20 and Type 3 truck loads.

Critical Section		Type 3S2 Legal Truck			Type 3-3 Legal Truck		
		DF	FE	MF	DF	FE	MF
Interior	Deck	3.74	2.27	4.45	3.96	2.51	4.45
	Flange	1.79	2.70	1.90	1.96	2.89	1.90
	Shear	6.40	6.69	6.15	6.78	7.08	6.51
Fascia	Deck	3.91	3.93	4.77	4.27	4.18	4.89
	Flange	2.10	3.66	2.56	2.29	3.75	2.62
	Shear	7.89	7.95	9.12	8.60	8.45	9.64

Table 8.6. ASD operating ratings for Type 3S2 and Type 3-3 truck loads.

8.7.3 LFD Rating Results

The LFD inventory ratings are presented in Table 8.7 and Table 8.8 for the three live load stress calculation methods. The operating ratings are not shown since they are all merely 167% of the published inventory ratings. Again, for the LFD philosophy, the distribution factor for interior girder forces is S/5.5 lanes of trucks to the girder, and the lever rule is used for the fascia girder.

Critical Section		HS-20 Design Load			Type 3 Legal Truck		
		DF	FE	MF	DF	FE	MF
Interior	Deck	1.71	0.91	1.83	2.27	1.23	2.40
	Flange	1.42	2.17	1.52	1.89	2.84	1.99
	Shear	2.94	2.87	2.73	4.04	3.85	3.68
Fascia	Deck	1.76	1.74	2.16	2.34	2.36	2.86
	Flange	1.50	2.64	1.85	2.00	3.48	2.45
	Shear	3.19	3.81	4.27	4.38	5.43	5.96

Table 8.7. LFD inventory ratings for HS-20 and Type 3 truck loads.

Critical Section		Type 3S2 Legal Truck			Type 3-3 Legal Truck		
		DF	FE	MF	DF	FE	MF
Interior	Deck	2.49	1.34	2.63	2.72	1.48	2.63
	Flange	2.07	3.10	2.18	2.26	3.32	2.18
	Shear	3.80	3.97	3.65	4.02	4.20	3.87
Fascia	Deck	2.57	2.58	3.13	2.80	2.74	3.21
	Flange	2.19	3.83	2.68	2.39	3.93	2.75
	Shear	4.12	4.72	5.41	4.36	5.01	5.72

Table 8.8. LFD inventory ratings for Type 3S2 and Type 3-3 truck loads.

The LFD load ratings for bending moment are generally quite a bit higher than when using the ASD philosophy. This is because LFD allows the full plastic moment of the section to be used for compact steel sections such as the rolled beams of the Hartbarger Bridge. In contrast, the ASD allowable stresses do not incorporate any increase for compact sections beyond first yield.

As with the ASD ratings, the LFD deck ratings using the FE model are quite low due to locally high deck stresses in the vicinity of a truck wheel. For interior girder bending, the modal flexibility based ratings are 7% higher than those using distribution factors. For bending in the fascia girder, the modal flexibility based ratings are 23% higher than the ratings using distribution factors. These rating improvements align very well with the ASD results. Also as

before, modal flexibility and finite element results apply less shear force to fascia girders and more to interior girders than distribution factors do.

8.7.4 LRFD Rating Results

For the LRFD philosophy, distribution factors were developed in a rational manner as described previously, and are different for shear and for moment. The distribution factors also provide modification factors for shear and moment based on the bridge skew. Since this bridge has zero skew, the modification factors are unity. For the structural arrangement of the Hartbarger Bridge, the distribution factor equations for more than one lane loaded (controlling) are:

Interior girder moment:

$$DF = 0.075 + \left(\frac{S}{14ft}\right)^{0.6}\left(\frac{S}{L}\right)^{0.2}\left(\frac{K_g}{L\,t_s^3}\right)^{0.1} \qquad \text{Equation 8.26.}$$

Fascia girder moment:

$$DF = e_m\left[0.075 + \left(\frac{S}{9.5ft}\right)^{0.6}\left(\frac{S}{L}\right)^{0.2}\left(\frac{K_g}{L\,t_s^3}\right)^{0.1}\right] \qquad \text{Equation 8.27.}$$

Interior girder shear:

$$DF = 0.2 + \left(\frac{S}{12ft}\right) - \left(\frac{S}{35ft}\right)^2 \qquad \text{Equation 8.28.}$$

Fascia girder shear:

$$DF = e_v\left[0.2 + \left(\frac{S}{12ft}\right) - \left(\frac{S}{35ft}\right)^2\right] \qquad \text{Equation 8.29.}$$

In the preceding equations, K_g, e_m, and e_v are found as:

$$K_g = n\left(I_x + A_g e_g^2\right) \qquad \text{Equation 8.30.}$$

$$e_m = 0.77 + \frac{d_e}{9.1ft}$$ Equation 8.31.

$$e_v = 0.6 + \frac{d_e}{10ft}$$ Equation 8.32.

Where:

$S =$ the girder spacing, in feet.

$L =$ the span length, in feet.

$t_s =$ the design slab thickness.

$n =$ the modular ratio between steel and concrete.

$I_x =$ the moment of inertia of the bare steel girder.

$A_g =$ the area of the bare steel girder.

$e_g =$ the distance between the C.G. of the deck and the C.G. of the girder.

$d_e =$ the distance from the center of fascia girder to the face of barrier.

The LRFD inventory ratings are presented in Table 8.9 and Table 8.10 for the three live load stress calculation methods.

Critical Section		HL-93 Design Load			Type 3 Legal Truck		
		DF	FE	MF	DF	FE	MF
Interior	Deck	1.63	0.87	1.69	3.33	1.76	3.41
	Flange	1.34	2.01	1.40	2.76	4.03	2.82
	Shear	2.43	2.95	2.77	5.31	5.79	5.54
Fascia	Deck	1.79	1.57	1.90	3.66	3.26	3.96
	Flange	1.52	2.30	1.62	3.11	4.79	3.36
	Shear	3.65	3.72	4.27	7.99	8.16	8.95

Table 8.9. LRFD inventory ratings for HL-93 and Type 3 truck loads.

Critical Section		Type 3S2 Legal Truck			Type 3-3 Legal Truck		
		DF	FE	MF	DF	FE	MF
Interior	Deck	3.65	1.91	3.74	3.99	2.11	3.74
	Flange	3.02	4.40	3.09	3.30	4.71	3.09
	Shear	5.00	5.98	5.49	5.29	6.32	5.82
Fascia	Deck	4.01	3.57	4.33	4.38	3.79	4.44
	Flange	3.41	5.26	3.68	3.72	5.39	3.77
	Shear	7.52	7.09	8.14	7.96	7.54	8.60

Table 8.10. LRFD inventory ratings for Type 3S2 and Type 3-3 truck loads.

Using LRFD, the results are similar to ASD and LFD. The finite element model overestimates deck stresses and underestimates bottom flange stresses at the critical bending section. The ratings using modal flexibility are again less conservative than the distribution factor based ratings. For the interior girder and HL-93 loading, the flange rating is 4% higher using modal flexibility. For the fascia girder, the flange rating is 7% higher. It is noteworthy that the LRFD distribution factors provide ratings that are much closer to the modal flexibility results than the other design philosophies, although this is to be expected with the more complex distribution factor equations.

8.8 CONCLUSIONS

The Hartbarger Bridge was load rated using three different methods for determining live load stress. The simplest and most commonly used method is the application of AASHTO distribution factors. The most computationally intensive method, which is only occasionally used in industry, is to perform loading in a detailed finite element model. The third method, which is developed herein, is to use a simple model developed from a measured modal flexibility matrix.

The modal flexibility matrix cannot be used directly for load rating since it is not possible to determine the needed internal structural forces without knowledge of local stiffness. A direct and simple solution to this problem is developed herein, and builds on previously published works.

This two-step method starts by solving the common issue of having measured flexibility of insufficient rank. The rank is increased by using a least-squares process to best fit a simple structural model to the measured data. An augmented flexibility matrix is then assembled that consists of the measured flexibility combined with estimated columns and rows for the unmeasured DOFs. The second step of the method disassembles the augmented flexibility matrix to determine local stiffness parameters for the simple structural model. With estimates of local stiffness based on the measured flexibility, it is then possible to determine internal forces due to any external loading pattern, including rating vehicles.

The ratings for the Hartbarger Bridge demonstrate that the modal flexibility method is less conservative than the distribution factor method. For the older ASD and LFD design philosophies, the ratings based on bending stress (which usually control) range from 7% to 22% higher for the modal flexibility method. For the current LRFD philosophy, which uses carefully calibrated distribution factors, the ratings based on bending stress range from 4% to 7% higher using modal flexibility.

Previous studies have shown that AASHTO distribution factors are at their best for simple-span bridges with no skew, such as the Hartbarger Bridge, and are less accurate for continuous spans and skewed bridges. Thus, larger increases in load rating can be expected using the modal flexibility rating method on more complex bridges. A rating increase based on modal testing could benefit bridge owners in situations where ratings (for legal loads especially) are less than unity. In a situation such as this, the higher ratings from the less conservative approach might demonstrate that load posting is not required, or that less restrictive posting can be used. Additionally, more accurate ratings can enable owners to better utilize their limited maintenance funds for managing and maintaining their aging bridge inventories.

An additional potential benefit to owners, although not demonstrable on the tested structure due to its good structural condition, is that loss of stiffness due to damage or deterioration will automatically be incorporated into the measured flexibility. The extracted local stiffness of elements will thus be lower, and this will be reflected in the ratings. However, it is noted that only generalized damage that decreases structural stiffness will cause this effect. Localized damage such as weld cracks, girder nicks, etc. will not usually decrease stiffness and thus will not change the load ratings. Detection and characterization of localized damage and defects is an open area of research that is not in the scope of this thesis.

The modal flexibility method also outperformed the rating results based on the calibrated finite element model. The FE model significantly overestimated deck stresses while underestimating bottom flange stresses in the vicinity of wheel loads. Although the deck in the FE model is composed of 969 plate elements generally of 1.5 square feet each, the mesh is too coarse for proper distribution of the heavy wheel loads. To give more accurate results, the mesh would have to be finer for any location where wheels would be applied, and the wheel point loads would have to be converted to area loads distributed across the plate elements. Additionally, the plate elements that comprise the girders would also have to be developed from a finer mesh to enable more accurate force dissipation. These types of refinements would increase the engineering time required (and thus the cost of the model), and would further lengthen solution time (although this is generally a minor issue with modern computers). In industry, less experienced personnel performing this work would possibly not be aware of the inaccurate results in any case, especially without results from an alternate method for comparison.

Overall, the use of measured modal flexibility for bridge rating is shown to be successful. The method provides results quite similar to those determined from standard industry practice, which

demonstrates that the method functions properly. Additionally, the new method provides load ratings that are on the order of 10% higher than standard industry ratings by using the actual flow of forces through the structure, as opposed to using conservative simplifying assumptions.

8.9 FUTURE WORK

The load rating performed herein was developed as a demonstration of the usefulness of the type of accurate modal flexibility matrix that can be captured using the tactile transducers in MIMO EMA testing of bridges. There is significant future work needed to validate the calculation of ratings with this method such as:

- Testing and rating of a variety of bridge configurations (various skews, continuous bridges, concrete girders).
- Statistical analysis of the effects of measurement noise, data collection errors, and modal parameter extraction errors in the accuracy of the ratings.
- Since the assumed simple structural model is not unique, analysis of the effects of assuming different model configurations.

CHAPTER NINE

THESIS CONCLUSION

9.1 INTRODUCTION

This chapter recapitulates and summarizes the broad range of work reported in this thesis. The first goal of the work was to determine the optimal manner in which to apply a tactile transducer based excitation system for MIMO EMA of short to medium-span bridges. The second goal was to develop a new method for directly using the identified modal parameters of a bridge to improve the load rating process. The various steps that were taken in order to achieve these goals are summarized in the following subsections, which parallel the chapters of this thesis.

9.2 CHARACTERIZATION OF TACTILE TRANSDUCERS AND POWER AMPLIFIERS

Tactile transducers and appropriately sized consumer subwoofer amplifiers are not manufactured with the intended use of MIMO EMA testing of bridges, and thus the manufacturers' specifications do not provide the types of information that would inform the application of such devices to MIMO EMA. Therefore, it was necessary to characterize the operational and performance characteristics of these components in a quantitative manner. The literature provided no framework for this characterization process, and thus a testing protocol was developed and implemented.

The testing was performed on several alternate tactile transducers and amplifiers. The selection of the best devices for use in the MIMO EMA system was validated by specific test results. Considering the three shakers tested, the shaker used for further work had the best low-frequency force output, the flattest response across a broad range of frequencies, and good signal

reproduction with low noise and distortion. Of the three amplifiers tested, the one used for further work had the best low-frequency gain and the least low-frequency distortion. This amplifier also provides two channels which each have adequate power to drive the TT shaker, and it also performed well with stochastic signals.

9.3 IN-DEPTH CHARACTERIZATION OF SHAKER AND AMPLIFIER

Additional testing of the best shaker and amplifier combination was undertaken with the goal of determining if a dedicated force transducer would be required at each input location for MIMO EMA. Ideally, the force output could be adequately characterized through controlled testing in the lab; however, this hypothesis was systematically evaluated to determine if force transducers could be neglected. Another goal was to determine if the shakers and amplifiers are uniform enough across their population that they could be used interchangeably. The literature did not provide guidance on performing an evaluation of this type, and a process was developed to establish the necessity of using force transducers with the novel MIMO EMA system.

The testing revealed than a TT reproduces a signal in a uniform manner, with variation in force output on the order of 2%. Much of the variation was attributed to heating of the device during operation, and thus allowing the shakers to warm up prior to production testing would reduce the variation in force. It was also found that the amplifier reproduces a signal with variation in voltage output on the order of 0.1%.

The population of TTs showed significant variation. It was apparent that different production runs of the devices incorporated design changes, and that the population acquired consisted of at least three different iterations. The average variation in force output across the population was on

the order of 7%, and the level of signal distortion was much higher for some of the devices than for others.

The population of amplifiers was more uniform than the shakers, with voltage output varying by an average of only about 2%. However, setting an equal gain on all amplifiers is essentially impossible since a dial potentiometer is used for this purpose. No production run differences were identified with the amplifiers, and all provided similar quality of reproduction.

It was also noted that structure response significantly affects the force output of the structure-mounted shakers. In the vicinity of natural frequencies of the structure, the force output of a shaker changed by up to 100% in comparison to the force output on a rigid mount.

Overall, the variation in shaker performance, amplifier gain settings, and structure interaction negated the idea that the shakers could be used without force transducers. However, the idea of roving force transducers was maintained since each run of a shaker in a particular setup was highly uniform.

9.4 EXCITATION TECHNIQUES

One of the most important aspects of modal testing is the proper selection and application of excitation signals. The signal type, force level, and spatial input locations all have consequences to the quality of the FRFs and extracted modal parameters. Since MIMO EMA of civil structures is only reported twice in the literature, and optimization of the inputs for this application is not reported, it was necessary to determine the best techniques for MIMO EMA excitation of short to medium-span bridges as part of the work of this thesis.

Many signal types were discussed and compared, and the multisine signal was selected as the best type of deterministic signal for MIMO EMA bridge testing. A multisine signal can be constructed in many ways, and can selectively be built and utilized in a manner that eliminates leakage and provides high SNR. The signal is also compatible with MIMO testing: merely changing the polarity of the input provides essentially orthogonal force inputs. Cyclic averaging is also enabled, reducing noise while practically eliminating leakage. Finally, deterministic signals allow the use of roving transducers.

Selection of the best force level of the input is a balance of two opposing criteria. A high force level provides the best SNR in consideration of ambient noise in the structure and electronics. However, higher force also excites nonlinearities in structures and causes noise and rattles to develop. Thus, an appropriate force level must be determined for each structure by exploring a range and selecting an amplitude that provides the best FRFs.

Development of a good spatial distribution of inputs is also important. The biggest danger is providing all input near the locations of modal nodes since a poorly excited mode is difficult to accurately identify. The most direct way to reduce this risk is to reduce the probability of providing all input at modal nodes. For symmetric structures, the shapes of some modes can be inferred prior to testing and the probable locations of modal nodes identified and avoided. Also for symmetric structures, the shakers should not be placed symmetrically. Symmetric placement increases the probability of all input occurring at nodes. Finally, increasing the number of inputs reduces the probability of only exciting nodal locations, and thus the proposed MIMO EMA using many low-cost shakers is beneficial in this regard.

9.5 DATA PROCESSING AND ANALYSIS METHODS

Data capture methods were explored and explained as they relate to the accuracy of experimental results. Quantization errors in digital sensors and in data acquisition devices were discussed, and the necessity of adequate resolution in both the time domain and the frequency domain were demonstrated. Methods of data averaging for noise reduction were also compared, and cyclic averaging was noted as the best way to reduce noise while also diminishing or eliminating leakage errors.

The calculation of FRFs was discussed for four different averaging methods, using both SIMO and MIMO excitation. The H1 algorithm was identified as the best for stochastic signals while the EIV algorithm performs best for deterministic signals. These algorithms assemble the FRFs into a larger transfer function from which modal parameters can be extracted.

Parameter extraction is performed using the CMIF technique. Although many competing algorithms exist, CMIF was selected since it is robust and since it could be developed in-house. This algorithm provides a method for identifying potential modes as unusually high singular values. Associated singular vectors are taken as estimates of modal vectors and are used to filter the transfer function, resulting in enhanced FRFs. Least-squares techniques are then used to estimate the modal damping and modal mass from the enhanced FRFs. Finally, modal flexibility is synthesized from the identified natural frequencies, damping, and modal mass.

9.6 LABORATORY BRIDGE MODEL TESTING

Testing of a model structure in a laboratory environment was performed to validate that the TTs will provide an EMA characterization of a large-scale bridge model that is comparable to using a more conventional excitation device. This testing was important since EMA is a totally different

use for the shakers than the manufacturer intended. Thus, the shakers had never been validated for this use by the maker or by any other researcher. The various tests were designed to use the TTs in the same manner that purpose-built shakers are typically used, enabling the functionality of the TTs to be evaluated in realistic situations.

The model structure was tested in several ways to provide a baseline for comparison. First, a static flexibility matrix was developed by applying large static loads to each DOF and measuring vertical displacements at all DOFs. This provided a baseline against which to compare synthesized modal flexibility matrices. Second, an industry-standard APS Dynamics shaker was used in a series of SIMO experiments to excite each DOF in turn and provide a high quality 15x15 transfer function. Both multisine and burst-random signals were used. Modal parameters extracted from this testing were used as a baseline against which to compare parameters from tactile transducer excitation.

The structure was also tested in several ways using the novel excitation system. First, a SIMO process was used with a single TT, and a 15x15 transfer function was produced. Second, a MIMO test with a particular spatial arrangement of four TTs was performed, and a 15x4 transfer function was produced. Third, another MIMO test with four TTs in a different spatial arrangement was performed. Fourth, a MIMO test with eight TTs and roving force transducers was performed, and a 15x8 transfer function was produced. All of the tests were repeated twice: once with multisine excitation, and once with burst-random excitation.

The testing validated several items. First, the multisine signal was found to provide results on par with the burst-random signal. Second, use of roving transducers was successful for frequencies below 70 Hz. Above 70 Hz, some of the TTs perform in a less uniform manner and this has

serious negative consequences for parameter identification. Third, the MIMO testing underperformed the SIMO testing since a significantly smaller amount of redundant information was available in the transfer function for MIMO. Also, the issues with SIMO that cause errors in real-world testing are generally nonexistent in a controlled laboratory environment.

Finally, the laboratory bridge model testing demonstrated that the TTs operating in a MIMO EMA environment provide accurate modal parameters. The modal flexibility matrix synthesized from these modal parameters also had good agreement with the measured static flexibility matrix.

9.7 TESTING OF AN IN-SERVICE HIGHWAY BRIDGE

The primary purpose of this testing was to evaluate the capabilities of the tactile transducer excitation system for MIMO EMA of a full-scale bridge. The literature only reports a single prior MIMO EMA bridge test, and that testing only utilized two shakers. Overall, the system performed very well, and many modes of the structure were identified. The results of this testing were compared to results from various tests performed previously by others, and the MIMO EMA system approach using TTs outperformed the other methods. The previous work included the two most common testing methods used in the field today, which are MRIT (hammer testing at many DOFs in turn) and OMA (ambient excitation only).

The bridge was tested using only four TTs due to budget constraints. Testing with many more shakers was desirable, but force transducers and recording channels were not available for additional shakers. The four shakers were moved to five different lines of DOFs, and both burst-random and multisine signals were used. A test using eight shakers and roving force transducers was also performed, although it is recognized that this is a less desirable testing method.

Secondary analysis was also performed to explore several other topics. The benefits of combining FRFs from experiments performed at different times were evaluated. For this testing, the larger combined transfer function provided better results for mode capture and modal mass, but the inconsistencies in the data caused an apparent increase in damping. This again indicates that the best testing method is to simultaneously excite as many DOFs as possible, further supporting the use of the inexpensive array of shakers.

The use of roving force transducers was also tested again. Eight TTs were used with multisine excitation, and the four force transducers were all relocated one time. This testing produced a 20x8 transfer function, and the modal parameters extracted were generally reasonable. However, combining data from separate experiments produced more accurate data and is easier to execute in the field. Thus, roving force transducers should be avoided in most situations.

The impact of allowing traffic to use the structure during testing was also evaluated. It was found that the large unmeasured force input from traffic causes serious errors. Although identification of natural frequencies was not affected, modal mass estimates were off by orders of magnitude. However, a bridge does not have to be closed to enable MIMO EMA testing with the TT system. Testing only has to be performed at times when traffic is not heavy, such as overnight. Data sets that are contaminated by traffic can simply be excluded during processing.

Finally, multisine and burst-random excitation were again compared. The use of multisine excitation provided more accurate modal parameters than burst-random, which is expected based on the theoretical advantages of the deterministic signal. However, burst-random signals are more traditionally used in EMA, and testing time is not significantly increased by using two

different signals. Thus, including burst-random excitation in future modal testing is reasonable, and provides an additional set of modal parameters for comparison and evaluation purposes.

9.8 BRIDGE LOAD RATING USING MEASURED MODAL FLEXIBILITY

Load rating of the Hartbarger Bridge was performed to evaluate a potential application for the high quality modal flexibility matrix that can be captured using the MIMO EMA excitation. It is again noted that none of the previous testing of this bridge provided modal parameters that could have been used for load rating. The parameters from MRIT were quite inaccurate and many modes were not found, and the OMA testing does not provide modal flexibility. Thus, the capability to extract accurate modal flexibility for a bridge structure is relatively novel.

The most advantageous use of modal flexibility in load rating is in the application of truck loads. The live load demand at a section is highly dependent on assumptions about the flow of force through the structure, and the measured modal flexibility matrix provides valuable information in this regard. The load distribution is also affected by damage, deterioration, and structural defects, which are automatically reflected in the extracted modal flexibility. Simplifying and conservative assumptions that are typically used in live load application can be avoided by use of measured flexibility, improving the accuracy of the load ratings. There is also a potential to alter the capacity of sections and to modify section parameters used in the calculation of dead load demand; however, the rating performed did not include these changes due to the excellent condition of the Hartbarger Bridge.

Measured modal flexibility cannot be directly used for live load application since the local stiffness of elements is not provided. Therefore, a two-step method was demonstrated that allows the estimation of local stiffness for an assumed simple model that connects the measured DOF.

In the first step, the rank of the flexibility matrix is increased by adding estimated flexibility of unmeasured DOF. In the second step, the augmented flexibility matrix is disassembled in a manner that provides local stiffness values for the assumed DOF connectivity model. For the Hartbarger Bridge, it was shown that the estimated local stiffness parameters were reasonable and were in good agreement with estimates based on actual section dimensions. A global stiffness matrix is then generated from the local stiffness values, and influence surfaces are generated to enable truck loading for maximum force response.

The rating results using modal flexibility were in good agreement but were slightly less conservative than those found using traditional distribution factors. This good agreement demonstrates that the new method works properly, since the distribution factors are known to be accurate for the bridge type analyzed. The literature demonstrates that the traditional distribution factors are not accurate for many bridges with more complex geometry, and thus application of the modal flexibility method to these structures should provide improved results. Also, widespread damage and deterioration will be reflected in measured flexibility, and thus will automatically be included in local stiffness. Not only will the use of modal flexibility provide more accurate live load demand, but the calculated local stiffness can be used to modify the section capacity and the dead load stresses.

A detailed finite element model was also used in the rating of the bridge. The use of detailed FE models is generally considered by industry to be the most accurate way to develop load ratings, however, there are many ways to get inaccurate results. It was found in this work that the FE model was generally too coarse at the points of load application. This coarseness resulted in deck stresses that were too high and bottom flange stresses that were unconservatively low. Calibrating a nominal FE model to field measurements is also a difficult problem that is still the

subject of ongoing research. Thus, the method developed herein that uses the measured modal flexibility matrix is a simpler and more direct way to improve load ratings than the use of FE modeling.

9.9 OVERALL SUMMARY OF CONCLUSIONS

The work reported in this thesis consisted of validating a novel excitation system for improved MIMO experimental modal analysis of certain classes of civil structures. Both laboratory testing and real-world field testing of the system were undertaken, and the results demonstrated that the system does provide more accurate modal parameters than those provided by other more commonly used excitation schemes. Research is advancing on many fronts to expand the use of measured modal parameters, and the new ability to capture accurate values will benefit the state of knowledge in this area.

Load rating of an in-service highway bridge was also performed to demonstrate one potential use of the captured modal results. The use of measured modal parameters produced rating values that were accurate. The method demonstrated also has the benefit of eliminating the generation and calibration of a detailed FE model, which is currently the most common way that measured parameters are used.

REFERENCES

AASHTO. (1994). “Guide Specifications for Distribution of Load for Highway Bridges ” American Association of State Highway and Transportation Officials (AASHTO), Washington, D.C.

AASHTO. (2002). “Standard Specifications for Highway Bridges, 17th Edition.” American Association of State Highway and Transportation Officials (AASHTO), Washington, D.C.

AASHTO. (2008). “Manual for Bridge Evaluation.” American Association of State Highway and Transportation Officials (AASHTO), Washington, D.C.

AASHTO. (2010). “LRFD Bridge Design Specifications, 5th Edition.” American Association of State Highway and Transportation Officials (AASHTO), Washington, D.C.

Agardh, L. (1991). "Modal Analysis of Two Concrete Bridges in Sweden." *Structural Engineering International*, 1(4), 35-39.

Aktan, A. E., Miller, R. A., Shahrooz, B. M., Zwick, M., Heckenmueller, M., Ho, I., Hrinko, W., and Toksoy, T. (1992). "Nondestructive And Destructive Testing Of A Reinforced Concrete Slab Bridge And Associated Analytical Studies." Rep. No. FHWA/OH-93/017, National Technical Information Service, Springfield, VA.

Aktan, A.E., Chuntavan, C., Lee, K., and Toksoy, T. (1993). "Structural Identification Of A Steel Stringer Bridge." *TRR*, 1393(1), 175-185.

Aktan, A. E., Dalal, V., Farhey, D. N., and Hunt, V. J. (1995). "Bridge Reliability Evaluation in the 21st Century." *Research Transformed into Practice: Implementation of NSF Research*, ASCE Publications, 493-505.

Aktan, A. E., Ciloglu, S.D., Grimmelsman, K.A., Pan, Q., and Catbas, F.N. (2005). “Opportunities And Challenges In Health Monitoring Of Constructed Systems By Modal Analysis.” *Proceedings of the International Conference on Experimental Vibration Analysis for Civil Engineering Structures*, Bordeaux, France.

Allemang, R. J., Rost, R. W., and Brown, D. L. (1983). "Multiple Input Estimation Of Frequency Response Functions: Excitation Considerations." Design and Production Engineering Technical Conference. ASME, Dearborn, MI, USA, ASME, New York, NY, USA.

Allemang, R.J. (1999). “Vibrations: Experimental Modal Analysis.” UC-SDRL, Cincinnati, OH.

Allemang, R. J. (2003). "The Modal Assurance Criterion–Twenty Years Of Use And Abuse." *Sound and Vibration*, 37(8), 14-23.

Allemang, R.J., and Brown, D.L. (2006). "A Complete Review Of The Complex Mode Indicator Function (CMIF) With Applications." *Proc. of the International Conference on Noise and Vibration Engineering ISMA2006*, Leuven, Belgium, 3209-3246.

Avitabile, P., Singhal, R., Peeters, B., and Leuridan, J. (2005). "Modal Parameter Estimation Approaches For Large Complicated Multiple Reference Tests (Then And Now)." *Conference Proceedings of the Society for Experimental Mechanics Series 2005*, Springer, New York, NY.

Barbaccia, T.,Grady. (2011). "The State of Our Bridges." *Better Roads*, 81(11), pp 8-9, 11-12, 15-19.

Bendat, J. S., and Piersol, A. G. (1980). "Engineering Applications of Correlation and Spectral Analysis." New York: John Wiley and Sons, Inc.

Brownjohn, J. M. W., Dumanoglu, A. A., Severn, R. T., and Taylor, C. A. (1987). "Ambient Vibration Measurements Of The Humber Suspension Bridge And Comparison With Calculated Characteristics." *Proceedings of the Institution of Civil Engineers* (London), 83, 561-600.

Cai, C. S. (2005). "Discussion on AASHTO LRFD Load Distribution Factors For Slab-On-Girder Bridges." *Pract.Periodical Struct.Des.Constr.*, 10(3), 171-176.

Catbas, F. N., Lenett, M., Aktan, A. E., Brown, D. L., Helmicki, A. J., and Hunt, V. (1998). "Damage Detection And Condition Assessment Of Seymour Bridge." *Proceedings of the International Modal Analysis Conference*, SEM, Santa Barbara, CA, USA, 1694-1702.

Catbas, F. N., Brown, D. L., and Aktan, A. E. (2004). "Parameter Estimation For Multiple-Input Multiple-Output Modal Analysis Of Large Structures." *J.Eng.Mech.*, 130(8), 921-930.

Catbas, F. N., Brown, D. L., and Aktan, A. E. (2006). "Use Of Modal Flexibility For Damage Detection And Condition Assessment: Case Studies And Demonstrations On Large Structures." *J.Struct.Eng.*, 132(11), 1699-1712.

Catbas, F.N. (2010). "Load Rating Using a Practical Analysis and Testing Method for Existing Reinforced Concrete T-Beam Bridges." *TRB 89th Annual Meeting Compendium of Papers*, TRB, Washington, D.C.

Chauhan, S., Phillips, A., and Allemang, R. (2008). "Damping Estimation Using Operational Modal Analysis." *Proceedings of the 26th International Modal Analysis Conference*, Springer, New York, NY, USA.

Cloutier, D., Avitabile, P., Bono, R., and Peres, M. (2009). "Shaker/Stinger Effects On Measured Frequency Response Functions." *Proceedings of the Twenty-Seventh International Modal Analysis Conference.* Orlando, FL, 9-12.

Coleman, J. (1996). "Bridge Inspection and Assessment - Virginia Department of Transportation." *Structural Materials Technology - An NDT Conference*, Technomic Publishing Company, Inc., Lancaster, PA, 233-234.

Cunha, A., and Caetano, E. (2006). "Experimental modal analysis of civil engineering structures." *Sound and Vibration*, 40(6), 12-20.

Davis, B., Barrett, A. R., and Murray, T.M. (2011). “Use Of A Force Plate Versus Armature Accelerometer For Measuring Frequency Response Functions.” *Experimental Techniques*, 35(1), 73-79.

Deckers, K., Guillaume, P., Lefeber, D., De Roeck, G., and Reynders, E. (2008). " Modal Testing Of Bridges Using Low-Weight Pneumatic Artificial Muscle Actuators." *Proceedings of the 26th International Modal Analysis Conference*, Springer, New York, NY, USA.

Deger, Y., Cantieni, R., Pietrzko, S., Ruecker, W., and Rohrmann, R. (1995). "Modal Analysis of a Highway Bridge; Experiment, Finite Element Analysis and Link." *Proceedings of the 13th International Modal Analysis Conference*, SPIE, 1141.

Dobrowiecki, T. P., Schoukens, J., and Guillaume, P. (2006). "Optimized Excitation Signals For MIMO Frequency Response Function Measurements." Instrumentation and Measurement, IEEE Transactions on, 55(6), 2072-2079.

Doebling, S. W., Farrar, C. R., and Cornwell, P. (1997). "Statistical Comparison Of Impact And Ambient Testing Results From The Alamosa Canyon Bridge." *Proceedings of the International Modal Analysis Conference – IMAC*, SEM, Bethel, CT, USA, 264-270.

Doebling, S.W. and Peterson, L.D. (1997). “Computing Statically Complete Flexibility from Dynamically Measured Flexibility.” *Journal of Sound and Vibration*, 205(5), 631-645.

Doebling, S.W., Peterson, L.D., and Alvin, K.F. (1998). “Experimental Determination of Local Structural Stiffness by Disassembly of Measured Flexibility Matrices.” *Journal of Vibration and Acoustics*, 120(10), 949-957.

Fladung, W. A., Phillips, A. W., and Brown, D. L. (1997). "Specialized Parameter Estimation Algorithms For Multiple Reference Testing." *Proceedings of the 15th International Modal Analysis Conference*, Orlando, FL, 1078-1087.

Gangone, M. V., Whelan, M. J., and Janoyan, K. D. (2009). "Wireless Sensing System For Bridge Condition Assessment And Health Monitoring." *Smart Sensor Phenomena, Technology, Networks, and Systems*, 7293(1).

Gangone, M. V., Whelan, M. J., and Janoyan, K. D. (2011). "Wireless Monitoring of a Multispan Bridge Superstructure for Diagnostic Load Testing and System Identification." *Computer-Aided Civil and Infrastructure Engineering*, 26(7), 560-579.

Giraldo, D. F., Song, W., Dyke, S. J., and Caicedo, J. M. (2009). "Modal Identification through Ambient Vibration: Comparative Study." *J.Eng.Mech.*, 135(8), 759-770.

Gokce, H. B., Catbas, F. N., and Frangopol, D. M. (2011). "Evaluation Of Load Rating And System Reliability Of Movable Bridge." *TRR*, 2251(1), 114-122.

Guillaume, P., Verboven, P., Vanlanduit, S., and Parloo, E. (2001). "Multisine Excitations- New Developments And Applications In Modal Analysis." IMAC-XIX: A Conference on Structural Dynamics, 1543-1549.

Gul, M., and Catbas, F. N. (2008). "Ambient Vibration Data Analysis for Structural Identification and Global Condition Assessment." *J.Eng.Mech*., 134(8), 650-662.

Haritos, N., Khalaf, H., and Chalko, T. (1995). "Modal Testing of a Skew Reinforced Concrete Bridge." *Proceedings of the 13th International Modal Analysis Conference*, SPIE, 703.

Hartle, R., Balan, T., Wingate, F., Vanderzee, P., and Lai, L. (2007). "Remote Health Monitoring and Load Modeling of Cracked Fracture Critical Bridge Components." *Rep. No. FHWA-PA-2006-036-040207-1*, National Technical Information Service, Springfield, VA.

Herrman, J. K. (2011). "Laboratory Evaluation Of Dynamic Characterization Methods For Rapid Condition Assessment Of Bridges." Master's Thesis, University of Arkansas.

Hunt, D. L. (1987). "A Modern Approach For Modal Testing Using Multiple Input Sine Excitation." Structures, Structural Dynamics and Materials Conference, 28th, Monterey, CA, and AIAA Dynamics Specialists Conference, Monterey, CA, Apr. 9, 10, Technical Papers. Part 2B.

Hunt, D. L., and Brillhart, R. D. (1991). "Modal Testing Using Multiple Input Random Excitation." *Proceedings Of The International Modal Analysis Conference.* Volume 2, 1495-1501.

Imamovic, N., and Ewins, D. (1997). "Optimization Of Excitation DOF Selection For Modal Tests." *Proceedings of the International Modal Analysis Conference*, Orlando, FL, v2, 1945-1951.

James, G.H. and Carne, T.G. (1993). "Damping Measurements from an Operating Wind Turbine: Preliminary Results and Procedures." *ASME Sol Energy Div Publ SED*, v14, ASME, New York, NY, 103-111.

Lang, G. F. (1997). "Electrodynamic Shaker Fundamentals." *Sound and Vibration*, 31(4), 14-23.

Lembregts, F., Snoeys, R., and Leuridan, J. (1987). "Application And Evaluation Of Multiple Input Modal Parameter Estimation." 5th International Modal Analysis Conference, London, England, 966-978.

Lenett, M., Griessmann, A., Helmicki, A. J., and Aktan, A. E. (1999). "Subjective and Objective Evaluations of Bridge Damage." *TRR*, 1688(1), 76-86.

Leuridan, J., and Vanderauweraer. A. (1986). "Comparison Of Recent Developments For Estimating Frequency Response Functions In Structural Analysis." *Proceedings of EUSIPCO-86: Third European Signal Processing Conference*, North-Holland, Amsterdam, Netherlands, 263-266.

Leurs, W., Deblauwe, F., and Lembregts, F. (1993). "Modal Parameter Estimation Based on Complex Mode Indicator Functions." *Proceedings of SPIE - The International Society for Optical Engineering*, v1923, 1035-1041.

Maas, S., Zurbes, A., Waldmann, D., Waltering, M., Bungard, V., and De Roeck, G. (2012). "Damage Assessment Of Concrete Structures Through Dynamic Testing Methods. Part 2: Bridge Tests." *Eng.Struct.*, 34(1), 483-494.

Maestri, R., Fernstrom, E., and Grimmelsman, K. (2012). "Dynamic Characterization Of Multiple Identical Spans Of A Steel Girder Bridge." 6th International Conference on Bridge Maintenance, Safety and Management, IABMAS 2012, Lake Maggiore, Italy, 3464-3471.

Maia, N., and Silva, J. (2001). "Modal Analysis Identification Techniques." *Philosophical Transactions of the Royal Society of London*. Series A: Mathematical, Physical and Engineering Sciences, 359(1778), 29-40.

Miller, R. A., Aktan, A. E., and Shahrooz, B. M. (1992). "Nondestructive And Destructive Testing Of A Three Span Skewed R. C. Slab Bridge." *Proceedings of Nondestructive Testing of Concrete Elements and Structures*, April 13, 1992 - April 15, ASCE, San Antonio, TX, USA, 150-161.

Miskovic, Z., Pavic, A., and Reynolds, P. (2009). "Effects Of Full-Height Nonstructural Partitions On Modal Properties Of Two Nominally Identical Building Floors." *Canadian Journal of Civil Engineering*, 36(7), 1121-1132.

Mitchell, L. and Elliot, K. (1984). "A Method for Designing Stingers for Use in Mobility Testing." *Proceedings of the Second International Modal Analysis Conference*. Volume 2, 872-876.

Napolitano, K., and Linehan, D. (2009). "Multiple Sine Sweep Excitation For Ground Vibration Tests." *Conference Proceedings of the Society for Experimental Mechanics, IMAC XXVII,* Springer, New York, NY.

Parloo, E., Cauberghe, B., Benedettini, F., Alaggio, R., and Guillaume, P. (2005). "Sensitivity-Based Operational Mode Shape Normalisation: Application To A Bridge." *Mechanical Systems and Signal Processing*, 19(1), 43-55.

Phares, B. M., Washer, G. A., Rolander, D. D., Graybeal, B. A., and Moore, M. (2004). "Routine Highway Bridge Inspection Condition Documentation Accuracy and Reliability." *J.Bridge Eng.*, 9(4), 403-413.

Pintelon, R., and Schoukens, J. (1998). "Measurement And Modeling Of Linear Systems In The Presence Of Non-Linear Distortions." *Proceedings Of The International Seminar On Modal Analysis*, KU Leuven, 451-458.

Pintelon, R., and Schoukens, J. (2001). "Measurement Of Frequency Response Functions Using Periodic Excitations, Corrupted By Correlated Input/Output Errors." 17th IEEE Instrumentation and Measurement Technology Conference, IEEE, USA, 1753-60.

Rao, D. K. (1987). "On The 'Glitches' In The Force Transmitted By An Electrodynamic Exciter To A Structure." 58th Shock and Vibration Symposium. Volume 1. NASA, Huntsville, AL, USA, 245-255.

Richardson, M. H. (1977). "Derivation of Mass, Stiffness and Damping Parameters From Experimental Modal Data." Hewlett Packard Company, Santa Clara Division, Santa Clara, CA.

Rotter, T., Kohoutek, R., and Marusiak, G. (1994). "Modal Analysis of Railway Bridge in Mlada Boleslav." *Proc. SPIE*, 2251(1), 1316.

Schoukens, J., Pintelon, R., Van Der Ouderaa, E., and Renneboog, J. (1988). "Survey Of Excitation Signals For FFT Based Signal Analyzers." Instrumentation and Measurement, IEEE Transactions on, 37(3), 342-352.

Schwarz, B., and Richardson, M. (2001). "Post-Processing Ambient And Forced Response Bridge Data To Obtain Modal Parameters." *Proceedings of the International Modal Analysis Conference – IMAC*, SEM, Santa Barbara, CA, USA, 829-835.

Sennett, R.E. (1994). "Matrix Analysis of Structures." Waveland Press, Inc., Prospect Heights, IL, USA.

Shelley, S. J., Lee, K. L., and Aktan, A. E. (1995). "Active-Control And Forced-Vibration Studied On Highway Bridge." *J.Struct.Eng.*, 121(9), 1306-1312.

Shih, C. Y., Tsuei, Y. G., Allemang, R. J., and Brown, D. L. (1988). " Complex Mode Indicator Function and Its Application to Spatial Domain Parameter Estimation." *Mechanical Systems and Signal Processing*, 2(4), 367-377.

Siswobusono, P., Chen, S., Jones, S., Callahan, D., Grimes, T., and Delatte, N. (2004). "Serviceability-Based Dynamic Load Rating Of a Lt20 Bridge." *Exp Tech*, 28(6), 33-36.

Sohn, H. (1998). "A Bayesian Probabilistic Approach to Damage Detection for Civil Structures." PhD diss., Stanford University.

Solomou, M., and Rees, D. (2003). "Measuring The Best Linear Approximation Of Systems Suffering Nonlinear Distortions: An Alternative Method." IEEE Transactions on Instrumentation and Measurement, 52(4), 1114-1119.

Stiltz, H.L. (1961). "Aerospace Telemetry, Volume 1." Prentice Hall, New York, NJ.

Suksawang, N., and Nassif, H. H. (2007). "Development Of Live Load Distribution Factor Equation For Girder Bridges." *TRR*, 2028(1), 9-18.

Tustin, W. (1991). "Shaker Displacement Limits Low-Frequency Vibration Testing." *EE: Evaluation Engineering*, 30(5), 162-163.

U.S. Government. (2004). "National Bridge Inspection Standards, Code of Federal Regulations", Title 23, Part 650. U.S. Government Printing Office, Washington, D.C.

Varoto, P. S., and De Oliveira, Leopoldo P. R. (2002). "Interaction Between A Vibration Exciter And The Structure Under Test." *Sound and Vibration*, 36(10), 20-26.

Vold, H., Kundrat, J., Rocklin, G., and Russel, R. (1982). “A Multi-Input Modal Estimation Algorithm For Mini-Computers.” *SAE Technical Papers*, Warrendale, PA, USA.

Vold, H., Crowley, J., and Rocklin, G. T. (1984). "New Ways Of Estimating Frequency Response Functions." *Sound and Vibration*, 18(11), 34-38.

Wang, X., Kangas, S., Padur, D., Liu, L., Swanson, J. A., Helmicki, A. J., and Hunt, V. J. (2005). "Overview of a Modal-Based Condition Assessment Procedure." *J.Bridge Eng*., 10(4), 460-467.

Ward, H. S. (1984). "Traffic Generated Vibrations and Bridge Integrity." *J.Struct.Eng*., 110(10), 2487-2498.

White, K., Minor, J., and Derucher, K. (1992). “Bridge Maintenance Inspection and Evaluation, Second Edition, Revised and Expanded.” Marcel Dekker, Inc., New York, NY, USA.

Wood, M., Friswell, M., and Penny, J. (1992). "Exciting Large Structures Using a 'Bolt Gun'." *Proceedings of the 10th International Modal Analysis Conference*, 233-235.

Yi, J., Cho, S., and Yun, C. (2011). "Two-Step Indirect Static Deflection Estimation of Bridges Based on Ambient Acceleration Measurements." *Exp Tech,* 35.

Yu, E., Skolnik, D., Whang, D. H., and Wallace, J. W. (2008). "Forced Vibration Testing Of A Four-Story Reinforced Concrete Building Utilizing The Nees@UCLA Mobile Field Laboratory." Earthquake Spectra, 24(4), 969-95.

Zhang, Z., and Aktan, A. E. (1996). "Conceptual Structural Identification Using Modal Test And Its Application On Nondestructive Evaluation." *Proceedings - The International Society for Optical Engineering*, SPIE, USA, 739-747.

Zhang, L. (2004). "An Overview Of Major Developments And Issues In Modal Identification." *Proceedings of the IMAC-XXII*, A Conf. on Structural Dynamics, Dearborn, MI, 1-8.

Zimmerman, R., and Hunt, D. (1985). "Multiple Input Excitation Using Burst Random for Modal Testing." Sound and Vibration, 255.

Zokaie, T., T. A. Osterkamp, and R. A. Imbsen. (1991). “Distribution of Wheel Loads on Highway Bridges.” *NCHRP Report 12-2611*. Transportation Research Board, National Research Council, Washington, DC.

Zokaie, T. (2000). "AASHTO-LRFD Live Load Distribution Specifications." *J.Bridge Eng*., 5(2), 131-138.

APPENDIX

BRIDGE LOAD RATING CALCULATIONS

Introduction:

PURPOSE: This worksheet is used to rate the Hartbarger bridge for various truck types using various methods (ASD, LFD, LRFD. Fascia and interior girders are rated.

REFERENCES: (A) AASHTO Standard Specifications for Highway Bridges, Seventeenth Edition, 2002.

(CE) AASHTO Manual for Condition Evaluation of Bridges, Second Edition with Interims through 2003.

(AR) AASHTO LRFD Bridge Design Specifications, Third Edition with Interims through 2005.

(BE) AASHTO Manual for Bridge Evaluation, Second Edition with Interims through 2013.

CREATED: 1/9/14 by EVF.

REVISED: None to date.

Introduction:

The second span of the Hartbarger bridge is rated herein. Rating is performed three different AASHTO design philosophies: ASD, LFD, and LRFD. Additionally, live load effect is calculated in three different ways: per AAHSTO distribution factors, using a calibrated finite element model, and using the results of modal testing.

For bending, stresses are used to rate since the section properties of the span changed during the construction process, preventing the superposition of moments.

For all methods, unfactored dead load effects are the same. For the legal rating vehicles, unfactored live load load effects are the same regardless of the design philosophy.

Rating of the bridge is performed at locations of maximum shear and maximum moment. Since this is a simple-span structure, and since the section properties do not vary along the length of a girder, maximum moment will occur at midspan and maximum shear will occur at the supports. Both fascia and interior girders are rated.

General information:

The general geometric data and material properties for the structure are as follows:

$L_{bridge} := 50ft$ $W_{bridge} := 27ft$

Girder Spacing:

$S := 7.5ft$

Steel properties:

$F_y := 50ksi$ $E := 29000ksi$ $\gamma_s := 490pcf$

W27x94 girders:

Top Flange: Web: Bottom Flange:

$b_c := 9.99in$ $t_w := 0.49in$ $b_t := 9.99in$ AISC

$t_c := 0.745in$ $D := 25.41in$ $t_t := 0.745in$

$A_g := 27.7 \cdot in^2$ $I_x := 3270 \cdot in^4$ $d := 26.9 \cdot in$

C12x20.7 intermediate diaphragms:

$W_d := 20.7 \cdot \frac{lb}{ft}$

Concrete Deck Properties:

$f'c := 3.5 \cdot ksi$ assumed based on age

$E_c := 1820 \cdot \sqrt{f'c \cdot ksi}$ $E_c = 3404.91 \cdot ksi$ AR C5.4.2.4

$\gamma_c := 150pcf$

$n := 9$ A 10.38.1.3

$t_{actual} := 8in$ nominal deck thickness per measurements at deck edge

$t_{design} := t_{actual} - 0.5in$ $t_{design} = 7.5 \cdot in$

$t_{haunch} := 0in$

Section Properties:

The section properties are found for noncomposite loads, long term composite loads, and short term composite loads.

Noncomposite:

For dead loads applied prior to deck hardening, the girder supports all loads.

$I_x = 3270 \cdot in^4$ $S_x := 243 \cdot in^3$ AISC

Long Term Composite:

For dead loads applied after the deck hardens, the long term composite section is used. The segment of slab that is considered part of the composite section is different for the fascia and interior girders, and thus thier properties need to be found separately.

Width of deck that contributes to interior girder properties:

$B := \min\left(\frac{L_{bridge}}{4}, S, 12 \cdot t_{design}\right)$ $B = 7.5\,ft$ A 10.38.3.1

Width of deck that contributes to fascia girder properties:

$B_f := \frac{B}{2} + 2.25 \cdot ft$ $B_f = 6\,ft$

Fascia LTC properties:

$A_g = 27.7 \cdot in^2$

$A_{deck} := \frac{B_f \cdot t_{design}}{3 \cdot n}$ $A_{deck} = 20 \cdot in^2$

$A_{ltc} := A_g + A_{deck}$ $A_{ltc} = 47.7 \cdot in^2$

$y := \frac{A_g \cdot \frac{d}{2} + A_{deck} \cdot \left(d + \frac{t_{design}}{2} \right)}{A_{ltc}}$ $y = 20.66 \cdot in$

$I_{gird} := I_x + A_g \cdot \left(y - \frac{d}{2} \right)^2$ $I_{gird} = 4710.65 \cdot in^4$

$I_{deck} := \frac{\frac{B_f}{3 \cdot n} \cdot t_{design}^{\,3}}{12} + A_{deck} \cdot \left(d + \frac{t_{design}}{2} - y \right)^2$ $I_{deck} = 2089.06 \cdot in^4$

$I_{f.ltc} := I_{gird} + I_{deck}$ $I_{f.ltc} = 6799.71 \cdot in^4$

$S_{bf.ltc} := \frac{I_{f.ltc}}{y}$ $S_{bf.ltc} = 329.1 \cdot in^3$

$S_{tf.ltc} := \frac{I_{f.ltc}}{d + t_{design} - y}$ $S_{tf.ltc} = 494.95 \cdot in^3$

Interior LTC properties:

$A_{deck} := \frac{B \cdot t_{design}}{3 \cdot n}$ $A_{deck} = 25 \cdot in^2$

$A_{ltc} := A_g + A_{deck}$ $A_{ltc} = 52.7 \cdot in^2$

$y := \frac{A_g \cdot \frac{d}{2} + A_{deck} \cdot \left(d + \frac{t_{design}}{2} \right)}{A_{ltc}}$ $y = 21.61 \cdot in$

$I_{gird} := I_x + A_g \cdot \left(y - \frac{d}{2} \right)^2$ $I_{gird} = 5114.15 \cdot in^4$

$I_{deck} := \frac{\frac{B}{3 \cdot n} \cdot t_{design}^{\,3}}{12} + A_{deck} \cdot \left(d + \frac{t_{design}}{2} - y \right)^2$ $I_{deck} = 2160.5 \cdot in^4$

$I_{i.ltc} := I_{gird} + I_{deck}$ $I_{i.ltc} = 7274.65 \cdot in^4$

$S_{bi.ltc} := \frac{I_{i.ltc}}{y}$ $S_{bi.ltc} = 336.64 \cdot in^3$

$$S_{ti.ltc} := \frac{I_{i.ltc}}{d + t_{design} - y} \qquad S_{ti.ltc} = 568.75 \cdot in^3$$

Short Term Composite:

For live loads applied after the deck hardens, the short term composite section is used. The segment of slab that is considered part of the composite section is different for the fascia and interior girders, and thus thier properties need to be found separately.

Fascia STC properties:

$$A_{deck} := \frac{B_f \cdot t_{design}}{n} \qquad A_{deck} = 60 \cdot in^2$$

$$A_{stc} := A_g + A_{deck} \qquad A_{stc} = 87.7 \cdot in^2$$

$$y := \frac{A_g \cdot \frac{d}{2} + A_{deck} \cdot \left(d + \frac{t_{design}}{2}\right)}{A_{stc}} \qquad y = 25.22 \cdot in$$

$$I_{gird} := I_x + A_g \cdot \left(y - \frac{d}{2}\right)^2 \qquad I_{gird} = 7105.66 \cdot in^4$$

$$I_{deck} := \frac{\frac{B_f}{n} \cdot t_{design}^{\,3}}{12} + A_{deck} \cdot \left(d + \frac{t_{design}}{2} - y\right)^2 \qquad I_{deck} = 2052.05 \cdot in^4$$

$$I_{f.stc} := I_{gird} + I_{deck} \qquad I_{f.stc} = 9157.7 \cdot in^4$$

$$S_{bf.stc} := \frac{I_{f.stc}}{y} \qquad S_{bf.stc} = 363.15 \cdot in^3$$

$$S_{tf.stc} := \frac{I_{f.stc}}{d + t_{design} - y} \qquad S_{tf.stc} = 997.29 \cdot in^3$$

Interior STC properties:

$$A_{deck} := \frac{B \cdot t_{design}}{n} \qquad A_{deck} = 75 \cdot in^2$$

$$A_{stc} := A_g + A_{deck} \qquad A_{stc} = 102.7 \cdot in^2$$

$$y := \frac{A_g \cdot \frac{d}{2} + A_{deck} \cdot \left(d + \frac{t_{design}}{2}\right)}{A_{stc}} \qquad y = 26.01 \cdot in$$

$$I_{gird} := I_x + A_g \cdot \left(y - \frac{d}{2}\right)^2 \qquad I_{gird} = 7640.37 \cdot in^4$$

$$I_{deck} := \frac{\frac{B}{n}\cdot t_{design}^{3}}{12} + A_{deck}\cdot\left(d + \frac{t_{design}}{2} - y\right)^{2} \qquad I_{deck} = 1965.69\cdot in^{4}$$

$$I_{i.stc} := I_{gird} + I_{deck} \qquad I_{i.stc} = 9606.06\cdot in^{4}$$

$$S_{bi.stc} := \frac{I_{i.stc}}{y} \qquad S_{bi.stc} = 369.31\cdot in^{3}$$

$$S_{ti.stc} := \frac{I_{i.stc}}{d + t_{design} - y} \qquad S_{ti.stc} = 1145.06\cdot in^{3}$$

Dead Load Calculations:

Dead loads are divided into those applied to the noncomposite steel section and those applied to the long-term composite section after the deck hardened.

Noncomposite Dead:

Girder self weight:

$$w_{girder} := 94\cdot\frac{lb}{ft}$$ AISC

Deck weight (per square foot of deck area):

$$w_{deck} := t_{actual}\cdot\gamma_c \qquad w_{deck} = 100\cdot psf$$

Intermediate diaphragms (each):

$$w_{dia} := S\cdot W_d \qquad w_{dia} = 155.25\,lb$$

Connection plates (each, based on field measurements):

$$w_{conn} := D\cdot 6\cdot in\cdot\frac{1}{2}\cdot in\cdot\gamma_s \qquad w_{conn} = 21.62\,lb$$

There are no SIP forms on this bridge, and no haunch.

Composite Dead:

Barrier curbs:

$$w_{barrier} := 400\cdot\frac{lb}{ft}$$

This bridge has no wearing surface, utilities, or luminaires.

Apply Dead Loads:

Dead loads per foot length of an interior and a fascia girder are found. Barrier load is distributed evenly to all girders as permitted by AASHTO 3.23.2.3.1.1.

Noncomposite dead load for an interior girder:

$$D_{int.nc} := w_{girder} + w_{deck}\cdot S + \frac{3\cdot w_{dia}}{L_{bridge}} + \frac{6\cdot w_{conn}}{L_{bridge}} \qquad D_{int.nc} = 855.91\,\frac{lb}{ft}$$

Composite dead load for an interior girder:

$$D_{int.ltc} := \frac{2 \cdot w_{barrier}}{4} \qquad D_{int.ltc} = 200 \frac{lb}{ft}$$

Noncomposite dead load for a fascia girder:

$$D_{fas.nc} := w_{girder} + w_{deck} \cdot \frac{S}{2} + w_{deck} \cdot 2.25 \cdot ft + \frac{3 \cdot w_{dia}}{2 \cdot L_{bridge}} + \frac{3 \cdot w_{conn}}{L_{bridge}} \qquad D_{fas.nc} = 699.95 \frac{lb}{ft}$$

Composite dead load for a fascia girder:

$$D_{fas.ltc} := \frac{2 \cdot w_{barrier}}{4} \qquad D_{fas.ltc} = 200 \frac{lb}{ft}$$

Calculate Unfactored Dead Load Forces:

Midspan moments and end shears are desired.

Interior Girder:

$$M_{int.nc} := \frac{D_{int.nc} \cdot L_{bridge}^{2}}{8} \qquad M_{int.nc} = 3209.66 \cdot kip \cdot in$$

$$M_{int.ltc} := \frac{D_{int.ltc} \cdot L_{bridge}^{2}}{8} \qquad M_{int.ltc} = 750 \cdot kip \cdot in$$

$$V_{int.nc} := \frac{D_{int.nc} \cdot L_{bridge}}{2} \qquad V_{int.nc} = 21.4 \cdot kip$$

$$V_{int.ltc} := \frac{D_{int.ltc} \cdot L_{bridge}}{2} \qquad V_{int.ltc} = 5 \cdot kip$$

Fascia Girder:

$$M_{fas.nc} := \frac{D_{fas.nc} \cdot L_{bridge}^{2}}{8} \qquad M_{fas.nc} = 2624.83 \cdot kip \cdot in$$

$$M_{fas.ltc} := \frac{D_{fas.ltc} \cdot L_{bridge}^{2}}{8} \qquad M_{fas.ltc} = 750 \cdot kip \cdot in$$

$$V_{fas.nc} := \frac{D_{fas.nc} \cdot L_{bridge}}{2} \qquad V_{fas.nc} = 17.5 \cdot kip$$

$$V_{fas.ltc} := \frac{D_{fas.ltc} \cdot L_{bridge}}{2} \qquad V_{fas.ltc} = 5 \cdot kip$$

ASD Section Capacities:

Section capacities are found using the AASHTO ASD design philosophy.

For bending, the top flange will not control since it is continuously braced by the deck and has less total stress than the bottom flange. Thus, only the tensile capacity of the bottom flange and the compressive capacity of the deck are needed:

$f_{s.allow} := 0.55 \cdot F_y$	bottom flange at the inventory level	CE T6.6.2.1-1
$f_{s.allow.op} := 0.75 \cdot F_y$	bottom flange at the operating level	CE T6.6.2.1-2
$f_{c.allow} := 1200 \cdot psi$	deck compression at the inventory level	CE 6.6.2.4.1
$f_{c.allow.op} := 1900 \cdot psi$	deck compression at the operating level	CE 6.6.2.4.1

For shear in a web without stiffeners, with a compact section, and with none of the web depth in bending compression for the composite section:

$f_{v.allow} := 0.33 \cdot F_y$	web at the inventory level	CE T6.6.2.1-1
$f_{v.allow.op} := 0.45 \cdot F_y$	web at the operating level	CE T6.6.2.1-2

ASD Load Rating with Distribution Factors:

Load ratings per AASHTO ASD are calculated. First, live load effects and rating factors are found using the AASHTO ASD distribution factors. Second, the same is found using the calibrated finite element model. Third, the same is found using the modal testing results.

AASHTO Live Load Distribution:

For interior girders, the distribution factor (wheels per girder) is:

$$DF_{int} := \frac{S}{5.5 \cdot ft} \qquad DF_{int} = 1.36$$ A T3.23.1

For fascia girders, the lever rule is to be used assuming a pinned support at the first interior girder. The wheel load closest to the barrier is placed at 2' off of the face per AASHTO F3.7.6A.

$$DF_{fas} := 1 \cdot wheel \cdot \frac{6.25 \cdot ft}{S} + 1 \cdot wheel \cdot \frac{0.25 \cdot ft}{S} \qquad DF_{fas} = 0.87$$

However, the distribution factor may not be less than:

$$DF_{fas} := \frac{S}{4 \cdot ft + 0.25 \cdot S} \qquad DF_{fas} = 1.28$$ A 3.23.2.3.1.5

Calculate the impact factor to account for dynamic effects:

$$IF := \frac{50 \cdot ft}{L_{bridge} + 125 \cdot ft} \qquad IF = 0.29$$ A 3.8.2.1

HS Truck Loading:

The maximum moment and shear for a single lane load are taken from AASHTO Appendix A for HS-20 loading

$M_{hs} := 627.9 \cdot kip \cdot ft$ $V_{hs} := 58.5 \cdot kip$

The force effect to an interior girder is thus:

$V_{hs.int} := V_{hs} \cdot \frac{DF_{int}}{2} \cdot (1 + IF)$ $V_{hs.int} = 51.28 \cdot kip$

$M_{hs.int} := M_{hs} \cdot \frac{DF_{int}}{2} \cdot (1 + IF)$ $M_{hs.int} = 6605.18 \cdot kip \cdot in$

The force effect to a fascia girder is:

$V_{hs.fas} := V_{hs} \cdot \frac{DF_{fas}}{2} \cdot (1 + IF)$ $V_{hs.fas} = 48.01 \cdot kip$

$M_{hs.fas} := M_{hs} \cdot \frac{DF_{fas}}{2} \cdot (1 + IF)$ $M_{hs.fas} = 6183.57 \cdot kip \cdot in$

HL-93 Truck Loading:

The LRFD HL-93 truck is just a combination of the HS-20 truck and the lane load.

$M_{hl} := M_{hs} + \frac{0.64 \cdot kip}{ft} \cdot \frac{L_{bridge}^2}{8}$ $M_{hl} = 9934.8 \cdot kip \cdot in$ AR 3.6.1.2.1

$V_{hl} := V_{hs} + \frac{0.64 \cdot kip}{ft} \cdot \frac{L_{bridge}}{2}$ $V_{hl} = 74.5 \cdot kip$

AASHTO Legal Truck Loading:

Three standard trucks are also provided by AASHTO that reflect typical highway traffic. These vehicles are commonly used in ratings since load posting is based on these vehicle arrangements. The maximum moments and shears from these vehicles are found and distributed to a girder.

$L := L_{bridge}$

Type 3 Truck:

$V_3 := 17 \cdot kip + 17 \cdot kip \cdot \frac{46 \cdot ft}{L} + 16 \cdot kip \cdot \frac{L - 19 \cdot ft}{L}$ $V_3 = 42.56 \cdot kip$

$M_3 := 17 \cdot kip \cdot \frac{L}{4} + 17 \cdot kip \cdot \frac{(L - 29 \cdot ft)}{2} + 16 \cdot kip \cdot \frac{(L - 40 \cdot ft)}{2}$ $M_3 = 5652 \cdot kip \cdot in$

Type 3S2 Truck:

$V_{3s2} := 15.5 \cdot kip + 15.5 \cdot kip \cdot \frac{46 \cdot ft}{L} + 15.5 \cdot kip \cdot \frac{24 \cdot ft}{L} + 15.5 \cdot kip \cdot \frac{20 \cdot ft}{L} + 10 \cdot kip \cdot \frac{9 \cdot ft}{L}$

$V_{3s2} = 45.2 \cdot kip$

$M_{3s2} := \frac{1}{4} \cdot [15.5 \cdot kip \cdot L + 15.5 \cdot kip \cdot (L - 2 \cdot 22 \cdot ft) + 15.5 \cdot kip \cdot (L - 2 \cdot 4 \cdot ft) + 10 \cdot kip \cdot (L - 2 \cdot 15 \cdot ft)]$

$M_{3s2} = 5157 \cdot kip \cdot in$

Type 3-3 Truck:

$V_{33} := 14 \cdot kip + 14 \cdot kip \cdot \frac{46 \cdot ft}{L} + 16 \cdot kip \cdot \frac{30 \cdot ft}{L} + 12 \cdot kip \cdot \frac{15 \cdot ft}{L} + 12 \cdot kip \cdot \frac{11 \cdot ft}{L}$ $V_{33} = 42.72 \cdot kip$

$$M_{33} := \frac{1}{4}\cdot[16\cdot kip\cdot L + 14\cdot kip\cdot(L - 2\cdot 16\cdot ft) + 14\cdot kip\cdot(L - 2\cdot 20\cdot ft) + 12\cdot kip\cdot(L - 2\cdot 15\cdot ft) + 12\cdot kip\cdot(L - 2\cdot 19\cdot ft)]$$

$$M_{33} = 4728\cdot kip\cdot in$$

And the force effects to the interior girders are:

$$V_{3.int} := V_3\cdot\frac{DF_{int}}{2}\cdot(1 + IF) \qquad V_{3.int} = 37.31\cdot kip$$

$$M_{3.int} := M_3\cdot\frac{DF_{int}}{2}\cdot(1 + IF) \qquad M_{3.int} = 4954.68\cdot kip\cdot in$$

$$V_{3s2.int} := V_{3s2}\cdot\frac{DF_{int}}{2}\cdot(1 + IF) \qquad V_{3s2.int} = 39.62\cdot kip$$

$$M_{3s2.int} := M_{3s2}\cdot\frac{DF_{int}}{2}\cdot(1 + IF) \qquad M_{3s2.int} = 4520.75\cdot kip\cdot in$$

$$V_{33.int} := V_{33}\cdot\frac{DF_{int}}{2}\cdot(1 + IF) \qquad V_{33.int} = 37.45\cdot kip$$

$$M_{33.int} := M_{33}\cdot\frac{DF_{int}}{2}\cdot(1 + IF) \qquad M_{33.int} = 4144.68\cdot kip\cdot in$$

And the force effects to the fascia girders are:

$$V_{3.fas} := V_3\cdot\frac{DF_{fas}}{2}\cdot(1 + IF) \qquad V_{3.fas} = 34.93\cdot kip$$

$$M_{3.fas} := M_3\cdot\frac{DF_{fas}}{2}\cdot(1 + IF) \qquad M_{3.fas} = 4638.42\cdot kip\cdot in$$

$$V_{3s2.fas} := V_{3s2}\cdot\frac{DF_{fas}}{2}\cdot(1 + IF) \qquad V_{3s2.fas} = 37.09\cdot kip$$

$$M_{3s2.fas} := M_{3s2}\cdot\frac{DF_{fas}}{2}\cdot(1 + IF) \qquad M_{3s2.fas} = 4232.19\cdot kip\cdot in$$

$$V_{33.fas} := V_{33}\cdot\frac{DF_{fas}}{2}\cdot(1 + IF) \qquad V_{33.fas} = 35.06\cdot kip$$

$$M_{33.fas} := M_{33}\cdot\frac{DF_{fas}}{2}\cdot(1 + IF) \qquad M_{33.fas} = 3880.12\cdot kip\cdot in$$

Calculate Load Ratings for Moment:

For ASD, the load ratings are simply found as:

$$RF := \frac{C - D}{L}$$ CE 6.5.1

Fascia Moment:

For moment for a fascia girder, the rating is the minimum of that found for compression in the deck and tension in the bottom flange.

Inventory Level:

$$RF_{hs.deck} := \left(f_{c.allow} - \frac{M_{fas.ltc}}{S_{tf.ltc} \cdot 3n}\right) \cdot \frac{S_{tf.stc} \cdot n}{M_{hs.fas}} \qquad RF_{hs.deck} = 1.66$$

$$RF_{hs.flange} := \left(f_{s.allow} - \frac{M_{fas.nc}}{S_x} - \frac{M_{fas.ltc}}{S_{bf.ltc}}\right) \cdot \frac{S_{bf.stc}}{M_{hs.fas}} \qquad RF_{hs.flange} = 0.85$$

Operating Level:

$$RF_{hs.deck} := \left(f_{c.allow.op} - \frac{M_{fas.ltc}}{S_{tf.ltc} \cdot 3n}\right) \cdot \frac{S_{tf.stc} \cdot n}{M_{hs.fas}} \qquad RF_{hs.deck} = 2.68$$

$$RF_{hs.flange} := \left(f_{s.allow.op} - \frac{M_{fas.nc}}{S_x} - \frac{M_{fas.ltc}}{S_{bf.ltc}}\right) \cdot \frac{S_{bf.stc}}{M_{hs.fas}} \qquad RF_{hs.flange} = 1.43$$

Interior Moment:

Inventory Level:

$$RF_{hs.deck} := \left(f_{c.allow} - \frac{M_{int.ltc}}{S_{ti.ltc} \cdot 3n}\right) \cdot \frac{S_{ti.stc} \cdot n}{M_{hs.int}} \qquad RF_{hs.deck} = 1.8$$

$$RF_{hs.flange} := \left(f_{s.allow} - \frac{M_{int.nc}}{S_x} - \frac{M_{int.ltc}}{S_{bi.ltc}}\right) \cdot \frac{S_{bi.stc}}{M_{hs.int}} \qquad RF_{hs.flange} = 0.67$$

Operating Level:

$$RF_{hs.deck} := \left(f_{c.allow.op} - \frac{M_{int.ltc}}{S_{ti.ltc} \cdot 3n}\right) \cdot \frac{S_{ti.stc} \cdot n}{M_{hs.int}} \qquad RF_{hs.deck} = 2.89$$

$$RF_{hs.flange} := \left(f_{s.allow.op} - \frac{M_{int.nc}}{S_x} - \frac{M_{int.ltc}}{S_{bi.ltc}}\right) \cdot \frac{S_{bi.stc}}{M_{hs.int}} \qquad RF_{hs.flange} = 1.23$$

Other Legal Vehicles:

Fascia Girder:

$$IR_{3.deck} := \left(f_{c.allow} - \frac{M_{fas.ltc}}{S_{tf.ltc} \cdot 3n}\right) \cdot \frac{S_{tf.stc} \cdot n}{M_{3.fas}} \qquad IR_{3.deck} = 2.21$$

$$IR_{3.flange} := \left(f_{s.allow} - \frac{M_{fas.nc}}{S_x} - \frac{M_{fas.ltc}}{S_{bf.ltc}} \right) \cdot \frac{S_{bf.stc}}{M_{3.fas}} \qquad IR_{3.flange} = 1.13$$

$$OR_{3.deck} := \left(f_{c.allow.op} - \frac{M_{fas.ltc}}{S_{tf.ltc} \cdot 3n} \right) \cdot \frac{S_{tf.stc} \cdot n}{M_{3.fas}} \qquad OR_{3.deck} = 3.57$$

$$OR_{3.flange} := \left(f_{s.allow.op} - \frac{M_{fas.nc}}{S_x} - \frac{M_{fas.ltc}}{S_{bf.ltc}} \right) \cdot \frac{S_{bf.stc}}{M_{3.fas}} \qquad OR_{3.flange} = 1.91$$

$$IR_{3s2.deck} := \left(f_{c.allow} - \frac{M_{fas.ltc}}{S_{tf.ltc} \cdot 3n} \right) \cdot \frac{S_{tf.stc} \cdot n}{M_{3s2.fas}} \qquad IR_{3s2.deck} = 2.43$$

$$IR_{3s2.flange} := \left(f_{s.allow} - \frac{M_{fas.nc}}{S_x} - \frac{M_{fas.ltc}}{S_{bf.ltc}} \right) \cdot \frac{S_{bf.stc}}{M_{3s2.fas}} \qquad IR_{3s2.flange} = 1.24$$

$$OR_{3s2.deck} := \left(f_{c.allow.op} - \frac{M_{fas.ltc}}{S_{tf.ltc} \cdot 3n} \right) \cdot \frac{S_{tf.stc} \cdot n}{M_{3s2.fas}} \qquad OR_{3s2.deck} = 3.91$$

$$OR_{3s2.flange} := \left(f_{s.allow.op} - \frac{M_{fas.nc}}{S_x} - \frac{M_{fas.ltc}}{S_{bf.ltc}} \right) \cdot \frac{S_{bf.stc}}{M_{3s2.fas}} \qquad OR_{3s2.flange} = 2.1$$

$$IR_{33.deck} := \left(f_{c.allow} - \frac{M_{fas.ltc}}{S_{tf.ltc} \cdot 3n} \right) \cdot \frac{S_{tf.stc} \cdot n}{M_{33.fas}} \qquad IR_{33.deck} = 2.65$$

$$IR_{33.flange} := \left(f_{s.allow} - \frac{M_{fas.nc}}{S_x} - \frac{M_{fas.ltc}}{S_{bf.ltc}} \right) \cdot \frac{S_{bf.stc}}{M_{33.fas}} \qquad IR_{33.flange} = 1.35$$

$$OR_{33.deck} := \left(f_{c.allow.op} - \frac{M_{fas.ltc}}{S_{tf.ltc} \cdot 3n} \right) \cdot \frac{S_{tf.stc} \cdot n}{M_{33.fas}} \qquad OR_{33.deck} = 4.27$$

$$OR_{33.flange} := \left(f_{s.allow.op} - \frac{M_{fas.nc}}{S_x} - \frac{M_{fas.ltc}}{S_{bf.ltc}} \right) \cdot \frac{S_{bf.stc}}{M_{33.fas}} \qquad OR_{33.flange} = 2.29$$

Calculate Load Ratings for Shear:

Fascia Shear for HS20 Load:

$$IR_V := \frac{f_{v.allow} \cdot D \cdot t_w - V_{fas.nc} - V_{fas.ltc}}{V_{hs.fas}} \qquad IR_V = 3.81$$

$$OR_V := \frac{f_{v.allow.op} \cdot D \cdot t_w - V_{fas.nc} - V_{fas.ltc}}{V_{hs.fas}} \qquad OR_V = 5.37$$

Interior Girder Shear for HS20 Load:

$$IR_V := \frac{f_{v.allow} \cdot D \cdot t_w - V_{int.nc} - V_{int.ltc}}{V_{hs.int}} \qquad IR_V = 3.49$$

$$OR_V := \frac{f_{v.allow.op} \cdot D \cdot t_w - V_{int.nc} - V_{int.ltc}}{V_{hs.int}} \qquad OR_V = 4.95$$

Other Legal Vehicles:

Interior Girder:

$$IR_V := \frac{f_{v.allow} \cdot D \cdot t_w - V_{int.nc} - V_{int.ltc}}{V_{3.int}} \qquad IR_V = 4.8$$

$$OR_V := \frac{f_{v.allow.op} \cdot D \cdot t_w - V_{int.nc} - V_{int.ltc}}{V_{3.int}} \qquad OR_V = 6.8$$

$$IR_V := \frac{f_{v.allow} \cdot D \cdot t_w - V_{int.nc} - V_{int.ltc}}{V_{3s2.int}} \qquad IR_V = 4.52$$

$$OR_V := \frac{f_{v.allow.op} \cdot D \cdot t_w - V_{int.nc} - V_{int.ltc}}{V_{3s2.int}} \qquad OR_V = 6.4$$

$$IR_V := \frac{f_{v.allow} \cdot D \cdot t_w - V_{int.nc} - V_{int.ltc}}{V_{33.int}} \qquad IR_V = 4.78$$

$$OR_V := \frac{f_{v.allow.op} \cdot D \cdot t_w - V_{int.nc} - V_{int.ltc}}{V_{33.int}} \qquad OR_V = 6.78$$

ASD Load Rating with Finite Element Live Load Stresses

Stresses in the critical elements are found using the calibrated Hartbarger finite element model. The deck surface of the model is loaded with unit loads and responses at the critical locations are collected. These responses are then used to create an influence surface for each critical stress. Automatic positioning of the various trucks is then performed for maximum response. The impact factor is not included in the FE analysis and must be applied to the resulting stresses. Two trucks of the same type are applied to the bridge for each loading case.

The results are as follows for the various truck loads and for an interior and a fascia girder:

HS Truck Interior:

$V_{int} := 40.74 \cdot kip \cdot (1 + IF)$ $V_{int} = 52.38 \cdot kip$

$f_{b.int} := 9.059 \cdot ksi \cdot (1 + IF)$ $f_{b.int} = 11.65 \cdot ksi$

$f_{t.int} := 0.934 \cdot ksi \cdot (1 + IF)$ $f_{t.int} = 1.2 \cdot ksi$

$$IR_{deck} := \left(f_{c.allow} - \frac{M_{int.ltc}}{S_{ti.ltc} \cdot 3n} \right) \cdot \frac{1}{f_{t.int}} \qquad IR_{deck} = 0.96$$

$$IR_{flange} := \left(f_{s.allow} - \frac{M_{int.nc}}{S_x} - \frac{M_{int.ltc}}{S_{bi.ltc}} \right) \cdot \frac{1}{f_{b.int}} \qquad IR_{flange} = 1.04$$

$$IR_v := \frac{f_{v.allow} \cdot D \cdot t_w - V_{int.nc} - V_{int.ltc}}{V_{int}} \qquad IR_v = 3.42$$

$$OR_{deck} := \left(f_{c.allow.op} - \frac{M_{int.ltc}}{S_{ti.ltc} \cdot 3n} \right) \cdot \frac{1}{f_{t.int}} \qquad OR_{deck} = 1.54$$

$$OR_{flange} := \left(f_{s.allow.op} - \frac{M_{int.nc}}{S_x} - \frac{M_{int.ltc}}{S_{bi.ltc}} \right) \cdot \frac{1}{f_{b.int}} \qquad OR_{flange} = 1.89$$

$$OR_v := \frac{f_{v.allow.op} \cdot D \cdot t_w - V_{int.nc} - V_{int.ltc}}{V_{int}} \qquad OR_v = 4.84$$

HS Truck Fascia:

$V_{fas} := 31.18 \cdot kip \cdot (1 + IF)$ $V_{fas} = 40.09 \cdot kip$

$f_{b.fas} := 7.527 \cdot ksi \cdot (1 + IF)$ $f_{b.fas} = 9.68 \cdot ksi$

$f_{t.fas} := 0.540 \cdot ksi \cdot (1 + IF)$ $f_{t.fas} = 0.69 \cdot ksi$

$$IR_{deck} := \left(f_{c.allow} - \frac{M_{fas.ltc}}{S_{tf.ltc} \cdot 3n} \right) \cdot \frac{1}{f_{t.fas}} \qquad IR_{deck} = 1.65$$

$$IR_{flange} := \left(f_{s.allow} - \frac{M_{fas.nc}}{S_x} - \frac{M_{fas.ltc}}{S_{bf.ltc}} \right) \cdot \frac{1}{f_{b.fas}} \qquad IR_{flange} = 1.49$$

$$IR_v := \frac{f_{v.allow} \cdot D \cdot t_w - V_{fas.nc} - V_{fas.ltc}}{V_{fas}} \qquad IR_v = 4.56$$

$$OR_{deck} := \left(f_{c.allow.op} - \frac{M_{fas.ltc}}{S_{tf.ltc} \cdot 3n} \right) \cdot \frac{1}{f_{t.fas}} \qquad OR_{deck} = 2.66$$

$$OR_{flange} := \left(f_{s.allow.op} - \frac{M_{fas.nc}}{S_x} - \frac{M_{fas.ltc}}{S_{bf.ltc}} \right) \cdot \frac{1}{f_{b.fas}} \qquad OR_{flange} = 2.52$$

$$OR_v := \frac{f_{v.allow.op} \cdot D \cdot t_w - V_{fas.nc} - V_{fas.ltc}}{V_{fas}} \qquad OR_v = 6.43$$

Type 3 Truck Interior:

$V_{int} := 30.43 \cdot kip \cdot (1 + IF)$ $V_{int} = 39.12 \cdot kip$

$f_{b.int} := 6.939 \cdot ksi \cdot (1 + IF)$ $f_{b.int} = 8.92 \cdot ksi$

$f_{t.int} := 0.689 \cdot ksi \cdot (1 + IF)$ $f_{t.int} = 0.89 \cdot ksi$

$$IR_{deck} := \left(f_{c.allow} - \frac{M_{int.ltc}}{S_{ti.ltc} \cdot 3n} \right) \cdot \frac{1}{f_{t.int}} \qquad IR_{deck} = 1.3$$

$$IR_{flange} := \left(f_{s.allow} - \frac{M_{int.nc}}{S_x} - \frac{M_{int.ltc}}{S_{bi.ltc}} \right) \cdot \frac{1}{f_{b.int}} \qquad IR_{flange} = 1.35$$

$$IR_v := \frac{f_{v.allow} \cdot D \cdot t_w - V_{int.nc} - V_{int.ltc}}{V_{int}} \qquad IR_v = 4.58$$

$$OR_{deck} := \left(f_{c.allow.op} - \frac{M_{int.ltc}}{S_{ti.ltc} \cdot 3n} \right) \cdot \frac{1}{f_{t.int}} \qquad OR_{deck} = 2.09$$

$$OR_{flange} := \left(f_{s.allow.op} - \frac{M_{int.nc}}{S_x} - \frac{M_{int.ltc}}{S_{bi.ltc}} \right) \cdot \frac{1}{f_{b.int}} \qquad OR_{flange} = 2.47$$

$$OR_v := \frac{f_{v.allow.op} \cdot D \cdot t_w - V_{int.nc} - V_{int.ltc}}{V_{int}} \qquad OR_v = 6.49$$

Type 3 Truck Fascia:

$V_{fas} := 21.91 \cdot kip \cdot (1 + IF)$ $V_{fas} = 28.17 \cdot kip$

$f_{b.fas} := 5.707 \cdot ksi \cdot (1 + IF)$ $f_{b.fas} = 7.34 \cdot ksi$

$f_{t.fas} := 0.399 \cdot ksi \cdot (1 + IF)$ $f_{t.fas} = 0.51 \cdot ksi$

$$IR_{deck} := \left(f_{c.allow} - \frac{M_{fas.ltc}}{S_{tf.ltc} \cdot 3n} \right) \cdot \frac{1}{f_{t.fas}} \qquad IR_{deck} = 2.23$$

$$IR_{flange} := \left(f_{s.allow} - \frac{M_{fas.nc}}{S_x} - \frac{M_{fas.ltc}}{S_{bf.ltc}}\right) \cdot \frac{1}{f_{b.fas}} \qquad IR_{flange} = 1.97$$

$$IR_v := \frac{f_{v.allow} \cdot D \cdot t_w - V_{fas.nc} - V_{fas.ltc}}{V_{fas}} \qquad IR_v = 6.49$$

$$OR_{deck} := \left(f_{c.allow.op} - \frac{M_{fas.ltc}}{S_{tf.ltc} \cdot 3n}\right) \cdot \frac{1}{f_{t.fas}} \qquad OR_{deck} = 3.59$$

$$OR_{flange} := \left(f_{s.allow.op} - \frac{M_{fas.nc}}{S_x} - \frac{M_{fas.ltc}}{S_{bf.ltc}}\right) \cdot \frac{1}{f_{b.fas}} \qquad OR_{flange} = 3.33$$

$$OR_v := \frac{f_{v.allow.op} \cdot D \cdot t_w - V_{fas.nc} - V_{fas.ltc}}{V_{fas}} \qquad OR_v = 9.15$$

Type 3S2 Truck Interior:

$V_{int} := 29.48 \cdot kip \cdot (1 + IF)$ $\qquad V_{int} = 37.9 \cdot kip$

$f_{b.int} := 6.355 \cdot ksi \cdot (1 + IF)$ $\qquad f_{b.int} = 8.17 \cdot ksi$

$f_{t.int} := 0.633 \cdot ksi \cdot (1 + IF)$ $\qquad f_{t.int} = 0.81 \cdot ksi$

$$IR_{deck} := \left(f_{c.allow} - \frac{M_{int.ltc}}{S_{ti.ltc} \cdot 3n}\right) \cdot \frac{1}{f_{t.int}} \qquad IR_{deck} = 1.41$$

$$IR_{flange} := \left(f_{s.allow} - \frac{M_{int.nc}}{S_x} - \frac{M_{int.ltc}}{S_{bi.ltc}}\right) \cdot \frac{1}{f_{b.int}} \qquad IR_{flange} = 1.48$$

$$IR_v := \frac{f_{v.allow} \cdot D \cdot t_w - V_{int.nc} - V_{int.ltc}}{V_{int}} \qquad IR_v = 4.72$$

$$OR_{deck} := \left(f_{c.allow.op} - \frac{M_{int.ltc}}{S_{ti.ltc} \cdot 3n}\right) \cdot \frac{1}{f_{t.int}} \qquad OR_{deck} = 2.27$$

$$OR_{flange} := \left(f_{s.allow.op} - \frac{M_{int.nc}}{S_x} - \frac{M_{int.ltc}}{S_{bi.ltc}}\right) \cdot \frac{1}{f_{b.int}} \qquad OR_{flange} = 2.7$$

$$OR_v := \frac{f_{v.allow.op} \cdot D \cdot t_w - V_{int.nc} - V_{int.ltc}}{V_{int}} \qquad OR_v = 6.69$$

Type 3S2 Truck Fascia:

$V_{fas} := 25.21 \cdot kip \cdot (1 + IF)$ $\qquad V_{fas} = 32.41 \cdot kip$

$f_{b.fas} := 5.195 \cdot ksi \cdot (1 + IF)$ $\qquad f_{b.fas} = 6.68 \cdot ksi$

$f_{t.fas} := 0.365 \cdot ksi \cdot (1 + IF)$ $\qquad f_{t.fas} = 0.47 \cdot ksi$

$$IR_{deck} := \left(f_{c.allow} - \frac{M_{fas.ltc}}{S_{tf.ltc} \cdot 3n} \right) \cdot \frac{1}{f_{t.fas}} \qquad IR_{deck} = 2.44$$

$$IR_{flange} := \left(f_{s.allow} - \frac{M_{fas.nc}}{S_x} - \frac{M_{fas.ltc}}{S_{bf.ltc}} \right) \cdot \frac{1}{f_{b.fas}} \qquad IR_{flange} = 2.16$$

$$IR_v := \frac{f_{v.allow} \cdot D \cdot t_w - V_{fas.nc} - V_{fas.ltc}}{V_{fas}} \qquad IR_v = 5.64$$

$$OR_{deck} := \left(f_{c.allow.op} - \frac{M_{fas.ltc}}{S_{tf.ltc} \cdot 3n} \right) \cdot \frac{1}{f_{t.fas}} \qquad OR_{deck} = 3.93$$

$$OR_{flange} := \left(f_{s.allow.op} - \frac{M_{fas.nc}}{S_x} - \frac{M_{fas.ltc}}{S_{bf.ltc}} \right) \cdot \frac{1}{f_{b.fas}} \qquad OR_{flange} = 3.66$$

$$OR_v := \frac{f_{v.allow.op} \cdot D \cdot t_w - V_{fas.nc} - V_{fas.ltc}}{V_{fas}} \qquad OR_v = 7.95$$

Type 3-3 Truck Interior:

$$V_{int} := 27.87 \cdot kip \cdot (1 + IF) \qquad V_{int} = 35.83 \cdot kip$$

$$f_{b.int} := 5.936 \cdot ksi \cdot (1 + IF) \qquad f_{b.int} = 7.63 \cdot ksi$$

$$f_{t.int} := 0.573 \cdot ksi \cdot (1 + IF) \qquad f_{t.int} = 0.74 \cdot ksi$$

$$IR_{deck} := \left(f_{c.allow} - \frac{M_{int.ltc}}{S_{ti.ltc} \cdot 3n} \right) \cdot \frac{1}{f_{t.int}} \qquad IR_{deck} = 1.56$$

$$IR_{flange} := \left(f_{s.allow} - \frac{M_{int.nc}}{S_x} - \frac{M_{int.ltc}}{S_{bi.ltc}} \right) \cdot \frac{1}{f_{b.int}} \qquad IR_{flange} = 1.58$$

$$IR_v := \frac{f_{v.allow} \cdot D \cdot t_w - V_{int.nc} - V_{int.ltc}}{V_{int}} \qquad IR_v = 5$$

$$OR_{deck} := \left(f_{c.allow.op} - \frac{M_{int.ltc}}{S_{ti.ltc} \cdot 3n} \right) \cdot \frac{1}{f_{t.int}} \qquad OR_{deck} = 2.51$$

$$OR_{flange} := \left(f_{s.allow.op} - \frac{M_{int.nc}}{S_x} - \frac{M_{int.ltc}}{S_{bi.ltc}} \right) \cdot \frac{1}{f_{b.int}} \qquad OR_{flange} = 2.89$$

$$OR_v := \frac{f_{v.allow.op} \cdot D \cdot t_w - V_{int.nc} - V_{int.ltc}}{V_{int}} \qquad OR_v = 7.08$$

Type 3-3 Truck Fascia:

$V_{fas} := 23.72 \cdot kip \cdot (1 + IF)$ $V_{fas} = 30.5 \cdot kip$

$f_{b.fas} := 5.066 \cdot ksi \cdot (1 + IF)$ $f_{b.fas} = 6.51 \cdot ksi$

$f_{t.fas} := 0.343 \cdot ksi \cdot (1 + IF)$ $f_{t.fas} = 0.44 \cdot ksi$

$$IR_{deck} := \left(f_{c.allow} - \frac{M_{fas.ltc}}{S_{tf.ltc} \cdot 3n} \right) \cdot \frac{1}{f_{t.fas}} \qquad IR_{deck} = 2.59$$

$$IR_{flange} := \left(f_{s.allow} - \frac{M_{fas.nc}}{S_x} - \frac{M_{fas.ltc}}{S_{bf.ltc}} \right) \cdot \frac{1}{f_{b.fas}} \qquad IR_{flange} = 2.21$$

$$IR_v := \frac{f_{v.allow} \cdot D \cdot t_w - V_{fas.nc} - V_{fas.ltc}}{V_{fas}} \qquad IR_v = 6$$

$$OR_{deck} := \left(f_{c.allow.op} - \frac{M_{fas.ltc}}{S_{tf.ltc} \cdot 3n} \right) \cdot \frac{1}{f_{t.fas}} \qquad OR_{deck} = 4.18$$

$$OR_{flange} := \left(f_{s.allow.op} - \frac{M_{fas.nc}}{S_x} - \frac{M_{fas.ltc}}{S_{bf.ltc}} \right) \cdot \frac{1}{f_{b.fas}} \qquad OR_{flange} = 3.75$$

$$OR_v := \frac{f_{v.allow.op} \cdot D \cdot t_w - V_{fas.nc} - V_{fas.ltc}}{V_{fas}} \qquad OR_v = 8.45$$

ASD Load Rating with Modal Flexibility Live Load Stresses

Stresses in the critical elements are found using the results of the modal analysis. Influence surfaces were generated using unit loads for the critical responses. Automatic positioning of the various trucks is then performed for maximum response. The impact factor is not included in the analysis and must be applied to the resulting forces. Two trucks of the same type are applied to the bridge for each loading case.

The results are as follows for the various truck loads and for an interior and a fascia girder:

HS Truck Interior:

$V_{int} := 42.97 \cdot kip \cdot (1 + IF)$ $V_{int} = 55.25 \cdot kip$

$M_{int} := 4788 \cdot kip \cdot in \cdot (1 + IF)$ $M_{int} = 6156 \cdot kip \cdot in$

$$IR_{deck} := \left(f_{c.allow} - \frac{M_{int.ltc}}{S_{ti.ltc} \cdot 3n} \right) \cdot \frac{S_{ti.stc} \cdot n}{M_{int}} \qquad IR_{deck} = 1.93$$

$$IR_{flange} := \left(f_{s.allow} - \frac{M_{int.nc}}{S_x} - \frac{M_{int.ltc}}{S_{bi.ltc}} \right) \cdot \frac{S_{bi.stc}}{M_{int}} \qquad IR_{flange} = 0.72$$

$$IR_v := \frac{f_{v.allow} \cdot D \cdot t_w - V_{int.nc} - V_{int.ltc}}{V_{int}} \qquad IR_v = 3.24$$

$$OR_{deck} := \left(f_{c.allow.op} - \frac{M_{int.ltc}}{S_{ti.ltc} \cdot 3n}\right) \cdot \frac{S_{ti.stc} \cdot n}{M_{int}} \qquad OR_{deck} = 3.1$$

$$OR_{flange} := \left(f_{s.allow.op} - \frac{M_{int.nc}}{S_x} - \frac{M_{int.ltc}}{S_{bi.ltc}}\right) \cdot \frac{S_{bi.stc}}{M_{int}} \qquad OR_{flange} = 1.32$$

$$OR_v := \frac{f_{v.allow.op} \cdot D \cdot t_w - V_{int.nc} - V_{int.ltc}}{V_{int}} \qquad OR_v = 4.59$$

HS Truck Fascia:

$$V_{fas} := 27.87 \cdot kip \cdot (1 + IF) \qquad V_{fas} = 35.83 \cdot kip$$

$$M_{fas} := 3901 \cdot kip \cdot in \cdot (1 + IF) \qquad M_{fas} = 5015.57 \cdot kip \cdot in$$

$$IR_{deck} := \left(f_{c.allow} - \frac{M_{fas.ltc}}{S_{tf.ltc} \cdot 3n}\right) \cdot \frac{S_{tf.stc} \cdot n}{M_{fas}} \qquad IR_{deck} = 2.05$$

$$IR_{flange} := \left(f_{s.allow} - \frac{M_{fas.nc}}{S_x} - \frac{M_{fas.ltc}}{S_{bf.ltc}}\right) \cdot \frac{S_{bf.stc}}{M_{fas}} \qquad IR_{flange} = 1.04$$

$$IR_v := \frac{f_{v.allow} \cdot D \cdot t_w - V_{fas.nc} - V_{fas.ltc}}{V_{fas}} \qquad IR_v = 5.11$$

$$OR_{deck} := \left(f_{c.allow.op} - \frac{M_{fas.ltc}}{S_{tf.ltc} \cdot 3n}\right) \cdot \frac{S_{tf.stc} \cdot n}{M_{fas}} \qquad OR_{deck} = 3.3$$

$$OR_{flange} := \left(f_{s.allow.op} - \frac{M_{fas.nc}}{S_x} - \frac{M_{fas.ltc}}{S_{bf.ltc}}\right) \cdot \frac{S_{bf.stc}}{M_{fas}} \qquad OR_{flange} = 1.77$$

$$OR_v := \frac{f_{v.allow.op} \cdot D \cdot t_w - V_{fas.nc} - V_{fas.ltc}}{V_{fas}} \qquad OR_v = 7.19$$

Type 3 Truck Interior:

$$V_{int} := 31.81 \cdot kip \cdot (1 + IF) \qquad V_{int} = 40.9 \cdot kip$$

$$M_{int} := 3653 \cdot kip \cdot in \cdot (1 + IF) \qquad M_{int} = 4696.71 \cdot kip \cdot in$$

$$IR_{deck} := \left(f_{c.allow} - \frac{M_{int.ltc}}{S_{ti.ltc} \cdot 3n}\right) \cdot \frac{S_{ti.stc} \cdot n}{M_{int}} \qquad IR_{deck} = 2.53$$

$$IR_{flange} := \left(f_{s.allow} - \frac{M_{int.nc}}{S_x} - \frac{M_{int.ltc}}{S_{bi.ltc}}\right) \cdot \frac{S_{bi.stc}}{M_{int}} \qquad IR_{flange} = 0.95$$

$$IR_v := \frac{f_{v.allow} \cdot D \cdot t_w - V_{int.nc} - V_{int.ltc}}{V_{int}} \qquad IR_v = 4.38$$

$$OR_{deck} := \left(f_{c.allow.op} - \frac{M_{int.ltc}}{S_{ti.ltc} \cdot 3n}\right) \cdot \frac{S_{ti.stc} \cdot n}{M_{int}} \qquad OR_{deck} = 4.06$$

$$OR_{flange} := \left(f_{s.allow.op} - \frac{M_{int.nc}}{S_x} - \frac{M_{int.ltc}}{S_{bi.ltc}}\right) \cdot \frac{S_{bi.stc}}{M_{int}} \qquad OR_{flange} = 1.73$$

$$OR_v := \frac{f_{v.allow.op} \cdot D \cdot t_w - V_{int.nc} - V_{int.ltc}}{V_{int}} \qquad OR_v = 6.2$$

Type 3 Truck Fascia:

$$V_{fas} := 19.97 \cdot kip \cdot (1 + IF) \qquad V_{fas} = 25.68 \cdot kip$$

$$M_{fas} := 2953 \cdot kip \cdot in \cdot (1 + IF) \qquad M_{fas} = 3796.71 \cdot kip \cdot in$$

$$IR_{deck} := \left(f_{c.allow} - \frac{M_{fas.ltc}}{S_{tf.ltc} \cdot 3n}\right) \cdot \frac{S_{tf.stc} \cdot n}{M_{fas}} \qquad IR_{deck} = 2.7$$

$$IR_{flange} := \left(f_{s.allow} - \frac{M_{fas.nc}}{S_x} - \frac{M_{fas.ltc}}{S_{bf.ltc}}\right) \cdot \frac{S_{bf.stc}}{M_{fas}} \qquad IR_{flange} = 1.38$$

$$IR_v := \frac{f_{v.allow} \cdot D \cdot t_w - V_{fas.nc} - V_{fas.ltc}}{V_{fas}} \qquad IR_v = 7.13$$

$$OR_{deck} := \left(f_{c.allow.op} - \frac{M_{fas.ltc}}{S_{tf.ltc} \cdot 3n}\right) \cdot \frac{S_{tf.stc} \cdot n}{M_{fas}} \qquad OR_{deck} = 4.36$$

$$OR_{flange} := \left(f_{s.allow.op} - \frac{M_{fas.nc}}{S_x} - \frac{M_{fas.ltc}}{S_{bf.ltc}}\right) \cdot \frac{S_{bf.stc}}{M_{fas}} \qquad OR_{flange} = 2.34$$

$$OR_v := \frac{f_{v.allow.op} \cdot D \cdot t_w - V_{fas.nc} - V_{fas.ltc}}{V_{fas}} \qquad OR_v = 10.03$$

Type 3S2 Truck Interior:

$$V_{int} := 32.07 \cdot kip \cdot (1 + IF) \qquad V_{int} = 41.23 \cdot kip$$

$$M_{int} := 3335 \cdot kip \cdot in \cdot (1 + IF) \qquad M_{int} = 4287.86 \cdot kip \cdot in$$

$$IR_{deck} := \left(f_{c.allow} - \frac{M_{int.ltc}}{S_{ti.ltc} \cdot 3n}\right) \cdot \frac{S_{ti.stc} \cdot n}{M_{int}} \qquad IR_{deck} = 2.77$$

$$IR_{flange} := \left(f_{s.allow} - \frac{M_{int.nc}}{S_x} - \frac{M_{int.ltc}}{S_{bi.ltc}}\right) \cdot \frac{S_{bi.stc}}{M_{int}} \qquad IR_{flange} = 1.04$$

$$IR_v := \frac{f_{v.allow} \cdot D \cdot t_w - V_{int.nc} - V_{int.ltc}}{V_{int}} \qquad IR_v = 4.34$$

$$OR_{deck} := \left(f_{c.allow.op} - \frac{M_{int.ltc}}{S_{ti.ltc} \cdot 3n}\right) \cdot \frac{S_{ti.stc} \cdot n}{M_{int}} \qquad OR_{deck} = 4.45$$

$$OR_{flange} := \left(f_{s.allow.op} - \frac{M_{int.nc}}{S_x} - \frac{M_{int.ltc}}{S_{bi.ltc}}\right) \cdot \frac{S_{bi.stc}}{M_{int}} \qquad OR_{flange} = 1.9$$

$$OR_v := \frac{f_{v.allow.op} \cdot D \cdot t_w - V_{int.nc} - V_{int.ltc}}{V_{int}} \qquad OR_v = 6.15$$

Type 3S2 Truck Fascia:

$$V_{fas} := 21.97 \cdot kip \cdot (1 + IF) \qquad V_{fas} = 28.25 \cdot kip$$

$$M_{fas} := 2698 \cdot kip \cdot in \cdot (1 + IF) \qquad M_{fas} = 3468.86 \cdot kip \cdot in$$

$$IR_{deck} := \left(f_{c.allow} - \frac{M_{fas.ltc}}{S_{tf.ltc} \cdot 3n}\right) \cdot \frac{S_{tf.stc} \cdot n}{M_{fas}} \qquad IR_{deck} = 2.96$$

$$IR_{flange} := \left(f_{s.allow} - \frac{M_{fas.nc}}{S_x} - \frac{M_{fas.ltc}}{S_{bf.ltc}}\right) \cdot \frac{S_{bf.stc}}{M_{fas}} \qquad IR_{flange} = 1.51$$

$$IR_v := \frac{f_{v.allow} \cdot D \cdot t_w - V_{fas.nc} - V_{fas.ltc}}{V_{fas}} \qquad IR_v = 6.48$$

$$OR_{deck} := \left(f_{c.allow.op} - \frac{M_{fas.ltc}}{S_{tf.ltc} \cdot 3n}\right) \cdot \frac{S_{tf.stc} \cdot n}{M_{fas}} \qquad OR_{deck} = 4.77$$

$$OR_{flange} := \left(f_{s.allow.op} - \frac{M_{fas.nc}}{S_x} - \frac{M_{fas.ltc}}{S_{bf.ltc}}\right) \cdot \frac{S_{bf.stc}}{M_{fas}} \qquad OR_{flange} = 2.56$$

$$OR_v := \frac{f_{v.allow.op} \cdot D \cdot t_w - V_{fas.nc} - V_{fas.ltc}}{V_{fas}} \qquad OR_v = 9.12$$

Type 3-3 Truck Interior:

$$V_{int} := 30.3 \cdot kip \cdot (1 + IF) \qquad V_{int} = 38.96 \cdot kip$$

$$M_{int} := 3335 \cdot kip \cdot in \cdot (1 + IF) \qquad M_{int} = 4287.86 \cdot kip \cdot in$$

$$IR_{deck} := \left(f_{c.allow} - \frac{M_{int.ltc}}{S_{ti.ltc} \cdot 3n}\right) \cdot \frac{S_{ti.stc} \cdot n}{M_{int}} \qquad IR_{deck} = 2.77$$

$$IR_{flange} := \left(f_{s.allow} - \frac{M_{int.nc}}{S_x} - \frac{M_{int.ltc}}{S_{bi.ltc}}\right) \cdot \frac{S_{bi.stc}}{M_{int}} \qquad IR_{flange} = 1.04$$

$$IR_v := \frac{f_{v.allow} \cdot D \cdot t_w - V_{int.nc} - V_{int.ltc}}{V_{int}} \qquad IR_v = 4.6$$

$$OR_{deck} := \left(f_{c.allow.op} - \frac{M_{int.ltc}}{S_{ti.ltc} \cdot 3n}\right) \cdot \frac{S_{ti.stc} \cdot n}{M_{int}} \qquad OR_{deck} = 4.45$$

$$OR_{flange} := \left(f_{s.allow.op} - \frac{M_{int.nc}}{S_x} - \frac{M_{int.ltc}}{S_{bi.ltc}}\right) \cdot \frac{S_{bi.stc}}{M_{int}} \qquad OR_{flange} = 1.9$$

$$OR_v := \frac{f_{v.allow.op} \cdot D \cdot t_w - V_{int.nc} - V_{int.ltc}}{V_{int}} \qquad OR_v = 6.51$$

Type 3-3 Truck Fascia:

$$V_{fas} := 20.79 \cdot kip \cdot (1 + IF) \qquad V_{fas} = 26.73 \cdot kip$$

$$M_{fas} := 2631 \cdot kip \cdot in \cdot (1 + IF) \qquad M_{fas} = 3382.71 \cdot kip \cdot in$$

$$IR_{deck} := \left(f_{c.allow} - \frac{M_{fas.ltc}}{S_{tf.ltc} \cdot 3n}\right) \cdot \frac{S_{tf.stc} \cdot n}{M_{fas}} \qquad IR_{deck} = 3.04$$

$$IR_{flange} := \left(f_{s.allow} - \frac{M_{fas.nc}}{S_x} - \frac{M_{fas.ltc}}{S_{bf.ltc}}\right) \cdot \frac{S_{bf.stc}}{M_{fas}} \qquad IR_{flange} = 1.55$$

$$IR_v := \frac{f_{v.allow} \cdot D \cdot t_w - V_{fas.nc} - V_{fas.ltc}}{V_{fas}} \qquad IR_v = 6.84$$

$$OR_{deck} := \left(f_{c.allow.op} - \frac{M_{fas.ltc}}{S_{tf.ltc} \cdot 3n}\right) \cdot \frac{S_{tf.stc} \cdot n}{M_{fas}} \qquad OR_{deck} = 4.89$$

$$OR_{flange} := \left(f_{s.allow.op} - \frac{M_{fas.nc}}{S_x} - \frac{M_{fas.ltc}}{S_{bf.ltc}}\right) \cdot \frac{S_{bf.stc}}{M_{fas}} \qquad OR_{flange} = 2.62$$

$$OR_v := \frac{f_{v.allow.op} \cdot D \cdot t_w - V_{fas.nc} - V_{fas.ltc}}{V_{fas}} \qquad OR_v = 9.64$$

LFD Section Capacities:

Section capacities are found using the AASHTO LFD design philosophy.

For bending, the compact steel section may be permitted to reach its full plastic capacity and thus moments must be used instead of stresses in the rating equations. The moment capacity for a fascia girder and for an interior girder is found below.

Fascia Girder Moment Capacity:

$b := B_f$ $b = 6\,ft$

$C1 := 0.85 \cdot f'c \cdot b \cdot t_{design}$ $C1 = 1606.5 \cdot kip$ A eq. 10-123

$C2 := A_g \cdot F_y$ $C2 = 1385 \cdot kip$ A eq. 10-124

$C := \min(C1, C2)$ $C = 1385 \cdot kip$

$a := \frac{C}{0.85 \cdot f'c \cdot b}$ $a = 6.47 \cdot in$ A eq. 10-125

Since 'a' is less than the design slab thickness, then the neutral axis at the plastic moment is in the slab.

$M_{u.f} := 0.85 \cdot f'c \cdot b \cdot a \cdot \frac{a}{2} + A_g \cdot F_y \cdot \left(\frac{d}{2} + t_{design} - a \right)$ $M_{u.f} = 24538.1 \cdot kip \cdot in$ A 10.50.1.1

Interior Girder Moment Capacity:

$b := B$ $b = 7.5\,ft$

$C1 := 0.85 \cdot f'c \cdot b \cdot t_{design}$ $C1 = 2008.13 \cdot kip$ A eq. 10-123

$C2 := A_g \cdot F_y$ $C2 = 1385 \cdot kip$ A eq. 10-124

$C := \min(C1, C2)$ $C = 1385 \cdot kip$

$a := \frac{C}{0.85 \cdot f'c \cdot b}$ $a = 5.17 \cdot in$ A eq. 10-125

Since 'a' is less than the design slab thickness, then the neutral axis at the plastic moment is in the slab.

$M_{u.i} := 0.85 \cdot f'c \cdot b \cdot a \cdot \frac{a}{2} + A_g \cdot F_y \cdot \left(\frac{d}{2} + t_{design} - a \right)$ $M_{u.i} = 25433.63 \cdot kip \cdot in$ A 10.50.1.1

For shear in a web without stiffeners, with a compact section, and with none of the web depth in bending compression for the composite section:

$f_{v.allow} := 0.58 \cdot F_y$ A 10.48.8.1

LFD Load Rating with Distribution Factors:

Load ratings per AASHTO LFD are calculated. Unfactored dead and live load forces are the same as for ASD, however, the capacity changes.

The LFD rating equation is:

$$RF := \frac{C - A_1 \cdot D}{A_2 \cdot L}$$ CE 6.5.3

$A_1 := 1.3$

$A_2 := 1.3$ at the operating level

$A_2 := 2.17$ at the inventory level

And the rating factors are:

HS20 Truck Interior:

$V_{int} := V_{hs.int}$ $V_{int} = 51.28 \cdot kip$

$M_{int} := M_{hs.int}$ $M_{int} = 6605.18 \cdot kip \cdot in$

$$IR_{deck} := \frac{M_{u.i} - A_1 \cdot M_{int.ltc}}{A_2 \cdot M_{int}}$$ $IR_{deck} = 1.71$

$$IR_{flange} := \frac{M_{u.i} - A_1 \cdot M_{int.nc} - A_1 \cdot M_{int.ltc}}{A_2 \cdot M_{int}}$$ $IR_{flange} = 1.42$

$$IR_v := \frac{f_{v.allow} \cdot D \cdot t_w - A_1 \cdot V_{int.nc} - A_1 \cdot V_{int.ltc}}{A_2 \cdot V_{int}}$$ $IR_v = 2.94$

$OR_{deck} := 1.67 \cdot IR_{deck}$ $OR_{deck} = 2.85$

$OR_{flange} := 1.67 \cdot IR_{flange}$ $OR_{flange} = 2.36$

$OR_v := 1.67 \cdot IR_v$ $OR_v = 4.9$

HS20 Truck Fascia:

$V_{fas} := V_{hs.fas}$ $V_{fas} = 48.01 \cdot kip$

$M_{fas} := M_{hs.fas}$ $M_{fas} = 6183.57 \cdot kip \cdot in$

$$IR_{deck} := \frac{M_{u.f} - A_1 \cdot M_{fas.ltc}}{A_2 \cdot M_{fas}}$$ $IR_{deck} = 1.76$

$$IR_{flange} := \frac{M_{u.f} - A_1 \cdot M_{fas.nc} - A_1 \cdot M_{fas.ltc}}{A_2 \cdot M_{fas}}$$ $IR_{flange} = 1.5$

$$IR_v := \frac{f_{v.allow} \cdot D \cdot t_w - A_1 \cdot V_{fas.nc} - A_1 \cdot V_{fas.ltc}}{A_2 \cdot V_{fas}}$$ $IR_v = 3.19$

$OR_{deck} := 1.67 \cdot IR_{deck}$ $OR_{deck} = 2.93$

$OR_{flange} := 1.67 \cdot IR_{flange}$ $OR_{flange} = 2.51$

$OR_{v} := 1.67 \cdot IR_{v}$ $OR_{v} = 5.32$

Type 3 Truck Interior:

$V_{int} := V_{3.int}$ $V_{int} = 37.31 \cdot kip$

$M_{int} := M_{3.int}$ $M_{int} = 4954.68 \cdot kip \cdot in$

$$IR_{deck} := \frac{M_{u.i} - A_1 \cdot M_{int.ltc}}{A_2 \cdot M_{int}}$$ $IR_{deck} = 2.27$

$$IR_{flange} := \frac{M_{u.i} - A_1 \cdot M_{int.nc} - A_1 \cdot M_{int.ltc}}{A_2 \cdot M_{int}}$$ $IR_{flange} = 1.89$

$$IR_{v} := \frac{f_{v.allow} \cdot D \cdot t_w - A_1 \cdot V_{int.nc} - A_1 \cdot V_{int.ltc}}{A_2 \cdot V_{int}}$$ $IR_{v} = 4.04$

$OR_{deck} := 1.67 \cdot IR_{deck}$ $OR_{deck} = 3.8$

$OR_{flange} := 1.67 \cdot IR_{flange}$ $OR_{flange} = 3.15$

$OR_{v} := 1.67 \cdot IR_{v}$ $OR_{v} = 6.74$

Type 3 Truck Fascia:

$V_{fas} := V_{3.fas}$ $V_{fas} = 34.93 \cdot kip$

$M_{fas} := M_{3.fas}$ $M_{fas} = 4638.42 \cdot kip \cdot in$

$$IR_{deck} := \frac{M_{u.f} - A_1 \cdot M_{fas.ltc}}{A_2 \cdot M_{fas}}$$ $IR_{deck} = 2.34$

$$IR_{flange} := \frac{M_{u.f} - A_1 \cdot M_{fas.nc} - A_1 \cdot M_{fas.ltc}}{A_2 \cdot M_{fas}}$$ $IR_{flange} = 2$

$$IR_{v} := \frac{f_{v.allow} \cdot D \cdot t_w - A_1 \cdot V_{fas.nc} - A_1 \cdot V_{fas.ltc}}{A_2 \cdot V_{fas}}$$ $IR_{v} = 4.38$

$OR_{deck} := 1.67 \cdot IR_{deck}$ $OR_{deck} = 3.91$

$OR_{flange} := 1.67 \cdot IR_{flange}$ $OR_{flange} = 3.34$

$OR_{v} := 1.67 \cdot IR_{v}$ $OR_{v} = 7.31$

Type 3S2 Truck Interior:

$V_{int} := V_{3s2.int}$ $V_{int} = 39.62 \cdot kip$

$M_{int} := M_{3s2.int}$ $M_{int} = 4520.75 \cdot kip \cdot in$

$IR_{deck} := \frac{M_{u.i} - A_1 \cdot M_{int.ltc}}{A_2 \cdot M_{int}}$ $IR_{deck} = 2.49$

$IR_{flange} := \frac{M_{u.i} - A_1 \cdot M_{int.nc} - A_1 \cdot M_{int.ltc}}{A_2 \cdot M_{int}}$ $IR_{flange} = 2.07$

$IR_v := \frac{f_{v.allow} \cdot D \cdot t_w - A_1 \cdot V_{int.nc} - A_1 \cdot V_{int.ltc}}{A_2 \cdot V_{int}}$ $IR_v = 3.8$

$OR_{deck} := 1.67 \cdot IR_{deck}$ $OR_{deck} = 4.16$

$OR_{flange} := 1.67 \cdot IR_{flange}$ $OR_{flange} = 3.45$

$OR_v := 1.67 \cdot IR_v$ $OR_v = 6.35$

Type 3S2 Truck Fascia:

$V_{fas} := V_{3s2.fas}$ $V_{fas} = 37.09 \cdot kip$

$M_{fas} := M_{3s2.fas}$ $M_{fas} = 4232.19 \cdot kip \cdot in$

$IR_{deck} := \frac{M_{u.f} - A_1 \cdot M_{fas.ltc}}{A_2 \cdot M_{fas}}$ $IR_{deck} = 2.57$

$IR_{flange} := \frac{M_{u.f} - A_1 \cdot M_{fas.nc} - A_1 \cdot M_{fas.ltc}}{A_2 \cdot M_{fas}}$ $IR_{flange} = 2.19$

$IR_v := \frac{f_{v.allow} \cdot D \cdot t_w - A_1 \cdot V_{fas.nc} - A_1 \cdot V_{fas.ltc}}{A_2 \cdot V_{fas}}$ $IR_v = 4.12$

$OR_{deck} := 1.67 \cdot IR_{deck}$ $OR_{deck} = 4.28$

$OR_{flange} := 1.67 \cdot IR_{flange}$ $OR_{flange} = 3.66$

$OR_v := 1.67 \cdot IR_v$ $OR_v = 6.88$

Type 3-3 Truck Interior:

$V_{int} := V_{33.int}$ $V_{int} = 37.45 \cdot kip$

$M_{int} := M_{33.int}$ $M_{int} = 4144.68 \cdot kip \cdot in$

$IR_{deck} := \frac{M_{u.i} - A_1 \cdot M_{int.ltc}}{A_2 \cdot M_{int}}$ $IR_{deck} = 2.72$

$$IR_{flange} := \frac{M_{u.i} - A_1 \cdot M_{int.nc} - A_1 \cdot M_{int.ltc}}{A_2 \cdot M_{int}} \qquad IR_{flange} = 2.26$$

$$IR_v := \frac{f_{v.allow} \cdot D \cdot t_w - A_1 \cdot V_{int.nc} - A_1 \cdot V_{int.ltc}}{A_2 \cdot V_{int}} \qquad IR_v = 4.02$$

$$OR_{deck} := 1.67 \cdot IR_{deck} \qquad OR_{deck} = 4.54$$

$$OR_{flange} := 1.67 \cdot IR_{flange} \qquad OR_{flange} = 3.77$$

$$OR_v := 1.67 \cdot IR_v \qquad OR_v = 6.71$$

Type 3-3 Truck Fascia:

$$V_{fas} := V_{33.fas} \qquad V_{fas} = 35.06 \cdot kip$$

$$M_{fas} := M_{33.fas} \qquad M_{fas} = 3880.12 \cdot kip \cdot in$$

$$IR_{deck} := \frac{M_{u.f} - A_1 \cdot M_{fas.ltc}}{A_2 \cdot M_{fas}} \qquad IR_{deck} = 2.8$$

$$IR_{flange} := \frac{M_{u.f} - A_1 \cdot M_{fas.nc} - A_1 \cdot M_{fas.ltc}}{A_2 \cdot M_{fas}} \qquad IR_{flange} = 2.39$$

$$IR_v := \frac{f_{v.allow} \cdot D \cdot t_w - A_1 \cdot V_{fas.nc} - A_1 \cdot V_{fas.ltc}}{A_2 \cdot V_{fas}} \qquad IR_v = 4.36$$

$$OR_{deck} := 1.67 \cdot IR_{deck} \qquad OR_{deck} = 4.67$$

$$OR_{flange} := 1.67 \cdot IR_{flange} \qquad OR_{flange} = 4$$

$$OR_v := 1.67 \cdot IR_v \qquad OR_v = 7.28$$

LFD Load Rating with Finite Element Live Load Stresses

Stresses in the critical elements are found as discussed previously.

The results are as follows for the various truck loads and for an interior and a fascia girder:

HS Truck Interior:

$V_{int} := 40.74 \cdot kip \cdot (1 + IF)$ $V_{int} = 52.38 \cdot kip$

$f_{b.int} := 9.059 \cdot ksi \cdot (1 + IF)$ $f_{b.int} = 11.65 \cdot ksi$

$f_{t.int} := 0.934 \cdot ksi \cdot (1 + IF)$ $f_{t.int} = 1.2 \cdot ksi$

$$IR_{deck} := \frac{M_{u.i} - A_1 \cdot M_{int.ltc}}{A_2 \cdot S_{ti.stc} \cdot f_{t.int} \cdot n} \qquad IR_{deck} = 0.91$$

$$IR_{flange} := \frac{M_{u.i} - A_1 \cdot M_{int.nc} - A_1 \cdot M_{int.ltc}}{A_2 \cdot S_{bi.stc} \cdot f_{b.int}} \qquad IR_{flange} = 2.17$$

$$IR_v := \frac{f_{v.allow} \cdot D \cdot t_w - A_1 \cdot V_{int.nc} - A_1 \cdot V_{int.ltc}}{A_2 \cdot V_{int}} \qquad IR_v = 2.87$$

$OR_{deck} := 1.67 \cdot IR_{deck}$ $OR_{deck} = 1.52$

$OR_{flange} := 1.67 \cdot IR_{flange}$ $OR_{flange} = 3.63$

$OR_v := 1.67 \cdot IR_v$ $OR_v = 4.8$

HS Truck Fascia:

$V_{fas} := 31.18 \cdot kip \cdot (1 + IF)$ $V_{fas} = 40.09 \cdot kip$

$f_{b.fas} := 7.527 \cdot ksi \cdot (1 + IF)$ $f_{b.fas} = 9.68 \cdot ksi$

$f_{t.fas} := 0.540 \cdot ksi \cdot (1 + IF)$ $f_{t.fas} = 0.69 \cdot ksi$

$$IR_{deck} := \frac{M_{u.f} - A_1 \cdot M_{fas.ltc}}{A_2 \cdot S_{tf.stc} \cdot f_{t.fas} \cdot n} \qquad IR_{deck} = 1.74$$

$$IR_{flange} := \frac{M_{u.f} - A_1 \cdot M_{fas.nc} - A_1 \cdot M_{fas.ltc}}{A_2 \cdot S_{bf.stc} \cdot f_{b.fas}} \qquad IR_{flange} = 2.64$$

$$IR_v := \frac{f_{v.allow} \cdot D \cdot t_w - A_1 \cdot V_{fas.nc} - A_1 \cdot V_{fas.ltc}}{A_2 \cdot V_{fas}} \qquad IR_v = 3.81$$

$OR_{deck} := 1.67 \cdot IR_{deck}$ $OR_{deck} = 2.91$

$OR_{flange} := 1.67 \cdot IR_{flange}$ $OR_{flange} = 4.41$

$OR_v := 1.67 \cdot IR_v$ $OR_v = 6.37$

Type 3 Truck Interior:

$V_{int} := 30.43 \cdot kip \cdot (1 + IF)$ $V_{int} = 39.12 \cdot kip$

$f_{b.int} := 6.939 \cdot ksi \cdot (1 + IF)$ $f_{b.int} = 8.92 \cdot ksi$

$f_{t.int} := 0.689 \cdot ksi \cdot (1 + IF)$ $f_{t.int} = 0.89 \cdot ksi$

$$IR_{deck} := \frac{M_{u.i} - A_1 \cdot M_{int.ltc}}{A_2 \cdot S_{ti.stc} \cdot f_{t.int} \cdot n}$$ $IR_{deck} = 1.23$

$$IR_{flange} := \frac{M_{u.i} - A_1 \cdot M_{int.nc} - A_1 \cdot M_{int.ltc}}{A_2 \cdot S_{bi.stc} \cdot f_{b.int}}$$ $IR_{flange} = 2.84$

$$IR_v := \frac{f_{v.allow} \cdot D \cdot t_w - A_1 \cdot V_{int.nc} - A_1 \cdot V_{int.ltc}}{A_2 \cdot V_{int}}$$ $IR_v = 3.85$

$OR_{deck} := 1.67 \cdot IR_{deck}$ $OR_{deck} = 2.06$

$OR_{flange} := 1.67 \cdot IR_{flange}$ $OR_{flange} = 4.74$

$OR_v := 1.67 \cdot IR_v$ $OR_v = 6.43$

Type 3 Truck Fascia:

$V_{fas} := 21.91 \cdot kip \cdot (1 + IF)$ $V_{fas} = 28.17 \cdot kip$

$f_{b.fas} := 5.707 \cdot ksi \cdot (1 + IF)$ $f_{b.fas} = 7.34 \cdot ksi$

$f_{t.fas} := 0.399 \cdot ksi \cdot (1 + IF)$ $f_{t.fas} = 0.51 \cdot ksi$

$$IR_{deck} := \frac{M_{u.f} - A_1 \cdot M_{fas.ltc}}{A_2 \cdot S_{tf.stc} \cdot f_{t.fas} \cdot n}$$ $IR_{deck} = 2.36$

$$IR_{flange} := \frac{M_{u.f} - A_1 \cdot M_{fas.nc} - A_1 \cdot M_{fas.ltc}}{A_2 \cdot S_{bf.stc} \cdot f_{b.fas}}$$ $IR_{flange} = 3.48$

$$IR_v := \frac{f_{v.allow} \cdot D \cdot t_w - A_1 \cdot V_{fas.nc} - A_1 \cdot V_{fas.ltc}}{A_2 \cdot V_{fas}}$$ $IR_v = 5.43$

$OR_{deck} := 1.67 \cdot IR_{deck}$ $OR_{deck} = 3.94$

$OR_{flange} := 1.67 \cdot IR_{flange}$ $OR_{flange} = 5.82$

$OR_v := 1.67 \cdot IR_v$ $OR_v = 9.07$

Type 3S2 Truck Interior:

$V_{int} := 29.48 \cdot kip \cdot (1 + IF)$ $V_{int} = 37.9 \cdot kip$

$f_{b.int} := 6.355 \cdot ksi \cdot (1 + IF)$ $f_{b.int} = 8.17 \cdot ksi$

$f_{t.int} := 0.633 \cdot ksi \cdot (1 + IF)$ $f_{t.int} = 0.81 \cdot ksi$

$$IR_{deck} := \frac{M_{u.i} - A_1 \cdot M_{int.ltc}}{A_2 \cdot S_{ti.stc} \cdot f_{t.int} \cdot n}$$ $IR_{deck} = 1.34$

$$IR_{flange} := \frac{M_{u.i} - A_1 \cdot M_{int.nc} - A_1 \cdot M_{int.ltc}}{A_2 \cdot S_{bi.stc} \cdot f_{b.int}}$$ $IR_{flange} = 3.1$

$$IR_v := \frac{f_{v.allow} \cdot D \cdot t_w - A_1 \cdot V_{int.nc} - A_1 \cdot V_{int.ltc}}{A_2 \cdot V_{int}}$$ $IR_v = 3.97$

$OR_{deck} := 1.67 \cdot IR_{deck}$ $OR_{deck} = 2.24$

$OR_{flange} := 1.67 \cdot IR_{flange}$ $OR_{flange} = 5.17$

$OR_v := 1.67 \cdot IR_v$ $OR_v = 6.63$

Type 3S2 Truck Fascia:

$V_{fas} := 25.21 \cdot kip \cdot (1 + IF)$ $V_{fas} = 32.41 \cdot kip$

$f_{b.fas} := 5.195 \cdot ksi \cdot (1 + IF)$ $f_{b.fas} = 6.68 \cdot ksi$

$f_{t.fas} := 0.365 \cdot ksi \cdot (1 + IF)$ $f_{t.fas} = 0.47 \cdot ksi$

$$IR_{deck} := \frac{M_{u.f} - A_1 \cdot M_{fas.ltc}}{A_2 \cdot S_{tf.stc} \cdot f_{t.fas} \cdot n}$$ $IR_{deck} = 2.58$

$$IR_{flange} := \frac{M_{u.f} - A_1 \cdot M_{fas.nc} - A_1 \cdot M_{fas.ltc}}{A_2 \cdot S_{bf.stc} \cdot f_{b.fas}}$$ $IR_{flange} = 3.83$

$$IR_v := \frac{f_{v.allow} \cdot D \cdot t_w - A_1 \cdot V_{fas.nc} - A_1 \cdot V_{fas.ltc}}{A_2 \cdot V_{fas}}$$ $IR_v = 4.72$

$OR_{deck} := 1.67 \cdot IR_{deck}$ $OR_{deck} = 4.31$

$OR_{flange} := 1.67 \cdot IR_{flange}$ $OR_{flange} = 6.39$

$OR_v := 1.67 \cdot IR_v$ $OR_v = 7.88$

Type 3-3 Truck Interior:

$V_{int} := 27.87 \cdot kip \cdot (1 + IF)$ $V_{int} = 35.83 \cdot kip$

$f_{b.int} := 5.936 \cdot ksi \cdot (1 + IF)$ $f_{b.int} = 7.63 \cdot ksi$

$f_{t.int} := 0.573 \cdot ksi \cdot (1 + IF)$ $f_{t.int} = 0.74 \cdot ksi$

$$IR_{deck} := \frac{M_{u.i} - A_1 \cdot M_{int.ltc}}{A_2 \cdot S_{ti.stc} \cdot f_{t.int} \cdot n}$$ $IR_{deck} = 1.48$

$$IR_{flange} := \frac{M_{u.i} - A_1 \cdot M_{int.nc} - A_1 \cdot M_{int.ltc}}{A_2 \cdot S_{bi.stc} \cdot f_{b.int}}$$ $IR_{flange} = 3.32$

$$IR_v := \frac{f_{v.allow} \cdot D \cdot t_w - A_1 \cdot V_{int.nc} - A_1 \cdot V_{int.ltc}}{A_2 \cdot V_{int}}$$ $IR_v = 4.2$

$OR_{deck} := 1.67 \cdot IR_{deck}$ $OR_{deck} = 2.48$

$OR_{flange} := 1.67 \cdot IR_{flange}$ $OR_{flange} = 5.54$

$OR_v := 1.67 \cdot IR_v$ $OR_v = 7.02$

Type 3-3 Truck Fascia:

$V_{fas} := 23.72 \cdot kip \cdot (1 + IF)$ $V_{fas} = 30.5 \cdot kip$

$f_{b.fas} := 5.066 \cdot ksi \cdot (1 + IF)$ $f_{b.fas} = 6.51 \cdot ksi$

$f_{t.fas} := 0.343 \cdot ksi \cdot (1 + IF)$ $f_{t.fas} = 0.44 \cdot ksi$

$$IR_{deck} := \frac{M_{u.f} - A_1 \cdot M_{fas.ltc}}{A_2 \cdot S_{tf.stc} \cdot f_{t.fas} \cdot n}$$ $IR_{deck} = 2.74$

$$IR_{flange} := \frac{M_{u.f} - A_1 \cdot M_{fas.nc} - A_1 \cdot M_{fas.ltc}}{A_2 \cdot S_{bf.stc} \cdot f_{b.fas}}$$ $IR_{flange} = 3.93$

$$IR_v := \frac{f_{v.allow} \cdot D \cdot t_w - A_1 \cdot V_{fas.nc} - A_1 \cdot V_{fas.ltc}}{A_2 \cdot V_{fas}}$$ $IR_v = 5.01$

$OR_{deck} := 1.67 \cdot IR_{deck}$ $OR_{deck} = 4.58$

$OR_{flange} := 1.67 \cdot IR_{flange}$ $OR_{flange} = 6.56$

$OR_v := 1.67 \cdot IR_v$ $OR_v = 8.37$

LFD Load Rating with Modal Flexibility Live Load Stresses

Stresses in the critical elements are found using the results of the modal analysis as discussed previously.

The results are as follows for the various truck loads and for an interior and a fascia girder:

HS Truck Interior:

$V_{int} := 42.97 \cdot kip \cdot (1 + IF)$ $V_{int} = 55.25 \cdot kip$

$M_{int} := 4788 \cdot kip \cdot in \cdot (1 + IF)$ $M_{int} = 6156 \cdot kip \cdot in$

$IR_{deck} := \frac{M_{u.i} - A_1 \cdot M_{int.ltc}}{A_2 \cdot M_{int}}$ $IR_{deck} = 1.83$

$IR_{flange} := \frac{M_{u.i} - A_1 \cdot M_{int.nc} - A_1 \cdot M_{int.ltc}}{A_2 \cdot M_{int}}$ $IR_{flange} = 1.52$

$IR_v := \frac{f_{v.allow} \cdot D \cdot t_w - A_1 \cdot V_{int.nc} - A_1 \cdot V_{int.ltc}}{A_2 \cdot V_{int}}$ $IR_v = 2.73$

$OR_{deck} := 1.67 \cdot IR_{deck}$ $OR_{deck} = 3.06$

$OR_{flange} := 1.67 \cdot IR_{flange}$ $OR_{flange} = 2.54$

$OR_v := 1.67 \cdot IR_v$ $OR_v = 4.55$

HS Truck Fascia:

$V_{fas} := 27.87 \cdot kip \cdot (1 + IF)$ $V_{fas} = 35.83 \cdot kip$

$M_{fas} := 3901 \cdot kip \cdot in \cdot (1 + IF)$ $M_{fas} = 5015.57 \cdot kip \cdot in$

$IR_{deck} := \frac{M_{u.f} - A_1 \cdot M_{fas.ltc}}{A_2 \cdot M_{fas}}$ $IR_{deck} = 2.16$

$IR_{flange} := \frac{M_{u.f} - A_1 \cdot M_{fas.nc} - A_1 \cdot M_{fas.ltc}}{A_2 \cdot M_{fas}}$ $IR_{flange} = 1.85$

$IR_v := \frac{f_{v.allow} \cdot D \cdot t_w - A_1 \cdot V_{fas.nc} - A_1 \cdot V_{fas.ltc}}{A_2 \cdot V_{fas}}$ $IR_v = 4.27$

$OR_{deck} := 1.67 \cdot IR_{deck}$ $OR_{deck} = 3.62$

$OR_{flange} := 1.67 \cdot IR_{flange}$ $OR_{flange} = 3.09$

$OR_v := 1.67 \cdot IR_v$ $OR_v = 7.13$

Type 3 Truck Interior:

$V_{int} := 31.81 \cdot kip \cdot (1 + IF)$ $V_{int} = 40.9 \cdot kip$

$M_{int} := 3653 \cdot kip \cdot in \cdot (1 + IF)$ $M_{int} = 4696.71 \cdot kip \cdot in$

$$IR_{deck} := \frac{M_{u.i} - A_1 \cdot M_{int.ltc}}{A_2 \cdot M_{int}} \qquad IR_{deck} = 2.4$$

$$IR_{flange} := \frac{M_{u.i} - A_1 \cdot M_{int.nc} - A_1 \cdot M_{int.ltc}}{A_2 \cdot M_{int}} \qquad IR_{flange} = 1.99$$

$$IR_v := \frac{f_{v.allow} \cdot D \cdot t_w - A_1 \cdot V_{int.nc} - A_1 \cdot V_{int.ltc}}{A_2 \cdot V_{int}} \qquad IR_v = 3.68$$

$OR_{deck} := 1.67 \cdot IR_{deck}$ $OR_{deck} = 4.01$

$OR_{flange} := 1.67 \cdot IR_{flange}$ $OR_{flange} = 3.32$

$OR_v := 1.67 \cdot IR_v$ $OR_v = 6.15$

Type 3 Truck Fascia:

$V_{fas} := 19.97 \cdot kip \cdot (1 + IF)$ $V_{fas} = 25.68 \cdot kip$

$M_{fas} := 2953 \cdot kip \cdot in \cdot (1 + IF)$ $M_{fas} = 3796.71 \cdot kip \cdot in$

$$IR_{deck} := \frac{M_{u.f} - A_1 \cdot M_{fas.ltc}}{A_2 \cdot M_{fas}} \qquad IR_{deck} = 2.86$$

$$IR_{flange} := \frac{M_{u.f} - A_1 \cdot M_{fas.nc} - A_1 \cdot M_{fas.ltc}}{A_2 \cdot M_{fas}} \qquad IR_{flange} = 2.45$$

$$IR_v := \frac{f_{v.allow} \cdot D \cdot t_w - A_1 \cdot V_{fas.nc} - A_1 \cdot V_{fas.ltc}}{A_2 \cdot V_{fas}} \qquad IR_v = 5.96$$

$OR_{deck} := 1.67 \cdot IR_{deck}$ $OR_{deck} = 4.78$

$OR_{flange} := 1.67 \cdot IR_{flange}$ $OR_{flange} = 4.08$

$OR_v := 1.67 \cdot IR_v$ $OR_v = 9.95$

Type 3S2 Truck Interior:

$V_{int} := 32.07 \cdot kip \cdot (1 + IF)$ $V_{int} = 41.23 \cdot kip$

$M_{int} := 3335 \cdot kip \cdot in \cdot (1 + IF)$ $M_{int} = 4287.86 \cdot kip \cdot in$

$$IR_{deck} := \frac{M_{u.i} - A_1 \cdot M_{int.ltc}}{A_2 \cdot M_{int}} \qquad IR_{deck} = 2.63$$

$$IR_{flange} := \frac{M_{u.i} - A_1 \cdot M_{int.nc} - A_1 \cdot M_{int.ltc}}{A_2 \cdot M_{int}} \qquad IR_{flange} = 2.18$$

$$IR_v := \frac{f_{v.allow} \cdot D \cdot t_w - A_1 \cdot V_{int.nc} - A_1 \cdot V_{int.ltc}}{A_2 \cdot V_{int}} \qquad IR_v = 3.65$$

$OR_{deck} := 1.67 \cdot IR_{deck}$ $OR_{deck} = 4.39$

$OR_{flange} := 1.67 \cdot IR_{flange}$ $OR_{flange} = 3.64$

$OR_v := 1.67 \cdot IR_v$ $OR_v = 6.1$

Type 3S2 Truck Fascia:

$V_{fas} := 21.97 \cdot kip \cdot (1 + IF)$ $V_{fas} = 28.25 \cdot kip$

$M_{fas} := 2698 \cdot kip \cdot in \cdot (1 + IF)$ $M_{fas} = 3468.86 \cdot kip \cdot in$

$$IR_{deck} := \frac{M_{u.f} - A_1 \cdot M_{fas.ltc}}{A_2 \cdot M_{fas}} \qquad IR_{deck} = 3.13$$

$$IR_{flange} := \frac{M_{u.f} - A_1 \cdot M_{fas.nc} - A_1 \cdot M_{fas.ltc}}{A_2 \cdot M_{fas}} \qquad IR_{flange} = 2.68$$

$$IR_v := \frac{f_{v.allow} \cdot D \cdot t_w - A_1 \cdot V_{fas.nc} - A_1 \cdot V_{fas.ltc}}{A_2 \cdot V_{fas}} \qquad IR_v = 5.41$$

$OR_{deck} := 1.67 \cdot IR_{deck}$ $OR_{deck} = 5.23$

$OR_{flange} := 1.67 \cdot IR_{flange}$ $OR_{flange} = 4.47$

$OR_v := 1.67 \cdot IR_v$ $OR_v = 9.04$

Type 3-3 Truck Interior:

$V_{int} := 30.3 \cdot kip \cdot (1 + IF)$ $V_{int} = 38.96 \cdot kip$

$M_{int} := 3335 \cdot kip \cdot in \cdot (1 + IF)$ $M_{int} = 4287.86 \cdot kip \cdot in$

$$IR_{deck} := \frac{M_{u.i} - A_1 \cdot M_{int.ltc}}{A_2 \cdot M_{int}} \qquad IR_{deck} = 2.63$$

$$IR_{flange} := \frac{M_{u.i} - A_1 \cdot M_{int.nc} - A_1 \cdot M_{int.ltc}}{A_2 \cdot M_{int}} \qquad IR_{flange} = 2.18$$

$$IR_v := \frac{f_{v.allow} \cdot D \cdot t_w - A_1 \cdot V_{int.nc} - A_1 \cdot V_{int.ltc}}{A_2 \cdot V_{int}} \qquad IR_v = 3.87$$

$OR_{deck} := 1.67 \cdot IR_{deck}$ $OR_{deck} = 4.39$

$OR_{flange} := 1.67 \cdot IR_{flange}$ $OR_{flange} = 3.64$

$OR_v := 1.67 \cdot IR_v$ $OR_v = 6.46$

Type 3-3 Truck Fascia:

$V_{fas} := 20.79 \cdot kip \cdot (1 + IF)$ $V_{fas} = 26.73 \cdot kip$

$M_{fas} := 2631 \cdot kip \cdot in \cdot (1 + IF)$ $M_{fas} = 3382.71 \cdot kip \cdot in$

$$IR_{deck} := \frac{M_{u.f} - A_1 \cdot M_{fas.ltc}}{A_2 \cdot M_{fas}}$$ $IR_{deck} = 3.21$

$$IR_{flange} := \frac{M_{u.f} - A_1 \cdot M_{fas.nc} - A_1 \cdot M_{fas.ltc}}{A_2 \cdot M_{fas}}$$ $IR_{flange} = 2.75$

$$IR_v := \frac{f_{v.allow} \cdot D \cdot t_w - A_1 \cdot V_{fas.nc} - A_1 \cdot V_{fas.ltc}}{A_2 \cdot V_{fas}}$$ $IR_v = 5.72$

$OR_{deck} := 1.67 \cdot IR_{deck}$ $OR_{deck} = 5.36$

$OR_{flange} := 1.67 \cdot IR_{flange}$ $OR_{flange} = 4.58$

$OR_v := 1.67 \cdot IR_v$ $OR_v = 9.55$

LRFD Load Rating Introduction

Load rating using the LRFD philosophy is about the same as using the other philosophies. The dead load forces do not change and the forces due to legal trucks do not change. The section capacities are found differently, load factors are applied, and the design live load becomes HL-93 instead of HS-20.

$$RF := \frac{C - \gamma_{DL} \cdot D}{\gamma_{LL} \cdot L}$$ BE 6A.4.2.1

$\gamma_{DL} := 1.25$ for components and attachments BE 6A.4.2.2

$\gamma_{LL} := 1.35$ for HL-93 truck at the operating level

$\gamma_{LL} := 1.75$ for HL-93 truck at the inventory level

$\gamma_{LL.l} := 1.4$ for legal loads, no separate inventory and operating levels BE 6A.4.4.2.3a-1

$C := \phi_c \cdot \phi_s \cdot \phi R_n$

$\phi_c := 1.0$ good bridge condition BE T6A4.2.3-1

$\phi_s := 1.0$ redundant system BE T6.4.2.4-1

LRFD Bending Capacity - Interior Girder

Finding the strength per LRFD is a lengthy process because of the inclusion of the plastic moment and the plastic neutral axis. The flowcharts Figure C6.4.4-1 and C6.4.5-1 in AASHTO will be followed for these calculations, and are attached for reference.

for flexure: $\phi_f := 1.00$ AR 6.5.4.2

for shear: $\phi_v := 1.00$

Step 1 - Check for Section Compactness:

Check Minimum Yield Strength:

$F_y \le 70ksi = 1$ Okay AR 6.10.6.2.2

Check Web Slenderness:

For webs without longitudinal stiffeners:

$D = 25.41 \cdot in$

$t_w = 0.49 \cdot in$

$\frac{D}{t_w} = 51.86$

$\frac{D}{t_w} \le 150 = 1$ Okay AR 6.10.2.1.1-1

Check Depth of Web in Compression:

This check is done at the plastic moment, and requires calculating the plastic neutral axis. The calculations used to find the PNA can be conservatively simplified by ignoring the reinforcing steel in the deck.

$$2\cdot\frac{D_{cp}}{t_w} \le 3.76\cdot\sqrt{\frac{E}{F_y}}$$ AR 6.10.6.2.2-1

At the plastic moment the force in the bottom (tension) flange is:

$P_t := F_y\cdot b_t\cdot t_t$ $P_t = 372.13\cdot kip$

And the force in the web is:

$P_w := F_y\cdot D\cdot t_w$ $P_w = 622.54\cdot kip$

And the force in the top (compression) flange is:

$P_c := P_t$ $P_c = 372.13\cdot kip$

And the force in the slab is:

$b_s := B$ $b_s = 7.5\,ft$

$P_s := 0.85f'c\cdot t_{design}\cdot b_s$ $P_s = 2008.12\cdot kip$

The location of the PNA will be in one of the following locations: AR T D6.1-1
Case 1: PNA lies in web
Case 2: PNA lies in top flange
Case 3: PNA lies in concrete deck

$t_s := t_{design}$

$$\begin{aligned}
PNA := \;& (case \leftarrow 3) \;\; \text{if } P_t + P_w + P_c < P_s \\
& (case \leftarrow 2) \;\; \text{if } P_t + P_w + P_c \ge P_s \\
& (case \leftarrow 1) \;\; \text{if } P_t + P_w \ge P_c + P_s \\
& y \leftarrow \frac{D}{2}\cdot\left(\frac{P_t - P_c - P_s}{P_w} + 1\right) \;\; \text{if } case = 1 \\
& y \leftarrow \frac{t_c}{2}\cdot\left(\frac{P_w + P_t - P_s}{P_c} + 1\right) \;\; \text{if } case = 2 \\
& y \leftarrow t_s\cdot\left(\frac{P_c + P_w + P_t}{P_s}\right) \;\; \text{if } case = 3 \\
& pna \leftarrow t_t + D - y \;\; \text{if } case = 1 \\
& pna \leftarrow t_t + D + t_c - y \;\; \text{if } case = 2 \\
& pna \leftarrow t_t + D + t_c + t_s - y \;\; \text{if } case = 3 \\
& pna
\end{aligned}$$

$PNA = 29.3\cdot in$ measured upwards from the bottom of the bottom flange:

Therefore, the depth of web in compression is zero:

$D_{cp} := 0 \cdot in$

And checking for compactness:

$2 \cdot \frac{D_{cp}}{t_w} \le 3.76 \cdot \sqrt{\frac{E}{F_y}} = 1$ Okay - Compact

Step 2 - Determine Plastic Moment:

Because the sections are compact, the bending strength is a function of the plastic moment. Therefore, the plastic moment must be found. The plastic moment equations use a variable 'y' which is measured from different points in the section depending on the location of the PNA. This variable will be found first:

$$y' := \begin{| } y \leftarrow t_t + D + t_c + t_s - PNA \\ y \leftarrow t_t + D + t_c - PNA \text{ if } P_t + P_w + P_c \ge P_s \\ y \leftarrow t_t + D - PNA \text{ if } P_t + P_w \ge P_c + P_s \\ y \end{|}$$

$y' = 5.1 \cdot in$

Now the plastic moment will be calculated:

$$M_p := \begin{| } d1 \leftarrow t_t + D \\ d2 \leftarrow d1 + t_c \\ d3 \leftarrow d2 + t_s \\ d_t \leftarrow |PNA - t_t| \\ d_w \leftarrow \left|PNA - t_t - \frac{D}{2}\right| \\ d_c \leftarrow \left|PNA - t_t - D - \frac{t_c}{2}\right| \\ d_s \leftarrow \left|PNA - t_t - D - t_c - \frac{t_s}{2}\right| \\ m \leftarrow (y')^2 \cdot \frac{P_s}{2 \cdot t_s} + P_c \cdot d_c + P_w \cdot d_w + P_t \cdot d_t \\ m \leftarrow \frac{P_c}{2 \cdot t_c} \cdot \left[(y')^2 + (t_c - y')^2\right] + P_s \cdot d_s + P_w \cdot d_w + P_t \cdot d_t \text{ if } P_t + P_w + P_c \ge P_s \\ m \leftarrow \frac{P_w}{2 \cdot D} \cdot \left[(y')^2 + (D - y')^2\right] + P_s \cdot d_s + P_c \cdot d_c + P_t \cdot d_t \text{ if } P_t + P_w \ge P_c + P_s \\ m \end{|}$$

$M_p = 2083.94 \cdot kip \cdot ft$

Step 3 - Determine Nominal Bending Strength:

There are two equations that may control the nominal bending strength, and the choice of which equation to use is based on the ratio of the depth of section in compression to the total depth of section. The following checks this ratio and then calculates the nominal bending strength:

$$M_{n.i} := \left| \begin{array}{l} D_t \leftarrow t_t + D + t_c + t_s \\ D_p \leftarrow D_t - PNA \\ m \leftarrow M_p \\ m \leftarrow M_p \cdot \left(1.07 - 0.7 \cdot \frac{D_p}{D_t}\right) \text{ if } D_p > 0.1 \cdot D_t \\ m \end{array} \right.$$

AR 6.10.7.1.2-1

AR 6.10.7.1.2-2

$M_{n.i} = 2013.34 \cdot kip \cdot ft$

LRFD Shear Capacity - Interior Girder

$V_n := C \cdot V_p$ AR 6.10.9.2-1

$k_w := 5.0$ no web stiffeners AR 6.10.9.2

$E_s := E$

$$C := \left| \begin{array}{l} c \leftarrow \frac{1.57 \cdot E_s \cdot k_w}{\left(\frac{D}{t_w}\right)^2 \cdot F_y} \\ c \leftarrow \frac{1.12}{\left(\frac{D}{t_w}\right)} \cdot \sqrt{\frac{E_s \cdot k_w}{F_y}} \text{ if } \frac{D}{t_w} \le 1.40 \cdot \sqrt{\frac{E_s \cdot k_w}{F_y}} \\ c \leftarrow 1.0 \text{ if } \frac{D}{t_w} < 1.12 \cdot \sqrt{\frac{E_s \cdot k_w}{F_y}} \\ c \end{array} \right.$$

AR 6.10.9.3.2-6

AR 6.10.9.3.2-5

AR 6.10.9.3.2-4

$C = 1$

$V_p := 0.58 \cdot F_y \cdot D \cdot t_w \qquad V_p = 361.08 \cdot kip$ AR 6.10.9.3.2-3

$V_{n.i} := C \cdot V_p \qquad V_{n.i} = 361.08 \cdot kip$

LRFD Bending Capacity - Fascia Girder

Finding the strength per LRFD is a lengthy process because of the inclusion of the plastic moment and the plastic neutral axis. The flowcharts Figure C6.4.4-1 and C6.4.5-1 in AASHTO will be followed for these calculations, and are attached for reference.

for flexure: $\phi_f := 1.00$ AR 6.5.4.2

for shear: $\phi_v := 1.00$

Step 1 - Check for Section Compactness:

Check Minimum Yield Strength:

$F_y \le 70ksi = 1$ Okay AR 6.10.6.2.2

Check Web Slenderness:

For webs without longitudinal stiffeners:

$D = 25.41 \cdot in$

$t_w = 0.49 \cdot in$

$\frac{D}{t_w} = 51.86$

$\frac{D}{t_w} \le 150 = 1$ Okay AR 6.10.2.1.1-1

Check Depth of Web in Compression:

This check is done at the plastic moment, and requires calculating the plastic neutral axis. The calculations used to find the PNA can be conservatively simplified by ignoring the reinforcing steel in the deck.

$2 \cdot \frac{D_{cp}}{t_w} \le 3.76 \cdot \sqrt{\frac{E}{F_y}}$ AR 6.10.6.2.2-1

At the plastic moment the force in the bottom (tension) flange is:

$P_t := F_y \cdot b_t \cdot t_t$ $P_t = 372.13 \cdot kip$

And the force in the web is:

$P_w := F_y \cdot D \cdot t_w$ $P_w = 622.54 \cdot kip$

And the force in the top (compression) flange is:

$P_c := P_t$ $P_c = 372.13 \cdot kip$

And the force in the slab is:

$b_s := B_f$ $b_s = 6\ ft$

$P_s := 0.85 f'c \cdot t_{design} \cdot b_s$ $P_s = 1606.5 \cdot kip$

The location of the PNA will be in one of the following locations:
Case 1: PNA lies in web AR T D6.1-1
Case 2: PNA lies in top flange
Case 3: PNA lies in concrete deck

$t_s := t_{design}$

$$PNA := \begin{| (case \leftarrow 3) \ \text{if} \ P_t + P_w + P_c < P_s \\ (case \leftarrow 2) \ \text{if} \ P_t + P_w + P_c \geq P_s \\ (case \leftarrow 1) \ \text{if} \ P_t + P_w \geq P_c + P_s \\ y \leftarrow \frac{D}{2}\cdot\left(\frac{P_t - P_c - P_s}{P_w} + 1\right) \ \text{if} \ case = 1 \\ y \leftarrow \frac{t_c}{2}\cdot\left(\frac{P_w + P_t - P_s}{P_c} + 1\right) \ \text{if} \ case = 2 \\ y \leftarrow t_s\cdot\left(\frac{P_c + P_w + P_t}{P_s}\right) \ \text{if} \ case = 3 \\ pna \leftarrow t_t + D - y \ \text{if} \ case = 1 \\ pna \leftarrow t_t + D + t_c - y \ \text{if} \ case = 2 \\ pna \leftarrow t_t + D + t_c + t_s - y \ \text{if} \ case = 3 \\ pna |$$

$PNA = 28.02\cdot in$ measured upwards from the bottom of the bottom flange:

Therefore, the depth of web in compression is zero:

$D_{cp} := 0\cdot in$

And checking for compactness:

$2\cdot\frac{D_{cp}}{t_w} \leq 3.76\cdot\sqrt{\frac{E}{F_y}} = 1$ Okay - Compact

Step 2 - Determine Plastic Moment:

Because the sections are compact, the bending strength is a function of the plastic moment. Therefore, the plastic moment must be found. The plastic moment equations use a variable 'y' which is measured from different points in the section depending on the location of the PNA. This variable will be found first:

$$y' := \begin{| y \leftarrow t_t + D + t_c + t_s - PNA \\ y \leftarrow t_t + D + t_c - PNA \ \text{if} \ P_t + P_w + P_c \geq P_s \\ y \leftarrow t_t + D - PNA \ \text{if} \ P_t + P_w \geq P_c + P_s \\ y |$$

$y' = 6.38\cdot in$

Now the plastic moment will be calculated:

$$M_p := \left| \begin{array}{l} d1 \leftarrow t_t + D \\ d2 \leftarrow d1 + t_c \\ d3 \leftarrow d2 + t_s \\ d_t \leftarrow \left| PNA - t_t \right| \\ d_w \leftarrow \left| PNA - t_t - \frac{D}{2} \right| \\ d_c \leftarrow \left| PNA - t_t - D - \frac{t_c}{2} \right| \\ d_s \leftarrow \left| PNA - t_t - D - t_c - \frac{t_s}{2} \right| \\ m \leftarrow (y')^2 \cdot \frac{P_s}{2 \cdot t_s} + P_c \cdot d_c + P_w \cdot d_w + P_t \cdot d_t \\ m \leftarrow \frac{P_c}{2 \cdot t_c} \cdot \left[(y')^2 + \left(t_c - y' \right)^2 \right] + P_s \cdot d_s + P_w \cdot d_w + P_t \cdot d_t \quad \text{if } P_t + P_w + P_c \geq P_s \\ m \leftarrow \frac{P_w}{2 \cdot D} \cdot \left[(y')^2 + (D - y')^2 \right] + P_s \cdot d_s + P_c \cdot d_c + P_t \cdot d_t \quad \text{if } P_t + P_w \geq P_c + P_s \\ m \end{array} \right.$$

$$M_p = 2011.26 \cdot kip \cdot ft$$

Step 3 - Determine Nominal Bending Strength:

There are two equations that may control the nominal bending strength, and the choice of which equation to use is based on the ratio of the depth of section in compression to the total depth of section. The following checks this ratio and then calculates the nominal bending strength:

$$M_{n.f} := \left| \begin{array}{l} D_t \leftarrow t_t + D + t_c + t_s \\ D_p \leftarrow D_t - PNA \\ m \leftarrow M_p \\ m \leftarrow M_p \cdot \left(1.07 - 0.7 \cdot \frac{D_p}{D_t} \right) \quad \text{if } D_p > 0.1 \cdot D_t \qquad \text{AR 6.10.7.1.2-1} \\ m \qquad \text{AR 6.10.7.1.2-2} \end{array} \right.$$

$$M_{n.f} = 1890.89 \cdot kip \cdot ft$$

LRFD Shear Capacity - Fascia Girder

$V_n := C \cdot V_p$ AR 6.10.9.2-1

$k_w := 5.0$ no web stiffeners AR 6.10.9.2

$E_s := E$

$$C := \begin{cases} c \leftarrow \dfrac{1.57 \cdot E_s \cdot k_w}{\left(\dfrac{D}{t_w}\right)^2 \cdot F_y} \\ c \leftarrow \dfrac{1.12}{\left(\dfrac{D}{t_w}\right)} \cdot \sqrt{\dfrac{E_s \cdot k_w}{F_y}} \quad \text{if} \quad \dfrac{D}{t_w} \le 1.40 \cdot \sqrt{\dfrac{E_s \cdot k_w}{F_y}} \\ c \leftarrow 1.0 \quad \text{if} \quad \dfrac{D}{t_w} < 1.12 \cdot \sqrt{\dfrac{E_s \cdot k_w}{F_y}} \\ c \end{cases}$$

AR 6.10.9.3.2-6, AR 6.10.9.3.2-5, AR 6.10.9.3.2-4

$C = 1$

$V_p := 0.58 \cdot F_y \cdot D \cdot t_w$ $V_p = 361.08 \cdot kip$ AR 6.10.9.3.2-3

$V_{n.f} := C \cdot V_p$ $V_{n.f} = 361.08 \cdot kip$

Determine Live Load Distribution Factors per LRFD:

The calculation of live load effects will use the distribution factors of LRFD Section 4.

$N_L := 2$ number of lanes $N_b := 4$ number of girders AR 3.6.1.1.1

Interior Girder:

The value of Kg is found using the bare girder section properties:

$e_g := \dfrac{D}{2} + t_c + \dfrac{t_s}{2}$ $e_g = 17.2 \cdot in$ AR 4.6.2.2.1

$K_g := n \cdot \left(I_x + A_g \cdot e_g^{\,2}\right)$ $K_g = 103182.91 \cdot in^4$ AR 4.6.2.2.1-1

Basic Distribution Factor for Moment:

There are a variety of limitations for using the empirical distribution factors, which are checked below:

$$check := \begin{cases} check \leftarrow 1 \quad \text{if} \quad S \ge 16.0ft \vee S \le 3.5ft \\ check \leftarrow 2 \quad \text{if} \quad t_s \le 4.5in \vee t_s \ge 12.0in \\ check \leftarrow 3 \quad \text{if} \quad N_b < 4 \\ check \leftarrow 4 \quad \text{if} \quad K_g \le 10000in^4 \vee K_g \ge 7000000in^4 \\ check \leftarrow \text{"OK to use following DF formula"} \quad \text{otherwise} \end{cases}$$

AR T4.6.2.2.2b-1

check = "OK to use following DF formula"

The bridge qualifies for use of the distribution factors, so the moment distribution factor for live load is calculated below.

For one lane loaded:

$$DF_{m1} := 0.06 + \left(\frac{S}{14\cdot ft}\right)^{0.4}\cdot\left(\frac{S}{L}\right)^{0.3}\cdot\left(\frac{K_g}{L\cdot t_s^{\,3}}\right)^{0.1} \qquad DF_{m1} = 0.46\cdot\frac{lanes}{beam}$$ AR T4.6.2.2.2b-1

For more than one lane loaded:

$$DF_{m2} := 0.075 + \left(\frac{S}{9.5\cdot ft}\right)^{0.6}\cdot\left(\frac{S}{L}\right)^{0.2}\cdot\left(\frac{K_g}{L\cdot t_s^{\,3}}\right)^{0.1} \qquad DF_{m2} = 0.62\cdot\frac{lanes}{beam}$$

And the controlling DF is:

$$DF_{m.i} := \max\left(DF_{m1}, DF_{m2}\right) \qquad DF_{m.i} = 0.62\cdot\frac{lanes}{beam}$$

Since the bridge skew is zero, no moment reduction factor is calculated.

Distribution Factor for Shear:

The bridge qualifies for use of the distribution factor based on the preceding checks, so the shear distribution factor is:

For one lane loaded:

$$DF_{v1} := 0.36 + \frac{S}{25\cdot ft} \qquad DF_{v1} = 0.66\cdot\frac{lanes}{beam}$$ AR T4.6.2.2.3a-1

For more than one lane loaded:

$$DF_{v2} := 0.2 + \frac{S}{12\cdot ft} - \left(\frac{S}{35\cdot ft}\right)^{2.0} \qquad DF_{v2} = 0.78\cdot\frac{lanes}{beam}$$

And the controlling DF is:

$$DF_{v.i} := \max\left(DF_{v1}, DF_{v2}\right) \qquad DF_{v.i} = 0.78\cdot\frac{lanes}{beam}$$

No skew correction factor is applied since the skew is zero.

Fascia Girder:

Basic Distribution Factor for Moment:

The distance, de, is defined a the distance between the web centerline of the exterior girder and the interior edge of the curb.

$$d_e := 0.75\cdot ft$$

There are a variety of limitations for using the empirical distribution factors, which are checked below:

check := | check ← 1 if $d_e \geq 5.5ft \vee d_e \leq -1.0ft$
| check ← "OK to use following DF formula" otherwise

AR T4.6.2.2.2d-1

check = "OK to use following DF formula"

The bridge qualifies for use of the distribution factors, so the moment distribution factor for live load is calculated below.

For one lane loaded, the lever rule is to be used which will result in the same answer as for ASD, except that a factor of 1.2 is applied for the multiple presence factor:

$$DF_{m1} := \frac{0.87}{2}\cdot 1.2 \qquad DF_{m1} = 0.52\cdot\frac{lanes}{beam}$$

For more than one lane loaded:

$$DF_{m2} := 0.075 + \left(\frac{S}{9.5\cdot ft}\right)^{0.6}\cdot\left(\frac{S}{L}\right)^{0.2}\cdot\left(\frac{K_g}{L\cdot t_s^{\,3}}\right)^{0.1} \qquad DF_{m2} = 0.62\cdot\frac{lanes}{beam}$$ AR 4.6.2.2.1-1

Except modified by em:

$$e_m := 0.77 + \frac{d_e}{9.1\cdot ft} \qquad e_m = 0.85$$ AR T4.6.2.2.2d-1

And the controlling DF is:

$$DF_{m.f} := \max\left(DF_{m1}, e_m\cdot DF_{m2}\right) \qquad DF_{m.f} = 0.53\cdot\frac{lanes}{beam}$$

Since the bridge skew is zero, no moment modification factor is calculated.

Distribution Factor for Shear:

The bridge qualifies for use of the distribution factor based on the preceding checks, so the shear distribution factor is:

For one lane loaded, the lever rule is used:

$$DF_{v1} := DF_{m1} \qquad DF_{v1} = 0.52\cdot\frac{lanes}{beam}$$ AR T4.6.2.2.3a-1

For more than one lane loaded:

$$DF_{v2} := 0.2 + \frac{S}{12\cdot ft} - \left(\frac{S}{35\cdot ft}\right)^{2.0} \qquad DF_{v2} = 0.78\cdot\frac{lanes}{beam}$$

Except modified by em:

$$e_m := 0.6 + \frac{d_e}{10\cdot ft} \qquad e_m = 0.68$$ AR T4.6.2.2.3b-1

And the controlling DF is:

$$DF_{v.f} := \max\left(DF_{v1}, e_m\cdot DF_{v2}\right) \qquad DF_{v.f} = 0.53\cdot\frac{lanes}{beam}$$

No skew correction factor is applied since the skew is zero.

$IM := 0.33$ Dynamic load allowance

LRFD Load Rating with Distribution Factors:

Load ratings per AASHTO LRFD are calculated.

HL-93 Loading Interior:

$V_{int} := V_{hl} \cdot DF_{v.i} \cdot (1 + IM)$ $V_{int} = 77.2 \cdot kip$

$M_{int} := M_{hl} \cdot DF_{m.i} \cdot (1 + IM)$ $M_{int} = 8163.3 \cdot kip \cdot in$

$$IR_{deck} := \frac{\phi_c \cdot \phi_s \cdot \phi_f \cdot M_{n.i} - \gamma_{DL} \cdot M_{int.ltc}}{\gamma_{LL} \cdot M_{int}}$$ $IR_{deck} = 1.63$

$$IR_{flange} := \frac{\phi_c \cdot \phi_s \cdot \phi_f \cdot M_{n.i} - \gamma_{DL} \cdot M_{int.ltc} - \gamma_{DL} \cdot M_{int.nc}}{\gamma_{LL} \cdot M_{int}}$$ $IR_{flange} = 1.34$

$$IR_v := \frac{\phi_c \cdot \phi_s \cdot \phi_v \cdot V_{n.i} - \gamma_{DL} \cdot (V_{int.nc} + V_{int.ltc})}{\gamma_{LL} \cdot V_{int}}$$ $IR_v = 2.43$

$OR_{deck} := IR_{deck} \cdot \frac{1.75}{1.35}$ $OR_{deck} = 2.11$

$OR_{flange} := IR_{flange} \cdot \frac{1.75}{1.35}$ $OR_{flange} = 1.74$

$OR_v := IR_v \cdot \frac{1.75}{1.35}$ $OR_v = 3.15$

HL-93 Loading Fascia:

$V_{fas} := V_{hl} \cdot DF_{v.f} \cdot (1 + IM)$ $V_{fas} = 52.11 \cdot kip$

$M_{fas} := M_{hl} \cdot DF_{m.f} \cdot (1 + IM)$ $M_{fas} = 6958.54 \cdot kip \cdot in$

$$IR_{deck} := \frac{\phi_c \cdot \phi_s \cdot \phi_f \cdot M_{n.f} - \gamma_{DL} \cdot M_{fas.ltc}}{\gamma_{LL} \cdot M_{fas}}$$ $IR_{deck} = 1.79$

$$IR_{flange} := \frac{\phi_c \cdot \phi_s \cdot \phi_f \cdot M_{n.f} - \gamma_{DL} \cdot M_{fas.ltc} - \gamma_{DL} \cdot M_{fas.nc}}{\gamma_{LL} \cdot M_{fas}}$$ $IR_{flange} = 1.52$

$$IR_v := \frac{\phi_c \cdot \phi_s \cdot \phi_v \cdot V_{n.f} - \gamma_{DL} \cdot (V_{fas.nc} + V_{fas.ltc})}{\gamma_{LL} \cdot V_{fas}}$$ $IR_v = 3.65$

$OR_{deck} := IR_{deck} \cdot \frac{1.75}{1.35}$ $OR_{deck} = 2.32$

$OR_{flange} := IR_{flange} \cdot \frac{1.75}{1.35}$ $OR_{flange} = 1.97$

$OR_v := IR_v \cdot \frac{1.75}{1.35}$ $OR_v = 4.73$

Type 3 Truck Interior:

$V_{int} := V_3 \cdot DF_{v.i} \cdot (1 + IM)$ $V_{int} = 44.1 \cdot kip$

$M_{int} := M_3 \cdot DF_{m.i} \cdot (1 + IM)$ $M_{int} = 4975.91 \cdot kip \cdot in$

$$IR_{deck} := \frac{\phi_c \cdot \phi_s \cdot \phi_f \cdot M_{n.i} - \gamma_{DL} \cdot M_{int.ltc}}{\gamma_{LL.l} \cdot M_{int}} \qquad IR_{deck} = 3.33$$

$$IR_{flange} := \frac{\phi_c \cdot \phi_s \cdot \phi_f \cdot M_{n.i} - \gamma_{DL} \cdot M_{int.ltc} - \gamma_{DL} \cdot M_{int.nc}}{\gamma_{LL.l} \cdot M_{int}} \qquad IR_{flange} = 2.76$$

$$IR_v := \frac{\phi_c \cdot \phi_s \cdot \phi_v \cdot V_{n.i} - \gamma_{DL} \cdot \left(V_{int.nc} + V_{int.ltc}\right)}{\gamma_{LL.l} \cdot V_{int}} \qquad IR_v = 5.31$$

Type 3 Truck Fascia:

$V_{fas} := V_3 \cdot DF_{v.f} \cdot (1 + IM)$ $V_{fas} = 29.77 \cdot kip$

$M_{fas} := M_3 \cdot DF_{m.f} \cdot (1 + IM)$ $M_{fas} = 4241.55 \cdot kip \cdot in$

$$IR_{deck} := \frac{\phi_c \cdot \phi_s \cdot \phi_f \cdot M_{n.f} - \gamma_{DL} \cdot M_{fas.ltc}}{\gamma_{LL.l} \cdot M_{fas}} \qquad IR_{deck} = 3.66$$

$$IR_{flange} := \frac{\phi_c \cdot \phi_s \cdot \phi_f \cdot M_{n.f} - \gamma_{DL} \cdot M_{fas.ltc} - \gamma_{DL} \cdot M_{fas.nc}}{\gamma_{LL.l} \cdot M_{fas}} \qquad IR_{flange} = 3.11$$

$$IR_v := \frac{\phi_c \cdot \phi_s \cdot \phi_v \cdot V_{n.f} - \gamma_{DL} \cdot \left(V_{fas.nc} + V_{fas.ltc}\right)}{\gamma_{LL.l} \cdot V_{fas}} \qquad IR_v = 7.99$$

Type 3s2 Truck Interior:

$V_{int} := V_{3s2} \cdot DF_{v.i} \cdot (1 + IM)$ $V_{int} = 46.84 \cdot kip$

$M_{int} := M_{3s2} \cdot DF_{m.i} \cdot (1 + IM)$ $M_{int} = 4540.12 \cdot kip \cdot in$

$$IR_{deck} := \frac{\phi_c \cdot \phi_s \cdot \phi_f \cdot M_{n.i} - \gamma_{DL} \cdot M_{int.ltc}}{\gamma_{LL.l} \cdot M_{int}} \qquad IR_{deck} = 3.65$$

$$IR_{flange} := \frac{\phi_c \cdot \phi_s \cdot \phi_f \cdot M_{n.i} - \gamma_{DL} \cdot M_{int.ltc} - \gamma_{DL} \cdot M_{int.nc}}{\gamma_{LL.l} \cdot M_{int}} \qquad IR_{flange} = 3.02$$

$$IR_v := \frac{\phi_c \cdot \phi_s \cdot \phi_v \cdot V_{n.i} - \gamma_{DL} \cdot \left(V_{int.nc} + V_{int.ltc}\right)}{\gamma_{LL.l} \cdot V_{int}} \qquad IR_v = 5$$

Type 3s2 Truck Fascia:

$V_{fas} := V_{3s2} \cdot DF_{v.f} \cdot (1 + IM)$ $V_{fas} = 31.61 \cdot kip$

$M_{fas} := M_{3s2} \cdot DF_{m.f} \cdot (1 + IM)$ $M_{fas} = 3870.08 \cdot kip \cdot in$

$$IR_{deck} := \frac{\phi_c \cdot \phi_s \cdot \phi_f \cdot M_{n.f} - \gamma_{DL} \cdot M_{fas.ltc}}{\gamma_{LL.l} \cdot M_{fas}} \qquad IR_{deck} = 4.01$$

$$IR_{flange} := \frac{\phi_c \cdot \phi_s \cdot \phi_f \cdot M_{n.f} - \gamma_{DL} \cdot M_{fas.ltc} - \gamma_{DL} \cdot M_{fas.nc}}{\gamma_{LL.l} \cdot M_{fas}} \qquad IR_{flange} = 3.41$$

$$IR_{v} := \frac{\phi_c \cdot \phi_s \cdot \phi_v \cdot V_{n.f} - \gamma_{DL} \cdot \left(V_{fas.nc} + V_{fas.ltc}\right)}{\gamma_{LL.l} \cdot V_{fas}} \qquad IR_{v} = 7.52$$

Type 3-3 Truck Interior:

$V_{int} := V_{33} \cdot DF_{v.i} \cdot (1 + IM)$ $V_{int} = 44.27 \cdot kip$

$M_{int} := M_{33} \cdot DF_{m.i} \cdot (1 + IM)$ $M_{int} = 4162.44 \cdot kip \cdot in$

$$IR_{deck} := \frac{\phi_c \cdot \phi_s \cdot \phi_f \cdot M_{n.i} - \gamma_{DL} \cdot M_{int.ltc}}{\gamma_{LL.l} \cdot M_{int}} \qquad IR_{deck} = 3.99$$

$$IR_{flange} := \frac{\phi_c \cdot \phi_s \cdot \phi_f \cdot M_{n.i} - \gamma_{DL} \cdot M_{int.ltc} - \gamma_{DL} \cdot M_{int.nc}}{\gamma_{LL.l} \cdot M_{int}} \qquad IR_{flange} = 3.3$$

$$IR_{v} := \frac{\phi_c \cdot \phi_s \cdot \phi_v \cdot V_{n.i} - \gamma_{DL} \cdot \left(V_{int.nc} + V_{int.ltc}\right)}{\gamma_{LL.l} \cdot V_{int}} \qquad IR_{v} = 5.29$$

Type 3-3 Truck Fascia:

$V_{fas} := V_{33} \cdot DF_{v.f} \cdot (1 + IM)$ $V_{fas} = 29.88 \cdot kip$

$M_{fas} := M_{33} \cdot DF_{m.f} \cdot (1 + IM)$ $M_{fas} = 3548.13 \cdot kip \cdot in$

$$IR_{deck} := \frac{\phi_c \cdot \phi_s \cdot \phi_f \cdot M_{n.f} - \gamma_{DL} \cdot M_{fas.ltc}}{\gamma_{LL.l} \cdot M_{fas}} \qquad IR_{deck} = 4.38$$

$$IR_{flange} := \frac{\phi_c \cdot \phi_s \cdot \phi_f \cdot M_{n.f} - \gamma_{DL} \cdot M_{fas.ltc} - \gamma_{DL} \cdot M_{fas.nc}}{\gamma_{LL.l} \cdot M_{fas}} \qquad IR_{flange} = 3.72$$

$$IR_{v} := \frac{\phi_c \cdot \phi_s \cdot \phi_v \cdot V_{n.f} - \gamma_{DL} \cdot \left(V_{fas.nc} + V_{fas.ltc}\right)}{\gamma_{LL.l} \cdot V_{fas}} \qquad IR_{v} = 7.96$$

LRFD Load Rating with Finite Element Live Load Stresses

HL-93 Truck Interior:

$V_{int} := 40.74 \cdot kip \cdot (1 + IM) + 9.4 \cdot kip$ $V_{int} = 67.45 \cdot kip$

$f_{b.int} := 9.059 \cdot ksi \cdot (1 + IM) + 2.762 \cdot ksi$ $f_{b.int} = 14.81 \cdot ksi$

$f_{t.int} := 0.934 \cdot ksi \cdot (1 + IM) + 0.239 \cdot ksi$ $f_{t.int} = 1.48 \cdot ksi$

$$IR_{deck} := \frac{\phi_c \cdot \phi_s \cdot \phi_f \cdot M_{n.i} - \gamma_{DL} \cdot M_{int.ltc}}{\gamma_{LL} \cdot S_{ti.stc} \cdot f_{t.int} \cdot n}$$ $IR_{deck} = 0.87$

$$IR_{flange} := \frac{\phi_c \cdot \phi_s \cdot \phi_f \cdot M_{n.i} - \gamma_{DL} \cdot M_{int.nc} - \gamma_{DL} \cdot M_{int.ltc}}{\gamma_{LL} \cdot S_{bi.stc} \cdot f_{b.int}}$$ $IR_{flange} = 2.01$

$$IR_v := \frac{\phi_c \cdot \phi_s \cdot \phi_v \cdot V_{n.i} - \gamma_{DL} \cdot V_{int.nc} - \gamma_{DL} \cdot V_{int.ltc}}{\gamma_{LL} \cdot V_{int}}$$ $IR_v = 2.78$

$OR_{deck} := \frac{1.75}{1.35} \cdot IR_{deck}$ $OR_{deck} = 1.13$

$OR_{flange} := \frac{1.75}{1.35} \cdot IR_{flange}$ $OR_{flange} = 2.6$

$OR_v := \frac{1.75}{1.35} \cdot IR_v$ $OR_v = 3.6$

HL-93 Truck Fascia:

$V_{fas} := 31.18 \cdot kip \cdot (1 + IM) + 9.63 \cdot kip$ $V_{fas} = 51.1 \cdot kip$

$f_{b.fas} := 7.527 \cdot ksi \cdot (1 + IM) + 2.608 \cdot ksi$ $f_{b.fas} = 12.62 \cdot ksi$

$f_{t.fas} := 0.540 \cdot ksi \cdot (1 + IM) + 0.165 \cdot ksi$ $f_{t.fas} = 0.88 \cdot ksi$

$$IR_{deck} := \frac{\phi_c \cdot \phi_s \cdot \phi_f \cdot M_{n.f} - \gamma_{DL} \cdot M_{fas.ltc}}{\gamma_{LL} \cdot S_{tf.stc} \cdot f_{t.fas} \cdot n}$$ $IR_{deck} = 1.57$

$$IR_{flange} := \frac{\phi_c \cdot \phi_s \cdot \phi_f \cdot M_{n.f} - \gamma_{DL} \cdot M_{fas.nc} - \gamma_{DL} \cdot M_{fas.ltc}}{\gamma_{LL} \cdot S_{bf.stc} \cdot f_{b.fas}}$$ $IR_{flange} = 2.3$

$$IR_v := \frac{\phi_c \cdot \phi_s \cdot \phi_v \cdot V_{n.f} - \gamma_{DL} \cdot V_{fas.nc} - \gamma_{DL} \cdot V_{fas.ltc}}{\gamma_{LL} \cdot V_{fas}}$$ $IR_v = 3.72$

$OR_{deck} := 1.67 \cdot IR_{deck}$ $OR_{deck} = 2.62$

$OR_{flange} := 1.67 \cdot IR_{flange}$ $OR_{flange} = 3.85$

$OR_v := 1.67 \cdot IR_v$ $OR_v = 6.22$

Type 3 Truck Interior:

$V_{int} := 30.43 \cdot kip \cdot (1 + IM)$ $V_{int} = 40.47 \cdot kip$

$f_{b.int} := 6.939 \cdot ksi \cdot (1 + IM)$ $f_{b.int} = 9.23 \cdot ksi$

$f_{t.int} := 0.689 \cdot ksi \cdot (1 + IM)$ $f_{t.int} = 0.92 \cdot ksi$

$$IR_{deck} := \frac{\phi_c \cdot \phi_s \cdot \phi_f \cdot M_{n.i} - \gamma_{DL} \cdot M_{int.ltc}}{\gamma_{LL.l} \cdot S_{ti.stc} \cdot f_{t.int} \cdot n} \qquad IR_{deck} = 1.76$$

$$IR_{flange} := \frac{\phi_c \cdot \phi_s \cdot \phi_f \cdot M_{n.i} - \gamma_{DL} \cdot M_{int.nc} - \gamma_{DL} \cdot M_{int.ltc}}{\gamma_{LL.l} \cdot S_{bi.stc} \cdot f_{b.int}} \qquad IR_{flange} = 4.03$$

$$IR_{v} := \frac{\phi_c \cdot \phi_s \cdot \phi_v \cdot V_{n.i} - \gamma_{DL} \cdot V_{int.nc} - \gamma_{DL} \cdot V_{int.ltc}}{\gamma_{LL.l} \cdot V_{int}} \qquad IR_{v} = 5.79$$

Type 3 Truck Fascia:

$V_{fas} := 21.91 \cdot kip \cdot (1 + IM)$ $V_{fas} = 29.14 \cdot kip$

$f_{b.fas} := 5.707 \cdot ksi \cdot (1 + IM)$ $f_{b.fas} = 7.59 \cdot ksi$

$f_{t.fas} := 0.399 \cdot ksi \cdot (1 + IM)$ $f_{t.fas} = 0.53 \cdot ksi$

$$IR_{deck} := \frac{\phi_c \cdot \phi_s \cdot \phi_f \cdot M_{n.f} - \gamma_{DL} \cdot M_{fas.ltc}}{\gamma_{LL.l} \cdot S_{tf.stc} \cdot f_{t.fas} \cdot n} \qquad IR_{deck} = 3.26$$

$$IR_{flange} := \frac{\phi_c \cdot \phi_s \cdot \phi_f \cdot M_{n.f} - \gamma_{DL} \cdot M_{fas.nc} - \gamma_{DL} \cdot M_{fas.ltc}}{\gamma_{LL.l} \cdot S_{bf.stc} \cdot f_{b.fas}} \qquad IR_{flange} = 4.79$$

$$IR_{v} := \frac{\phi_c \cdot \phi_s \cdot \phi_v \cdot V_{n.f} - \gamma_{DL} \cdot V_{fas.nc} - \gamma_{DL} \cdot V_{fas.ltc}}{\gamma_{LL.l} \cdot V_{fas}} \qquad IR_{v} = 8.16$$

Type 3S2 Truck Interior:

$V_{int} := 29.48 \cdot kip \cdot (1 + IM)$ $V_{int} = 39.21 \cdot kip$

$f_{b.int} := 6.355 \cdot ksi \cdot (1 + IM)$ $f_{b.int} = 8.45 \cdot ksi$

$f_{t.int} := 0.633 \cdot ksi \cdot (1 + IM)$ $f_{t.int} = 0.84 \cdot ksi$

$$IR_{deck} := \frac{\phi_c \cdot \phi_s \cdot \phi_f \cdot M_{n.i} - \gamma_{DL} \cdot M_{int.ltc}}{\gamma_{LL.l} \cdot S_{ti.stc} \cdot f_{t.int} \cdot n} \qquad IR_{deck} = 1.91$$

$$IR_{flange} := \frac{\phi_c \cdot \phi_s \cdot \phi_f \cdot M_{n.i} - \gamma_{DL} \cdot M_{int.nc} - \gamma_{DL} \cdot M_{int.ltc}}{\gamma_{LL.l} \cdot S_{bi.stc} \cdot f_{b.int}} \qquad IR_{flange} = 4.4$$

$$IR_{v} := \frac{\phi_c \cdot \phi_s \cdot \phi_v \cdot V_{n.i} - \gamma_{DL} \cdot V_{int.nc} - \gamma_{DL} \cdot V_{int.ltc}}{\gamma_{LL.l} \cdot V_{int}} \qquad IR_{v} = 5.98$$

Type 3S2 Truck Fascia:

$V_{fas} := 25.21 \cdot kip \cdot (1 + IM)$ $V_{fas} = 33.53 \cdot kip$

$f_{b.fas} := 5.195 \cdot ksi \cdot (1 + IM)$ $f_{b.fas} = 6.91 \cdot ksi$

$f_{t.fas} := 0.365 \cdot ksi \cdot (1 + IM)$ $f_{t.fas} = 0.49 \cdot ksi$

$$IR_{deck} := \frac{\phi_c \cdot \phi_s \cdot \phi_f \cdot M_{n.f} - \gamma_{DL} \cdot M_{fas.ltc}}{\gamma_{LL.l} \cdot S_{tf.stc} \cdot f_{t.fas} \cdot n} \qquad IR_{deck} = 3.57$$

$$IR_{flange} := \frac{\phi_c \cdot \phi_s \cdot \phi_f \cdot M_{n.f} - \gamma_{DL} \cdot M_{fas.nc} - \gamma_{DL} \cdot M_{fas.ltc}}{\gamma_{LL.l} \cdot S_{bf.stc} \cdot f_{b.fas}} \qquad IR_{flange} = 5.26$$

$$IR_v := \frac{\phi_c \cdot \phi_s \cdot \phi_v \cdot V_{n.f} - \gamma_{DL} \cdot V_{fas.nc} - \gamma_{DL} \cdot V_{fas.ltc}}{\gamma_{LL.l} \cdot V_{fas}} \qquad IR_v = 7.09$$

Type 3-3 Truck Interior:

$V_{int} := 27.87 \cdot kip \cdot (1 + IM)$ $V_{int} = 37.07 \cdot kip$

$f_{b.int} := 5.936 \cdot ksi \cdot (1 + IM)$ $f_{b.int} = 7.89 \cdot ksi$

$f_{t.int} := 0.573 \cdot ksi \cdot (1 + IM)$ $f_{t.int} = 0.76 \cdot ksi$

$$IR_{deck} := \frac{\phi_c \cdot \phi_s \cdot \phi_f \cdot M_{n.i} - \gamma_{DL} \cdot M_{int.ltc}}{\gamma_{LL.l} \cdot S_{ti.stc} \cdot f_{t.int} \cdot n} \qquad IR_{deck} = 2.11$$

$$IR_{flange} := \frac{\phi_c \cdot \phi_s \cdot \phi_f \cdot M_{n.i} - \gamma_{DL} \cdot M_{int.nc} - \gamma_{DL} \cdot M_{int.ltc}}{\gamma_{LL.l} \cdot S_{bi.stc} \cdot f_{b.int}} \qquad IR_{flange} = 4.71$$

$$IR_v := \frac{\phi_c \cdot \phi_s \cdot \phi_v \cdot V_{n.i} - \gamma_{DL} \cdot V_{int.nc} - \gamma_{DL} \cdot V_{int.ltc}}{\gamma_{LL.l} \cdot V_{int}} \qquad IR_v = 6.32$$

Type 3-3 Truck Fascia:

$V_{fas} := 23.72 \cdot kip \cdot (1 + IM)$ $V_{fas} = 31.55 \cdot kip$

$f_{b.fas} := 5.066 \cdot ksi \cdot (1 + IM)$ $f_{b.fas} = 6.74 \cdot ksi$

$f_{t.fas} := 0.343 \cdot ksi \cdot (1 + IM)$ $f_{t.fas} = 0.46 \cdot ksi$

$$IR_{deck} := \frac{\phi_c \cdot \phi_s \cdot \phi_f \cdot M_{n.f} - \gamma_{DL} \cdot M_{fas.ltc}}{\gamma_{LL.l} \cdot S_{tf.stc} \cdot f_{t.fas} \cdot n} \qquad IR_{deck} = 3.79$$

$$IR_{flange} := \frac{\phi_c \cdot \phi_s \cdot \phi_f \cdot M_{n.f} - \gamma_{DL} \cdot M_{fas.nc} - \gamma_{DL} \cdot M_{fas.ltc}}{\gamma_{LL.l} \cdot S_{bf.stc} \cdot f_{b.fas}} \qquad IR_{flange} = 5.39$$

$$IR_v := \frac{\phi_c \cdot \phi_s \cdot \phi_v \cdot V_{n.f} - \gamma_{DL} \cdot V_{fas.nc} - \gamma_{DL} \cdot V_{fas.ltc}}{\gamma_{LL.l} \cdot V_{fas}} \qquad IR_v = 7.54$$

LRFD Load Rating with Modal Flexibility Live Load Stresses

Stresses in the critical elements are found using the results of the modal analysis as discussed previously.

The results are as follows for the various truck loads and for an interior and a fascia girder:

HL-93 Loading Interior:

$V_{int} := 42.97 \cdot kip \cdot (1 + IM) + 10.44 \cdot kip$ $V_{int} = 67.59 \cdot kip$

$M_{int} := 4788 \cdot kip \cdot in \cdot (1 + IM) + 1501 \cdot kip \cdot in$ $M_{int} = 7869.04 \cdot kip \cdot in$

$$IR_{deck} := \frac{\phi_c \cdot \phi_s \cdot \phi_f \cdot M_{n.i} - \gamma_{DL} \cdot M_{int.ltc}}{\gamma_{LL} \cdot M_{int}} \qquad IR_{deck} = 1.69$$

$$IR_{flange} := \frac{\phi_c \cdot \phi_s \cdot \phi_f \cdot M_{n.i} - \gamma_{DL} \cdot M_{int.nc} - \gamma_{DL} \cdot M_{int.ltc}}{\gamma_{LL} \cdot M_{int}} \qquad IR_{flange} = 1.4$$

$$IR_v := \frac{\phi_c \cdot \phi_s \cdot \phi_v \cdot V_{n.i} - \gamma_{DL} \cdot V_{int.nc} - \gamma_{DL} \cdot V_{int.ltc}}{\gamma_{LL} \cdot V_{int}} \qquad IR_v = 2.77$$

$OR_{deck} := \frac{1.75}{1.35} \cdot IR_{deck}$ $OR_{deck} = 2.19$

$OR_{flange} := \frac{1.75}{1.35} \cdot IR_{flange}$ $OR_{flange} = 1.81$

$OR_v := \frac{1.75}{1.35} \cdot IR_v$ $OR_v = 3.6$

HL-93 Loading Fascia:

$V_{fas} := 27.87 \cdot kip \cdot (1 + IM) + 7.54 \cdot kip$ $V_{fas} = 44.61 \cdot kip$

$M_{fas} := 3901 \cdot kip \cdot in \cdot (1 + IM) + 1344 \cdot kip \cdot in$ $M_{fas} = 6532.33 \cdot kip \cdot in$

$$IR_{deck} := \frac{\phi_c \cdot \phi_s \cdot \phi_f \cdot M_{n.f} - \gamma_{DL} \cdot M_{fas.ltc}}{\gamma_{LL} \cdot M_{fas}} \qquad IR_{deck} = 1.9$$

$$IR_{flange} := \frac{\phi_c \cdot \phi_s \cdot \phi_f \cdot M_{n.f} - \gamma_{DL} \cdot M_{fas.nc} - \gamma_{DL} \cdot M_{fas.ltc}}{\gamma_{LL} \cdot M_{fas}} \qquad IR_{flange} = 1.62$$

$$IR_v := \frac{\phi_c \cdot \phi_s \cdot \phi_v \cdot V_{n.f} - \gamma_{DL} \cdot V_{fas.nc} - \gamma_{DL} \cdot V_{fas.ltc}}{\gamma_{LL} \cdot V_{fas}} \qquad IR_v = 4.27$$

$OR_{deck} := \frac{1.75}{1.35} \cdot IR_{deck}$ $OR_{deck} = 2.47$

$OR_{flange} := \frac{1.75}{1.35} \cdot IR_{flange}$ $OR_{flange} = 2.09$

$OR_v := \frac{1.75}{1.35} \cdot IR_v$ $OR_v = 5.53$

Type 3 Truck Interior:

$V_{int} := 31.81 \cdot kip \cdot (1 + IM)$ $V_{int} = 42.31 \cdot kip$

$M_{int} := 3653 \cdot kip \cdot in \cdot (1 + IM)$ $M_{int} = 4858.49 \cdot kip \cdot in$

$$IR_{deck} := \frac{\phi_c \cdot \phi_s \cdot \phi_f \cdot M_{n.i} - \gamma_{DL} \cdot M_{int.ltc}}{\gamma_{LL.l} \cdot M_{int}} \qquad IR_{deck} = 3.41$$

$$IR_{flange} := \frac{\phi_c \cdot \phi_s \cdot \phi_f \cdot M_{n.i} - \gamma_{DL} \cdot M_{int.nc} - \gamma_{DL} \cdot M_{int.ltc}}{\gamma_{LL.l} \cdot M_{int}} \qquad IR_{flange} = 2.82$$

$$IR_v := \frac{\phi_c \cdot \phi_s \cdot \phi_v \cdot V_{n.i} - \gamma_{DL} \cdot V_{int.nc} - \gamma_{DL} \cdot V_{int.ltc}}{\gamma_{LL.l} \cdot V_{int}} \qquad IR_v = 5.54$$

Type 3 Truck Fascia:

$V_{fas} := 19.97 \cdot kip \cdot (1 + IM)$ $V_{fas} = 26.56 \cdot kip$

$M_{fas} := 2953 \cdot kip \cdot in \cdot (1 + IM)$ $M_{fas} = 3927.49 \cdot kip \cdot in$

$$IR_{deck} := \frac{\phi_c \cdot \phi_s \cdot \phi_f \cdot M_{n.f} - \gamma_{DL} \cdot M_{fas.ltc}}{\gamma_{LL.l} \cdot M_{fas}} \qquad IR_{deck} = 3.96$$

$$IR_{flange} := \frac{\phi_c \cdot \phi_s \cdot \phi_f \cdot M_{n.f} - \gamma_{DL} \cdot M_{fas.nc} - \gamma_{DL} \cdot M_{fas.ltc}}{\gamma_{LL.l} \cdot M_{fas}} \qquad IR_{flange} = 3.36$$

$$IR_v := \frac{\phi_c \cdot \phi_s \cdot \phi_v \cdot V_{n.f} - \gamma_{DL} \cdot V_{fas.nc} - \gamma_{DL} \cdot V_{fas.ltc}}{\gamma_{LL.l} \cdot V_{fas}} \qquad IR_v = 8.95$$

Type 3S2 Truck Interior:

$V_{int} := 32.07 \cdot kip \cdot (1 + IM)$ $V_{int} = 42.65 \cdot kip$

$M_{int} := 3335 \cdot kip \cdot in \cdot (1 + IM)$ $M_{int} = 4435.55 \cdot kip \cdot in$

$$IR_{deck} := \frac{\phi_c \cdot \phi_s \cdot \phi_f \cdot M_{n.i} - \gamma_{DL} \cdot M_{int.ltc}}{\gamma_{LL.l} \cdot M_{int}} \qquad IR_{deck} = 3.74$$

$$IR_{flange} := \frac{\phi_c \cdot \phi_s \cdot \phi_f \cdot M_{n.i} - \gamma_{DL} \cdot M_{int.nc} - \gamma_{DL} \cdot M_{int.ltc}}{\gamma_{LL.l} \cdot M_{int}} \qquad IR_{flange} = 3.09$$

$$IR_v := \frac{\phi_c \cdot \phi_s \cdot \phi_v \cdot V_{n.i} - \gamma_{DL} \cdot V_{int.nc} - \gamma_{DL} \cdot V_{int.ltc}}{\gamma_{LL.l} \cdot V_{int}} \qquad IR_v = 5.49$$

Type 3S2 Truck Fascia:

$V_{fas} := 21.97 \cdot kip \cdot (1 + IM)$ $V_{fas} = 29.22 \cdot kip$

$M_{fas} := 2698 \cdot kip \cdot in \cdot (1 + IM)$ $M_{fas} = 3588.34 \cdot kip \cdot in$

$$IR_{deck} := \frac{\phi_c \cdot \phi_s \cdot \phi_f \cdot M_{n.f} - \gamma_{DL} \cdot M_{fas.ltc}}{\gamma_{LL.l} \cdot M_{fas}} \qquad IR_{deck} = 4.33$$

$$IR_{flange} := \frac{\phi_c \cdot \phi_s \cdot \phi_f \cdot M_{n.f} - \gamma_{DL} \cdot M_{fas.nc} - \gamma_{DL} \cdot M_{fas.ltc}}{\gamma_{LL.l} \cdot M_{fas}} \qquad IR_{flange} = 3.68$$

$$IR_{v} := \frac{\phi_c \cdot \phi_s \cdot \phi_v \cdot V_{n.f} - \gamma_{DL} \cdot V_{fas.nc} - \gamma_{DL} \cdot V_{fas.ltc}}{\gamma_{LL.l} \cdot V_{fas}} \qquad IR_{v} = 8.14$$

Type 3-3 Truck Interior:

$V_{int} := 30.3 \cdot kip \cdot (1 + IM)$ $V_{int} = 40.3 \cdot kip$

$M_{int} := 3335 \cdot kip \cdot in \cdot (1 + IM)$ $M_{int} = 4435.55 \cdot kip \cdot in$

$$IR_{deck} := \frac{\phi_c \cdot \phi_s \cdot \phi_f \cdot M_{n.i} - \gamma_{DL} \cdot M_{int.ltc}}{\gamma_{LL.l} \cdot M_{int}} \qquad IR_{deck} = 3.74$$

$$IR_{flange} := \frac{\phi_c \cdot \phi_s \cdot \phi_f \cdot M_{n.i} - \gamma_{DL} \cdot M_{int.nc} - \gamma_{DL} \cdot M_{int.ltc}}{\gamma_{LL.l} \cdot M_{int}} \qquad IR_{flange} = 3.09$$

$$IR_{v} := \frac{\phi_c \cdot \phi_s \cdot \phi_v \cdot V_{n.i} - \gamma_{DL} \cdot V_{int.nc} - \gamma_{DL} \cdot V_{int.ltc}}{\gamma_{LL.l} \cdot V_{int}} \qquad IR_{v} = 5.82$$

Type 3-3 Truck Fascia:

$V_{fas} := 20.79 \cdot kip \cdot (1 + IM)$ $V_{fas} = 27.65 \cdot kip$

$M_{fas} := 2631 \cdot kip \cdot in \cdot (1 + IM)$ $M_{fas} = 3499.23 \cdot kip \cdot in$

$$IR_{deck} := \frac{\phi_c \cdot \phi_s \cdot \phi_f \cdot M_{n.f} - \gamma_{DL} \cdot M_{fas.ltc}}{\gamma_{LL.l} \cdot M_{fas}} \qquad IR_{deck} = 4.44$$

$$IR_{flange} := \frac{\phi_c \cdot \phi_s \cdot \phi_f \cdot M_{n.f} - \gamma_{DL} \cdot M_{fas.nc} - \gamma_{DL} \cdot M_{fas.ltc}}{\gamma_{LL.l} \cdot M_{fas}} \qquad IR_{flange} = 3.77$$

$$IR_{v} := \frac{\phi_c \cdot \phi_s \cdot \phi_v \cdot V_{n.f} - \gamma_{DL} \cdot V_{fas.nc} - \gamma_{DL} \cdot V_{fas.ltc}}{\gamma_{LL.l} \cdot V_{fas}} \qquad IR_{v} = 8.6$$